Multifunctional materials based on task-specific ionic liquids : from fundamental to next generation of hybrid electrochemical devices and artifical skin

Thuan Nguyen Pham Truong

Thèse de doctorat

de l'Université Sorbonne Paris Cité

Préparée à l'Université Paris Diderot

Ecole doctorale Chimie Physique et Chimie Analytique de Paris Centre

ED388

Laboratoire ITODYS – Equipe SIELE

Multifunctional materials based on task-specific ionic liquids : From fundamental to next generation of hybrid electrochemical devices and artificial skin

Matériaux multifonctionnels à base de liquides ioniques à tâches spécifiques : De l'étude fondamentale à la nouvelle génération de dispositifs électrochimiques et de peau artificielle

Par Thuan – Nguyen PHAM – TRUONG

Thèse de doctorat de Chimie

Dirigé par Prof. Hyacinthe Randriamahazaka et Dr. Jalal Ghilane

Présentée et soutenue publiquement à Paris le 29 novembre 2018

Président du jury : DR./Dr. Philippe Hapiot – Université Rennes 1

Rapporteurs : Prof. Alexander Kuhn – ENS de Chimie, de Biologie et de Physique

Prof. Sabine Szunerits – Université Lilles 1

Examinateurs : Prof. Qing Wang – Université Nationale de Singapour

Prof. Martin Pumera – Université de Chimie et de Technologies de Prague

Directeur de thèse : Prof. Hyacinthe Randriamahazaka - Université Paris Diderot

Co-directeur de thèse : Dr. Jalal Ghilane – Université Paris Diderot

Université PARIS DIDEROT PARIS 7

Paris Diderot University
Sorbonne Paris Cité

Doctoral School DS 388

Interfaces Traitements Organisation et Dynamique des Systèmes Laboratory

THESIS

MULTIFUNCTIONAL MATERIALS BASED ON TASK-SPECIFIC IONIC LIQUIDS : FROM FUNDAMENTAL TO NEXT GENERATION OF HYBRID ELECTROCHEMICAL DEVICES AND ARTIFICIAL SKIN

Presented by
Thuan-Nguyen Pham-Truong

A dissertation submitted in partial fulfillment of requirements for the degree of Doctorate

PARIS
DEFENSE DATE
NOVEMBER 29TH, 2018

JURY MEMBERS

Prof. Alexander Kuhn	National Engineering School of Chemistry, Biology and Physic	Reviewer
Prof. Sabine Szunerits	Lille University of Science and Technology	Reviewer
Dr. Philippe Hapiot	University of Rennes 1	Examiner
Prof. Martin Pumera	University of Chemistry and Technology Prague	Examiner
Prof. Qing Wang	National University of Singapore	Examiner
Dr. Jalal Ghilane	Sorbonne Paris Cité University	Co-Supervisor
Prof. Hyacinthe Randriamahazaka	Sorbonne Paris Cité University	Supervisor

Université Paris Diderot
Sorbonne Paris Cité

Ecole Doctorale ED388

Laboratoire Interfaces Traitements Organisation
et Dynamique des Système

THESE

MATÉRIAUX MULTIFONCTIONNELS À BASE DE LIQUIDES IONIQUES À TÂCHES SPÉCIFIQUES: DE L'ÉTUDE FONDAMENTALE À LA NOUVELLE GÉNÉRATION DE DISPOSITIFS ÉLECTROCHIMIQUES ET DE PEAU ARTIFICIELLE

Presenté par
Thuan-Nguyen Pham-Truong

PARIS
DATE DE SOUTENANCE
29 NOVEMBRE 2018

MEMBRES DU JURY

Prof. Alexander Kuhn	ENS de Chimie, de Biology et de Physique	Rapporteur
Prof. Sabine Szunerits	Université Lille 1	Rapporteur
Dr. Philippe Hapiot	Université Rennes 1	Examinateur
Prof. Martin Pumera	University of Chemistry and Technology Prague	Examinateur
Prof. Qing Wang	National University of Singapore	Examinateur
Dr. Jalal Ghilane	Université Sorbonne Paris Cité	Co-Directeur de thèse
Prof. Hyacinthe Randriamahazaka	Université Sorbonne Paris Cité	Directeur de thèse

ACKNOWLEDGMENTS

This dissertation represents not only the individual work at the keyboard, it is about 3 years of collective work at Laboratory of Interfaces Traitements Organisation et Dynamique des Système (ITODYS), especially within the SIELE group (Surface – Ionic Liquid – Electrochemistry and Energy). My experience in the group has been fulfilled with challenges, opportunities and of course plenty of memories. Throughout these years, I have been given unique opportunities thanks to which I have learned a lot of new things. Accordingly, this thesis presents different results that I have achieved and accumulated in 3 years with the aids from many individuals who I wish to acknowledge.

First and foremost, I would like to express my sincere gratitude to my advisor, Prof. Hyacinthe Randriamahazaka. I am indebted to him for giving me the PhD position and guiding me at this early stage of my research career. He gave me a lot of opportunities to work in different interesting projects with international collaborators. I would like also to thank him for teaching me how to work efficiently and for giving me authority to develop my ideas. I appreciate all his precious contributions to make my PhD journey so productive and stimulating. Beside the work in the laboratory, he also encouraged me to participate to diverse thematic schools and international conferences. It has been a great honor to be one of his students.

I am heartily thankful to my co-supervisor, Dr. Jalal Ghilane whose guidance, support and patience enabled me to finalize this thesis. He has been supportive since the first to the last day of my journey in the group. I am really appreciated his contributions of precious times and knowledges through daily discussion to resolve every problem. It is very constructive and comfortable to discuss with him about my ideas, thoughts and even personal issues. The enthusiasm that he has in scientific research is motivational for me. I am also thankful for the excellent example he has shown as a talented researcher. Beside the professional qualities, I am also admired about his personal qualities. Especially, his office is always open for consultation and discussion.

I am thankful to the all members of the Committee, Prof. Sabine Szunerits, Prof. Alexander Kuhn, Res.Dir/ Dr. Philippe Hapiot, Prof. Marin Pumera and Prof. Qing Wang for participation to my thesis jury and for their valuable discussion and critical reading of my manuscript that make my dissertation ameliorated.

I would like to express my gratitude to all the staff of the SIELE group, A/P. Myriana Hemadi, A/P Frédéric Lafolet and to all the interns, Ms. Lydia Merakeb, Mr. Thomas Petenzi, Ms. Ouiza Mebarki, Mr. Taha Yassine Ben Brahim, Ms. Christine Ranjan, Ms. Wendy Toko, for their contributions to the work and for the pleasant working atmosphere.

My sincere thanks will go to Dr. Philippe Decorse for the XPS measurements, discussions and his kindness.

Being an ITODYS member, I would like to express my sincere thanks to all of the ITODYS staff, especially A/P Thanh Ha Duong for joyful parties she organized.

I gratefully acknowledge Prof. Qing Wang for accepting me in his group and for preparing all of the necessary stuffs for my visit. I also would like to thank all of his group's member for exciting collaborative works.

My warm thank to the group of Prof. François Tran Van (PCM2E) at Tours University, especially Dr. Cédric Desgranges for the helpful training on supercapacitor and battery.

I would to thank the Doctoral School of Physical and analytical chemistry, Paris Centre for scholarship and administrative support during my doctoral studies. I am so grateful to the Tech Transfer Accelerator Network (SATT, IDF INNOV) for financial support for our work in supercabattery (1st maturation process) and redox-flow battery (pre-maturation stage).

Also, I would like to thank University of Sorbonne Paris Cité (USPC) and National University of Singapore (NUS) for the grant for the short-term exchange program.

Words are never enough for expressing my gratitude to all my friends Yong Ai, Eswaran Murugasen, Van Bui-Thi-Tuyet, Van Quynh Nguyen, Van Quyen Nguye, Thi Hong Lien Han, Thi Tuyet Mai Nguyen, Thi Thuy Nguyen, Thien Thanh Nguyen, Thi Thu Vu, Thi Thuy Khue Nguyen, Ha Anh Nguyen who support me and share good moments during my PhD life. Many thanks go to them for joyful times that we spent together. The PhD life with all of you is one of my best memories.

I am very much indebted to my wife, Vy Huynh, who has supported me in every possible way to go to the final stage of this work. Big thank to her for her understanding and sharing with me all of the moments in my life since we met each other. And I'm so thankful to have her in my life.

I owe a lot to my parents, who unconditionally encouraged and supported me at every stages of my life. Mom and dad, I have no words to acknowledge their sacrifices. One of the greatest titles in the world is parents, and one of the biggest blessings in the world is to have parents. "Thank you for everything."

Finally, through this report, I would like to express my heartfelt thanks to all those who contribute directly or indirectly to this humble work.

Thuan Nguyen PHAM TRUONG

Paris, November 2018

I am enough of the artist to draw freely upon my imagination. Imagination is more important than knowledge. Knowledge is limited. Imagination encircles the world.

Albert Einstein,

What Life Means to Einstein: An Interview by George Sylvester Viereck, The Saturday Evening post, 26 october 1929, p.117.

SUMMARY

Increasing demand of energy requires massive investment for exploration and utilization of renewable energy sources in the energy balance. However, due to the intermittence of the current renewable sources, the generated electricity must be stored under other forms to correlate the fleeting production and the continuous consumption. Despite available commercialized systems, seeking for new materials and new approaches for resolving this problem is still matter of interest for scientific researches. Highlighted advancements have recently oriented the community towards the utilization of nanoscale materials for efficient energy storage and conversion. Although the advantages given by existing nanomaterials for diverse applications, especially in the energy field, their performance is still lower than theoretical purposes. Consequently, tailoring the physical-chemical properties at the molecular scale becomes crucial not only for boosting the activities of the existed materials but also for creating a new type of molecular entities for storing and releasing the energy. Accordingly, this PhD work aim to develop new family of materials based on ionic liquid that exhibits a multifunctionality towards energy applications. Our work is based on the knowhow in surface functionalization and material preparation by simple methods to build up electrochemical systems that can be utilized in various applications. Thus, this thesis will report different results obtained by following this direction and is composed of six chapters:

Chapter 1 reports an overview of ionic liquid and polymeric ionic liquid. We propose to review the available literature on the redox-IL from solution to immobilized substrates. Through this chapter, we will achieve the following points: (1) Report the possible uses of ionic liquids in electrochemistry; (2) Discuss about the physical-chemical behaviors of these compounds in solution, (3) Show the immobilization of (Redox-active)–ionic liquids onto different substrates: from thin layer to polymer and (4) Highlight recent advances using polymeric ionic liquids for diverse applications.

Chapter 2 will be devoted to different electrochemical assisted approaches for the immobilization of (redox)-ionic liquids to the electrode surface. We will focus on generating a thin layer and polymeric film based ionic liquid. Furthermore, the different characteristics of the new interfaces will be reported.

Chapter 3 concentrates on the use of the polymer ionic liquid modified electrodes as emerging catalyst and as template for the generation of hybrid materials towards activation of small molecules.

Chapter 4 studies the reactivity at micro/nanometer scale of diverse materials, including single layer graphene, polymeric redox – ionic liquid, using the scanning electrochemical microscopy (SECM).

Chapter 5 reports the potential applications of redox ionic liquid and focus on providing the preliminary results towards the fabrication of flexible substrates with interesting functionalities: possibility to convert the friction to electricity and energy storage by using polymeric redox ionic liquids. These studies open a new opportunity to elaborate flexible, wearable and implantable devices.

Finally, some concluding remarks are given to summarize different results obtained in the previous chapters. Besides, different perspectives will be given by using ionic liquid as main material for developing different energy storage and conversion systems.

Keywords: Energy storage and conversion, artificial skin, electrocatalysis, scanning electrochemical microscopy, ionic liquids, polymers, triboelectricity, surface functionalization.

RESUME

Le développement durable nécessite des investissements massifs pour l'exploration et l'utilisation des sources d'énergie renouvelables dans le bilan énergétique. Parmi diverses formes de l'énergie, l'électricité est sans doute la forme la plus souhaitable pour les usages quotidiens. Cependant, en raison de l'intermittence des sources d'énergie renouvelables, l'électricité doit être stockée sous d'autres formes afin de corréler la production éphémère et la consommation en continue. Malgré la présence des systèmes commerciaux de stockage d'énergie, la recherche de nouveaux matériaux et de nouvelles approches pour résoudre ce problème est toujours en cours et attire également une grande attention. Les récents progrès ont poussé la communauté scientifique vers l'utilisation de matériaux à l'échelle nanométrique pour des systèmes de stockage et de conversion de l'énergie. Bien que ces derniers offrent des avantages pour réduire les émissions de gaz à effet de serre, leurs performances sont encore inférieures aux valeurs théoriques. Dans ce contexte, l'ingénierie à l'échelle moléculaire devient cruciale non seulement pour créer un nouveau type d'entités moléculaires mais aussi pour augmenter les performances des matériaux existants. Dans ce contexte, nous proposons d'utiliser une nouvelle famille de matériaux à base de liquides ioniques pour diverses d'applications, comprenant celles dans le domaine énergétique et pour le long terme, dans la fabrication de la peau artificielle, ces objectifs font l'objet de ces travaux de thèse. Cette dissertation est composée de cinq chapitres.

Le chapitre 1 présente différents aspects des liquides ioniques (LIs) et des polymères à base de LI décrites dans la littérature. Via ce chapitre, nous envisageons d'atteindre les points suivants : (1) Décrire les utilisations possibles des liquides ioniques en électrochimie ; (2) Discuter des comportements physico-chimiques de ces composés en solution, (3) Montrer l'immobilisation de liquides ioniques (Redox-actifs) sur différents substrats : de couches minces aux polymères et (4) Mettre en évidence les travaux marquant portant sur l'utilisation des polymères ioniques liquides dans diverses applications.

Le chapitre 2 présente différentes approches électrochimiques pour l'immobilisation de liquides ioniques rédox à la surface de l'électrode. De plus, les différentes caractéristiques des nouvelles interfaces seront reportées. Le chapitre 3 se concentre sur l'utilisation des polymères LIs comme catalyseurs émergents et comme matrices pour la génération de matériaux hybrides vers l'activation de petites molécules (ORR, OER, HER). Le chapitre 4 étudie la réactivité à l'échelle micro / nanométrique de divers matériaux, y compris les polymères liquides ioniques électro-actifs, en utilisant la microscopie électrochimique à balayage (SECM). Le chapitre 5 présente les résultats préliminaires de la fabrication de substrats flexibles avec des fonctionnalités intéressantes : possibilité de convertir le frottement en électricité et stockage d'énergie en utilisant des liquides ioniques redox polymériques. Ces études ouvrent de nouvelles opportunités pour élaborer des dispositifs flexibles, portables et implantables.

Mot-clés : Stockage et conversion d'énergie, peau artificielle, electrocatalyse, microscopy électrochimique à balayage, liquides ioniques, polymères, triboelectricité, functionalisation de surface.

GLOSSARY

AFM	Atomic Force Microscopy
SEM	Scanning Electron Microscopy
TEM	Transmission Electron Microscopy
SECM	Scanning ElectroChemical Microscopy
XPS	X-ray Photoelectron Spectroscopy
FT-IR	Fourier Transform Infrared Spectroscopy
UV-Vis	Ultraviolet – Visible Spectroscopy
NMR	Nuclear Magnetic Resonance Spectroscopy
DLS	Dynamic Light Scattering
GCPL	Galvanostatic Cycling with Potential Limitation
CED	Coulombic Efficiency Determination
SMG	Special Modular Galvano
EIS	Electrochemical Impedance Spectroscopy
CV	Cyclic Voltammetry
LSV	Linear Sweep Voltammetry
CA	ChronoAmperommetry
MW	Microwave
SI-ATRP	Surface-Initiated Atom Transfer Radical Polymerization
RFLB	Redox-flow lithium battery
WE	Working Electrode
CE	Counter Electrode
Ref	Reference Electrode
UME	UltraMicroElectrode
SCE	Saturated Calomel Electrode
RHE	Reversible Hydrogen Electrode
E	Potential
EW	Potential window
E_p	Peak potential
ΔE	Peak-to-peak Separation
E^0	Standard potential
η	Overpotential
k	Electron transfer rate constant

α	Charge transfer coefficient
i	Current
j	Current density
i_p	Peak current
K-L	Koutecky-Levich
PCET	Proton coupled electron transfer
ICET	Ion coupled electron transfer
δ	Chemical shift
ppm	Parts per million
C	Concentration
hrs	Hours
MeCN	Acetonitrile
DMF	Dimethylformamide
DCM	Dichloromethane
IL	Ionic liquid
PIL	Poly(ionic liquid)
TFSI	Bis(trifluoromethanesulfonyl)amide
Fc	Ferrocene
Fc^+	Ferrocenium
AQ	Anthraquinone
PMDETA	Pentamethyl-diethylenetriamine
PAMI	Poly(1-allyl-3-methylimidazolium)
EMIES	1-ethyl-3-methylimidazolium ethylsulfate
$TBAPF_6$	Tetra n-butylammonium hexafluorophosphate
C-Dots	Carbon Dots
NPs	Nanoparticles
GC	Glassy Carbon Electrode
ITO	Indium Tin Oxide

GENERAL OUTLINE

PREFACE AND GENERAL INTRODUCTION

Life, the magnificent process, appears on Earth billions of years ago. Beginning from non-living chemical substances, e.g. carbon, nitrogen and water, numerous reactions and transformations conducted to the formation of autonomous systems with open-ended evolutionary capacities, that defined living-systems[1,2]. Depending on the evolution level, the living-structures are very diverse. Though, whatever the creatures are, from the simplest primitive life-form like bacteria to the most complex creature, human; there are always a protective layer, named "skin". The latter acts as a barrier between the inner parts of creatures and the surrounding environment. To ensure the protection role, the skin which has a unique double-layer's structure must cover the whole body, resulting to the largest and heaviest organ[3]. Besides, it can also perform multiple tasks, such as regulating body temperature, preventing adsorption of harmful irradiations, acting as body's sensory device, preventing loss of moisture, avoiding penetration of liquid, dirt and chemical products[4]. However, by suffering serious damages (diseases, injuries, etc.), the body cannot act fast enough to manufacture necessary tissues to heal the wound.

Inspired from the nature, artificial skin (AS) that mimed natural skin has been nowadays widely investigated and developed. Among various approaches for producing artificial skin, synthetic membrane can provide a fully flexible system bearing desired functionalities resulting from surface modifications which can be not only used in medicine but also in material sciences (e.g. soft robotic)[5,6]. In this context, our research group desires to embark on this field by providing our expertise in energy by using an expanding class of material, ionic liquid. The final goal of this research is to develop flexible functionalized transparent film for fabrication of electronic skin. Beside the basic roles of human skin, the layer should have a highly energetical autonomy, i.e. it can generate necessary electricity using environmental sources, and has other task-specific functions.

During the past 2 decades, the notion "ionic liquid" and its derivatives attract a rising research interest as solvent – electrolyte for electrochemical processes. However, the recent studies show the ability to use ionic liquids (IL) and ionic liquid-based polymers (PIL), labeled task-specific ionic liquids, as main components for a large spectrum of applications. Despite the development of these materials, the number of reports is relatively limited and the fundamental understanding of IL and PIL properties is still opened for further investigations.

The first chapter is reserved for recent advances from fundamental researches to practical uses in the field of ionic liquid. Being used as green solvent, ionic liquids and its derivatives are quite harmful for environment and human health. To resolve this problem, different approaches have been proposed to immobilize ionic liquid onto various substrates to reduce the quantity of IL and to generate new interesting interfaces from thin layer ionic liquid to polymeric ionic liquid. In this context, self-assembled monolayer and electrochemical tools are among the most powerful techniques to graft IL and PIL onto material surfaces from nanoscale to large area.

The IL-modified substrates exhibit unusual behaviors compared to other organic materials providing the possibility to use them in sensing, catalysis, energy applications, and so on. In parallel with the traditional ionic liquids, redox-active ionic liquids (RIL) and redox-active polymer ionic liquids appear as new candidates for the integration in electrochemical processes. They have been successfully used as electro-responsive materials for reversible electrochemical switchable wettability and electrochemical energy storage[7].

Before going to further applications using (electroactive)ionic liquids, the attachment of the molecules onto electrode becomes crucial task towards the formation of multifunctional and flexible substrates with well-controlled physical-chemical properties. In the continuation of the previous works, we propose in the chapter 2, by means of electrochemical approaches, the surface functionalization of novel redox-active ionic liquids with different morphologies ranging from very thin layer to dense polymer film. The simultaneous presence of both charges from the backbone and redox-active groups at the surface generates unusual properties[8–11].

In the chapter 3, we mainly focus on the utilization of poly (ionic liquid) based materials as an efficient catalyst towards the activation of small molecules (H_2, O_2, H_2O, etc.). The electrocatalytic performance of the hybrid materials by embedding the nanoparticles (Au, Pt/C, C dots, etc.) inside the polymer brush-like structure is fully described in this chapter. Interestingly, the cationic properties of the polymer backbone, the poly(ionic liquid) can be used as a host-guest platform for capturing metal ions. Later, it can also act as template for the electrochemical generation of metal clusters under self-electrolytic conditions[12,13].

The chapter 4 is mainly reserved to the use of poly(ferrocenated-IL) in scanning electrochemical microscopy application. Thus, the polymerization of FcIL onto ultramicroelectrode increases the sensibility of the surface of the ultramicroelectrode (UME). Consequently, the modified UME can detect the presence of conductive substrates without using mediator in solution. From preliminary results, we propose to use the immobilized probe SECM for surface mapping to prevent border effect caused by the diffusion of the mediator in solution. This chapter is also devoted to the investigation of the local properties of graphene and modified graphene supported onto flexible and transparent substrate[14,15].

The chapter 5 will shed light on the potential use of the ionic liquid in energy[16]. Thus, we will present the preliminary results for the elaboration of flexible electrodes for further developing of artificial skin by using different approaches. Each family of substrates presents also potential uses in various applications such as wearable supercapacitors and triboelectric nanogenerators.

The last part of this dissertation is reserved for some concluding remarks and the prospects based on the ongoing works.

REFERENCES

(1) Ruiz-Mirazo, K.; Peretó, J.; Moreno, A. A Universal Definition of Life: Autonomy and Open-Ended Evolution. *Orig. life Evol. Biosph.* **2004**, *34* (3), 323–346.

(2) Peretó, J. Controversies on the Origin of Life. *Int. Microbiol.* **2005**, *8* (1), 23–31.

(3) Pappas, A. Lipids and Skin Health. *Lipids Ski. Heal.* **2015**, 1–359.

(4) Tortora, G. J.; Derrickson, B. *Principles of Anatomy and Physiology*; 2000; Vol. 86.

(5) Ng, S. F.; Rouse, J. J.; Sanderson, F. D.; Eccleston, G. M. The Relevance of Polymeric Synthetic Membranes in Topical Formulation Assessment and Drug Diffusion Study. *Arch. Pharm. Res.* **2012**, *35* (4), 579–593.

(6) Yannas, I. V.; Burke, J. F. Design of an Artificial Skin. I. Basic Design Principles. *J. Biomed. Mater. Res.* **1980**, *14* (1), 65–81.

(7) **Pham-Truong, T.-N.;** Ghilane, J.; Randriamahazaka, H. *Redox-Active Immobilized Ionic Liquids and Polymer Ionic Liquids*; Ali Eſtekhar, Ed.; Royal Society of Chemistry, 2018, 225-261.

(8) **Pham-Truong, T.-N.**; Randriamahazaka, H.; Ghilane, J. Redox Monomer Ionic Liquid Based on Quaternary Ammonium: From Electrochemistry to Polymer Brushes. *Electrochem. commun.* **2017**, *82* (July), 25–29.

(9) **Pham-Truong, T. N.;** Lafolet, F.; Ghilane, J.; Randriamahazaka, H. Surface Functionalization with Redox Active Molecule Based Imidazolium via Click Chemistry. *Electrochem. commun.* **2016**, *70*, 13–17.

(10) **Pham-Truong, T.-N.**; Randriamahazaka, H.; Ghilane, J. Platinum/Poly(N-Ferrocenylmethyl-N-Allylimidazolium Bromide) Quasi-Reference Electrode for Electrochemistry in Non-Aqueous and Ionic Liquid Solutions. *Electrochem. commun.* **2016**, *73*, 5–9.

(11) Randriamahazaka, H.; Ghilane, J.; Trippe-Allard, G.; Bui-Thi-Tuyet, V.; **Pham Truong, T. N.;** Electroactive ionic liquids and surface-modified substrates containing them. *WO2017/191481A1*

(12) **Pham Truong, T. N.;** Randriamahazaka, H.; Ghilane, J. Polymer Brushes Ionic Liquid as a Catalyst for Oxygen Reduction and Oxygen Evolution Reactions. *ACS Catal.* **2018**, *8* (2), 869–875.

(13) **Pham-Truong, T. N.;** Petenzi, T.; Ranjan, C.; Randriamahazaka, H.; Ghilane, J. Microwave Assisted Synthesis of Carbon Dots in Ionic Liquid as Metal Free Catalyst for Highly Selective Production of Hydrogen Peroxide. *Carbon N. Y.* **2018**, *130*, 544–552.

(14) **Pham-Truong, T. N.;** Deng, B.; Liu, Z.; Randriamahazaka, H.; Ghilane, J. Local Electrochemical Reactivity of Single Layer Graphene Deposited on Flexible and Transparent Plastic Film Using Scanning Electrochemical Microscopy. *Carbon N. Y.* **2018**, *130*, 566–573.

(15) Yan, R.; Ghilane, J.; Phuah, K. C.; **Pham Truong, T. N.;** Adams, S.; Randriamahazaka, H.; Wang, Q. Determining Li^{+} -Coupled Redox Targeting Reaction Kinetics of Battery Materials with Scanning Electrochemical Microscopy. *J. Phys. Chem. Lett.* **2018**, *9* (3), 491–496.

(16) Zhou, M.; Huang, Q.; **Pham Truong, T. N.;** Ghilane, J.; Zhu, Y. G.; Jia, C.; Yan, R.; Fan, L.; Randriamahazaka, H.; Wang, Q. Nernstian-Potential-Driven Redox-Targeting Reactions of Battery Materials. *Chem* **2017**, *3* (6), 1036–1049.

CHAPTER 1

IONIC LIQUIDS AND POLYMERS: FROM MOLECULAR CONCEPT TO FUNCTIONAL MATERIALS

This chapter provides an overview of (redox-active) – ionic liquids and polymer based ionic liquids. The flexible design of these new families of ionic liquids allows for the tuning of various properties. Furthermore, these compounds can act as active materials for diverse applications. In this chapter, different approaches and procedures for immobilizing redox-active ionic liquids, from thin layers to polymers, are mentioned and discussed. Importantly, polymer ionic liquids have largely contributed to recent advances in polymer sciences and are becoming key materials in different fields, such as energy storage (batteries, supercapacitors), energy conversion (actuators), and information processing (sensors). The highlighted reports cited below provide strong evidences on multifunctional aspects of ionic liquid-based materials which are considered as the background and starting point of my Ph.D. works described in this thesis.

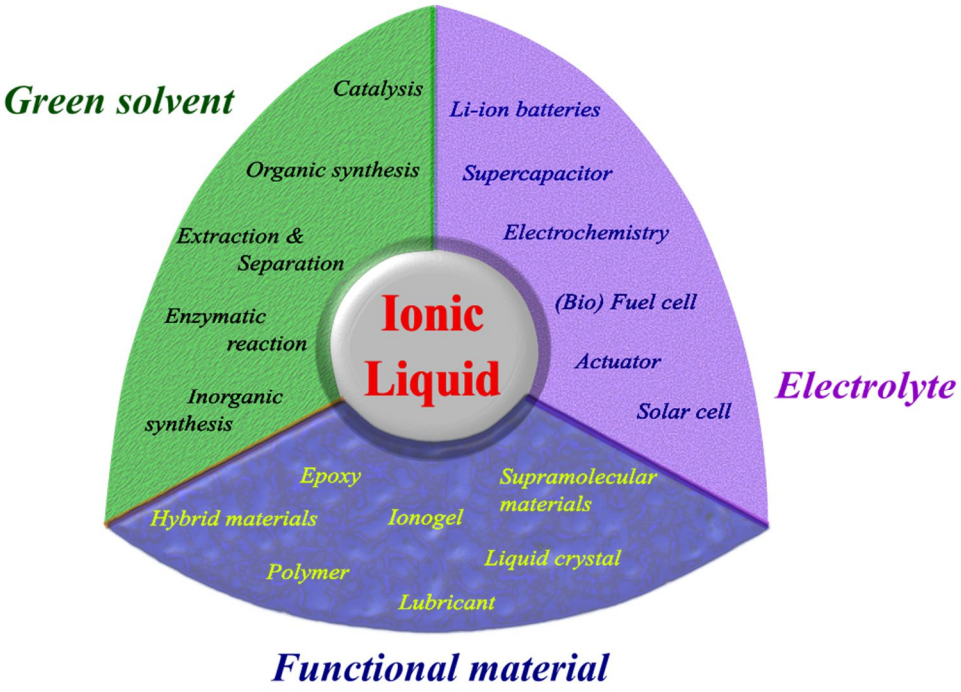

OUTLINE

1.1 INTRODUCTION

Although the first synthesized ionic liquid was reported at the beginning of the last century, we had to wait until the 1990s to see the great innovation of this family of compounds. Since then, ionic liquids and their derivatives have attracted a lot of interest from the scientific world and have become a real multidisciplinary field. So, what makes ionic liquids different from other compounds? According to the common definition, an ionic liquid is a molten salt with a melting temperature below 100 °C. However, according to the structures and properties of various ionic liquids reported in the literature, an alternative definition of ionic liquid can be attributed as salts that contains at least one organic component (cation and/or anion) and in which the ions are poorly coordinated results to highly polar compounds. Importantly, ionic liquid can melt without any decomposition. The characteristics that can be attributed to ionic liquids are a wide liquidus range, very low vapor pressure, and thermal stability with unusual solvent properties. These properties make ionic liquids one of the best choices as solvents for green chemistry and for sustainability science. Overcome with knowledge about ionic liquids at this time, researchers' and scientists' imaginations make ionic liquids rather more useful than only being used in organic synthesis. Thus, the limits are being further pushed to tailor the physical-chemical properties of ionic liquids by generating new structures for use in the field of electrochemistry, in which the development of this type of compound becomes unlimited.

1.2 ELECTROCHEMISTRY IN IONIC LIQUIDS

In 1982, dialkylimidazolium chloroaluminate-based ionic liquids were the very first room-temperature ionic liquids (RTILs) to enter the electrochemistry field for use in the electrodeposition of aluminum, according to the reported work by Wilkes and co-workers[1]. Since then, different studies have been performed to investigate the electrochemical behaviors not only of ionic liquids themselves, but also of other materials in ionic liquids. From an electrochemical point of view, ionic liquids simultaneously play the role of a solvent and a supporting electrolyte. A good electrolyte for electrochemical measurements and for devices should exhibit a strong resistance to electro-oxidation and reduction. This behavior is indicated by a large electrochemical window (EW). For different families of ionic liquids (imidazolium, pyrrolidium, ammonium, etc.), a broad EW was observed (3.5 to 6 V), which depends upon the composition of the ionic liquid as listed in Table 1.1. Compared with the usual organic solvents in use nowadays, whose EWs result partially from the interactions between the electrolyte and the solvent, the EW of ionic liquids is as an intrinsic value that is characteristic for each ionic liquid structure. In addition, the vapor pressure of RTILs is much lower than that of other organic solvents providing strong stability over time, which is extremely beneficial for long-term, non-volatile electrochemical devices. By possessing advantageous electrochemical properties, ionic liquids are being used in numerous applications in the electrochemistry field, especially for electrodeposition processes. Indeed, a large variety of metals, metal oxides and semiconductors have been deposited in ionic liquid media.

Table 1.1 Typical electrochemical windows of different types of ionic liquid.

Ionic liquid[*Ref*]	**Cathodic potential limit (V)**	**Anodic potential limit (V)**	**Electrochemical window (V)**	**Reference electrode**	**Working electrode**
[1-Et-3-MeIm$^+$] [TFSI$^-$][2]	-1.8	2.3	4.1	I^-/I_3^-	Pt
[1-Et-3-MeIm$^+$] [OTf$^-$][2]	-1.7	2	3.7	I^-/I_3^-	Pt
[1-Bu-3-MeIm$^+$] [BF_4^-][3]	-1.6	2.5	4.1	Pt QRE	Pt
[1-Bu-3-MeIm$^+$] [PF_6^-][3]	-1.6	2.55	4.15	Pt QRE	Pt
[1,2-Me_2-3-PrIm$^+$] [Tf_3C^-][4]	0.28	5.65	5.37	Li^+/Li	GC
[1,2-Me_2-3-PrIm$^+$] [TFSI$^-$][4]	0.2	5.4	5.2	Li^+|Li	GC
[1-Me-3-PrPyrro$^+$] [TFSI][5]	-2.5	2.8	5.3	Ag Wire	Pt
[1-Bu-3-MePyrro$^+$] [TFSI][6]	-3	2.5	5.5	Ag|Ag^+	GC
[Et_3HexAmm$^+$] [TFSI][7]	-2.5	2	4.5	Ag|Ag^+	GC
[ButPyri$^+$][BF_4^-][8]	-1	2.4	3.4	Ag wire	Pt
[Et_3S^+][TFSI][9]	-2	2.7	4.7	Pt	GC
[But_3S^+][TFSI][9]	-2.1	2.8	4.8	Pt	GC

1.2.1 Electrodeposition of Metals, Metal Alloys and Semiconductors

As mentioned in the previous subsection, the first metal to be electrodeposited in an ionic liquid was aluminum. The main problem with this process is that the precursor, $AlCl_3$, which is a Lewis acid, is highly sensitive to the presence of water, which induces the formation of basic $AlCl_3$ and as a consequence inhibits the electrodeposition process. However, this deposition process becomes much more feasible in ionic liquid medium[10] and the morphology of the deposits can also be controlled[11]. From this successful process, a large number of metals and

metal alloys (Pd, Cu, Fe, Al–Mn, etc.) have been electrodeposited onto different substrates in ionic liquid media[12–14].

Besides the electrodeposition of different metals, the electrodeposition of semiconductors in ionic liquids has also been investigated. Only a few published studies mention the use of ionic liquids for the electrodeposition of semiconductors[14–16]. Despite the feasibility of generating different SCs on a surface (IV, III–V, and p-type SCs) from these solvents, the main problem with this process is the homogeneity of the generated surface.

1.2.2 Electropolymerization of Conducting Polymers

In this context, it would be remiss not to discuss the possible electro-polymerization of conducting polymers in ionic liquid media. High quality, homogeneous and smooth-surface poly(3-alkylthiophene)s were electrochemically prepared in [1-But-3-MeIm$^+$][PF_6^-] as promising materials for electrochromic devices[17]. Another typical example is the electrochemical polymerization of poly(aniline), which is well-known for its use in energy applications. In addition, CF_3COOH–doped poly(aniline) nanotubule structures, with a diameter of around 120 nm, were obtained after electrochemical polymerization in an IL solution containing aniline monomers and trifluoroacetic acid[18] (Figure 1.1).

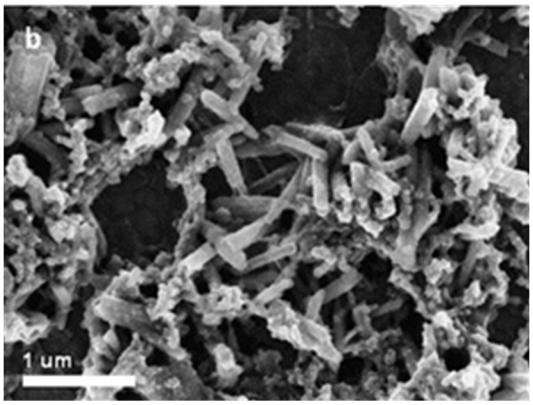

Figure 1.1 SEM images of PANI deposited onto ITO synthesized from $BMIPF_6$ containing 1.0 M CF_3COOH.

Others conducting polymers have also been electrochemically synthesized in ionic liquids, such as poly(pyrrole)[19], poly(p-phenylene)[20] and poly(3,4-ethylenedioxythiophene)[21]. Compared to a classical solvent, the use of ionic liquids as an electrolytic medium provides different morphological structures and offers new interface properties.

1.3 REDOX-ACTIVE IONIC LIQUIDS

In the previous subsection, the different aspects of electrochemistry in ionic liquids were briefly described. Nevertheless, the potential of ionic liquids in electrochemistry is much more considerable than just being limited to their use as a solvent–electrolyte. Recently, new families of ionic liquids known as “task specific ionic liquids” have been introduced that are based on ionic liquids bearing functional groups. As an example, the introduction of a redox group to an ionic liquid framework led to the formation of a new class of ionic liquids labeled as redox-

active ionic liquids. The first redox-active ionic liquids were prepared by Grätzel's group in 2004; they contained a redox active counter-anion ([I^-] and [$SeCN^-$]) and were successfully used in a dye sensitized solar cell system[22]. R. Balasubramanian et al.[23] in 2006 reported the electrochemical behaviors of ferrocenated imidazolium compounds whose ferrocenyl group is connected to the imidazolium ring by an organic linker (Figure 1.2, left). This work shows that the viscosity of the redox ionic liquid depends on the length of the linker and the side chains. In Figure 1.2, right, the electrochemical response of the undiluted ferrocenated ionic liquid is strongly influenced by the temperature and, as a consequence, the viscosity of the medium following the Williams–Landel–Ferry (WLF) model[24]. Compared to the electrochemical behavior of ferrocene in solution, a positive shift in terms of the formal potential is observed for the ferrocenated ionic liquid. Indeed, linking an electron attractor group (imidazolium) to the ferrocene induces a withdrawing effect due to the positive charge. The electron density of ferrocene decreases, resulting in a lower energy level of the highest occupied molecular orbital (HOMO) and in an increase of the oxidation potential[25].

Recently, a hybrid redox system based on imidazolium ionic liquids was investigated by X. Chen et al.[26] A mixture of 2 redox ionic liquids containing imidazolium functionalized with 2,2,6,6-tetramethyl-piperidinyl-1-oxyl ([$MeIm^+$–TEMPO][$TFSI^-$]) and [1-Pro-3-$MeIm^+$][I^-] was used to produce a Grätzel-type cell. The reported bi-redox couple electrolyte showed strong absorption only in the UV region and a higher redox potential compared with the I^-/I_3^- redox couple. Later, a bi-redox ionic liquid molecule was reported by O. Fontaine et al.[27,28] In these studies, a series of ionic liquids containing anions and cations that are functionalized with anthraquinone (AQ) and TEMPO moieties, respectively, was electrochemically studied (Figure 1.3).

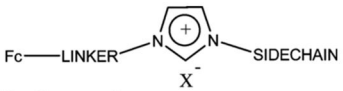

Fc - Ferrocenyl

	linker	side chain	η, cP (25 °C)[b]
1	C_4H_8	CH_3 or C_4H_9	na[c]
2	C_6H_{12}	CH_3 or C_4H_9	8.5×10^3
3	COO−C_3H_6	CH_3 or C_4H_9	1.4×10^7
4	COO−C_6H_{12}	CH_3 or C_4H_9	5.8×10^5
5	COO−$C_{11}H_{22}$	CH_3 or C_4H_9	1.6×10^5
6	COO−$C_2H_4OC_2H_4$	CH_3 or C_4H_9	5.4×10^5
7	COO−C_3H_6	$C_2H_4OCH_3$	na[c]
8	COO−C_6H_{12}	$C_2H_4OCH_3$	na[c]

[a] X = Br^-, PF_6^-, or BF_4^-. All ILs listed are either fluid or glassy materials except for **1**·CH_3·Br, **2**·CH_3·Br, and **2**·CH_3·PF_6, which are solids. [b] All viscosities are for X = PF_6 and side chain = C_4H_9. [c] Not measured.

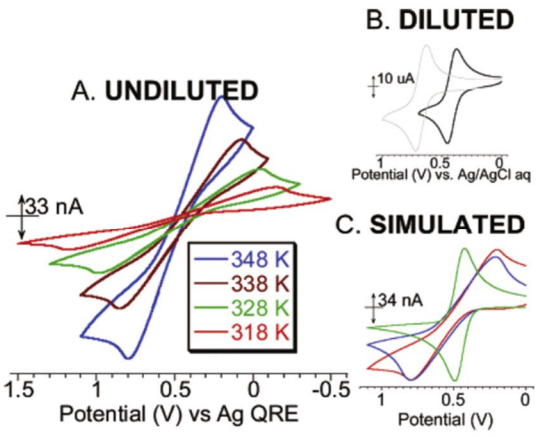

Figure 1.2 (Left) Intrinsically Electroactive Ionic Liquids, (Right) (A) CV (10 mV/s) of undiluted 8.PF_6 at 12.5 µm radius Pt micro disk electrode, in vacuum at indicated temperatures. (B) CV of 1,CH_3,PF_6 (right curve) and carboxylated 3,CH_3,PF_6 (left curve) in dilute CH_2Cl_2 solution with 0.2 M $TBAClO_4$ electrolyte. (C) Digital simulation (blue curve) CV (10 mV/s) of undiluted 8.PF_6 at 75 °C, compared to experimental result (red curve). The green curve is ideal CV with no iRUNC effect.

Tethering redox-active moieties onto both the cation and the anion allows the density of the redox-active groups in the liquid state to be increased up to the bulk density of a redox-active solid. In addition, the bi-redox IL provided double the specific energy in a supercapacitor based on activated carbon and graphene oxide electrodes compared to the same approach without redox active groups. At the same time, the power capability and cycling stability were maintained. The enhanced capacitance is sustained for 2000 cycles without degradation. Moreover, the bi-redox IL enabled high-capacity/high rate charge storage, overcoming a major hurdle for high-energy supercapacitors, opening up a wide new field for redox materials and their applications.

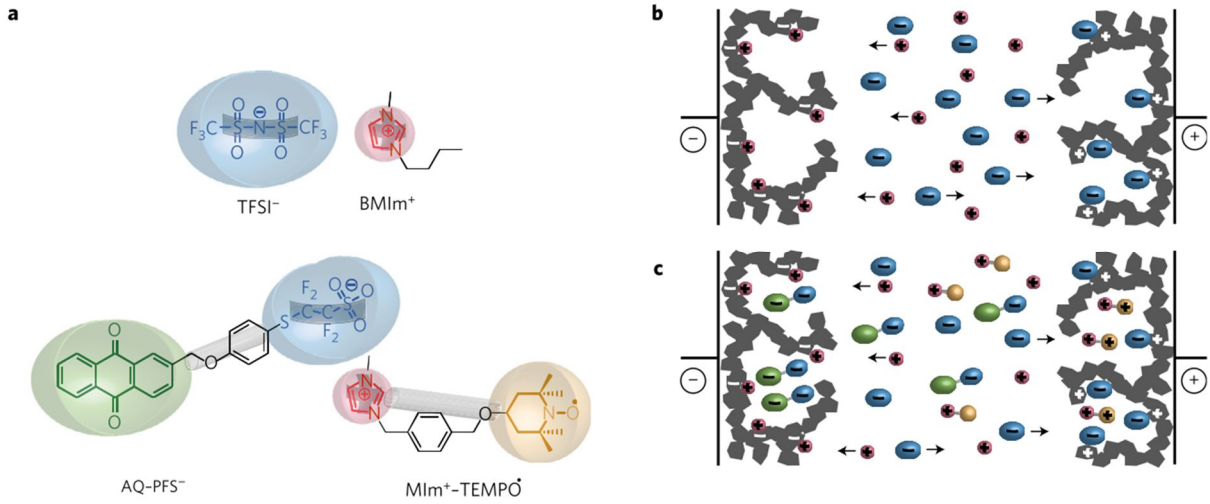

Figure 1.3 Comparison of charge storage in EDLC with IL electrolyte and the bi-redox IL-enhanced pseudo-capacitor. a) Structure of the herein used BMImTFSI IL and the bi-redox IL comprising a perfluorosulfonate anion bearing anthraquinone (AQ–PFS^{-}) and a methyl imidazolium cation bearing TEMPO (MIm^{+}–TEMPO$^{\bullet}$). b) and c) Charge storage in a purely capacitive EDLC comprising porous carbon electrodes and an IL electrolyte.

1.4 IMMOBILIZATION OF IONIC LIQUIDS AND REDOX-ACTIVE IONIC LIQUIDS

1.4.1 Introduction

From laboratory research to real-life applications, the role of surface modification with organic layers is always crucial. Indeed, the atoms at the surface of a material behave completely different compared to the bulk atoms because of the leakage in terms of the coordination number. As a consequence, they have a different free energy, density of states, structure and reactivity. Thus, the attachment of organic molecules onto the surface is considered to be a facile approach to provide novel physical-chemical properties to the materials[29,30]. The immobilization of organic molecules has been successfully integrated in several applications, including smart surfaces, molecular electronics, photovoltaics, catalysis and surface wettability, and several reviews have been devoted to this topic and related applications[31–38]. It is well-known that the surface atoms are more reactive than the other atoms in the bulk of the material, which implies the enhancement of the physisorption and chemisorption of molecules from the ambient environment at the surface.

Introducing an organic layer onto the surface could act as an organic barrier for protection and/or to generate new interfaces involving novel properties, which can be helpful in different fields such as anti-corrosion, super-hydrophobic/super-hydrophilic surfaces, inks and paints, etc. Ionic liquids could also be deposited onto a surface, providing new properties to the interface[39–42].

1.4.2 Approaches to form Thin Layers of Ionic Liquids

Self-assembled monolayers (SAMs) of organic molecules consist of organic assemblies formed by the well-arranged adsorption of organic molecules that have a specific functionalized head group from the solution or the gas phase onto the surface of a solid or onto the surface of a liquid (in the case of liquid metals and its alloys). The most widely studied branch of SAMs is the adsorption of alkanethiols on gold, silver and copper. The strong affinity of thiols (–SH) for the surface of noble metals is the key factor leading to the generation of well-defined organic layers that have other functionalities at the exposed interface.

Thiol-terminated imidazolium-based ionic liquids have been immobilized onto Au substrates by dipping the Au substrate into a millimolar ethanolic solution of the thiol-terminated IL for a few hours[39]. This procedure is widely used for the formation of alkanethiols derivatives on gold substrates (Figure 1.4). Actually, a well-defined structure of the SAM can only be achieved by immersing the substrate for a few hours in order to overcome the slow rearrangement rate of the adsorbates. Different parameters such as temperature, purity of the adsorbate, concentration of oxygen in the solution, solvent, immersion time, etc., should be considered to achieve a good SAM. A generalized scheme of the surface modification of a noble metal by a thiol-terminated IL SAM is presented in Figure 1.4.

B. Lee et al[39] also demonstrated direct counter-anion exchange from the 1.9 nm IL-SAM layer by simple immersion of the ionic liquid-modified substrate into different solutions containing the target counter-anion.

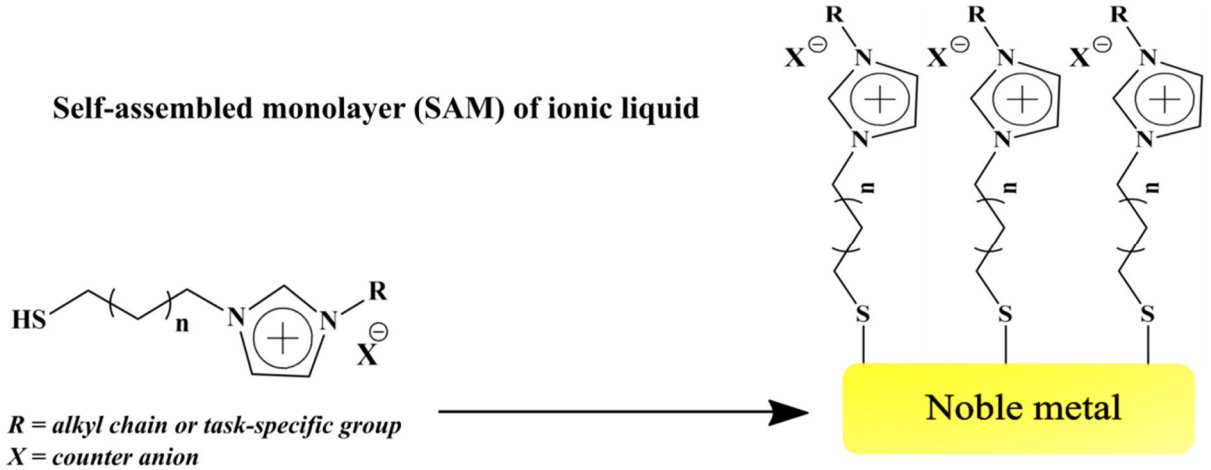

Figure 1.4 Self-assembled monolayer of thiol-functionalized imidazolium based ionic liquid on noble metal (Au, Ag, Cu, etc.).

The influence of the counter-anion on the water wettability of the substrate was also demonstrated. Different counter-anions were found to influence the water contact angle of the substrate in the following order: $TFSI^- > PF_6^- > CF_3SO_3^- > ClO_4^- > BF_4^- > Br^-$. Shortly after this work, an IL-SAM on a gold substrate was reported to be able to exhibit selective redox-switchable behaviors toward Ru^{3+}/Ru^{2+} in the presence of $[Fe(CN)_6]^{3-}$ as a counter-anion[40]. The electrons pass through the IL-SAM layer in the presence of $[Fe(CN)_6]^{3-}$ showing the redox signal of the Ru^{3+}/Ru^{2+} couple. However, the detected signal is cutoff by adding SCN^- or OCN^- into the solution. A self-assembled monolayer of ionic liquid was also applied to gold nanoparticles in order to selectively detect counter-anions[43] or to make a new class of enzymatic biosensors[44] by studying the displacement of the plasmonic band of the IL-functionalized Au nanoparticles.

Besides the formation of a self-assembled monolayer using thiol-terminated ILs on noble metal surfaces, IL-SAMs can also be formed on hydroxyl modified surfaces by using alkoxysilanes bearing imidazolium moieties. As reported by B. Gadenne et al.[45], well-ordered silica particles were synthesized via template-directed polycondensation of triethoxysilylated imidazolium. The materials prepared via this technique depend strongly on the length of the alkyl side chain. Whereas a short alkyl chain (methyl, allyl) gave a lamellar structure, longer chains lead to the formation of nanostructured silica with hexagonal symmetry, which can be attributed to the micellar arrangement of the surfactant molecules. In the case of short chains, the ionic liquid molecules interact only with the polar head of the surfactant, while in the case of longer chains, in addition to the interaction described for the previous case, the alkyl chain of the ionic liquid can also interact with the hydrophobic tail of the surfactant by being incorporated into a micellar arrangement. More recently, the surface of modified silica gels functionalized with a monolayer of covalently attached 1-(1-trimethoxysilane) propyl-2,3-dimethyl-imidazolium chloride, tetrafluoroborate or hexafluorophosphate ionic moieties was used to catalyze the aldol reaction. Later, M. Zhang et al.[46] proposed the use of silica spheres modified with an ionic liquid to make stationary phases for HPLC, thanks to their facile preparation, high bonding amount and excellent design ability as illustrated in Figure 1.5. Besides the alkoxysilane group, other functional groups can be used for the formation of a self-assembled monolayer via a condensation process, such as alkyl phosphonium-bearing ionic liquids[47].

In parallel with the self-assembled monolayers of ionic liquids with highly oriented molecules, the electrochemical grafting of a thin layer of ionic liquid with an electrochemically assisted method is also considered to be an efficient way to immobilize ionic liquid moieties onto a conductive substrate. This method involves the generation of radicals from oxidizable or reducible group by applying a suitable potential to the substrate. Although this technique is one of the most powerful, there are very few reports on electrochemically assisted surface functionalization with molecules based on ionic liquids.

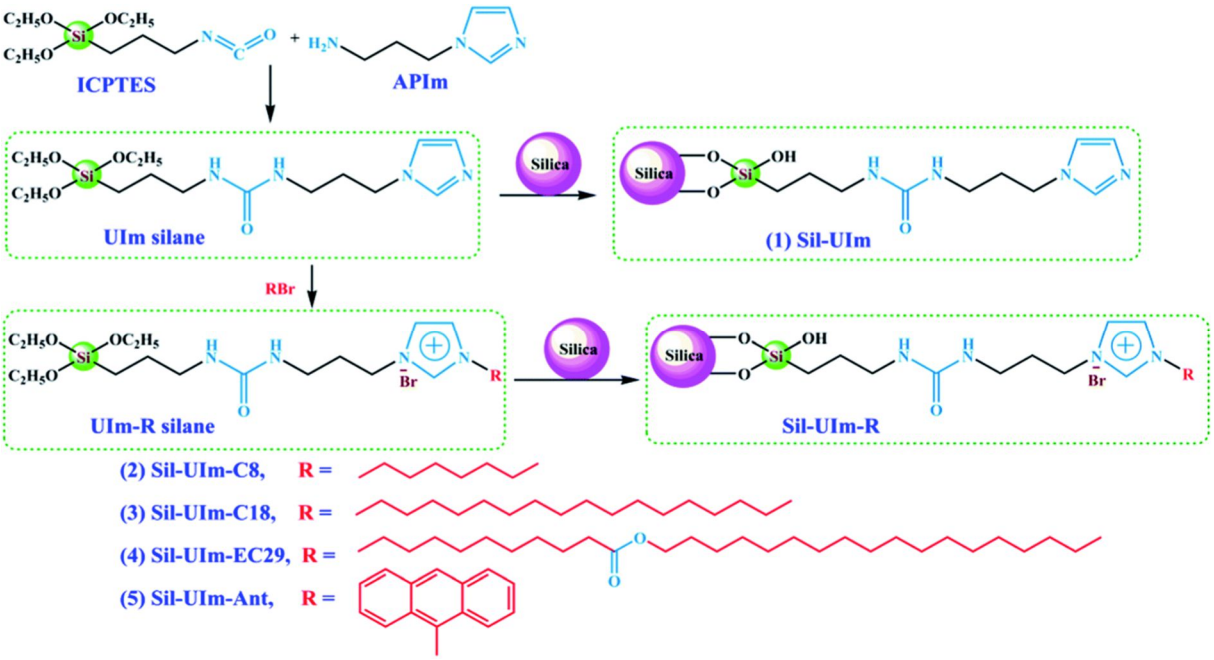

Figure 1.5 Synthetic strategy for SCIL stationary phases

Electrochemically assisted oxidative grafting of ionic liquid moieties can be carried out in one or multiple steps. To the best of our knowledge, there are very few reports that mention the oxidative grafting of an ionic liquid. The oxidative grafting of a redox-molecule-based ionic liquid onto an electrode surface was firstly reported by M. Gomez-Mingot et al.[48] In this report, N-(2-aminoethyl)-N-(4-nitrophenylethylimidazolium) bromide was grafted onto a glassy carbon electrode via electrochemical oxidation of the amine group at around 1.2 V vs. SCE. During the grafting process, aminyl radicals that were electrochemically generated near the electrode surface reacted rapidly with the surface leading to the formation of a thin ionic liquid layer (Figure 1.6).

The immobilization of the ionic liquid on the surface was evidenced by XPS. Figure 1.6 shows the electrochemical characterization of the modified electrode recorded in 0.1 M sulfuric acid aqueous solution and exhibits the presence of a reduction wave at −0.4 V vs. SCE corresponding to the irreversible reduction of the nitro group. Next, during the second cycle, a new redox reversible signal of the generated NHOH/NO group is observed at 0.3 V. These results give rise to a promising material functionalization technique, which combines the attachment of ionic liquids to the surface, the presence of a redox active interface, and the ability to perform anion exchange.

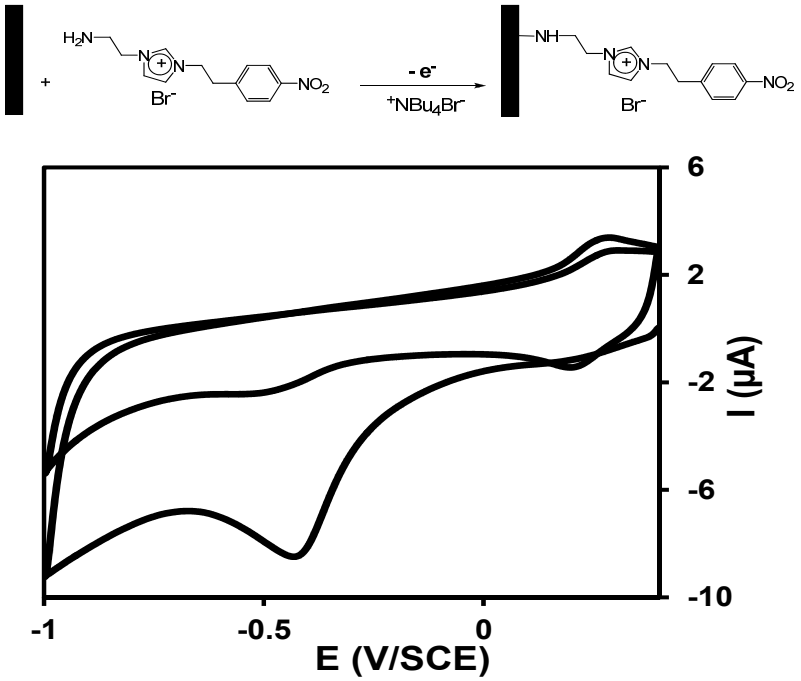

Figure 1.6 Schematic illustrating the grafting of redox based ionic liquid through the electrochemical oxidation of primary amine onto a carbon electrode and the cyclic voltammetry of carbon modified electrode in 0.1 M H_2SO_4. Scan rate 0.1 $V.s^{-1}$.

Later on, the immobilization of a ferrocene-based ionic liquid onto a carbon electrode using a stepwise procedure was investigated[49]. The general procedure is based on the electrochemical grafting of a first layer bearing terminal groups that can be engaged in a chemical reaction, followed by a second step to attach the desired molecules. Figure 1.7 presents an example of this two-step procedure leading to the immobilization of ferrocene-based ionic liquid moieties through aryl–aryl coupling. First, oxidative grafting of 2-(4-aminophenyl) acetic acid was performed onto a glassy carbon electrode. Next, in the presence of sodium nitrite and perchloric acid, a diazotization reaction occurs at the surface leading to the conversion of the attached NH_2 head group into a diazonium group. The latter is accessible for further transformation. Indeed, the Gomberg–Bachmann reaction through aryl–aryl coupling allows the attachment of an aryl radical to one of the cyclopentadienyl moieties of the ferrocene-based ionic liquid[50]. In this work, the immobilization of the ferrocene-based ionic liquid was evidenced by electrochemical characterization, showing the reversible redox signal of the ferrocene group.

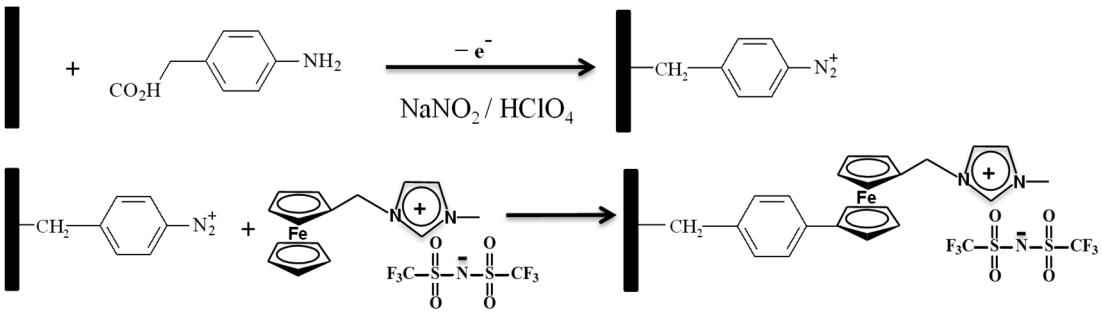

Figure 1.7 Strategy for the stepwise process for the immobilization of ferrocene based ionic liquid.

In parallel with oxidative grafting, electrochemical reductive grafting of ionic liquids has also been a subject of scientific investigation. Among the different functional groups, diazonium derivatives are the most investigated molecules for electrochemical grafting. S. Bouden et al.[42] immobilized a bi-redox ionic liquid, 1-nitrophenylethyl-3-methylferrocenylimidazolium TFSI, onto an electrode surface by the electrochemical reduction of in situ-generated diazonium functional groups (Figure 1.8). By sweeping the potential to the cathodic side (from −0.2 V to −1.1 V vs. SCE) in an acidic MeCN solution containing a bi-redox ionic liquid, nitro-phenyl groups in the vicinity of the electrode surface were reduced via 6 electron pathways to give amines, which were transformed into diazonium groups in the presence of sodium nitrite under acidic conditions. Under negative potential, the in situ-generated diazonium groups within the diffusion layer were reduced into radicals and then attached rapidly to the electrode surface. Compared to the previously reported electrochemically assisted grafting, this approach leads to generate the diazonium within the diffusion layer avoiding or minimizing the spontaneous grafting observed when the diazonium is generated in the electrochemical cell.

The immobilized ionic liquid layer was evidenced by XPS and electrochemistry by observing the signature of the ferrocene moieties (Figure 1.8). This new approach leads to the generation of a multifunctional material bearing redox-active molecules and ionic liquid components. This new interface shows versatile applications toward electrochemically switchable wettability.

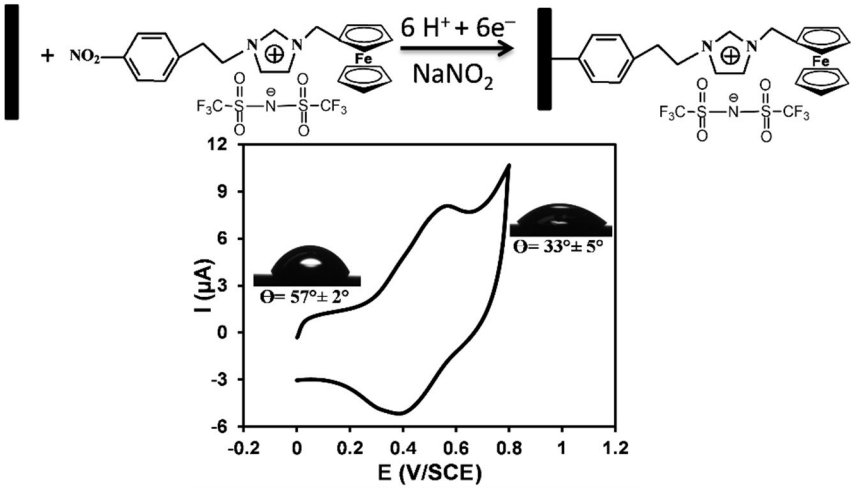

Figure 1.8 Proposed pathway for the electrochemical grafting of ferrocene based ionic liquid molecule. Cyclic voltammogram of grafted electrode in acetonitrile solution containing 0.1 M LiTFSI as supporting electrolyte, scan rate 0.1 $V.s^{-1}$. Inset: contact angles obtained on modified electrode before and after electrochemical oxidation.

Recently, a simple and general route for the immobilization of molecules containing an ionic liquid framework was proposed as shown in Figure 1.9. Inspired by the classical synthesis of ionic liquids, surface-initiated synthesis was reported. This process is based on building the ionic liquid structure on the surface. Thus, a bromide-terminated layer was immobilized on the electrode surface, and the modified surface was then immersed in a solution containing

imidazole derivatives. The generated structures provide multifunctional systems containing ions, immobilized cations and mobile anions, and redox species[41].

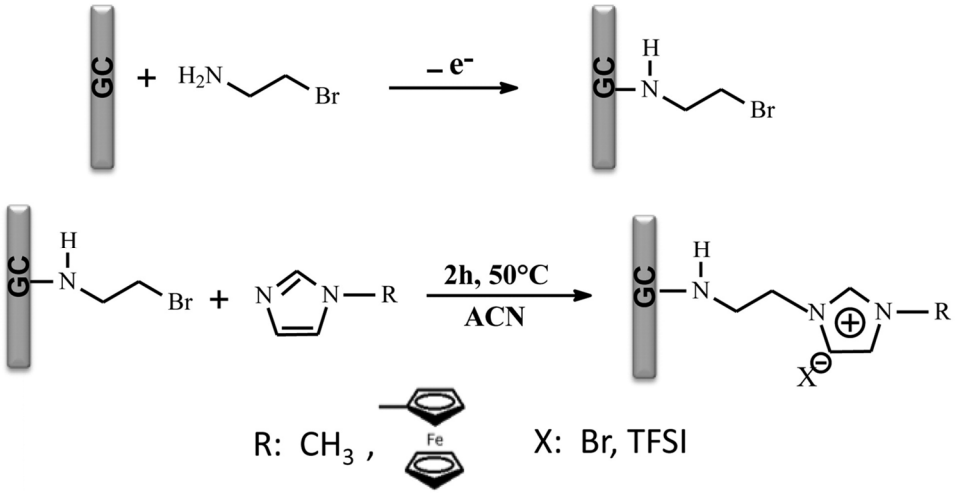

Figure 1.9 Proposed approach for the surface-initiated attachment of molecules based ionic liquid.

Originally, J. Ghilane et al.[51] proposed a novel route for the surface modification of Pt electrode using a bi-redox system containing an imidazolium-based ionic liquid. The procedure is based on electrochemical reductive activation of the electrode materials. Briefly, the cathodic polarization of the electrode material in dry organic electrolytic solution conduces to the generation of new phase. Unlike the classical surface modification methods, described above, the latter is accompanied by the intercalation of the electrolyte cation within the electrode materials. In a recent work, the cathodic polarization of Pt electrode at −2.2 V vs. SCE in the presence of 1-ferrocenylethyl-3-methylimidazolium TFSI as a supporting electrolyte (0.1 M) in dry acetonitrile solution was investigated. As a result, Pt reduction occurs concomitant with the insertion of the supporting electrolyte cation, generating a new metal–organic phase, [$Pt_n^{\delta-}$, $A^{\delta+}$, AX] (where A^+ is the cation and X^- is the anion electrolyte), as illustrated in Figure 1.10. This surface functionalization procedure changes greatly the nature of the starting material by forming ferrocene imidazolium platinide-like phases.

Furthermore, a second redox molecule was introduced by spontaneous reaction between a 4-nitrophenyldiazonium tetrafluoroborate salt and the reduced platinum phase. Indeed, thanks to the reducing power of the cathodically activated platinum, the spontaneous reduction of diazonium occurs leading to the attachment of nitrophenyl groups onto the reduced Pt, as shown in Figure 1.10. As a result, bi-redox molecules were attached onto the Pt, with the ferrocenyl-based ionic liquid inside the Pt and nitro-phenyl at the surface. The electrochemical and XPS characterizations confirm the presence of two redox systems on the Pt surface (Figure 1.10).

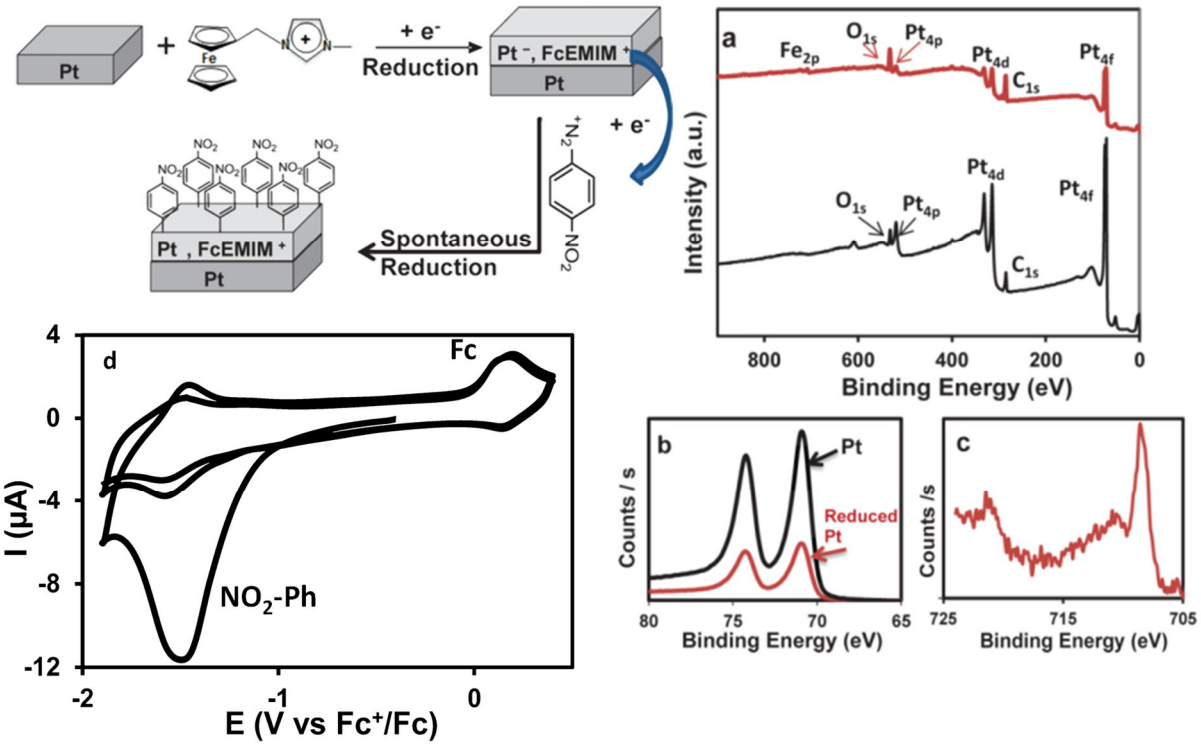

Figure 1.10 Schematic illustrating the spontaneous grafting of nitrophenyl layer onto activated platinium. (a) XPS survey scans of platinum substrate (black line) without any polarization and (red line) after a 200 s cathodic polarization at −2.2 V in ferrocene based ionic liquid. High resolution XPS spectra for (b) Pt(4f) and (c) Fe(2p) core level. (d) Electrochemical characterization of modified Pt electrode in solution containing 0.1 M of Bu_4NBF_4 in ACN. Scan rate was 0.1 V s^{-1}.

1.5 POLYMER IONIC LIQUIDS

Recent developments in polymer science have allowed the synthesis of various polyelectrolytes that are continuously being introduced with controlled morphology, such as linear polymers, nano/micro particles, and dendritic and star structures. The term poly(ionic liquid) (PIL) refers to a subclass of polyelectrolytes that feature an ionic liquid (IL) species in each monomer repeating unit, connected through a polymeric backbone to form a macromolecular structure[52]. In the last decade, poly(ionic liquid)s have been widely investigated as new polyelectrolytes, leading to rapid growth in terms of publications and applications in diverse fields[53–58].

Ohno et al. were the pioneers on reporting PILs as solid electrolytes in electrochemical applications[59–61]. These studies inspired researchers to use PILs with different structures and properties in several applications. There are some reviews provided by Firestone, Long, Texter, Mecerreyes and Antonietti that summarize the synthesis, characterization, and applications of PILs[52,62–67]. In this subsection, the state-of-the-art in this area will be described, presenting a systematic view of the preparation and typical properties of PILs that have already been reported in the literature.

1.5.1 Synthetic Route and Structure of PILs

Monomer-based ionic liquids have been studied leading to the emergence of novel solid materials bearing ionic liquid frameworks. Several reviews were devoted to this new class of ionic polymer, highlighting the formation of new structures, new interfacial properties and potential applications[62,63,68]. Depending on the nature of the polymeric backbone, two types of PIL are classified, called polymerized cationic ionic liquids and polymerized anionic ionic liquids. For each series of PILs, different approaches can be used, such as direct polymerization of ionic liquid monomers or modification of polymeric polymers by forming repeating units containing ionic liquids. In 1973, the first PILs were synthesized by Salamone et al[69]. However, this work did not receive much attention from the scientific community at that time, and we had to wait until the 1990s for the next reports by Ohno et al. on the free radical polymerization of ionic liquids. Since the importance of polymer-based ionic liquids has been recognized, numerous publications have appeared reporting different structures of ionic liquid monomers bearing commonly vinyl or acryloyl groups, as shown in Figure 1.11.

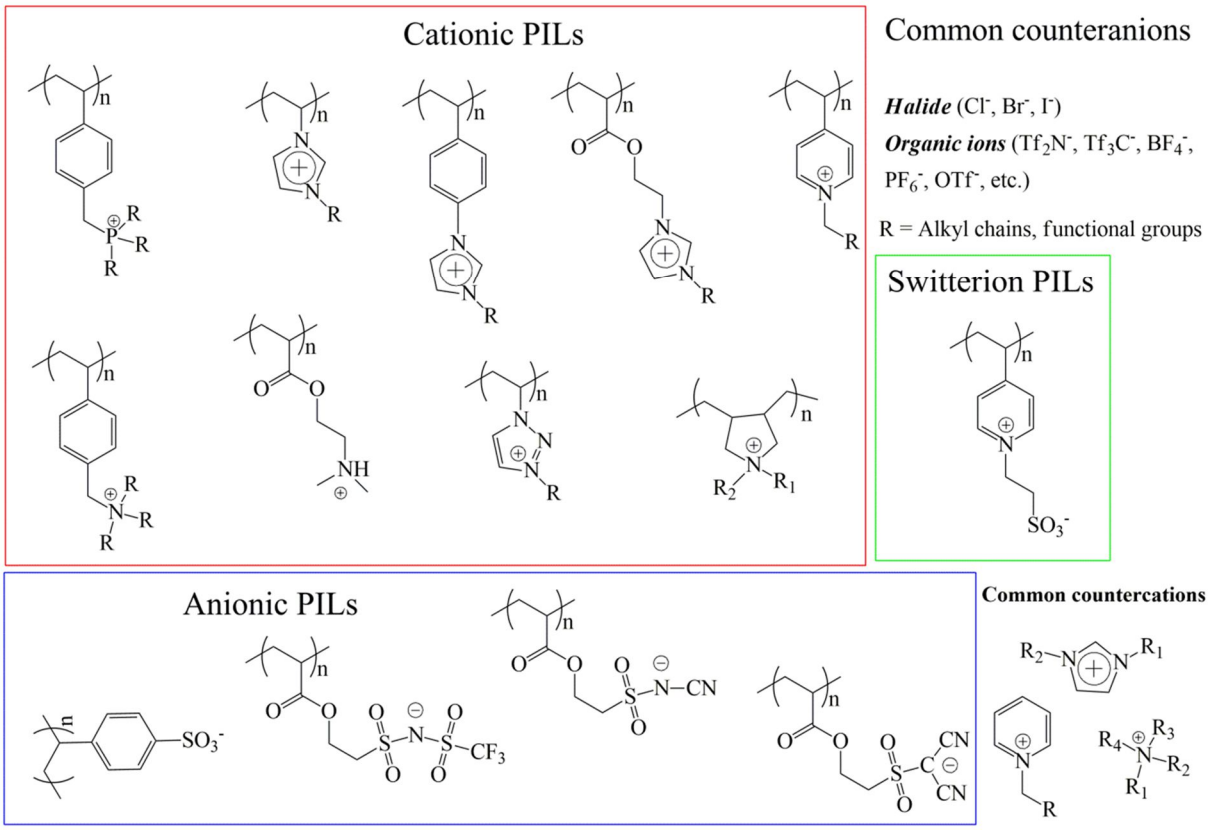

Figure 1.11 Examples of Poly(ionic liquid) chemical structures

Vinyl-functionalized ionic liquid monomers can be prepared in a one-step synthesis via a quaternization reaction by mixing halo-alkane molecules bearing vinyl groups and N – R imidazolium molecules (R = alkyl, redox-active or other functional groups). Further anion exchange might offer interesting properties to the monomer. Acryloyl-functionalized ionic liquid monomers can be synthesized in a 3-step process. Firstly, (meth)acryloyl chloride is

treated with a hydroxyl-containing halo-alkane resulting in the corresponding ester. In the second step, the as-prepared halo-alkane bearing a (meth)acryloyl group is added leading to a quaternization reaction where the imidazolium is connected to the (meth)acryloyl group. Finally, most of the PILs can be commonly synthesized by conventional radical polymerization. In addition, other polymerization approaches can also be applied for PIL systems, such as atom transfer radical polymerization (ATRP)[70,71] and reversible addition–fragmentation transfer polymerization (RAFT)[72,73]. The only part that determines the structure and properties of the PIL is the chemical structure of the ionic liquid monomer. Most PILs were successfully synthesized in bulk solution, in micro-emulsions or in dispersed media. However, it has been shown to be feasible to polymerize ionic liquids onto material surfaces by surface-initiated atom transfer radical polymerization (SI-ATRP)[58,74]. In addition to linear polymers, cross-linked PIL networks have been synthesized by classical radical polymerization. To achieve a PIL network, an ionic liquid monomer bearing bi–, tri–, or multi–vinyl/acryloyl groups must first be prepared. The cross-linking reaction is initiated under thermal- or photoactivation leading to the formation of a PIL network[75].

Beside these polymeric structures, block polymers have received some attention thanks to their ability to provide new and well-defined structures. Indeed, hyperbranched[76–81], dendrimeric[82–85] and star-like[86–91] poly- and oligo(ionic liquid)s have been successfully synthesized. A hyperbranched PIL with an onion-like topography, containing a poly(1,3-diether) core, a polar imidazolium inner shell and a non-polar outer alkyl shell, was synthesized[76]. This system was proven to be highly stable under harsh conditions resulting in it being a promising material for use in nano-reactors and as a host for various functional materials. K. Pu et al.[92] reported a novel route to prepare fluorescent core–shell nanoparticles based on a hyper-branched PIL (HCPE) for cell imaging. Hyper-branched cationic poly-fluorine (PF) constitutes the core component of the HPCE and serves as a stable light-emitting center. This PF is covered by linear poly(ethylene glycol) (PEG), which acts as a passive layer on the macromolecular surface and, moreover, adds good cyto-compatibility properties to the whole structure. Because of the shape persistence of the rigid core, the HCPE molecules form single-molecular nano-spheres, facilitating their uptake for cell imaging. In a number of publications, star-like PIL structures were synthesized by using mainly polyhedral oligomeric silsesquioxane (POSS)-bearing ionic liquids and tetraalkylammonium compounds[88,93,94].

For smart material applications, redox-active PILs have great potential. This class of PIL is made from an ionic liquid monomer bearing redox-active sites. Like others PILs, redox-active PILs can be synthesized either in bulk solution or onto surface. X. Sui et al.[95] reported the preparation of cross-linkable PILs bearing ferrocene moieties by using a PES – PIL hydrogel as described in Figure 1.12.

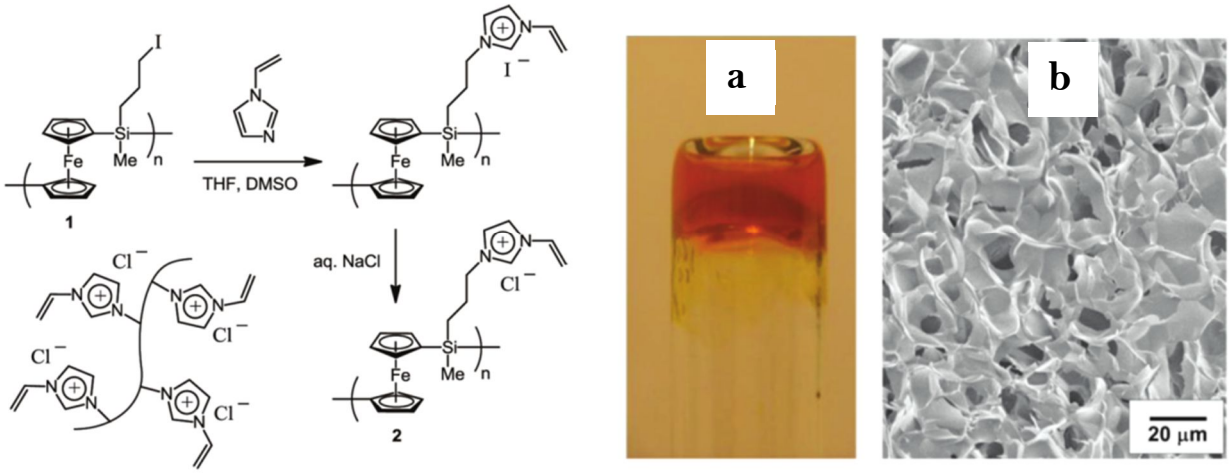

Figure 1.12 ***(Left)*** Synthesis of Cross-Linkable PFS-PIL ***(Right)*** ***(a)*** Photograph of a PFS-PIL macroscopic hydrogel; ***(b)*** SEM image of a PFS-PIL hydrogel after freeze-drying.

Poly(ferrocenyl(3-iodopropyl)-methylsilane) was mixed with 1-vinylimidazolium leading to quaternarization. A PES – PIL hydrogel (Figure 1.12) was then prepared by performing photo-initiated polymerization under UV-irradiation in the presence of a photo-initiator (Irgacure 2959). A relatively low glass transition and high decomposition temperature was observed for the PES – PIL (T_g = 48 °C, T_d = 350 °C). Reversible oxidation and the reverse reaction were carried out by adding an oxidant and a reducer to the hydrogel, leading to a color change of the gel. This work highlighted the feasibility of this new class of redox-responsive organometallic polymers. Later, Randriamahazaka et al. prepared surfaces functionalized with poly(3– (2–methacryloyloxyethyl) –1– (N– (ferrocenylmethyl)imidazolium TFSI)) by using SI-ATRP[74,96]. The initiator was first immobilized onto the surface by electrochemical oxidation of the primary amine in aqueous solution. The polymerization process was performed by dipping the surface-initiated electrode into an ionic liquid solution containing a millimolar concentration of the monomer, a catalytic amount of activator, a small amount of deactivator and a complexing agent under an inert atmosphere (Figure 1.13).

The thickness of the polymer film was followed over time by both electrochemistry and surface characterization techniques (XPS, AFM, and SEM) as illustrated in Figure 1.13. The Fc-PIL-modified electrodes were electrochemically characterized in usual organic solvents and ionic liquid media, showing a high stability with a small decrease in the ferrocene signal. Interestingly, it was proven that the Fc-PIL could act as a self-double layer. Indeed, the ferrocene electrochemical signal of the attached poly(FcIL) was observed in free-supporting electrolyte acetonitrile solution. The authors also demonstrated a possible application of the poly(FcIL) as an electrochemically reversible surface wettability system and as an electrochemical sensor for catalytic activity toward the oxidation of tyrosine.

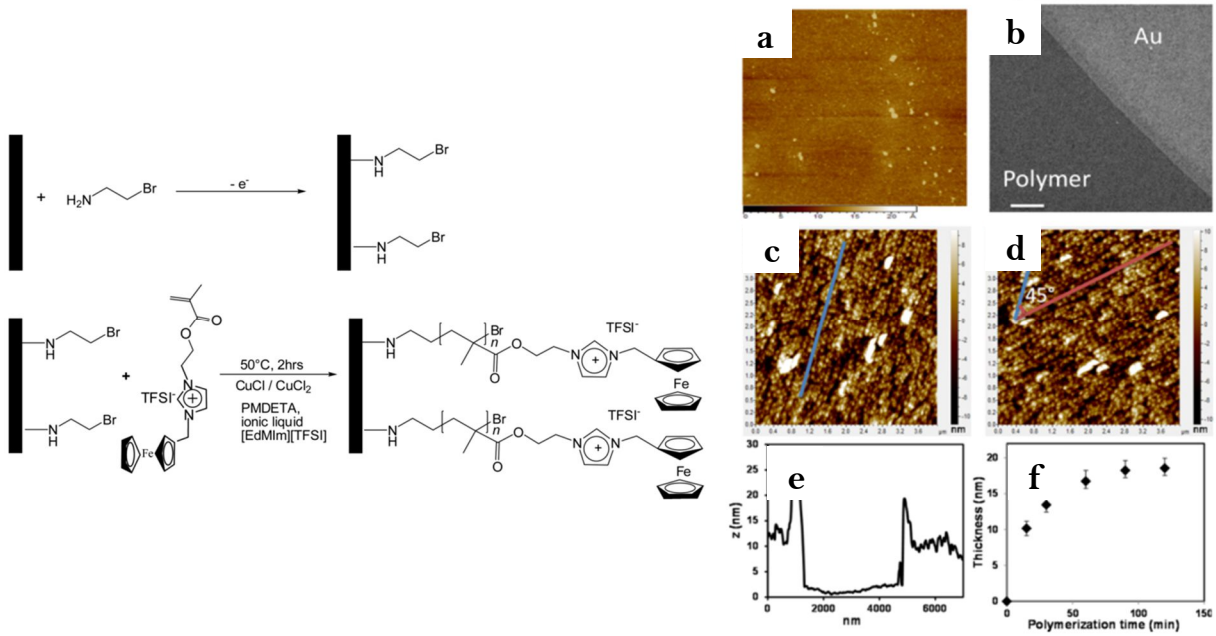

Figure 1.13 (Left) Attachment of initiator layer through electrochemical oxidative grafting of bromo-ethylamine followed by polymerization using ATRP in ionic liquid media ***(Right) (a)*** AFM topography image of Au modified with the initiator layer. ***(b)*** SEM image of the poly(FcIL) growth on Au. Scale bare 1 μm. ***(c)*** AFM topography image of poly(FcIL) onto Au substrate, image size 4 × 4 μm2. (d) AFM topography image performed in the same area as in c using scan angle of 45°. ***(e)*** Cross-section after scratch AFM experiment. ***(f)*** Evolution of poly(FcIL) film thickness as a function of polymerization time for the SI-ATRP.

1.5.2 Physicochemical Properties

Poly(ionic liquid)s are used nowadays as important ionic polyelectrolytes for solid state devices. Recent studies have been performed in order to gain insight into the intrinsic properties of PILs (ionic conductivity, glass transition temperature, decomposition, etc.). Different parameters should be taken into consideration for influencing the ionic conductivity of PILs. The nature of the cation can strongly affect the ionic conductivity of the PIL. Thus, when changing the cation from ammonium, to imidazolium or pyrrolium, the conductivity changes considerably (10^{-7} S cm^{-1}, 3×10^{-7} S.cm^{-1} and 3×10^{-6} S.cm^{-1}, respectively)[97]. In addition, the length of the spacer also plays an important role. It was proven that shortening the spacer between the cation and the polymeric main chain results in a decrease in the conductivity. As an example, the conductivity changes from 2.4×10^{-10} S.cm^{-1} to 3.2×10^{-6} S.cm^{-1} when the spacer is changed from ethyl to undecyl in poly(imidazolium)-based ILs[97]. When introducing a flexible spacer, such as poly- or oligo(ethylene oxide), a drastic increase in the conductivity was recorded with a 2 orders of magnitude enhancement (10^{-4} S.cm^{-1}) compared to the equivalent alkyl spacer[98]. Unlike for cationic PILs, in the case of anionic PILs, the spacer has to be as short as possible to get a high conductivity[59]. When keeping the same cation ($EtMeIm^+$), the conductivity increases from poly(p-styrenesulfonate) ($\sigma = 1.1 \times 10^{-8}$ S.cm^{-1}) to poly(sulfonate) ($\sigma = 1.1 \times 10^{-4}$ S.cm^{-1}). The explanation for this change might be attributed to

the size effect of the anion on the mobility of the imidazolium cation. In summary, the ionic conductivity of a PIL is partially due to the degree of freedom of the positively charged ion, either in the main chain or free in the anionic polymer matrix. This is evidenced by the augmentation of the conductivity with an increase in the length of the spacer for cationic polymers and a decrease in the linker length for anionic PILs. Moreover, for cationic PILs, the anions also have an impact on the conductivity of the corresponding PIL. The influence of different anions on the conductivity of poly(1-Et-3-MeIm$^+$) was investigated and found to be in the following order (50 Hz, 20 °C): $CF_3SO_3^-$ (6.52×10^{-11} S.cm^{-1}) < $(CF_3SO_2)_2N^-$ (1.27×10^{-10} S.cm^{-1}) < $(CN)_2N^-$ (2.09×10^{-6} S.cm^{-1})[99]. For 1-[2-(methacryloyloxy)ethyl]-3-butylimidazolium based PIL, the influence of anions was also investigated where PF_6^- ($2.5.10^{-6}$ S.cm^{-1}) < BF_4^- (5.10^{-6} S.cm^{-1}) < $CF_3SO_3^-$ (1.25×10^{-5} S.cm^{-1}) < $(CF_3SO_2)_2N^-$ (3.2×10^{-4} S.cm^{-1}) at 110 °C[100]. This effect is attributed to several parameters, including the anion size, the delocalization of the negative charge and the ability of the anion to interact with the polymer backbone. Besides the impact of the PIL structure on its conductivity, the environment also plays an important role. Typically, the addition of an ionic liquid solution to the polymer matrix results in an enhancement in the ionic conductivity of PIL electrolytes. The ionic conductivities were 6.76×10^{-3} S.cm^{-1}, 2.92×10^{-3} S.cm^{-1} and 5.83×10^{-3} S.cm^{-1} for the IL-, poly[BVIm$^+$][TFSI$^-$]/IL mixture- and poly[BVIm$^+$][HIm$^+$][TFSI$^-$]/IL mixture-based electrolytes, respectively[101]. Other parameters should also be taken into consideration, such as the water content in the PIL matrix or the impact of the co-block polymer on the final conductivity, etc.

In parallel with the ionic conductivity of the PIL, the thermal properties of the material are a key factor that makes PILs interesting materials for various applications. Generally, ionic liquids and poly(ionic liquid)s have rather low T_g values in comparison to other salts. As there is a relationship between conductivity and T_g, the parameters mentioned above also have an impact on T_g. At the same temperature, a PIL that has a lower T_g is more flexible and more dynamic than the others, resulting in a high mobility of the residual ions. Poly[VIm][TMEN][TFSI] bearing 2 cations (imidazolium and ammonium) exhibits a relatively high glass transition temperature of around 106.6 °C[102] compared to mono-cationic PILs (T_g = 80 °C for poly[2-(methacryloyloxy) ethyl]-N,N,N-trimethylammonium] and 28 °C for poly[1-[2-(methacryloyloxy) ethyl]-3-methylimidazolium][97]). The introduction of boron into the IL monomer structure causes the corresponding polymer to have a very low glass transition temperature (T_g = −59 °C to −45 °C)[103]. It has been empirically accepted that there is a linear relationship between the ionic conductivity and the glass transition temperature (when a PIL has a lower glass transition temperature, its conductivity is higher).

1.6 APPLICATIONS OF POLY(IONIC LIQUID)S

1.6.1 Nano-structuration

Since ionic liquids and poly(ionic liquid)s were considered as advanced materials for green chemistry, new efforts to make micro/nano-structures from and/or with poly(ionic liquid)s have been launched. Among the different forms of nano-structuration, nanoparticles, which are the bridge between the bulk material and molecules, have attracted a great interest. Recently, poly(ionic liquid) nanoparticles with controllable, tunable shapes and well-organized inner structural domains below 5 nm were reported for the first time[78,104]. It was also reported that a small change in the chemical structure of the ionic liquid monomers or the pH of the medium changes the morphology of the synthesized particles. As a consequence, by increasing the length of the alkyl chain of 1-vinyl-1,2,4-triazolium-type ionic liquids, self-assembled wasp-like ellipsoids and onion-like particles were obtained. This results from the energy balance between 3 components, the hydrophobic side chain, the positively charged triazolium and the surface energy of the particle. Indeed, with a longer hydrophobic tail (TILM-C_{16}Br), the exposure of the surface to the aqueous phase is energetically unfavorable, which causes a morphological change from lamellar ellipsoid to vesicular particles. Understanding the physical-chemical properties and the self-ordering in a complex polymer system can be utilized to make functional polymer nanoparticles.

Benefitting from the extremely low vapor pressure of RTILs, poly(ionic liquid)s were prepared under high vacuum using focused ion beam (FIB)[105] and electron beam (EB) irradiation[106] (Figure 1.14).

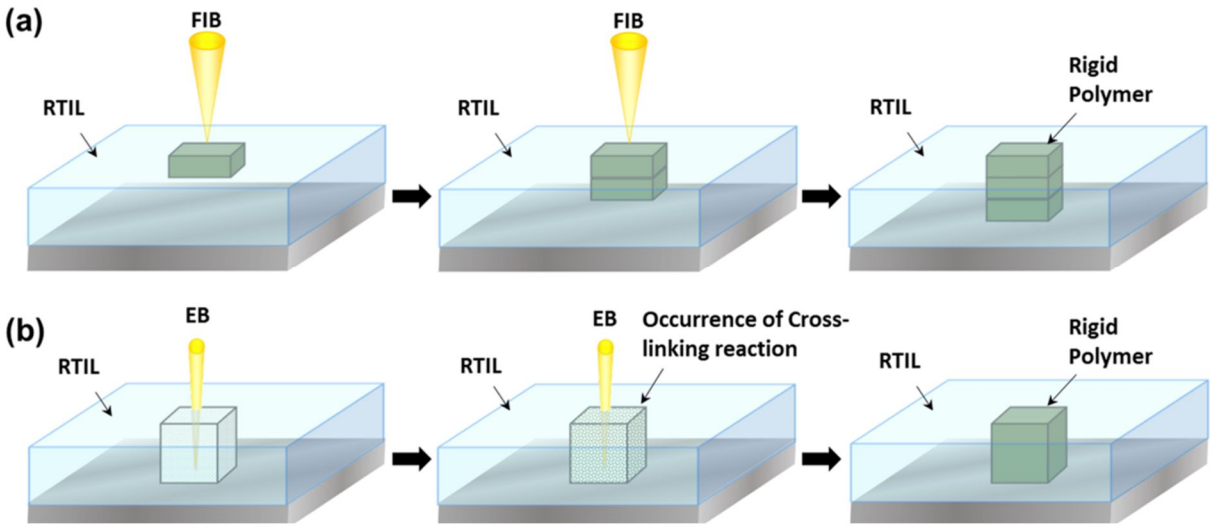

Figure 1.14 Illustrations of the polymer formation mechanism for ***(a)*** the FIB-RTIL method and ***(b)*** the EB-RTIL method.

These techniques use high energy particles to generate radicals inside the ionic liquid monomer, which makes the polymerization process possible. The difference between the two techniques is related to the penetration distance of the irradiated beam. The polymerization using FIB

irradiation is carried out at the ionic liquid/vacuum interface, while electron beams (EB) penetrate deeper inside the liquid resulting in polymerization throughout the whole irradiated volume (Figure 1.15).

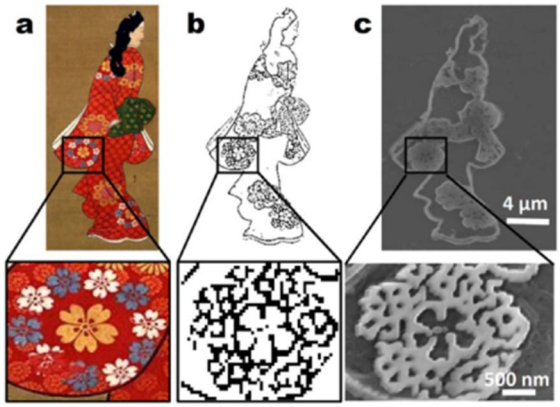

Figure 1.15 (a) A famous Japanese picture titled, ‘‘Beauty Looking Back.’’ This picture was painted by a Japanese artist, Moronobu Hishikawa, in the Edo period. ***(b)*** Bitmap image of ‘‘Beauty Looking Back’’ created for the FIB drawing. ***(c)*** SEM image of a 2D polymer structure fabricated from the bitmap image. The enlarged view of the flower painted on the ‘‘Kimono’’ is shown under each picture. The irradiation conditions for fabrication of this structure were the ion dose of 100.10^{15} ions.cm^{-2} and the number of scanning of 33 times.

The resolution of the FIB and EB approaches can reach sub-hundred nanometer scales (Figure 1.16).

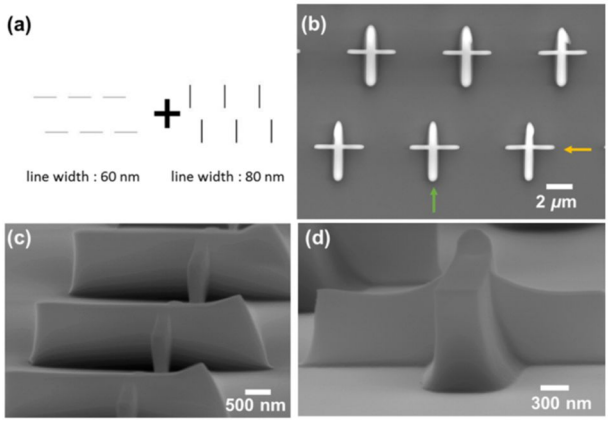

Figure 1.16 Cross-shaped structures prepared by two-step irradiation: ***(a)*** irradiation design indicating the two-step irradiation, ***(b)*** top-view SEM image of deposited structures, ***(c, d)*** side-view SEM images observed from the direction represented in ***(b)*** by ***(c)*** orange and ***(d)*** green arrows. The dose condition was 200 mC.cm^{-2}.

The development of these techniques for making poly(ionic liquid)s with well-defined patterns can be helpful to fabricate micro-devices and micro-machines, or even for ionic liquid-based electronic devices. However, the biggest drawback of the ion/electron beam techniques is that they are time consuming, high cost, and only suitable for small-scale fabrication, so they are

not suitable for industrial production. Large-area preparation of ionic liquid patterns is continuously improving through ongoing researches. A mesoporous ionic liquid network was successfully prepared by using a hard-template of silica nanoparticles, in which the ionic liquid was grown by polymerization at the interstitial voids, resulting in inorganic–organic networks. By etching the silica template in 1 M NaOH, a mesoporous ionic liquid structure is produced with a specific surface area of around 150 – 220 $m^2.g^{-1}$.

On the other hand, based on poly(ionic liquid)s, different nanostructured materials have already been made. Briefly, imidazolium-based ionic liquid polymers were used as precursors for the preparation of mesoporous graphitic carbon materials[107,108]. Typically, 1-vinyl-3-ethylimidazolium bromide (IL–a), 1-vinyl-3-ethylimidazolium dicyanamide (IL–b),1-vinyl-3-cyanomethylimidazolium bromide (IL–c), and 1-vinyl-3-cyanopropylimidazolium bromide (il-IL–d) were pyrolyzed at 900 °C–1000 °C in the presence of $FeCl_2$, and the polymerization process occurred simultaneously with the carbonization process resulting highly conductive, mesoporous, n-doped graphitic carbon materials. These recent results opened a new and facile route to prepare interesting metal-free materials for energy applications.

1.6.2 Switchable Devices

Like some chameleons, PILs can adapt their behaviors upon external stimuli or environmental change. Researchers in the field of polymer materials have been trying to mimic this interesting behavior for the last three decades. Their efforts have given birth to a novel concept, smart polymers. By following this rational idea, poly(ionic liquid)s with their unique properties were used for the construction of smart polymers for switchable devices. Among different aspects, the wettability of the material surface plays an important role for self-cleaning materials and anticorrosion. As ionic liquids and poly(ionic liquid)s are sensitive to water, PILs can be used for the efficient switchable wetting of surfaces based on counter-anion exchange. X. He et al.[58] reported the preparation of poly[1-(4-vinylbenzyl)-3-butylimidazoliumPF_6] by SI-ATRP on a silicon wafer and its application to static tunable-wettability surfaces. The as-prepared PIL with PF_6^- as anion showed a rather hydrophobic response (95°). Then ion exchange was carried out by dipping the substrate into NaCl solution, which promoted the formation of a hydrophilic surface due to the formation of PIL – Cl^- (contact angle = 41°). By switching again from Cl^- to PF_6^- anions, the hydrophobic behavior was reversed leading to reversible and tunable wetting of the surface (Figure 1.17a and b).

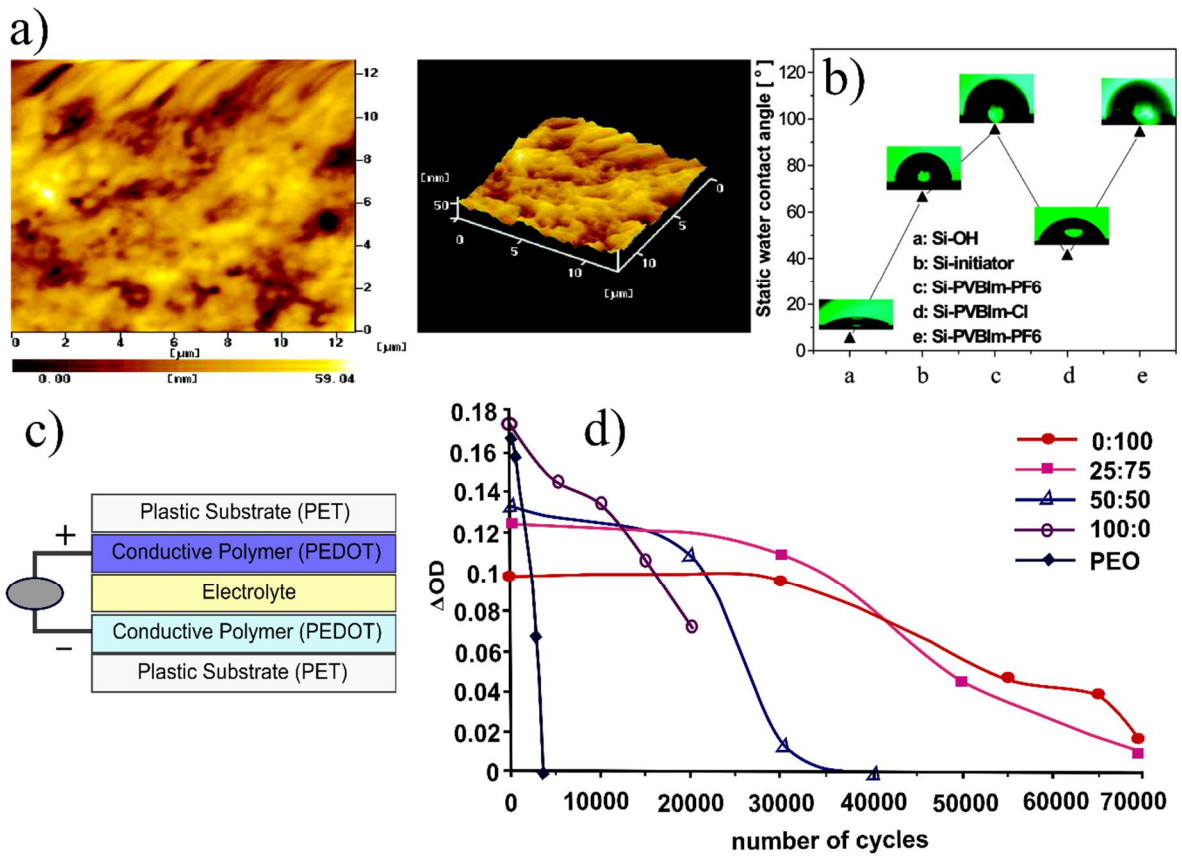

Figure 1.17 (a) AFM topography and 3D image of the PVBIm-PF6 brush modified silicon surface; ***(b)*** Changes in static water contact angles corresponding to various surfaces of silicon substrates. The ***insets*** show five photographs of the shapes of water droplets on different surfaces; ***(c)*** All-polymeric five-layer electrochromic device configuration; ***(d)*** Variation of ΔOD as a function of the number of cycles for ECDs using polymer electrolytes with different ratios [$EMIm^+$][Br^-]: poly[$ViEtIm^+$][Br^-] and using PEO/lithium triflate electrolyte.

Based on the same ion exchange concept, switchable permeability poly(ionic liquid) hollow particles were prepared via the SaPSeP method[57]. $TFSI^-$ and Br^- were chosen as exchangeable anions for the surface wetting study. As expected, the particles containing $TFSI^-$ exhibited hydrophobic behavior, whereas the particles containing Br^- exhibited a hydrophilic response. The concept of ion exchange is interesting, but it is not suitable for practical use. Electroactive PILs have entered the field as novel materials for electro-stimuli-switchable devices. The redox-active PILs are based on concerted electron transfer coupled with anion transport. Randriamahazaka et al.[74] introduced poly(3-(2-methacryloyloxyethyl)-1-(N-(ferrocenylmethyl) imidazolium TFSI)) prepared by SI-ATRP for this concept. The contact angle in the neutral state of the redox PIL-modified Au substrate was determined to be around 90°, while after oxidizing the ferrocene moieties, the contact angle decreased to rather hydrophilic (60°) and vice versa. Originally, PEDOT-bearing ionic liquid moieties were demonstrated to be eligible not only for tunable wettability surfaces but also for electrochromic devices.[109]

A reversible hydrophobic/hydrophilic switch was observed depending on the nature of the counter-anion. Higher fluorinated anions yield higher contact angles. By flushing LiTFSI solution onto a rough surface, the contact angle was determined to be around 107 ± 3°, while when flushing $LiBF_4$ solution onto the same surface, the contact angle decreased dramatically to 24 ± 3°. This process was fully reversible. By heating/cooling oxidized PEDOT – $ImBF_4Cl$ between 20 °C and 70 °C, the color of the membrane changes reversibly from blue to purple. Previously, this group also proposed the assembly of a symmetric device in which the PIL layer is sandwiched between 2 PEDOT–electrochromic layers[110]. Different IL/PIL mixtures were tested for their ECD performance. It was found that the poly[1-vinyl-3-ethylIm$^+$][Br$^-$]/ [1-vinyl-3-ethylIm$^+$][Br$^-$] mixture (75:25) offered the best performance, exceeding 70000 pulsed cycles (0 and 3 V) (Figure 1.17c and d). However, no long-life requirements are needed, giving preference to using mixtures with a higher content of IL in order to get a higher optical contrast (ΔOD). This is a promising result for the development of higher performance ECD using PILs rather than traditional polyelectrolytes.

1.6.3 Energy Applications

Supercapacitors

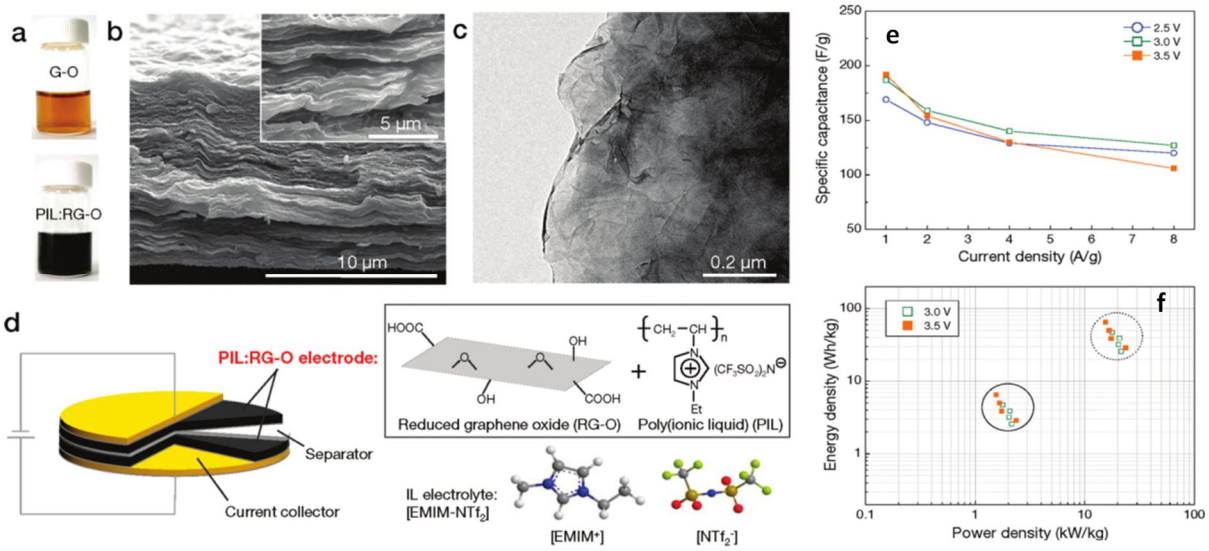

Figure 1.18 (a) Optical images of a suspension of a graphene oxide (G-O) in propylene carbonate (PC) and a poly(ionic liquid) modified reduced graphene oxide (PIL:RG-O) in PC; ***(b)*** Scanning electron microscopy (SEM) and ***(c)*** transmission electron microscopy (TEM) image of PIL:RG-O platelets; ***(d)*** Schematic diagram of the supercapacitor based on the PIL:RG-O electrodes and ionic liquid electrolyte (EMIM-NTf2); ***(e)*** Plot of specific capacitance versus the current density. (f) Plot of energy density versus power density at operating voltages of 3.0 and 3.5 V. The energy and power density were normalized to the total mass of the two electrodes employed including the electrolyte and current collector (solid circle) and the mass of two PIL: RG-O (dashed circle).

Electrochemical capacitors or supercapacitors are referred to "electric double-layer capacitors" or "pseudo-capacitors". The term double-layer refers to capacitors that physically store electrical charge at the surface–electrolyte interface, which has a high surface-area, while

pseudo-capacitors are related to a fast surface redox reaction[111]. Supercapacitors can be used as a complement to batteries or as an alternative solution for energy storage. Since the development of ionic liquids and poly(ionic liquid)s, they have been considered to be interesting materials for supercapacitors thanks to the ionic species contained inside their structures. In the past 5 years, poly(ionic liquid)s have started to be used in high performance supercapacitors. T. Kim and co-workers[112] investigated the energy storage possibility of a poly(1-ethyl- 3-vinylimidazolium) TFSI–modified graphene electrode (Figure 1.18).

The poly(ionic liquid) is linked to reduced-graphene oxide (rGO) through non-covalent interactions (cation – π interactions) resulting in a hybrid structure with advantageous performance for energy storage. A synergetic effect due to the hybrid rGO and poly(ionic liquid) was revealed by using cyclic voltammetry and galvanostatic charge–discharge with a specific capacitance of around 187 $F.g^{-1}$, a power density of 2.4 $kW.h^{-1}$ and an energy density of 6.5 $W.h.kg^{-1}$ as shown in Figure 1.18e and f. Recently, a zwitterionic poly(ionic liquid) gel electrolyte, poly(propylsulfonate dimethylammonium propylmethacrylamide), deposited on a flexible graphene electrode was reported to have a high stability (10000 charge–discharge cycles) and a high volume capacitance (300.8 $F.cm^{-3}$ at 0.8 $A.cm^{-3}$)[54]. A bi-redox ionic liquid bearing anthraquinone in the anion and tetramethylpiperidinyl-1-oxyl (TEMPO) in the cation has been proposed to enhance the performance of supercapacitors[27]. In this work, the specific energy of the supercapacitors based on activated carbon and graphene oxide electrodes could be doubled with the use of a bi-redox ionic liquid electrolyte (Figure 1.19). An immobilized redox-PIL based on imidazolium bearing ferrocene and anthraquinone was also proven to provide not only electrochromic properties but also electrochemical energy storage[96]. Beside these highlighted works, other structures have also been investigated that exhibit an electrochemical response toward energy storage[56,113,114].

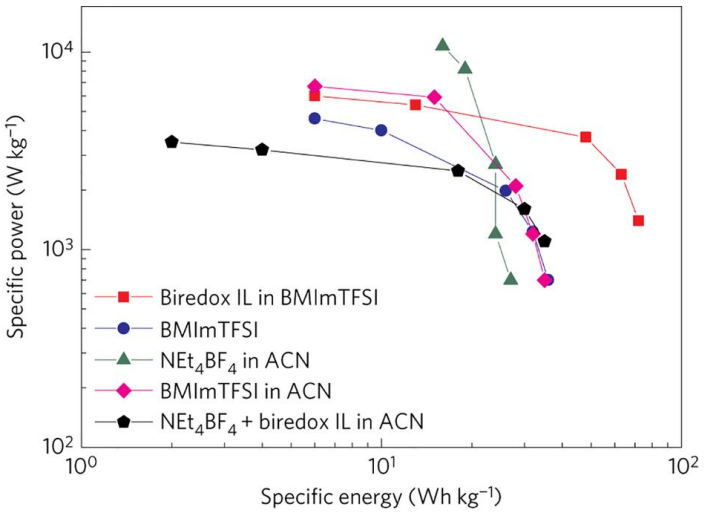

Figure 1.19 Ragone plot of supercapacitors using various electrolytes. 0.5 M biredox IL in BMImTFSI is compared to other electrolytes in symmetric PICA-based supercapacitors: 0.5 M NEt_4BF_4 in acetonitrile (ACN), 0.5 M BMImTFSI in acetonitrile and 0.5 M NEt_4BF_4 + 0.5 M biredox IL in acetonitrile. Energy and power densities are relative to the weight of PICA carbon in both electrodes.

Li-ion batteries

Li-ion batteries, which were first reported by M. S. Whittingham[115], were commercialized by Sony in 1991. Since their initial introduction, Li-ion batteries have become the most produced and consumed batteries in the world. Due to the nativity of the technique, polymer electrolytes have already been used in order to prevent the decomposition of the organic electrolyte, and in the worst case, explosions or fires caused by using a liquid electrolyte. However, we had to wait until 2010 for the first report on the use of poly(diallyldimethylammoniumTFSI) as a polyelectrolyte for Li-ion batteries[116]. This ternary polymer electrolyte was proven to have good mechanical and chemical stability with an ionic conductivity above 10^{-4} S.cm^{-1}. This material was tested as both an electrolyte separator and a binder for the cathode material in Li/LFP batteries. The resulting battery was able to deliver 140 mA.h.g^{-1} with good capacity retention up to the medium current rate (C/5) at 40 °C. Later, M. Li et al.[117,118] reported the use of an ion gel based on guanidinium polymeric ionic liquids for rechargeable Li-batteries. It was found that their system showed good activity for Li/LFP batteries (discharge capacity around 140 mA.h.g^{-1} at C/10). However, the working temperature is relatively high for industrial applications (T = 80 °C). To fix this problem, K. Yin et al.[102] proposed the use of a di-cationic polymeric ionic liquid (Figure 1.20), poly(N,N,N-trimethyl-N-(1-vinlyimidazolium-3-ethyl)-ammonium TFSI). The Li/LFP cell assembled with this polyelectrolyte can deliver discharge capacities of about 160 mA.h.g^{-1}, 140 mA.h.g^{-1} and 120 mA.h.g^{-1} at 40 °C, 30 °C and 25 °C, respectively. It should be noted that the batteries exhibited good capacity retention at each temperature.

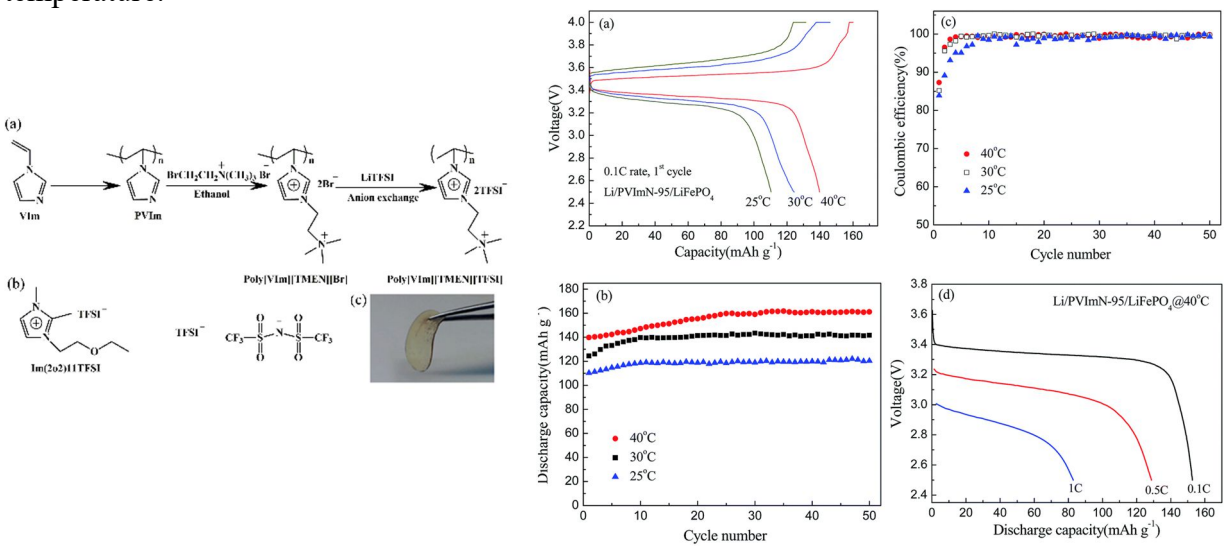

Figure 1.20 (Left) (a) Synthetic route of the imidazolium-tetraalkylammonium-based PIL. ***(b)*** Structure of IM(2o2)11TFSI. ***(c)*** Picture of a PIL-LiTFSI-IM(2o2)11TFSI electrolyte (PVImN-95 sample) ***(Right)*** Cell performance of Li/PVImN-95/$LiFePO_4$ cells. ***(a)*** Charge–discharge curves for initial cycles at three temperatures, ***(b)*** cycling performance of cells at 0.1 C as a function of temperatures, ***(c)*** cycle-number dependence of coulombic efficiency and ***(d)*** discharge curves of selected half cycles at various current rates at 40 °C, charging at 0.1 C rate and discharging at various current rates.

Toward effective ion-conducting channels with high ionic conductivity, surface-initiated atom transfer radical polymerization (ATRP) of poly(N,N-diethyl-N-(2-methacryloylethyl)-N-methylammonium TFSI) on monodisperse silica particles (SiO_2 NPs with d = 130 nm) was performed and reported by Sato et al.[119] Living radical polymerization of the ionic liquid monomer lead to the formation of a SiO_2/poly(ionic liquid) core–shell structure in which the polymer layer had M_n = 25000 and M_w/M_n = 1.13 at a monomer conversion of around 53%. By casting the hybrid particles onto an ionic liquid solution, N,N-diethyl-N-(2-methoxyethyl)-N-methylammonium TFSI, colloidal crystals were formed with an adequate composition of PSiP/DEME-TFSI (75:25 wt.%), and a solid film was formed with enough physical strength to maintain the film shape. The fabricated solid electrolyte was tested in bipolar Li batteries where two unit-cells were connected with a bipolar electrode of $Li_4Ti_5O_{12}$ and $LiMn_2O_4$ layers. The charge and discharge operation were observed between 3.0 and 6.0 V, twice as high as the unit-cell voltage (Figure 1.20). In addition, the discharge specific capacity was found to be at the mA.h scale (2.3 mA.h) with 95% coulombic efficiency, which was the best performance for a leak- and vapor-free (solid) bipolar LIB of prismatic aluminum-laminated, thin film-type. Very recently, Y. Yuan et al.[120,121] demonstrated that poly(ionic liquid)s act as efficient binders for strong improvement of the charge transfer between the solvent/salt, binder/salt and active material. Different choices of polymer moieties can give more stable binders in the high voltage region in order for them to be applied to cathode materials such as $LiCoPO_4$.

Fuel Cells

Polymer electrolytes that can conduct protons or hydroxyl groups have been investigated to develop electrolyte membranes for fuel cells[122–127]. A variety of PILs have already been used for ion-exchange membranes in fuel cells. Recent reports from Y. Feng et al.[128–130] have opened up a promising route to prepare anion-exchange membranes in alkaline media. C2-substituted imidazolium PILs exhibit a high ionic conductivity above 10^{-2} S.cm^{-1} with excellent stability over time for up to 60 h in 2 M KOH without any deterioration (poly[$DMVIm^+$][Br^-]). However, serious care has to be taken when preparing fuel cells with PILs bearing imidazolium rings because the imidazolium can undergo a ring opening reaction at high temperature in concentrated alkaline solution leading to the degradation of the membrane. Very recently, a membrane based on different quaternary ammonium triblock copolymers was reported to have advantageous properties for use as an anion – exchange membrane[131]. A small amount of degradation of the membrane was observed after exposure to 1 M of NaOH at 80 °C for 4 weeks. During a full life test for 110 h at 60 °C and 80 °C, even though the cell voltage decreased over time, there was no sign of degradation of the membrane. High fuel cell performance with a peak power density of 223 mW.cm^{-2} was observed at 60 °C. When the temperature is raised up to 80 °C, the maximum power density was obtained (240 mW.cm^{-2}). Membranes based on PILs represent an important innovation in the development and application of fuel cells.

Solid State Dye-sensitized Solar Cells (SS-DSSCs)

The use of poly(ionic liquid)s in solid state DSSCs was first investigated by studying the behaviors of poly(ionic liquid)s containing iodide as a counter-anion[132,133]. PILs can prevent problems caused by ionic liquid electrolytes, such as leakage of the liquid electrolyte and the evaporation of iodine in solution. A poly(pyridinium)-based IL containing iodide as a counter-anion/SWNTs was found to exhibit high performance (η = 3.7% under 100 mW.cm^{-2} illumination) and good stability for more than 1000 h at room temperature without sealing[133]. Poly(1-vinyl-3-propylimidazolium) iodide also gave a similar light-to-electricity conversion efficiency of 3.73 % under 10 mW.cm^{-2} illumination[132]. Later, poly(1-[(4-ethenylphenyl)methyl]-3-butyl-imidazolium iodide) (PEBII)[134] was used as a solid electrolyte in a DSSC. The polymer was casted directly onto the prepared photoelectrode and then covered with a counter-electrode. The as-prepared solid state DSSC showed a higher performance of up to 5.93 % at 100 mW.cm^{-2}, which is one of the highest energy conversion efficiencies reported for N719 dye-based, I_2-free solid state DSSCs. A bis-imidazolium-based poly(IL), poly(1-butyl-3-(1-vinylimidazolium-3-hexyl) imidazolium TFSI), which was mixed with a RTIL solution containing I_2, gave a quasi-solid-state gel electrolyte[101]. The resultant DSSCs exhibit a higher efficiency than those based on the mono-cationic PIL poly(1-butyl-3-vinylimidazoliumTFSI) (η = 5.92 %). These results provide a novel method to synthesize (quasi) solid-state DSSCs for future applications.

Electrochemical actuators

The concept of an electromechanical actuator involves the migration of charged species and the solvation shell under an electric field to the electrode surface. When these species pile up near the electrode surface, they create an over pressure at the electrode, which leads to the deformation of the material.

A flexible thin membrane, which was originally flat, tends to exhibit spontaneous bending depending on the applied electric field. From this notion, Long et al. developed a triblock and penta-block copolymer in which one of the components is a poly(ionic liquid)[135–137]. The polymer materials were swelled in different ionic liquids in order to achieve an effective actuation response at low applied potential (typically < 4 V). Mechanical property characterization using dynamic mechanical analysis displayed well-defined rubbery plateaus with high modulus storage (around 700 MPa). It should be noted that the fabrication of the ionic liquid-containing n-block copolymer afforded tunable polarity toward polar guest molecules, such as ionic liquids. The incorporation of an ionic liquid into the polymer matrix increased the ionic conductivity, which can decrease the response time and increase the curvature amplitude to 0.26 mm^{-1} within 20 s. The device then decayed back to the original position during 46 s and bent to the other side (cathode) with a final curvature of 0.67 mm^{-1} after 120 s.

Very recently, J. Yuan and co-workers[138–140] reported a series of materials based on poly(ionic liquid)s for multi-responsive behavior driven by solvent molecule adsorption. This novel approach can turn any inert object into an actuator by coating it with a cationic poly(ionic liquid). The PILTFSI/C–pillar[5]arene membrane exhibits an unprecedented fast actuation speed in response to acetone stimulus (Figure 1.21).

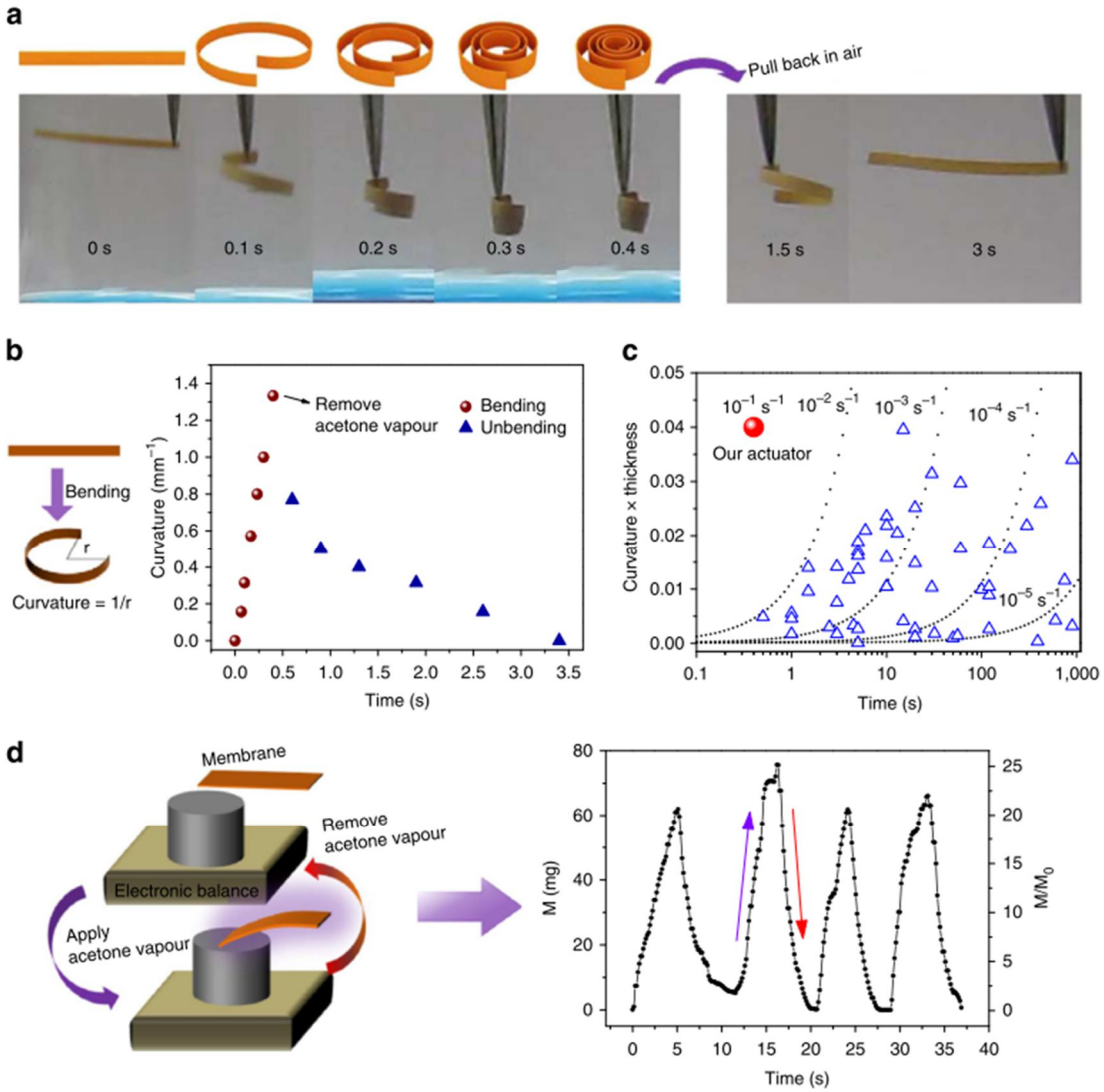

Figure 1.21 Actuation of the membrane actuator. ***(a)*** Adaptive movement of a PILTFSI/C-pillar[5]arene membrane (1mmx20mmx30mm) placed in acetone vapor (24 kPa, 20°C, left) and then back in air (right). Note: acetone solvent is stained in blue; ***(b)*** Plot of curvature against time for the membrane actuator in (a); on the left: a schematic of how the curvature is calculated; ***(c)*** Plot of curvature x thickness against time for the membrane actuator in (a) and from literature results (blue triangle) compared with lines of constant actuation speed; ***(d)*** Plot of the force generated by membrane actuator in (a) against time when the membrane was exposed to acetone vapor (24 kPa, 20°C) and air alternatively; M is the force that the actuator exerted on the balance; M_0 is the weight of the actuator membrane. On the left: schematic illustration of the experimental force measurement set-up.

Under acetone vapor (24 kPa, 20 °C), the flat membrane bent rapidly into a closed loop within 0.1 s, with the top surface inwards (Figure 1.21a), and the twisting continued until the maximum

curvature was reached (after 0.4 s). After removing the membrane from the acetone vapor chamber, the ribbon switched back to the initial form after 2 s. The actuators were tested under harsh conditions. After storage in liquid nitrogen, the membrane was cooked for 24 h at 150 °C under high pressure (100 MPa). The treated membrane remained active but with a slower response rate (0.5 s for bending into a semicircle). This novel concept opens a new route for making soft actuators that can work with a huge number of materials, like human hair, or complex systems by capture of perfume or tea tree oil vapor[139].

Sensors

The worldwide increase in human health troubles and environmental pollution has been a driving force for the development of analytical techniques that can help to quantify target substances. Following this direction, poly(ionic liquid)s have also been used for making sensor devices. K. Cui et al.[141] reported the use of fluorescent nanoparticles (FLNPs) based on poly(ionic liquid)s for the selective detection of copper ions. Their FLNPs were synthesized by mixing poly(pyridinium)-based ionic liquids with fluorescent organic molecules (2-(4-amino-2-hydroxyphenyl) benzothiazole derivatives) and additional secondary ions (azo-compounds bearing different groups). The inter-connection and the hydrophobic balance between these 3 components resulted in their assembly into nanoparticles, in which the fluorescent organic molecules quench the poly(ionic liquid) and secondary ion in the inner part of the particles, while free poly(ionic liquid) chains cover the outside part of the particles. The FL molecule–poly(ionic liquid) complex structure is crucial for enhancing the fluorescence properties of the organic molecules. Indeed, a common problem with FL organic molecules is photo-bleaching in the presence of oxygen in the solution. By using a poly(ionic liquid) as the backbone, the final complex leads not only to enhanced FL intensity, with an increase in thermal stability and overall stability, but also retardation of the photo-bleaching problem. In addition, these nanoparticles exhibit highly selective recognition for copper ions due to the formation of a AHBTA–Cu^{2+} complex, which dramatically decreases the FL intensity (down to 10%). For pH sensing applications, Q. Zhao et al. demonstrated that poly(ionic liquid)-coated optical fibers can provide a high pH sensing performance with a fast response time as shown in Figure 1.22 (right)[142]. The charged membrane using poly[1-cyanomethyl-3-vinylimidazolium TFSI] and poly(acrylic acid) was activated by immersion in aqueous ammonia resulting in the formation of a thin layer of macro pores, followed by a thick layer of nanopores (Figure 1.22 (left)). The activated membrane is stable in both aqueous and non-aqueous solution with high sensibility (2.04 and −2.48 nm per pH unit corresponding to acidic and basic medium, respectively).

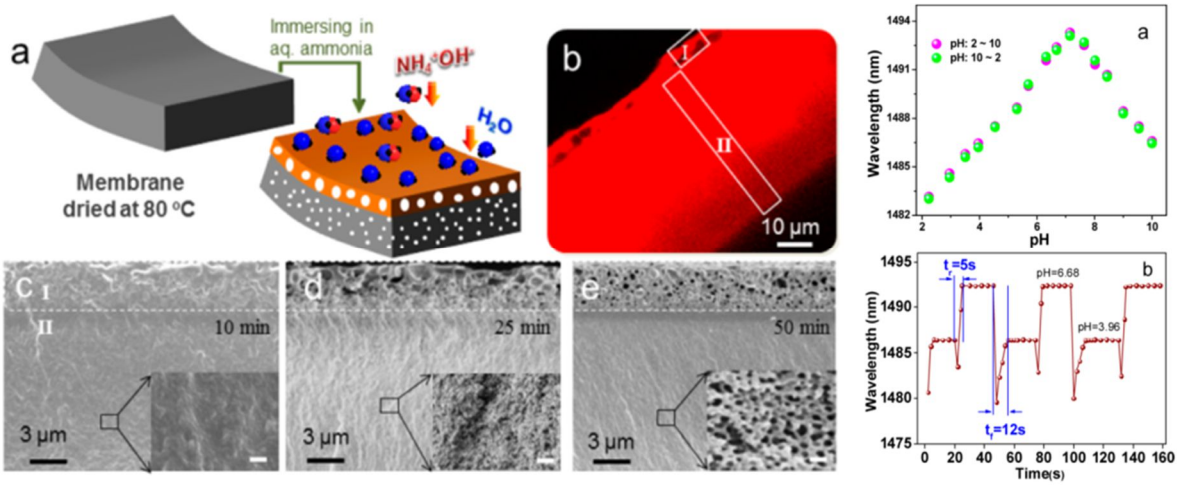

Figure 1.22 (Left) (a) Cartoon illustrating pore generation controlled by the diffusion of aqueous NH3 into the membrane. ***(b)*** Fluorescent confocal laser scanning microscopy image of the PPM cross section after the film was soaked for 2 h in 0.2 wt % aqueous NH_3 doped with 15 ppm rhodamine B. ***(c−e)*** Time-dependent cross-section structures of the membrane soaked in 0.2 wt % aqueous NH3 for 10, 25, and 50 min, respectively. Scale bars in the insets are 100 nm. ***(Right) (a)*** Response of the TCFMI pH sensor versus pH. ***(b)*** Dynamic responses of the TCFMI pH sensor in solutions with pH alternating between 6.68 and 3.96.

Poly(ionic liquid)s were also used for detecting bio-molecules such as dopamine, a neurotransmitter that is released by neurons to send a signal to other cells in order to control our feelings. 1-Vinyl-3-ethylimidazolium bromide that was polymerized onto poly(pyrrole)-modified graphene oxide (PIL/PPy/GO) was used for dopamine detection in the presence of ascorbic acid[53]. For the PPy/GO and GO electrodes, the oxidation signals of 3 mM of l-ascorbic acid (AA) and 2 μM of dopamine (DA) cannot be distinguished, resulting in 1 oxidation peak at around 0.4 V vs. Ag/AgCl. However, in the case of PIL/PPy/GO, two clearly separated peaks were observed at 0.18 V and 0.4 V for the oxidation of AA and DA, respectively. This result was explained by a double catalysis system where the hybrid material catalyzed the oxidation of AA by shifting the oxidation potential to a lower value (from 0.4 V to 0.18 V vs. Ag/AgCl) and the oxidation of DA by enhancing the current intensity. The double catalysis system is applicable in real-life because in biological media, AA and DA always coexist with a concentration ratio of around 100 to 1000, and the PIL/PPy/GO -modified GC electrode can identify the presence of DA at the same concentration ratio as reported. On the other hand, the detection limit of this system reaches 73.3 nM and the linear range is determined to be between 4 and 18 μM. Beside these cited applications of poly(ionic liquid)s, these materials can also be used for the determination of humidity[143] and for the detection of hydrogen peroxide[144].

1.7 CONCLUDING REMARKS

During the past two decades, ionic liquids and their derivatives have attracted increasing research interest as solvent–electrolytes for electrochemical processes. Recent studies have indicated the feasibility of using ionic liquids and ionic liquid-based polymers, called task-specific ionic liquids, as the main component for a large spectrum of applications. Despite the development of these materials, the number of reports is relatively limited and a fundamental understanding of IL and PIL properties is still open for further investigations. In this chapter, we have attempted to provide recent advances from fundamental research into practical uses in the field of ionic liquids. Even when being used as a green solvent, ionic liquids and their derivatives are quite harmful to the environment and human health. To resolve this problem, different approaches have been proposed in order to immobilize the ionic liquid onto various substrates, which can reduce the quantity of IL required and generate new interesting interfaces from thin layer ionic liquids to polymeric ionic liquids. In this context, self-assembled monolayers and electrochemical tools are among the most powerful techniques to graft ILs and PILs onto material surfaces from the nanoscale to a large area. These IL–modified substrates exhibit unusual behaviors compared to other organic materials, providing the possibility to use them for sensor, catalysis and energy applications, and so on. In parallel with the traditional ionic liquids, redox-active ionic liquids (Redox-IL) and redox-active polymer ionic liquids have appeared as new candidates for integration into electrochemical processes. By introducing ionic liquid moieties onto redox active compounds, the intrinsic properties of both the ionic liquid and the redox-active group change, resulting in multifunctional materials. These materials have been successfully used as electro-responsive materials for reversible electrochemically switchable wettability and electrochemical energy storage. We expect that redox-active ILs and polymers will boost the whole field of ionic liquids toward multifunctional materials and will open up possibilities for their integration into various applications.

1.8 REFERENCES

(1) Wilkes, J. S.; Levisky, J. A.; Wilson, R. A.; Hussey, C. L. Dialkylimidazolium Chloroaluminate Melts: A New Class of Room-Temperature Ionic Liquids for Electrochemistry, Spectroscopy, and Synthesis. *Inorg. Chem.* **1982**, *237* (1980), 1263–1264.

(2) Bonhôte, P.; Dias, A.-P.; Armand, M.; Papageorgiou, N.; Kalyanasundaram, K.; Grätzel, M. Hydrophobic, Highly Conductive Ambient-Temperature Molten Salts. *Inorg. Chem.* **1996**, *35* (5), 1168--1178.

(3) Schroder, U.; Wadhawan, J. D.; Compton, R. G.; Marken, F.; Suarez, P. a Z.; Consorti, C. S.; Souza, F. De. Water-Induced Accelerated Ion Diffusion: Voltammetric Studies in [BMIM][BF4]. *New J. Chem.* **2000**, *24*, 1009–1015.

(4) Koch, V. R.; Dominey, L. A.; Nanjundiah, C.; Ondrechen, M. . The Intrinsic Anodic Stability of Several Anions Comprising Solvent-Free Ionic Liquids. *J. Electrochem. Soc.* **1996**, *143* (3), 798–803.

(5) Barisci, J. N.; Wallace, G. G.; MacFarlane, D. R.; Baughman, R. H. Investigation of Ionic Liquids as Electrolytes for Carbon Nanotube Electrodes. *Electrochem. commun.* **2004**, *6* (1), 22–27.

(6) MacFarlane, D.; Meakin, P. Pyrrolidinium Imides: A New Family of Molten Salts and Conductive Plastic Crystal Phases. *J. Phys. Chem. B* **1999**, *103* (20), 4164–4170.

(7) Sun, J.; Forsyth, M.; Macfarlane, D. R. Room-Temperature Molten Salts Based on the Quaternary Ammonium Ion. *J. Phys. Chem. B* **1998**, *102* (44), 8858–8864.

(8) Noda, A.; Watanabe, M. Highly Conductive Polymer Electrolytes Prepared by in Situ Polymerization of Vinyl Monomers in Room Temperature Molten Salts. *Electrochim. Acta* **2000**, *45* (8), 1265–1270.

(9) Matsumoto, H.; Matsuda, T.; Miyazaki, Y. Room Temperature Molten Salts Based on Trialkylsulfonium Cations and Bis(Trifluoromethylsulfonyl)Imide. *Chem. Lett.* **2000**, *29* (12), 1430–1431.

(10) El Abedin, S. Z.; Moustafa, E. M.; Hempelmann, R.; Natter, H.; Endres, F. Additive Free Electrodeposition of Nanocrystalline Aluminium in a Water and Air Stable Ionic Liquid. *Electrochem. commun.* **2005**, *7* (11), 1111–1116.

(11) Jiang, T.; Chollier Brym, M. J.; Dubé, G.; Lasia, A.; Brisard, G. M. Electrodeposition of Aluminium from Ionic Liquids: Part I-Electrodeposition and Surface Morphology of Aluminium from Aluminium Chloride (AlCl3)-1-Ethyl-3-Methylimidazolium Chloride ([EMIm]Cl) Ionic Liquids. *Surf. Coatings Technol.* **2006**, *201* (1–2), 1–9.

(12) Endres, F.; Bukowski, M.; Hempelmann, R.; Natter, H. Electrodeposition of Nanocrystalline Metals and Alloys from Ionic Liquids. *Angew. Chemie - Int. Ed.* **2003**, *42*, 3428–3430.

(13) El Abedin, S. Z.; Pölleth, M.; Meiss, S. A.; Janek, J.; Endres, F. Ionic Liquids as Green Electrolytes for the Electrodeposition of Nanomaterials. *Green Chem.* **2007**, *9* (6), 549–553.

(14) Endres, F. Ionic Liquids: Solvents for the Electrodeposition of Metals and Semiconductors. *ChemPhysChem* **2002**, *3* (2), 144–154.

(15) Zein El Abedin, S.; Saad, A. Y.; Farag, H. K.; Borisenko, N.; Liu, Q. X.; Endres, F. Electrodeposition of Selenium, Indium and Copper in an Air- and Water-Stable Ionic Liquid at

Variable Temperatures. *Electrochim. Acta* **2007**, *52* (8 SPEC. ISS.), 2746–2754.

(16) Mann, O.; Pan, G. B.; Freyland, W. Nanoscale Electrodeposition of Metals and Compound Semiconductors from Ionic Liquids. *Electrochim. Acta* **2009**, *54* (9), 2487–2490.

(17) Pang, Y.; Li, X.; Ding, H.; Shi, G.; Jin, L. Electropolymerization of High Quality Electrochromic Poly(3-Alkyl-Thiophene)s via a Room Temperature Ionic Liquid. *Electrochim. Acta* **2007**, *52* (20), 6172–6177.

(18) Wei, D.; Kvarnström, C.; Lindfors, T.; Ivaska, A. Polyaniline Nanotubules Obtained in Room-Temperature Ionic Liquids. *Electrochem. commun.* **2006**, *8* (10), 1563–1566.

(19) Pringle, J. M.; Forsyth, M.; Wallace, G. G.; Macfarlane, D. R. Solution - Surface Electropolymerization : A Route to Morphologically Novel Poly (Pyrrole) Using an Ionic Liquid. *Macromolecules* **2006**, *39*, 7193–7195.

(20) Zein El Abedin, S.; Borissenko, N.; Endres, F. Electropolymerization of Benzene in a Room Temperature Ionic Liquid. *Electrochem. commun.* **2004**, *6* (4), 422–426.

(21) Liu, K.; Hu, Z.; Xue, R.; Zhang, J.; Zhu, J. Electropolymerization of High Stable Poly(3,4-Ethylenedioxythiophene) in Ionic Liquids and Its Potential Applications in Electrochemical Capacitor. *J. Power Sources* **2008**, *179* (2), 858–862.

(22) Wang, P.; Zakeeruddin, S. M.; Moser, J. E.; Humphry-Baker, R.; Graetzel, M. A Solvent-Free, SeCN-/(SeCN)3- Based Ionic Liquid Electrolyte for High-Efficiency Dye-Sensitized Nanocrystalline Solar Cells. *J. Am. Chem. Soc.* **2004**, *126* (23), 7164–7165.

(23) Balasubramanian, R.; Wang, W.; Royce W. Redox Ionic Liquid Phases: Ferrocenated Imidazoliums. *J. Am. Chem. Soc.* **2006**, *128* (31), 9994–9995.

(24) Mirkhani, S. A.; Gharagheizi, F.; Ilani-Kashkouli, P.; Farahani, N. Determination of the Glass Transition Temperature of Ionic Liquids: A Molecular Approach. *Thermochim. Acta* **2012**, *543*, 88–95.

(25) Fontaine, O.; Lagrost, C.; Ghilane, J.; Martin, P.; Trippé, G.; Fave, C.; Lacroix, J. C.; Hapiot, P.; Randriamahazaka, H. N. Mass Transport and Heterogeneous Electron Transfer of a Ferrocene Derivative in a Room-Temperature Ionic Liquid. *J. Electroanal. Chem.* **2009**, *632* (1–2), 88–96.

(26) Chen, X. J.; Xu, D.; Qiu, L. H.; Li, S. C.; Zhang, W.; Yan, F. Imidazolium Functionalized TEMPO/Iodide Hybrid Redox Couple for Highly Efficient Dye-Sensitized Solar Cells. *J. Mater. Chem. A* **2013**, *1* (31), 8759–8765.

(27) Mourad, E.; Coustan, L.; Freunberger, S. A.; Mehdi, A.; Vioux, A.; Favier, F.; Fontaine, O. Biredox Ionic Liquids: Electrochemical Investigation and Impact of Ion Size on Electron Transfer. *Electrochim. Acta* **2015**, *206*, 513–523.

(28) Mourad, E.; Coustan, L.; Lannelongue, P.; Zigah, D.; Mehdi, A.; Vioux, A.; Freunberger, S. A.; Favier, F.; Fontaine, O. Biredox Ionic Liquids with Solid-like Redox Density in the Liquid State for High-Energy Supercapacitors. *Nat. Mater.* **2016**, *1* (November).

(29) Love, J. C.; Estroff, L. A.; Kriebel, J. K.; Nuzzo, R. G.; Whitesides, G. M. Self-Assembled Monolayers of Thiolates on Metals as a Form of Nanotechnology. *Chem. Rev.* **2005**, *105* (4), 1103–1169.

(30) Bélanger, D.; Pinson, J. Electrografting: A Powerful Method for Surface Modification. *Chem. Soc. Rev.* **2011**, *40* (7), 3995–4048.

(31) Uhlmann, P.; Ionov, L.; Houbenov, N.; Nitschke, M.; Grundke, K.; Motornov, M.; Minko, S.; Stamm, M. Surface Functionalization by Smart Coatings: Stimuli-Responsive Binary Polymer Brushes. *Prog. Org. Coatings* **2006**, *55* (2), 168–174.

(32) Anthony, J. E. Functionalized Acenes and Heteroacenes for Organic Electronics. *Chem. Rev.* **2006**, *106* (12), 5028–5048.

(33) Querner, C.; Reiss, P.; Bleuse, J.; Pron, A. Chelating Ligands for Nanocrystals' Surface Functionalization. *J. Am. Chem. Soc.* **2004**, *126* (37), 11574–11582.

(34) Dong, A.; Ye, X.; Chen, J.; Kang, Y.; Gordon, T.; Kikkawa, J. M.; Murray, C. B. A Generalized Ligand-Exchange Strategy Enabling Sequential Surface Functionalization of Colloidal Nanocrystals. *J. Am. Chem. Soc.* **2011**, *133* (4), 998–1006.

(35) Kakade, B. a.; Pillai, V. K. Tuning the Wetting Properties of Multiwalled Carbon Nanotubes by Surface Functionalization. *J. Phys. Chem. C* **2008**, *112* (9), 3183–3186.

(36) Forrest, S. R. The Path to Ubiquitous and Low-Cost Organic Electronic Appliances on Plastic. *Nature* **2004**, *428* (6986), 911–918.

(37) Wang, Q. H.; Hersam, M. C. Room-Temperature Molecular-Resolution Characterization of Self-Assembled Organic Monolayers on Epitaxial Graphene. *Nat. Chem.* **2009**, *1* (3), 206–211.

(38) Lao, C.; Li, Y.; Wong, C. P.; Wang, Z. L. Enhancing the Electrical and Optoelectronic Performance of Nanobelt Devices by Molecular Surface Functionalization. *Nano Lett.* **2007**, *7* (5), 1323–1328.

(39) Lee, B. S.; Chi, Y. S.; Lee, J. K.; Choi, I. S.; Song, C. E.; Namgoong, S. K.; Lee, S. G. Imidazolium Ion-Terminated Self-Assembled Monolayers on Au: Effects of Counteranions on Surface Wettability. *J. Am. Chem. Soc.* **2004**, *126* (2), 480–481.

(40) Chi, Y. S.; Hwang, S.; Lee, B. S.; Kwak, J.; Choi, I. S.; Lee, S. G. Anion Exchange-Promoted Ru3+/2+ Redox Switch in Self-Assembled Monolayers of Imidazolium Ions on a Gold Electrode. *Langmuir* **2005**, *21* (10), 4268–4271.

(41) Bouden, S.; Gómez-Mingot, M.; Randriamahazaka, H.; Ghilane, J. Surface Initiated Immobilization of Molecules Contained in an Ionic Liquid Framework. *Anal. Chem.* **2016**, *88* (1), 1017–1021.

(42) Bouden, S.; Trippé-Allard, G.; Ghilane, J.; Randriamahazaka, H. Electrochemical Immobilization of Redox Active Molecule Based Ionic Liquid. *Electrochem. commun.* **2015**, *58*, 65–68.

(43) Itoh, H.; Naka, K.; Chujo, Y. Synthesis of Gold Nanoparticles Modified with Ionic Liquid Based on the Imidazolium Cation. *J. Am. Chem. Soc* **2004**, *126* (10), 3026–3027.

(44) Ratel, M.; Provencher-Girard, A.; Shuo Zhao, S.; Breault-Turcot, J.; Labrecque-Carbonneau, J.; Branca, M.; Pelletier, J. N.; Schmitzer, A. R.; Masson, J.-F. Imidazolium-Based Ionic Liquid Surfaces for Biosensing. *Anal. Chem.* **2013**, *85* (12), 5770–5777.

(45) Gadenne, B.; Hesemann, P.; Moreau, J. J. E. Supported Ionic Liquids: Ordered Mesoporous Silicas Containing Covalently Linked Ionic Species. *Chem. Commun.* **2004**, 1768–1769.

(46) Zhang, M.; Chen, J.; Qiu, H.; Mallik, A. K.; Takafuji, M.; Ihara, H. Homogenous Formation and Quaternization of Urea-Functionalized Imidazolyl Silane and Its Immobilization on Silica for Surface-Confined Ionic Liquid Stationary Phases. *RSC Adv.* **2014**, *4* (65), 34654–34658.

(47) Marins, J. a.; Soares, B. G.; Silva, a. a.; Livi, S. Silica Prepared in the Presence of Alkylphosphonium-Based Ionic Liquids and Its Performance in Electrorheological Fluids. *RSC Adv.* **2014**, *4* (92), 50925–50931.

(48) Gomez-Mingot, M.; Bui-Thi-Tuyet, V.; Trippe-Allard, G.; Ghilane, J.; Randriamahazaka, H. Oxidative Grafting of a Redox-Molecule-Based Ionic Liquid onto an Electrode Surface: Anion Exchange within a Layer. *ChemElectroChem* **2014**, *1* (9), 1467–1470.

(49) Bui-Thi-Tuyet, V.; Trippe-Allard, G.; Ghilane, J.; Randriamahazaka, H. Surface Functionalization of Ferrocene Based Ionic Liquid onto Carbon Surface Using Stepwise Grafting. *J. Electroanal. Chem.* **2014**, *713*, 28–31.

(50) Hazimeh, H.; Pioge, S.; Combellas, C.; Podvorica, F. I. Radical Chemistry from Diazonium-Terminated Surfaces. *Chem. Mater.* **2013**, *25*, 605–612.

(51) Ghilane, J.; Lacroix, J. C. Formation of a Bifunctional Redox System Using Electrochemical Reduction of Platinum in Ferrocene Based Ionic Liquid and Its Reactivity with Aryldiazonium. *J. Am. Chem. Soc.* **2013**, *135* (12), 4722–4728.

(52) Yuan, J.; Mecerreyes, D.; Antonietti, M. Poly(Ionic Liquid)s: An Update. *Prog. Polym. Sci.* **2013**, *38* (7), 1009–1036.

(53) Mao, H.; Liang, J.; Zhang, H.; Pei, Q.; Liu, D.; Wu, S.; Zhang, Y.; Song, X. M. Poly(Ionic Liquids) Functionalized Polypyrrole/Graphene Oxide Nanosheets for Electrochemical Sensor to Detect Dopamine in the Presence of Ascorbic Acid. *Biosens. Bioelectron.* **2015**, *70*, 289–298.

(54) Peng, X.; Liu, H.; Yin, Q.; Wu, J.; Chen, P.; Zhang, G.; Liu, G.; Wu, C.; Xie, Y. A Zwitterionic Gel Electrolyte for Efficient Solid-State Supercapacitors. *Nat. Commun.* **2016**, *7* (May), 11782.

(55) Qiu, B.; Lin, B.; Yan, F. Ionic Liquid/Poly(Ionic Liquid)-Based Electrolytes for Energy Devices. *Polym. Int.* **2013**, *62* (3), 335–337.

(56) Zhou, T.; Gao, X.; Dong, B.; Sun, N.; Zheng, L. Poly(Ionic Liquid)s Hydrogels Exhibiting Superior Mechanical and Electrochemical Properties as Flexible Electrolytes. *J. Mater. Chem. A Mater. energy Sustain.* **2015**, *4*, 1112–1118.

(57) Nakamura, R.; Tokuda, M.; Suzuki, T.; Minami, H. Preparation of Poly(Ionic Liquid) Hollow Particles with Switchable Permeability. *Langmuir* **2016**, *32* (10), 2331–2337.

(58) He, X.; Yang, W.; Pei, X. Preparation , Characterization , and Tunable Wettability of Poly (Ionic Liquid) Brushes via Surface-Initiated Atom Transfer Radical Polymerization. *Macromolecules* **2008**, *41*, 4615–4621.

(59) Ohno, H.; Yoshizawa, M.; Ogihara, W. Development of New Class of Ion Conductive Polymers Based on Ionic Liquids. *Electrochim. Acta* **2004**, *50* (2–3 SPEC. ISS.), 255–261.

(60) Ogihara, W.; Washiro, S.; Nakajima, H.; Ohno, H. Effect of Cation Structure on the Electrochemical and Thermal Properties of Ion Conductive Polymers Obtained from Polymerizable Ionic Liquids. *Electrochim. Acta* **2006**, *51* (13), 2614–2619.

(61) Washiro, S.; Yoshizawa, M.; Nakajima, H.; Ohno, H. Highly Ion Conductive Flexible Films Composed of Network Polymers Based on Polymerizable Ionic Liquids. *Polymer (Guildf).* **2004**, *45* (5), 1577–1582.

(62) Yuan, J.; Antonietti, M. Poly(Ionic Liquid)s: Polymers Expanding Classical Property Profiles. *Polymer (Guildf).* **2011**, *52* (7), 1469–1482.

(63) Mecerreyes, D. Polymeric Ionic Liquids: Broadening the Properties and Applications of Polyelectrolytes. *Prog. Polym. Sci.* **2011**, *36* (12), 1629–1648.

(64) Shaplov, A. S.; Marcilla, R.; Mecerreyes, D. Recent Advances in Innovative Polymer Electrolytes Based on Poly(Ionic Liquid)S. *Electrochim. Acta* **2015**, *175* (March), 18–34.

(65) Lu, J.; Yan, F.; Texter, J. Advanced Applications of Ionic Liquids in Polymer Science. *Prog. Polym. Sci.* **2009**, *34* (5), 431–448.

(66) Green, M. D.; Long, T. E. Designing Imidazole-Based Ionic Liquids and Ionic Liquid Monomers for Emerging Technologies. *Polym. Rev.* **2009**, *49* (4), 291–314.

(67) Green, O.; Grubjesic, S.; Lee, S.; Firestone, M. A. The Design of Polymeric Ionic Liquids for the Preparation of Functional Materials. *J. Macromol. Sci. R , Part C Polym. Rev.* **2009**, *49* (May 2013), 339–360.

(68) Shaplov, A. S.; Marcilla, R.; Mecerreyes, D. Recent Advances in Innovative Polymer Electrolytes Based on Poly(Ionic Liquid)S. *Electrochim. Acta* **2015**, *175*, 18–34.

(69) Salamone, J. C.; Israel, S. C.; Taylor, P.; Snider, B. Synthesis and Homopolymerization Studies of Vinylimidazolium Salts. *Polymer (Guildf).* **1973**, *14* (12), 639–644.

(70) He, H.; Zhong, M.; Luebke, D.; Nulwala, H.; Matyjaszewski, K. Atom Transfer Radical Polymerization of Ionic Liquid Monomer: The Influence of Salt/Counterion on Polymerization. *J. Polym. Sci. Part A Polym. Chem.* **2014**, *52* (15), 2175–2184.

(71) He, H.; Luebke, D.; Nulwala, H.; Matyjaszewski, K. Synthesis of Poly(Ionic Liquid)s by Atom Transfer Radical Polymerization with Ppm of Cu Catalyst. *Macromolecules* **2014**, *47* (19), 6601–6609.

(72) Mori, H.; Yanagi, M.; Endo, T. RAFT Polymerization of N-Vinylimidazolium Salts and Synthesis of Thermoresponsive Ionic Liquid Block Copolymers. *Macromolecules* **2009**, *42* (21), 8082–8092.

(73) Vijayakrishna, K.; Jewrajka, S. K.; Ruiz, A.; Marcilla, R.; Pomposo, J. A.; Mecerreyes, D.; Taton, D.; Gnanou, Y. Synthesis by RAFT and Ionic Responsiveness of Double Hydrophilic Block Copolymers Based on Ionic Liquid Monomer Units. *Macromolecules* **2008**, *41* (17), 6299–6308.

(74) Bui-Thi-Tuyet, V.; Trippe-Allard, G.; Ghilane, J.; Randriamahazaka, H. Surface and Electrochemical Properties of Polymer Brush-Based Redox Poly(Ionic Liquid). *ACS Appl. Mater. Interfaces* **2016**, *8* (42), 28316–28324.

(75) Wilke, A.; Yuan, J.; Antonietti, M.; Weber, J. Enhanced Carbon Dioxide Adsorption by a Mesoporous Poly(Ionic Liquid). *ACS Macro Lett.* **2012**, *1* (8), 1028–1031.

(76) Schüler, F.; Kerscher, B.; Beckert, F.; Thomann, R.; Mülhaupt, R. Hyperbranched Polymeric Ionic Liquids with Onion-like Topology as Transporters and Compartmentalized Systems. *Angew. Chemie - Int. Ed.* **2013**, *52*, 455–458.

(77) Shevchenko, V. V; Stryutsky, A. V; Klymenko, N. S.; Gumenna, M. A.; Fomenko, A. A.; Bliznyuk, V. N.; Trachevsky, V. V; Davydenko, V. V; Tsukruk, V. V. Protic and Aprotic Anionic Oligomeric Ionic Liquids. *Polymer (Guildf).* **2014**, *55* (16), 3349–3359.

(78) Yuan, J.; Soll, S.; Drechsler, M.; Mueller, A. H. E.; Antonietti, M. Mesostructure Formation and Directional Alignment in One Step Self-Assembly of Poly (Ionic Liquid) S : Polymerization ,

Mesostructure Formation and Directional Alignment in One Step. *J. Am. Chem. Soc.* **2011**, *133*, 17556–17559.

(79) Canilho, N.; Scholl, M.; Klok, H.; Mezzenga, R.; Muse, C.; Fribourg, C.-; Polyme, L.; Mate, I.; Fe, Ä. P. Thermotropic Ionic Liquid Crystals via Self-Assembly of Cationic Hyperbranched Polypeptides and Anionic Surfactants. *Macromolecules* **2007**, *40*, 8374–8383.

(80) Schadt, K.; Kerscher, B.; Thomann, R.; Mu, R. Structured Semi Fl Uorinated Polymer Ionic Liquids for Metal Nanoparticle Preparation and Dispersion in Fluorous Compartments. *Macromolecules* **2013**, *46*.

(81) Kerscher, B.; Appel, A.; Thomann, R.; Mu, R. Treelike Polymeric Ionic Liquids Grafted onto Graphene Nanosheets. *Macromolecules* **2013**, *46*.

(82) Porphyrins, D.; Tomioka, N.; Takasu, D. Electrostatic Assembly of Dendrimer Electrolytes : Negatively and Positively Charged. *Angew. Chemie - Int. Ed.* **1998**, *37*, 1531–1534.

(83) Huang, J.; Luo, H.; Liang, C.; Sun, I. W.; Baker, G. A.; Dai, S. Hydrophobic Brønsted Acid - Base Ionic Liquids Based on PAMAM Dendrimers with High Proton Conductivity and Blue Photoluminescence. *J. Am. Chem. Soc* **2005**, *127*, 12784–12785.

(84) Marcos, M.; Alcala, R.; Serrano, L. Photosensitive Ionic Nematic Liquid Crystalline Complexes Based on Dendrimers and Hyperbranched Polymers and a Cyanoazobenzene Carboxylic Acid †. *Chem. Mater.* **2008**, *20* (22), 5209–5217.

(85) Vergara, J.; Cano, M.; Barber, J.; Romero, P.; Serrano, L.; Ros, M. B. Mesomorphism from Bent-Core Based Ionic Dendritic Macromolecules. *Chem. Mater.* **2011**, *23*, 4931–4940.

(86) Mori, H.; Ebina, Y.; Kambara, R.; Nakabayashi, K. Temperature-Responsive Self-Assembly of Star Block Copolymers with Poly (Ionic Liquid) Segments. *Polym. J.* **2012**, *44* (6), 550–560.

(87) Stathatos, E.; Jovanovski, V.; Orel, B.; Jerman, I.; Lianos, P. Dye-Sensitized Solar Cells Made by Using a Polysilsesquioxane Polymeric Ionic Fluid as Redox Electrolyte. *J. Phys. Chem. C* **2007**, *111*, 6528–6532.

(88) Jovanovski, V.; Orel, B.; Jes, R.; Angela, S. Novel Polysilsesquioxane - I - / I 3 - Ionic Electrolyte for Dye-Sensitized Photoelectrochemical Cells. *J. Phys. Chem. B* **2005**, *109*, 14387–14395.

(89) Jeon, J.-H.; Tanaka, K.; Chujo, Y. POSS Fillers for Modulating the Thermal Properties Of. *RSC Adv.* **2013**, *3*, 2422–2427.

(90) Tan, J.; Sun, X.; Feng, S.; Zhang, C. Dalton Transactions. *Dalton Trans.* **2013**, *42*, 4337–4339.

(91) Majumdar, P.; Lee, E.; Gubbins, N.; Stafslien, S. J.; Daniels, J.; Thorson, C. J.; Chisholm, B. J. Synthesis and Antimicrobial Activity of Quaternary Ammonium-Functionalized POSS (Q-POSS) and Polysiloxane Coatings Containing Q-POSS. *Polymer (Guildf).* **2009**, *50* (5), 1124–1133.

(92) Pu, K.; Li, K.; Shi, J.; Liu, B. Fluorescent Single-Molecular Core - Shell Nanospheres of Hyperbranched Conjugated Polyelectrolyte for Live-Cell Imaging. *Chem. Mater.* **2009**, *21*, 3816–3822.

(93) Cardiano, P.; Lazzara, G.; Manickam, S.; Mineo, P.; Milioto, S.; Lo, S. POSS – Tetraalkylammonium Salts : A New Class of Ionic Liquids [‡]. *Eur. J. Inorg. Chem.* **2012**, 5668–5676.

(94) Manickam, S.; Cardiano, P.; Mineo, P. G.; Lo, S. Star-Shaped Quaternary Alkylammonium Polyhedral Oligomeric Silsesquioxane Ionic Liquids. *Eur. J. Inorg. Chem.* **2014**, 2704–2710.

(95) Sui, X.; Hempenius, M. A.; Vancso, G. J. Redox-Active Cross-Linkable Poly(Ionic Liquid)S. *J. Am. Chem. Soc* **2012**, *9*, 4023–4025.

(96) Randriamahazaka, H.; Ghilane, J.; Trippe-Allard, G.; Bui-Thi-Tuyet, V.; Pham-Truong, T. N. Electroactive ionic liquids and surface-modified substrates containing them. *Fr. Pat. 370121D36047, PCT/FR2016/051069* 2016.

(97) Shaplov, A. S.; Lozinskaya, E. I.; Ponkratov, D. O.; Malyshkina, I. A.; Vidal, F.; Aubert, P.; Okatova, V.; Pavlov, G. M.; Komarova, L. I.; Wandrey, C.; Vygodskii, Y. S. Bis (Trifluoromethylsulfonyl) Amide Based " Polymeric Ionic Liquids ": Synthesis , Purification and Peculiarities of Structure – Properties Relationships. *Electrochim. Acta* **2011**, *57*, 74–90.

(98) Yoshizawa, M.; Ohno, H. Molecular Brush Having Molten Salt Domain for Fast Ion Conduction. *Chem. Lett.* **1999**, 889–890.

(99) Vygodskii, Y. S.; Mel, O. A.; Lozinskaya, E. I.; Shaplov, A. S.; Malyshkina, I. A.; Gavrilova, N. D.; Lyssenko, K. A.; Antipin, M. Y.; Golovanov, D. G.; Korlyukov, A. A.; Ignat, N.; Welz-biermann, U. The Influence of Ionic Liquid ' s Nature on Free Radical Polymerization of Vinyl Monomers and Ionic Conductivity of the Obtained Polymeric Materials. *Polym. Adv. Technol.* **2007**, *18*, 50–63.

(100) Ye, Y.; Elabd, Y. A. Anion Exchanged Polymerized Ionic Liquids : High Free Volume Single Ion Conductors. *Polymer (Guildf).* **2011**, *52* (5), 1309–1317.

(101) Chen, X.; Zhao, J.; Zhang, J.; Qiu, L.; Xu, D.; Zhang, H.; Han, X.; Sun, B.; Fu, G.; Zhang, Y.; Yan, F. Bis-Imidazolium Based Poly(Ionic Liquid) Electrolytes for Quasi-Solid-State Dye-Sensitized Solar Cells. *J. Mater. Chem.* **2012**, *22* (34), 18018.

(102) Yin, K.; Zhang, Z.; Li, X.; Yang, L.; Tachibana, K.; Hirano, S. Polymer Electrolytes Based on Dicationic Polymeric Ionic Liquids: Application in Lithium Metal Batteries. *J. Mater. Chem. A* **2015**, *3* (1), 170–178.

(103) Matsumi, N.; Sugai, K.; Miyake, M.; Ohno, H. Polymerized Ionic Liquids via Hydroboration Polymerization as Single Ion Conductive Polymer Electrolytes. *Macromolecules* **2006**, *39*, 6924–6927.

(104) Zhang, W.; Kochovski, Z.; Lu, Y.; Schmidt, B. V. K. J.; Antonietti, M.; Yuan, J. Internal Morphology-Controllable Self-Assembly in Poly(Ionic Liquid) Nanoparticles. *ACS Nano* **2016**, *10* (8), 7731–7737.

(105) Kuwabata, S.; Minamimoto, H.; Inoue, K.; Imanishi, A.; Hosoya, K.; Uyama, H.; Torimoto, T.; Tsuda, T.; Seki, S. Three-Dimensional Micro/Nano-Scale Structure Fabricated by Combination of Non-Volatile Polymerizable RTIL and FIB Irradiation. *Sci. Rep.* **2014**, *4*, 3722.

(106) Minamimoto, H.; Irie, H.; Uematsu, T.; Tsuda, T.; Imanishi, A.; Seki, S.; Kuwabata, S. Polymerization of Room-Temperature Ionic Liquid Monomers by Electron Beam Irradiation with the Aim of Fabricating Three-Dimensional Micropolymer/Nanopolymer Structures. *Langmuir* **2015**, *31* (14), 4281–4289.

(107) Yuan, J.; Giordano, C.; Antonietti, M. Ionic Liquid Monomers and Polymers as Precursors of Highly Conductive, Mesoporous, Graphitic Carbon Nanostructures. *Chem. Mater.* **2010**, *22* (17), 5003–5012.

(108) Zhang, P.; Yuan, J.; Fellinger, T. P.; Antonietti, M.; Li, H.; Wang, Y. Improving Hydrothermal Carbonization by Using Poly(Ionic Liquid)S. *Angew. Chemie - Int. Ed.* **2013**, *52* (23), 6028–6032.

(109) Döbbelin, M.; Tena-Zaera, R.; Morcilla, R.; Iturri, J.; Moya, S.; Pomposo, J. A.; Mecerreyes, D. Multiresponsive PEDOT-Ionic Liquid Materials for the Design of Surfaces with Switchable Wettability. *Adv. Funct. Mater.* **2009**, *19* (20), 3326–3333.

(110) Marcilla, R.; Alcaide, F.; Sardon, H.; Pomposo, J. A.; Pozo-Gonzalo, C.; Mecerreyes, D. Tailor-Made Polymer Electrolytes Based upon Ionic Liquids and Their Application in All-Plastic Electrochromic Devices. *Electrochem. commun.* **2006**, *8* (3), 482–488.

(111) Simon, P.; Gogotsi, Y. Materials for Electrochemical Capacitors. *Nat. Mater.* **2008**, *7* (11), 845–854.

(112) Kim, T. Y.; Lee, H. W.; Stoller, M.; Dreyer, D. R.; Bielawski, C. W.; Ruoff, R. S.; Suh, K. S. High-Performance Supercapacitors Based on Poly(Ionic Liquid)-Modified Graphene Electrodes. *ACS Nano* **2011**, *5* (1), 436–442.

(113) Trigueiro, J. P. C.; Lavall, R. L.; Silva, G. G. Supercapacitors Based on Modified Graphene Electrodes with Poly(Ionic Liquid). *J. Power Sources* **2014**, *256*, 264–273.

(114) Kang, Y. J.; Yoo, Y.; Kim, W. 3-V Solid-State Flexible Supercapacitors with Ionic-Liquid-Based Polymer Gel Electrolyte for AC Line Filtering. *ACS Appl. Mater. Interfaces* **2016**, *8* (22), 13909–13917.

(115) Whittingham, M. S. Electrical Energy Storage and Intercalation Chemistry. *Science (80-.).* **1976**, *192*, 1126–1127.

(116) Appetecchi, G. B.; Kim, G. T.; Montanino, M.; Carewska, M.; Marcilla, R.; Mecerreyes, D.; De Meatza, I. Ternary Polymer Electrolytes Containing Pyrrolidinium-Based Polymeric Ionic Liquids for Lithium Batteries. *J. Power Sources* **2010**, *195* (11), 3668–3675.

(117) Li, M.; Yang, L.; Fang, S.; Dong, S.; Hirano, S. I.; Tachibana, K. Polymer Electrolytes Containing Guanidinium-Based Polymeric Ionic Liquids for Rechargeable Lithium Batteries. *J. Power Sources* **2011**, *196* (20), 8662–8668.

(118) Li, M.; Yang, L.; Fang, S.; Dong, S.; Hirano, S. I.; Tachibana, K. Polymerized Ionic Liquids with Guanidinium Cations as Host for Gel Polymer Electrolytes in Lithium Metal Batteries. *Polym. Int.* **2012**, *61* (2), 259–264.

(119) Sato, T.; Morinaga, T.; Marukane, S.; Narutomi, T.; Igarashi, T.; Kawano, Y.; Ohno, K.; Fukuda, T.; Tsujii, Y. Novel Solid-State Polymer Electrolyte of Colloidal Crystal Decorated with Ionic-Liquid Polymer Brush. *Adv. Mater.* **2011**, *23* (42), 4868–4872.

(120) Grygiel, K.; Lee, J. S.; Sakaushi, K.; Antonietti, M.; Yuan, J. Thiazolium Poly(Ionic Liquid)s: Synthesis and Application as Binder for Lithium-Ion Batteries. *ACS Macro Lett.* **2015**, *4* (12), 1312–1316.

(121) Lee, J.-S.; Sakaushi, K.; Antonietti, M.; Yuan, J. Poly(Ionic Liquid) Binders as Li + Conducting Mediators for Enhanced Electrochemical Performance. *RSC Adv.* **2015**, *5* (104), 85517–85522.

(122) Díaz, M.; Ortiz, A.; Vilas, M.; Tojo, E.; Ortiz, I. Performance of PEMFC with New Polyvinyl-Ionic Liquids Based Membranes as Electrolytes. *Int. J. Hydrogen Energy* **2014**, *39* (8), 3970–3977.

(123) Wojnarowska, Z.; Knapik, J.; Díaz, M.; Ortiz, A.; Ortiz, I.; Paluch, M. Conductivity Mechanism in Polymerized Imidazolium-Based Protic Ionic Liquid [HSO 3 –BVIm][OTf]: Dielectric Relaxation Studies. *Macromolecules* **2014**, *47* (12), 4056–4065.

(124) Deavin, O. I.; Murphy, S.; Ong, A. L.; Poynton, S. D.; Zeng, R.; Herman, H.; Varcoe, J. R. Anion-Exchange Membranes for Alkaline Polymer Electrolyte Fuel Cells: Comparison of Pendent Benzyltrimethylammonium- and Benzylmethylimidazolium-Head-Groups. *Energy Environ. Sci.* **2012**, *5* (9), 8584–8597.

(125) Wang, J.; Li, S.; Zhang, S. Novel Hydroxide-Conducting Polyelectrolyte Composed of an Poly(Arylene Ether Sulfone) Containing Pendant Quaternary Guanidinium Groups for Alkaline Fuel Cell Applications. *Macromolecules* **2010**, *43* (8), 3890–3896.

(126) Ye, Y.; Elabd, Y. A. Relative Chemical Stability of Imidazolium-Based Alkaline Anion Exchange Polymerized Ionic Liquids. *Macromolecules* **2011**, *44* (21), 8494–8503.

(127) Qiu, B.; Lin, B.; Si, Z.; Qiu, L.; Chu, F.; Zhao, J.; Yan, F. Bis-Imidazolium-Based Anion-Exchange Membranes for Alkaline Fuel Cells. *J. Power Sources* **2012**, *217*, 329–335.

(128) Lin, B.; Qiu, L.; Qiu, B.; Peng, Y.; Yan, F. A Soluble and Conductive Polyfluorene Ionomer with Pendant Imidazolium Groups for Alkaline Fuel Cell Applications. *Macromolecules* **2011**, *44* (24), 9642–9649.

(129) Lin, B.; Qiu, L.; Lu, J.; Yan, F. Cross-Linked Alkaline Ionic Liquid-Based Polymer Electrolytes for Alkaline Fuel Cell Applications. *Chem. Mater.* **2010**, *22* (24), 6718–6725.

(130) Lin, B.; Dong, H.; Li, Y.; Si, Z.; Gu, F.; Yan, F. Alkaline Stable C2-Substituted Imidazolium-Based Anion-Exchange Membranes. *Chem. Mater.* **2013**, *25* (9), 1858–1867.

(131) Mohanty, A. D.; Ryu, C. Y.; Kim, Y. S.; Bae, C. Stable Elastomeric Anion Exchange Membranes Based on Quaternary Ammonium-Tethered Polystyrene-b-Poly(Ethylene-Co-Butylene)-b-Polystyrene Triblock Copolymers. *Macromolecules* **2015**, *48* (19), 7085–7095.

(132) Azaceta, E.; Marcilla, R.; Sanchez-Diaz, A.; Palomares, E.; Mecerreyes, D. Synthesis and Characterization of Poly(1-Vinyl-3-Alkylimidazolium) Iodide Polymers for Quasi-Solid Electrolytes in Dye Sensitized Solar Cells. *Electrochim. Acta* **2010**, *56* (1), 42–46.

(133) Kawano, R.; Katakabe, T.; Shimosawa, H.; Nazeeruddin, M. K.; Graetzel, M.; Matsui, H.; Kitamura, T.; Tanabe, N.; Watanabe, M. Solid-State Dye-Sensitized Solar Cells Using Polymerized Ionic Liquid Electrolyte with Platinum-Free Counter Electrode. *Phys. Chem. Chem. Phys.* **2010**, *12* (8), 1916–1921.

(134) Chi, W. S.; Koh, J. K.; Ahn, S. H.; Shin, J.-S.; Ahn, H.; Ryu, D. Y.; Kim, J. H. Highly Efficient I2-Free Solid-State Dye-Sensitized Solar Cells Fabricated with Polymerized Ionic Liquid and Graft Copolymer-Directed Mesoporous Film. *Electrochem. commun.* **2011**, *13* (12), 1349–1352.

(135) Green, M. D.; Wang, D.; Hemp, S. T.; Choi, J. H.; Winey, K. I.; Heflin, J. R.; Long, T. E. Synthesis of Imidazolium ABA Triblock Copolymers for Electromechanical Transducers. *Polym. (United Kingdom)* **2012**, *53* (17), 3677–3686.

(136) Gao, R.; Wang, D.; Heflin, J. R.; Long, T. E. Imidazolium Sulfonate-Containing Pentablock Copolymer–ionic Liquid Membranes for Electroactive Actuators. *J. Mater. Chem.* **2012**, *22* (27), 13473.

(137) Wu, T.; Wang, D.; Zhang, M.; Heflin, J. R.; Moore, R. B.; Long, T. E. RAFT Synthesis of ABA Triblock Copolymers as Ionic Liquid-Containing Electroactive Membranes. *ACS Appl. Mater.*

Interfaces **2012**, *4* (12), 6552–6559.

(138) Zhao, Q.; Dunlop, J. W. C.; Qiu, X.; Huang, F.; Zhang, Z.; Heyda, J.; Dzubiella, J.; Antonietti, M.; Yuan, J. An Instant Multi-Responsive Porous Polymer Actuator Driven by Solvent Molecule Sorption. *Nat. Commun.* **2014**, *5*, 4293.

(139) Zhao, Q.; Heyda, J.; Dzubiella, J.; Täuber, K.; Dunlop, J. W. C.; Yuan, J. Sensing Solvents with Ultrasensitive Porous Poly(Ionic Liquid) Actuators. *Adv. Mater.* **2015**, *27* (18), 2913–2917.

(140) Song, H.; Lin, H.; Antonietti, M.; Yuan, J. From Filter Paper to Functional Actuator by Poly(Ionic Liquid)-Modified Graphene Oxide. *Adv. Mater. Interfaces* **2016**, *3* (12), 1–7.

(141) Cui, K.; Lu, X.; Cui, W.; Wu, J.; Chen, X.; Lu, Q. Fluorescent Nanoparticles Assembled from a Poly(Ionic Liquid) for Selective Sensing of Copper Ions. *Chem. Commun. (Camb).* **2011**, *47* (3), 920–922.

(142) Zhao, Q.; Yin, M.; Zhang, A. P.; Prescher, S.; Antonietti, M.; Yuan, J. Hierarchically Structured Nanoporous Poly(Ionic Liquid) Membranes: Facile Preparation and Application in Fiber-Optic PH Sensing. *J. Am. Chem. Soc.* **2013**, *135* (15), 5549–5552.

(143) Wang, L. L.; Duan, X.; Xie, W.; Li, Q.; Wang, T. Highly Chemoresistive Humidity Sensing Using Poly(Ionic Liquid)S. *Chem. Commun.* **2016**, *52* (54), 8417–8419.

(144) Wang, Q.; Yun, Y. Nonenzymatic Sensor for Hydrogen Peroxide Based on the Electrodeposition of Silver Nanoparticles on Poly(Ionic Liquid)-Stabilized Graphene Sheets. *Microchim. Acta* **2013**, *180* (3–4), 261–268.

CHAPTER 2

SURFACE MODIFICATIONS USING ELECTROACTIVE IONIC LIQUIDS AND APPLICATIONS

The combination of redox-active molecules and conventional ionic liquids attracts an intense attention for a large spectrum of applications. In this context, we propose a series of redox molecules based ionic liquid, (redox-IL) by introducing oxidative and/or reducible groups to the imidazolium's and ammonium's structure. Unlike conventional redox-active molecules, (redox)-ionic liquids provide multiple role in electrochemistry, i.e, simultaneously act as solvent, supporting electrolyte and electrochemical active materials. Recently, the use of ionic liquid in electrochemistry evolve from their strict use as solution (as solvent and supporting electrolyte) to the electrode interface through various immobilization strategies. Among the most powerful approaches, electrochemistry has been widely used for functionalizing conducting substrates and/or semiconductor. Bearing suitable chemical functions, the task-specific ionic liquids can be immobilized onto electrode surfaces from direct electrochemical grafting to electrochemistry assisted pathways. We provide different approach to modify the electrode surface with redox-IL from thin layer to polymers. It has been observed that at the electrified surfaces, the (Redox-active) ionic liquids behave differently when compared to conventional Redox molecules. In this context, the electrochemical responses of immobilized Redox-IL are investigated to understand the electrochemistry of such interfaces. The scheme bellow summarizes the approach used in this chapter. Thus, in the first part we will focus on the immobilization of thin layer based redox ionic liquid, while the second part will be devoted to the immobilization of redox polymer based ionic liquid.

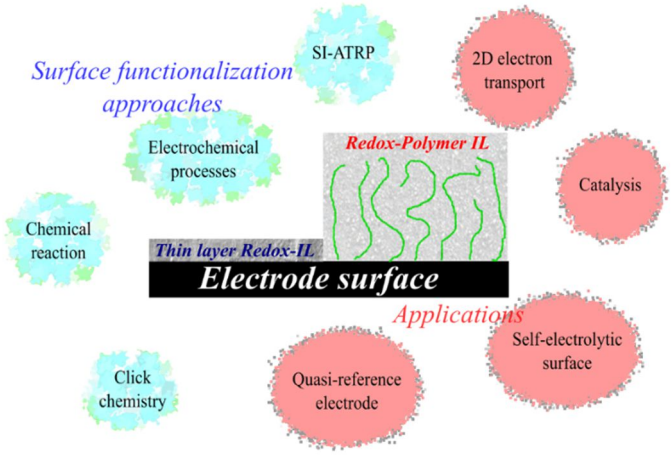

Keywords: (Redox)-ionic liquids, polymers, thin layer, surface functionalization, chemical reactions, electrochemistry, applications.

OUTLINE

2.1 INTRODUCTION

Sustainable development requires massive investment for exploration and utilization of renewable energy sources in the energy balance. Among various forms, electricity is undoubtedly the most desirable energy input for daily uses. However, due to the intermittence of the current renewable sources, the electricity must be stored under other forms in order to correlate the fleeting production and the continuous consumption. Despite the presence of commercial energy storage systems, seeking for new materials and new approaches for resolving this problem is still in progress and also attracts a wide attention from scientific community. Recent advancements have pushed the community towards the utilization of nanoscale materials for efficient energy storage and conversion systems. Even though the advantages given by available nanomaterial, their performance is still lower than theoretical purposes. In this context, tailoring the physical-chemical properties at the molecular level becomes crucial not only for boosting the performance of the existing materials but also for creating new type of molecular entities for storing and releasing the energy. Following this concept, an old discovery of ionic liquids has been awakened and they become one of the best candidates for settling the energetic problems[1,2]. This family of compounds is nowadays upcoming major research field by offering relevant ability in different applications, Interestingly, an infinity of ionic liquids can be obtained resulting from the possibility to tailor the physical-chemical properties at molecular level. Moreover, the coupling of classical ionic liquid with electrochemical active groups leads to the formation of a promising multifunctional molecules that have been demonstrated to be suitable for energy storage[3–6], labeled redox-active ionic liquids. Aside from using (redox-active)-ionic liquid as active material in solution, the surface functionalization using these molecules is also matter of interest for boosting the performance of the substrates, resulting from the generation of new interfaces. For this purpose, it is well known that electrochemistry offers powerful tools for immobilizing organic compounds onto the conductive substrates including electroactive ionic liquids[7,8]. It has also demonstrated that the modified substrates provide promising results for a large spectrum of applications[9–13].

In this context, our group develops a new family of task-specific ionic liquids that exposes well-defined redox behaviors. These compounds can be immobilized onto various conductor and semi-conductor surfaces and thus resolve the problem related to the high cost and leakage of ionic liquid for further implementation in solid-state devices. In the continuation of the previously reported works from our group[8,14–18], other routes have been developed for attaching new redox-ionic liquids onto electrode surfaces via the formation of thin layer and polymer films containing electroactive ionic liquid framework. Through this chapter, various electroactive ionic liquids bearing single and bi-redox moieties are introduced for surface functionalization via different electrochemical based approaches. We will report the

functionalization of material surfaces by proposing 2 novel routes: thin layer and polymer of redox-active ionic liquid (redox-IL).

2.2 MONOLAYER OF FERROCENE BASED IONIC LIQUID VIA CLICK CHEMISTRY

Even though the feasibility of the one-step electrochemical procedure has been reported, the organic synthesis pathway remains complex with multistep reactions. Indeed, the immobilization of molecules based ionic liquid requires the synthesis of molecule bearing the anchoring (diazonium, thiol, amine….) and the functional groups. The introduction of the anchoring group reduces the possibility to implant other interesting functionalities. In the continuation of the works reported in our group on the immobilization of thin layer of ionic liquid via direct electrochemical deposition methods, we propose to use a two-step procedure, in which a primary layer will be immobilized onto the electrode followed by a chemical reaction to immobilize the ionic molecules onto the surface, e.g. click chemistry.

"Click Chemistry" is a term that was introduced by Kolb, Finn and Sharpless in 2001[19] to describe reactions that assemble two molecular blocks together by a single step. Among different possible “click” reactions (thiol-ene, oxime, Diels-Alder, etc.), the copper(I)–catalyzed azide alkyne cycloaddition (Cu-AAC) is presented as the most exploited one[20]. Briefly, the Cu-AAC is a branch of Huisgen 1,3-dipolar cycloaddition that produces 1,4-disubstituted (1,2,3)-triazole from a terminal alkyne and an aliphatic azide in presence of Cu(I) catalyst under mild conditions. Even though several Cu(I) sources have been reported, the initial Fokin – Sharpless catalyst ($CuSO_4$ + Sodium L-ascorbate) remains the most practical and used up-to-date. Later, the reaction mechanism has been clarified and evidenced by Fokin et al. in 2013 demonstrating the participation of di-nuclear copper into the reaction pathway as presented in the scheme 2.1[21].

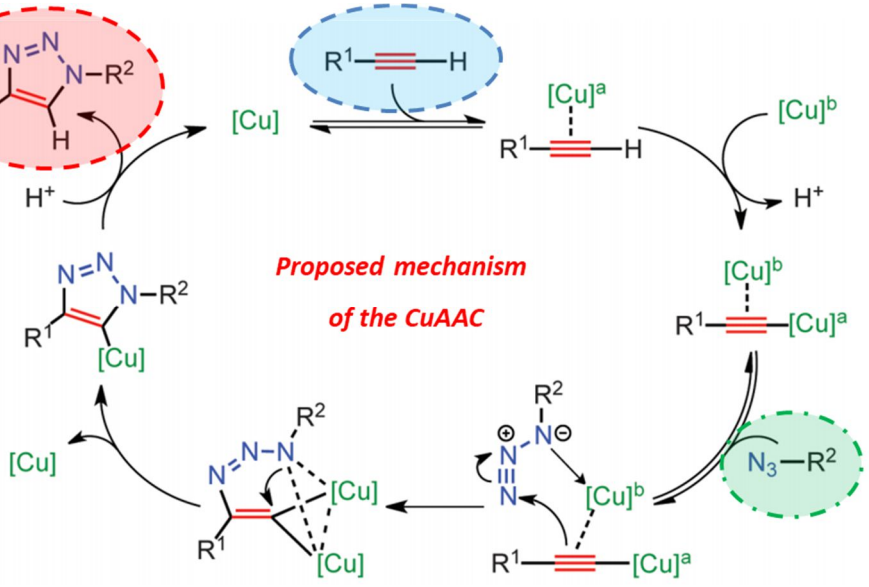

Scheme 2.1 Mechanism of Cu-AAC click reaction

Thanks to the advantages of the click reactions, the procedure has been successfully applied to modify different substrates for a large spectrum of applications[22,23]. This approach involves an immobilization step of either azide- or alkyne-based molecules onto the substrate surface followed by click reaction in the presence of copper catalyst. Despite the attractive properties of the immobilized ionic liquids, so far, there is no report on surface functionalization of ionic liquid onto the electrode surface using click chemistry. Within this context, we purpose to functionalize the electrode surface with electroactive ionic liquid using click chemistry, affording novel electrochemical active interface.

The 1-ferrocenylmethyl-3-propargylimidazolium bromide (FcPIm) was synthesized according to the procedure described in the appendices. Before grafting onto electrode surface, the electrochemical behavior of the as-synthetized 1-ferrocenylmethyl-3-propargylimidazolium bromide (FcPIm) was investigated and the cyclic voltammograms were recorded on ITO electrode in MeCN solution containing 1 mM of FcPIm and 0.1 M of $TBAPF_6$ as shown in the Figure 2.1. The recorded CV (red curve) displays a reversible electrochemical signal at a standard potential of 0.57 V/ SCE attributed to the response of FcPIm molecule. Due to the introduction of electron withdrawing effect induced by imidazolium ring, the electrochemical response of ferrocene moieties is strongly influenced, resulting to a positive shift in term of standard potential ($\Delta E° = 150$ mV compared to Fc^+/Fc redox couple). This positive potential shift is similar to the reported works on ferrocenated imidazolium compounds[24].

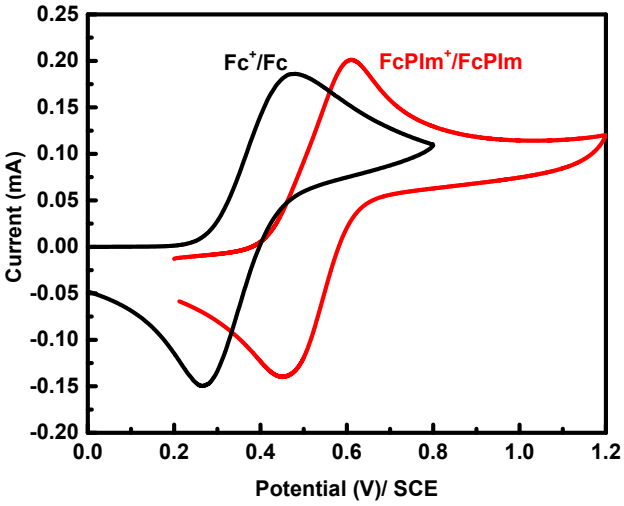

Figure 2.1 Cyclic voltammograms recorded on ITO substrates by using (black curve) 1 mM of Fc and (red curve) 1 mM of $[FcPIm^+][Br^-]$ in MeCN solution containing 0.1 M of $TBAPF_6$ as supporting electrolyte

After that, the surface functionalization using this molecule was performed by following the electrochemical – chemical procedure as illustrated in the Scheme 2.2.

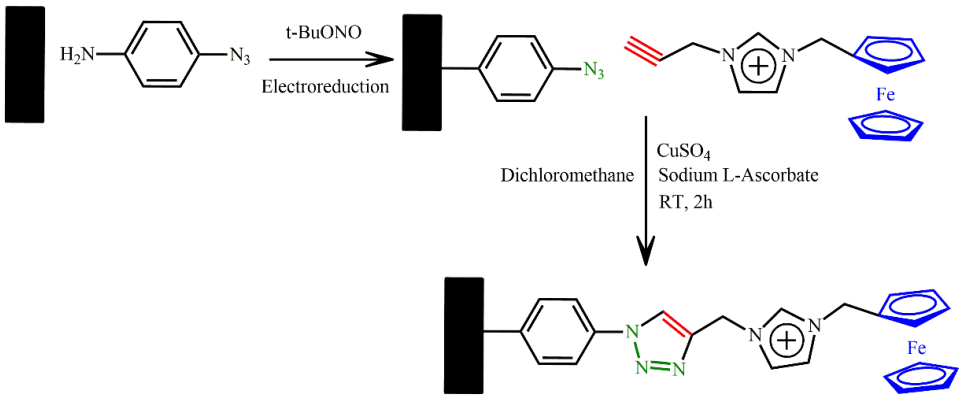

Scheme 2.2 Immobilization procedure of [FcPIm$^+$][Br$^-$] (FPI) onto electrode surface via click chemistry

The electrochemical step was performed via electroreduction of diazonium generated in-situ from 4-azidoaniline. Briefly, in electrolytic solution containing 1 mM of 4-azidoaniline and 0.1 M $TBAPF_6$ in acetonitrile, the diazotization agent was added, i.e. tert-Bu-NO (3 equiv.). In the presence of the nitrosium source, 4-azidoaniline was rapidly transformed in situ to the corresponding diazonium cation[25]. Then, the generated 4-azidophenyldiazonium was electrochemically reduced under cathodic polarization on an ITO substrate using different number of electro-grafting cycles. Precisely, the potential was kept sweeping from 0.4 V to -0.8 V/ SCE for the first cycle and from 0 V to -0.8 V for the further cycles. A reduction peak located at -0.35 V vs SCE was observed and is attributed to the reduction of diazonium. Besides, the reduction current was dramatically decreased from the 2nd cycle that indicates the attachment of the radical onto the electrode surface by forming a thin organic layer and the blocking effect due to the presence of the film (Figure 2.2).

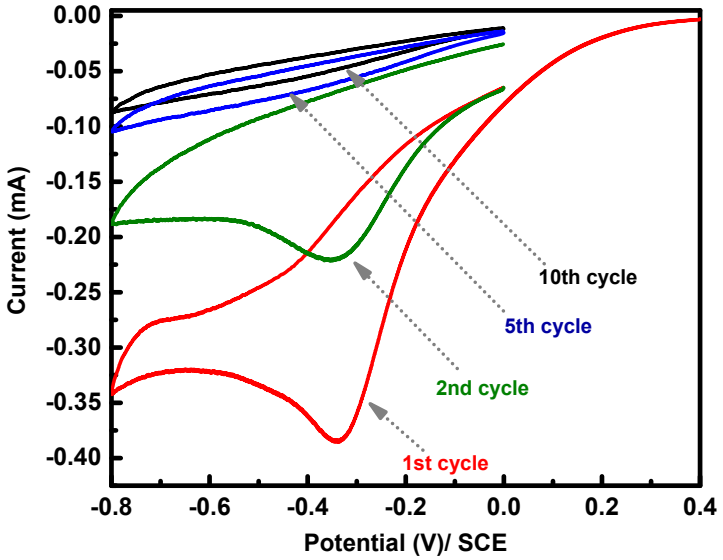

Figure 2.2 Cyclic voltammograms for the reduction of 1 mM of 4-azidophenyldiazonium in MeCN solution with 0.1 M of $TBAPF_6$ by using ITO electrodes.

Later, the azido-modified ITO substrates were immersed into a dichloromethane solution containing 5 mM of [$FcPIm^+$][Br^-] and a catalytic amount of aqueous solution of $CuSO_4$ and sodium L-ascorbate required for Cu(I)AAC reaction. The mixture was rigorously stirred, and the reaction was kept at room temperature for 2 hrs. The electrodes were removed from the solution, washed successively with distilled water, acetone, acetonitrile under sonication (35 kHz, 10 min).

The modified electrode, prepared by 1 cycle of electrochemical reduction of 4-azidoaniline followed by click reaction, was transferred to an electrolytic MeCN solution and the CVs were recorded and presented in the Figure 2.3a. The voltammogram shows a fully reversible redox signal at 0.57 V/ SCE corresponding to the presence of [$FcPIm^+$][Br^-] at the electrode surface. In addition, the peak-to-peak separation around 20 mV, and the linear variation of the peak current as function of the scan rate (Figure 2.S1) confirm that the ferrocene-based ionic liquid was successfully immobilized onto the electrode surface through the Cu-AAC click chemistry process.

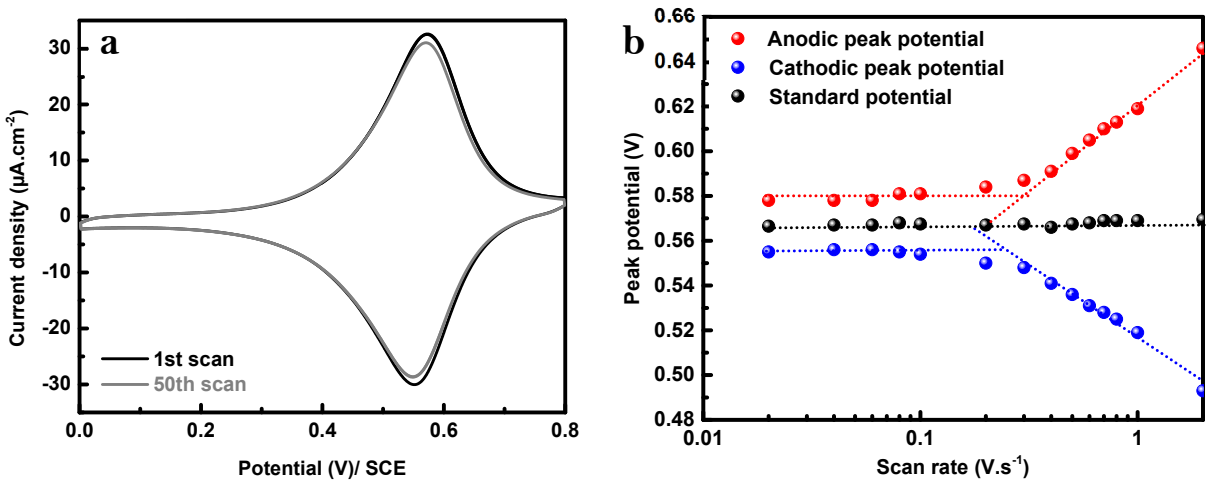

Figure 2.3 (a) Cyclic voltammograms of immobilized [$FcPIm^+$][Br^-] in MECN solution containing 0.1 M of Bu_4NPF_6. 1st scan (black line) and 50th scan (grey line); ***(b)*** Variation of the peak potentials as function of the scan rate.

Besides, the full width at half maximum of the peak is found to be around 150 mV which is higher than the theoretical value (90 mV) suggesting the occurrence of a strong interaction between [$FcPIm^+$][Br^-] moieties at the top layer. Furthermore, after 50 scans, the current density was remained at 99 % compared to the 1st scan, indicating the high stability of the attached film. This behavior makes it possible to evaluate the electron transfer rate constant at the interface/immobilized layer via utilization of Laviron's formalism[26].

$$E_{p,a} = E^0 + \frac{RT}{(1-\alpha)nF}\ln\frac{1-\alpha}{|m|} \quad (2.1) \text{ and } E_{p,c} = E^0 + \frac{RT}{\alpha nF}\ln\frac{\alpha}{|m|} \quad (2.2)$$

$$\text{with } m = \frac{RTk_s}{Fnv} \quad (2.3)$$

$$\text{when } v \to 0, \lim_{v\to 0}(E_{p,a}) = \lim_{v\to 0}(E_{p,c}) = E^0 \qquad (2.4)$$

Consequently, the equation 2.2 becomes

$$\lim_{v\to 0}\alpha = m \quad (2.5), \text{ resulting to } k_{app} = \frac{\alpha n F v_c}{RT} = \frac{(1-\alpha) n F v_a}{RT} \quad (2.6) \text{ with } \alpha = \frac{v_a}{v_a + v_c} \quad (2.7)$$

where v the scan rate, E^0 the formal potential, n the number of transferred electron and α the charge transfer coefficient.

From the variation of the peak potentials as function of the scan rate (Figure 2.3b) the electron transfer rate constant for the present system was found to be 43 s^{-1} with a charge transfer coefficient around 0.5. The observed electron transfer is attributed to the electron tunneling from the redox layer to the electrode surface through a short insulator barrier induced by the presence of the primary azide layer. The measured k_{app} is comparable to that reported for a self-assembled monolayer of alkyl ferrocene attached to a silicon substrate[27]. The surface coverage of the attached ferrocene molecules was determined from the integration of the charge of the anodic peak and was estimated to be 1.9×10^{14} molecules.cm^{-2} (Table 2.1). The reported values of the surface coverage are close to that expected for a close-packed ferrocene monolayer[28], highlighting the efficiency of the click chemistry process. In addition, there was a negligible change in the surface coverage as a function of the number of electrochemical reduction cycles of 4-azidophenyldiazonium, providing further evidence that the ferrocene based ionic liquid layer had reached saturation (Table 2.1) at the extreme layer of the film. In addition, the primary layer has a compact structure, i.e. free of pinhole effect.

Table 2.1 Variation of the surface coverage in function of the number of electro-grafting cycles

Number of electro-grafting cycles	**1**	**2**	**3**	**5**	**7**	**10**
Surface concentration (molecules.cm^{-2})	$1.97.10^{14}$	$1.93.10^{14}$	$1.99.10^{14}$	$2.01.10^{14}$	$2.07.10^{14}$	$2.11.10^{14}$

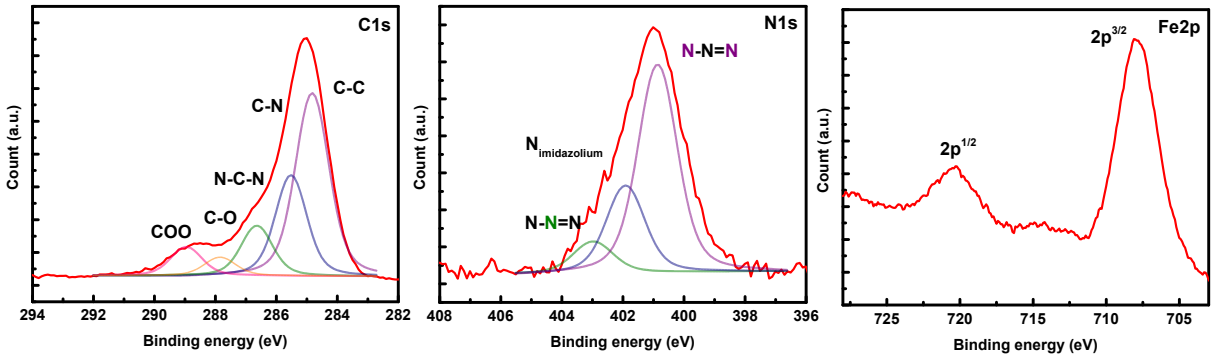

Figure 2.4 High resolution XPS spectrum of ***(a)*** C(1s); ***(b)*** N(1s) and ***(c)*** Fe(2p) of FPI modified ITO electrode by using 1 electrochemical reduction cycle.

The XPS analysis of the modified ITO reveals the presence of available elements from the molecular structure of the attached layers, such as C(1s), N(1s) and Fe(2p). It is observed that the deconvolution of the C(1s) peak exhibits 5 components which correspond to C – C(H) (285 eV), C – N (286.1 eV), N–C–N (287 eV), C–O (288 eV) and COO (288.5 eV) bonds[29][1]. The presence of C-O and COO peaks could be attributed to the surface contamination. Furthermore, the N(1s) spectrum shows a peak at 402 eV which is attributed the nitrogen from imidazolium ring[14] and two peaks at 400.5 and 403 eV which comes from the N-N=N of the azide groups[1],[30]. The presence of the redox system in FcPIm is confirmed by the presence of two peaks at 708.2 and 720.8 eV which are attributed to Fe($2p^{3/2}$) and Fe($2p^{1/2}$) component, in agreement with the previously reported values for immobilized ferrocene moieties on the electrode surfaces[27].

To evaluate the topography and the thickness of the attached layer, AFM was performed as shown in the Figure 2.5. As results, the AC AFM 2D image (inset) presents a homogenous film with a roughness less than 2 nm for all of the samples. Later, the AFM tapping mode was changed to contact mode in which the scratching tests were performed. This technique consists to apply strong loading forces to the tip to remove the attached molecules during the scan. The measured thickness of the film via AFM scratch experiment is around 3.5 nm for the sample prepared using one electrografting cycle followed by click reaction.

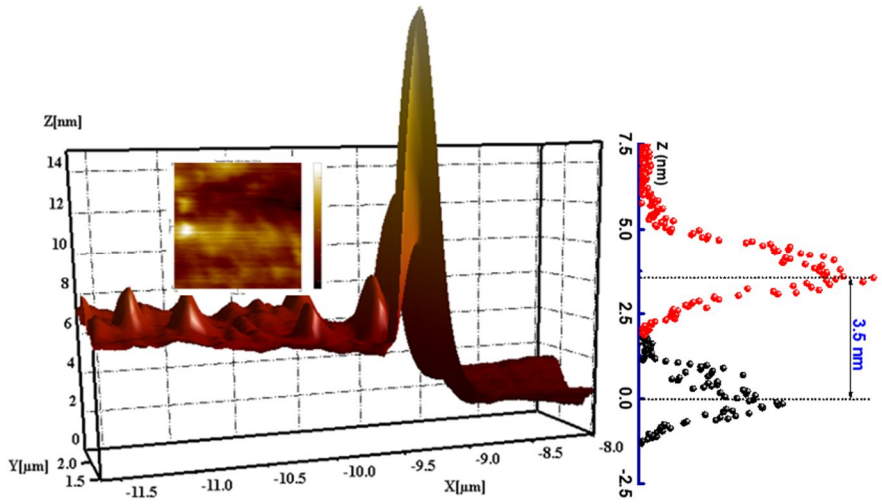

Figure 2.5 2D AFM image (10 µm × 10 µm) of ITO/Fc-grafted layer based on 1 cycle electrochemical reduction of 4-azidophenyldiazonium, and AFM scratch profiles of modified ITO.

To correlate the thickness of the primary layer and the electron transfer through it, the apparent electron transfer constant and the thickness of the grafted layer of different samples were calculated and plotted in the figure 2.6. The black curve displays the variation of the thickness of the attached layer (the primary layer and the FcPIm) as function of the electrografting cycles number measured by AFM scratch experiment. The curve shows that the increase of the number of electro-grafting cycles induces an increase of the thickness of the final modified electrodes.

[1]xpssimplified.com/elements/carbon.php

The latter reaches a saturated level around 10 nm after 5 electrochemical reduction cycles. This thickness consists of a top monolayer of ferrocenyl-based ionic liquid and 8 nm of the linker layer. The measured electron transfer rate (red curve) shows a decay as function of the number of the electrografting cycles. This behavior is expected since the primary layer act as a barrier against the electron transfer. Thus, for a thicker layer the electron transfer rate is attenuated.

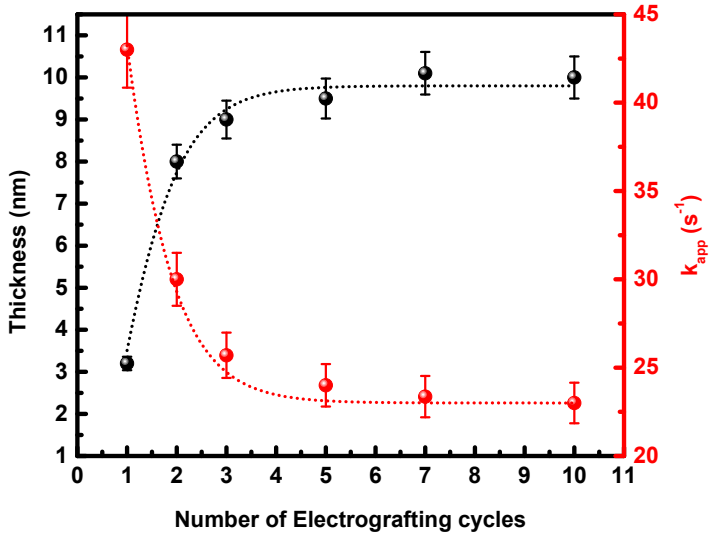

Figure 2.6 Variation of the thickness of the Fc-grafted layer (black) and the apparent electron transfer constant (red) as function of the number of electro-grafting cycles.

As a result, the electron transfer rate constant decreases exponentially with the thickness of the barrier as displayed in the figure 2.6. The observed saturation of the electron transfer rate after 5 cycles could be related to the presence of silent Fc moieties, not detectable by electrochemistry. However, the AFM scratch experiments confirm the saturation of the thickness of the primary attached layer and roll out the previous hypothesis.

In summary, we have shown that it is possible to immobilize a task-specific ionic liquid onto an electrode surface by coupling the electrochemical reduction of 4-azidophenyldiazonium and click reaction (Cu(I)AAC) by using 1-ferrocenylmethyl-3-propargylimidazolium. The presence of a monolayer of Fc-based imidazolium was evidenced by following the redox signal of Fc head groups. The presence of the imidazolium ring influences the arrangement of the molecules at the surface and the electron transport inside the active layer.

2.3 THIN LAYER OF BI-REDOX IONIC LIQUID MOLECULE FOR GENERATION OF MULTI-REDOX STATE SURFACE

In the literature, different procedures have been reported for the immobilization of redox active molecules[31,32]. However, most of the reported works focused on the immobilization of either donor or acceptor redox group while only a little attention has been devoted to the immobilization of bi-redox molecules. Within this context, we make attempt to immobilize a bi-redox ionic liquid bearing simultaneously an electron donor (D) and acceptor (A), resulting to a functional surface with multi-redox states.

It is noted that the previous methodology requires an ionic liquid molecule bearing an alkyne group that make the synthesis of bi-redox molecules more complex. However, the feasibility of chemical reaction onto previously modified electrode surface could overcome the synthesis drawback. Thus, various chemical reactions could be adapted (click chemistry, peptide coupling, Gomberg-Bachmann reaction, etc.) leading to a more flexible method for the attachment of the desired molecule at the electrode surface. Typically, the Gomberg – Bachmann reaction is an aryl – aryl reaction coupling based on diazonium derivatives and aryl component. In this part, 1-ethyleneamidoanthraquinone-3-ferrocenemethylimidazolium TFSI ([FcIm$^+$AQ][TFSI$^-$]) was synthesized and used for surface functionalization. The ionic liquid-based molecule contains two-redox centers, namely ferrocene and anthraquinone. First, the electrochemical behavior of [FcIm$^+$AQ][TFSI$^-$] in electrolytic solution was investigated. The figure 2.7a shows the electrochemical signal of the [FcIm$^+$AQ][TFSI$^-$] in MeCN solution. Two reversible systems located at 0.55 V and -0.7 V/ SCE are attributed to the Fc and AQ moieties within the molecule's structure. It is noted that in non-protic solution, the reduction of AQ followed one electron pathway, affording radical anion, i.e. AQ + 1e$^-$ ⇋ AQ$^{\bullet-}$. Therefore, the current intensity of these two components should be equal, which is not satisfied in this case. The current intensity of the AQ is far lower than the values obtained with Fc head, suggesting a difference of solvation of these 2 heads. As a consequence, unequal diffusion coefficients are expected. By performing CVs with different scan rate ranging from 10 mV.s^{-1} to 100 V.s^{-1}, a linear relationship between the peak current and the v$^{1/2}$ (figure 2.7b) indicates diffusional regime of the molecules. By using Randle – Sevcik equation, the diffusion coefficients are found to be around 6.58.10^{-6} cm^2.s^{-1}, 3.71.10^{-6} cm^2.s^{-1}, 9.03.10^{-6} cm^2.s^{-1} and 3.25.10^{-6} cm^2.s^{-1} for AQ, AQ$^{\bullet-}$, Fc, Fc$^+$, respectively.

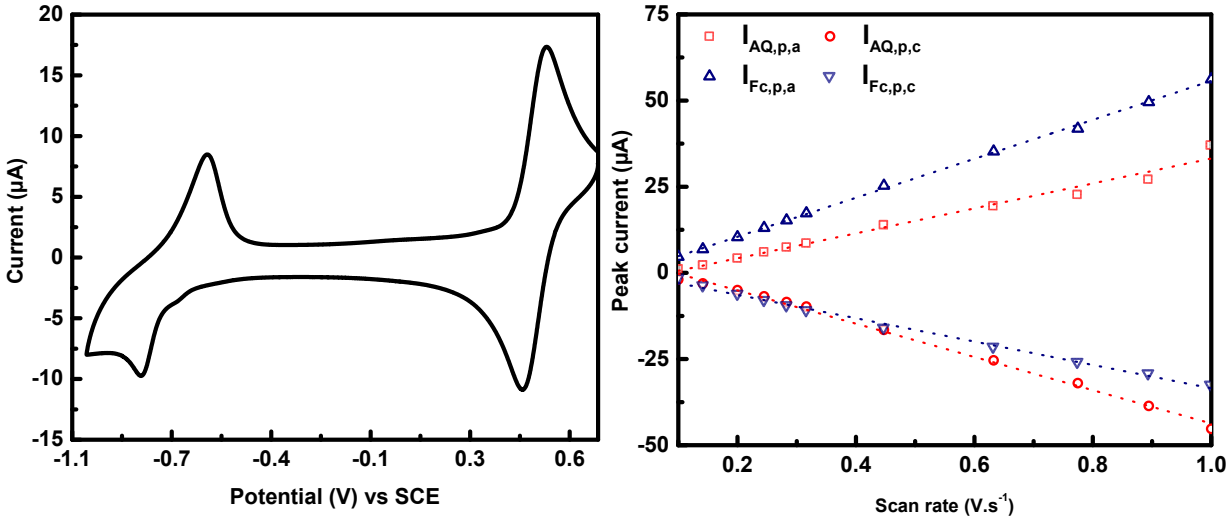

Figure 2.7 (a) CV recorded in MeCN solution containing 1 mM of [FcIm$^+$AQ][TFSI$^-$] and 0.1 M $TBAPF_6$; ***(b)*** Variation of the peak current in function of the square root of the scan rate (v$^{1/2}$).

Next, the bi-redox molecule based ionic liquid was immobilized onto electrode surface using the Gomberg-Bachmann reaction at the surface (Scheme 2.3).

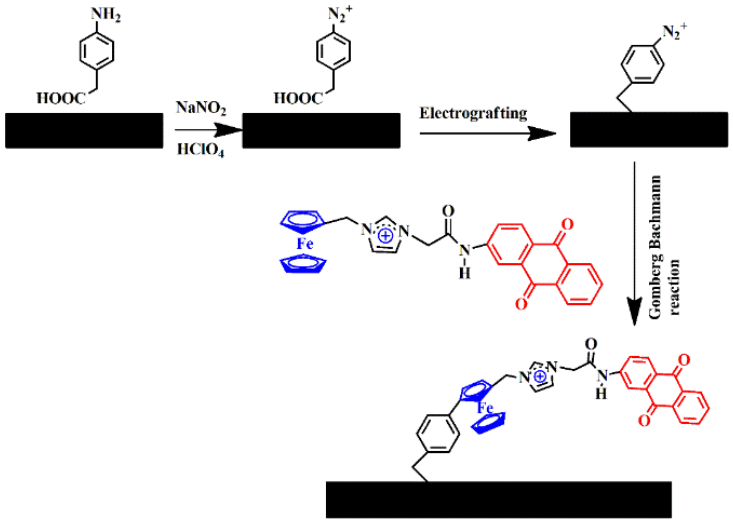

Scheme 2.3. Immobilization of [FcIm$^+$AQ][TFSI$^-$] onto electrode surface via Gomberg-Bachmann reaction

The molecule used in this work is composed from a ferrocene moiety, which can undergo one electron process (D-group), and anthraquinone moiety, which is involved in 2-electron and 2-proton reduction process (A-group) in acidic media as below:

$$Fc \rightleftarrows Fc^+ + 1e^- \qquad \text{(Electron donor)}$$

$$AQ + 2e^- + 2H^+ \rightleftarrows AQH_2 \qquad \text{(Electron acceptor) in protic condition}$$

As shown in the scheme 2.3, the immobilization of the molecule is occurred through E-C procedure. First, the linker is grafted onto electrode surface via electrochemical oxidation of carboxylic group from the 4-aminophenylacetic acid in presence of diazotization agents ($HClO_4$ and $NaNO_2$ 20 equiv./10 equiv., respectively).

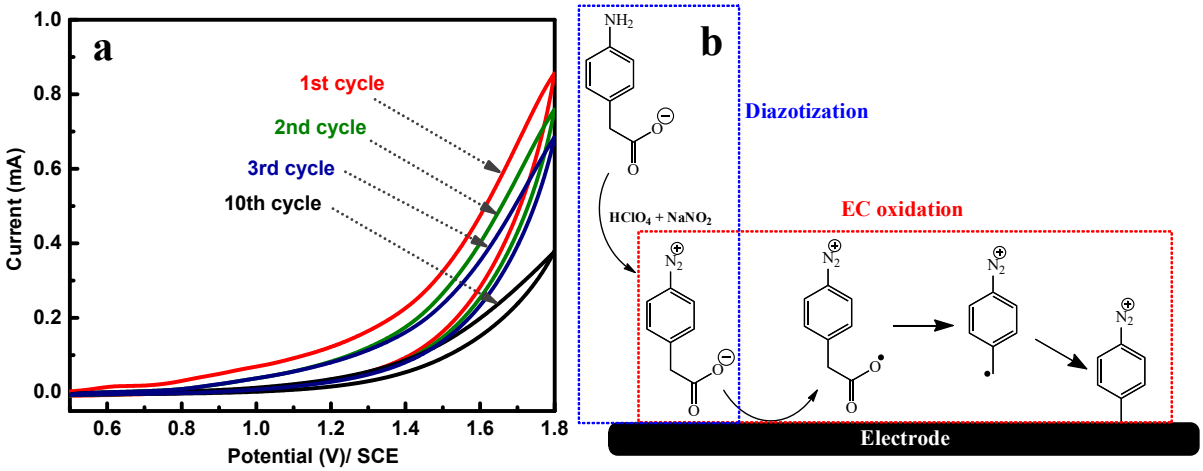

Figure 2.8 ***(a)*** Cyclic voltammograms for the reduction of 1 mM of 4-aminophenylacetic acid in aqueous solution with 0.1 M of KCl in presence of diazotization agents (10 equiv. $NaNO_2$ and 20 equiv. $HClO_4$); ***(b)*** Grafting mechanism.

The addition of these reactants ensures a total conversion of amine onto diazonium group which can either prevent the attachment from the amine side via oxidation of amine group and serve for further transformations. By sweeping the potential from 0.5 to 1.8 V/SCE, the absence of

the characteristic oxidation peak of amine at 1.25 V/ SCE is observed, confirming the occurrence of the diazotization reaction. The anodic current observed at the potential higher than 1.4 V corresponds to the oxidation of carboxylic group and the formation of radicals which are quickly attached to the electrode surface[33] (Figure 2.8). Next, the treated electrodes were immersed into MeCN solution containing 5 mM of the FcAQIm. After 2hrs at room temperature, the electrodes were removed from the solution, rinsed thoroughly with MeCN and dried under Ar stream.

Different available redox-states are revealed by using cyclic voltammetry in aqueous solution containing 0.1 M of HTFSI. As displayed in the Figure 2.9a, the electrochemical signature of the immobilized layer was observed at 0.3 V and -0.2 V/ SCE corresponding to the responses of Fc and AQ moieties, respectively. According to the quantity of charge measured separately from the voltammogram, the surface concentration of the Fc and AQ moieties is calculated to be $\Gamma_{Fc} = 1.78.10^{-10}$ and $\Gamma_{AQ} = 1.99.10^{-10}$ mol.cm^{-2} corresponding to saturated monolayer of [FcIm$^+$AQ][TFSI$^-$].

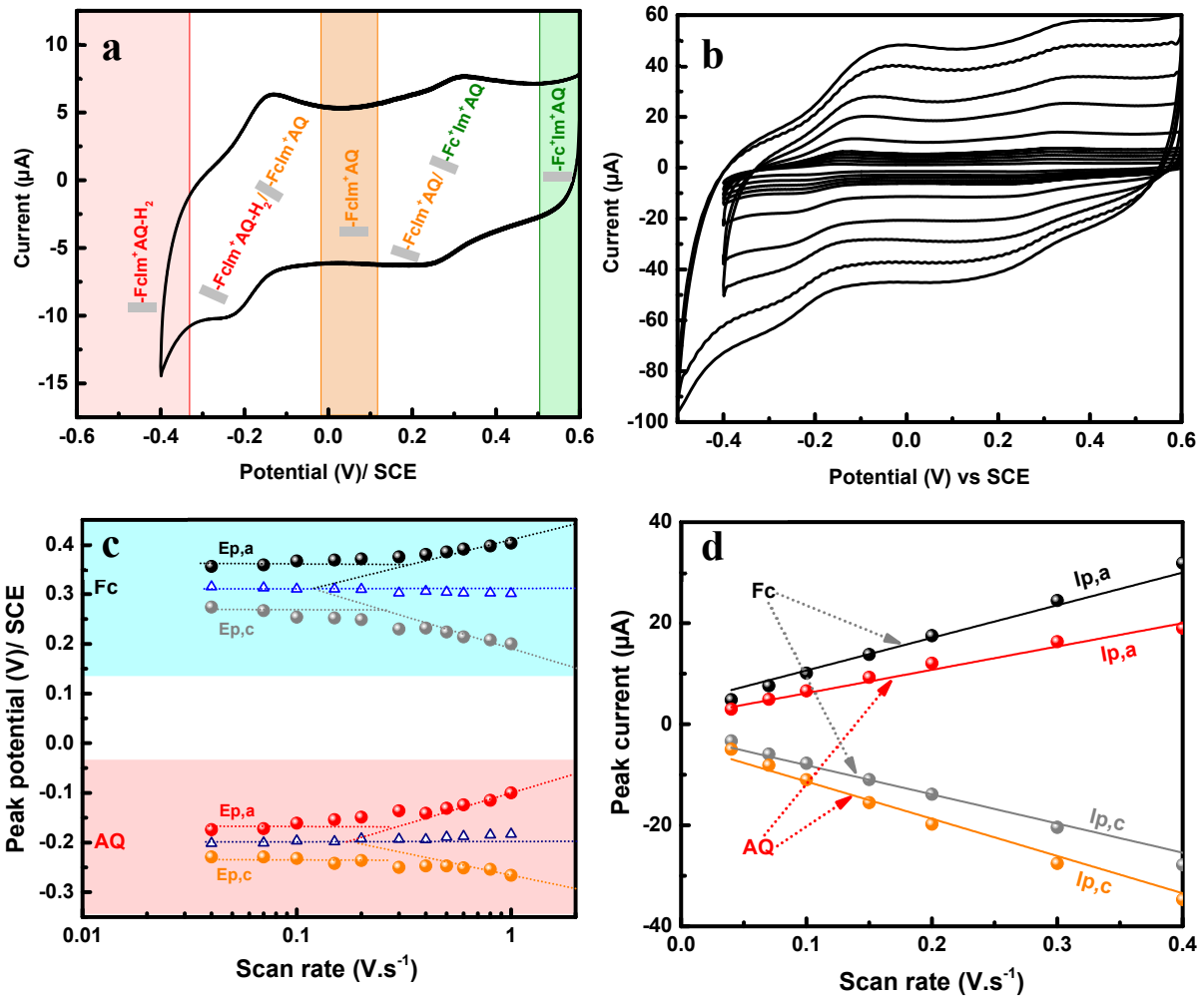

Figure 2.9 Cyclic voltammograms of immobilized [FcIm$^+$AQ][TFSI$^-$] in aqueous solution containing 0.1 M of HTFSI: ***(a)*** at v = 0.1 V.s^{-1}, ***(b)*** at different scan rates from 10 mV.s^{-1} to 1 V.s^{-1}; Variation of ***(c)*** the peak potential and ***(d)*** peak current in function of the scan rate.

For comparison, the surface coverage of alkyl thiol-terminated anthraquinone via self-assembled monolayer on Au is $2.8.10^{-10}$ mol.cm^{-2} and the value for Fc is around $4.0.10^{-10}$ mol.cm^{-2} [34]. In addition, as presented in the voltammogram, 3 different redox-states were identified as followed:

$$\underset{\text{State}[-1]}{AQH_2 - Im^+ - Fc} \xrightleftharpoons[2e^- + 2H^+]{} \underset{\text{State}[0]}{AQ - Im^+ - Fc} \xrightleftharpoons[1e^-]{} \underset{\text{State}[+1]}{AQ - Im^+ - Fc^+}$$

In acidic condition, the electrochemical switching window from the state [-1] to [+1] through [0] is about 0.8 V, i.e. [-0.3 V; 0.5 V/ SCE], which is reasonable for achieving stable system without degradation and enable for different variety of substrates. In addition, different to reported work on electrochemical multi-state redox systems by using self-assemble monolayer of bi-component system[34]. Briefly, monolayer of thiol-terminated anthraquinone was deposited onto Au wafer. Then the modified Au electrode was dipped into thiol-terminated ferrocene solution affording mixed layer via adsorption/desorption of AQ-based molecule. It has been demonstrated that the ratio Γ_{AQ}/Γ_{Fc} is ranging from 5 to 10. In our case, bi-redox molecules provide equimolar system where $\Gamma_{AQ}/\Gamma_{Fc} = 1$, simplify the preparation process and also increase the reproducibility. Furthermore, via Gomberg-Bachmann reaction, the FcAQIm molecules are covalently attached onto the electrode surface providing stronger stability for the modified electrode. Indeed, the stability of the film was confirmed by cycling in HTFSI for 100 scans from -0.4 V to 0.6 V vs. SCE resulting to a decrease of 3 % in term of current. It indicates that the film is strongly stable which is suitable for further investigations of charge transfer rate. Thus, by performing CV at different scan rate ranging from 10 mV.s^{-1} to 1 V.s^{-1}, linear relationship between the peak current and the scan rate was obtained which is typically characteristic of immobilized redox system onto electrode surface (Figure 2.9d). Furthermore, the electron transfer rate constants calculated from the variation of the peak potential in function of the scan rate exhibit a value of 22 s^{-1} (Fc) and 25 s^{-1}(AQ) (Figure 2.9c). These values are comparable with the ones reported via click chemistry. These values result from the formation of multilayer of diazonium. The oxidation of carboxylic groups conducts to the formation of radicals at the vicinity of the electrode surface. Consequently, the latter can interact with the surface resulting to the formation of the first organic layer. Furthermore, other radicals can also react with the existing layer via electrophilic substitution. In the previous case, 8 nm primary layer (4-azidophenyl film) induces an electron transfer rate constant of the FcPIm top layer of 23 s^{-1}. Similarly, the thickness of the whole layer is expected around 10 nm in which the diazonium layer is around 8 nm. The values were then confirmed by AFM scratch experiment.

Interestingly, the attached molecule contains immobilized imidazolium center that is positively charged and a labile anion that should be presented within the layer. This composition provides an ionic layer attached to the surface. Previous work reported in our group highlight the capability of using this ionic layer as a self-double layer leading to perform electrochemical measurement in the absence of supporting electrolyte[35]. The capacitive behavior of the layer was investigated by sweeping the potential in the capacitive region between -0.1 and 0.1 V using different scan rate (Figure 2.9a). The electrical double layer generated by the FcAQIm-modified electrode changed compared to bare GC electrode (Figure 2.10b).

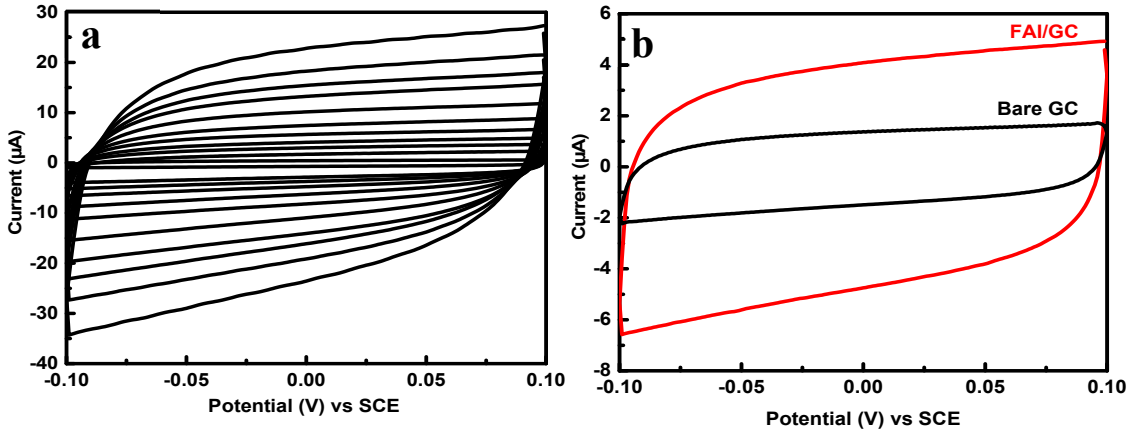

Figure 2.10 Cyclic voltammograms of immobilized [FcIm$^+$AQ][TFSI$^-$] in aqueous solution containing 0.1 M of HTFSI: ***(a)*** at different scan rate ranging from 10 mV.s^{-1} to 0.8 V.s^{-1}; ***(b)*** at v = 0.1 V.s^{-1} when compared with bare GC (black curve)

Indeed, the electrical double layer is referred to the equilibrium properties of the electrode as capacitance and surface tension of an electrode surface in solution containing salts. In the present case, the interface of electrode can be separated into 2 sub-interfaces: solid/ionic liquid interface and ionic liquid/water one.

To ensure the electroneutrality of the film, ionic transport from the aqueous phase to the ionic liquid layer is unavoidable with ionic fluxes $J_i = -D_i \nabla c_i - \frac{z_i F}{RT} D_i \nabla \phi + u c_i$ (2.9) where D_i, c_i, z_i, ϕ, u correspond to the diffusion coefficient, concentration, charge number of species i, electric potential and velocity, respectively. The electrical potential can be described by Poisson – Boltzmann theory for monovalent ions as:

$$\phi(x) = -\frac{2k_B T}{e} \ln\left[\frac{1+\gamma \exp(-z/\lambda_D)}{1-\gamma \exp(-z/\lambda_D)}\right] \quad (2.10)$$

with Debye screening length $\lambda_D = \sqrt{\frac{\varepsilon_r \varepsilon_0 k_B T}{2 c_0 e^2}}$ (2.11)

At the interface, the double layer capacitance is composed of capacitive contribution of both aqueous phase and ionic liquid layer. It is known that $C_d = \frac{C_d^{aq}.C_d^{IL}}{C_d^{aq} + C_d^{IL}} = \frac{\partial \sigma}{\partial(\phi^S - \phi^\infty)}$ (2.12) is the

capacity to store a charge density $\sigma = -\varepsilon_r \varepsilon_0 \frac{\partial \phi}{\partial x}$ (2.13) at x = 0 in response to a perturbation potential[36].

In presence of applied potential, the result for double layer capacitance is given as followed[37]:

$$C = \frac{dQ}{dE} = \frac{C_d^{aq}.C_d^{IL}}{C_d^{aq} + C_d^{IL}} \left\{ 1 + \frac{e}{C_d^{aq}} \left[\frac{d\Gamma_{aq}^{+}}{dE} - \frac{d\Gamma_{aq}^{-}}{dE} \right] - \frac{e}{C_d^{IL}} \left[\frac{d\Gamma_{IL}^{+}}{dE} - \frac{d\Gamma_{IL}^{-}}{dE} \right] \right\} \quad (2.14)$$

with Γ the interfacial concentration of ions. In our case, an assumption that the surface concentration of anion in the aqueous phase should be equal to the concentration of the imidazolium cation can be taken into consideration. Consequently, due to the high concentration of ionic species located within the ionic liquid layer, an increase of the double layer capacitance is observed as shown in the figure 2.9. The linear evolution of the capacitive current as function of the scan rate was derived from the figure 2.9a by following the equation below:

$i_C = -C_d \frac{dE}{dt}$ (2.15) where the slope indicates the value of the double layer capacitance, which is found to be around 570 μF.cm^{-2} (compared to 140 μF.cm^{-2} for bare GC).

In conclusion, the attachment of a bi-redox molecule onto the electrode surface was carried out by stepwise reaction. The novel interface exhibits interesting electrochemical behaviors, including multi-redox state and a high double layer capacitance. These properties come from the high ionic density of the immobilized species and the formation of the double junction at the electrode surface. This approach open promising ways for further uses as ternary memory and EGOFET-based sensor application

2.4 POLY(ELECTROACTIVE IONIC LIQUID) FILM BY ELECTROCHEMICAL POLYMERIZATION

In the previous parts, the electrode surface was modified by a thin film of electroactive ionic liquid varying from mono to biredox molecules. In addition to the thin film approach, the polymerization of ionic liquids is also an interesting process for generating novel interfaces. In the literature, the polymerization of ionic liquid is mainly performed via 3 routes[38,39]: polymerization or crosslinking of monomer ionic liquid, doping with ionic liquids and direct polymerization of IL-based monomer. In the literature, polymers bearing electroactive units were found to be interesting materials for a large spectrum of applications as organic and molecular electronics, (bio)analytical biosensors, (photo)electrochemical actuators, smart surfaces and energy storage and conversion materials. In this part, poly(1-allyl-3-ferrocenylmethylimidazolium bromide), poly(FcIL), was deposited on a platinum wire by

electrochemical reduction of its corresponding monomer. The polymer film characterized by electrochemical methods.

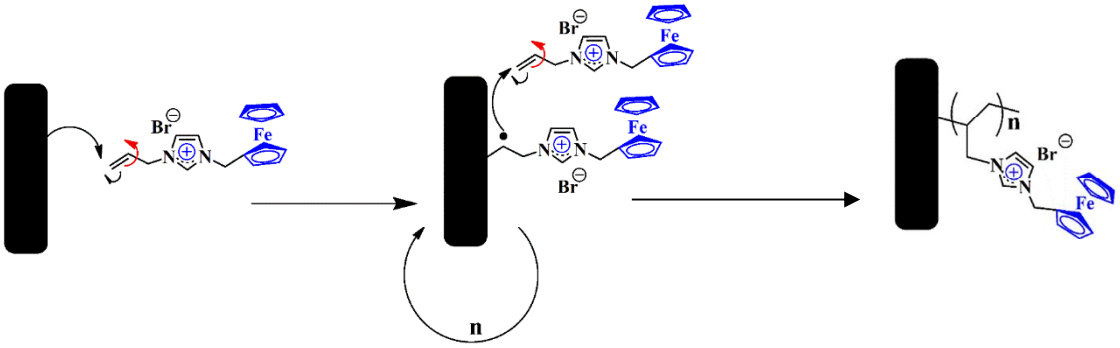

Scheme 2.4 Cathodic polymerization of 1-allyl-3-ferrocenylmethylimidazolium bromide

As reported in the literature, Poly(vinylferrocene) modified electrodes have been prepared by several polymerization methods, including electrochemical ones. Indeed, Leech et al.[40] reported that the electrochemical reduction of vinylferrocene monomer provides a stable and compact electroactive polymer film. This procedure was followed to polymerize 1-allyl-3-ferrocenylmethylimidazolium bromide monomer on a platinum electrode. The electrochemical polymerization was carried out with a three-electrode setup using a Pt wire as the working electrode, a stainless-steel mesh as the counter electrode and Ag|AgCl as the reference electrode. Platinum wire was immersed in a solution containing 5 mM of 1-allyl-3-ferrocenylmethylimidazolium bromide and 0.1 M of $TBAPF_6$ in MeCN. The solution was deoxygenated by argon flow for 30 min.

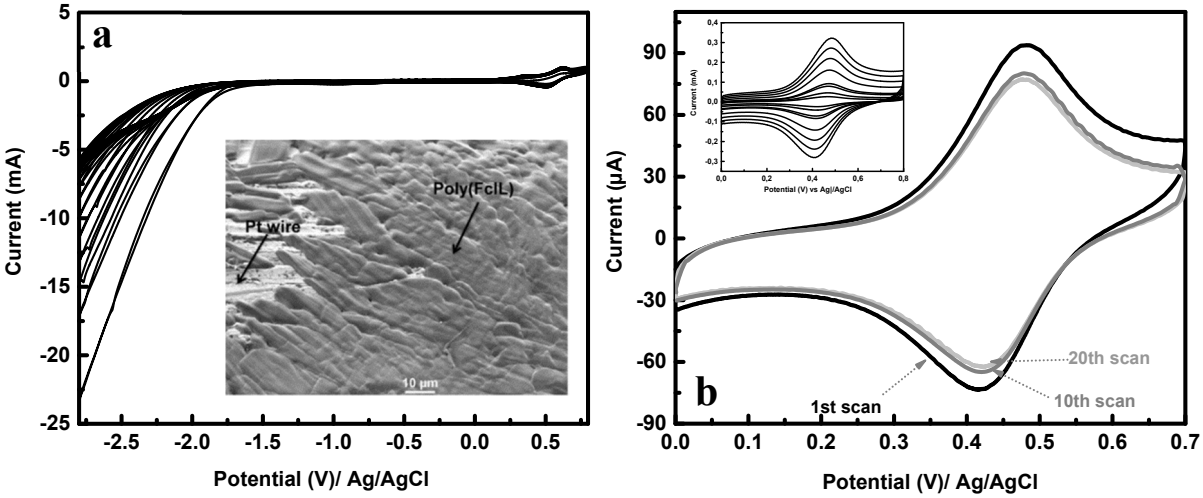

Figure 2.11 ***(a)*** Cyclic voltammetry at Pt wire in an acetonitrile solution containing 5 mM of 1-allyl-3-ferrocenylmethylimidazolium bromide monomer and 0.1 M $TBAPF_6$, ***inset*** represents the SEM image of Pt/Poly(FcIL); ***(b)*** cyclic voltammetry of polymer-coated Pt wire in MeCN containing 0.1 M TBAPF6, 1st scan (black), 10th scan (gray) and 20th scan (light gray). Inset: variation of the CVs as function of the scan rate.

Continuous cycling by using cyclic voltammetry technique (20 cycles) over the potential range from 0.8 to −2.8 V vs Ag|AgCl was performed, as shown in Figure 2.11a. During the first scan, a reversible redox signal attributed to the ferrocenyl group linked to the vinyl imidazolium

monomer was observed at 0.5 V. Scanning to negative potential shows a reduction current starting from −1.8 V, which is assigned to the reduction of the allyl group. From this potential, the allyl group was reduced to form corresponding radical anion which can attached to the electrode surface. Upon continuous cycling the reduction current decreased due to the formation of an electronically insulating film, indicating that the polymer had been formed. After a few cycles, the current was saturated, and the film thickness reached its limit. After the polymerization, the modified electrode was rinsed carefully with acetonitrile. A yellow film was visually observed on the platinum wire, indicating the formation of a polymer film. The modified wire was characterized by SEM which shows the presence of a dense and homogeneous polymer film coated the Pt wire (inset Fig.2.11a). In the literature, poly(vinylferrocene) has been produced under the same conditions, showing similar behavior, and the film was found to be stable and free of large pinholes[40]. To check for the presence of polymer on the electrode, the latter was characterized by cyclic voltammetry in MeCN solution containing 0.1 M $TBAPF_6$. The redox signal of the immobilized ferrocenyl groups was observed at 0.47 V/ Ag|AgCl as illustrated in Fig.2.11b. The peak-to-peak separation was found to be around 30 mV and the current intensity was slightly decreased after 10 cycles, corresponding to desorption of weakly attached units. After that, there was no further significant change in current intensity observed upon cycling, indicating the high stability of the polymer film.

It is worth noting that one of the frequently encountered drawbacks in ionic liquid environment is related to the selection of an appropriate reference electrode (RE). Because of the unique physical-chemical requirements, the choice of REs for electrochemical measurements in ionic liquids and deep eutectic solvents is very restricted. Currently, saturated calomel electrode (SCE) and Ag|AgCl are widely used as REs in non-aqueous solutions. However, these electrodes generate an undesirable liquid junction between the aqueous phase inside the electrode and the non-aqueous phase from the bulk solution, as well as causing diffusion of water from the RE to the solution, resulting in undesirable contamination. An ideal reference electrode should be stable over time, i.e. the reference potential does not drift or shows minimal drift (ideally < 10 mV per day)[41]. The RE commonly reported in the literature for use in ionic liquids is based on a metal/ metal ion system ($Ag|Ag^+$). This RE was fabricated by immersing Ag wire in an ionic liquid solution containing a silver salt[42–44]. Despite the moderate stability of these REs, the presence of a small amount of water inside the electrode may cause the formation of silver nanoparticles in a solution containing Ag^+ and the ionic liquid anion ($TFSI^-$). In addition, these types of electrodes can cause undesirable electrochemical signals due to the diffusion of Ag^+ from the RE into the test solution. To overcome this issue, quasi-reference electrodes (QREs) based on metallic wires (silver or platinum) have been proposed[45]. In this case, an internal reference such as ferrocene is frequently employed to calibrate the reference electrode against the commonly used reference system. However, the latter exhibits a potential

drift with time during a series of electrochemical measurements due to the formation of metal oxide. Recently Kötz et al. proposed activated carbon as a convenient QRE for use in non-aqueous media[46,47]. In addition, solid state QREs based on metallic wire coated with polymers have also been proposed for electro- chemical investigations in non-aqueous solutions[48–50]. Within this context, the Pt coated with partially oxidized poly(FcIL) could be used as a quasi-reference electrode by following the argument that the ionic liquid-based polymer is stable in ionic liquid solution.

However, after cycling for several cycles, the ferrocene units were in a neutral state and the electrode is not ready for use as a reference electrode. A second step is necessary to partially oxidize the attached layer. To this end, a half wave potential was applied (0.4 V) during 20 s, producing a partially oxidized polymer film. The quantity of the charge introduced during the partial oxidation process is 150 µC.cm^{-2}.

The stability of the as-prepared RE was investigated by performing several electrochemical tests in an ionic liquid and a non-aqueous solution in the presence of a redox system. In this study, acetonitrile (MeCN) was chosen as the non-aqueous solution and 1-ethyl-3-methylimidazolium bis(trifluoromethane)sulfonimide (EMITFSI) as the ionic liquid. Cyclic voltammograms were recorded in the presence of 1 mM Fc using a glassy carbon electrode as the working electrode and Pt/poly(FcIL) as the reference electrode in electrolytic acetonitrile solution (Fig. 2.12b) and in the ionic liquid (EMITFSI) (Fig. 2.12c).

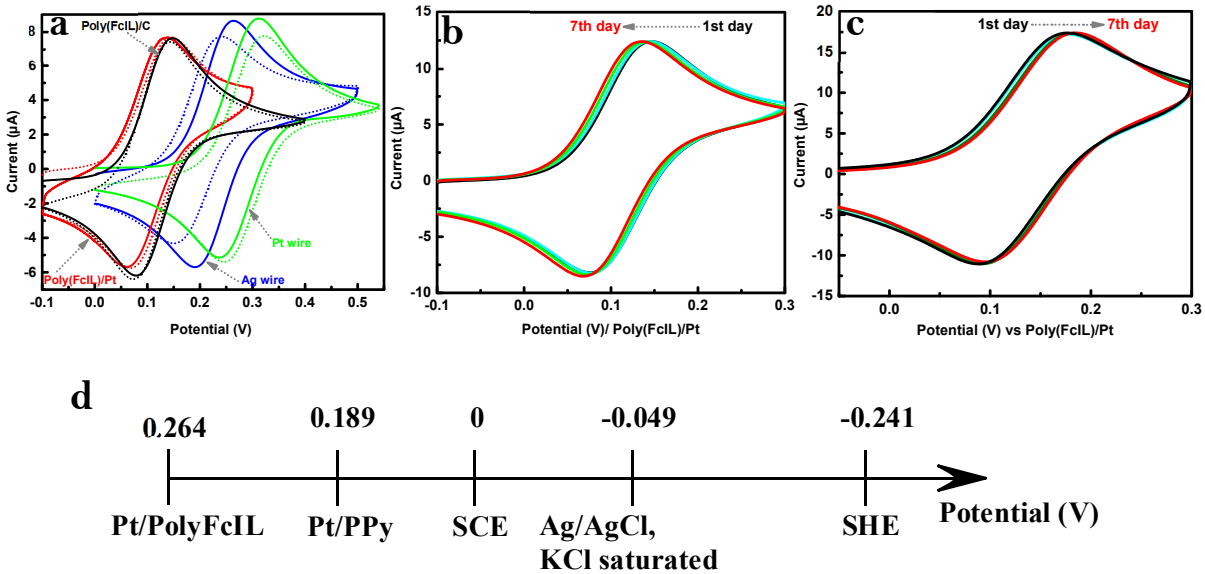

Figure 2.12 (a) CVs in EMITFSI solution containing 1 mM Fc, 1st scan (solid line), 500th scan (dotted line). Red curves: Pt/poly(FcIL) as reference electrode, black curves: C/poly(FcIL) as reference electrode, blue curves: Ag wire as reference electrode and gray curves: Pt wire as reference electrodes; Cyclic voltammetry onto GC electrode in solution containing 1 mM ferrocene using Pt/poly(FcIL) as reference electrode over times ***(b)*** in acetonitrile containing 0.1 M $TBAPF_6$; ***(c)*** in EMITFSI solution; ***(d)*** scheme showing the potential of Pt/poly(FcIL) versus other reference electrodes.

In all the tested solutions, the redox couple exhibits the typical features of a reversible redox system. The $E_{1/2}$ of the ferrocene in solution was 0.112 V versus Pt/poly(FcIL). CVs were also recorded over 7 days using the same Pt/poly(FcIL) reference electrode, which was washed and kept in air without any protection between the measurements. Five series of 20 cycles were performed each day. During this period, a small drift in potential is observed (7 mV in EMITFSI and 12 mV in MeCN after 7 days), demonstrating an excellent stability of the Pt/poly(FcIL) reference electrode in ionic liquid and electrolytic acetonitrile solution (Table S2.1). The stability of the reference electrode is higher in the ionic liquid. Fig. 2.12a compares the CVs of 1 mM Fc in ionic liquid, EMITFSI, using an Ag wire (shown in blue), a Pt wire (gray) and Pt/poly(FcIL) (red) as quasi-reference electrodes. After 500 scans, a negligible potential drift (< 5 mV) was observed in the case of the Pt/poly(FcIL) QRE, while this value increases to 50 mV under the same conditions when using an Ag wire as QRE and reaches 25 mV for a Pt wire. For similar investigations in acetonitrile solution, the potential drift was found to be < 10 mV with the Pt/poly(FcIL) reference electrode while a larger potential drift (> 70 mV) was observed for an Ag wire. These results demonstrate the superior stability of the proposed QRE compared to bare Ag or Pt wire. A similar experiment was also performed using a carbon rod covered with poly(FcIL) as a reference electrode and the potential drift was found to be around 5 mV after 500 cycles (Fig. 2.12a black curves). From the above results, the potential of the Pt/poly(FcIL) reference electrode is 0.264 V vs SCE or 0.505 V vs SHE in acetonitrile solution containing 0.1 M of $TBAPF_6$ (Fig.2.11d).

As highlighted in a previous study, the performance of the reference electrode can be affected by the anions present in the supporting electrolyte[29]. The potential of the Pt/poly(FcIL) QRE is strongly dependent on the ease with which the anions can move from the bulk solution into the polymer film. To investigate the influence of the supporting electrolyte anions, the open circuit potential (OCP) of a Pt/poly(FcIL) electrode, fabricated in MeCN with PF_6^- as a counter-ion, was studied in MeCN solution containing different anions.

Table 2.2 Open circuit potential (OCP) of Pt/poly(FcIL) reference electrode in acetonitrile solution containing different supporting electrolyte anions.

Supporting electrolyte (0.1 M)	Bu_4NOH	Bu_4NCl	Bu_4NClO_4	Bu_4NBF_4	$Bu_4NPF_6^-$	$Bu_4NCF_3SO_4$	Bu_4NHSO_4	Bu_4NBr
OCP of Pt/Poly(FcIL) (V) vs SCE	-0.455	0.174	0.188	0.246	0.251	0.368	0.377	0.722
Supporting electrolyte	LiTFSI (0.1 M)		Pure EMITFSI		1mM Np-EMITFSI		Np^--EMITFSI	
OCP of Pt/Poly(FcIL) (V) vs SCE	0.504		0.358		0.23		0.176	

The results are summarized in Table 2.2. The Pt/poly(FcIL) electrode was immersed in the solution for 10 min prior to the electrochemical measurements. As expected, the OCP depends on the nature of the anion used. The OCP variation might be amplified by the presence of the imidazolium ring, which also has an exchangeable counter-ion. Despite the problem of ion exchange, the stability of the reference electrode is important in all electrolytes. CVs recorded in MeCN containing 1 mM Fc solution with $TBAPF_6$ using Pt/poly(FcIL) as a reference

electrode before and after several electrochemical measurements in different supporting electrolytes show a negligible change in standard redox potential (lower than 5 mV). Finally, the OCP variation could be eliminated by placing the reference electrode in a Teflon tube with frit which improves the stability of the reference electrode.

An ideal reference electrode should have a non-polarizable interface in which the potential does not vary with the current flow within the electrode. To explain the behavior of the redox poly(FcIL) as a reference electrode, we invoke the thermodynamic feature of the system, for instance the chemical capacitance. Pelton introduced and defined the chemical capacitance C_{ij} of a species i with respect to species j as:

$$C_{ij} = \left(\frac{\partial \mu_i}{\partial n_j}\right)^{-1}_{T,P} = \left(\frac{\partial^2 G}{\partial n_j^{\,2}}\right)^{-1}_{T,P} \quad (2.16)$$

Where μ_i is the chemical potential of i, n_j is the number of moles of j, and G is the Gibbs energy. According to the definition of the chemical potential, $\mu_{ij(\partial G/\partial n_i)}$, one has the reciprocal relationship $C_{ij} = C_{ji}$. For an electrochemical reaction $Ox + e^- \leftrightharpoons Red$, the redox potential E is defined as:

$$E = E^{0'} + \frac{RT}{F}\ln\left(\frac{a_{Ox}}{a_{Red}}\right) \quad (2.17)$$

where $E^{0\prime}$ is the formal potential of the redox couple and a_{Ox} and a_{Red} are the activities of the oxidized and reduced species. At the equilibrium $dE = -d\mu_{e-}$, where μ_{e-} represents the chemical potential of the electron in the supporting metallic electrode. Then dE/dn_j can be calculated from the chemical capacitance of the electron $C_{e-,j}$ by

$$\frac{dE}{dn_j} = -\frac{1}{F.C_{e^-,j}} \quad (2.18)$$

According to Eq. (2.18), the chemical capacitance is related to the "redox potential-buffering". This equation is directly related to Figure 2.10b, indicating that an electrochemical system with a large chemical capacitance can accept a large amount of electric charge with only a small change in the electrical potential. The chemical capacitance plays an important role in the field of electrochemical energy storage and particularly in batteries, where the energy stored chemically can be viewed as a chemical capacitor.

In summary, we propose a facile route to fabricate a Pt/poly(FcIL) reference electrode. The latter exhibits strong stability to repetitive electrochemical measurements over a long period. The QRE has several advantages compared to a conventional reference electrode, including the absence of contamination and liquid junction problems. The Pt/poly(FcIL) quasi-reference electrode was found to be stable for 7 days in acetonitrile and in ionic liquid solutions. The QRE could be made at a small scale and used as a RE in microelectrochemical cells as an alternative to silver wire. The stability of the QRE could be enhanced by placing the Pt/poly(FcIL) in a Teflon tube with frit. Moreover, as the temperature window of ionic liquids

is larger than that of other materials, we anticipate that the RE could be used over a wider range of temperatures and pressures than conventional reference electrodes.

2.5 POLY(ELECTROACTIVE IONIC LIQUID) BRUSHES BY SI-ATRP

Even though the important application of poly(FcIL) coated Pt wire in electrochemistry as reference electrode, the main drawback of the polymerization by means of electrochemical reduction comes from the uncontrollable nano-structuration of the final polymer film. In order to perform a nanostructured polymer, other polymerization methods should be used. To this end, surface-initiated atom transfers radical polymerization (SI-ATRP) has been reported to achieve immobilized brush-like structure of the polymer at the electrode surface. The ATRP process is widely used in material science to achieve controllable architecture and molecular weight of polymer. This procedure was discovered independently by J-S Wang and K. Matyjaszewski[51] and by M. Sato et al[52] in 1995 as an expansion of transition metal catalyzed atom transfer radical addition (ATRA) (Eq. 2.19 – 2.21). The first reaction involved during the polymerization process is referred to the Kharasch addition or metal-catalyzer free radical addition of $CXCl_3$ (X is halogen atom) to alkenes.

$$\left[M^{n}\right] + CXCl_3 \rightleftarrows \left[M^{n+1}\right]Cl + \bullet CXCl_2 \qquad (2.19)$$

$$RR'C = CH_2 + \bullet CXCl_2 \rightleftarrows RR'\dot{C} - CH_2 - CXCl_2 \qquad (2.20)$$

$$RR'\dot{C} - CH_2 - CXCl_2 + \left[M^{n+1}\right]Cl \rightleftarrows RR'ClC - CH_2 - CXCl_2 + \left[M^{n}\right] \qquad (2.21)$$

The repetitive addition of alkenes to the radical species can occur if the radical generated during the second step (Eq. 2.20) has comparable reactivity before and after the radicalization and the latter must be sufficiently stabilized. This is the basis of the atom transfer radical polymerization (ATRP). The general mechanism of ATRP is presented as followed:

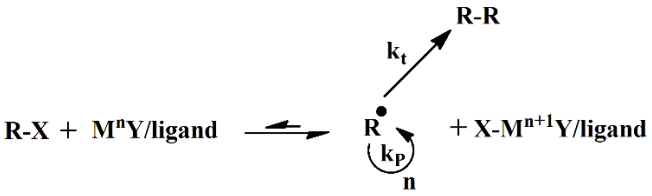

k_t rate constant for the terminaison step

k_P rate constant for the propagation step

Later, Surface-initiated ATRP has been developed to perform the polymerization onto the substrate surface[53,54]. The SI-ATRP process is based on the immobilization of thin initiator layer bearing halide terminator. In the literature several initiators have been described and attached to the surface by means of various grafting procedure including electrochemically assisted method[55,56].

In our case, the immobilization of initiator layer was performed using the oxidative grafting of primary amine, 2-bromoethylamine, yielding to a bromide terminated electrode.

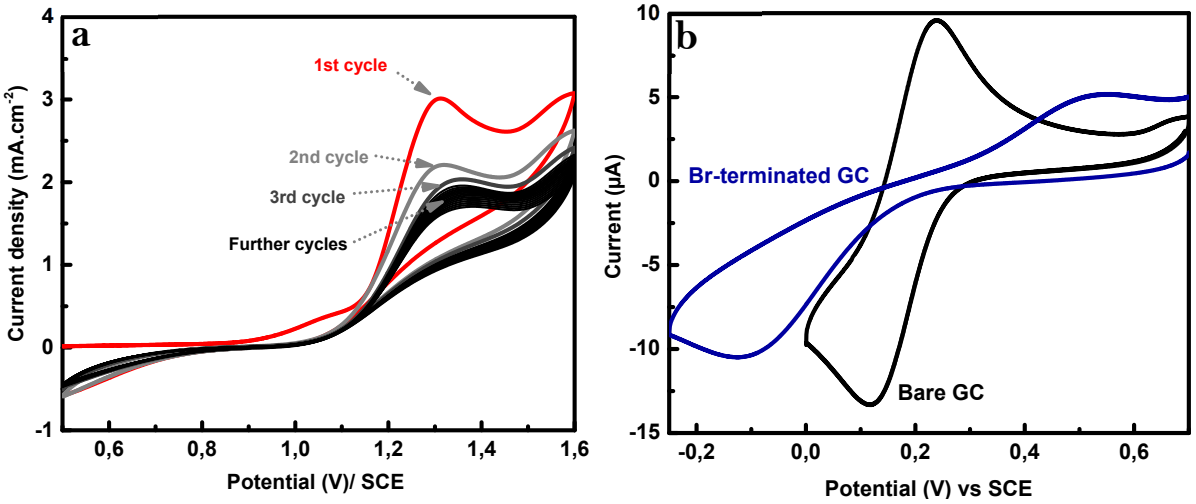

Figure 2.13 (a) Cyclic voltammograms for the oxidation of 3 mM of 2-bromoethylamine hydrobromide in aqueous solution with 0.1 M of $LiClO_4$; ***(b)*** Cyclic voltammograms in aqueous solution containing 0.1 M KCl and 1 mM of $K_3Fe(CN)_6$ by using (black) bare glassy carbon electrode and (blue) Bromide terminated electrode

Briefly, by sweeping the potential from 0.5 V to 1.6 V/ SCE, an irreversible oxidation peak was observed at 1.2 V/ SCE (Fig.2.13a) corresponding to the oxidation of primary amine function to aminyl radical. Unlike single electrochemical step formation of radical by means of electrochemical reduction of diazonium's salt derivatives, aminyl species are more difficult to attach to the electrode surface due to the complexity of the system via multistep reactions as shown in the Scheme 2.3 and 2.S1[57]. Nevertheless, the oxidation current is strongly decreased from the second scan that indicates the formation of a thin initiator film onto the electrode surface and its blocking behavior. Besides, the immobilization of a thin layer of the 2-bromoethylamine onto the electrode surface was evidenced by characterization in aqueous solution containing 1 mM of $K_3Fe(CN)_6$ and 0.1 M of supporting electrolyte resulting to 2 different behaviors (Figure 2.12). For bare GC electrode, well-defined reversible signal (ΔE = 70 mV) was observed at 0.15 V/ SCE corresponding to the reduction of the $[Fe(CN)_6]^{3-}$ to $[Fe(CN)_6]^{4-}$. Interestingly, the recorded CV signal for Br-terminated GC electrode exhibits an extremely high ΔE (around 700 mV), suggesting low electron transfer rate towards inner-sphere electroactive mediator attributed to the presence of the chemisorbed species, 2-bromoethylamine, at the electrode surface.

Following that, the modified electrode with the initiator layer was immersed in solution containing the redox ionic liquid monomer and all the necessary reagents (CuCl, $CuCl_2$ and PMDETA as activator, deactivator and complexing agent, respectively) as presented in the scheme 2.3. After keeping the polymerization for 2 hrs under inert atmosphere, the electrodes were removed from the solution, successively rinsed with distilled water, acetone and MeCN, respectively. Later, the polymer modified electrodes were characterized using different analytical and electrochemical tools.

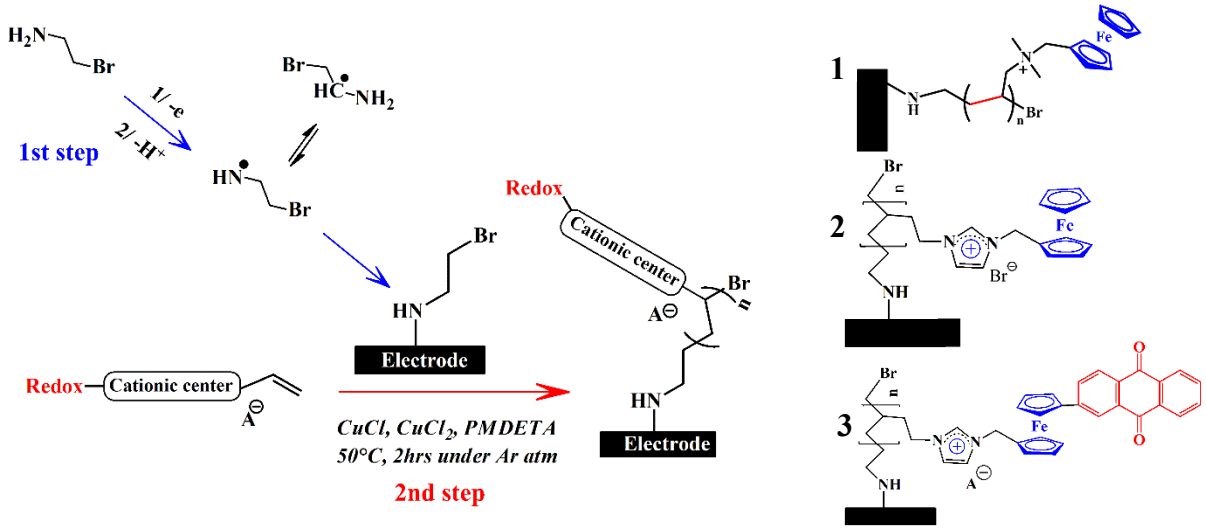

Scheme 2.3 Scheme illustrating the SI-ATRP procedure of some typical poly(redox-active ionic liquids)

For this chapter, three different monomers, listed below, will be used for functionalization of the electrode surface as illustrated in the scheme 2.3.

1. N,N-dimethyl-N-ferrocenylmethyl-prop-2-en-1-ammonium bromide
2. 1-allyl-3-ferrocenylmethylimidazolium bromide
3. 1-allyl-3-(1-anthraquinone-1'-methyl)ferrocenylimidazolium bromide

2.5.1 Poly(N,N-dimethyl-N-ferrocenylmethyl-prop-2-en-1-ammonium bromide)

Before immobilizing the N,N-dimethyl-N-ferrocenylmethyl-prop-2-en-1-ammonium bromide onto the electrode surface, the electrochemical behaviors of the quaternary ammonium ionic liquid were investigated in solution as shown in the figure 2.14.

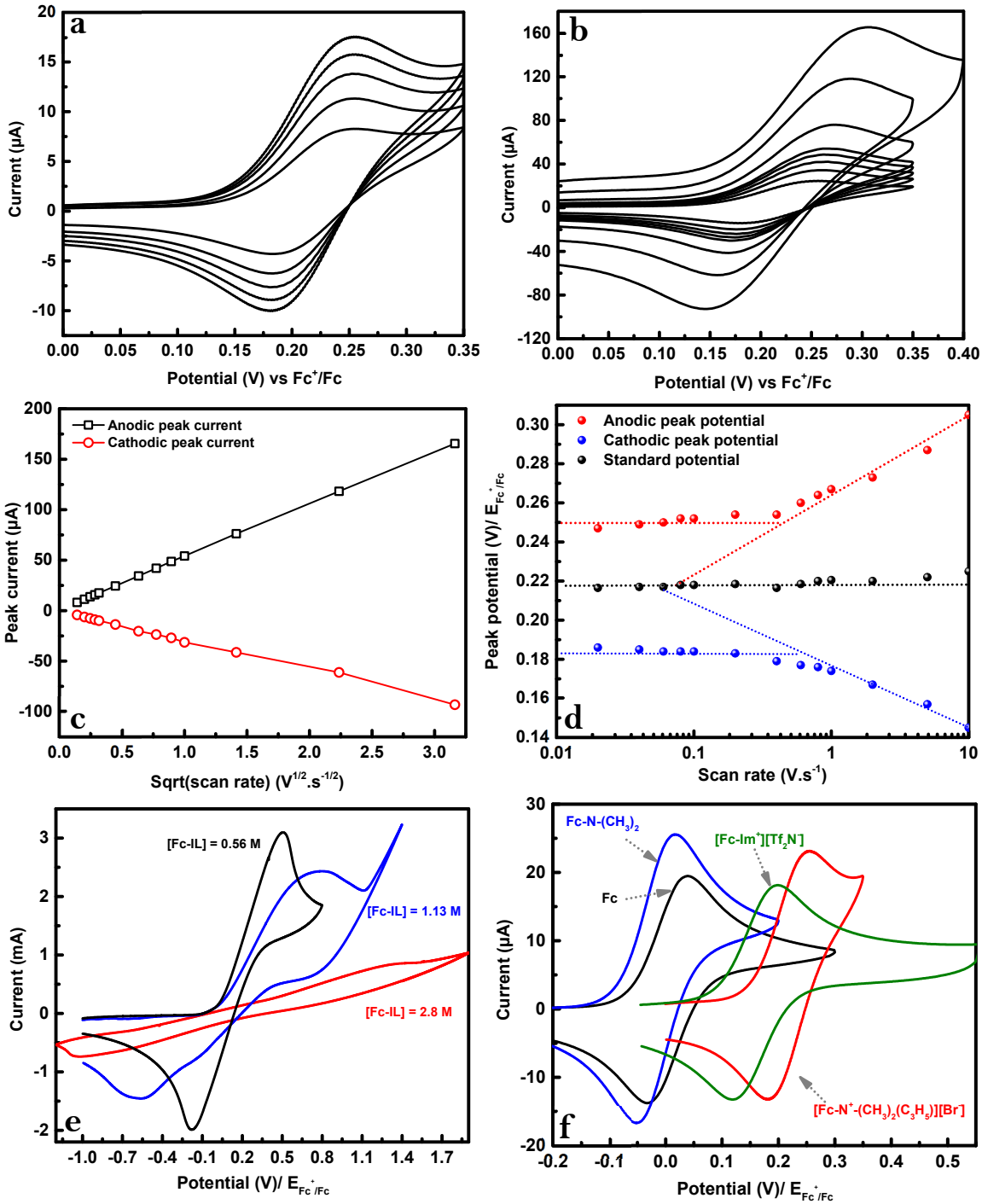

Figure 2.14 Cyclic voltammograms of the N,N-dimethyl-N-ferrocenylmethyl-prop-2-en-1-ammonium bromide monomer recorded at different scan rates : ***(a)*** from 20 $mV.s^{-1}$ to 0.1 $V.s^{-1}$; ***(b)*** from 0.1 $V.s^{-1}$ to 10 $V.s^{-1}$; ***(c)*** Variation of the oxidation peak current in function of the scan rate; ***(d)*** Variation of the peak potentials in function of the scan rate; ***(e)*** CV's of undiluted redox monomer ionic liquid and diluted in acetonitrile, scan rate 0.1 $V.s^{-1}$; ***(f)*** CV's of different Fc derivatives in MeCN solution containing 0.1 M of Bu_4NPF_6, scan rate 0.1 $V.s^{-1}$

The electrochemical behavior of the synthesized molecule was studied by cyclic voltammetry. Fig.1.14a-b exhibit a reversible signal at 0.22 V/ Fc^+/Fc corresponding to ferrocenyl ammonium redox couple. Besides that, the evolution of the redox signal as function of the scan rate shows linear relation between the peak current and $v^{1/2}$, as shown in Figure 2.14c, suggesting that the system is under diffusion-controled regime. A difference in the slope of the anodic and cathodic part is observed suggesting the change in the diffusion coefficient of the oxidized and reduced species. This linearity leads to determine the diffusion coefficient of the redox molecule using the Randles-Sevčik equation and values of 7.6×10^{-6} and 2.4×10^{-6} $cm^2.s^{-1}$ were measured for $D_{Fc\text{-ammonium}}$ and $D_{Fc^+\text{-ammonium}}$, respectively.

Fig.2.14e shows the electrochemical response of highly conccentrated ferrocene quaternary ammonium ionic liquid and diluted ones in acetonitrile. For a saturated ionic liquid in MeCN, the concentration is around 2.8 M and the recorded CV shows a weak oxidation and reduction peaks with a large peak potential separation caused by a large solution resistance (iR Ohmic drop) and the high viscosity. However, after gradually diluting with acetonitrile the electrochemical response exhibits more defined oxidation and reduction peaks and the redox signal is well defined at a concentration of 0.56 M. This experiment evidences the possibility to record the electrochemical signal of ferrocene based ammonium ionic liquid at a concentration higher than 1 M. Besides, the electrochemical signal of different Fc-based derivatives shows the important role of the substituents. Indeed, by linking the Fc moiety to a tertiary amine group, the standard potential has tendancy to shift to negative value ($E^0_{Fc^+\text{-N/Fc-N}}$ = -0.05 V vs $E^0_{Fc^+/Fc}$) while the substituent becomes cation center, the electron withdrawing effect (EWE) induces positive shift. To summarize, the EWE effect induced by different substituent increase in the following order : $-N(CH_3)_2$ < Ø < –Imidazolium < –Quaternary ammonium (Fig.2.14f).

After investigating the electrochemical properties of the monomer in solution, the surface functionalization by using SI-ATRP procedure was performed. The analysis of the polymer was started by the investigation of the chemical composition at the extreme surface using X-ray photoelectron spectroscopy (XPS) as illustrated in the figure 2.15.

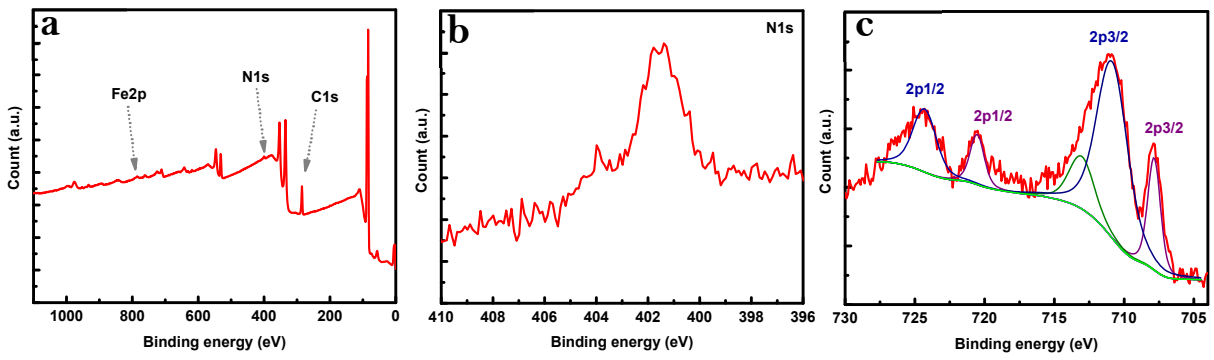

Figure 2.15 (a) XPS survey spectrum of Poly(N,N-dimethyl-N-ferrocenylmethyl-prop-2-en-1-ammonium; ***(b)*** and ***(c)*** high resolution XPS spectra of N(1s) and Fe(2p)

The deconvolution of the C(1s) spectra exhibits the presence of 4 components at binding energy of 285, 285.8, 286.6 and 288.3 eV. The peak at 285 eV is attributed to the binding energy of carbon atom derived from the C in hydrocarbons (C-C and C-H), while the peak at 285.8 eV is attributed to C-O band. The band at 286.5 eV is attributed to C-N bonds of the quaternary ammonium. The small signal at 288.3 eV is linked to -COO from the surface contamination. The XPS spectrum of N(1s) (Figure 2.15b) shows the presence of peak at 402 eV corresponding to N in the ammonium groups[57]. Finally, the Fe(2p3/2) signal (Figure 2.15c) displays two peaks at 708 and 710.4 eV attributed to Fe(II) (ferrocene in its reduced state) and Fe (III) (in the form of ferrocenium), respectively. The other peaks at 721 and 724 eV correspond to the signal of Fe(2p1/2) of Fe(II) and Fe (III), respectively[58]. The presence of ferrocenium could be due to the oxidation of ferrocene under X-ray irradiation. Besides, a small signal of Br^- is observed corresponding to the anion of the Poly(ferrocenyl quaternary ammonium) ionic liquid. The atomic percentage of the C(1s) is around 45% while the Br shows a value around 3%. In addition, the atomic ratio N/Fe is about 1.2, which suggests that the observed surface species is derived from Poly(ferrocenyl quaternary ammonium) (theoretical ratio N/Fe = 1). The polymer film thickness was measured by AFM scratch experiment and an average thickness of 25 nm was obtained which is similar to the previously reported work[35].

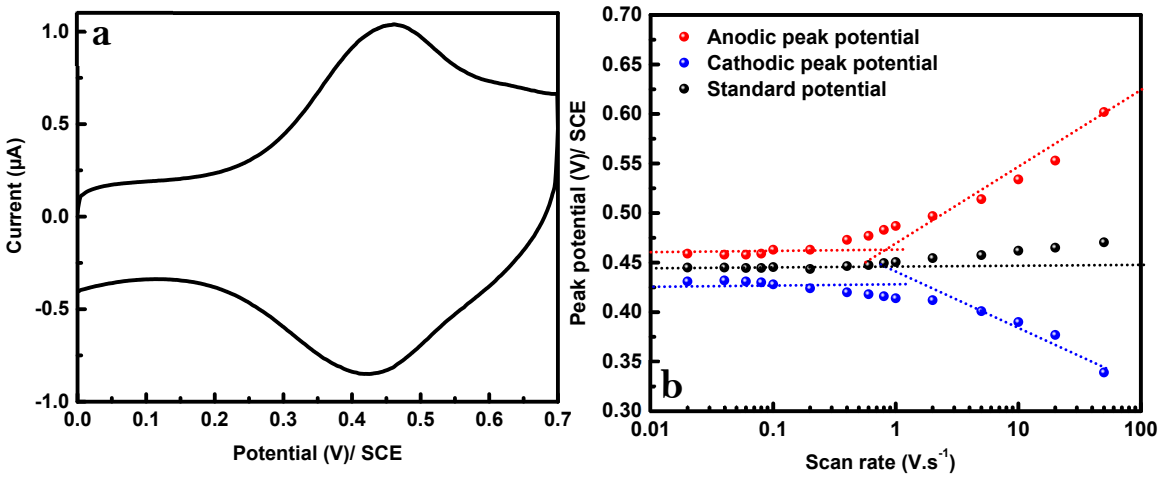

Figure 2.16 (a) CV response of the attached Poly(ferrocenyl quaternary ammonium) onto GC electrode in acetonitrile solution containing 0.1 M Bu_4NPF_6, 0.1 V/s; ***(b)*** Variation of the peak potentials in function of the scan rate.

Figure 2.16 displays the electrochemical response of the Poly(ferrocenyl quaternary ammonium) modified GC electrode in electrolytic acetonitrile solution. The recoded CV shows the presence of a well-defined reversible redox system at 0.45 V/ SCE attributed to the redox couple Fc^+/Fc within the polymer backbone. This electrochemical signal confirms the success of the SI-ATRP polymerization using Fc quaternary ammonium monomer. The peak-to-peak potential is almost 0 V confirming the attachment of the Fc onto the electrode surface. The coulometric investigations lead to determine the surface coverage and an average value of $1.2.10^{-9}$ mol·cm^{-2} was estimated by using the formula $\Gamma = Q/nFA$ where Q is the charge

collected from the anodic peak, n the number of exchanged electron and A the area of the electrode. Compared to previous works, the average grafting densities of the Poly(ferrocenyl quaternary ammonium) brushes is ranged from 0.3 to 0.8 chains.nm^{-2}.[17]

The electrochemical responses of the polymer were performed at different scan rates as illustrated in Figure 2.S2a-c. This investigation clearly shows a linear variation of the peak current versus the scan rate suggesting the presence of non-diffusive process (Fig.S2.2d). Besides that, for higher scan rate (above 1 V.s^{-1}) the redox signal of ferrocene starts to deviate from fully reversible system indicating that the system is limited by the electron transfer rate. The linear dependency of the E_p vs Log(v) leads to determine the apparent electron transfer rate constant which is found to be around 120 s^{-1} highlighting the presence of fast electron transfer of the attached ferrocenyl groups. Several parameters could explain the fast electron transfer rate including the structure of the polymer in the form of brushes, the short distance of the initiator (the ferrocene units are close to the electrode and the electron transfer could occur easily across this layer) and the composition of the polymer which includes positive and negative charges. Indeed, the presence of ions within the film may enhance the electron hopping process and consequently the electron transfer rate.

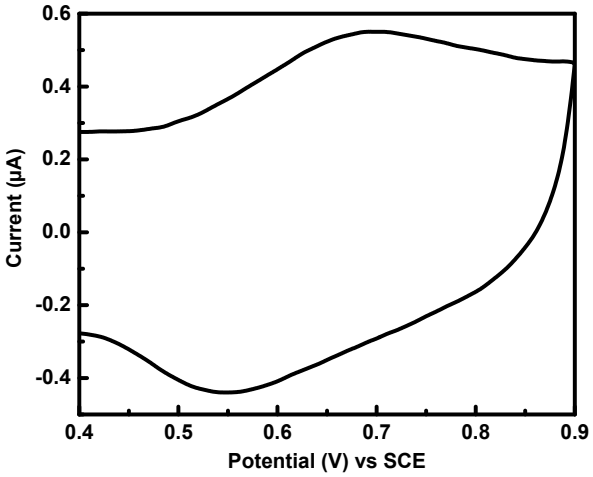

Figure 2.17 CV responses of the Poly(FcN_4)/GC in acetonitrile free of electrolyte.

Poly(ionic liquids) refer to a subclass of polyelectrolytes that contain an ionic liquid (IL) species in each monomer repeating unit, connected through a polymeric backbone to form a macromolecular structure. They are considered as interesting materials for electrochemical applications (batteries, supercapacitor, and solid electrolyte) thanks to the presence of ionic species inside the structure. Having these characteristics, the electrochemical responses of the generated polymer was performed in acetonitrile solution in the absence of supporting electrolyte (Fig.2.17). The curve shows clearly the presence of oxidation and reduction waves corresponding to the Fc^+/Fc redox couple despite the absence of supporting electrolyte. Compared to the CV in Fig.2.16a the peaks currents are slightly lowered, and the peaks potentials are shifted to more positive potential. This result could suggest that (i) the generated polymer brushes act as self-supporting electrolyte thanks to the presence of cation and the anion

within the film, (ii) The first oxidized ferrocene could induce electron hopping and participate to the oxidation of the adjacent ferrocene minimizing the need of ion ingress and egress from the solution to the polymer film, (iii) the oxidation/reduction of the Fc units is not limited by the rate of counter-ion migration into/out of the polymer.

The modulation of the properties of interfaces such as the variation of the wettability is of high interest. Figure 2.18 shows the contact angle (CA) variation, for the Poly(ferrocenyl quaternary ammonium) attached onto ITO substrate, after electrochemical switch and anions exchanges

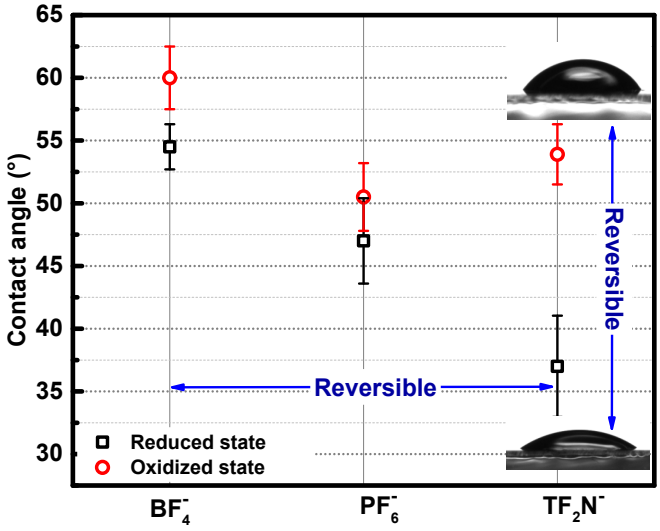

Figure 2.18 Contact angles obtained for Poly(ferrocenyl quaternary ammonium) deposited onto ITO substrate before and after electrochemical oxidation and anions exchanges.

Interestingly, whatever the used anion the electrochemical oxidation induces increase of the CA. Besides the electrochemical modulation of the CA, the latter could also be tuned by anions exchange as illustrated in Figure 2.18. The electrochemical and anions exchanges processes, for contact angle modulation, are fully reversible. Furthermore, a common behavior was observed with a higher the contact angle's value for the oxidized state of the polymer. Within 3 different anions, the most pronounced change is attributed to the case of TFSI anion. In the reduced state, the CA was measured to be around 38° while in the oxidized state, the CA is increased to 55°. This phenomenon can be explained by the electron transfer coupled ion transport (ICET), i.e. $Fc \leftrightharpoons Fc^{+} + 1\ e^{-} + 1\ A^{-}$. ICET process induces additional hydrophobic anions to the final configuration of the oxidized state polymer/electrode resulting to a more hydrophobic film (data not shown).

2.5.2 Poly(1-allyl-3-ferrocenylmethylimidazolium bromide)

The same procedure was applied to the redox monomer-based imidazolium affording immobilized Poly(1-allyl-3-ferrocenylmethylimidazolium bromide) on the electrode surface (configuration 2 in Scheme 2.3). As shown in the figure 2.19a the electrochemical response of the poly(FcIL) attached onto GC electrode surface, a reversible signal at 0.55 V vs. SCE with a $\Delta E \approx 10$ mV attributed to the immobilized Fc moieties within the polymer structure.

Furthermore, the electron transfer in between the redox-active layer and GC electrode is revealed via investigations the variation of the peak potential and the peak current in function of the scan rate. It is found that the apparent electron transfer rate constant is around 177 s^{-1}. This value is comparable with the previously published work by using 3-(2-methacryloyloxy ethyl)-1-(N-ferrocenylmethyl) imidazolium monomer[17].

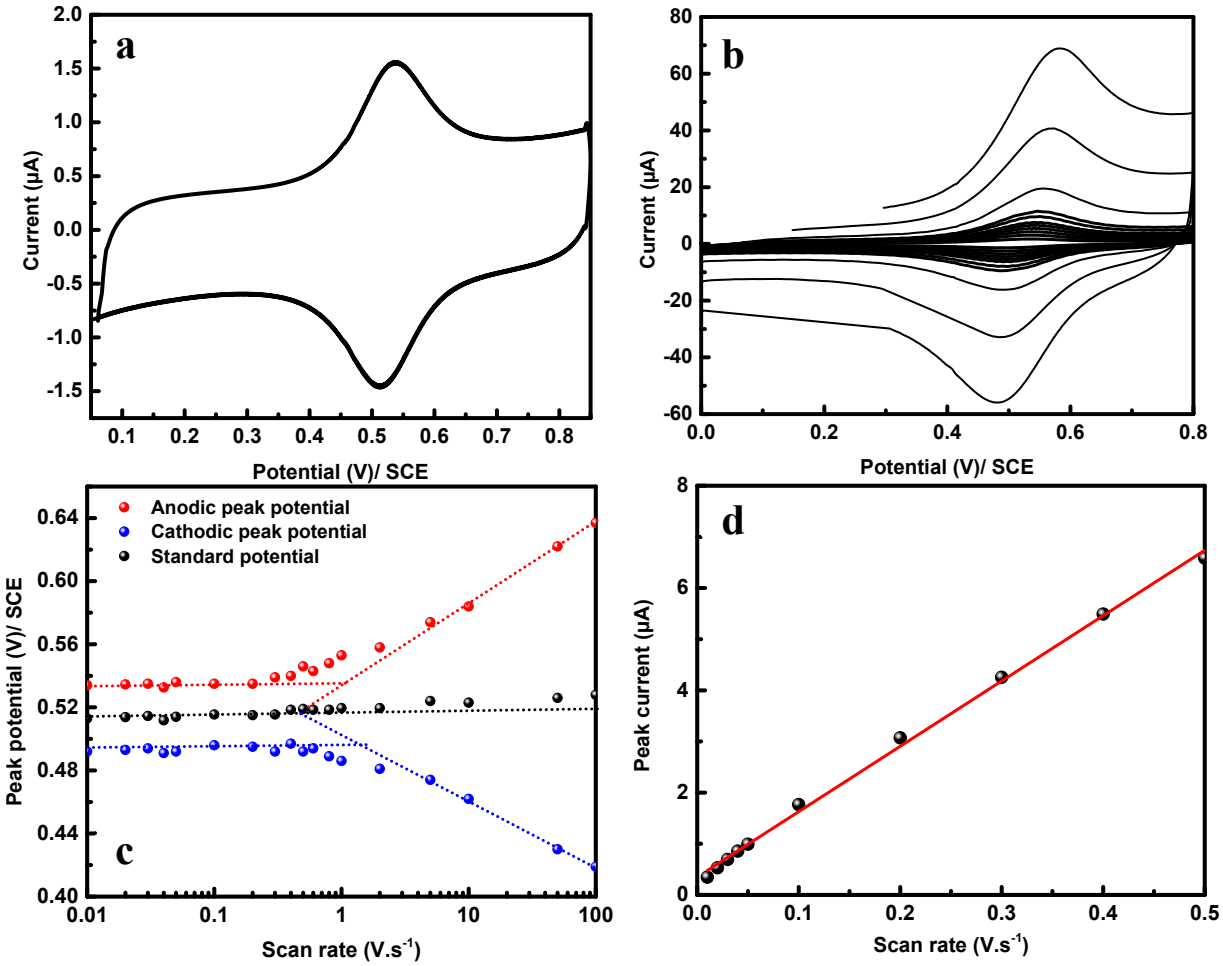

Figure 2.19 Cyclic voltammograms of the Poly(1-allyl-3-ferrocenylmethylimidazolium bromide) modified GC electrode recorded at different scan rates : ***(a)*** 0.1 $V.s^{-1}$; ***(b)*** from 0.01 $V.s^{-1}$ to 10 $V.s^{-1}$ in MeCN solution containing 0.1 M Bu_4NPF_6; ***(c)*** Variation of the peak potentials in function of the scan rate; ***(d)*** Variation of the oxidation peak current in function of the scan rate

Also, the linear variation of the oxidation peak current in function of the scan rate indicates non-diffusive species from and to the electrode surface that again, confirms the immobilization of the polymeric ferrocene based ionic liquid onto electrode surface. Similar to the Poly(N,N-dimethyl-N-ferrocenylmethyl-prop-2-en-1-ammonium bromide), the high resolution spectrum of Fe(2p) shows the Fe ($2p^{1/2}$) and Fe ($2p^{3/2}$) signal at 721 eV and 708 eV indicating the presence of Fc on the surface of the electrode. The polymerization can be extended to others substrates like ITO deposited on PET, Ni foam, Au, Pt, etc. As shown in the figure 2.20, the immobilized ferrocene signals were recorded by using ITO on PET and Ni foam electrode. Unlike fast electron transfer rate constant within GC electrode, the modified ITO and Ni foam exhibit lower

electron transfer rate with high peak-to-peak separation, around 100 mV and 200 mV for ITO/PET and Ni foam, respectively.

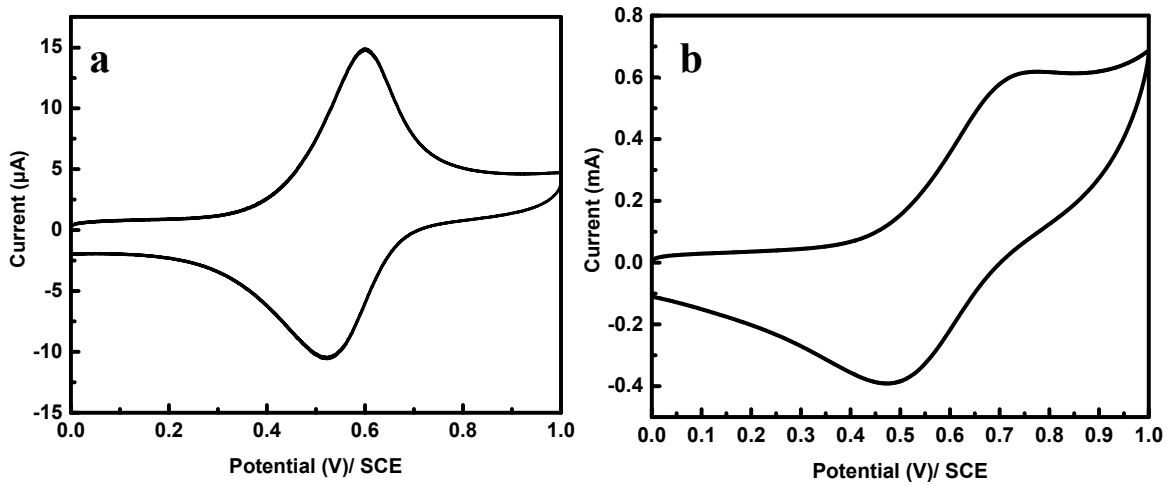

Figure 2.20 Cyclic voltammograms of the Poly(1-allyl-3-ferrocenylmethylimidazolium bromide) modified ***(a)*** ITO/PET and ***(b)*** Ni foam electrode in MeCN solution containing 0.1 M of Bu_4NPF_6

2.5.3 Poly(1-allyl-3-(1-anthraquinone-1'-methyl)ferrocenylimidazolium bromide)

In this part, the polymerization of bi-redox monomer based ionic liquid will be performed. The polymerization of the bi-redox polymeric ionic liquid is performed as followed. A solution containing 3.5mM de 1-allyl-3-ferrocenylmethylimidazolium bromide in 10ml of anhydrous MeCN was mixed with a second solution containing 3.7mM of anthraquinone diazonium salt dissolved in 10 ml of anhydrous MeCN. The mixture was sonicated for 30 minutes and served as polymerization medium to modify the electrodes by following similar condition as precedingly reported (Scheme 2.4). After 2 hrs of polymerization, the electrodes were removed from the solution, rinse thoroughly with MeCN, acetone and dried under Ar stream.

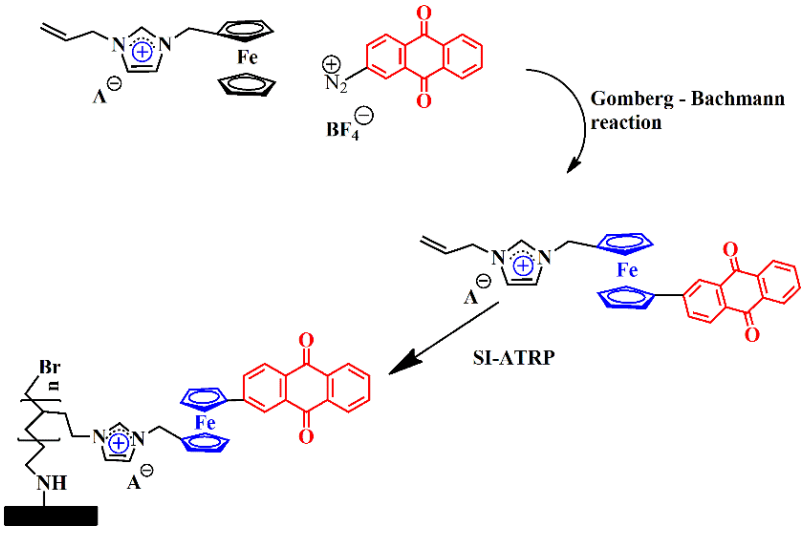

Scheme 2.4 Polymerization procedure of bi-redox ionic liquid monomer

The electrochemical behaviors of the Poly(AQFcIm) were investigated by using cyclic voltammetry in aqueous solution containing 0.1 M of HTFSI. The figure 2.21 a-b shows a series

of cyclic voltammograms of the modified electrode by changing the sweeping rate from 40 $mV.s^{-1}$ up to 10 $V.s^{-1}$.

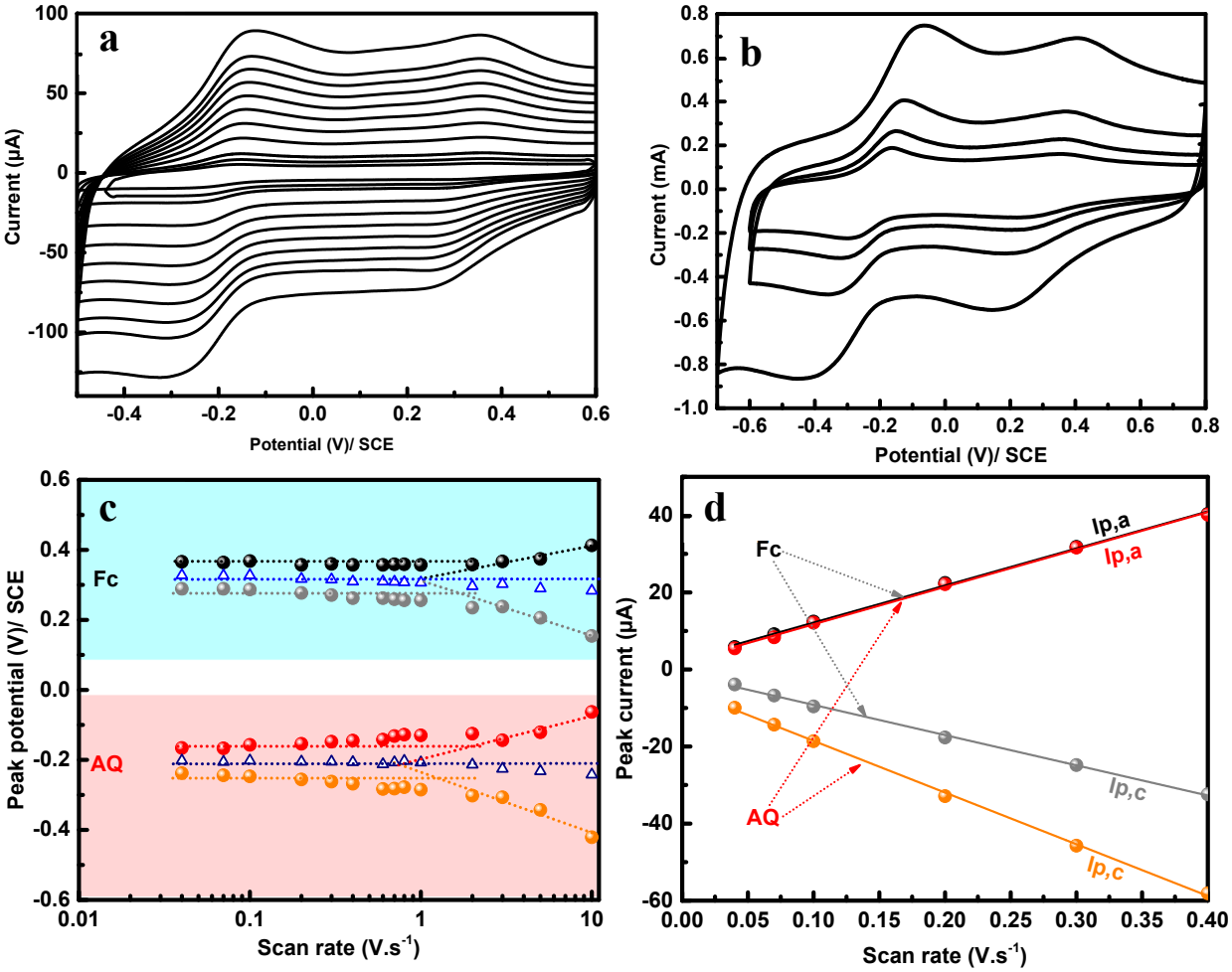

Figure 2.21 Cyclic voltammograms of the Poly(1-allyl-3-(1-anthraquinone-1'-methyl)ferrocenylimidazolium bromide) modified GC electrode recorded at different scan rates: ***(a)*** from 40 $mV.s^{-1}$ to $1V.s^{-1}$ and ***(b)*** from 1 to 10 $V.\ s^{-1}$ in aqueous solution containing 0.1 M HTFSI; ***(c)*** Variation of the peak potentials in function of the scan rate; ***(d)*** Variation of the peak current in function of the scan rate.

The CVs show 2 reversible systems at 0.35 V and -0.2 V/SCE which are assigned to the electrochemical responses of the immobilized Fc^{+}/Fc and AQH_2/AQ couples. For low scan rate (below 1 $V.s^{-1}$), the signal of both components, Fc and AQ, displays clearly full – reversible system with relatively low peak – to – peak separation (< 30 mV). At higher scan rate, the ΔE starts to increase, suggesting the deviation from the reversible system by the limitation of the electron transfer kinetic of the electrochemical active heads. From the evolution of the peak potentials as function of the scan rate (Figure 2.21c), the apparent electron transfer rate constant is calculated around 190 s^{-1} (α = 0.48) and 136 s^{-1} (α = 0.49) for Fc and AQ moieties, respectively. The value obtained for the Fc moieties is comparable with the ones measured for immobilized ferrocene onto electrode surface (0.1 s^{-1} to 200 s^{-1})[27,59]. The high value of the electron transfer rate constant can be attributed to the organization as brush-like chains at the surface of electrode which has already been demonstrated in the previous work[17]. The higher

value when compared to the polymer vinyl ferrocene (130 s^{-1})[59] is attributed to either the presence of the imidazolium center and the nanostructuration of the layer. Thus, the electron transfer at this interface is attributed to the combination of two distinct phenomena, the electron transfer via tunneling effect and the electron transport through the successive electron hopping. At the vicinity of the GC surface (< 5-10 nm), the ET is ensured by the electron tunneling through the thin initiator layer. In addition, due to the extremely high concentration of labile anion inside the polymer film, the electron coupled ion transfer is in a favor situation where the following transformation ($Fc \leftrightharpoons Fc^+ + 1\ e^- + 1\ A^-$) is fortified by high ionic transport inside the film. Besides, the nano-structuration by the formation of brush-like structure generates not only the electron hopping channels along the brushes but also a more flexible system that may change the viscoelastic properties of the polymer ionic liquid layer. The present approach provides a thick layer of bi-redox molecules with the surface concentration of $2.2.10^{-9}$ $mol.cm^{-2}$ and $1.9.10^{-9}$ $mol.cm^{-2}$ for AQ (n = 2) and Fc (n = 1) moieties, respectively which give a molecular weight (MW) in the order of 10^4 $g.mol^{-1}$.

Similar to the results mentioned in the previous part, the presence of bi-redox polymer layer induces the generation of multi-redox states at the surface with higher current density by keeping the same ratio of the oxidative and reducible heads ($\Gamma_{AQ}/\Gamma_{Fc} \sim 1$). As previously reported, the presence of the single FcAQIm layer at the surface of electrode enhances strongly the double layer capacitance of the latter. The phenomenon is so far amplified by functionalizing the electrode with the polymer layer. As shown in the figure 2.22, the double layer capacitance provided by the modified electrode is calculated to be around 30 times higher than the value for bare GC.

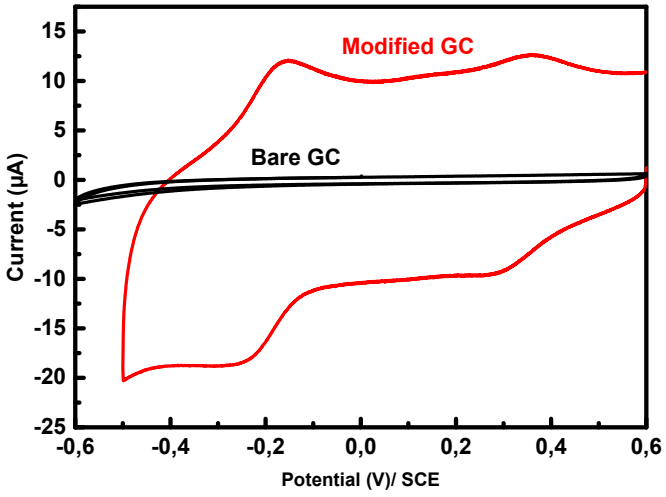

Figure 2.22 Cyclic voltammograms of the Poly(1-allyl-3-(1-anthraquinone-1'-methyl) ferrocenyl imidazolium bromide) modified GC electrode (red line) and Bare GC (black line) in aqueous solution containing 0.1 M HTFSI.

To get further information about the electrochemical responses of the poly(AQFcIm)/GC as function of the chemical environment, different voltammograms were recorded in various solutions ranging from ionic liquid, MeCN to aqueous solution as presented in the table 2.3.

Table 2.3 *Influence of solvents to the electrochemical response of the bi-redox system (v = 0.1 V.s^{-1})*

Milieu	E°(Fc) (V)/SCE	E°(AQ) (V)/SCE	ΔE° (V)	Relative capacitance C_{mod}/C_{bare}
1mM of 1-allyl-3-(1-anthraquinone-1'-methyl)ferrocenylimidazolium bromide in solution				
Pure EMITFSI	0.46	-0.43	0.89	
0.1 M EMITFSI/ACN	0.56	-0.74	1.30	
0.1 M HTFSI/ACN	0.46	0.12	0.34	
0.1 M $LiClO_4$/ACN	0.47	-0.80	1.27	
Poly(1-allyl-3-(1-anthraquinone-1'-methyl)ferrocenylimidazolium bromide) modified GC electrode				
Pure EMITFSI	0.47	-0.59	1.06	9.6
0.1 M HTFSI/H_2O	0.32	-0.20	0.52	30.9
0.1 M HTFSI/ACN	0.44	0.04	0.40	15.8
0.1 M EMITFSI/ACN	0.49	-0.57	1.06	14.1
0.1 M $LiClO_4$/ACN	0.44	-0.91	1.35	12.1

As expected, the standard potential of the Fc and AQ moieties changes in function of the solvent and the supporting electrolyte, resulting to a change of the potential window ($\Delta E^0 = E^0_{Fc} - E^0_{AQ}$) from 0.4 V in acidified MeCN (0.1 M HTFSI) to 1.4 V in 0.1 M $LiClO_4$/MeCN. Furthermore, a change of the double layer capacitance is also observed. For comparison, the relative capacitance, which reflect the ratio of the capacitance obtained with the modified electrode and the one obtained with bare GC, is calculated for different solvent. Interestingly, for all of the media, an increase of the capacitance is detected with the ratio ranging from 9.6 (EMITFSI) to 30 (HTFSI/H_2O). The remarkable difference in the capacitance ratio is further demonstrated by electrochemical impedance and electrochemical quartz crystal microbalance, and attributed to the concerted mechanism (ICET), in which water molecules are not involved in the solvation of the polymer layer (data not shown). In the other words, it is due to the insertion of the TFSI anion into the polymer film that causes the formation of the double electrified interfaces, GC/Poly(AQFcIm) and Poly(AQFcIm)/aqueous phase.

In the literature, it is well – known that the reduction of immobilized anthraquinone is attributed to the heterogeneous proton-coupled electron transfer (PCET)[60], i.e. $AQ + 2e^- + 2H^+ \rightleftharpoons AQH_2$. It means that the reaction rate is depending on the electron flux and the concentration of proton in the solution, suggesting a possibility to correlate the measured current to the pH of the solution. Owing anthraquinone moieties within the polymer structure, the relationship between the anodic peak potential and the pH can be obtained via Nernst equation:

$$E_{peak} = E^0 + \frac{2.3RTm}{nF} pH \quad (2.22)$$

Indeed, different CVs were recorded as function of the concentration of proton, i.e. as function of the pH of the solution. As presented in the figure 2.20 the anodic i-V curves of the poly(AQFcIm)/GC for a pH ranging from 1.2 to 0.6. Interestingly, the electrochemical response of the AQ moieties change in function of the pH while the signal of Fc part remains at the same potential ($E_{p,a}$ = 0.45V/SCE). Precisely, the peak potential attributed to anthraquinone shifts to more negative values by increasing the pH of the solution. By plotting the variation of the ΔE^0 in function of the pH, a linear relationship is obtained with a slope about 0.076. The R^2 value of the linear fit is 0.99, indicating a good agreement with the linearity of the data. Based on these results, the Fc part can be used as internal reference, resulting to development of new electrochemical pH sensors.

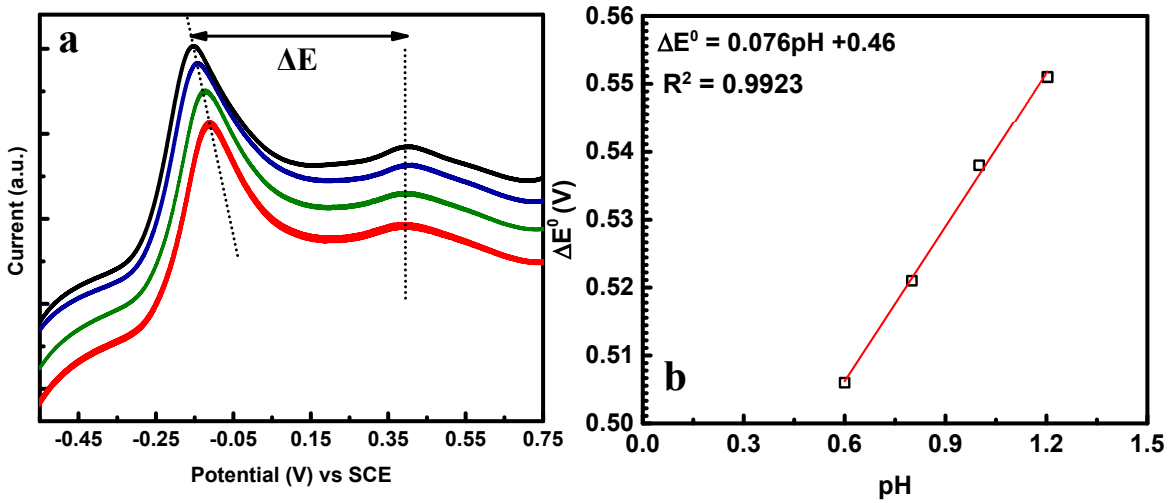

Figure 2.23 (a) CVs of the Poly(AFAI)/GC in aqueous HTFSI solutions at different pH ranging from (black curve) 1.2, (blue) 1, (green) 0.8 to (red) 0.6; ***(b)*** evolution of the ΔE^0 as function of the pH

2.6 CONCLUSION

Increasing demand for energy requires exploration and utilization of highly efficient materials for storing and releasing energy to satisfy the mismatching between the production and the consumption of energy. In this context, molecular design of new material, ionic liquid and redox-active ionic liquid attract immense attention from scientific community. Profiting an infinite possible structure, these novel family of compounds opens up new avenue for tailoring the physical-chemical properties at molecular level. Moreover, the attachment of these molecules onto substrate's surface offers new interfaces with interesting and unique properties.

Within this chapter, different electrochemical related routes were performed in order to functionalize the electrode surface with redox-IL, such as electrochemical reduction of diazonium salt coupled click chemistry or oxidative grafting of carboxylic group followed by Gomberg – Bachmann reaction, affording thin layer of redox and bi-redox ionic liquid molecules.

In addition to thin layer Redox-IL, the surface functionalization with polymer redox-IL has also been investigated. Our approach with poly(redox-IL) was carried out by using Surface-Initiated Atom Transfer Radical Polymerization (SI-ATRP) and direct electro-polymerization leading to the formation of polymer redox ionic liquid films at the substrate surface.

The radical polymerization initiated by cathodic polarization leads to the formation of dense and thick film coated the electrode surface. Pt/poly(FcIL) was proven to be able for practical use as highly stable quasi-reference electrode in non-aqueous solutions and in ionic liquid media.

In the other hand, the poly(Fc-IL) modified electrode prepared by SI-ATRP was electrochemically characterized in usual organic solvent and ionic liquid media showing high stability. Interestingly, it was proven that the Poly(Fc-IL) exhibits as self-electrolyte properties leading to the detection of the ferrocene redox signal in free-supporting electrolyte solution. We also demonstrate the possible applications of the poly(FcIL) as electrochemically reversible surface wettability system and as electrochemical sensor.

2.7 REFERENCES

(1) Qiu, B.; Lin, B.; Yan, F. Ionic Liquid/Poly(Ionic Liquid)-Based Electrolytes for Energy Devices. *Polym. Int.* **2013**, *62* (3), 335–337.

(2) Zhang, G.-R.; Etzold, B. J. M. Ionic Liquids in Electrocatalysis. *J. Energy Chem.* **2016**, *25* (2), 199–207.

(3) Truong, T. N. P.; Randriamahazaka, H.; Ghilane, J. Redox Monomer Ionic Liquid Based on Quaternary Ammonium: From Electrochemistry to Polymer Brushes. *Electrochem. commun.* **2017**, *82* (July), 25–29.

(4) Zhao, Q.; Dunlop, J. W. C.; Qiu, X.; Huang, F.; Zhang, Z.; Heyda, J.; Dzubiella, J.; Antonietti, M.; Yuan, J. An Instant Multi-Responsive Porous Polymer Actuator Driven by Solvent Molecule Sorption. *Nat. Commun.* **2014**, *5*, 4293.

(5) Lin, B.; Qiu, L.; Lu, J.; Yan, F. Cross-Linked Alkaline Ionic Liquid-Based Polymer Electrolytes for Alkaline Fuel Cell Applications. *Chem. Mater.* **2010**, *22* (24), 6718–6725.

(6) Peng, X.; Liu, H.; Yin, Q.; Wu, J.; Chen, P.; Zhang, G.; Liu, G.; Wu, C.; Xie, Y. A Zwitterionic Gel Electrolyte for Efficient Solid-State Supercapacitors. *Nat. Commun.* **2016**, *7* (May), 11782.

(7) Bélanger, D.; Pinson, J. Electrografting: A Powerful Method for Surface Modification. *Chem. Soc. Rev.* **2011**, *40* (7), 3995–4048.

(8) Ghilane, J.; Trippe-Allard, G.; Lacroix, J. C. Grafting of Imidazolium Ion-Terminated Layer Using Electrochemical Reduction of Diazonium: Redox Active Counter Anion Exchange within the Layer. *Electrochem. commun.* **2013**, *27*, 73–76.

(9) Hughes, M.; Shaffer, M. S. P.; Renouf, A. C.; Singh, C.; Chen, G. Z.; Fray, D. J.; Windle, A. H. Electrochemical Capacitance of Nanocomposite Films Formed by Coating Aligned Arrays of Carbon Nanotubes with Polypyrrole. *Adv. Mater.* **2002**, *14* (5), 382–385.

(10) Anothumakkool, B.; Guyomard, D.; Gaubicher, J.; Madec, L. Interest of Molecular Functionalization for Electrochemical Storage. *Nano Res.* **2017**, *10* (12), 4175–4200.

(11) Saha, S.; Samanta, P.; Murmu, N. C.; Kim, N. H.; Kuila, T.; Lee, J. H. Electrochemical Functionalization and In-Situ Deposition of the SAA@rGO/h-BN@Ni Electrode for Supercapacitor Applications. *J. Ind. Eng. Chem.* **2017**, *52*, 321–330.

(12) Khalil, I.; Julkapli, N. M.; Yehye, W. A.; Basirun, W. J.; Bhargava, S. K. Graphene-Gold Nanoparticles Hybrid-Synthesis, Functionalization, and Application in a Electrochemical and Surface-Enhanced Raman Scattering Biosensor. *Materials (Basel).* **2016**, *9* (6), 406.

(13) Bachman, J. C.; Kavian, R.; Graham, D. J.; Young Kim, D.; Noda, S.; Nocera, D. G.; Shao-Horn, Y.; Lee, S. W. Electrochemical Polymerization of Pyrene Derivatives on Functionalized Carbon Nanotubes for Pseudocapacitive Electrodes. *Nat. Commun.* **2015**, *6* (May), 1–9.

(14) Bouden, S.; Gómez-Mingot, M.; Randriamahazaka, H.; Ghilane, J. Surface Initiated Immobilization of Molecules Contained in an Ionic Liquid Framework. *Anal. Chem.* **2016**, *88* (1), 1017–1021.

(15) Ghilane, J.; Fontaine, O.; Martin, P.; Lacroix, J. C.; Randriamahazaka, H. Formation of Negative Oxidation States of Platinum and Gold in Redox Ionic Liquid: Electrochemical Evidence. *Electrochem. commun.* **2008**, *10* (8), 1205–1209.

(16) Bouden, S.; Trippé-allard, G.; Ghilane, J.; Randriamahazaka, H. Electrochemistry Communications Electrochemical Immobilization of Redox Active Molecule Based Ionic Liquid. *Electrochem. commun.* **2015**, *58*, 65–68.

(17) Bui-Thi-Tuyet, V.; Trippe-Allard, G.; Ghilane, J.; Randriamahazaka, H. Surface and Electrochemical Properties of Polymer Brush-Based Redox Poly(Ionic Liquid). *ACS Appl. Mater. Interfaces* **2016**, *8* (42), 28316–28324.

(18) Bui-Thi-Tuyet, V.; Trippe-Allard, G.; Ghilane, J.; Randriamahazaka, H. Surface

Functionalization of Ferrocene Based Ionic Liquid onto Carbon Surface Using Stepwise Grafting. *J. Electroanal. Chem.* **2014**, *713*, 28–31.

(19) Kolb, H. C.; Finn, M. G.; Sharpless, K. B. Click Chemistry: Diveverse Chemical Funtion from a Few Good Reactions. *Angew. Chemie - Int. Ed.* **2001**, *40*, 2004–2021.

(20) Liang, L.; Astruc, D. The Copper(I)-Catalyzed Alkyne-Azide Cycloaddition (CuAAC) "Click" Reaction and Its Applications. An Overview. *Coord. Chem. Rev.* **2011**, *255* (23–24), 2933–2945.

(21) Worrell, B. T.; Malik, J. a.; Fokin, V. V. Direct Evidence of a Dinuclear. *Science.* **2013**, *340* (I), 457–460.

(22) Li, S.; Wang, L.; Yu, F.; Zhu, Z.; Shobaki, D.; Chen, H.; Wang, M.; Wang, J.; Qin, G.; Erasquin, U. J.; Ren, L.; Wang, Y.; Cai, C. Copper-Catalyzed Click Reaction on/in Live Cells. *Chem. Sci.* **2017**, *8* (3), 2107–2114.

(23) Lummerstorfer, T.; Hoffmann, H. Click Chemistry on Surfaces: 1,3-Dipolar Cycloaddition Reactions of Azide-Terminated Monolayers on Silica. *J. Phys. Chem. B* **2004**, *108* (13), 3963–3966.

(24) Ghilane, J.; Lacroix, J. C. Formation of a Bifunctional Redox System Using Electrochemical Reduction of Platinum in Ferrocene Based Ionic Liquid and Its Reactivity with Aryldiazonium. *J. Am. Chem. Soc.* **2013**, *135* (12), 4722–4728.

(25) Strzemińska, I.; Sainte Rose Fanchine, S.; Anquetin, G.; Reisberg, S.; Noël, V.; Pham, M. C.; Piro, B. Grafting of a Peptide Probe for Prostate-Specific Antigen Detection Using Diazonium Electroreduction and Click Chemistry. *Biosens. Bioelectron.* **2016**, *81*, 131–137.

(26) Laviron, E. General Expression of the Linear Potential Sweep Voltammogram in the Case of Diffusionless Electrochemical Systems. *J. Electroanal. Chem. Interfacial Electrochem.* **1979**, *101* (1), 19–28.

(27) Fabre, B.; Hauquier, F. Single-Component and Mixed Ferrocene-Terminated Alkyl Monolayers Covalently Bound to Si(111) Surfaces. *J. Phys. Chem. B* **2006**, *110* (13), 6848–6855.

(28) Chidsey, C. E. D.; Bertozzi, C. R.; Putvinski, T. M.; Mujsce, A. M. Coadsorption of Ferrocene-Terminated and Unsubstituted Alkanethiols on Gold: Electroactive Self-Assembled Monolayers. *J. Am. Chem. Soc.* **1990**, *112* (11), 4301–4306.

(29) Aydogan Gokturk, P.; Salzner, U.; Nyulászi, L.; Ulgut, B.; Kocabas, C.; Suzer, S. XPS-Evidence for in-Situ Electrochemically-Generated Carbene Formation. *Electrochim. Acta* **2017**, *234*, 37–42.

(30) Tu, Q.; Zhao, L.; Han, X.; Wang, D. E.; Yuan, M. Sen; Tian, C.; Wang, J. A Visualized Method for Cu2+ion Detection by Self-Assembling Azide Functionalized Free Graphene Oxide Using Click Chemistry. *RSC Adv.* **2016**, *6* (98), 95628–95632.

(31) Fukuzumi, S.; Lee, Y. M.; Nam, W. Immobilization of Molecular Catalysts for Enhanced Redox Catalysis. *ChemCatChem* **2018**, *10* (8), 1686–1702.

(32) Noël, J. M.; Sjöberg, B.; Marsac, R.; Zigah, D.; Bergamini, J. F.; Wang, A.; Rigaut, S.; Hapiot, P.; Lagrost, C. Flexible Strategy for Immobilizing Redox-Active Compounds Using in Situ Generation of Diazonium Salts. Investigations of the Blocking and Catalytic Properties of the Layers. *Langmuir* **2009**, *25* (21), 12742–12749.

(33) Hazimeh, H.; Piogé, S.; Pantoustier, N.; Combellas, C.; Podvorica, F. I.; Kanoufi, F. Radical Chemistry from Diazonium-Terminated Surfaces. *Chem. Mater.* **2013**, *25* (4), 605–612.

(34) Casado-montenegro, J.; Marchante, E.; Crivillers, N.; Rovira, C.; Mas-torrent, M. Donor / Acceptor Mixed Self-Assembled Monolayers for Realising a Multi-Redox-State Surface. *ChemPhysChem* **2016**, *17*, 1810–1814.

(35) Bui-Thi-Tuyet, V.; Trippé-Allard, G.; Ghilane, J.; Randriamahazaka, H. Surface and Electrochemical Properties of Polymer Brush-Based Redox Poly(Ionic Liquid). *ACS Appl. Mater. Interfaces* **2016**.

(36) Momotenko, D.; Pereira, C. M.; Girault, H. H. Differential Capacitance of Liquid/Liquid Interfaces of Finite Thicknesses: A Finite Element Study. *Phys. Chem. Chem. Phys.* **2012**, *14* (32), 11268–11272.

(37) Daikhin, L. I.; Urbakh, M. Double Layer Capacitance and a Microscopic Structure of Electrified Liquid-Liquid Interfaces. *J. Electroanal. Chem.* **2003**, *560* (1), 59–67.

(38) Lu, J.; Yan, F.; Texter, J. Advanced Applications of Ionic Liquids in Polymer Science. *Prog. Polym. Sci.* **2009**, *34* (5), 431–448.

(39) Anderson, E. B.; Long, T. E. Imidazole- and Imidazolium-Containing Polymers for Biology and Material Science Applications. *Polymer (Guildf).* **2010**, *51* (12), 2447–2454.

(40) Ju, H.; Leech, D. Electrochemistry of Poly(Vinylferrocene) Formed by Direct Electrochemical Reduction at a Glassy Carbon Electrode. *J. Chem. Soc. Faraday Trans.* **1997**, *93* (7), 1371–1375.

(41) Barrosse-Antle, L. E.; Bond, A. M.; Compton, R. G.; O'Mahony, A. M.; Rogers, E. I.; Silvester, D. S. Voltammetry in Room Temperature Ionic Liquids: Comparisons and Contrasts with Conventional Electrochemical Solvents. *Chemistry - An Asian Journal*. **2010**, 5, 202–230.

(42) Katayama, Y.; Fukui, R.; Miura, T. Electrodeposition of Cobalt from an Imide-Type Room-Temperature Ionic Liquid. *J. Electrochem. Soc.* **2007**, *154* (10), D534-D537

(43) Rogers, E. I.; Silvester, D. S.; Jones, S. E. W.; Aldous, L.; Hardacre, C.; Russell, A. J.; Davies, S. G.; Compton, R. G. Electrochemical Kinetics of $Ag|Ag^{+}$ and $TMPD|TMPD^{+\bullet}$ in the Room-Temperature Ionic Liquid $[C_4Mpyrr][NTf_2]$; toward Optimizing Reference Electrodes for Voltammetry in RTILs. *J. Phys. Chem.* **2007**, 13957–13966.

(44) Langmaier, J.; Samec, Z. Cyclic Voltammetry of Ion Transfer across a Room Temperature Ionic Liquid Membrane Supported by a Microporous Filter. *Electrochem. commun.* **2007**, *9* (10), 2633–2638.

(45) Bonnaud, C.; Billard, I.; Papaiconomou, N.; Chainet, E.; Lepretre, J. C. Rationale for the Implementation of Reference Electrodes in Ionic Liquids. *Phys. Chem. Chem. Phys.* **2016**, *18* (11), 8148–8157.

(46) Weingarth, D.; Foelske-Schmitz, A.; Wokaun, A.; Kötz, R. PTFE Bound Activated Carbon - A Quasi-Reference Electrode for Ionic Liquids. *Electrochem. commun.* **2012**, *18* (1), 116–118.

(47) Ruch, P. W.; Cericola, D.; Hahn, M.; Kötz, R.; Wokaun, A. On the Use of Activated Carbon as a Quasi-Reference Electrode in Non-Aqueous Electrolyte Solutions. *J. Electroanal. Chem.* **2009**, *636* (1–2), 128–131.

(48) Peerce, P. J.; Bard, A. J. Polymer Films on Electrodes Part i. the Application of Poly(Vinylferrocene)-Coated Platinum Electrodes as Reference Electrodes in Acetonitrlle. *J. Electroanal. Chem.* **1980**, *108*, 121–125.

(49) Vonau, W.; Oelßner, W.; Guth, U.; Henze, J. An All-Solid-State Reference Electrode. *Sensors Actuators, B Chem.* **2010**, *144* (2), 368–373.

(50) Kannuck, R. M.; Bellama, J. M.; Blubaugh, E. A.; Durst, R. A. Cross-Linked Poly(Vinylferrocene)-Modified Reference Electrode for Nonaqueous Electrochemistry. *Anal. Chem.* **1987**, *59* (10), 1473–1475.

(51) Wang, J. S.; Matyjaszewski, K. Controlled/"Living" Radical Polymerization. Atom Transfer Radical Polymerization in the Presence of Transition-Metal Complexes. *J. Am. Chem. Soc.* **1995**, *117* (20), 5614–5615.

(52) Kato, M.; Kamigaito, M.; Sawamoto, M.; Higashimura, T. Polymerization of Methyl Methacrylate with the Carbon Tetrachloride/Dichlorotris-(Triphenylphosphine)Ruthenium(II)/ Methylaluminum Bis(2,6-Di-Tert-Butylphenoxide) Initiating System: Possibility of Living Radical Polymerization. *Macromolecules* **1995**, *28* (5), 1721–1723.

(53) Edmondson, S.; Osborne, V. L.; Huck, W. T. S. Polymer Brushes via Surface-Initiated Polymerization. *Chem Soc Rev* **2004**, No. 33, 14–22.

(54) Perruchot, C.; Khan, M. A.; Kamitsi, A.; Armes, S. P.; Von Werne, T.; Patten, T. E. Synthesis of Well-Defined, Polymer-Grafted Silica Particles by Aqueous ATRP. *Langmuir* **2001**, *17* (15), 4479–4481.

(55) Singh, N.; Wang, J.; Ulbricht, M.; Wickramasinghe, S. R.; Husson, S. M. Surface-Initiated Atom Transfer Radical Polymerization: A New Method for Preparation of Polymeric Membrane Adsorbers. *J. Memb. Sci.* **2008**, *309* (1–2), 64–72.

(56) Kim, J.-B.; Bruening, M. L.; Baker, G. L. Surface-Initiated Atom Transfer Radical Polymerization on Gold at Ambient Temperature. *J. Am. Chem. Soc.* **2000**, *122* (31), 7616–7617.

(57) Adenier, A.; Chehimi, M. M.; Gallardo, I.; Pinson, J.; Vilà, N. Electrochemical Oxidation of Aliphatic Amines and Their Attachment to Carbon and Metal Surfaces. *Langmuir* **2004**, *20* (19), 8243–8253.

(58) Bouden, S.; Trippé-Allard, G.; Ghilane, J.; Randriamahazaka, H. Electrochemical Immobilization of Redox Active Molecule Based Ionic Liquid. *Electrochem. commun.* **2015**, *58*, 65–68.

(59) Dalchiele, E. A.; Aurora, A.; Bernardini, G.; Cattaruzza, F.; Flamini, A.; Pallavicini, P.; Zanoni, R.; Decker, F. XPS and Electrochemical Studies of Ferrocene Derivatives Anchored on N- and p-Si(1 0 0) by Si-O or Si-C Bonds. *J. Electroanal. Chem.* **2005**, *579* (1), 133–142.

(60) Abhayawardhana, A. D.; Sutherland, T. C. Heterogeneous Proton-Coupled Electron Transfer of an Aminoanthraquinone Self-Assembled Monolayer. *J. Phys. Chem. C* **2009**, *113* (12), 4915–4924.

2.8 APPENDICES

Synthesis of electroactive ionic liquids

1. N-ferrocenylmethylimidazole

25 g of trimethylammonium ferrocene iodide (64.8 mmol, 1equiv.) and 5.4 g of imidazole (79 mmol, 1.22 equiv.) were dissolved in 140 ml of dimethylformamide (DMF). The solution was refluxed for 2 hours. Then 150 ml of distilled water was added into the balloon and the black solid precipitate was eliminated by filtration. The product was recovered by decantation with diethyl ether (3x 100 ml). The organic layer was washed 1 time with distilled water (100 ml) to eliminate DMF traces. The organic phase was dried with $MgSO_4$. Diethyl ether was evaporated to obtain orange powder. Yield: 45% (8.23 g)

1H NMR (DMSO-d6) δ(ppm): 4.15 (t, J = 2.0 Hz, 2H), 4.18 (s, 5H), 4.31 (t, J = 2Hz, 2H), 4.90 (s, 2H), 6.83 (s, 1H), 7.15 (s, 1H), 7.64 (s, 1H).

2. 1-allyl-3-ferrocenylmethylimidazolium bromide

0.91 ml (10.5 mmol) of allyl bromide was added into a solution containing 1.2 g (4.5 mmol) of N-ferrocenylmethylimidazole in 40 ml of chloroform under stirring. The mixture was then refluxed for 2h then the solvent and unreacted starting materials were evaporated under reduced pressure. The yield of this reaction was 95 %.

1H NMR (DMSO-d6) δ(ppm): 4.22 (m, 7H), 4.45 (t, J = 1.6Hz, 2H), 4.83 (m, 2H), 5.26 (s, 2H), 5.33-5.36 (m, 2H), 6.04 (m, 1H), 7.71 (s, 1H), 7.81(s, 1H), 9.23 (s, 1H).

3. 1-ferrocenylmethyl-3-propargylimidazolium bromide

Propargyl bromide (1.6 mL, 21 mmol) and N-ferrocenylmethylimidazole (1.6 g, 6 mmol) were dissolved in chloroform, and the mixture was then refluxed for 2 h at 70 °C. The solvent and unreacted propargyl bromide were removed by evaporation under reduced pressure to give 2.08 g of a yellow brown oil (yield 90 %).

1H NMR (400 MHz, DMSO-d6) δ(ppm): 3.83 (s, 1H), 4.22 (m, 7H), 4.45 (t, J = 1.6 Hz, 2H), 5.15 (s, 2H), 5.18 (s, 2H), 7.76 (s, 1H), 7.81(s,1H), 9.25 (s, 1H).

4. N-allyl-N,N-dimethyl-N-ferrocenylmethylammonium bromide

First, the (dimethylaminomethyl)ferrocene (2.43 g, 10 mmol) and allyl bromide (2.42 g, 20 mmol) were dissolved in CH_2Cl_2 and the mixture was heated overnight at 55°C. Then the mixture was cooled down to room temperature and the solvent with unreacted allyl bromide were evaporated under reduced pressure. Finally, the residue was recrystallized using CH_2Cl_2/hexane (1: 20 v/v) resulting orange powder. The purified product was filtered and dried under vacuum 1 day before use. Yield: 96% (3.5 g)

1H NMR (400 MHz, DMSO-d6) δ(ppm): 3.30 (s, 6H), 3.39 (t, 2H), 3.81 (d, 2H), 4.26 (s, 5H), 4.37 (s, 2H), 4.46 (t, 2H), 5.63 (m, 2H), 6.09 (m, 1H).

5. Chloroethyleneamidoanthraquinone

In a three-necked flask, 2-aminoanthraquinone (1.0 g, 4.5 mmol), pyridine (0.5 ml, 6.2 mmol) and 60ml of dichloromethane were mixed under vigorous stirring at 0°C. Solution of chloroacetylchloride (0.4 ml, 5.4 mmol) in 20 ml of dichloromethane was then added drop wise. After stirring 4 h, the solution was filtered and extracted with 20 ml HCl 3M. The organic layer was washed with 20 ml of saturated NaCl and recovered by decantation. A large amount of MgSO4 was added into the organic phase to eliminate water traces. The solvent was evaporated to obtain a brown residue. The crude product was further dissolved in 100 ml of dichloromethane and 100 ml of hexane was slowly added into the solution. The purified product was recrystallized in the mixture and then was filtered and dried under vacuum.

Yield: 42.7% (0.55 g)

1H NMR ($CDCl_3$) δ(ppm): 4.27 (s, 2H), 7.82 (m, 2H), 8.23 (d, J = 2.4 Hz, 1H), 8.32 (m, 4H), 8.6 (s, 1H)

6. 1-ethyleneamidoanthraquinone-3-Ferrocenemethylimidazolium iodide

0.1 g of chloroethyleneamidoanthraquinone (0.33 mmol) was mixed with 0.094 g of N-ferrocenylmethylimidazole (0.35 mmol) and a catalytic amount of sodium iodide in 20 ml of acetone/dichloromethane (50:50 v/v).

The reaction was performed under vigorous stirring at room temperature for 60 hrs. Then the product was recovered by filtration and washed with distilled water. The brown powder was obtained and dried under vacuum for 1 day. Yield: 69.5% (0.13 g)

1H NMR ($CDCl_3$) δ(ppm): 4.27 (m, 7H), 4.46 (t, J = 2 Hz, 2H), 5.26 (s, 2H), 5.28 (s, 2H), 7.82 (s, 1H), 7.91 (s, 1H), 8.04 (m, 2H), 8.2 (m, 1H), 8.24 (m, 3H), 8.47 (m, 1H), 9.15 (s, 1H), 11.18 (s,1H).

7. 1-ethyleneamidoanthraquinone-3-Ferrocenemethylimidazolium TFSI

0.13 g of 1-ethyleneamidoanthraquinone-3-Ferrocenemethylimidazolium iodide (0.25 mmol) was added into a solution containing 20 ml of distilled water and 0.2 g of lithium bis(trifluoromethylsulfonyl)imide (0.75 mmol). The solution was then heated at 70°C for 24 hours to obtain a brown powder. The product was washed thoroughly with distilled water and dried under vacuum for 1 day. Yield: 87% (0.17 g)

1H NMR ($CDCl_3$) δ(ppm): 4.27 (m, 7H), 4.45 (t, J = 2 Hz, 2H), 5.26 (s, 2H), 5.28 (s, 2H), 7.81 (s, 1H), 7.92 (s, 1H), 8.04 (m, 2H), 8.18 (m, 1H), 8.24 (m, 3H), 8.47 (m, 1H), 9.15 (s, 1H), 11.18 (s, 1H).

19F NMR ($CDCl_3$) δ(ppm): -78.88 (s, 6F)

8. 1-ethyleneamidoanthraquinone-3-vinylimidazolium iodide

In the solution containing 1-vinylimidazole (0.094 g, 0.9 mmol) and a catalytic amount of sodium iodide (0.14 g, 1 mmol) in 20 ml de acetone/dichloromethane (50/50 v/v), chloroethyleneamidoanthraquinone (0.27 g, 0.9 mmol) was added. The mixture was kept under stirring at room temperature for 1 day. After the reaction, the precipitate was filtered and washed 5 times with distilled water. The crude product was further recrystallized in a solution of dichloromethane/hexane and the purified one was appeared as brown powder.

Yield: 94% (0.3 g).

1H RMN (DMSO-d6) δ(ppm): 5.39 (s, 2H), 5.5 (m, 1H), 6.05 (m, 1H), 7.47(q, J = 8.8Hz, 1H), 7.82 (s, 1H), 7.9 (s, 1H), 7.93 (m, 2H) , 8.08 (m, 1H), 8.22 (m, 3H), 8.29 (d, J = 2Hz, 1H), 9.52 (s, 1H), 11.53 (s, 1H).

Electrochemistry

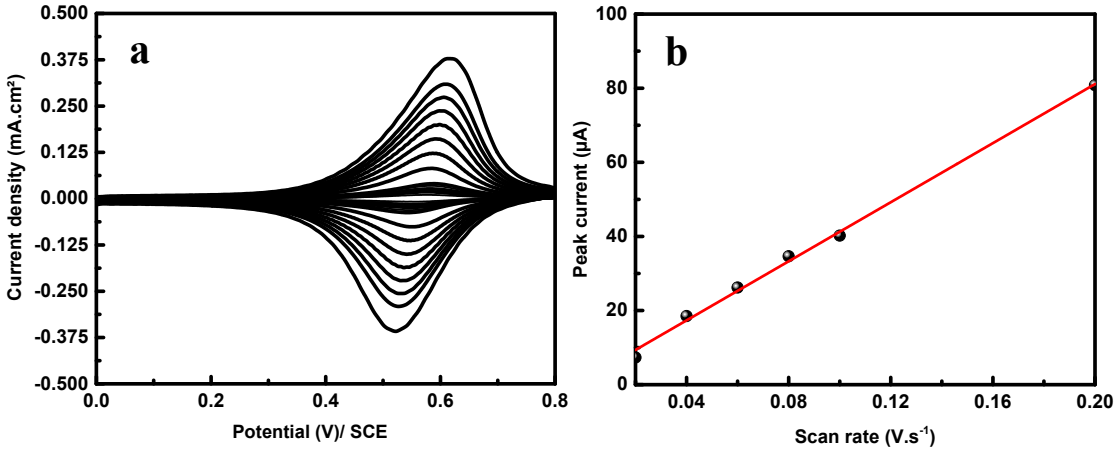

Figure 2.S1 (a) Cyclic voltammograms of immobilized ferrocene-based ionic liquid in MeCN solution containing 0.1 M of $TBAPF_6$ as function of the scan rate (10 $mV.s^{-1}$ to 2 $V.s^{-1}$); ***(b)*** Variation of the oxidation peak current in function of the scan rate.

Table S2.1 Variation of the standard potential (V) over time in MeCN and in EMITFSI solution by using Pt/poly(FcIL) reference electrode

Time/Day	**0**	**1**	**2**	**3**	**7**
MeCN	0.135	0.134	0.137	0.140	0.153
EMITFSI	0.112	0.112	0.111	0.109	0.103

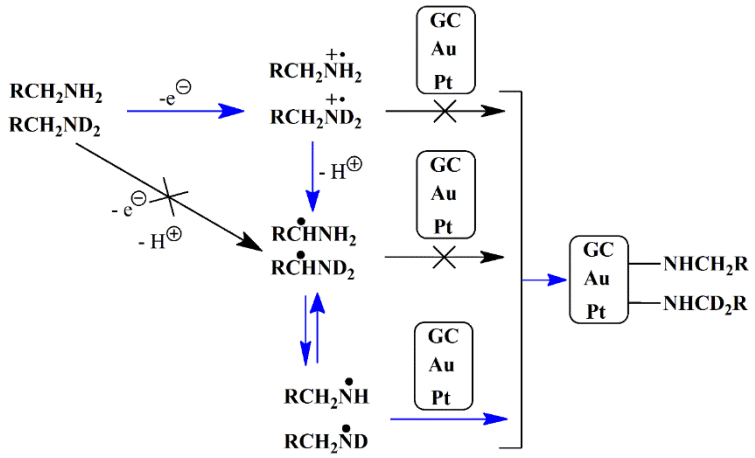

Scheme 2.S1 Scheme illustrating the electrochemical oxidation process by using primary amine

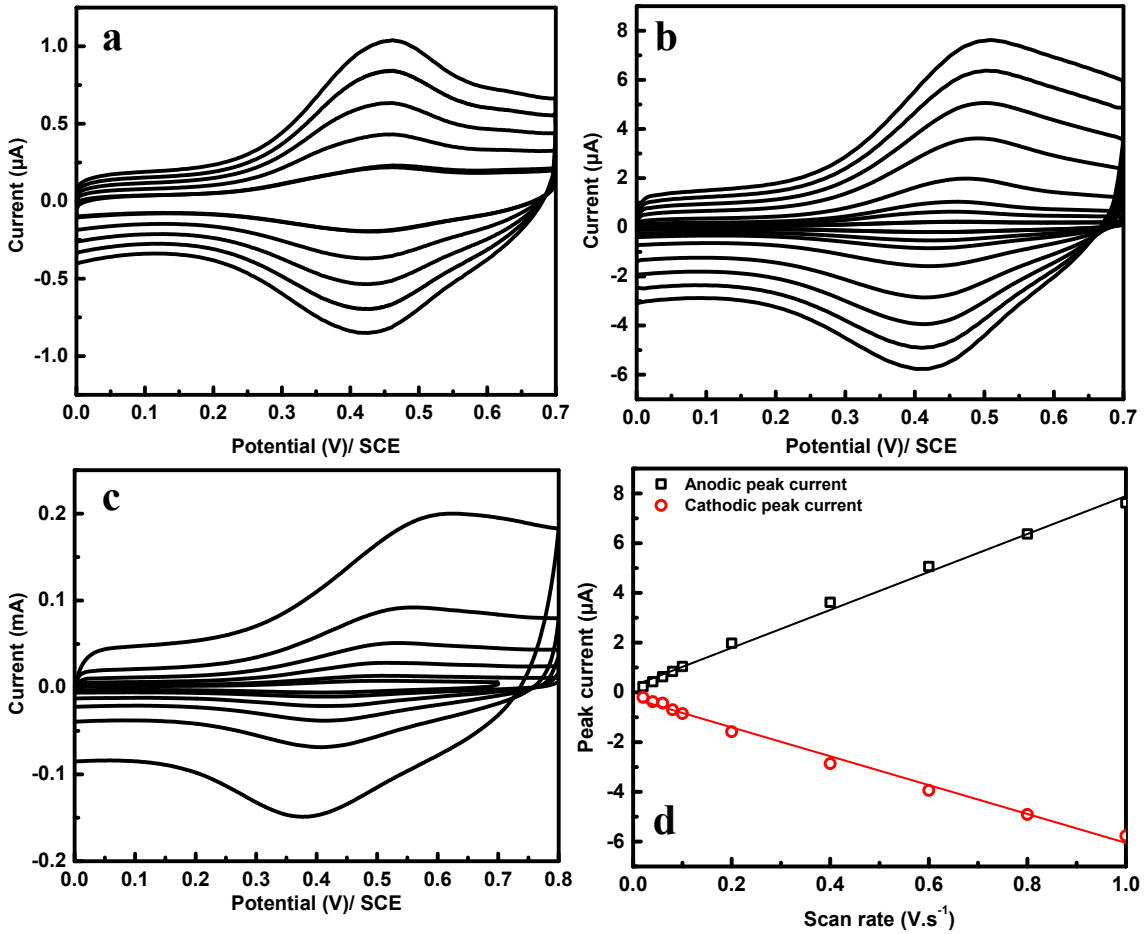

Figure 2.S2 Cyclic voltammograms of the polymer/GC electrode recorded at different scan rates: ***(a)*** from 20 $mV.s^{-1}$ to 0.1 $V.s^{-1}$; ***(b)*** from 0.1 $V.s^{-1}$ to 1 $V.s^{-1}$; ***(c)*** from 1 $V.s^{-1}$ to 50 $V.s^{-1}$; ***(d)*** Variation of the peak current in function of the scan rate.

CHAPTER 3

IONIC LIQUID-BASED MATERIALS TOWARDS ELECTROCHEMICAL ACTIVATION OF SMALL MOLECULES

In the past few years, ionic liquids have been demonstrated to be suitable as additives for enhancing the catalytic performance of different materials. However, there are numerous open questions about the role of the family of compounds in the field of electrocatalysis. In this chapter, we try to develop different routes to employ ionic liquids and the polymeric ionic liquids as catalysts in electrochemical activation of small molecules.

Keywords: *Microwave, Solvent, nanoparticles, facile preparation, surface modification, polymer brushes, selectivity, stability, platform, hybrid materials, oxygen reduction and evolution reactions, hydrogen evolution reaction*

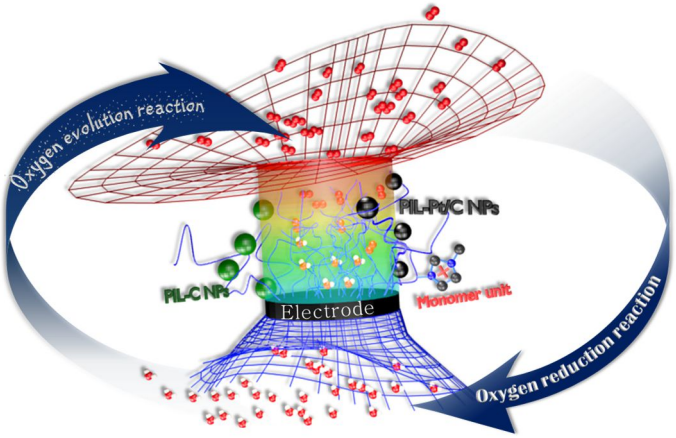

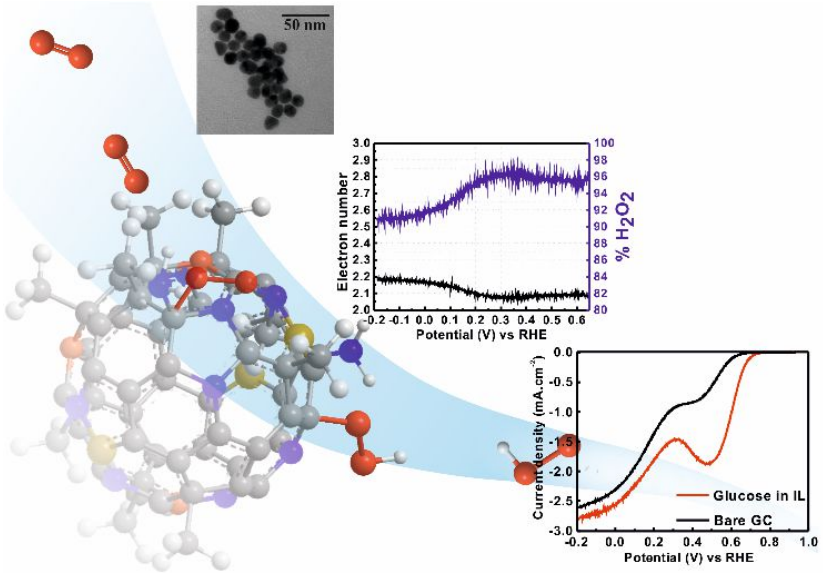

OUTLINE

3.1 INTRODUCTION

Small molecules, such as hydrogen, oxygen, nitrogen and carbon dioxide, etc., take part in our life not only by forming a protective atmosphere against cosmic rays but also through participation in metabolism. Once these molecules entered into the interior of the living systems, successive chemical transformations occur to maintain life. One typical example is the photosynthesis in plants which transforms CO_2 and water into carbohydrate and oxygen by using solar energy. Inspired from the nature, numerous investigations have been performed to point out safe and efficient ways to convert renewable energy into chemical energy and later, into electricity. Typically, most of the electricity is produced by combustion of fossil fuels. However, this approach causes severe consequences to the world economy and ecology, including the fuel resource dependency and climate change.

Within this context, electrochemical energy storage and conversion systems including rechargeable metal-air batteries and regenerative fuel cells, have been considered as promising systems thanks to their high energy density and environmental benignity. These energy technologies are composed, in principle, of 4 main reactions: oxygen reduction and evolution reactions, hydrogen oxidation and evolution reactions (ORR, OER, HER, HOR, respectively) that involve hydrogen (H_2) and oxygen (O_2)[1]. While hydrogen and oxygen evolution reactions are important to produced H_2 and O_2 from water via water splitting, the ORR is a crucial reaction in fuel cells and metal – air batteries. However, large activation barrier requires non – negligible energy input to generate the product, which lowers the transformation efficiency. Consequently, seeking for efficient and low – cost electrocatalysts, i.e. materials that can accelerate the electrochemical reaction by minimizing the activation energy and increasing the kinetic, attracts wide attention[2–7]. To obtain higher catalytic activity, two approaches can be parallelly considered, either preparing novel materials or changing the elaborations methods by using existing materials. Looking into the literature, electro-catalysts could be classified in three categories, noble-metals, transition metals and carbonaceous catalysts[8–10]. To improve the catalytic performance, several approaches have been investigated and reported. For example, Pt alloyed with other metals such as Co, Ni, Fe or bimetallic Pt core-shell exhibited an enhanced performance and stability[1,11]. For transition metals, composite materials proved to be able to reach performance comparable to Pt based materials[6,12–14]. Carbonaceous catalysts based on (doped) – nanocarbon[15–17] (graphene, nanotube, nanofiber, polymer, organic/organometallic compounds and carbon quantum dots) have been demonstrated to be a good alternative as a new generation of low-cost catalysts. However, whatever the selected catalyst concepts, they still suffer from multiple problems such as crossover effect and thus the durability for Pt based catalysts[18], metal dissolution along with the low conductivity for non-precious metals[19], the complicated preparation procedure and the strict synthesis conditions, e.g. carbonization at high temperature (700 – 1200 °C), for carbonaceous catalysts[20]. Besides that, the choice of catalyst for a reaction of interest is found to be restraint, e.g. for OER reaction, oxides of transition

metal[21] have been demonstrated as the best candidate while Pt – based catalysts exhibit excellent performance towards ORR and HER[11,22]. Several studies were devoted to the most recent achievements in the development and the design of catalysts for multifunctional purpose, such as bi-functional catalyst for ORR and OER[23,24]. The ongoing challenge is to design new catalysts that rationalize several parameters including the performance, the stability, the tolerance, and to some extent the bi/multi-functionality. Within this chapter, we will describe the use of ionic liquid as a starting material to generate a new class of electrocatalyst. Our strategy is based on two different approaches, the first one is the use of molecules based ionic liquid to generated carbon doped nano-material and the second one is based on the use of polymer ionic liquid as electrocatalyst.

3.2 IONIC LIQUID-BASED CARBON DOTS BY MICROWAVE ASSISTED SYNTHESIS: NEW APPROACH FOR SELECTIVE H_2O_2 PRODUCTION

In this part we will describe the generation of nano-carbon starting from ionic liquid solvent. The synthesis of carbon dots (C-dots) was performed in ionic liquid, 1-ethyl-3-methylimidazolium ethylsulfate (EMIES), using the microwave assisted solvothermal method. Possessing similar functions as a household microwave, the laboratory microwave reactor provides faster synthesis than conventional hydro/solvo-thermal methods with higher product yield at controllable high temperature and pressure. Inspiring from the caramelization of sugar at high temperature, a solution containing glucose (and L-glutamine) was heated in a microwave reactor affording to the formation of carbon nanodots. In the following works, we will describe the possible formation of C-dots in ionic liquid and their characteristics.

3.2.1 Synthesis and surface characterizations

Synthesis of carbon dots via microwave assisted method.

The microwave (MW) assisted synthesis is referred to a solvothermal process that involves the use of solvent under moderate to high pressure and temperature to facilitate the interactions between reactants during synthesis[24]. Thus, by irradiating the reaction mixture under microwave, polar solvent molecules, such as water, dimethylformamide (DMF), etc., are undergone sinusoidal electromagnetic field. Consequently, these molecules interact strongly with the field by flipping its orientation rapidly and bumping into surrounding ones to produce heat. Unlike conventional heating methods where the heat diffuses from the wall into the core side, microwave heating provides homogeneous baking temperature due to the deep penetration of the microwave inside the solution.

Profiting numerous advantages offered by MW synthesis, we propose to use bottom – up approach to construct the carbon dots from bio – based molecules, such as glucose and amino acids, in ionic liquid solvent. As reported in the literature, thermal treatment of glucose conducts to the formation of carbon particles by means of multi – step carbonization[24]. Nevertheless, high temperature and long reaction time are required, which can be avoided by using MW

heating. Typically, the time scale can be reduced up to 1 or 2 orders of magnitude. For this study, three C-dots were synthesized and labelled, C-dots – 1 generated from mixtures of ionic liquid and glucose/glutamine, C-dots – 2 generated from mixtures of ionic liquid and glucose and C-dots – 3 generated from mixtures of water and glucose/glutamine. Figure 3.1 summarizes the typical synthetic route of C-dots in ionic liquid and the solution color change while increasing the baking temperature.

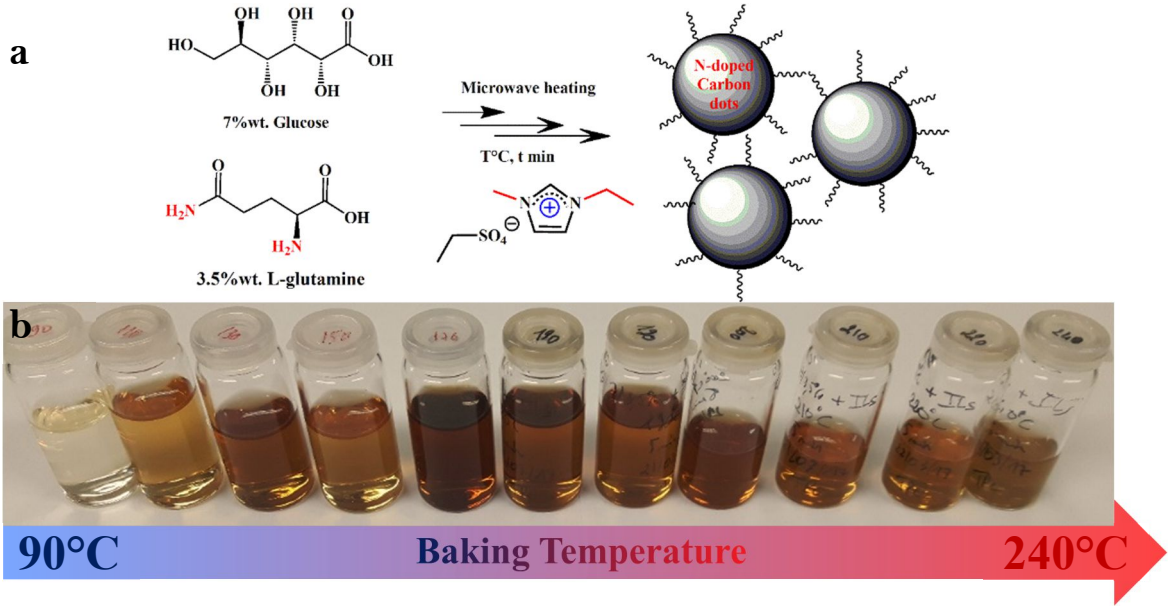

Figure 3.1 (a) Typical Synthetic pathway of Carbon dots in ionic liquids media; ***(b)*** Corresponding samples at different baking temperature.

Synthesis of C-dots – 1 and 3

The syntheses of C-dots – 1 and 3 were carried out in a monomodal microwave reactor (Anton Paar 300). Typically, 1.4 g of glucose and 0.7 g of glutamine were dissolved under vigorous stirring in 20 ml of 1-ethyl-3-methylimidazolium ethylsulfate (EMIES) (C-dots – 1) or in 20 ml of distilled water (C-dots – 3) resulting to clear transparent solution. Then the mixture was poured into a special-purpose vial for heating via microwave irradiation. The temperature ramp was constantly kept at $1°C.s^{-1}$. Different C-dots samples were obtained by varying the baking temperatures. After 5 min of heating, the solution was cooled down to room temperature followed by dialysis using cellulose membrane (Spectra/Por® Dialysis Tubing with MWCO = 7 kDa) for 48 hrs. Finally, the dialyzed suspensions of C-dots were centrifugated at 8000 rpm for 20 minutes to eliminate non-desired agglomerations and the supernatants were collected resulting to yellowish solutions and were ready for further uses.

Synthesis of C-dots – 2

Similar procedure was used for fabricating C-dots – 2. Briefly, 1.4 g of glucose was dissolved in 20 ml of EMIES ionic liquid (C-dots – 2). Then, the solutions were heated with the microwave assisted method for 5 minutes at controlled temperatures with a temperature ramp

at 1°C.s^{-1}. Once the solutions were cooled down to room temperature, the C-dots solutions were purified by dialysis (MWCO = 7 kDa) followed by centrifugation as previously described.

For all the C-dots several baking temperatures were investigated as illustrated in Table 3.1. However, the results of surface characterizations described in this chapter will be focused on one selected temperature for each C-dots, namely 170° for C-dots – 1, 200° for C-dots – 2 and 150° for C-dots – 3.

Table 3.1. Summary of synthetic conditions for different C-dots

Samples	Temperature (°C)												
Gluc-Glut in IL (C-dots – 1)	90	110	130		150		170		190	200	210	220	240
Gluc in IL (C-dots – 2)						160		180		200		220	240
Gluc-Glut in H_2O (C-dots – 3)				140	150	160	170	180	190	200		220	

Surface characterization

The generated C-dots were first characterized using FT-IR, XPS, UV-Vis spectroscopies techniques and transmission electron microscopy (TEM).

The FT-IR spectrum of C-dots – 1 (Fig.3.2a) shows a broad peak at 3300 cm^{-1} corresponding to stretching vibration of O-H groups. The peaks at 2920, 2850 and 750 cm^{-1} correspond to the stretching vibrations of aromatic and aliphatic C-H[25].

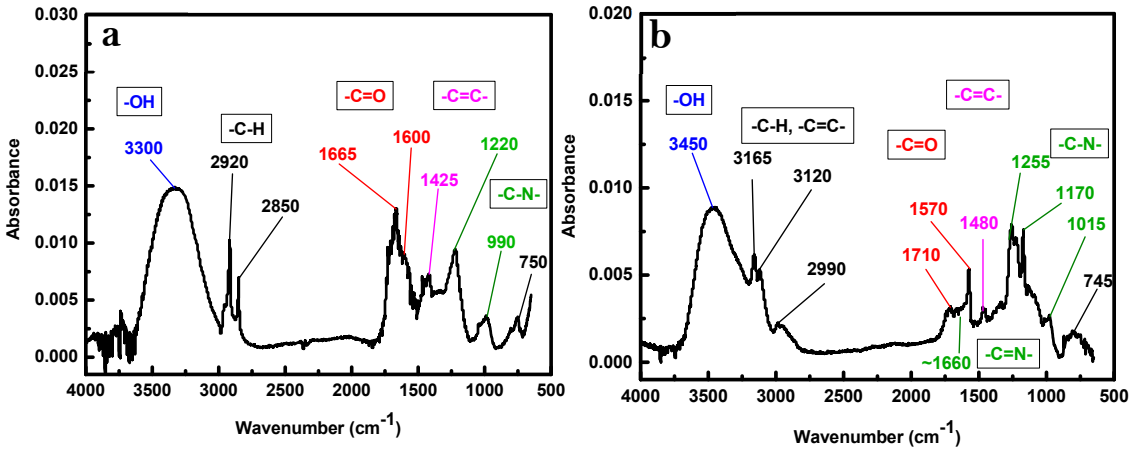

Figure 3.2 FT-IR spectrum of ***(a)*** C - dots -1; ***(b)*** C - dots -2

Besides that, the C=O stretching vibrations were observed at 1665 and 1600 cm^{-1} [26]. The peaks located at 1220 and 990 cm^{-1} are attributed to the stretching and bending vibrations of C-N group[27]. For further comparison, the generated C - dots -2 (at 200 °C) were also characterized by FT-IR as illustrated in Figure. 3.2b. The spectrum displays the same characteristics as those reported in Figure. 3.2a, thus the peaks corresponding to the O-H, C-H, C=O, and C=N were observed at similar wavelengths. Interestingly, the presence of -C – N vibrations for C-dots – 2 indicates the participation of the solvent, 1-ethyl-3-methylimidazolium ethyl-sulfate, to the formation of the final product. In addition, a peak at 1480 cm^{-1} corresponding to C=C stretching

vibration and a peak at 1660 cm^{-1} related to the C=N vibration are detected highlighting that the C-dots – 2 contain more conjugated structure. The FT-IR analyses reveal the presence of imidazole or imidazolium structure suggesting that the latter remain on the surface. These results confirm the formation of N doped C - dots in the ionic liquid media with or w/o the presence of additional nitrogen source (L-glutamine). Thus, the ionic liquid could be used as source of nitrogen doping.

Further information about the chemical composition and the surface state of different elements existed on the carbon dots was revealed by X-ray photoelectron spectroscopy (XPS). From the survey spectra (Figure 3.3a), 4 fundamental elements of the as-prepared carbon dots are identified as C(1s), O(1s), N(1s) and S(2p).

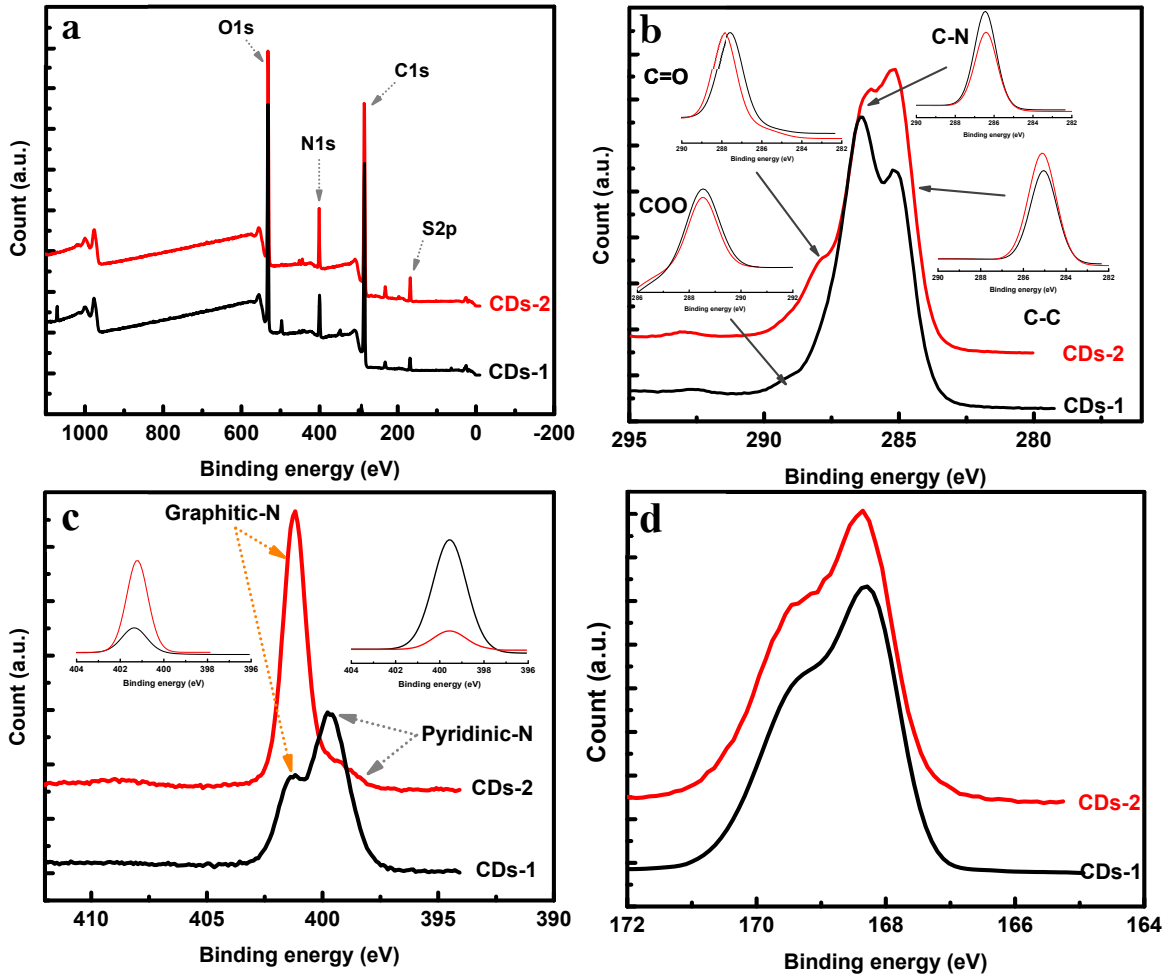

Figure 3.3 ***(a)*** XPS survey spectrum of C - dots -1 and -2, ***(b)***, ***(c)*** and ***(d)*** high resolution XPS spectra of C(1s, N(1s) and S(2p). ***Inset figures*** display the deconvolution of the experimental spectra.

The deconvolution of the C(1s), from high resolution spectrum (Fig.3.3b. inset), exhibits the presence of 4 components at the binding energies of 285, 286.1, 287.5 and 288.5 eV. The latter could be attributed to the binding energy (BE) of carbon atoms derived from the carbon backbone, amide group (C – N) from imidazolium ring, carbonyl group (C = O) and small contribution of carboxyl group (—COO), respectively. Besides, a π – π* satellite peak located at 292.5 eV corresponds to a typical conjugated system. For comparison, the C – N/ C – C ratio

is found to be around 0.66 and 1.02 for C-dots – 1 and – 2 which is coherent with the FT – IR results mentioned previously. Moreover, the N(1s) signal of C - dots -1 (Fig. 3.3c – black curve) shows 2 components at 398.8 and 401.5 eV corresponding to typical pyridinic – and graphitic – N structure[27]. The ratio N_g/N_p is found to be around 0.36 resulting to a pyridinic N – rich structure of the C-dots – 1. Whereas, the opposite behavior was obtained with the C-dots – 2 whose ratio N_g/N_p is equal to 7.4 resulting to graphitic N – rich structure. Even though the atomic percentage is remaining similar for both types of C - dots (Table 3.2), the chemical states change in function of the composition of the reactants.

Table 3.2 Atomic composition of C - dots.

Element	***C***	***N***	***O***	***S***
C-dots – 1 (% at.)	64.9	8.1	24.6	2.4
C-dots – 2 (% at.)	65.2	7.8	23.9	3
C-dots – 3 (% at.)	61.4	5.7	32.9	0

As discussed in the previous part about the contribution of the solvent molecule to the formation of the C-dots, sulfur XPS signal was recorded as shown in the figure 3.3d and displays 2 components at 168 eV and 169.5 eV that are attributed to $S(2p_{3/2})$ and $S(2p_{1/2})$ peaks due to the spin – orbit coupling. The binding energy of S is 168 eV suggesting the presence of sulfur oxide originated from the ionic liquid anion. The presence of this element confirms the presence of the ionic liquid anion at the extreme surface.

For comparison, the carbon dots synthetized in water in the presence of glucose and glutamine mixture (7% wt. and 3.5 % wt. – C-dots – 3), the percentage of C(1s) is found to be in the same range. However, the percentage of nitrogen decreases strongly from 8 % to 5.7 % and the quantity of oxygen increase up to 32.9 %, confirming the insertion of ionic liquid into C-dots structure. Furthermore, the use of EMIES solvent resolves the problem from the limited solubility of glutamine in water during the carbonization. In addition, the N(1s) of C-dots – 3 is composed from 4 components (Pyridinic –, Pyrrolic –, Graphitic – and Oxidized – N) (Figure 3.S1) instead of bi-component in the present cases. The difference of composition by using EMIES solvent maybe due to its viscosity that reduces the nucleation and growth rates of the C - dots resulting to more controllable structure.

To complement the physical – chemical properties of the as – prepared carbon dots, the absorption and fluorescent spectra were recorded using aqueous dispersion of the carbon dots. In general, the C - dots have been referred to nano-sized carbon particles that composed of C, H, O and doping agent, as S, N, P, etc[28]. The notion is far different from reported graphene quantum dots (GQDs) which are oxygen-free and contain only sp^2-hybridized C and H (presence of doping elements is possible). Furthermore, GQDs do not emit light (i.e. non-fluorescent). Consequently, C-dots have a more comprehensive definition compared to graphene dots. As presented in the figure 3.4a, a broad absorption band was observed from 425

nm to 200 nm indicating continuum of the degenerated energy level of the C-dots – 1. By exciting the C - dots solution with different wavelengths ranging from 350 nm to 550 nm, the corresponding fluorescent spectra were recorded. As shown in the figure 3.4a and c, two behaviors have been revealed. By increasing the excitation wavelength, the fluorescent intensity increases and reaches the maximum at 520 nm in blue – green region (λ_{exc} = 425 nm) followed by a decrease of the PL intensity. Furthermore, the emission peak position exhibits a red shift from 500 nm (λ_{exc} = 350 nm) to 600 nm (λ_{exc} = 550 nm), i.e. blue – green to orange emission. The behavior can be attributed to quantification of the energy levels for a quantum dot[28,29].

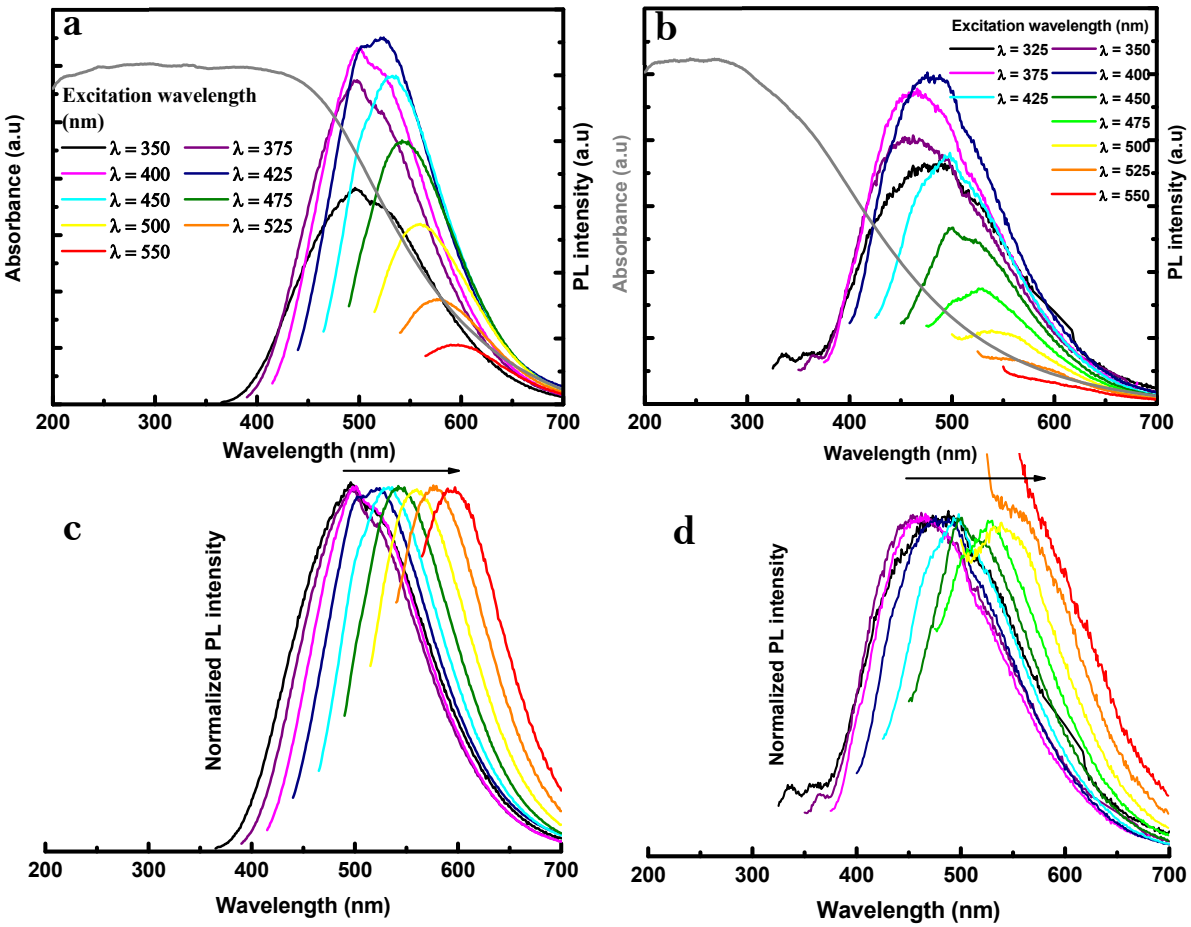

Figure 3.4 UV-Visible and Fluorescence spectra of ***(a, c)*** C-dots – 1 and ***(b, d)*** C-dots – 2

In QDs, the charge carriers are confined in all three dimensions corresponding to the spherical morphology observed with TEM, and because of this characteristic, the energy level of electrons and the corresponding holes can be demonstrated as discrete[30,31]. The band gap values can be defined, in this circumstance, as the difference between highest occupied molecular orbital (HOMO) and lowest unoccupied molecular orbital (LUMO) states. In addition, the density of state for each level depends strongly to the local concentration of doping states. These discrete energy levels cause the evolution in term of emission wavelength followed different excitation energies. In the other hand, according to the previous study[32], the strong electron withdrawing ability of nitrogen atoms causes a distortion in the π-π* structure of the conjugated

C planes which cause intra-band exciton annihilation (i.e. the π–π* electron–hole recombination enhancement).

Similar behaviors were observed with C-dots – 2. However, unlike C-dots – 1, the plateau of absorbance is narrower (< 350 nm) indicating a larger band – gap generated by this family of QDs. Besides, by exciting the suspension with various excitation wavelengths, the highest PL intensity is found to be at 480 nm which is attributed to λ_{exc} = 400 nm. For a fair comparison, by using λ_{exc} = 425 nm, the emission peak is located at 500 nm resulting to a blue – shift with C-dots – 2. As far as our knowledge, the photo-luminescent properties with a quantum yield ranging from 5 to 30 % are attributed to almost synthetized carbon dots, i.e. carbon clusters with nanometer scale[28]. However, the exact mechanism of the photo-excitation (single/multi – photon excitation) is remained at observational stage and required extensive investigations.

Even though the carbon dots do not swell in water, aggregation can be observed by comparing the distribution in size by using 2 different techniques (Dynamic Light Scattering and TEM). As shown in the figure 3.5 a, the hydrodynamic diameter of the carbon dots remains similar for both types of particles (~ 100 nm). However, TEM image (Fig. 3.5b) shows a size distribution ranging about 12 ± 2 nm. Additional information about the surface charge of the C-dots can be determined by using Zeta potential measurements affording a value of -25 ± 6 mV and – 30 ± 6 mV for C-dots – 1 and – 2, respectively. All these results confirm the possibility to generate N doped C - dots using EMIES as nitrogen source.

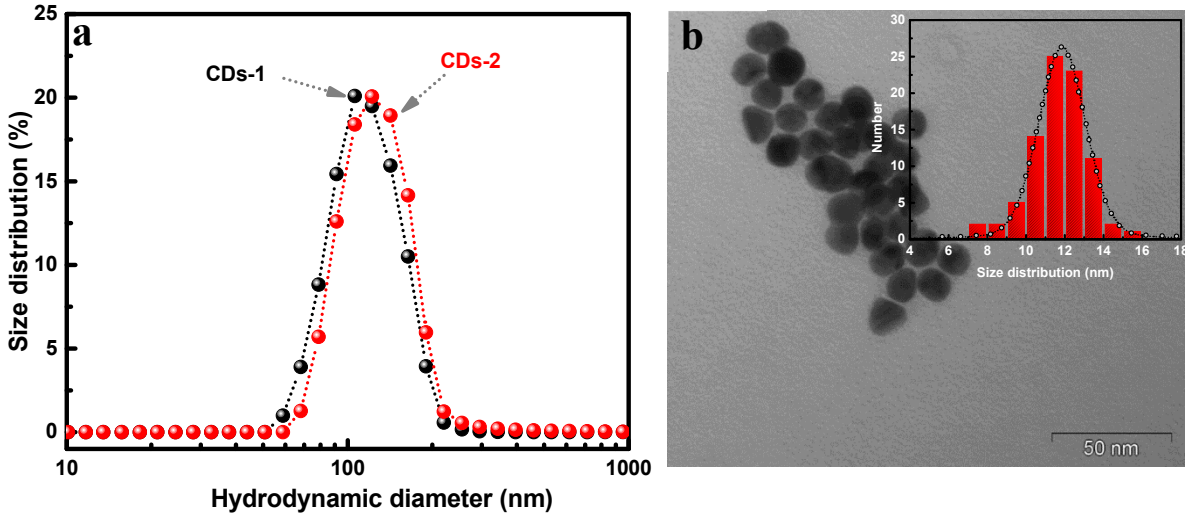

Figure 3.5 ***(a)*** Size distribution by DLS of (black) C - dots -1 and (red) C - dots -2; ***(b)*** TEM image of C- dots - 2. ***(Inset)*** Histogram of size distribution obtained by TEM

3.2.2 Electrochemical investigations of C-dots – 1

The oxygen reduction reaction, ORR, has been investigated by using C-dots – 1 suspension. First, the C-dots – 1 generated from a mixture of glucose and glutamine in ionic liquid at different temperatures were tested using linear sweep voltammetry (LSV) at rotating ring disk electrode (RRDE). The C-dots were mixed in Nafion/EtOH (5% v/v) solution and deposited onto RRDE electrode. All the results concerning the electrocatalytic performances were

repeated using at least 5 different films. Figure 3.6a shows the LSV of various C-dots – 1 (obtained at different temperatures) performed in 0.1 M O_2-saturated KOH solution at 1600 rpm with 10 $mV.s^{-1}$ as scan rate.

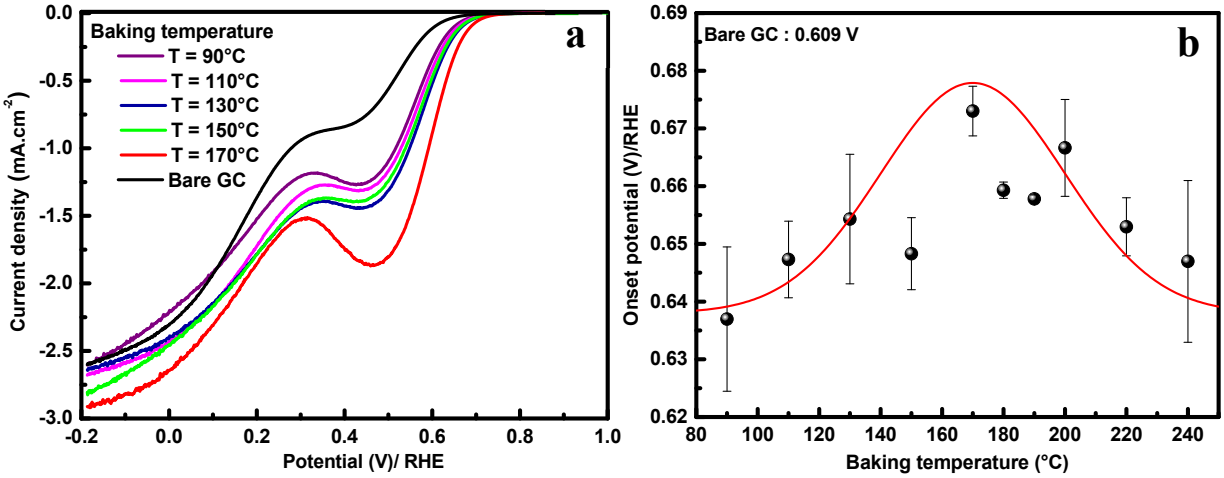

Figure 3.6 (a) the ORR polarization curves, in O_2-saturated 0.1 M KOH solution, using RRDE at rotation 1600 rpm with 10 mV/s scan rate for C-dots – 1 synthesized at different temperatures; ***(b)*** Variation of the onset potential (V) in function of the baking temperature.

The polarization curves show clearly that the all of the N – doped C-dots – 1 exhibit pronounced ORR electrocatalytic activity when compared to bare GC (black curve). The curves show two reduction waves, suggesting the occurrence of the ORR probably through a consecutive two electron steps with the generation of peroxides as an intermediate. From these curves, 2 important parameters for evaluating the catalytic activity of a given catalyst, onset potential and current density, can be revealed. While the onset potential represents the thermodynamic barrier of the reaction, herein the oxygen reduction, the current density displays the kinetic of the reaction. In some context, the current density is more appreciated than the onset potential for assessing the activity of a catalyst. In the literature, even though there is confusion about the determination of the onset potential, there are 2 different ways, either the onset potential is determined as the potential where the current starts to deviate from the baseline[33] or it is determined as the intersection between tangents from non – faradic zone and faradic zone[34]. In this dissertation, the second method will be applied.

As shown in the Figure 3.6b, the evolution of the onset potential of various samples with the synthetic temperature ranging from 90 °C to 240 °C exhibits gaussian-like curve with an optimum at 170 °C (E_{onset} = 0.675 ± 0.007 V vs. RHE). Indeed, the C-dots – 1 sample prepared at 170 °C displays the best performance towards the ORR as attested by not only more positive onset potential but also higher current density.

In order to get more insight about the performance of the C-dots – 1 towards ORR, the electrochemical investigations were complemented by performing the LSV on RRDE at various rotation rates (Figure 3.7a). The selected sample is the C-dots – 1 prepared using glucose/glutamine (7 %: 3.5% wt.) in EMIES at 170 °C. Figure 3.7a displays the observed

current at the disk and ring electrodes showing two reduction waves that are both attributed to two – electron reduction process affording hydrogen peroxide as intermediate.

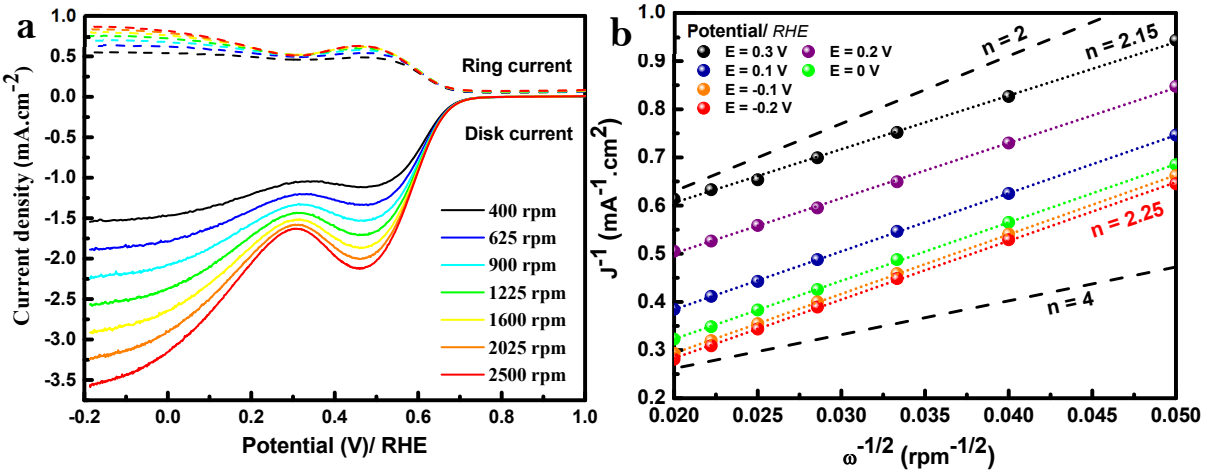

Figure 3.7 (a) ORR polarization curves in O_2-saturated 0.1 M KOH solution using RRDE of C-dots – 1 sample generated at 170 °C at different rotations speeds, ***(b)*** Koutecky-Levich plots at different potentials.

As the potential of electrode becomes negative, the limiting current is observed pointing out that the diffusion process becomes dominant during the reduction process. Nevertheless, the limiting current decreases at more negative potential, i.e. ranging from 0.45 to 0.3 V/ RHE, affording peak – like rather than normal plateau – current. Moreover, the peak current becomes more pronounced by increasing the rotation speed (ω) suggesting that the catalytic activity is lowered in this potential range. This phenomenon can be attributed to the inhibition of the catalyst's surface by temporal adsorption of the intermediate products. At lower potential, the reduction current increases again and reaches a second plateau (E < 0 V/ RHE), putting forward for consideration the regeneration of active sites at the catalyst surface.

From the LSV results, the variation of the limiting current was plotted as function of the square root of the rotation rate (Koutecky-Levich (K-L) plot) as shown in Figure 3.7b. Linear relationship between j^{-1} and $\omega^{-1/2}$ was obtained, confirming that the reduction at the electrode obeys the Koutecky – Levich equation as followed[35]:

$$\frac{1}{j_{lim}} = \frac{1}{j_k} + \frac{1}{j_{lev}} \qquad (3.1)$$

Where the diffusion controlled current (Levich current)

$j_{Lev} = 0.201nFAD^{\frac{2}{3}}\omega^{\frac{1}{2}}\nu^{\frac{-1}{6}}C$ (3.2) with n, A, D, C, ω, υ corresponding to the overall number of transferred electrons, surface area of the electrode (cm^2), diffusion coefficient ($cm^2.s^{-1}$) and bulk concentration ($mol.cm^{-3}$) of O_2, rotation speed (rpm) and kinematic viscosity ($cm.s^{-1}$) of the electrolyte solution. The value 0.201 is replaced by 0.62 if the unit of the rotation speed is reported in $rad.s^{-1}$.

While j_k represents the kinetic controlled current, which can be determined from the intercept of the K – L curves and related to several parameters as:

$j_k = nFAK_{O_2}\Gamma_{catalyst}C$ (3.3) where K_{O2} and $\Gamma_{catalyst}$ represent the rate constant of the chemical reaction which limits the plateau current and the concentration of the active sites.

The value of the transferred electron number n varies from 2.25 to 2.15 within the potential ranging from 0.3 to -0.2 V/ RHE indicating the production of hydrogen peroxide (Figure 3.7b). These values suggest that the ORR catalyzed by the N-doped C-dots – 1 occurs preferentially via two electron transfer pathways. Next, the electrochemical activity of the C-dots – 1 for oxygen reduction to produce hydrogen peroxide was quantified using the ring current. Indeed, the active materials deposited at the disk electrode reduce oxygen via different possible pathways including 2 – electron and 4 – electron ones to produce H_2O_2 and water. However, only hydrogen peroxide can be further electroactive. Under mass diffusion, the disk – generated hydrogen peroxide reaches the ring electrode where positive potential is applied to oxidize them to oxygen and water with a factor of efficiency (N).

The ORR current on the disk electrode is assumed as $j_D = j_{2e} + j_{4e}$ (3.4) where j_{2e} and j_{4e} correspond to the current serves for 2 – electron and 4 – electron ORR, respectively. As a result, eq3.1 induces following equation:

$$\frac{j_D}{n_e} = \frac{j_{2e}}{2} + \frac{j_{4e}}{4} \qquad (3.5)$$

As described, the ring current represents the necessary charge to oxidize H_2O_2, which is given by $j_{2e} = j_R / N$ ORR with N the collecting coefficient number.

By arranging equation 3.3, the equation 3.4 can be easily obtained, which can be further used to calculate the number of electrons from RRDE measurements.

$$n_e = \frac{4J_D}{J_D + J_R / N} \qquad (3.6)$$

The hydrogen peroxide percentage is estimated using the formula:

$$\%H_2O_2 = 100.\frac{4 - n_e}{2} = \frac{200J_R / N}{J_D + J_R / N} \qquad (3.7)$$

Thus, the ring current shows positive values due to the oxidation of H_2O_2 at a potential of 1.2 V/ RHE. Figure 3.8 displays the variation of the transferred electron number and the efficiency of hydrogen peroxide production as a function of the potential. Overall, the C-dots catalyze the oxygen reduction reaction mainly by 2 – electron process for a large potential window from 0.7 V to -0.2 V/RHE with the number of transferred electrons ranging from 2.15 to 2.25 corresponding to a quantity of hydrogen peroxide around 87 to 93 %. Despite similar electron number was collected in this potential range, this 2 – electron reduction occurs at 2 different potential ranges, i.e. [0.7 V; 0.2 V] and [0.1 V; -0.2 V], suggesting the co-existence of 2 kinds of active sites that have different electrocatalytic performance.

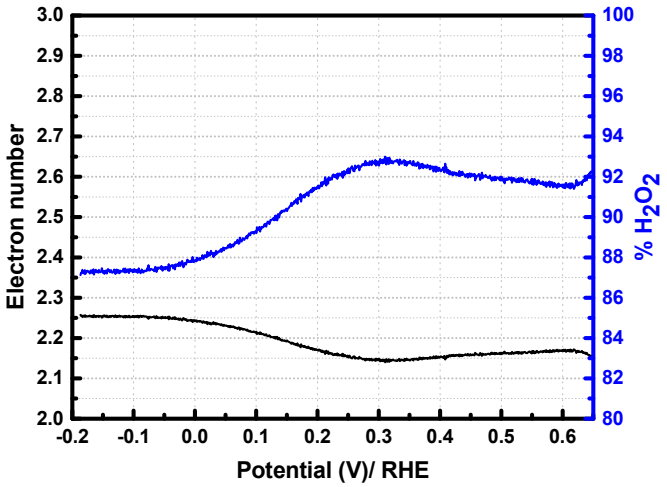

Figure 3.8 Variation of the electron number and the hydrogen peroxide percentage as function of the potential for C-dots – 1 sample.

The number of exchanged electron and percentage of hydrogen peroxide were calculated for the remaining samples at different baking temperature as shown in the figure 3.9.

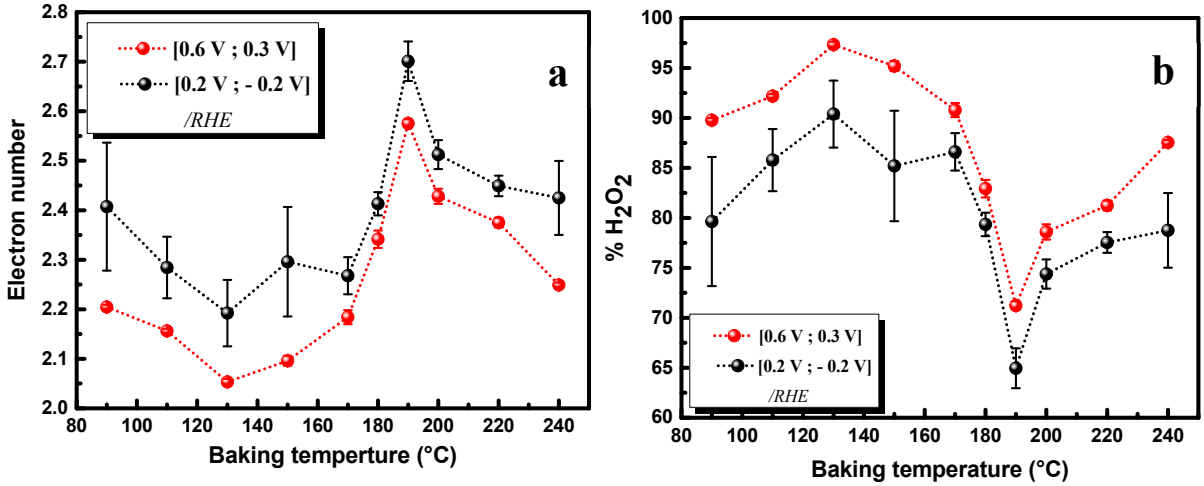

Figure 3.9 Variation of ***(a)*** the electron number and ***(b)*** the hydrogen peroxide percentage as function of the baking temperature for C-dots – 1 samples

For all the samples, the number of exchanged electron is lower in the first potential range (red dots), i.e. [0.7 V;0.2 V/ RHE], than the second range (black dots) ([0.1 V; -0.2 V/RHE]). Therefore, the percentage of generated hydrogen peroxide is higher in the first region resulting to higher selectivity towards 2-electron pathway's product.

Furthermore, the samples with baking temperature lower than 170 °C exhibit, in average, asymptotically an overall electron number of 2. While, the samples prepared at a temperature higher than 170 °C, provide an electron number higher than 2.3, corresponding to a quantity of hydrogen peroxide less than 75 %. By taking only the n_e and $\%H_2O_2$ into account, the C-dots prepared at 130 °C present highest selectivity towards production of hydrogen peroxide (n_e = 2.05 and $\%H_2O_2$ = 97 %). However, the later unveils higher overpotential (20-30 mV) and lower current density ($j_{130°C}/j_{170°C}$ = 0.75) compare to C-dots/170°C. By considering different

factors, optimal synthetic condition for C-dots – 1 to achieve the best performance is 170 °C for 5 min under microwave irradiation.

For complementing the influence of the EMIES solvent onto the selectivity of the C-dots towards generation of hydrogen peroxide, C-dots – 3 synthetized using a mixture of glucose/ glutamine (7%: 3.5% wt.) in water at 170 °C were evaluated for ORR. The latter gives higher electron number (n_e = 2.4) and percentage of H_2O_2 around 80%, suggesting a large loss of selectivity. As a result, EMIES has greatly contributed not only to the formation of the carbon dots as doping source but also to the enhancement of the catalytic activity of ORR toward H_2O_2 production. The ORR activity of nitrogen doped carbon matrix is attributed to the adjacent carbon atoms to the nitrogen due to the polarization generated by the difference of electronegativity of these elements. It has been demonstrated, by means of experiences and theoretical calculations that the selectivity towards formation of hydrogen peroxide of nitrogen – doped carbon materials is strongly depended not only on the atomic percentage of the nitrogen inside the material but also on the configuration of the nitrogen including oxidized quaternary– , pyridinic–, graphitic– and pyrrolic– nitrogen[36]. It is found that higher selectivity is obtained with high content of graphitic nitrogen which are located far from edge site of the graphite sheet[37,38]. Having already described previously that the ratio of N_g/N_p for C-dots – 2 is found to be 16 times higher than the value found for C-dots – 1, the C-dots – 2 are expected to provide a higher selectivity towards production of hydrogen peroxide. Within this context, different samples C-dots – 2 synthetized at different temperatures were then evaluated.

3.2.3 Electrochemical investigations of C - dots -2

The electrochemical catalytic activity of C-dots – 2 generated in the presence of 7 % wt. of glucose in ionic liquid solution (EMIES) under microwave at different baking temperature during 5 min was investigated. Figure 3.10 shows the electrochemical responses of different C-dots – 2 towards the ORR.

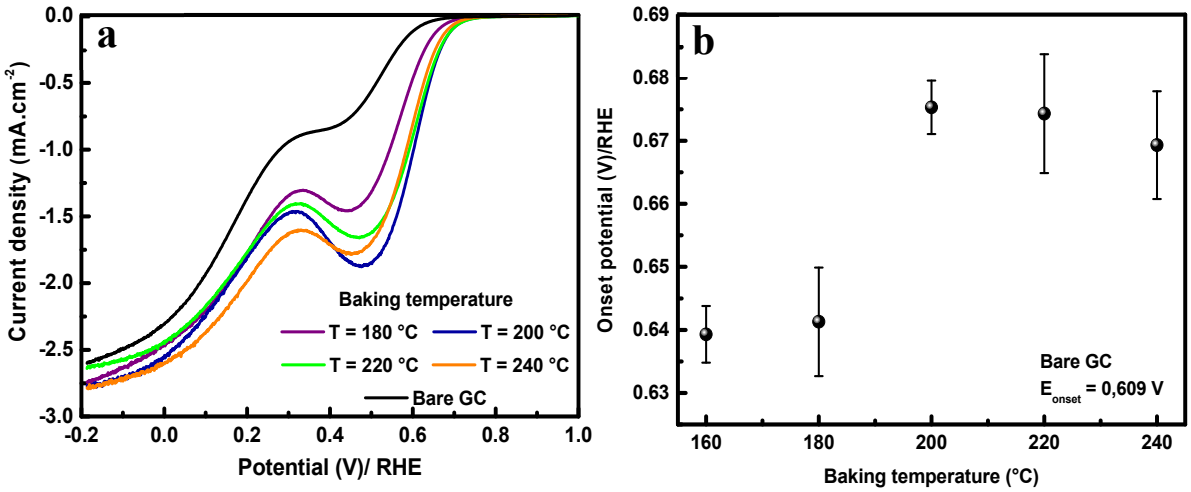

Figure 3.10 (a) the ORR polarization curves, in O2-saturated 0.1 M KOH solution, using RRDE at rotation 1600 rpm with 10 mV/s scan rate for C-dots – 1 synthesized at different temperatures; ***(b)*** Variation of the half-wave potential (V) in function of the baking temperature.

As displayed, the catalytic activity varies in function of the conditions of preparation (temperature). The C-dots prepared at 200 °C exhibit the most pronounced catalytic activity by both owing more positive onset potential (E_{onset} = 0.68 V/RHE) and higher current density (2 $mA.cm^{-2}$ at 0.5 V/ RHE) than other samples.

To get insight the catalytic activity of these particles, polarization curves at different rotation speeds were recorded for the C-dots prepared at 200 °C during 5 minutes in O_2 – saturated alkaline solution. As illustrated in the Figure 3.11a, the shape of the LSV curves appears similar to the responses of C-dots – 1.

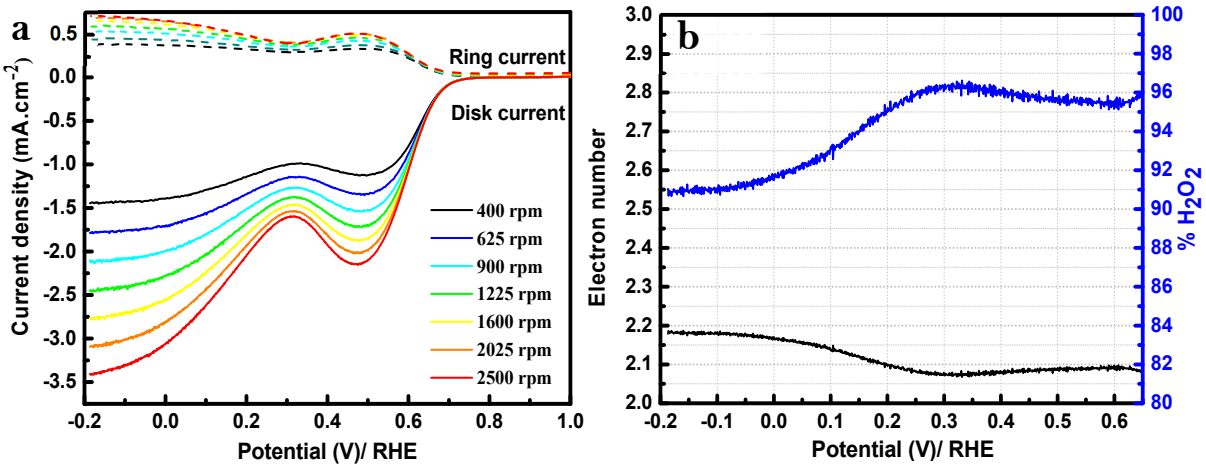

Figure 3.11 (a) ORR polarization curves in O_2-saturated 0.1 M KOH solution using RRDE of C-dots – 2 sample generated at 170 °C at different rotations speeds; ***(b)*** Variation of the electron number and the hydrogen peroxide percentage as function of the potential for C-dots – 2 sample.

Briefly, 2 reduction waves, at the potential ranging from 0.7 V to 0.3 V and from 0.3 V to -0.2 V/RHE, were obtained resulting from different active sites inside the particles. Importantly, as expected, the selectivity of the C-dots – 2 towards production of hydrogen peroxide is boosted by decreasing the number of electrons ranging from 2.05 to 2.15. Despite the presence of non – desirable quantity of pyridinic – N that lowers the selectivity of the C-dots, the percentage of H_2O_2 is retained superior to 90 % over a large range of potential from 0.6 V down to -0.2 V/RHE, i.e. the active potential window is calculated to be at least 0.8 V.

In addition, the Figure 3.12 displays a general picture of the evolution of the selectivity of the as – prepared C-dots in function of the synthetized temperature. In the first potential window, [0.6 V; 0.2 V], all of the C-dots samples exhibits higher catalytic activity ($\%H_2O_2$ > 85%). However, the catalytic performance decreases in the second potential range where the C-dots at 200 °C expose less variation than the others, indicating best performance in both potential windows.

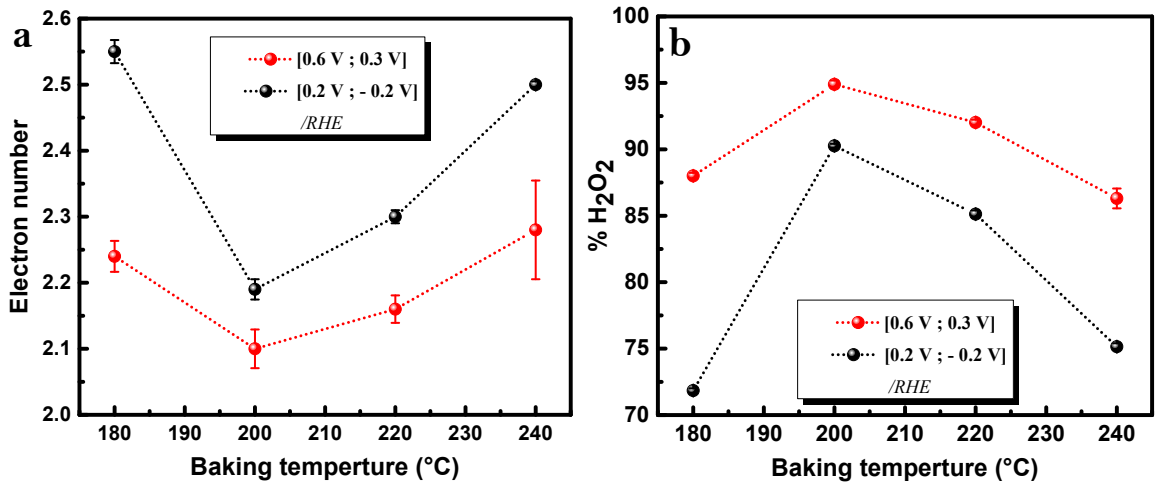

Figure 3.12 Variation of ***(a)*** the electron number and ***(b)*** the hydrogen peroxide percentage as function of the baking temperature for C-dots – 2 samples

Compared to the C-dots – 1 (generated in IL glucose/glutamine at/170 °C), an increase of 5 % of hydrogen peroxide is obtained over the studied potential range, confirming the role of the graphitic – N which is more abundant in the present product. However, the temperature needed to prepare the C-dots – 2 is 30 °C higher than in case of the C-dots – 1, suggesting difficult insertion of the EMIES molecules to the glucose induced carbon network. This difference could be due to the ring opening reaction of the EMIES by nucleophilic addition followed by elimination at the carbon atom adjacent to 2 nitrogen atoms (C (2)) as illustrated in Scheme 3.1[39].

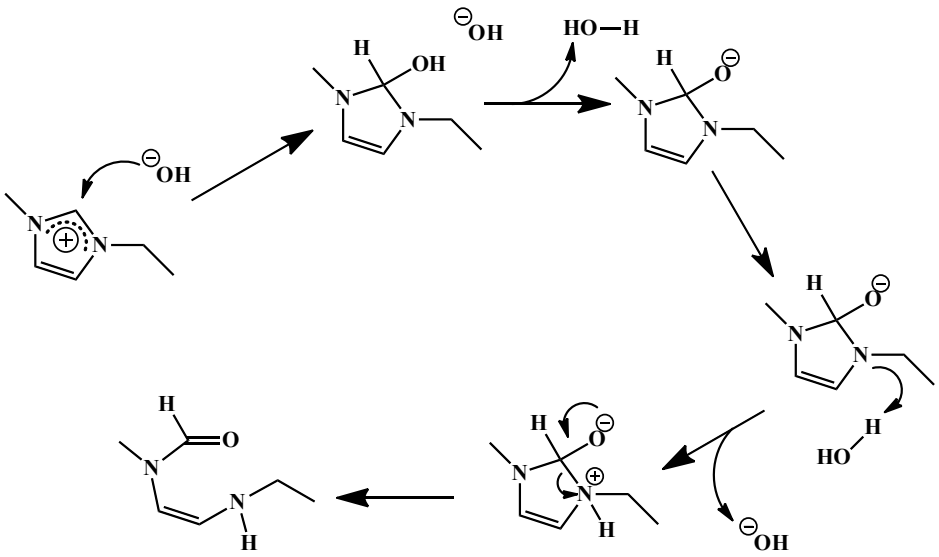

Scheme 3.1 Ring – opening reaction of EMIES[35]

Looking into the literature, efficient catalysts for reducing oxygen via 2-electron pathways with high percentage of H_2O_2 (> 85 %) have already been reported. Nevertheless, all of the reported selectivity is maintained within relatively narrow potential window. Interestingly, in this present work, the C-dots synthetized by carbonization of glucose in ionic liquid (EMIES) under

microwave irradiation offer wider accessible potential range with a comparable selectivity towards formation of hydrogen peroxide. A comparison between different types of C-dots prepared by microwave assisted method in the present work and previously reported results in the literature is presented in the table 3.3

Table 3.3 ORR parameters obtained on different C-dots and the comparison with the literature

Samples	Onset Potential (V)/RHE	Number of electrons at [0.7V; 0.3V]	Number of electrons at [0.1V; -0.2V]	Maximum of $\%H_2O_2$	Potential range (V) $\%H_2O_2 > 90$ %
C-dots – 1 *(Glucose/Glutamine in EMIES)*	0.67	2.2	2.4	90	0.4
C-dots – 2 *(Glucose in EMIES)*	0.68	2.05	2.15	95	0.8
C-dots – 3 *(Glucose/Glutamine in H_2O)*	0.65	2.2	2.6	85	Ø
C-dots – 4 *(Glucose in H_2O)*	0.67	2.7	2.5	75	Ø
Mesoporous N–doped C[40]	0.5	2.1		93	0.4
PtHg/C NPs[41]	0.75	2.2		90	0.3
Fe_3O_4 NPs on graphene[42]	0.75	2.7		68	Ø
Hierarchically porous carbon[43]	0.3	2.1		80 – 95	0.3
Co/C composite[44]	0.55	2.05		80 – 90	0.4
RF – AQ/Vulcan[45]	0.25	2.2		85	Ø
Mesoporous N–doped carbon[46]	0.5	2.1		96	0.2

In order to explain the origin of the enhanced catalytic activity and selectivity of the as – prepared C-dots, mechanistic investigation was performed via the study of the evolution of Koutecky – Levich lines in function of the applied potential. After each 5 mV in the first potential range of [0.637 V; 0.562 V] and in the second range of [0.212 V; 0.062 V] where the reaction is controlled by the electron transfer kinetic, the variation of j^{-1} as function of $\omega^{-1/2}$ was plotted as shown in the Figure 3.13a and b.

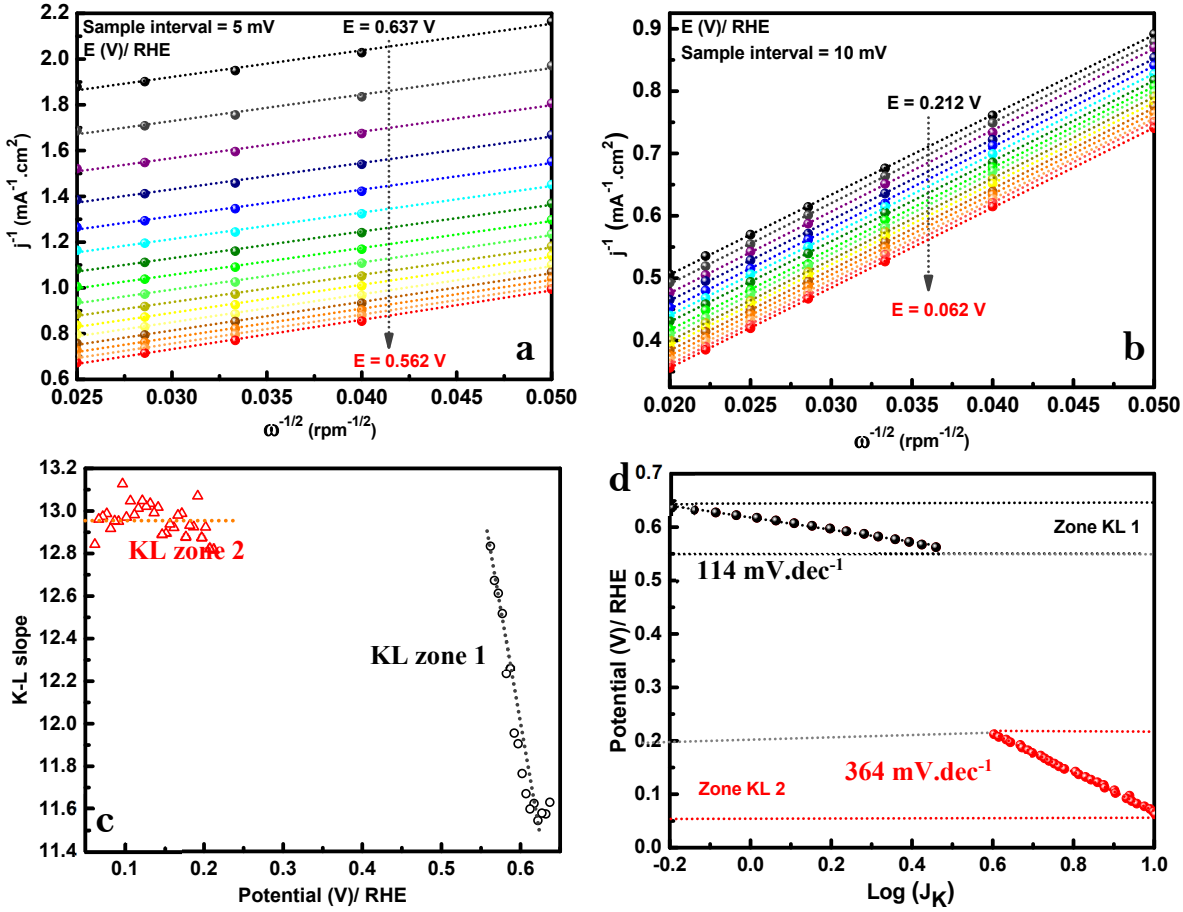

Figure 3.13 Koutecky-Levich plots at different potentials range from ***(a)*** 0.637 V to 0.562 V, ***(b)*** 0.212 V to 0.062 V vs RHE; ***(c)*** Evolution of the K – L slope as function of the potential and ***(d)*** Tafel plot for C-dots – 2 sample

All the plotted curves exhibit linear relationship following Koutecky – Levich equations. Nevertheless, the slope of the K– L lines changes as the potential range change, indicating the variation of the kinetic current, j_K. To follow the evolution of the j_K, the current – intercept of each line was calculated, giving $1/j_K$.

Figure 3.13 displays the corresponding Tafel plot in which the variation of the potential in function of the logarithm of the j_K is followed in the 2 potential ranges. As the kinetic of the oxygen reaction is relatively slow, i.e. the overpotential is large, the current density is calculated as: $j = j^0_{O_2} \exp(\frac{n\alpha F\eta}{RT})$ (Eq.3.8) where η the overpotential, α the transfer coefficient and j^0 the exchange current density.

For the electron transfer, there are two distinct notions, labelled the electron transfer coefficient (α) and the factor of symmetry (β). Even though it is widely known that the value of α is around 0.5, this term seems to be source of confusion. It comes from a specific situation that the value of α is equal to the one of β. Consequently, these concepts should be clarified.

At the early stage of electrochemistry, it was proposed that the electron transfer kinetic is mainly attributed to the neutralization of ions at the vicinity of the surface by an electron from the

electrode without paying attention about how it happens. Later, the quantum mechanics proposed a clear explanation of the way electron leaves the surface, i.e. tunneling effect. From the basics of quantum mechanics, when the Fermi level of the electrode and the available orbital of the species are adjusted at the same energy, the electron can tunnel between the electrode and the molecules without any loss of energy. Considering a system where the acceptor molecule is attached to the electrode surface via an electron transfer (Scheme 3.2).

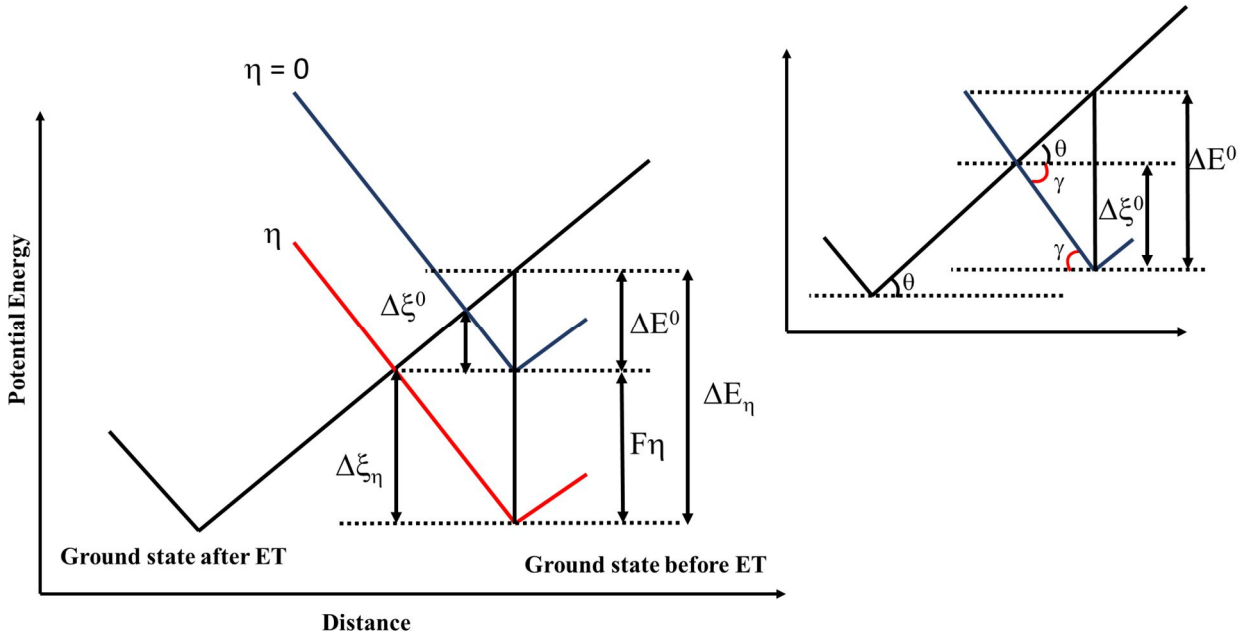

Scheme 3.2 Shift in energy – distance curve caused by application of an overpotential[47]

It is noted that the bond activation energy ($\Delta\xi$) is less than the original gap energy (ΔE), resulting to the following equation[47]

$$\frac{\Delta\xi^0}{\Delta E^0} < 1 \qquad (3.9)$$

By assuming that the energy – distance follows linear relationship as presented and by using intercept theorem for different triangles, the equation 3.9 can be represented as:

$$\frac{\Delta\xi^0}{\Delta E^0} = \frac{\Delta\xi_\eta}{\Delta E_\eta} = \frac{\Delta\xi + (\Delta\xi_\eta - \Delta\xi^0)}{\Delta E^0 + \eta F} = \frac{\Delta\xi^0 + \Delta(\Delta\xi)}{\Delta E^0 + \eta F} \qquad (3.10)$$

which can be satisfied only if $\frac{\Delta\xi^0}{\Delta E^0} = \frac{\Delta(\Delta\xi)}{\eta F} = \beta$ (3.11). The β value represents the ratio between the activation energy that makes the tunneling happened and the energy gap of non-activated bond.

From the scheme 3.2, inset, the value of β is equal to $\frac{\Delta\xi^0}{\Delta E^0} = \beta = \frac{\tan(\gamma)}{\tan(\theta) + \tan(\gamma)}$ (3.12)

If the slopes of the energy – distance are roughly equal, the equation 3.12 becomes

$\beta \cong 0.5 \quad (3.13)$ with $\tan(\gamma) \cong \tan(\theta)$

However, even though the use of 0.5 in different electrochemical equations, this value must not be attributed to the symmetry factor, but it has to be referred to the transfer coefficient (α).

By considering a multi-electron reaction: $A + ne^- \leftrightarrows Z$ in which the rate – determining step is assumed as: $O + re^- \leftrightarrows P$ where r the number of electrons involved in the RDS (r = 0 consists to a chemical determining step while r = 1 indicates electron transfer step). During the transformation from A to Z, $n = s + r\,\nu + s'$ where ν the number of molecules produced by the RDS needed for next step; s, s' are the number of electrons involved before and after the RDS, respectively. The reaction from A to Z can be decomposed as a consecutive sequence of different reactions as:

$$A + e - \underset{}{\overset{\text{Step1}}{\longleftrightarrow}} B + e - \underset{}{\overset{\text{Step2}}{\longleftrightarrow}} C + e - \underset{}{\longleftrightarrow} \ldots\ldots \underset{}{\longleftrightarrow} M + e - \underset{}{\overset{\text{Step s}-1}{\longleftrightarrow}} N + e - \underset{}{\overset{\text{Step s}}{\longleftrightarrow}} O$$

$$\nu(O + re^-) \underset{}{\overset{\text{Step s to s}+\nu}{\longleftrightarrow}} \nu P$$

$$\nu P + e - \underset{}{\overset{\text{Step s}+\nu+1}{\longleftrightarrow}} Q + e - \underset{}{\overset{\text{Step s}+\nu+2}{\longleftrightarrow}} R + e - \underset{}{\longleftrightarrow} \ldots\ldots \underset{}{\longleftrightarrow} X + e - \underset{}{\overset{\text{Step n}-1}{\longleftrightarrow}} Y + e - \underset{}{\overset{\text{Step n}}{\longleftrightarrow}} Z$$

The cathodic current for the reaction is calculated as

$$\left|i_{cath}\right| = Fk_O.C_O \exp\left(\frac{-r\beta F(E - E_r)}{RT}\right) = Fk_O.C_O \exp\left(\frac{-r\beta F\eta}{RT}\right) (3.14)$$ [48]

where E_r the potential of the interfacial reaction at equilibrium, which is defined by $E_r = E_{eq}^0 + \frac{RT}{rF}\ln\left[\frac{a_P}{a_O}\right]$ [49], E_{eq}^0 is the standard equilibrium potential.

Assumed that the total reaction is treated by using pseudo-equilibrium method where only the rate determining step is slower than others and alone control the overall reaction rate while other steps are in the equilibrium conditions. By using this hypothesis, the concentration of different species involved in the first step is:

$$K_1.C_A \exp\left(\frac{-\beta F\eta}{RT}\right) = C_B \exp\left(\frac{-(1-\beta)F\eta}{RT}\right) \quad (3.15)$$

conducting to $C_B = K_1.C_A \exp\left(\frac{-F\eta}{RT}\right) (3.16)$

with the K the equilibrium constant, which is define by $\Delta G^0 = -RT\ln(K)$, conducting to

$$K = \frac{C_{prod}}{C_{react}} = \exp\left(\frac{-\Delta G^0{}_{react-prod}}{RT}\right)$$

Accordingly, $C_C = K_2.C_B \exp\left(\frac{-F\eta}{RT}\right) = K_1.K_2.C_A \exp\left(\frac{-2F\eta}{RT}\right) (3.17).$

Via consecutive sequence, the concentration of O is: $C_O = \left[\prod_{i=1}^{s} K_i\right]^{1/\nu}.C_A \exp\left(\frac{-sF\eta}{RT}\right) (3.18),$

resulting to

$$\left|i_{cath}\right| = Fk_O.C_O \exp(\frac{-r\beta F\eta}{RT}) = Fk_O.\left[\prod_{i=1}^{s} K_i\right]^{1/\nu}.C_A \exp(\frac{-\frac{s}{\nu}F\eta}{RT}).\exp(\frac{-r\beta F\eta}{RT})$$

$$= Fk_O.\left[\prod_{i=1}^{s} K_i\right]^{1/\nu}.C_A.\exp(-\frac{(\frac{s}{\nu}+r\beta)F\eta}{RT}) = i^0_{cath}\exp(-\frac{(\frac{s}{\nu}+r\beta)F\eta}{RT}) \quad (3.19)$$

$$\text{with } i^0_{cath} = Fk_O.\left[\prod_{i=1}^{s} K_i\right]^{1/\nu}.C_A \text{, labelled exchange current}$$

For the backward reaction, the same argument is followed where

$$K_n.C_Z \exp(\frac{-\beta F\eta}{RT}) = C_Y \exp(\frac{-(1-\beta)F\eta}{RT}) \quad (3.20), \text{ suggesting } C_Y = K_n.C_Z \exp(\frac{F\eta}{RT}) \quad (3.21)$$

$$\text{Then, } C_P = \left[\prod_{i=s+\nu+1}^{n} K_i\right]^{1/\nu}.C_z^{1/\nu} \exp(\frac{s'F\eta}{RT}) \quad (3.22), \text{ conducting to}$$

$$i_{an} = Fk_P.C_P \exp(\frac{r(1-\beta)F\eta}{RT}) = Fk_P.\left[\prod_{i=n}^{s+\nu+1} K_i\right]^{1/\nu}.C_z^{1/\nu} \exp(\frac{\frac{s'}{\nu}F\eta}{RT}).\exp(\frac{r(1-\beta)F\eta}{RT})$$

$$= Fk_P.\left[\prod_{i=s+\nu+1}^{n} K_i\right]^{1/\nu}.C_z^{1/\nu}.\exp\left\{\frac{\left[\frac{s'}{\nu}+r(1-\beta)\right]F\eta}{RT}\right\} \quad (3.23)$$

by replacing s' = n – s – r ν and $i^0_{an} = Fk_P.\left[\prod_{i=n}^{s+\nu+1} K_i\right]^{1/\nu}.C_z^{1/\nu}$, the anodic current becomes

$$i_{an} = i^0_{an}\exp\frac{\left(\frac{n-s}{\nu}-r\beta\right)F\eta}{RT} \quad (3.23b)$$

Consequently, the measured current is given by

$$i = i_{an} - i_{cath} = i^0_{an}\exp\frac{\left(\frac{n-s}{\nu}-r\beta\right)F\eta}{RT} - i^0_{cath}\exp(-\frac{(\frac{s}{\nu}+r\beta)F\eta}{RT}) \quad (3.24)$$

Assumed that the system is in quasi-equilibrium condition, $i^0_{an} = i^0_{cath}$,

$$i = i_{an} - i_{cath} = i^0\left[\exp\frac{\left(\frac{n-s}{\nu}-r\beta\right)F\eta}{RT} - \exp(-\frac{(\frac{s}{\nu}+r\beta)F\eta}{RT})\right] \quad (3.24b)$$

The transfer coefficient for the anodic and cathodic reactions are given below:

$$\alpha_a = \frac{n-s}{\nu} - r\beta \quad (3.25) \quad \text{and} \quad \alpha_c = \frac{s}{\nu} + r\beta \quad (3.26)$$

The plot of η = f(log(j)) gives a linear relationship with a slope of 2.3RT/αF, called Tafel slope. This value represents how fast the overpotential increases with the current density and has been used to investigate the reaction pathways. Taking an example of the ORR via 4-electron pathway in which the first reduction step is RDS, the transfer coefficient is determined as $\alpha_c = \frac{s}{\nu} + r\beta = 0.5$, suggesting a theoretical Tafel slope of 120 mV.dec^{-1}. For C-dot system, in these 2 regions where the reaction is controlled by the electron transfer kinetic, the linearity of the curves E = f(log(j_K)) results in to 2 different Tafel slopes with a value of 114 mV.dec^{-1} (KL1) and 364 mV.dec^{-1} (KL2) as reported in the figure 3.13d. The inequality of the Tafel slope in the two region induces a difference of either the mechanism or the rate – determining step (RDS) in function of the applied potential. In the literature, these values are referred to an associative mechanism (Eq.3.27 – 3.33 and scheme 3.3)[3] in which the oxygen – oxygen bond - cleavage is not involved as the second step (Eq. 3.28).

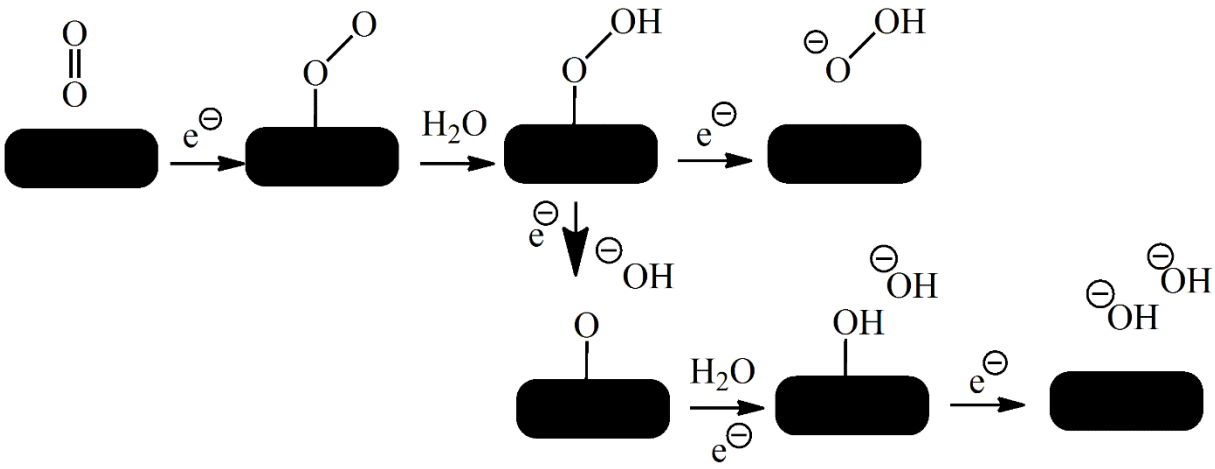

Scheme 3.3 Oxygen reduction reaction via 2-electron and 2+2-electron pathway

$$O_2 + * \rightarrow O_{2\,(ads)} \qquad (Eq.3.27)$$

$$O_{2\,(ads)} + e^- \rightarrow OO^-_{(ads)} \qquad (Eq.3.28)$$

$$OO^-_{(ads)} + H_2O \rightarrow OOH_{(ads)} + OH^- \qquad (Eq.3.29)$$

$$OOH_{(ads)} + e^- \rightarrow HOO^- \qquad (Eq.3.30)\ -2-electron\ pathways$$

$$OOH_{(ads)} + e^- \rightarrow O_{(ads)} + OH^- \qquad (Eq.3.31)$$

$$O_{(ads)} + H_2O + e^- \rightarrow OH_{(ads)} + OH^- \qquad (Eq.3.32)$$

$$OH_{(ads)} + e^- \rightarrow OH^- + * \qquad (Eq.3.33)$$

$$\Big\} -2+2-electron\ pathways$$

Furthermore, figure 3.13c displays the calculated slopes for different K – L lines. A small variation of the slope in the first KL region (zone 2) is observed, which is not the case in the second region (zone 1), suggesting an evolution of the diffusion-controlled regime that is compromise with the K – L equations. As discussed in the precedent part, the j_{Lev} depends on a single parameter that is the rotation speed under saturated oxygen condition. However, in

realistic conditions by considering the influence of the interface between the catalyst and electrolytic solution, the mass transport is less important than the adsorption of the electroactive species on the catalytic sites. During catalytic reaction involving adsorbed electroactive species, the concentration of oxygen depends not only on the bulk concentration of the species but also the coverage percentage at the catalyst surface, noted θ^{50}. It is denoted for 1st order reaction, the reaction rate is defined as $v = k\theta = j/nF$ with k the rate constant. Consequently, in the same kinetic regime, the slope must be constant, and the K-L lines is differed only by the kinetic current, i.e. the activation barrier induced by the applied potentials. As results, the non – parallel behavior of the K – L lines in the first potential range indicates that the oxygen reduction is not 1st order one, suggesting the first electron transfer as rate – determining step (RDS) (Eq.3.17). Consequently, the reaction can be presented as $v = k_1\theta_0[O_2] – k_2\theta_1[e]$ with θ_0 and θ_1 denote the surface coverage of empty sites and of $O_{2(ads)}$, respectively. Moreover, the calculated Tafel slope of 114 $mV.dec^{-1}$, which is practically equal to 120 $mV.dec^{-1}$, has been reported in the literature as the typical value of Tafel slope for the first electron transfer as RDS. In the second K – L zone at the potential ranging below 0.2 V/RHE, the K – L lines are found to be parallel resulting to a 1st order reaction with a Tafel slope of 364 $mV.dec^{-1}$, suggesting the protonation of $O_2^{-}{}_{ads}$ to HO_{2ads} (Eq. 3.29).

In summary, carbon dots have been successfully synthesized by means of microwave assisted methods using bio-based materials and ionic liquid. The glucose and glutamine in ionic liquid as starting materials lead to the formation of nitrogen doped carbon dots. Surface analyses confirm the presence of pyridinic and graphitic nitrogen and imidazolium and ionic liquid anion at the CDs surface. In addition, the nitrogen of the ionic liquid within the imidazolium ring successfully replaced the nitrogen source (glutamine). In this case, the generated CDs exhibits only the presence of graphitic nitrogen. The synthesized CDs were tested towards the oxygen reduction reaction. As a result, both CDs show a promising activity towards the ORR with a high selectivity towards the hydrogen peroxide production. The CDs generated in the presence of glucose and ionic liquid exhibit outstanding performance and selectivity for the ORR through the 2-electron pathway with an efficiency of H_2O_2 production up to 90% over a large potential range 0.8 V. This work not only demonstrates the possibility to generate nanoscale doped carbon dots in ionic liquid, but also provides an efficient metal-free catalyst for H_2O_2 production.

3.3 POLY(IONIC LIQUIDS) AS NOVEL CATALYST TOWARDS OXYGEN REDUCTION REACTION AND OXYGEN EVOLUTION REACTION

In the previous part, we reported the utilization of an ionic liquid molecule, EMIES, as solvent and doping agent for fabricating highly selective C-dots towards generation of H_2O_2. It has been clearly demonstrated the important role of the ionic liquid (EMIES) in the catalytic performance of the synthetized particles. Following this directive reflection, we attempt to investigate the use of polymer brushes ionic liquid, poly(IL), as an emerging catalyst for ORR. This part will be devoted to answer the question on the potential use of poly(IL) as catalyst. We will describe the surface characterization of the generated poly(IL), the electrochemical properties of the electrode/poly(IL) interface and the electrocatalytic performance.

3.3.1 Structural characterization

Following the analogous procedure detailed in the chapter 2 for preparing polymeric ionic liquid functionalized substrates by SI – ATRP, the 1-methyl-3-vinyl imidazolium TFSI (VImM) was used as monomer (Scheme 3.4) for the upcoming studies.

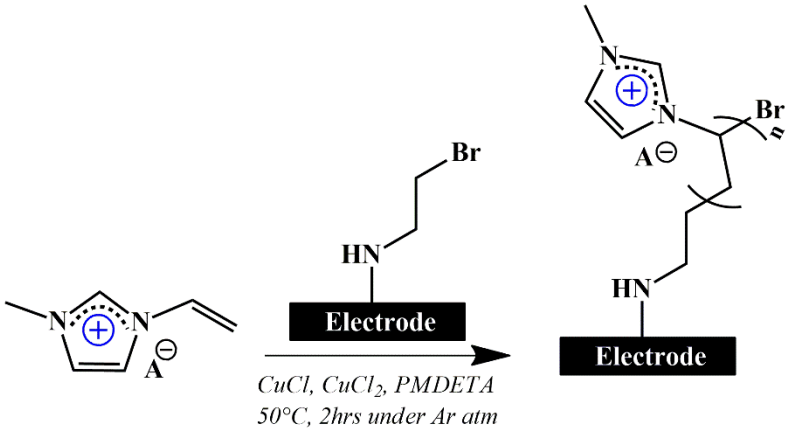

Scheme 3.4 Scheme illustrating the SI-ATRP process

Following the SI-ATRP polymerization, the surface analyses were performed by investigating the chemical composition of the polymer using X-ray photoelectron spectroscopy (XPS). Figure 3.14b represents the survey spectrum of the polymer ionic liquid, Poly(1-methyl-3-vinylimidazolium), abbreviated Poly(VImM), modified Au wafer using SI – ATRP. Typical signals of chemical elements from the polymer framework are observed, including C(1s), O(1s) and N(1s). As reported in the inset table, the atomic percentage of nitrogen and carbon is found to be around 10 % and 34%, respectively. It results to a ratio C/N about 3.4 times which is relatively close to the theoretical value obtained from the chemical structure of the monomer (C/N = 3), indicating the presence of the Poly(VImM) onto the Au surface. Figure 3.14c and d display the core level high resolution spectra of C(1s) and N(1s) elements. The deconvolution of the C(1s) spectrum exhibits the presence of 4 components at binding energy of 285.2, 286.5, 287.2, and 288.9 eV which can be attributed to the binding energy of carbon atom derived from the C backbone (C−C), amide (C−N), (−C=N) group from imidazolium ring, and −COO from

the surface contamination, respectively[51]. The main N(1s) signal appears at 401.7 eV is attributed to imine group from imidazolium ring[51].

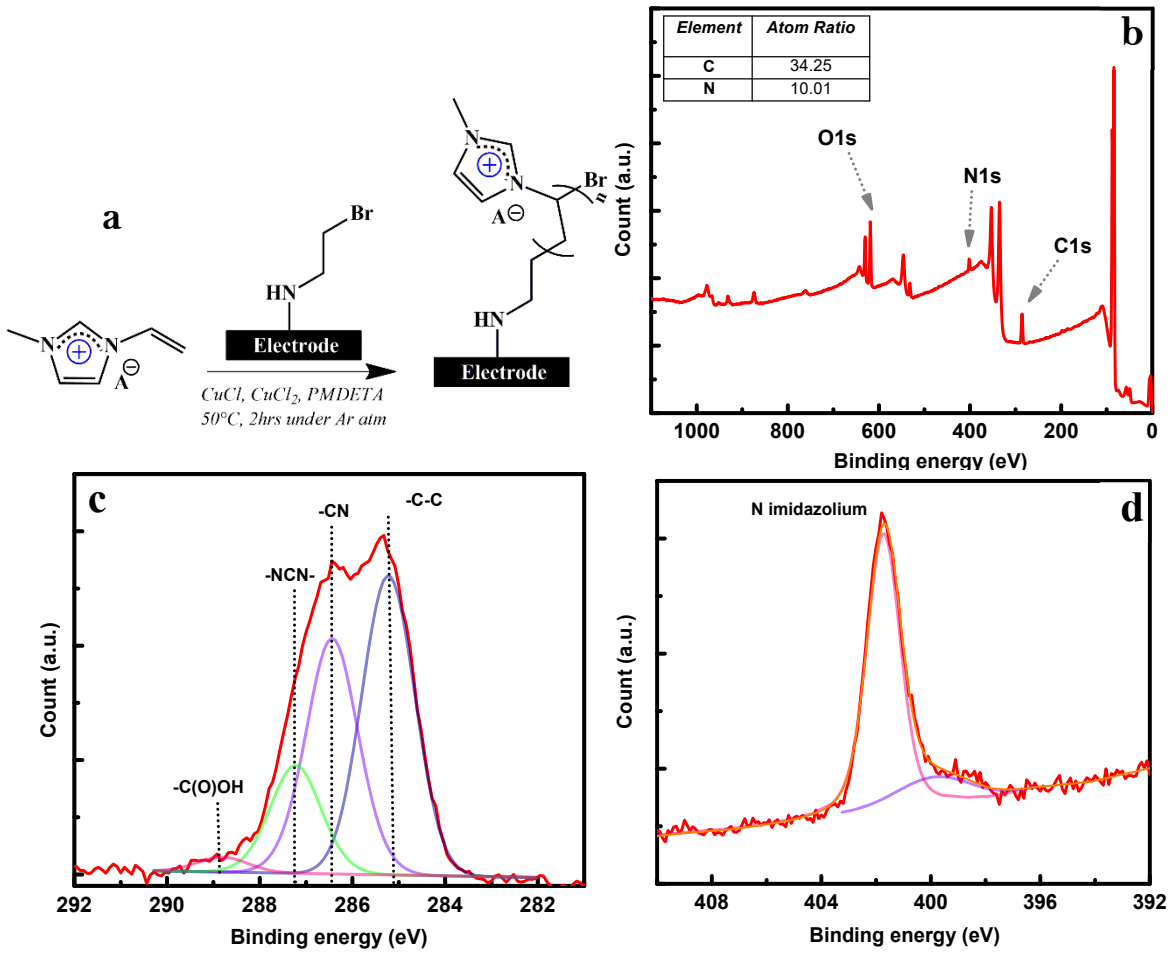

Figure 3.14 (a) Scheme illustrating the SI-ATRP process; ***(b)*** XPS survey spectrum of Poly([EMI$^+$][A$^-$]; ***(c)*** and ***(d)*** high resolution XPS spectra of C1s and N1s

Furthermore, the presence of the polymer layer was then visualized by scanning electron microscopy (SEM) and atomic force microscopy (AFM). The SEM image (Figure 3.15a) shows 2 distinguishable regions via difference of contrast. The bright side represents non – modified Au wafer where the dark – side reveals an increase of the altitude, marking the existence of the polymer layer. To get further information about the nano-structuration of the film, AFM was performed. The 2D-AFM image exhibits homogeneous and grainy directional structure of the poly(VImM) (Figure 3.15b). Furthermore, the 3D-AFM confirms the organization of the polymer units in a brush-like structure with an average thickness around 18 nm (AFM scratch – test by using contact mode) (Figure 3.15c, d). Overall, the morphological and structural analyses confirm the formation of nanostructured poly(VImM) brushes at the electrode surface.

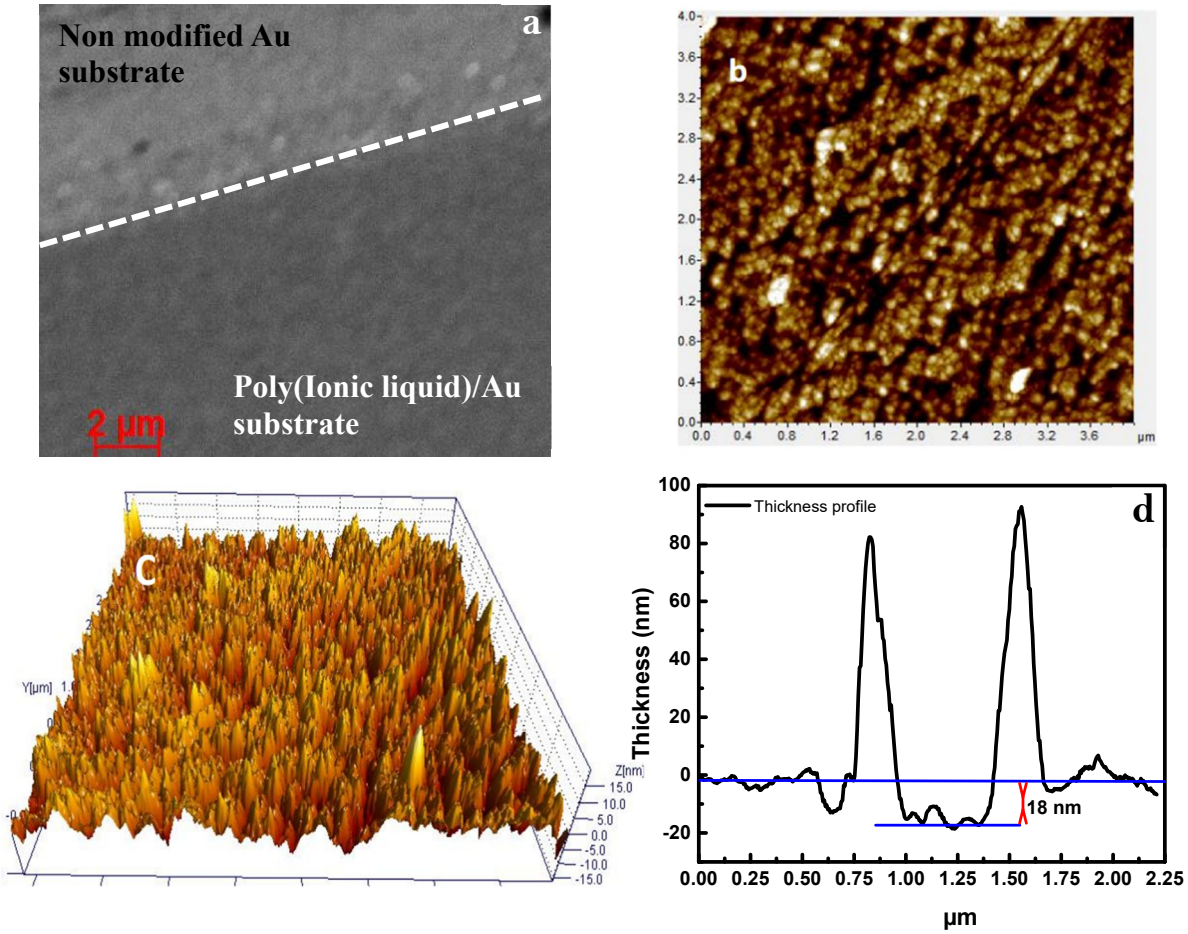

Figure 3.15 SEM and AFM investigations. ***(a)*** SEM image of poly(VImM) onto Au substrate. ***(b)*** and ***(c)*** AFM topography and 3D AFM image of poly(VImM), image size 4×4 µm2. ***(d)*** Cross section after AFM scratch experiment.

3.3.2 Electrochemical behaviors of poly(ionic liquid).

Prior to assess the catalytic performance of the polymeric ionic liquid layer, the electron-transfer properties at the Poly(VImM) interface were evaluated in the presence of outer-sphere (ferrocene methanol) and inner-sphere (potassium ferricyanide) redox probes. The electron transfer in an outer-sphere system occurs by tunneling across a thin layer of solvent, while an inner-sphere system requires a strong interaction with the electrode[52]. The cyclic voltammetry's (CV's) of modified glassy carbon with a bromide initiator layer (GC/Br initiator) and GC/Poly(VImM) were performed in the presence of ferrocene methanol and potassium ferricyanide (Figure 3.16a).

For FcMeOH (green curves), both electrodes depicted a well-defined reversible redox system with a peak-to-peak separation, ΔE, of 60 mV, highlighting the presence of fast electron transfer, despite the presence of the thin initiator layer and the poly(VImM) brushes. Conversely, the CV's responses of ferricyanide (bleu curves) show different behaviors. Thus, on GC/Br initiator (bleu dashed line), the ΔE is extremely high, 700 mV, suggesting low electron transfer rate attributed to the presence of the initiator layer that act as a barrier against the electron transfer of the inner sphere redox probe. Whereas, the CV recorded on

GC/Poly(VImM) exhibits a reversible electrochemical signal and shows a decrease of ΔE to 60 mV indicating fast electron transfer.

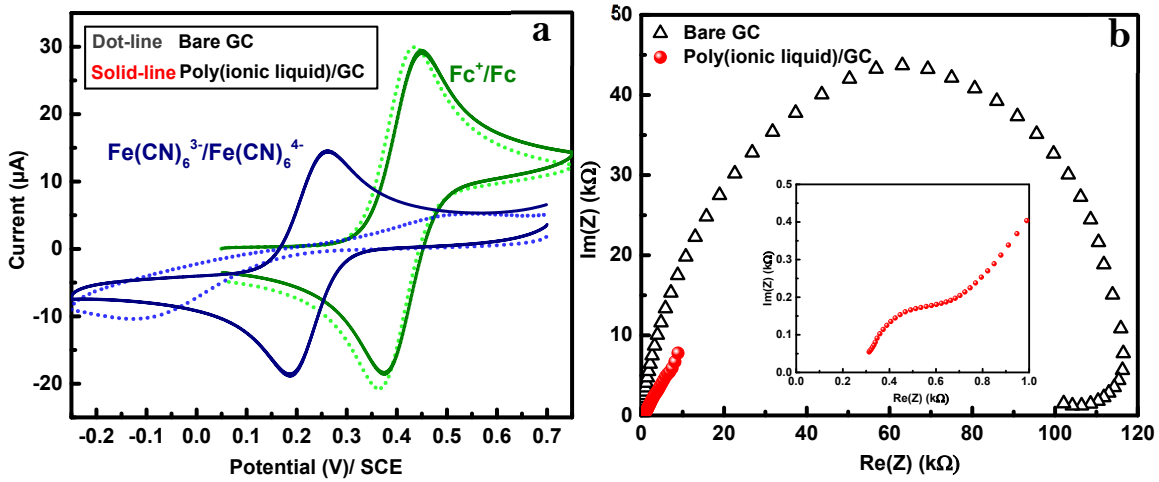

Figure 3.16 ***(a)*** CV response for bare GC and poly(VImM) electrode in the presence of ferrocene methanol, FcMeOH, and potassium ferricyanide ($K_3Fe(CN)_6$) at 1 mM in 0.1 M KOH aqueous solution; ***(b)*** Electrochemical impedance spectroscopy at bare and poly(VImM) GC electrodes in the presence of 1 mM potassium ferricyanide in 0.1 M KOH at a frequency of 100 kHz to 1 Hz.

The reason for such behavior is linked to the poly(VImM) brush structure which has a labile anion that could be replaced by ferricyanide. The anion exchange of ferricyanide within grafted ionic liquid layer has been already reported by our group[53]. In this situation, the ferricyanide interacts strongly with the polymer film leading to anion exchange and, therefore, the incorporation of ferricyanide moieties within the polymer. The presence of ferricyanide in the vicinity of the electrode promotes the electron transfer of ferricyanide at the polymer solution interface. To confirm this result, the charge-transport properties were characterized by monitoring the charge-transfer resistance (R_{CT}) at the electrode−electrolyte interface. Figure 3.16b shows the electrochemical impedance spectroscopy (EIS) plots at GC/Br initiator and GC/polymer electrodes in the presence of 1 mM $[Fe(CN)_6]^{3-/4-}$ in 0.1 M KOH at a frequency of 100 kHz to 1 Hz. The RCT value for GC/Br initiator is found to be 35 kΩ while the GC/Poly(VImM) displays a value around 307 Ω. This result demonstrates the fast electron transfer of the inner sphere redox probe at the polymer surface.

3.3.3 Performance of Poly(ionic liquid) towards ORR and OER

The mechanism of the oxygen reduction reaction has not been well established yet, but several steps were clearly identified, including the oxygen adsorption, oxygen bond cleavage, and the release of the intermediates[3]. The ORR is an inner-sphere redox reaction that involves several key steps, including oxygen adsorption, O−O band splitting. As the Poly(VImM) accelerate the electron transfer of the inner-sphere system, the electrocatalytic activities of this polymer toward the ORR was investigated.

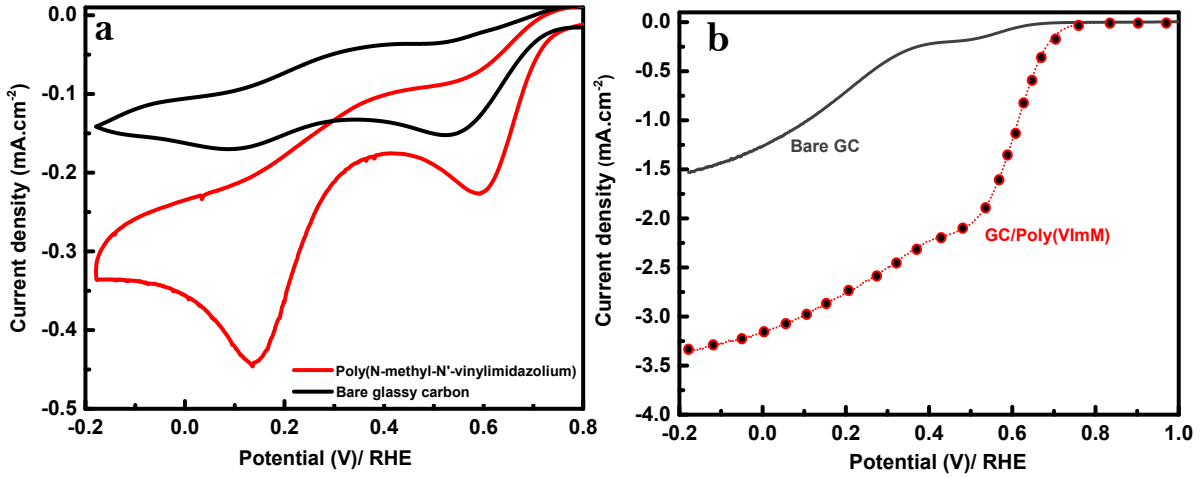

Figure 3.17 (a) CV and ***(b)*** LSV at 900 rpm of bare GC and GC/poly(VImM) in O_2-saturated 0.1 M KOH solution.

Figure 3.17a compares the cyclic voltammograms recorded on the bare GC and GC/poly(VImM) electrodes in an O_2-saturated aqueous alkaline solution. The CV depicts two typical reduction waves for oxygen reduction occurring probably through the peroxide route. Compared to bare GC, the as-prepared GC/poly(VImM) shows a pronounced electrocatalytic ORR activity as attested by the positive onset potential shift (80 mV) and the increase of the peak current density (from 0.18 to 0.45 $mA.cm^{-2}$). Compared to the state-of-the-art noble-metal-free catalysts, the performance of the poly(IL) is still lower[19,20]. However, the observed catalytic activity combined with the facile synthesis of the polymer, in the absence of carbonization step, supports the potential use of poly(VImM) as a metal-free electrocatalyst for the ORR.

To get more insight about the performance of the poly(VImM) toward ORR, linear sweep voltammetry (LSV) using rotating disk electrode (RDE) was performed. Figure 3.17b shows clearly that the GC/poly(VImM) electrode exhibits pronounced ORR electrocatalytic activity when compared with bare GC. The onset potential is 0.68 V vs RHE, and the limiting diffusion current density is 2 times higher than that of bare GC (at −0.2 V). The investigations were complemented by performing the LSV on rotating-ring disk electrode (RRDE) at various rotation rates (Figure 3.18a).

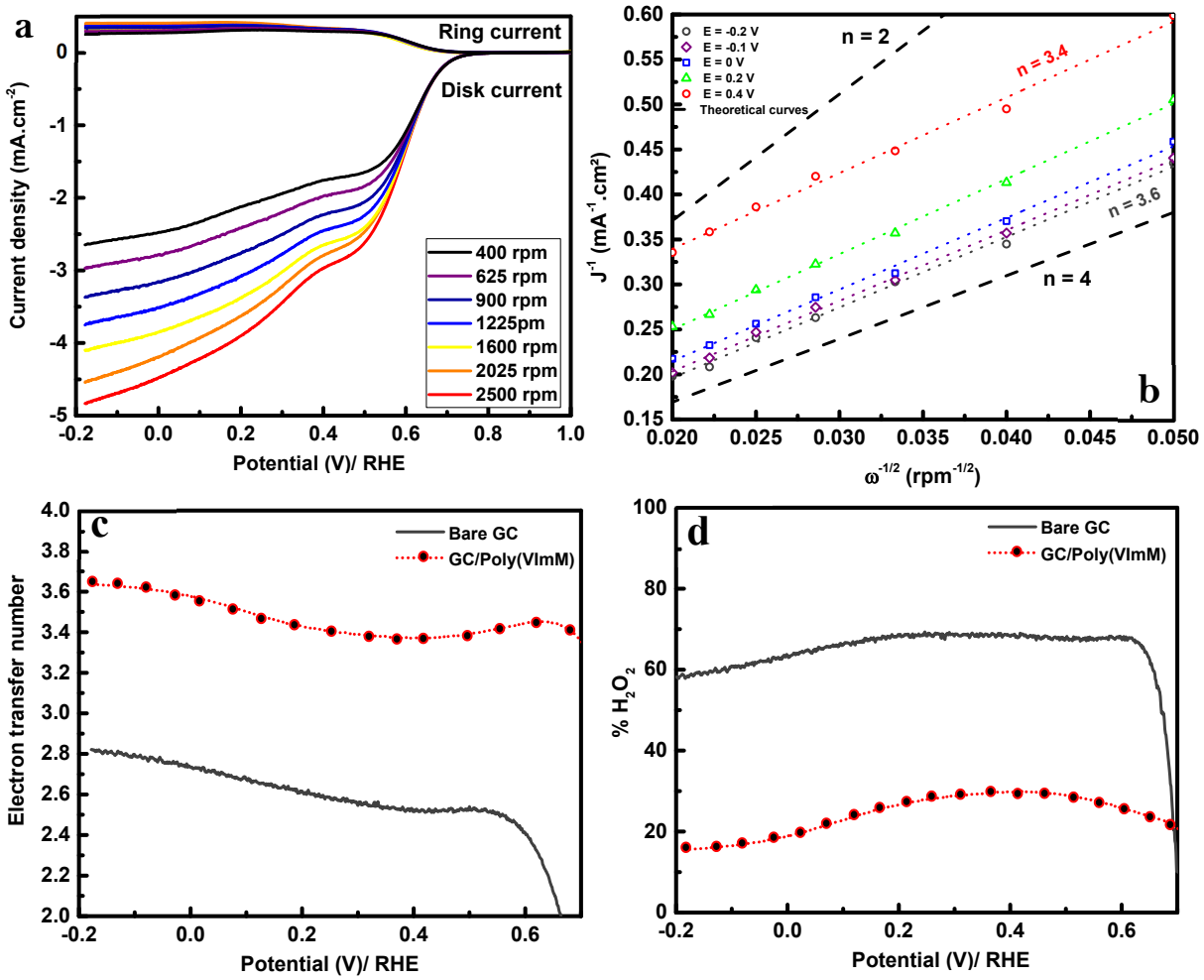

Figure 3.18 (a) ORR polarization curves using RRDE at different rotations speeds for GC/poly(VImM) electrode; ***(b)*** The Koutecky-Levich plots for GC/poly(VImM) electrode at different potentials; ***(c)*** Evolution of electron transfer number as function of the potential; ***(d)*** Variation of the hydrogen peroxide percentage at bare GC and poly(VImM) as function of the potential obtained from RRDE plots in O_2-saturated 0.1 M KOH solution.

The curves show a two-reduction process, suggesting the occurrence of the ORR through consecutive two electron steps with the generation of peroxides as intermediates. The Koutecky−Levich (K−L) plot was performed to determine the number of electrons, n, involved in the reduction process. Linear relationship between j^{-1} and $\omega^{-1/2}$ was observed at different potentials and the value of *n* varies from 3.4 to 3.6 within the potential range of 0.4 to −0.2 V (Figure 3.19c). These values suggest that the ORR catalyzed by the poly(VImM) involves two- and four-electron transfer pathways. In addition, the average yield of HO_2^- is about 20% within the potential range 0.6 to −0.2 V (Figure 3.18d). These results suggest the preferential occurrence of ORR through four-electron process.

The Tafel plot (Figure 3.19) shows a slope of 78 and 97 mV.dec^{-1} for GC/poly(VImM) and bare GC, respectively, demonstrating the improved kinetics and ORR performance. In the literature, metal-free catalysts involving carbon-based materials and doped carbon with different heteroatoms have been reported[15]. These materials were prepared using different

thermal processes at a temperature range from 700 to 1000 °C[54,55]. However, in our study, the poly(VImM) was used as prepared without additional thermal treatments. Based on the above results, it is concluded that the poly(VImM) exhibits clearly an enhancement of ORR.

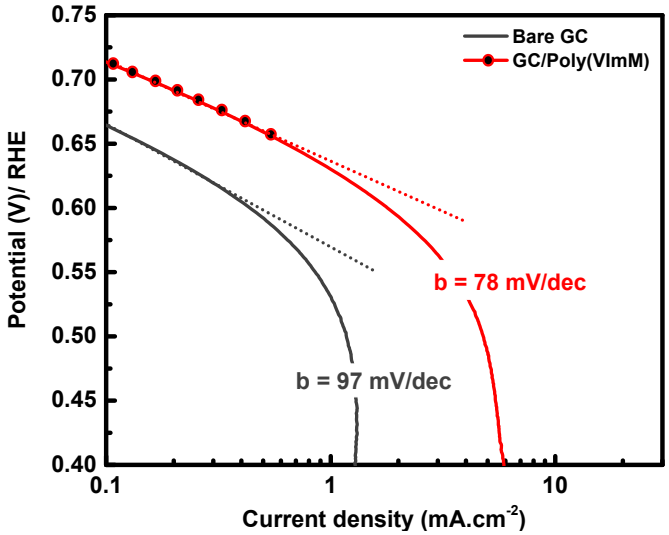

Figure 3.19 Tafel plot for (blue) Bare GC and (red) GC/Poly(VImM)

Based on the above results, the poly(VImM) exhibits clearly an enhanced ORR activity that could be explained by two factors – explicitly the chemical composition of the poly(VImM) and the brush organization. Indeed, the origin of the catalytic properties can be attributed to the presence of nitrogen atoms (electron-rich dopant) in the imidazolium ring that induces a high electron density and, consequently, generates a positive charge density of carbon atom located between the nitrogen atoms. The hierarchical polymer brush structure enhances the electron transfer and also the accessibility of water and oxygen[51,56]. In addition, the presence of positive and negative charges within the polymer could induce several effects, including the enhancement of oxygen solubility in the vicinity of the electrode material, favor the oxygen adsorption, and participate in the release of intermediates species through electrostatic interaction[57]. In recent works, the covering of nanocarbon-based catalysts with an ionic liquid layer showed improved ORR kinetics[58,59]. In a similar way as observed in an ionic liquid, the poly(ionic liquid) could enable the formation of a preferential water channel that assists proton transportation between the imidazolium and water molecules[60]. Furthermore, previous works have reported that imidazolium has acidic proton at the position 2, which could promote the interaction with oxygen molecules. Even though the fundamental understanding and the origin of C−H···O hydrogen bond is still a matter of debate, Singh et al.[61] reported that the strong interaction between the hydrogen within the imidazolium ring and oxygen atom occurred at C(2)−H. Gewirth et al.[62] demonstrate the role of proton-coupled electron transfer (PCET) in the modulation of the ORR mechanism. In our case, the acidic character of the C(2)−H could act as a proton carrier and thus enhance the catalytic activity through the efficient O−O bond activation/cleavage.

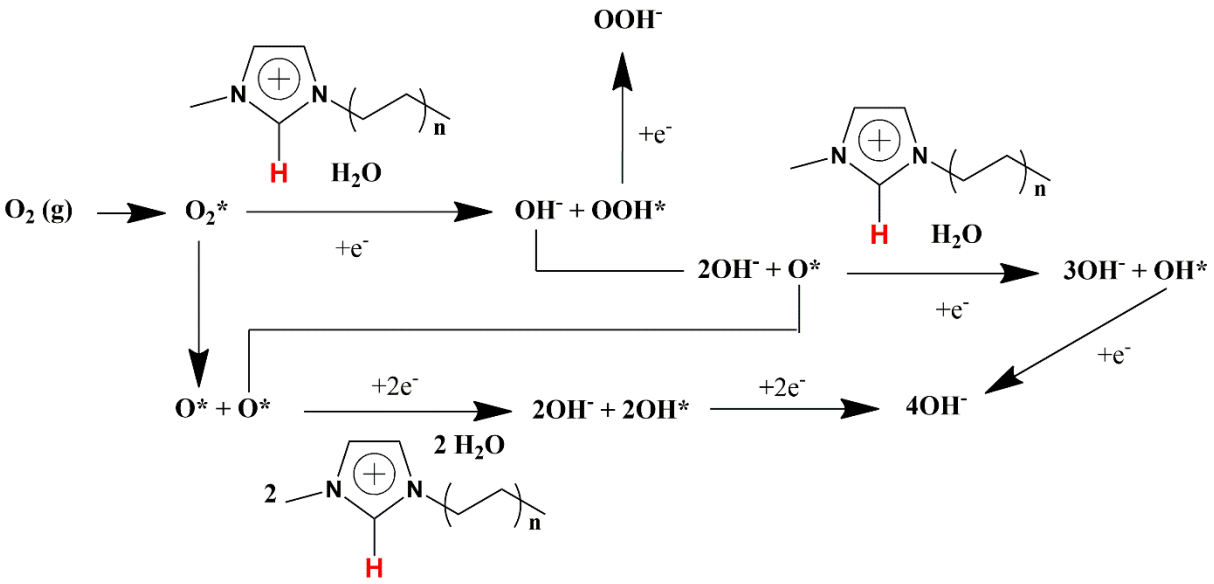

Figure 3.20 Proposed mechanism for oxygen reduction within Poly(VImM) layer

To confirm the crucial role of C(2)−H, the latter was replaced by a C(2)–CH_3 group within the monomer structure. Next, the SI – ATRP was applied to the new monomer and the catalytic activity of poly(VImMM) was evaluated. Figure 3.21a, orange curve, shows a poor O_2 reduction activity, which is comparable to the non-modified GC electrode. This result was further confirmed by the high yield of HO_2^- around 70% and a number of electron transfer around 2 to 2.5 (Figures 3.21b). Thus, the replacement of hydrogen by a methyl group at position 2 inhibits the oxygen reduction activity, confirming the important role of acidic proton on C(2) in the imidazolium.

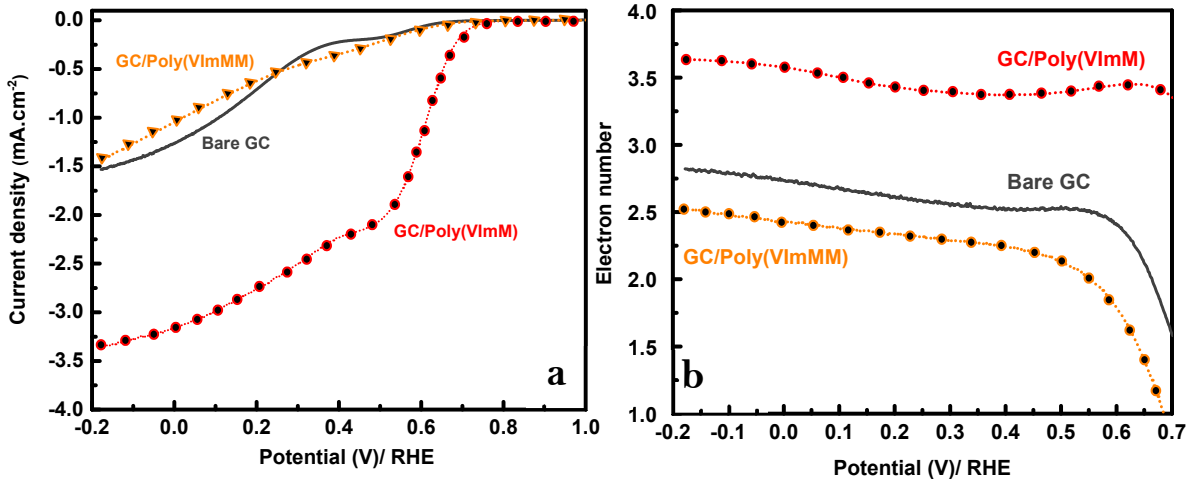

Figure 3.21 (a) ORR polarization curves using RRDE and ***(b)*** Variation of the electron number in function of the potential for (black) Bare GC, (blue) GC/Poly(VImMM) and (red) GC/Poly(VImM)

Besides, the brush organization of the poly(VImM) plays also an important role in the observed catalytic activity. In additional experiments, the poly(VImM) was performed using direct electrochemical reduction leading to the formation of a homogeneous film onto GC electrode (e-poly(VImM)) as reported in the previous chapter (Chapter 2). Besides, 1-(1-aminoethyl)-3-

(p-nitrophenyl)ethylimidazolium was grafted onto electrode surface, by means of electrochemical reduction of in-situ generated diazonium group, affording thin compact film of ionic liquid modified GC (d-IL). Thus, the electrochemical behaviors of the modified surface with compact films in redox probes solution, FcMeOH and $K_3Fe(CN)_6$, displayed high peak – to – peak separation in both solutions, suggesting a strong blocking effect. As consequent, for oxygen reduction, the diffusion of oxygen inside the polymeric film is strongly affected. It has been demonstrated that the nanodiffusion inside the electrocatalytic film and the catalytic performance of the material are strongly coupled[63]. Subsequently, ORR activity on e-poly(VImM) and d-IL was evaluated, showing lower activity (similar to that recorded for bare GC) when compared with the polymer generated using the SI-ATRP process (Figure 3.22). Indeed, the hierarchical polymer brush structure enhances the electron transfer and also the accessibility of water and oxygen. This experiment evidences the important role of the brush like structure in ORR activity.

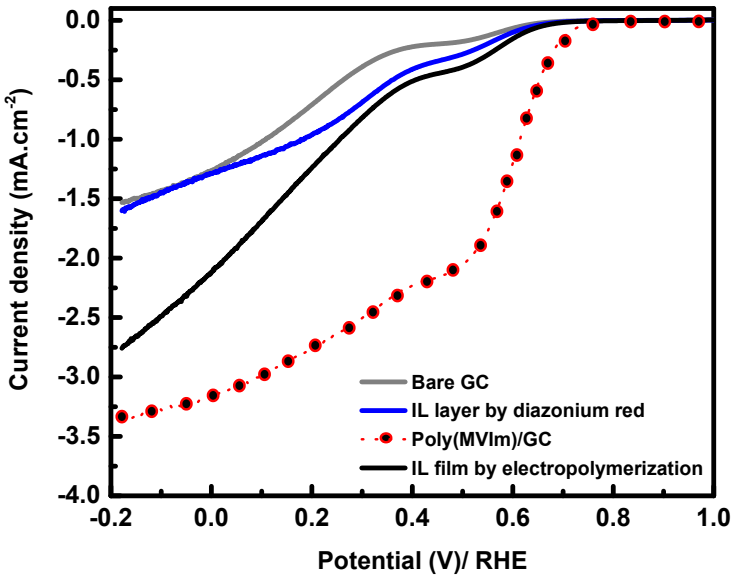

Figure 3.22 ORR polarization curves using RRDE for different morphologies prepared by various approaches

The stability of the polymeric film was evaluated by chronoamperometry (j vs. t) under diffusion-controlled conditions at 900 rpm in O_2– saturated alkaline solution for 10000 seconds. As presented in the figure 3.23, by applying a fixe potential at 0.4 V/RHE, the current retention is remained at 100 % during the time-lapse of 10000s. For comparison, the commercial Vulcan X72 (Pt/C) was used as reference that exposed dramatically decrease to 80 % after the same period. Even though the current density provided by the polymer layer is still far from the value given by Pt/C catalyst, the presented result indicates a strong stability of the Poly(VImM)/GC towards oxygen reduction reaction resulting from the covalent bonding of the polymer and the electrode via SI -ATRP process.

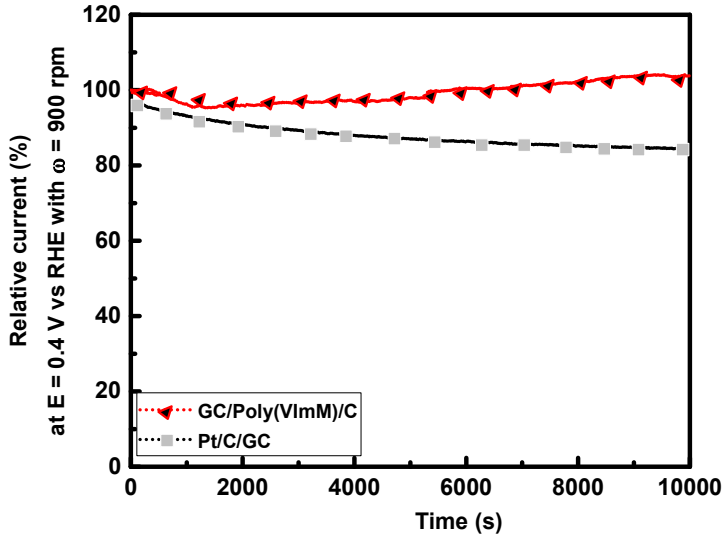

Figure 3.23 Stability of (red) GC/Poly(VImM) and (black) Bare GC under amperometric conditions at 0.4 V/ RHE with rotation speed of 900 rpm in O_2-saturated 0.1 M KOH solution

Beside the ORR, the oxygen evolution reaction (OER) is another important reaction for energy storage and conversion systems, particularly regenerative fuel cell. The challenge within this topic is to find bifunctional catalysts presenting an efficient catalytic activity toward the ORR and OER. The electrocatalytic activity for the OER of the as-prepared poly(VImM) was evaluated in alkaline solution (Figure 3.24).

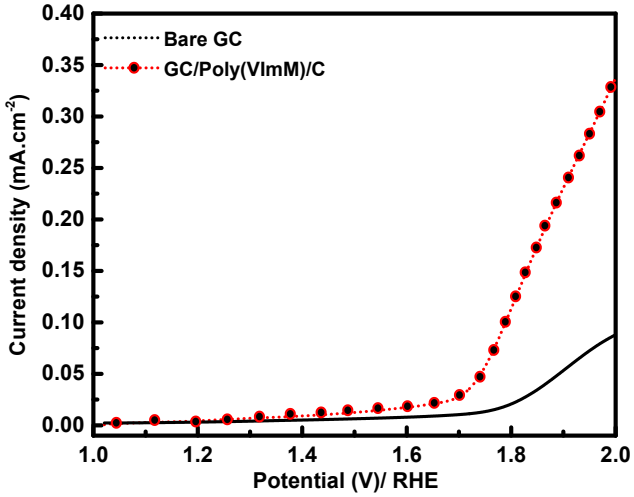

Figure 3.24 OER polarization curves using RRDE for (black) Bare GC and (red) GC/Poly(VImM)

The catalytic performance of the substrate in presence of the polymer layer is strongly enhanced with an increase of the current density of 1 order of magnitude and a notable decrease of the onset potential (150 mV). For similar reasons as described above, the enhancement of the OER activity could be linked to the chemical composition and to the surface organization in brush-like structure of the poly(VImM). In the literature, carbon-based catalysts have been investigated for OER; thus, nitrogen-doped carbon (N/C) nanomaterials exhibit notable activity. This activity was linked to the carbon (adjacent to N atoms) carrying positive charge

that favor the adsorption of OH^-. In our case, the OER activity can be attributed to the presence of nitrogen (electron rich dopant) in imidazolium generating a high electron density and as consequence generating a positive charge density of carbon that adsorb OH^- and thus accelerating the catalytic cycle of OER.

3.4 POLY(IONIC LIQUIDS) AS TEMPLATE FOR GENERATING HYBRID CATALYST MATERIALS

Owing high density of cation and anion within the polymer layer, the latter can be further used as host – guest platform for receiving other materials in order to generate hybrid catalysts that possess higher catalytic performance and multifunctional character. In this part, the potential use of the poly(VImM) as a host guest platform for other catalysts has been investigated. In this subsection, we will investigate the effect of adding nanoparticles onto the polymer brushes structures on the electrocatalytic performance of the hybrid material, poly(IL)/NP, toward ORR. Thus, we will investigate the case of the C-dots (case of C-dots 2 and 3 generated in glucose ionic liquid and mixture glucose/glutamine in H_2O, respectively), commercial Pt/C nanoparticles and Au nanoparticles.

3.4.1 Poly(ionic liquid) and Carbon dots

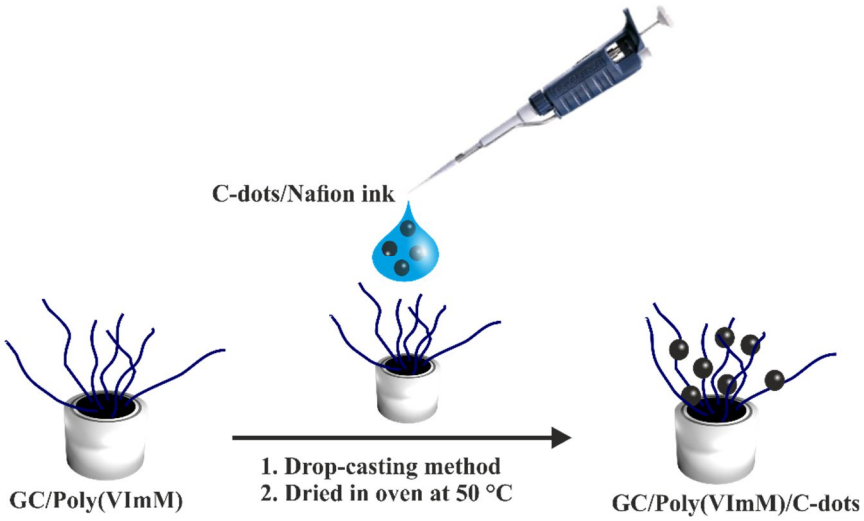

Figure 3.25 Scheme illustrating the deposition procedure of CDs on poly(IL)

To evaluate the electrocatalytic performance of our materials, the N-doped CDs, microwave assisted CDs preparation in glucose ionic liquid, were deposited onto bare glassy carbon and onto poly(VImM) modified glassy carbon electrodes as presented in the figure 3.25. Figure 3.26a displays the LSVs curves recorded as function of the rotation speed, from 400 to 2500 rpm, at scan rate 10 $mV.s^{-1}$. In this case, two reduction waves were observed with all the studied materials. To evaluate the influence of the C-dots, Poly(VImM) modified GC was used as prepared without further addition of C black. The electron transfer number calculated with RRDE is 3.2, which is coherent with the value found by using Koutecky-Levich plots. The electron number varied in two steps, the first step from 0.7 V to 0.3 V/ RHE that gave an

electron number around 3.2 while the second step from 0.1 V to -0.2 V/ RHE gave a n_e around 3.4. From 0.3 V to 0.1 V, a transition can be observed indicating the two-successive- step mechanism for oxygen reduction reaction occurring at the modified electrode. The mechanism is then confirmed by observing the quantity of produced hydrogen peroxide, which followed the two-step variation of n_e. Precisely, the main product at the first reduction wave is hydrogen peroxide (40%), then the percentage of H_2O_2 is reduced during the second reduction wave (30%).

Interestingly, by adding C-Dots – 3 to the modified GC, the calculated electron transfer number using K-L plots, was found to be at n_e = 3.5 at 0.6 V vs. RHE which was strongly enhanced compared with the electron number provided by each component. In addition, from 0 to -0.2 V vs. RHE, the electron number reaches saturation level close to 4 electrons (n_e = 3.9). The results are evidenced by calculating the n_e and the quantity of hydrogen peroxide using eq. (3.6) and (3.7) as shown in Fig.3.26c. The quantity of hydrogen peroxide decreases and reaches a lowest value around 5 % at -0.2 V vs. RHE. This result indicates the high selectivity for ORR activity of the prepared material by forming water as final product.

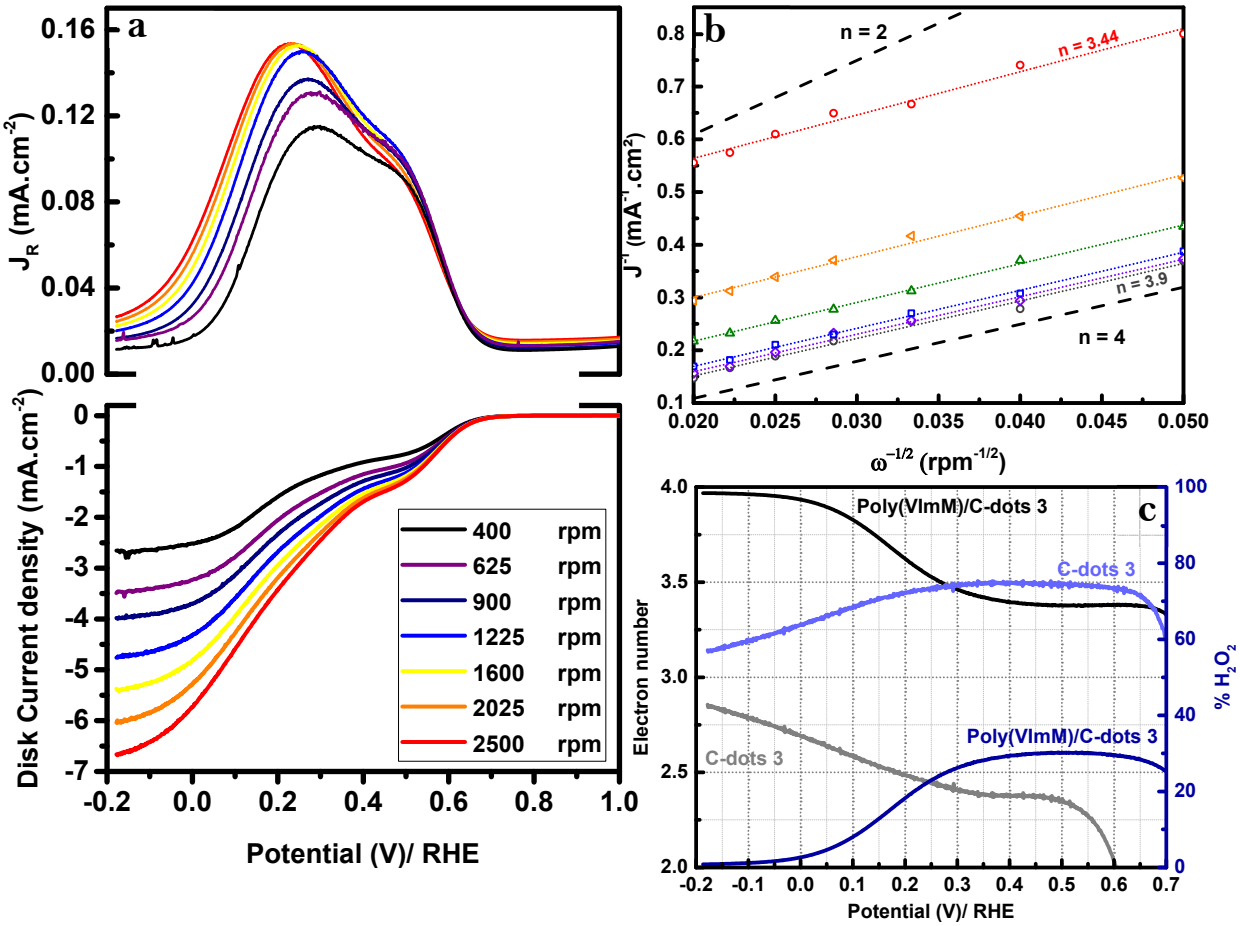

Figure 3.26 (a) ORR polarization curves using RRDE at different rotations speeds for GC/poly(VImM)/C-dots-3 in O_2-saturated 0.1 M KOH solution; ***(b)*** Koutecky-Levich plot for GC/poly(VImM)/C - dots -3 in function of the potential; ***(c)*** Evolution of the electron number and $\%H_2O_2$ as function of the potential of (dark curves) GC/poly(VImM)/C-dots -3 and (pale curves) GC/C-dots -3

The observed change of the catalytic reduction of ORR is certainly related to the synergetic effect between the Poly(IL) and CDs. The combination poly(IL) and C-dots3 may generate and expose a new catalytic site more favorable for the ORR following the $4e^-$ pathway. The enhancement of the ORR performance of the hybrid material might correspond to a strong interaction between the positive charge provided by imidazolium ring and the N-doped C-Dots. According to the reported work about the interaction between ionic liquid (EMI^+SCN^-) and graphene surface, different interactions can be occurred at this interface[64]. The π-π stacking effect between the imidazolium aromatic ring and the conjugated C planes of the graphene can be one of the factors for the adhesion of the C-Dots onto poly(VImM). However, as the synthetized C-Dots contains partially amorphous structure, the present π-π stacking effect cannot be considered as main interaction between the 2 components. The electrostatic interaction could explain the synergetic effect. Indeed, the positive charge of imidazolium ring can attract the nitrogen and oxygen contained functional groups (ζ-$E_{C\text{-}dots\text{–}3}$ = -24 ± 5 mV). The electrostatic interaction involves the decrease of the electron density of not only the most acidic proton of imidazolium ring but also the nearby carbon active sites from the pyridinic nitrogen (N_P) of the C-Dots. This effect could favor the adsorption of oxygen and the reduction process should be easier following the mechanism below. The polarization curves show the absence of peak – like current as in the previous studies using C-dots, suggesting that the graphitic nitrogen (N_g) is not involved into the interaction between the polymer chain and the C-dots. In our case, the N_g is incorporated into the carbon network while the N_p atoms are located at the edge side, providing a higher probability to interact with the polymer.

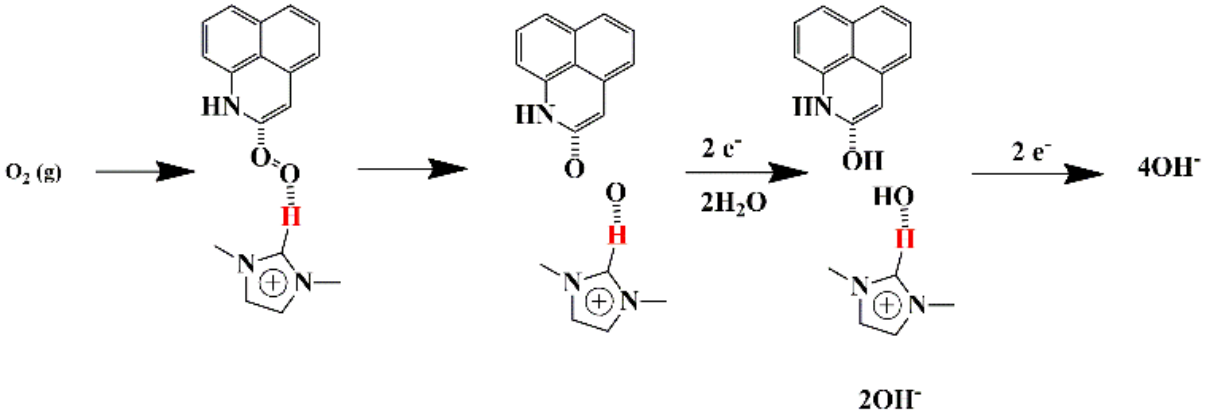

Figure 3.27 Proposed mechanism for oxygen reduction within Poly(VImM)/C-dots 3

As described in the previous part, the dissociative mechanism in the case of poly(VImM) is strongly unfavorable because of the high flexibility of the chains. By embedding the C dots inside the film, the degree of freedom of the polymer brushes decreases leading to a less flexible system and higher ionic transport. The electrostatic interaction between the ionic liquid polymer and the N-doped C dots generates new active sites in which the oxygen can interact with both components as shown in Fig.3.27. In addition, the size of the C dots is around ten nm corresponding to a surface area around 314 nm^2 with a high concentration of nitrogen functional

groups. Resulting from the large surface of the C dots, a large quantity of the ionic liquid-C active sites of C dots can be formed leading to the formation of high concentration of the dual active sites at the interface C dots and poly(ionic liquid). This process can be associated to a dissociative mechanism, where the oxygen binds to the catalyst surface via two adjacent active sites under conditions where the distance between 2 active sites has to be equal to the length of the molecular oxygen bond. We suggest that the molecular oxygen migrates into the active site, one head is linked to the C(2) of imidazolium ring by hydrogen bonding while the other head is linked to the C(2') of the C dots which is adjacent to the nitrogen functional group. The O = O bond is broken with one oxygen atom at C dots surface and one oxygen atom adsorbed at ionic liquid chain.

In order to demonstrate clearly the important role of polymeric ionic liquid during the oxygen reduction reaction, the as-prepared C-dots 2, microwave assisted CDs preparation in a mixture glucose/glutamine in H_2O, were used. In term of current density, it is clearly displayed that in the first potential range, [0.7V; 0.3V], the current density provided by polymer/C-dots hybrid is lower than that value obtained using only C-dots system (Figure 3.28a).

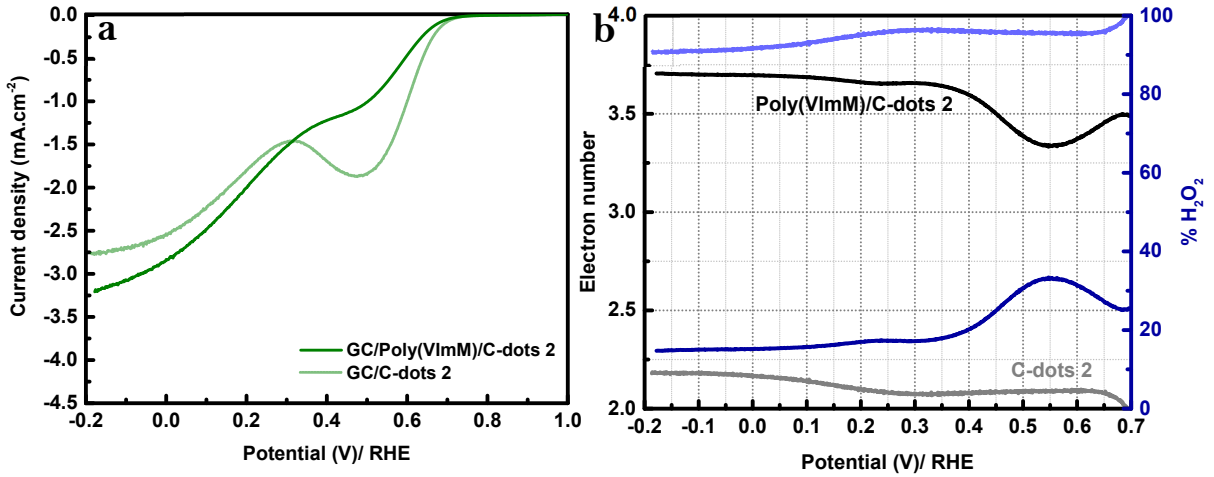

Figure 3.28 (a) ORR polarization curves using RRDE and ***(b)*** Variation of the electron number in function of the potential for (dark curves) GC/Poly(VImM)/C-dots 2 and (pale curves) GC/C-dots 2

It indicates that the diffusion inside the catalytic film change in the presence of the polymeric film. Being discussed for multiple times in previous parts that the Poly(VImM) brushes create water channel to conduct oxygen molecules to the active sites. As supposed that the interaction between the imidazolium rings and pyridinic nitrogen is crucial in the current system, the oxygen is oriented towards the duel active sites (C(2)–H ⋯ C/N_p) leading to a hindrance of the N_g catalytic sites. However, in lower potential region, the current density of the substrate in presence of polymer chains is higher when compared to the value offered by GC/C-dots 2, which is coherent with the proposed mechanism. The figure 3.28b shows that the number of exchanged electrons is strongly enhanced from 2 – 2.2 to 3.4 – 3.7 for two potential windows. Consequently, the percentage of hydrogen peroxide decreases down to 20% in the potential ranging from 0.2 to -0.2 V/ RHE by using GC/Poly(VImM)/C-dots 2.

The figure 3.29 summarizes the number of transferred electron and quantity of hydrogen peroxide generated at -0.2 V/ RHE. Significantly, the poly(vinyl imidazole) shows a restraint affinity towards C-dots with similar number of electron and hydrogen peroxide rate in presence and in absence of C-dots, confirming the crucial role of the cationic properties of the polymeric ionic liquid layer. Briefly, we have investigated a facile route for making efficient full organic electrocatalyst toward oxygen reduction reaction. The hybrid material poly(ionic liquid)/C-dots-3 exhibits a high selectivity for reducing oxygen to water (95 %) at -0.2 V vs RHE. Our preliminary results demonstrate that the interaction between ionic liquid and carbon-based materials is strongly involved into the reduction mechanism. In addition, our approach provides green materials with low cost means catalysts for further applications in metal-air batteries, fuel cell, etc.

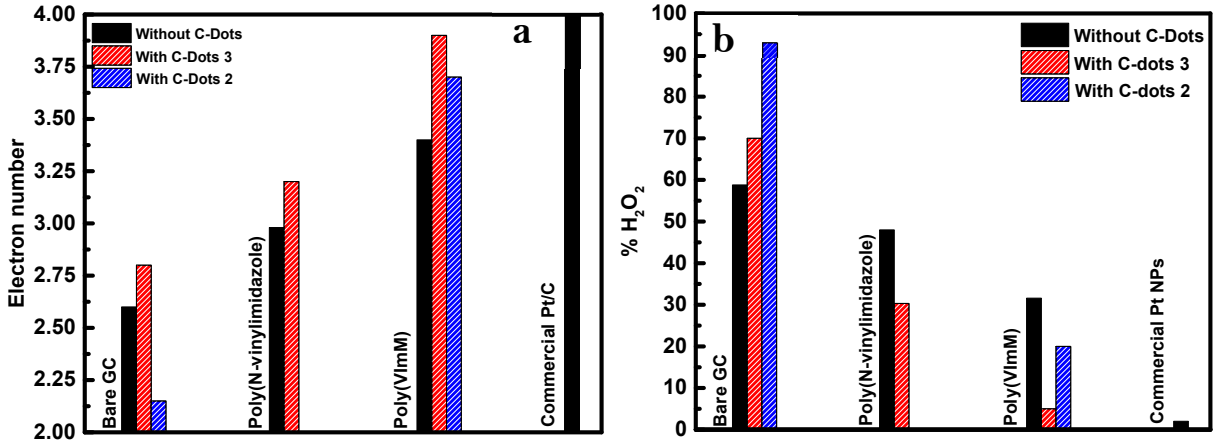

Figure 3.29 Summary on the electrocatalytic performance in presence (red) and in absence (black) of C- dots -3: ***(a)*** electron number and ***(b)*** quantity of hydrogen peroxide at -0.2 V/ RHE.

3.4.2 Poly(ionic liquid) and metallic NPs

In this part, the most efficient catalyst platinum catalyst, commercial Pt/C, was introduced by a drop casting over the poly(VImM), and the catalytic performance of the hybrid material was investigated (Figure 3.30). As expected for Pt/C, the curve shows a single-step plateau (Figure 3.30b grey curve) corresponding to the ORR reduction through $4e^-$ process. Interestingly, when the Pt/C catalyst is supported onto poly(VImM)/GC an increase in the ORR activity is observed as attested by the positive half-wave potential shift (+40 mV) and the increase of the limiting current density from −4.5 to −5 mA cm^{-2} (Figure 3.30b red curve). This was also confirmed by measuring the *n* value and the $\%HO_2^-$ involved in the ORR process (Figure 3.31). As an example, at 0.3 V the n is 3.97 ± 0.02 and the $\%HO_2^-$ is below 1% for Pt/C/poly(VImM), while for Pt/ C the n value is 3.92 ± 0.03 and the $\%HO_2^-$ is 3%. The Tafel slope, measured in the low overpotential, of Pt/C/poly(VImM) is 54 ± 4 mV dec^{-1}, which is smaller than that of Pt/C (59 ± 3 mV dec^{-1}), suggesting the high intrinsic catalytic activity of the hybrid material (Figure 3.S4).

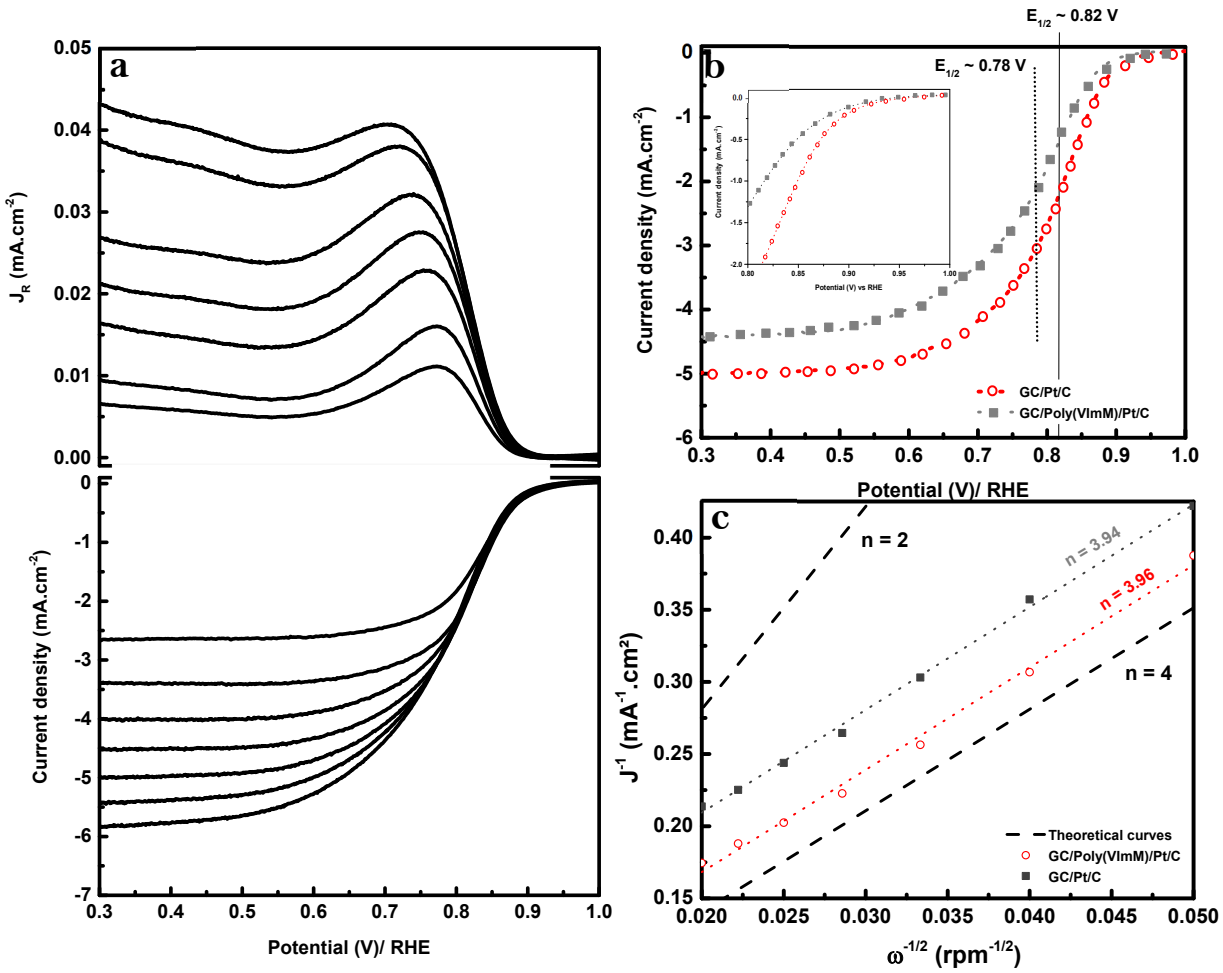

Figure 3.30 ***(a)*** ORR polarization curves using RRDE at different rotations speeds for GC/poly(VImM)/Pt/C electrode; ***(b)*** ORR polarization curves using RRDE at 1600 rpm for (grey) GC/Pt/C, (red) GC/poly(VImM)/Pt/C in O_2-saturated 0.1 M KOH solution; ***(c)*** Koutecky-Levich plot for (grey) GC/Pt/C, (red) GC/poly(VImM)/Pt/C in function of the potential.

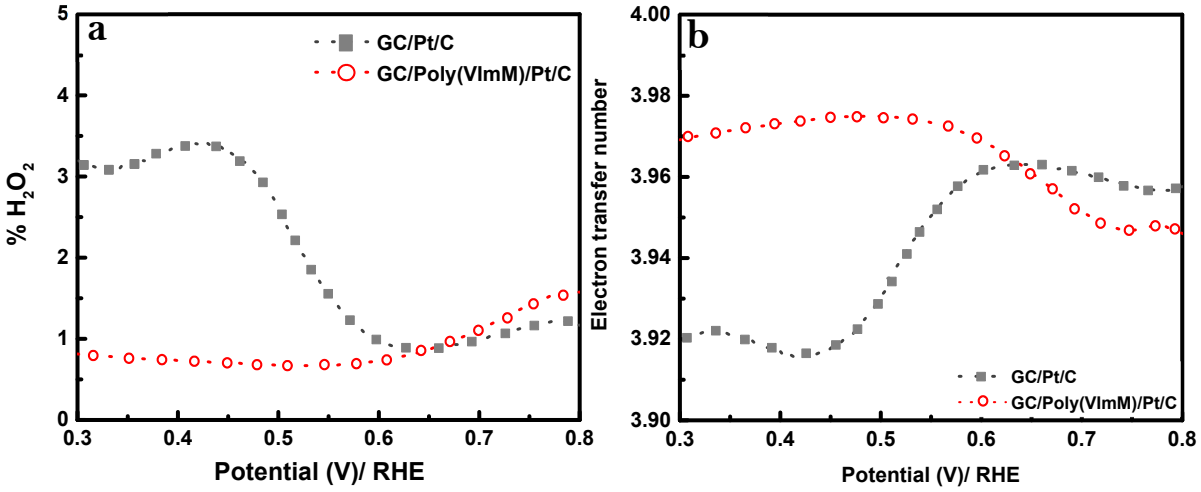

Figure 3.31 ***(a)*** Evolution of electron transfer number as function of the potential; ***(b)*** Variation of the hydrogen peroxide percentage at GC/Pt/C and GC/poly(VImM)/Pt/C as function of the potential obtained from RRDE plots in O_2-saturated 0.1 M KOH solution.

The Pt/C/poly(VImM) catalyst exhibits a slight improvement in ORR activity that is linked to the presence of the poly(IL). Indeed, this enhanced activity could be explained by several factors, including the synergetic effect of the hybrid catalyst, the role of the poly(VImM) in improving the interface between the Pt/C and the GC thanks to a lower charge transfer resistance, and the improved dispersion of the catalyst.

To bring more insight about this point, similar investigations were performed using Au nanoparticles as catalyst. It is well – known that Au is an inefficient catalyst for ORR. In this experiment, Au NPs were added onto poly(VImM)/GC and their ORR catalytic performances were evaluated and compared to the Au NPs deposited onto GC. Our results show that the Au NPs display oxygen reduction occurring through the peroxide route with an electron-transfer number around 2.7 within a potential range 0.2 V to −0.2 V (Figure 3.32b).

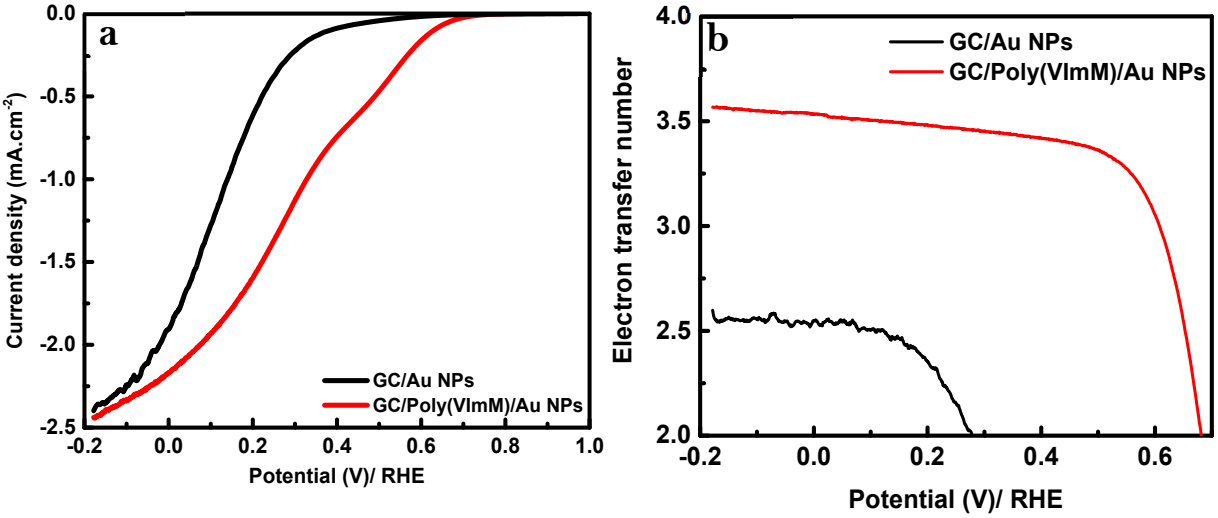

Figure 3.32 (a) ORR polarization curves using RRDE at 1600 rpm for (black) GC/Au NPs and (red) GC/poly(VImM)/Au NPs in O_2-saturated 0.1 M KOH solution; ***(b)*** Variation of the exchanged electron number as function of the potential.

However, for AuNPs that are drop cast onto poly(VImM)/GC, a higher catalytic activity is observed (Figure 3.32a), and the onset potential is shifted by 150 mV when compared with the AuNPs/GC catalyst. In addition, the electron-transfer number for the hybrid catalyst is found to be around 3.5 over a potential range 0.5 to −0.2 V. These results confirm the presence of a synergetic effect between the AuNPs and the poly(VImM). Even if the initial material shows an inefficient catalytic performance towards the ORR, its deposition onto ply(IL) provide to the hybrid material higher performance.

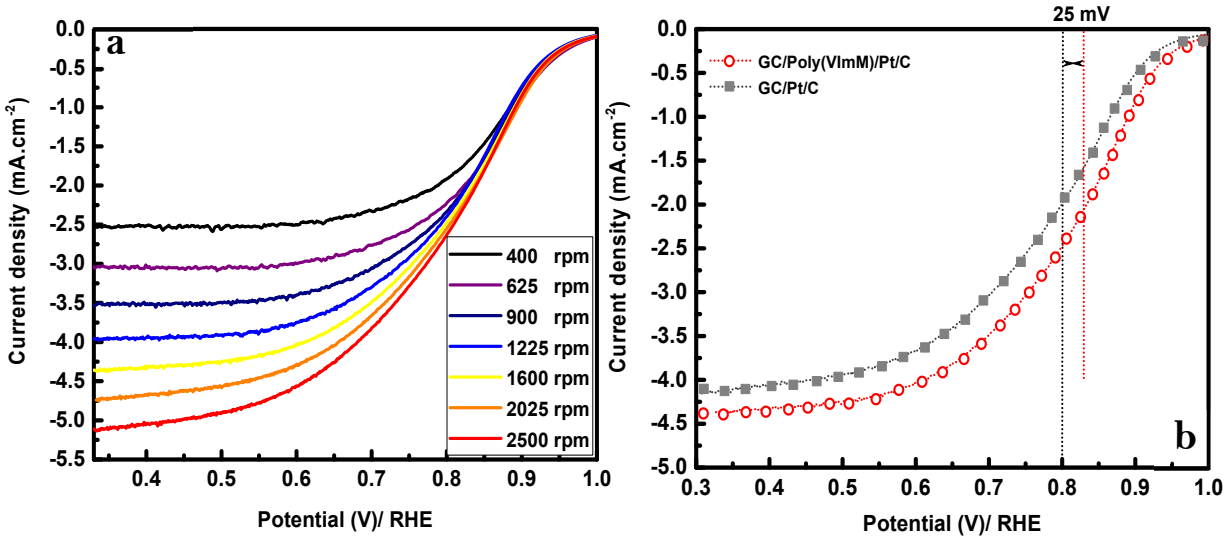

Figure 3.33 ***(a)*** ORR polarization curves using RRDE at different rotations speeds for GC/poly(VImM)/Pt/C electrode; ***(b)*** ORR polarization curves using RRDE at 1600 rpm for (grey) GC/Pt/C, (red) GC/poly(VImM)/Pt/C in O_2-saturated 0.1 M $HClO_4$ solution

The electrocatalytic performances of the Pt/C/poly(VImM) were also investigated in acidic media. Figure 3.33a shows the LSV curves for Pt/C/poly(VImM) at various rotation speeds in 0.1 M $HClO_4$.The curves exhibit a reduction plateau suggesting a diffusion-controlled regime within the potential range of 0.3 to 0.6 V/ RHE. Figure 3.33b shows the improved catalytic activity of Pt/C/ poly(VImM) for ORR when compared with the Pt/C, in acidic media, as attested by the positive potential shift around 25 mV along with the increase of the limiting current density. Furthermore, the n value and the $\%H_2O_2$ of Pt/C/poly(VImM) are found to be 4 and 0.1% over the potential range 0.9 to 0.3 V/ RHE (Figure 3.S6), confirming that the ORR in acidic media occurs exclusively via a $4e^-$ pathway ($O_2 + 4H^+ + 4e^- \rightarrow 2H_2O$).

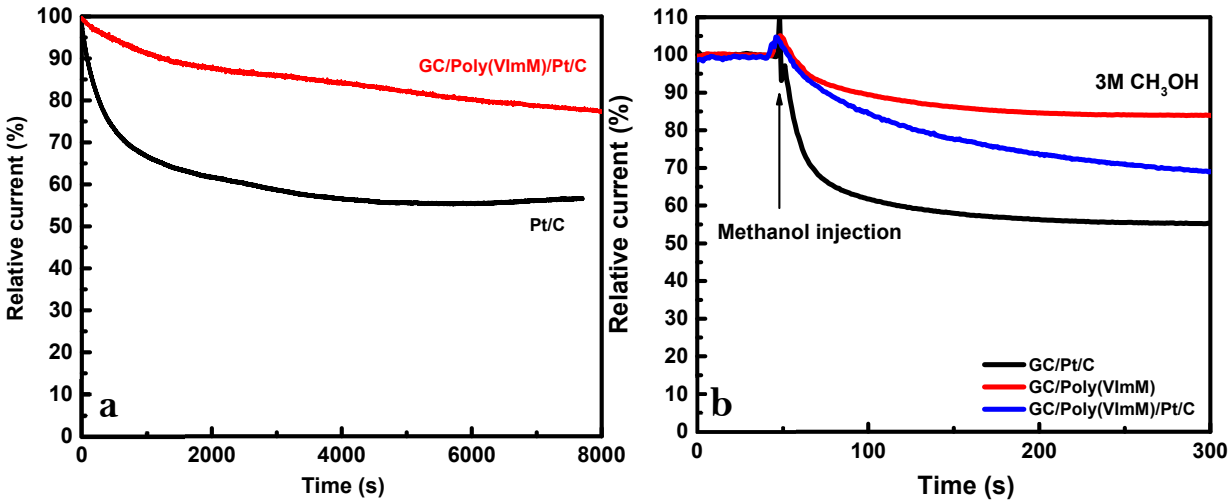

Figure 3.34 Variation of the relative current ***(a)*** in 0.1 M O_2 – saturated KOH solution at E = 0.4 V/ RHE and ω = 1600 rpm and ***(b)*** after the methanol injection by using bare GC, poly(VImM), Pt/C and poly(VImM)/Pt/C.

The Pt based catalysts suffer from multiple limitations, including the vulnerability to the crossover reactions. Within this problematic characteristic, methanol tolerance of Pt/C/poly(VImM) was evaluated. The Pt/C exhibits an instantaneous relative current decay to 55% after methanol injection (Figure 3.34b), whereas a less-pronounced variation is observed for poly(VImM) and Pt/C/poly(VImM) with a current attenuation to 85 and 75%, respectively.

Besides the ORR, the oxygen evolution reaction OER is another challenge for energy storage and conversion systems. Iridium and ruthenium oxides are the efficient electro-catalysts for the OER[65]. Several reviews were devoted to the most recent achievements in the development and the design of catalysts for ORR and OER[66–68]. The ongoing challenge is to design new catalysts that rationalize several parameters including the performance, the stability, the tolerance, and to some extent the bi-functionality. To this end, the bi-functionality of these materials towards ORR and OER is further explored.

The electrocatalytic activity of poly(VImM) after incorporation of Pt/C toward the OER was evaluated in alkaline solution. Figure 3.35a shows that the poly(VImM) has a catalytic activity when compared with bare GC, but lower than that observed for Pt/C which is an inefficient catalyst for OER. One is noted that even if the poly(VImM) displays catalytic activity, it is still far below than the iridium and ruthenium oxide catalysts. More interestingly, the hybrid material based on Pt/C/poly(VImM) exhibits pronounced catalytic activity compared with Pt/C.

Figure 3.35b compares the catalytic activity of Pt/C and Pt/C/poly(VImM) in alkaline media. The Pt/C/poly(VImM) offered higher current densities and lower overpotentials for both ORR and OER reactions when compared with Pt/C. The overpotential of the hybrid material at 2 $mA.cm^{-2}$ is almost 200 mV lower than that for Pt/C. As a result, the poly(IL)/Pt shows a potential use as a bi-functional catalyst for ORR and OER. This study provides simple and new strategies for preparing poly(IL)-based catalyst or hybrid materials that combine the poly(IL) and other metal catalysts.

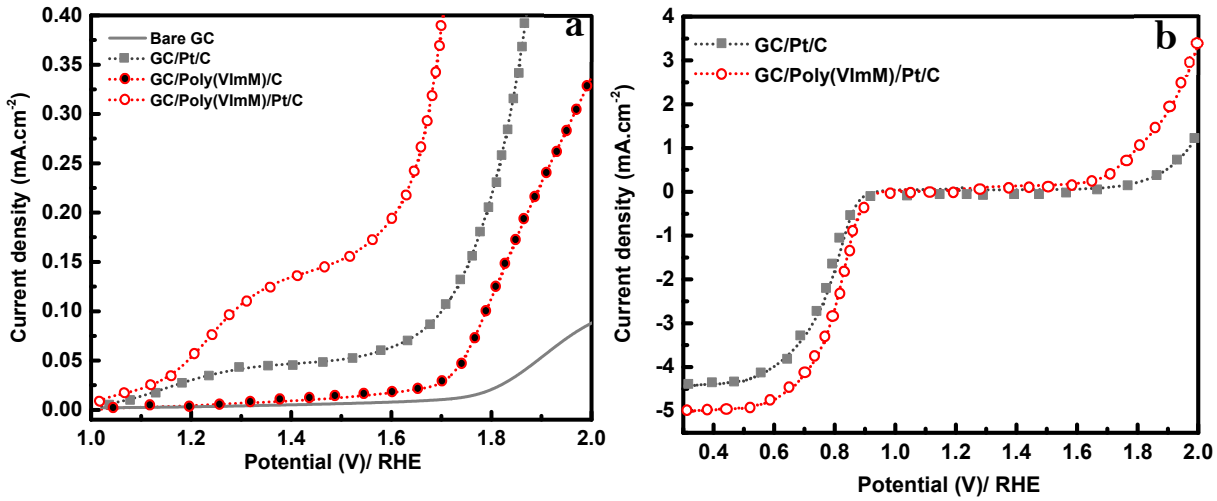

Figure 3.35 (a) OER polarization curves at 10 mV/s and 1600 rpm in O_2-saturated 0.1 M KOH solution recorded on bare GC, poly(VImM), Pt/C and poly(VImM)/Pt/C. ***(b)*** LSV plots comparing the ORR and OER in in O_2-saturated 0.1 M KOH solution at Pt/C and poly(VImM)/ Pt/C catalyst.

3.5 POLY(IONIC LIQUIDS) AS TEMPLATE FOR ELECTRODEPOSITION OF METALLIC NANOPARTICLES

In the previous parts, we demonstrated the possible use of immobilized polymeric ionic liquid layer as active material towards oxygen reactions. Besides that, the polymer ionic liquid was successfully used as a platform for host guesting other catalysts providing a synergetic effect to the hybrid materials. Even though the increase of the catalytic activity of the as – prepared substrates, the interface between ionic liquid moieties and the particles is relatively vague. In this part, the poly(IL) is used as a nanostructured platform for guiding the electrochemical deposition of metallic nanoparticles. The poly(1-allyl-3-methylimidazolium) (PAMI) is prepared by means of surface-initiated atom transfer radical polymerization as reported in our previous works. Next, the electrochemical deposition of metal onto GC/poly(IL) has been performed. It has been demonstrated that the hybrid materials possess bi-functionality towards oxygen reactions (ORR and OER). In this part, we would like to introduce a multifunctional aspect of the polymeric ionic liquid-based materials. Thus, the catalytic reaction, hydrogen evolution reaction (HER), has been chosen to evaluate the catalytic performance of the materials. Being known as the best candidate for hydrogen evolution reaction, noble metals were used, including palladium and platinum.

3.5.1 Electrochemical deposition of M NPs (M = Pt, Pd) in presence of immobilized PIL and its catalytic performance

The metal is deposited onto the electrode surface, GC/poly(IL), by chronoamperometry technique, which consists to apply a fixed potential in the presence of metallic salt (Na_2PdCl_4 or K_2PtCl_4) dissolved in aqueous solution (Figure 3.36).

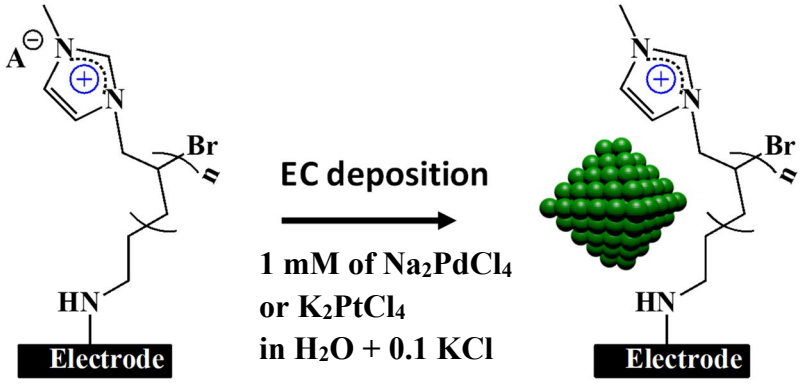

Figure 3.36 Procedure for Electrochemical deposition of nanoparticles onto GC/PAMI substrates

Depending on the applied potential, the nucleation and growth of the metallic structure at the GC/poly(IL) are different, resulting from the difference of thermodynamic barrier. To cover a large window of deposition potential, different samples were prepared with a deposition potential ranging from 0.2 V to -1 V/ SCE at a fixed time (100 s). Afterwards, the electrodes were then rinsed thoroughly with water and characterized in aqueous acidic solution. As shown in the Figure 3.S6c, the typical electrochemical response of Pd decorated GC/poly(IL) electrode

was recorded in N_2-saturated 0.5 M H_2SO_4 solution. At a potential higher than 0.7 V, an anodic peak is observed corresponding to the oxidation of Pd NPs. These oxidized species are reduced at 0.4 V. Besides that, the reduction peak at the potential ranging from 0V to -0.4 V corresponds to the proton reduction/hydrogen adsorption and the reverse peak attributed to hydrogen evolution/desorption. Similar CV's shape for Pt NPs decorated GC/poly(IL) was also observed as presented in the Fig.3.S6d. Briefly, the transformation of metallic platinum into oxide is occurred at 1.3 V/ SCE and the reverse reaction is located at 1.2 V/ SCE. Even though the hydrogen adsorption peak is hindered by the HER, the anodic peak indicates a strong desorption of theH_2 molecule from the Pt surface. These electrochemical characterizations confirm the electrodeposition of Pd and Pt over the GC/poly(IL) electrode.

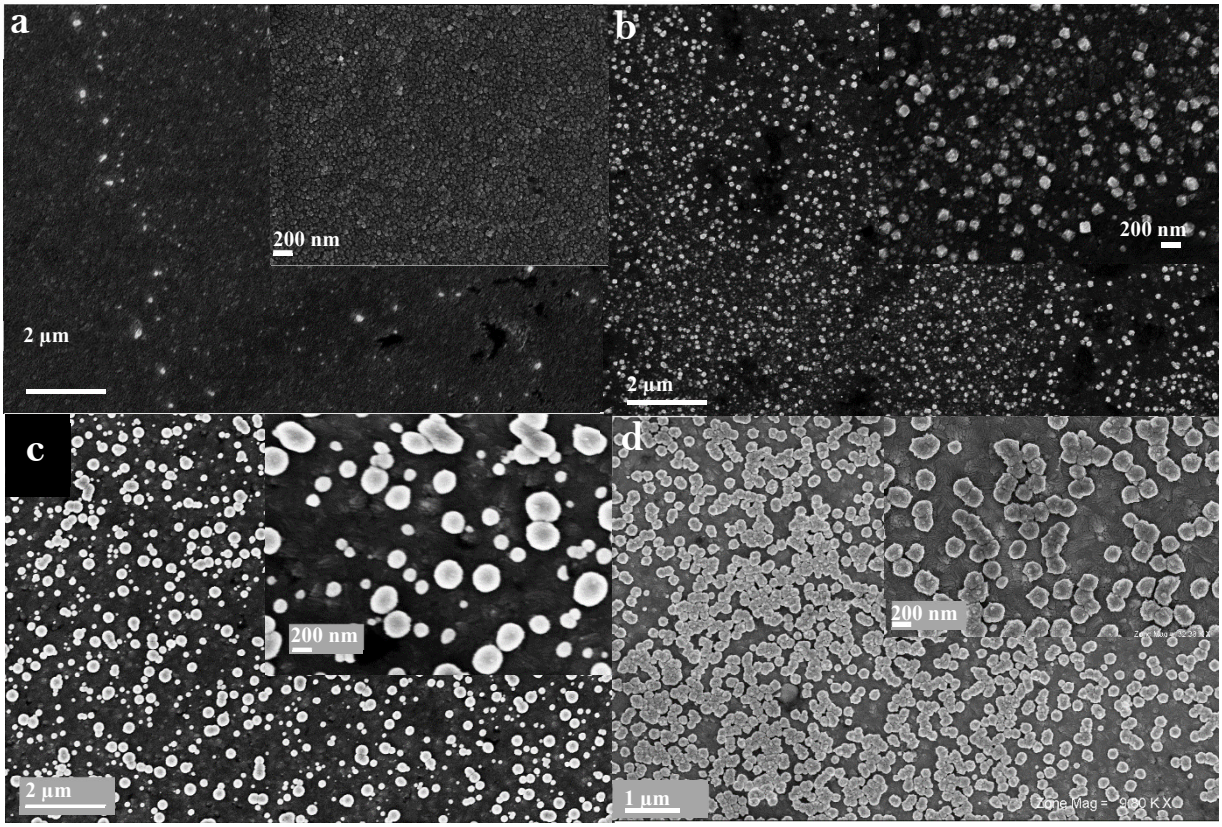

Figure 3.37 SEM images of ***(a)*** ITO/PAMI/Pd NPs; ***(b)*** ITO/Pd NPs deposited at -0.2 V/ SCE and ***(c)*** ITO/PAMI/Pt NPs; ***(d)*** ITO/Pt NPs deposited at -0.6 V/ SCE

Scanning Electron Microscopy (SEM) leads to determine the size and the morphology of the deposited materials. Typical images of the samples prepared by depositing Pt or Pd on GC/poly(IL) electrodes are presented in the figure 3.37a,c. The remaining images Figure 3.37b,d display the samples prepared in the absence of the polymer layer. The SEM revealed that the morphology and the size of the particles deposited onto ITO are different depending on the presence or the absence of the polymeric ionic liquid layer. Common behavior for both metals is the formation of nanoparticles after the electrochemical deposition. The size of the particles decreases in the presence of the poly(IL) layer. For Pd NPs deposited onto ITO/poly(IL) a smooth surface was obtained with a very dense layer composed from small

particles (< 50 nm) (Figure 3.37.a) while nanocubes with larger size (up to 200 nm) were obtained in the absence of the PAMI layer (Figure 3.37b). In the case of the platinum particles, smaller nanospheres were observed in the presence of the PAMI (Figure 3.37c). By depositing metallic nanoparticles via chronoamperometry technique, the measured current is composed of 3 components, including the double layer charge contribution, the 2D-instantaneous nucleation and 3D nucleation with diffusion-controlled growth[69–71]. From the SEM images, the formation of 3D nanoparticles was observed, conducting to elimination of the 2D contribution. Indeed, the currents recorded in the figure 3.S6a-b can be attributed to:

$$j = j_{ads} + j_{3D-dc} \quad (3.34)$$

Where $j_{ads} = k_1 \exp(-k_2 t)$ (3.35) is the current attributed to the ions adsorption which is based on the Langmuir-type adsorption–desorption equilibrium with $k_1 = k_2.q_{ads}$ and q_{ads} is the total charge density due to the adsorption process

And the $j_{3D-dc} = \frac{zfD^{1/2}C}{\pi^{1/2}t^{1/2}}\left\{1 - \exp\left[-2\sqrt{2}\pi^{3/2}N_0C^{1/2}V_m^{1/2}D\left(t - \frac{1-\exp(-At)}{A}\right)\right]\right\}$ (3.36) is attributed to the 3D-nucleation controlled by diffusion (zf, D, C, t, N_0, V_m, and A correspond to the molar charge transferred during electrodeposition, diffusion coefficient, bulk concentration of electrolyte, number of active sites, molar volume of the deposit and the nucleation rate constant). The relationship between the nucleation rate constant and the deposition potential is given by:

$A(E) = A^0 \exp\left(-\frac{(n_c+\alpha)ze_0}{kT}E\right)$ (3.37) leading to the number of atoms in critical nucleus is

$n_c = \frac{kT}{ze_0}\left(-\frac{d\ln A}{dE}\right) - \alpha$ (3.38) where A_0 is a constant which depends on the n_c, k is the Boltzmann constant, α cathodic charge transfer coefficient and e_0 the elementary charge.

In summary, by simplifying with $p_1 = \frac{zfD^{1/2}C}{\pi^{1/2}}$ and $p_2 = 2\sqrt{2}\pi^{3/2}N_0C^{1/2}V_m^{1/2}D$, the final current is given by $j = k_1\exp(k_2 t) + \frac{p_1}{t^{1/2}}\left\{1 - \exp\left[-p_2\left(t - \frac{1-\exp(-At)}{A}\right)\right]\right\}$ (3.39) resulting from the mechanism of Langmuir – type adsorption/desorption equilibrium followed by 3D nucleation under diffusion-controlled regime. Consequently, the measured current, especially the nucleation rate constant varies with the applied potential. It could result to a difference of the final crystallographic configuration of the deposited nanoparticles, leading to a difference of catalytic activity of the nanoparticles in function of the deposition potential. Even though the mechanistic investigation of nucleation and growth of the nanoparticles is still at the spectacular stage, it is still possible to conclude that the nucleation of nanoparticles is strongly affected by

the concentration of metallic ions at the vicinity of the electrode surface. By combining the SEM images and the polymer brushes structure, possible explanation can come from the high density of cations within the film that are converted to numerous nucleation sites for the formation of the final film. Consequently, smaller size particles are obtained by using poly(IL) as template, i.e. higher specific surface area, rather than big particles in the absence of PAMI.

The hydrogen evolution reaction is evaluated by using the samples prepared at different deposition potential ranging from 0.2 V to -1 V/ SCE. The LSV polarization curves were recorded in N_2 -saturated 0.5 M H_2SO_4. The HER on GC/poly(IL)/Pd NPs starts at low cathodic potential, resulting to a low overpotential after which the reduction current increases rapidly. Compared to the bare GC electrode, all the modified electrodes exhibit strong catalytic activity towards HER. As the growth of the particles are different by changing the deposition potential, their activity is considerably varied (Figure 3.38a), involving the onset potential and the current density (Figure 3.38b). The sample prepared by applying a potential at -0.2 V/SCE exhibits the most positive onset potential (-0.22 V/RHE) at a current density of 20 $mA.cm^{-2}$.

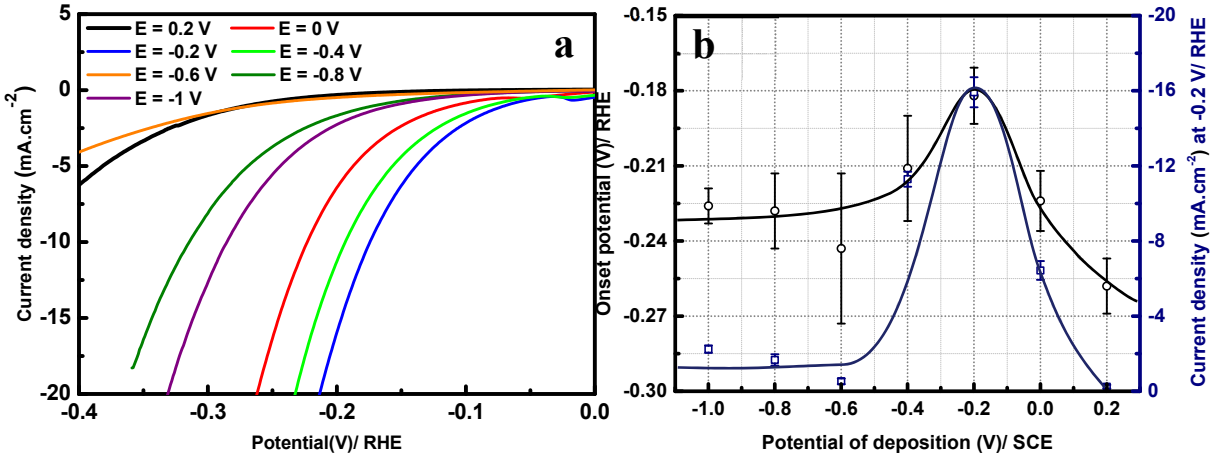

Figure 3.38 ***(a)*** HER polarization curve (LSV) at 10 mV.s-1 in 0.5 M H_2SO_4 aqueous solution on GC/PAMI/Pd NPs deposited at different potentials; ***(b)*** Variation of onset potential as function of deposition potential.

It is well – known that the proton reduction can follow 2 pathways depending on the surface state of the catalyst either the Volmer – Heyrovsky or the Volmer – Tafel mechanism. Being considered as model catalytic reaction, the HER is a typical example of two – electron transfer reaction with an intermediate (H – * where "*" denotes catalytic site). The detailed reactions are given below[72]:

$$\text{Volmer step:} \quad H^+ + e^- + * \rightarrow H* \qquad b = \frac{2.3RT}{\beta F} \approx 120\,mV.dec^{-1} \qquad (3.40)$$

$$\text{Heyrovsky step:} \quad H* + H^+ + e^- \rightarrow H_2 + * \qquad b = \frac{2.3RT}{(1+\beta)F} \approx 40\,mV.dec^{-1} \qquad (3.41)$$

$$\text{Tafel step:} \quad 2H* \rightarrow H_2 \qquad b = \frac{2.3RT}{2F} \approx 30\,mV.dec^{-1} \qquad (3.42)$$

The reaction rate is largely depended on the adsorption of the proton onto the catalyst surface, i.e. the adsorption free energy (ΔG_H). If the binding energy is too low, the adsorption becomes rate determining step, RDS, (Volmer step) whereas if the binding energy is too strong, the desorption step becomes rate determining step (Heyrovsky/Tafel step). To correlate the reaction rate and the mechanism, Tafel slope is used. The Tafel step is pointed as RDS if the corresponding slope is around 30 mV.dec^{-1} (Eq.3.42). The value indicating Heyrovsky step as RDS is calculated to be 40 mV.dec^{-1} (Eq.3.41). Tafel slope of 120 mV.dec^{-1} is attributed to the surface coverage of adsorbed hydrogen or Volmer step (Eq.3.40).

Relying onto the literature, it has already been demonstrated that the adsorption of hydrogen into the noble metal lattice results to either the formation of metal hydride surface at positive potential/ reversible H^+/H_2 potential, so – called underpotential deposited hydrogen (H-UPD), or overpotential – deposited hydrogen, H-OPD, which is generated below H^+/H_2 potential. It has been demonstrated that H-OPD are intermediates for the reduction reaction while the H-UPD remain spectator during the process[72]. Several works reported that Pd – based materials are suitable for hydrogen storage, H-UPD, issue from strong permeability and high solubility of hydrogen at Pd surface[73,74]. Thus, the adsorption of H-OPD may be limiting factor for the catalytic performance of the Pd – based materials. In our case, values close to 120 mV.dec^{-1} have been obtained for all of the samples (Figure 3.39a), suggesting that the adsorption of the hydrogen into the catalyst surface is the limiting step.

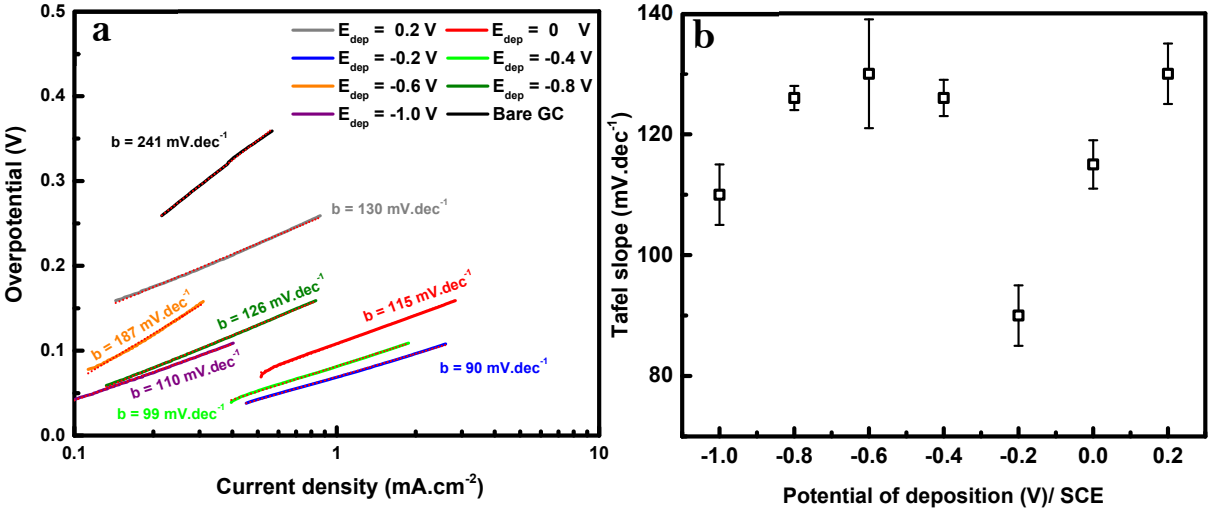

Figure 3.39 ***(a)*** Tafel slope towards HER in 0.5 M H_2SO_4 aqueous solution on GC/PAMI/Pd NPs deposited at different potentials; ***(b)*** Variation of onset potential as function of deposition potential.

The evolution of the Tafel slope as function of the deposition potential is reported in the Figure 3.39b. The GC/poly(IL)/Pd NPs prepared at -0.2 V/SCE exhibits the lowest Tafel slope of 90 mV.dec^{-1}, suggesting improvement of the adsorption of the H-OPD. However, the value of the Tafel slope is relatively subjective since the latter depends on the choice of the j-V region and the iR-drop correction. Therefore, the only possible conclusion that can be announced is the exclusion of combination and ion – atom reactions as the limiting steps. Despite the need of

more powerful analysis tools for achieving exact mechanism, the clear standpoint is that the electrochemical deposition in the presence of the immobilized ionic liquid layer enhances the adsorption of hydrogen.

In the absence of the polymeric ionic liquid layer, the GC/Pd NPs electrode prepared under the same conditions exhibits lower catalytic activity compared to the electrode in the presence of the ionic liquid polymer (PAMI), resulting from a higher overpotential (η_{PdNPs} = 240 mV vs. $\eta_{PAMI/PdNPs}$ = 215 mV at 20 mA.cm^{-2}) (Figure 3.40a). Figure 3.40, inset, shows the Tafel plot for GC/Pd NPs and GC/poly(IL)/Pd NPs, indicating a lower slope, i.e. higher H – adsorption rate, for the electrode containing the poly(IL). This result is further confirmed by the electrochemical impedance spectroscopy tests. As shown in the Figure 3.40b, the charge transfer resistance is lower in the presence of the polymer ionic liquid layer (1 kΩ compared to 3.5 kΩ), suggesting a higher electron transfer between the catalyst and the electrode surface. From these results, we could confirm that the presence of polymeric ionic liquids influences not only the nano-structuration of the metallic layer but also its catalytic performance.

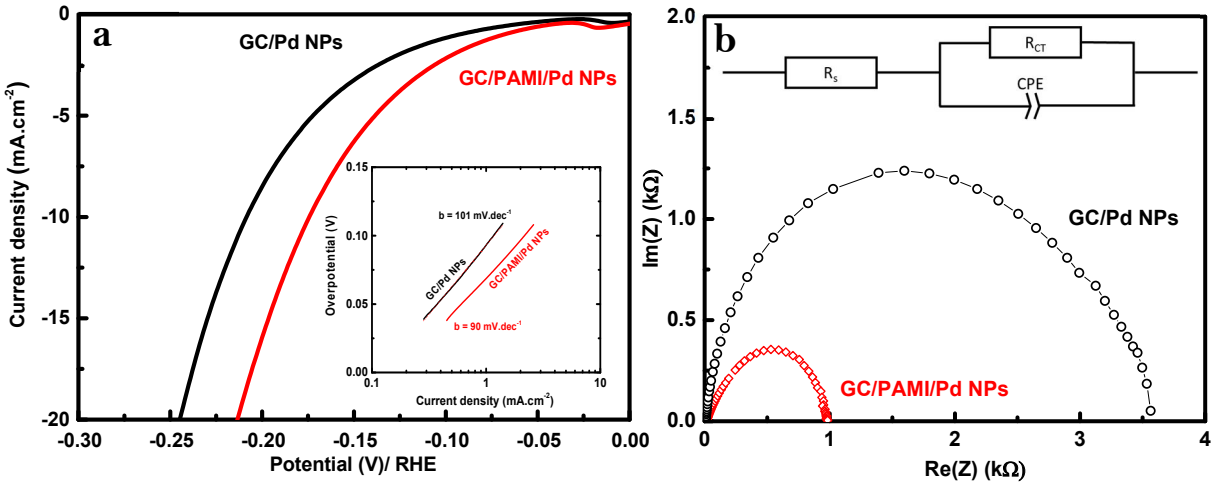

Figure 3.40 (a) HER polarization curve (LSV) at 10 mV.s-1 in 0.5 M H_2SO_4 aqueous solution (inset) Corresponding Tafel plot; ***(b)*** EIS curve recorded at -0.2 V/ RHE on GC/Pd NPs and GC/PAMI/Pd NPs deposited at -0.2 V/ SCE, (inset) Equivalent Randle circuit.

Even though improvement of the catalytic activity through the presence of poly(IL), the performance of the poly(IL)/Pd is still far from the activity of platinum, which is referred as one of the best electrocatalysts towards HER. Indeed, similar approach has been performed to Pt based catalysts. The electrochemical deposition was performed onto GC/ poly(IL)electrodes using different deposition potential during 100s in aqueous solution containing Na_2PtCl_4 as Pt precursor. Afterwards, the catalytic activity of different electrodes was evaluated towards HER in 0.5 M N_2–saturated H_2SO_4 solution as displayed in the figure 3.41. The performance of GC/PAMI/Pt NPs varies as function of the deposition potential as observed for the Pd – based electrodes. From the figure 3.41b, one notices that the highest onset potential is obtained at -50 mV/ RHE corresponding to the sample prepared under amperometric conditions at -0.6 V/ SCE.

This sample shows an overpotential of 70 mV at 20 mA.cm^{-2} which is among the most efficient catalysts towards HER[5,75–77]

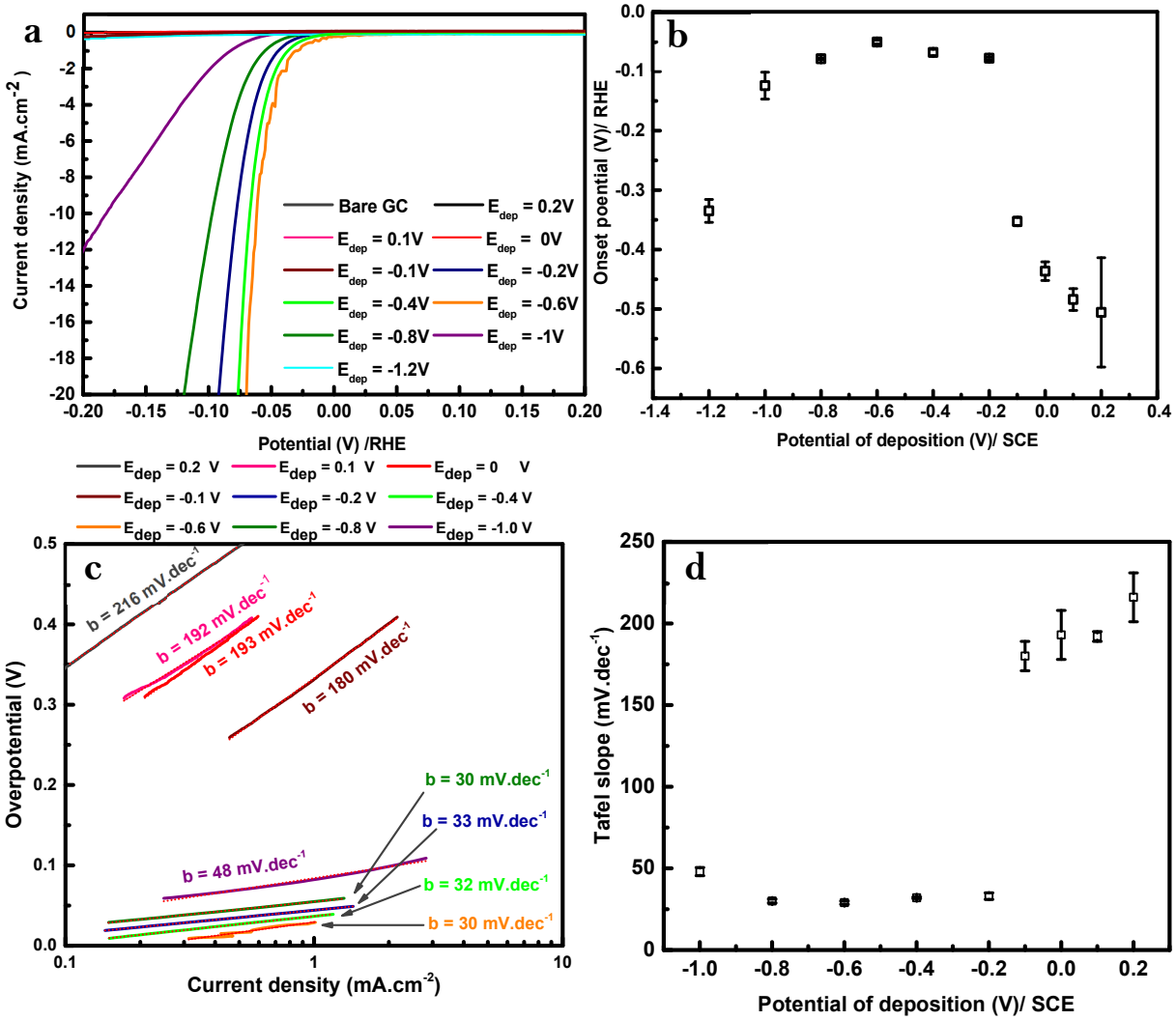

Figure 3.41 ***(a)*** HER polarization curve (LSV) at 10 mV.s-1 in 0.5 M H_2SO_4 aqueous solution on GC/PAMI/Pt NPs deposited at different potentials; Variation of ***(b)*** onset potential and ***(c,d)*** Tafel slope as function of deposition potential.

Next, the Tafel curves were plotted and the slope were calculated from different samples (Figure 3.41c, d). It has already been demonstrated that the Volmer – Tafel mechanism occurs when the H – coverage is very high ($\theta \sim 1$), which is known for Pt surface[72]. In the deposition potential ranging from -0.2 V to -0.8 V/ SCE, the Tafel slopes are found to be around 30 mV.dec^{-1}, indicating that the Tafel step is rate determining step which is coherent with reported works[6,78]. As an interesting result, the presence of polymeric ionic liquid increases the catalytic activity of the platinum particles. Indeed, the Pt based electrode in the presence of poly(IL) shows a higher catalytic activity with an overpotential of 70 mV at 20 mA.cm^{-2} compared to 100 mV obtained in the absence of the poly(IL). Besides, the charge transfer is evaluated by using EIS, resulting to a 40-times lower R_{CT} in case of GC/ poly(IL)/Pt NPs at η = 70 mV (Figure 3.42).

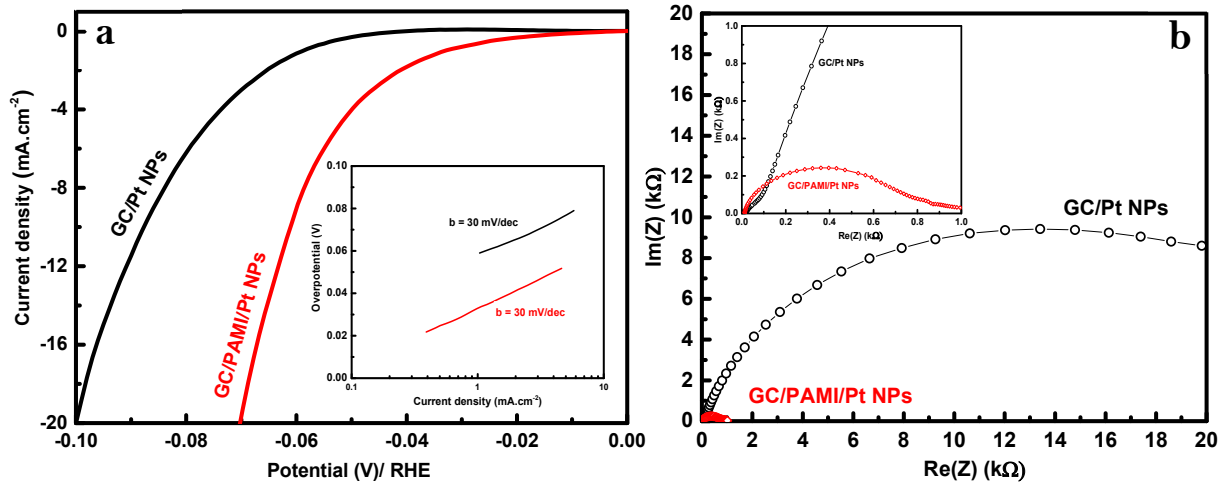

Figure 3.42 (a) HER polarization curve (LSV) at 10 $mV.s^{-1}$ in 0.5 M H_2SO_4 aqueous solution (inset) Corresponding Tafel plot; ***(b)*** EIS curve recorded at -70 mV/ RHE on GC/Pt NPs and GC/PAMI/Pt NPs deposited at -0.6 V/ SCE.

The enhancement of the catalytic performance towards HER confirm the importance of the polymeric ionic liquid. The crucial role of the polymer ionic liquid can be attributed to different factor. Firstly, as discussed in the previous part, the concentration of metallic anion is higher inside the layer rather than in the bulk, suggesting higher nucleation and growth rate due to diffusion-controlled system. Secondly, the organization of the polymer layer, i.e. brush – like structure, can participate to the orientation of the deposited metallic structure. Finally, the non – negligible interaction of the polymer layer and the deposited particles may also enhance the hydronium conduction and charge transfer rate at this interface.

Even though additional analyses must be performed to achieve deep understanding about the origin of the catalytic enhancement, at the current stage, it is clear that the presence of polymeric ionic liquid layer boosts the catalytic performance of the deposited materials, whether palladium or platinum or others. However, the limited availability and extremely high cost of noble – metal-based catalysts restrict their use in mass production. Consequently, seeking for a new approach to reduce the quantity of the catalyst by maintaining its activity becomes important task for cost effective system. Based on the observation concerning the possible anion capture within the polymer ionic liquids layer, we propose to use the latter as host – guest template to capture the metallic anions via ion exchange followed by electrochemical deposition in electrolytic – free solution affording nanocluster decorated poly(IL) nanofilm.

3.5.2 Metal clusters decorated Polymeric ionic liquid nanofilm as catalyst

Relying on advantageous performance offered by metal – based catalyst, nanosized structures have been proposed to both decrease the needed quantity of material and the increase of the catalytic activity, via the increase of the active site number and the specific area. The nanomaterial can be obtained by using several approaches as chemical synthesis, electrochemical deposition, etc. Recently, K. Tang and al[79] reported the electrochemical deposition of Pt on edge-rich layered WS_2 nanosheets and demonstrate the increase of the catalytic activities of the generated structure toward the HER. Thus, very small amount of Pt nanoparticle is found to be enough for boosting the system up to commercial Pt/C. However, the deposition of Pt is strongly dependent on the chemical composition, crystalline structure and morphology of the substrate (WS_2).

From aforementioned concept, the purpose of this part is to prove the possibility to generate nanoclusters of noble metal by the anion capturing property of polymeric ionic liquid, e.g. poly(1-allyl-3-methylimidazolium). The imidazolium skeleton of the as-prepared poly(IL) film creates extremely high cationic charge density at the interface between the electrode/solution interface. The electrostatic attraction allows strong molecular interaction between the imidazolium rings and metal-based anion (XCl_4^{2-}, X = Pt, Pd). The specific feature allows the poly(IL) modified electrode receiving a large density of metal precursors, which acts as reservoir for further electrochemical deposition of clusters (Figure 3.43).

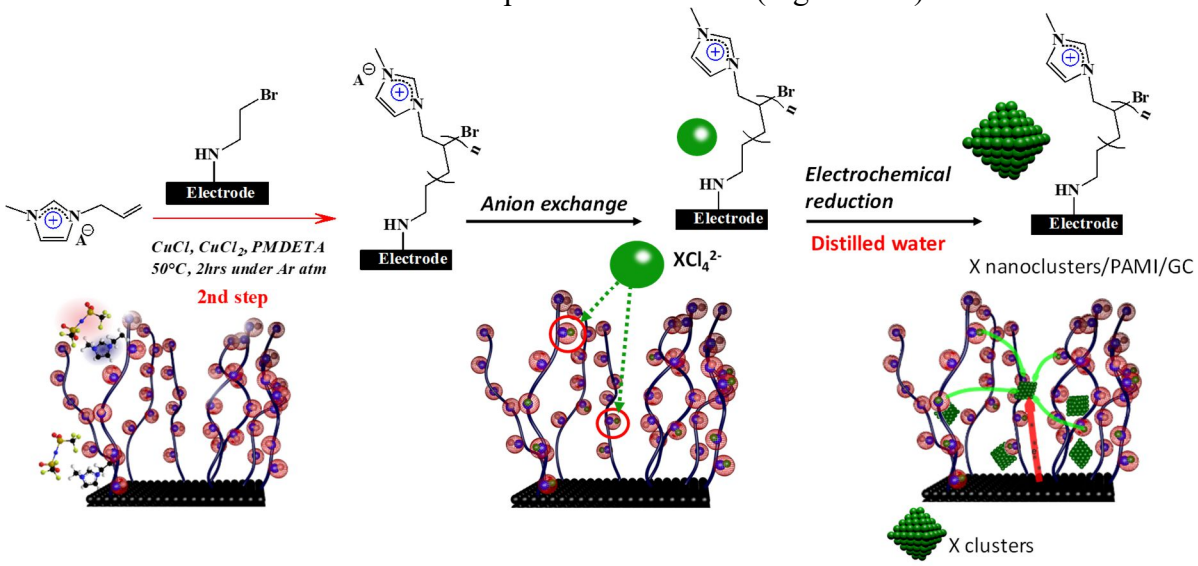

Figure 3.43 Typical procedure to generate X_{exc} (Pt, Pd, etc.) nanoparticles decorated GC/PAMI.

The electrochemical nucleation and growth of the nanoparticles can be occurred in distilled water under self-electrolytic conditions (without any additional supporting electrolyte). The electrochemistry in electrolytic – free solution is reported in the previous works[51]. Thus, by applying a cathodic potential, the anions (XCl_4^{2-}, X = Pt, Pd) inside the film can act as both precursor and metal reservoir for growing the nanoparticles. After the polymerization, the electrode was immersed in solution containing the metallic salt during 2h. Next, the electrode

was rinsed thoroughly and transferred into the electrochemical cell. After the electrochemical deposition in aqueous solution, the presence of clusters was first evidenced by the electrochemical characterization in aqueous acidic solution (0.5 M H_2SO_4). The typical signal of the Pd^0 (Figure 3.44a) and Pt^0 (Figure 3.44b) were obtained as described in the previous part. However, the current intensity attributed to the oxidation of Pd, Pt particles is lower than in the previous cases, that the deposition had been performed in the presence of metallic salts in solution. It is noted that even the concentration at the vicinity of the electrode is higher in the current case, the quantity of anion is still scanty within very thin layer of polymer. Thus, the quantity of X^0 (X = Pd, Pt) generated in this case must be lower.

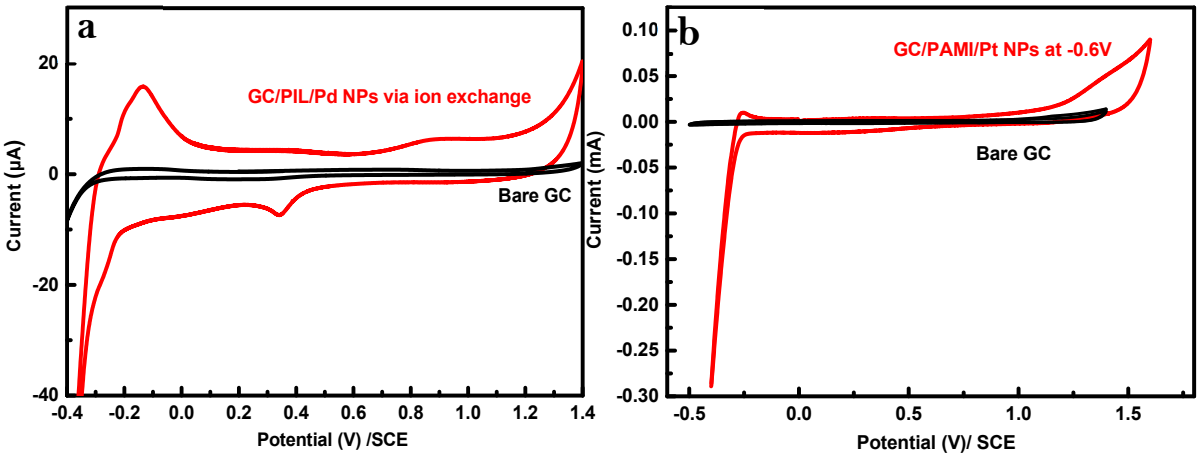

Figure 3.44 CV of ***(a)*** GC/PAMI/Pd_{exc} NPs and ***(b)*** GC/PAMI/Pt_{exc} NPs recorded in aqueous solution containing 0.5 M of H_2SO_4.

X-ray photoelectron spectroscopy (XPS) was used to follow the change in the atomic composition of the surface of different substrates. After anion exchange, the high-resolution spectra of the Pd(3p) exhibits lump signal of the Pd^{2+} ($3p^{3/2}$ and $3p^{1/2}$) centered at 337 eV and 343 eV, indicating the presence of $PdCl_4^{2-}$ within the polymer film (blue curve Figure 3.45a). Interestingly, after the electrochemical deposition, well – defined peaks at lower binding energy 335 eV and 341 eV appear corresponding to Pd^0 confirming the formation of metallic Pd inside the polymeric film (red curve Figure 3.45a). In addition, the variation of the signals provided by Cl(2p) confirm the hypothesis. Precisely, the appearance of Cl signal at 198 eV and 199 eV, attributed to $2p^{3/2}$ and $2p^{1/2}$ respectively, confirms that the $PdCl_4^{2-}$ is caught inside the polymer layer (blue curve Figure 3.45b). Next, a decrease of the Cl^- contribution after the electrodeposition (red curve Figure 3.45b) is observed confirming the formation of metallic Pd. Moreover, the nitrogen signal at 401.5 eV is still visible confirming the presence of imidazolium.

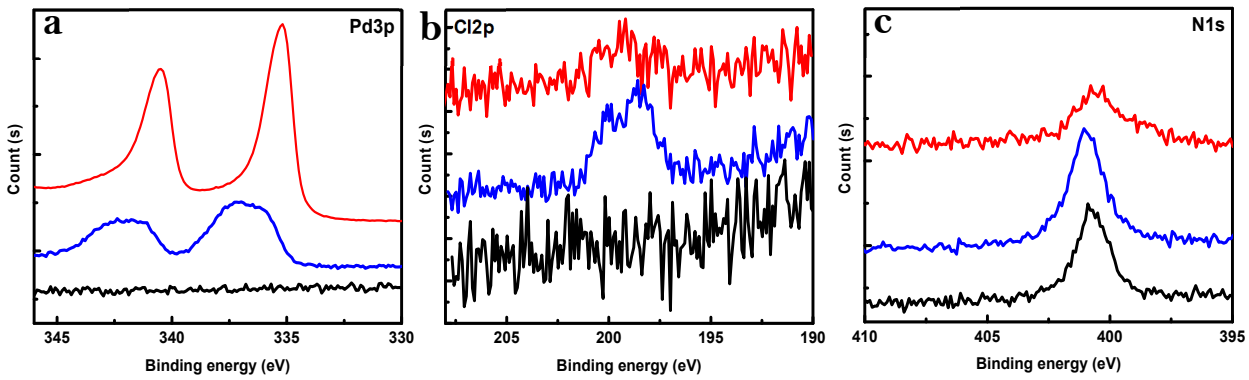

Figure 3.45 High resolution XPS spectra of ***(a)*** Pd(3p), ***(b)*** Cl(2p) and ***(c)*** N(1s) of (black curves) GC/PAMI, (blue curves) GC/PAMI/$PdCl_4^{2-}$ and (red curves) GC/PAMI/Pd NPs, respectively.

Even though the evidences about the presence of Pd and Pt particles from cyclic voltammetry and XPS measurements are confirmed, the SEM images do not display visible nanoparticles. The slight difference of contrast is attributed to the ITO surface that is similar to non – modified ITO. This result is attributed to the minute size of the metallic particles that cannot be detected by SEM (lower than 5 nm). Besides, as the deposition occurs only inside the polymer film, the generated particles must be retained in the layer and attached to the polymer brushes (Figure 3.S8).

Afterwards, the catalytic performance of the prepared electrodes toward the HER was evaluated. Figure 3.46a shows clearly that the presence of Pd_{exc} NPs inside the polymer layer enhances strongly the catalytic activity of the final electrode when compared to the Bare GC and GC/PAMI (black and grey curves, respectively). Typically, the GC/ poly(IL)/Pd_{exc} NPs deposited at -0.2 V/SCE exhibits the lowest onset potential around -0.18 V/ RHE and an overpotential of 310 mV for a current density about 20 $mA.cm^{-2}$. Compared to non-modified electrode, an overpotential of 650 mV is required to reach the same current density.

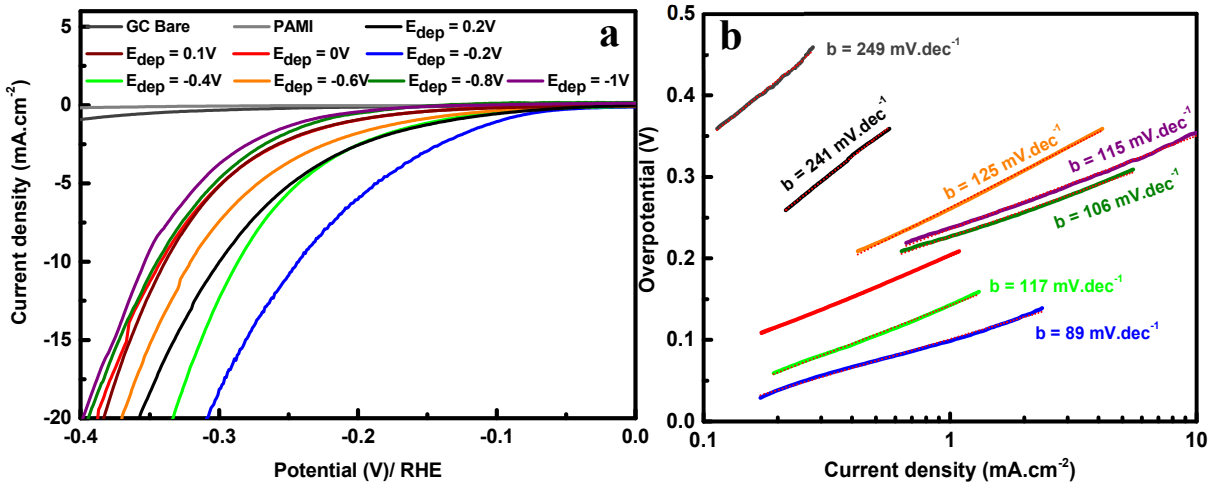

Figure 3.46 ***(a)*** HER polarization curve (LSV) at 10 $mV.s^{-1}$ in 0.5 M H_2SO_4 aqueous solution on GC/PAMI/Pd NPs deposited at different potentials; ***(b)*** Variation of onset potential as function of deposition potential and ***(c, d)*** Tafel slope as function of deposition potential.

The kinetic is evaluated by plotting the Tafel curves for samples prepared at different potential ranging from 0.2 V to -1 V/ RHE. The prepared samples exhibit Tafel slopes ranging from 125 $mV.dec^{-1}$ to 89 $mV.dec^{-1}$. Interestingly, the sample deposited at -0.2 V/ SCE shows a Tafel slope value of 89 $mV.dec^{-1}$, indicating a higher adsorption rate by decreasing Volmer step limitation.

To get more insight about the charge transfer kinetic, electrochemical impedance spectroscopy was performed at different overpotential for the sample prepared at -0.2 V/ SCE. The Nyquist and Bode diagrams are presented in the Figure 3.47.

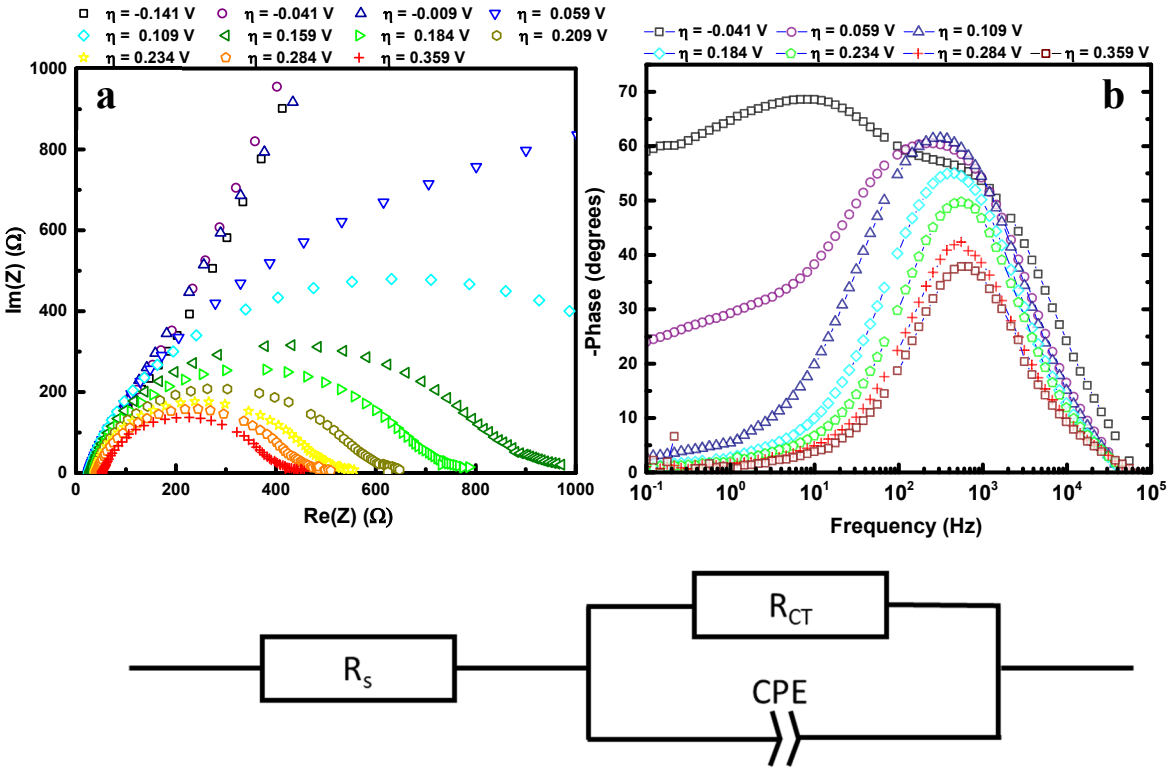

Figure 3.47 (a) Nyquist plot and ***(b)*** Bode plot at different overpotential towards HER by using GC/PAMI/Pd NPs electrode at different overpotentials; ***(c)*** Equivalent circuit used for the EIS fitting.

As displayed in the Figure 3.47, the GC/ poly(IL)/Pd^{exc} NPs exhibits single semicircle for all of the used overpotentials, suggesting that the equivalent circuit can be constructed by single time constant. In real environment, the pure capacitor is rarely observed due the electrode roughness[80,81], where introduction of constant phase element. This concept reflects somehow the deviation from the ideal electrical double layer capacitor. Mathematically, the CPE's impedance is described as:

$\frac{1}{Z} = Y = Q^0.(j\varpi)^{\alpha}$ (3.37) with Q^0 ($S.s^{\alpha}$) has the numeric value of the admittance Y for ω = 1 $rad.s^{-1}$. The exponent value (α) indicates the behavior of the CPE and could be resulted from the following equation, α = 1/(D-1) (3.38)[80]. For a rough and fractal surface, the dimension (D) is in between 2 and 3. For a smooth 2D surface, the value of α is equal to unity and for a highly

contorted surface (D = 3), α = 0.5. For α = 1, the CPE resembles a pure capacitor while when α = 0, the CPE become a pure resistance. At an intermediate value of exponent (α), the capacitance is calculated from CPE via following equation:

$$C_{eff} = Q^{1/\alpha}(R_s^{-1} + R_{CT}^{-1})^{(1-\alpha)/\alpha} \quad (3.39)$$

Consequently, the potential dependence of the resistance and of the capacitance (R-CPE circuit) reflects the kinetic of the HER process. Indeed, the charge transfer resistance decreases from 8250 Ω at η = 60 mV to 500 Ω at η = 200 mV. In addition, the variation of $\log(R_{CT}^{-1})$ as function of the overpotential was plotted as shown in the Figure 3.S9a, resulting to a linear relationship at low overpotential. The calculated Tafel slope is 83 $mV.dec^{-1}$ for the GC/ poly(IL)/Pd^{exc} NPs obtained from the EIS data. In addition to the value of the charge transfer resistance, the capacitance derived from the CPE is another important parameter. For calculation of capacitance, the exponent and CPE are required. The variation of the α and calculated capacitance are presented in the figure 3.S9c. In the overpotential ranged from 0 V to 0.4 V, α exhibits a slightly variation ranging from 0.80 to 0.89, which correspond to a phase angle in between 80° and 90° (given as αx90°). As the "capacitance" is classed in parallel with the charge transfer resistance, the Nyquist plot become a semi-circle whose center is depressed by an angle of (1-α).90° (3.40), i.e. 10° - 20°. Furthermore, the application of high overpotential conducts to a decrease of the double layer capacitance from 0.14 $mF.cm^{-2}$ at 60 mV (approximately 40 $mF.mg^{-1}$) to 0.04 $mF.cm^{-2}$ at 200 mV (~15 $mF.mg^{-1}$). These variations could be attributed to the partial blockage of the electrode surface by the generated hydrogen species resulting to the formation of microbubbles. The high values of the double layer capacitance for the particles decorated polymer ionic liquids highlight the ionic character of the polymer and the small size of the particles, indicating large specific surface areas[51].

Besides, the characteristic time for the electron transfer across the catalyst – electrolyte interface can be approximately estimated as the time constant, i.e. τ = RC (3.41), where smaller τ represents higher electron transfer rate. As presented in the figure 3.S9b, the evolution of τ in function of the potential shows a diminution of 3 orders of magnitude from 0 V to -0.17 V/RHE, suggesting an increase of the electron transfer kinetic correspond to the drop of the measured current in this potential range. In addition, below -0.2 V/RHE, the time's values reach a saturation at around (10^{-3} s). The value in this case reflects purely the charge transfer kinetic and excludes other contributions. Similar values were obtained suggesting that the Volmer step is the RDS during the reduction process.

The overpotential needed to reach 20 $mA.cm^{-2}$ at the GC/poly(IL)/Pdexc NPs is found to be around 310 mV compared to 250 and 210 mV obtained for GC/Pd NPs and GC/ poly(IL)/Pd NPs, respectively (Figure 3.48a).

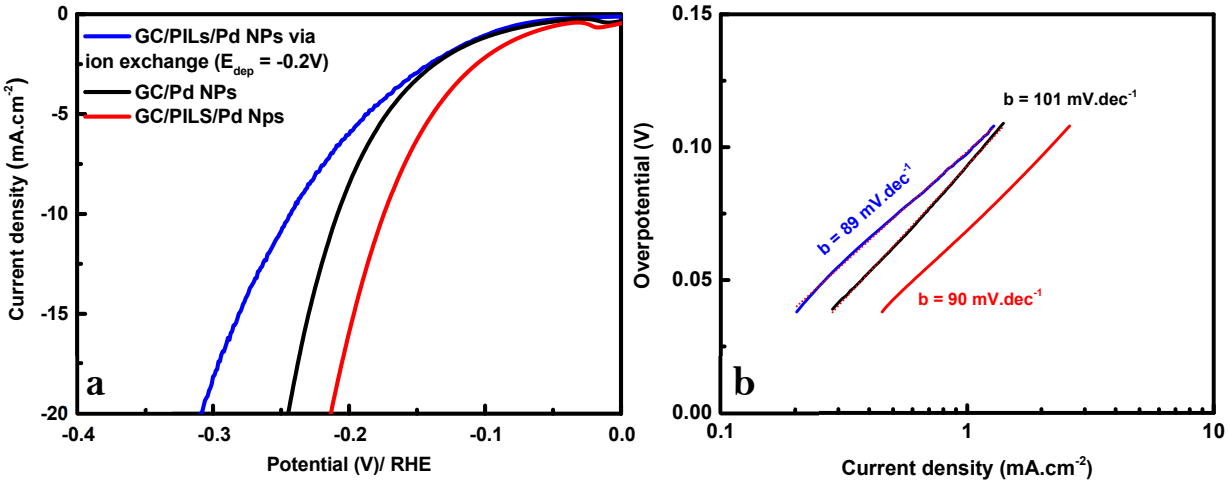

Figure 3.48 (a) HER polarization curve (LSV) at 10 mV.s^{-1} in 0.5 M H_2SO_4 aqueous solution on GC/Pd NPs (black); GC/ poly(IL)/Pd NPs (red); GC/PIL/Pd NPs via ion exchange (blue) and ***(b)*** Corresponding Tafel plot.

However, the sample prepared via ion exchange displays promising route to decrease the quantity of the active materials, herein noble metals, at least in the range of 2 orders of magnitude. In addition, in term of Tafel slope, the obtained value is around 89 mV.dec^{-1} (Figure 3.48b) which is similar to the one obtained when using GC/ poly(IL)/Pd NPs, confirming the enhancement of the adsorption of H-OPD onto Pd surface.

For upgrading the performance of the polymeric ionic liquid-based materials, similar procedure was applied to platinum. All of the prepared samples exhibit strong activity towards HER (Figure 3.S10). One notices that the electrode prepared by electrodeposition at -0.6 V/ SCE displays the highest performance with an overpotential of 195 mV at 20 mA.cm^{-2}. The corresponding Tafel slope was also calculated and found to be 49 mV.dec^{-1}. The obtained value is relatively ambiguous to have a clear idea about the exact mechanism for this substrate. One conclusion is the exclusion of the Volmer step as RDS. Even though the hybrid material exhibits high efficiency towards HER, the slope of the current in the Faradic zone is very low compared to other Pt – based catalysts. Possible explanation could be related to the disconnection between different particles inducing a high catalyst resistance. In order to get insight to the kinetic, EIS measurements were performed (Figure 3.S11) and present a decrease of double layer capacitance from 0.16 mF.cm^{-2} at 60 mV (~32 mF.mg^{-1}) to 0.075 mF.cm^{-2} at 200 mV (~14 mF.mg^{-1}) with a Tafel plot of 53 mV.dec^{-1} (Figure 3.S12). As the calculations are performed by assuming that all the imidazolium cations interact with the metallic anions (2 Im^+ : 1 A^-). It is probable that the diminution of the mass specific capacitance is related to the affinity of the $PtCl_4^{2-}$ to the imidazolium cation and the deposition process resulting to amorphous structure of Pt particles. Once compared with the GC/Pt NPs and GC/ poly(IL)/Pt NPs, the performance of GC/ poly(IL)/Pt^{exc} NPs is found to be lower with an over potential of 195 mV compared to 100 mV and 70 mV at the same current density of 20 mA.cm^{-2} (Figure 3.49). Nevertheless, the

gain in term of catalyst quantity is a great advantage of the current purpose compared to other preparation method.

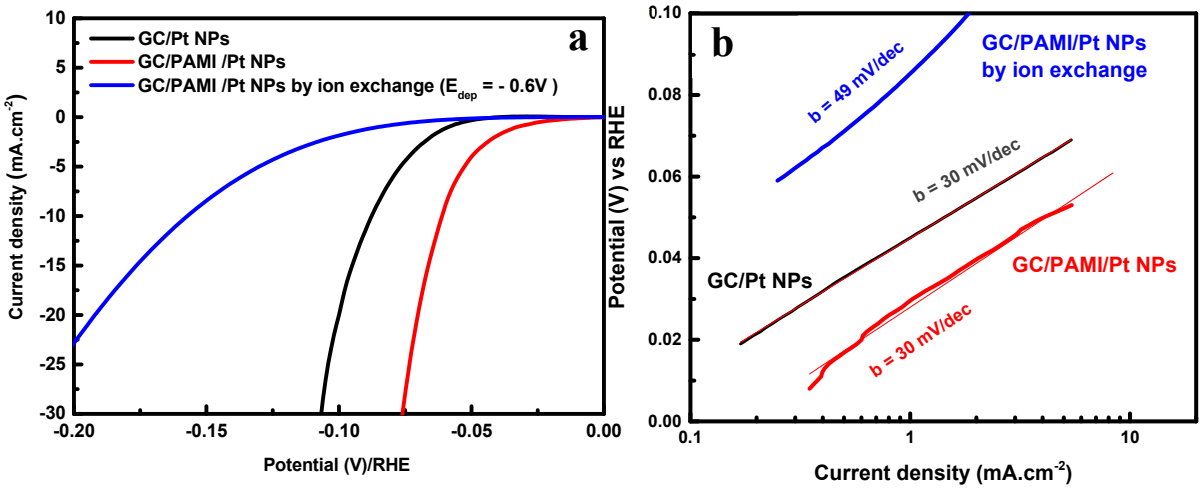

Figure 3.49 ***(a)*** HER polarization curve (LSV) at 10 mV.s^{-1} in 0.5 M H_2SO_4 aqueous solution on GC/Pt NPs (black); GC/PAMI/Pt NPs (red); GC/PAMI/Pt NPs via ion exchange (blue) and ***(b)*** Corresponding Tafel plot.

In summary, poly(IL) modified electrodes have been successfully used as a host-guest template for capturing metallic ions that serve as precursor for the electrochemical generation of metal clusters. The metal nanoparticles decorated poly(IL)/GC has also been studied for electrocatalytic activation of small molecules (HER and ORR) with relatively high performance. The simplicity of the material elaboration combined to the number of possible polymer-based ionic liquids (estimated around 10^4 molecules), the current approach opens up new class of electrocatalysts.

3.6 CONCLUSION

Seeking for highly efficient and cost-effective catalysts towards electrochemical activation of small molecules is the key process in developing renewable technologies. Possessing unique properties to be salt in the liquid phase at room temperature, the ionic liquid has been demonstrated as a promising candidate for elaboration of hybrid materials for multi-purposes in the fields of electrocatalysis. The chemical structure and the morphology of the immobilized polymer film generate water channels that enhance the diffusion of the target molecules from the bulk to the vicinity of the electrode. This specific character has been used for enhancing the catalytic activity of different materials from carbon dots to platinum-based particles towards oxygen reactions. Even more interesting, the cationic skeleton of the polymer can act as template to catch the anions from the bulk, affording a new and facile approach for preparing nanofilm of metal-organic framework that exhibit high performance towards catalytic activation of different molecules. In summary, within this humble work, the immobilized polymer ionic liquid has been used as active materials and template for generating efficient catalysts towards oxygen reactions (ORR, OER) and hydrogen evolution reaction (HER).

In the first part, nanometer scale doped carbon dots (CDs) were prepared using the microwave-assisted method in the presence of bio-based materials and ionic liquid (1-ethyl-3-methylimidazolium ethylsulfate). First, glutamine and glucose in ionic liquid were used as carbon and nitrogen source. Next to that, CDs were generated in the absence of glutamine while using the ionic liquid as source of nitrogen. As a result, both C-Dots materials exhibit a pronounced electrocatalytic activity with a prevalent 2-electron pathway leading to the formation of hydrogen peroxide. More interestingly, the C-Dots generated in the presence of glucose and ionic liquid display a selective 2-electron reduction of O_2, with H_2O_2 production higher than 90% for a potential range up to 0.8 V.

In the second part, we develop a polymer ionic liquid brushes, poly(IL), as an emerging catalyst for ORR. Our results show that the poly(IL) presents a promising electrocatalytic activity which is correlated to the chemical composition and the nano-structuration of the polymer. We demonstrate the use of poly(IL) as a host guest platform for Pt catalyst providing to the hybrid material a more efficient catalytic activity, stability and tolerance to crossover reaction. These performances were attributed to the synergetic effect between the poly(IL) and the Pt catalysts. We also reveal the potential use of poly(IL) and the hybrid poly(IL)/Pt as efficient bifunctional catalysts for ORR and oxygen evolution reaction OER. We anticipate that the simple preparation and the capability to design tasks specific poly(IL) can provide a new class of material for energy applications.

In the last part, the ionic properties of the immobilized polymeric ionic liquids have been used for growing the particles inside the layer. First approach consists to perform electrochemical deposition in the presence of metal salts solution. The presence of the polymer layer changes the morphology of the electrodeposited nanoparticles. Thus, the hybrid materials exhibit an enhancement of the catalytic performance. In a second approach, the polymer ionic liquid is used as a host -guest template to capture the metallic anion, followed by electrochemical deposition under self-electrolytic condition in distilled water. The final nanofilm displays a strong catalytic activity with a low catalyst loading (up to 2 orders of magnitude).

3.7 REFERENCES

(1) Jiao, Y.; Zheng, Y.; Jaroniec, M.; Qiao, S. Z. Design of Electrocatalysts for Oxygen- and Hydrogen-Involving Energy Conversion Reactions. *Chem. Soc. Rev.* **2015**, *44* (8), 2060–2086.

(2) McCrory, C. C. L.; Jung, S.; Peters, J. C.; Jaramillo, T. F. Benchmarking Heterogeneous Electrocatalysts for the Oxygen Evolution Reaction. *J. Am. Chem. Soc.* **2013**, *135* (45), 16977–16987.

(3) Ge, X.; Sumboja, A.; Wuu, D.; An, T.; Li, B.; Goh, F. W. T.; Hor, T. S. A.; Zong, Y.; Liu, Z. Oxygen Reduction in Alkaline Media: From Mechanisms to Recent Advances of Catalysts. *ACS Catal.* **2015**, *5* (8), 4643–4667.

(4) Wang, S.; Yu, D.; Dai, L.; Chang, D. W.; Baek, J. B. Polyelectrolyte-Functionalized Graphene as Metal-Free Electrocatalysts for Oxygen Reduction. *ACS Nano* **2011**, *5* (8), 6202–6209.

(5) Wang, P.; Zhang, X.; Zhang, J.; Wan, S.; Guo, S.; Lu, G.; Yao, J.; Huang, X. Precise Tuning in Platinum-Nickel/Nickel Sulfide Interface Nanowires for Synergistic Hydrogen Evolution Catalysis. *Nat. Commun.* **2017**, *8*, 1–9.

(6) Li, Y.; Wang, H.; Xie, L.; Liang, Y.; Hong, G.; Dai, H. MoS2 Nanoparticles Grown on Graphene: An Advanced Catalyst for the Hydrogen Evolution Reaction. *J. Am. Chem. Soc.* **2011**, *133* (19), 7296–7299.

(7) Falkowski, J. M.; Surendranath, Y. Metal Chalcogenide Nanofilms: Platforms for Mechanistic Studies of Electrocatalysis. *ACS Catal.* **2015**, *5* (6), 3411–3416.

(8) Zheng, Y.; Jiao, Y.; Jaroniec, M.; Qiao, S. Z. Advancing the Electrochemistry of the Hydrogen-Evolution Reaction through Combining Experiment. *Angew. Chemie - Int. Ed.* **2015**, *54* (1), 52–65.

(9) Zou, X.; Zhang, Y. Noble Metal-Free Hydrogen Evolution Catalysts for Water Splitting. *Chem. Soc. Rev.* **2015**, *44* (15), 5148–5180.

(10) Suen, N.-T.; Hung, S.-F.; Quan, Q.; Zhang, N.; Xu, Y.-J.; Chen, H. M. Electrocatalysis for the Oxygen Evolution Reaction: Recent Development and Future Perspectives. *Chem. Soc. Rev.* **2017**, *46* (2), 337–365.

(11) Wang, D.; Xin, H. L.; Hovden, R.; Wang, H.; Yu, Y.; Muller, D. a.; DiSalvo, F. J.; Abruña, H. D. Structurally Ordered Intermetallic Platinum–cobalt Core–shell Nanoparticles with Enhanced Activity and Stability as Oxygen Reduction Electrocatalysts. *Nat. Mater.* **2012**, *12* (1), 81–87.

(12) Hong, W. T.; Risch, M.; Stoerzinger, K. A.; Grimaud, A.; Suntivich, J.; Shao-Horn, Y. Toward the Rational Design of Non-Precious Transition Metal Oxides for Oxygen Electrocatalysis. *Energy Environ. Sci.* **2015**, *8* (5), 1404–1427.

(13) Guo, S.; Zhang, X.; Zhu, W.; He, K.; Su, D.; Mendoza-Garcia, A.; Ho, S. F.; Lu, G.; Sun, S. Nanocatalyst Superior to Pt for Oxygen Reduction Reactions: The Case of Core/Shell Ag(Au)/CuPd Nanoparticles. *J. Am. Chem. Soc.* **2014**, *136* (42), 15026–15033.

(14) Kong, D.; Cha, J. J.; Wang, H.; Lee, H. R.; Cui, Y. First-Row Transition Metal Dichalcogenide Catalysts for Hydrogen Evolution Reaction. *Energy Environ. Sci.* **2013**, *6* (12), 3553.

(15) Zhou, M.; Wang, H.-L.; Guo, S. Towards High-Efficiency Nanoelectrocatalysts for Oxygen Reduction through Engineering Advanced Carbon Nanomaterials. *Chem. Soc. Rev.* **2016**, *45* (5), 1273–1307.

(16) Wang, S.; Zhang, L.; Xia, Z.; Roy, A.; Chang, D. W.; Baek, J. B.; Dai, L. BCN Graphene as Efficient Metal-Free Electrocatalyst for the Oxygen Reduction Reaction. *Angew. Chemie - Int. Ed.* **2012**, *51* (17), 4209–4212.

(17) Yang, L.; Jiang, S.; Zhao, Y.; Zhu, L.; Chen, S.; Wang, X.; Wu, Q.; Ma, J.; Ma, Y.; Hu, Z. Boron-Doped Carbon Nanotubes as Metal-Free Electrocatalysts for the Oxygen Reduction Reaction. *Angew. Chemie* **2011**, *123* (31), 7270–7273.

(18) Borup, R.; Meyers, J.; Pivovar, B.; Kim, Y. S.; Mukundan, R.; Garland, N.; Myers, D.; Wilson, M.; Garzon, F.; Wood, D.; Zelenay, P.; More, K.; Stroh, K.; Zawodzinski, T.; Boncella, J.; McGrath, J. E.; Inaba, M.; Miyatake, K.; Hori, M.; Ota, K.; Ogumi, Z.; Miyata, S.; Nishikata, A.; Siroma, Z.; Uchimoto, Y.; Yasuda, K.; Kimijima, K. I.; Iwashita, N. Scientific Aspects of Polymer Electrolyte Fuel Cell Durability and Degradation. *Chem. Rev.* **2007**, *107* (10), 3904–3951.

(19) Tang, H.; Wang, D. Molecular Architecture of Cobalt Porphyrin Multilayers on Reduced Graphene Oxide Sheets for High Performance Oxygen Reduction Reaction. *Angew. Chemie* **2013**, *125*, 5695–5699.

(20) Men, B.; Sun, Y.; Li, M.; Hu, C.; Zhang, M.; Wang, L.; Tang, Y.; Chen, Y.; Wan, P.; Pan, J. Hierarchical Metal-Free Nitrogen-Doped Porous Graphene/Carbon Composites as an Efficient Oxygen Reduction Reaction Catalyst. *ACS Appl. Mater. Interfaces* **2016**, *8* (2), 1415–1423.

(21) Suntivich, J.; May, K. J.; Gasteiger, H. a; Goodenough, J. B.; Shao-horn, Y. A Perovskite Oxide Optimized for Molecular Orbital Principles. *Science (80-.).* **2011**, *334* (December), 2010–2012.

(22) Liu, S.; Mu, X.; Duan, H.; Chen, C.; Zhang, H. Pd Nanoparticle Assemblies as Efficient Catalysts for the Hydrogen Evolution and Oxygen Reduction Reactions. *Eur. J. Inorg. Chem.* **2017**, *2017* (3), 535–539.

(23) Liang, Y.; Li, Y.; Wang, H.; Zhou, J.; Wang, J.; Regier, T.; Dai, H. Co3O4 Nanocrystals on Graphene as a Synergistic Catalyst for Oxygen Reduction Reaction. *Nat. Mater.* **2011**, *10* (10), 780–786.

(24) Mao, S.; Wen, Z.; Huang, T.; Hou, Y.; Chen, J. High-Performance Bi-Functional Electrocatalysts of 3D Crumpled Graphene–cobalt Oxide Nanohybrids for Oxygen Reduction and Evolution Reactions. *Energy Environ. Sci.* **2014**, *7* (2), 609–616.

(25) Shu, Y.; Lu, J.; Mao, Q. X.; Song, R. S.; Wang, X. Y.; Chen, X. W.; Wang, J. H. Ionic Liquid Mediated Organophilic Carbon Dots for Drug Delivery and Bioimaging. *Carbon N. Y.* **2017**, *114*, 324–333.

(26) Niu, W. J.; Zhu, R. H.; Yan-Hua; Zeng, H. B.; Cosnier, S.; Zhang, X. J.; Shan, D. One-Pot Synthesis of Nitrogen-Rich Carbon Dots Decorated Graphene Oxide as Metal-Free Electrocatalyst for Oxygen Reduction Reaction. *Carbon N. Y.* **2016**, *109*, 402–410.

(27) Xiao, D.; Yuan, D.; He, H.; Gao, M. Microwave Assisted One-Step Green Synthesis of Fluorescent Carbon Nanoparticles from Ionic Liquids and Their Application as Novel Fluorescence Probe for Quercetin Determination. *J. Lumin.* **2013**, *140*, 120–125.

(28) Wolfbeis, O. S. An Overview of Nanoparticles Commonly Used in Fluorescent Bioimaging. *Chem. Soc. Rev.* **2015**, *44* (14), 4743–4768.

(29) Wang, Y.; Zhu, Y.; Yu, S.; Jiang, C. Fluorescent Carbon Dots: Rational Synthesis, Tunable Optical Properties and Analytical Applications. *RSC Adv.* **2017**, *7* (65), 40973–40989.

(30) Lei, K. W.; West, T.; Zhu, X. Y. Template-Assembly of Quantum Dot Molecules. *J. Phys. Chem. B* **2013**, *117* (16), 4582–4586.

(31) Robel, I.; Kuno, M.; Kamat, P. V. Size-Dependent Electron Injection from Excited CdSe Quantum Dots into TiO2 Nanoparticles. *J. Am. Chem. Soc.* **2007**, *129* (14), 4136–4137.

(32) Favaro, M.; Carraro, F.; Cattelan, M.; Colazzo, L.; Durante, C.; Sambi, M.; Gennaro, A.; Agnoli, S.; Granozzi, G. Multiple Doping of Graphene Oxide Foams and Quantum Dots: New Switchable Systems for Oxygen Reduction and Water Remediation. *J. Mater. Chem. A* **2015**, *3* (27), 14334–14347.

(33) Botz, A. J. R.; Nebel, M.; Rincón, R. A.; Ventosa, E.; Schuhmann, W. Onset Potential Determination at Gas-Evolving Catalysts by Means of Constant-Distance Mode Positioning of Nanoelectrodes. *Electrochim. Acta* **2015**, *179*, 38–44.

(34) Lu, G.; Yang, H.; Zhu, Y.; Huggins, T.; Ren, Z. J.; Liu, Z.; Zhang, W. Synthesis of a Conjugated Porous Co(II) Porphyrinylene–ethynylene Framework through Alkyne Metathesis and Its

Catalytic Activity Study. *J. Mater. Chem. A* **2015**, *3* (9), 4954–4959.

(35) Prodromidis, M. I.; Karayannis, M. I. Enzyme Based Amperometric Biosensors for Food Analysis Enzyme Based Amperometric Biosensors for Food Analysis. **2015**, *4109* (January).

(36) Guo, D.; Shibuya, R.; Akiba, C.; Saji, S.; Kondo, T.; Nakamura, J. Active Sites of Nitrogen-Doped Carbon Materials for Oxygen Reduction Reaction Clarified Using Model Catalysts. *Science (80-.).* **2015**, *351* (6271), 1–24.

(37) Sidik, R. A.; Anderson, A. B.; Subramanian, N. P.; Kumaraguru, S. P.; Popov, B. N. O 2 Reduction on Graphite and Nitrogen-Doped Graphite : Experiment and Theory. *J. Phys. Chem. B* **2006**, *110* (4), 1787–1793.

(38) Sharifi, T.; Hu, G.; Wagberg, T. Formation of Active Sites for Oxygen Reduction Reactions by Transformation of Nitrogen Functionalities in Nitrogen-Doped Carbon Nanotubes. *ACS Nano* **2012**, *10* (6), 8904–8912.

(39) Long, H.; Pivovar, B. Hydroxide Degradation Pathways for Imidazolium Cations : A DFT Study. *J. Phys. Chem. C* **2014**, *118*, 9880–9888.

(40) Park, J.; Nabae, Y.; Hayakawa, T.; Kakimoto, M. A. Highly Selective Two-Electron Oxygen Reduction Catalyzed by Mesoporous Nitrogen-Doped Carbon. *ACS Catal.* **2014**, *4* (10), 3749–3754.

(41) Siahrostami, S.; Verdaguer-Casadevall, A.; Karamad, M.; Deiana, D.; Malacrida, P.; Wickman, B.; Escudero-Escribano, M.; Paoli, E. a; Frydendal, R.; Hansen, T. W.; Chorkendorff, I.; Stephens, I. E. L. S.; Stephens, I. E.; Rossmeisl, J. Enabling Direct H2O2 Production through Rational Electrocatalyst Design. *Nat. Mater.* **2013**, *12* (December), 1137–1143.

(42) Barros, W. R. P.; Wei, Q.; Zhang, G.; Sun, S.; Lanza, M. R. V.; Tavares, A. C. Oxygen Reduction to Hydrogen Peroxide on Fe3O4nanoparticles Supported on Printex Carbon and Graphene. *Electrochim. Acta* **2015**, *162*, 263–270.

(43) Liu, Y.; Quan, X.; Fan, X.; Wang, H.; Chen, S. High-Yield Electrosynthesis of Hydrogen Peroxide from Oxygen Reduction by Hierarchically Porous Carbon. *Angew. Chemie* **2015**, *127*, 6941–6945.

(44) Bonakdarpour, A.; Esau, D.; Cheng, H.; Wang, A.; Gyenge, E.; Wilkinson, D. P. Preparation and Electrochemical Studies of Metal-Carbon Composite Catalysts for Small-Scale Electrosynthesis of H2O2. *Electrochim. Acta* **2011**, *56* (25), 9074–9081.

(45) Wang, A.; Bonakdarpour, A.; Wilkinson, D. P.; Gyenge, E. Novel Organic Redox Catalyst for the Electroreduction of Oxygen to Hydrogen Peroxide. *Electrochim. Acta* **2012**, *66*, 222–229.

(46) Fellinger, T. P.; Hasché, F.; Strasser, P.; Antonietti, M. Mesoporous Nitrogen-Doped Carbon for the Electrocatalytic Synthesis of Hydrogen Peroxide. *J. Am. Chem. Soc.* **2012**, *134* (9), 4072–4075.

(47) Bockris, J. O.; Reddy, A. K. . *Modern Electrochemistry*; Springer Science & Business Media, 1970.

(48) Bockris, J. O.; Reddy, A. K. .; Gamboa-Aldeco, M. *Modern Electrochemistry 2A: Fundamentals of Electrodics*, 2nd Editio.; Kluwer Academic Pubhishers, 2002.

(49) Lefebvre, M. C. Establishing the Link Between Multistep Electrochemical Reaction Mechanisms and Experimental Tafel Slopes. *Mod. Asp. Electrochem.* **1999**, No. 32, 249–300.

(50) Shinagawa, T.; Garcia-Esparza, A. T.; Takanabe, K. Insight on Tafel Slopes from a Microkinetic Analysis of Aqueous Electrocatalysis for Energy Conversion. *Sci. Rep.* **2015**, *5* (August), 1–21.

(51) Bui-Thi-Tuyet, V.; Trippe-Allard, G.; Ghilane, J.; Randriamahazaka, H. Surface and Electrochemical Properties of Polymer Brush-Based Redox Poly(Ionic Liquid). *ACS Appl. Mater. Interfaces* **2016**, *8* (42), 28316–28324.

(52) Ghilane, J.; Hauquier, F.; Lacroix, J. C. Oxidative and Stepwise Grafting of Dopamine Inner-Sphere Redox Couple onto Electrode Material: Electron Transfer Activation of Dopamine. *Anal.*

Chem. **2013**, *85* (23), 11593–11601.

(53) Ghilane, J.; Trippe-Allard, G.; Lacroix, J. C. Grafting of Imidazolium Ion-Terminated Layer Using Electrochemical Reduction of Diazonium: Redox Active Counter Anion Exchange within the Layer. *Electrochem. commun.* **2013**, *27*, 73–76.

(54) Guo, C.; Liao, W.; Li, Z.; Sun, L.; Chen, C. Easy Conversion of Protein-Rich Enoki Mushroom Biomass to a Nitrogen-Doped Carbon Nanomaterial as a Promising Metal-Free Catalyst for Oxygen Reduction Reaction. *Nanoscale* **2015**, *7* (38), 15990–15998.

(55) Zhu, J.; He, C.; Li, Y.; Kang, S.; Shen, P. K. One-Step Synthesis of Boron and Nitrogen-Dual-Self-Doped Graphene Sheets as Non-Metal Catalysts for Oxygen Reduction Reaction. *J. Mater. Chem. A* **2013**, *1* (46), 14700.

(56) Armand, M.; Endres, F.; MacFarlane, D. R.; Ohno, H.; Scrosati, B. Ionic-Liquid Materials for the Electrochemical Challenges of the Future. *Nat. Mater.* **2009**, *8* (8), 621–629.

(57) Snyder, J.; Fujita, T.; Chen, M. W.; Erlebacher, J. Oxygen Reduction in Nanoporous Metal-Ionic Liquid Composite Electrocatalysts. *Nat. Mater.* **2010**, *9* (11), 904–907.

(58) Qiao, M.; Tang, C.; Tanase, L. C.; Teodorescu, C. M.; Chen, C.-M.; Zhang, Q.; Titirici, M. Oxygenophilic Ionic Liquids Promote the Oxygen Reduction Reaction in Pt-Free Carbon Electrocatalysts. *Mater. Horiz.* **2017**, *4*, 895–899.

(59) Martinaiou, I.; Wolker, T.; Shahraei, A.; Zhang, G. R.; Janßen, A.; Wagner, S.; Weidler, N.; Stark, R. W.; Etzold, B. J. M.; Kramm, U. I. Improved Electrochemical Performance of Fe-N-C Catalysts through Ionic Liquid Modification in Alkaline Media. *J. Power Sources* **2018**, *375*, 222–232.

(60) Zhang, G.-R.; Etzold, B. J. M. Ionic Liquids in Electrocatalysis. *J. Energy Chem.* **2016**, *25* (2), 199–207.

(61) Singh, D. K.; Rathke, B.; Kiefer, J.; Materny, A. Molecular Structure and Interactions in the Ionic Liquid 1-Ethyl-3-Methylimidazolium Trifluoromethanesulfonate. *J. Phys. Chem. A* **2016**, *120* (31), 6274–6286.

(62) Barile, C. J.; Tse, E. C. M.; Li, Y.; Sobyra, T. B.; Zimmerman, S. C.; Hosseini, A.; Gewirth, A. a. Proton Switch for Modulating Oxygen Reduction by a Copper Electrocatalyst Embedded in a Hybrid Bilayer Membrane. *Nat. Mater.* **2014**, *13* (6), 619–623.

(63) Costentin, C.; Di Giovanni, C.; Giraud, M.; Savéant, J. M.; Tard, C. Nanodiffusion in Electrocatalytic Films. *Nat. Mater.* **2017**, *16* (10), 1016–1021.

(64) Pensado, A. S.; Malberg, F.; Gomes, M. F. C.; Pádua, A. A. H.; Fernández, J.; Kirchner, B. Interactions and Structure of Ionic Liquids on Graphene and Carbon Nanotubes Surfaces. *RSC Adv.* **2014**, *4* (35), 18017–18024.

(65) Lee, Y.; Suntivich, J.; May, K. J.; Perry, E. E.; Shao-Horn, Y. Synthesis and Activities of Rutile IrO_2 and RuO_2 Nanoparticles for Oxygen Evolution in Acid and Alkaline Solutions. *J. Phys. Chem. Lett.* **2012**, *3* (3), 399–404.

(66) Zhao, Q.; Yan, Z.; Chen, C.; Chen, J. Spinels: Controlled Preparation, Oxygen Reduction/Evolution Reaction Application, and Beyond. *Chem. Rev.* **2017**, *117* (15), 10121–10211.

(67) Chen, D.; Chen, C.; Baiyee, Z. M.; Shao, Z.; Ciucci, F. Nonstoichiometric Oxides as Low-Cost and Highly-Efficient Oxygen Reduction/Evolution Catalysts for Low-Temperature Electrochemical Devices. *Chem. Rev.* **2015**, *115* (18), 9869–9921.

(68) Gu, X. K.; Samira, S.; Nikolla, E. Oxygen Sponges for Electrocatalysis: Oxygen Reduction/Evolution on Nonstoichiometric, Mixed Metal Oxides †. *Chem. Mater.* **2018**, *30* (9), 2860–2872.

(69) Milchev, A. Electrochemical Phase Formation on a Foreign Substrate—basic Theoretical Concepts and Some Experimental Results. *Contemp. Phys.* **1991**, *32* (5), 321–332.

(70) Palomar-Pardavé, M.; González, I.; Batina, N. New Insights into Evaluation of Kinetic Parameters for Potentiostatic Metal Deposition with Underpotential and Overpotential Deposition Processes. *J. Phys. Chem. B* **2000**, *104* (15), 3545–3555.

(71) Rezaei, M.; Tabaian, S. H.; Haghshenas, D. F. Nucleation and Growth of Pd Nanoparticles during Electrocrystallization on Pencil Graphite. *Electrochim. Acta* **2012**, *59*, 360–366.

(72) Conway, B. E.; Tilak, B. V. Interfacial Processes Involving Electrocatalytic Evolution and Oxidation of H2, and the Role of Chemisorbed H. *Electrochim. Acta* **2002**, *47* (22–23), 3571–3594.

(73) Green, T.; Britz, D. Kinetics of the Deuterium and Hydrogen Evolution Reactions at Palladium in Alkaline Solution. *J. Electroanal. Chem.* **1996**, *412* (1–2), 59–66.

(74) Zalineeva, A.; Baranton, S.; Coutanceau, C.; Jerkiewicz, G. Octahedral Palladium Nanoparticles as Excellent Hosts for Electrochemically Adsorbed and Absorbed Hydrogen. *Sci. Adv.* **2017**, *3* (2), 1–11.

(75) Dasgupta, N. P.; Liu, C.; Andrews, S.; Prinz, F. B.; Yang, P. Atomic Layer Deposition of Platinum Catalysts on Nanowire Surfaces for Photoelectrochemical Water Reduction. *J. Am. Chem. Soc.* **2013**, *135* (35), 12932–12935.

(76) Raoof, J. B.; Ojani, R.; Kiani, A.; Rashid-Nadimi, S. Fabrication of Highly Porous Pt Coated Nanostructured Cu-Foam Modified Copper Electrode and Its Enhanced Catalytic Ability for Hydrogen Evolution Reaction. *Int. J. Hydrogen Energy* **2010**, *35* (2), 452–458.

(77) Begum, H.; Ahmed, M. S.; Jeon, S. Highly Efficient Dual Active Palladium Nanonetwork Electrocatalyst for Ethanol Oxidation and Hydrogen Evolution. *ACS Appl. Mater. Interfaces* **2017**, *9* (45), 39303–39311.

(78) Popczun, E. J.; Read, C. G.; Roske, C. W.; Lewis, N. S.; Schaak, R. E. Highly Active Electrocatalysis of the Hydrogen Evolution Reaction by Cobalt Phosphide Nanoparticles. *Angew. Chemie - Int. Ed.* **2014**, *53* (21), 5427–5430.

(79) Tang, K.; Wang, X.; Li, Q.; Yan, C. High Edge Selectivity of In Situ Electrochemical Pt Deposition on Edge-Rich Layered WS2Nanosheets. *Adv. Mater.* **2018**, *30* (7), 1–7.

(80) Mulder, W. H.; Sluyters, J. H.; Pajkossy, T.; Nyikos, L. Tafel Current at Fractal Electrodes. Connection with Admittance Spectra. *J. Electroanal. Chem.* **1990**, *285* (1–2), 103–115.

(81) Pajkossy, T. Impedance of Rough Capacitive Electrodes: The Role of Surface Disorder. *J. Electroanal. Chem.* **1998**, *448* (1), 139–142.

3.8 APPENDICES

Preparation of catalytic ink.

Pt/C and C black NPs inks: The catalytic inks were prepared as followed. 2.8 mg of catalyst (Pt/C or C black NPs) was dispersed in 0.5 ml of 5% Nafion/EtOH under sonication for 30 min. Then 10 µl of as-prepared catalytic ink was drop-casted onto glassy carbon (GC) electrode or poly(VImM) supported GC leading to a coverage density of 0.23 $mg.cm^{-2}$. The film was then dried before use.

Au NPs ink: 100 µL of suspension of Au NPs in toluene was mixed with 250 µL of absolute ethanol followed by addition of 15 µL of Nafion® 117 solution. The as-prepared mixture was sonicated for 3 times ten-minutes. 10 µL of the solution was drop casted onto the glassy carbon electrodes. And the film was dried before use.

C-dots ink: 200 µL of purified suspension of carbon dots was mixed with 500 µL of absolute ethanol followed by addition of 25 µL of Nafion® 117 solution. The as-prepared mixture was sonicated for 3 times ten-minutes. Finally, 10 µL of the solution was drop casted onto the glassy carbon part of a rotating disk electrode. After drying, the catalytic film was homogeneously formed on the electrode and was used for further electrochemical measurements.

Instrumentation.

Electrochemistry: For catalytic performance evaluations, a E7R9 ThinGap Fixed-Disk RRDE tips with 320 µm gap ($A_{GC\ disk}$ = 0.247 cm^2, $A_{Pt\ ring}$ = 0.187 cm^2) was used as working electrode, a stainless-steel mesh and saturated calomel electrode were used as counter electrode and reference electrode, respectively. In all experiments, the potential was converted to Reversible Hydrogen Electrode (RHE) via the following equation:

E (/RHE) = E (/SCE) + 0.241 + 0.059*pH

The electrochemical measurements are controlled with a CHI920C bipotentiostat (CH Instruments, Austin, Texas). For oxygen reduction and evolution reaction measurements, 0.1 M KOH solution was used as electrolyte and bubbled with purified oxygen gas for 30 minutes. During the measurements, the solution was kept under O_2 atmosphere.

The electrochemical tests including cyclic voltammetry, linear sweep voltammetry (LSV), electrochemical impedance spectroscopy (EIS) and scanning electrochemical microscopy (SECM) were performed using CHI920C bipotentiostat (CH Instruments, Austin, Texas).

Spectroscopy: XPS measurements of the modified electrodes were performed using a Thermo VG Scientific ESCALAB 250 system fitted with a micro focused, monochromatic Al Kα (hν = 1486.6 eV) 200 W X-ray source. Infrared spectra were obtained using Fourier-transform infrared spectroscopy (FT-IR) via a Thermoscientific (Nicolet 8700). UV-Visible and Fluorescence measurements were accomplished using a Cary 4000 (Varian) and a Aminco Bowman – Series 2 (Bioritech), respectively.

Microscopy: The distribution in size of the as-prepared carbon dots was obtained via DLS measurements (Zetasizer NanoZS) and TEM image using a JEOL JEM 100CX. The SEM images were taken by MEB-FEG Zeiss (Zeiss SUPRA 40). The AFM investigations were performed in tapping mode at room temperature with a Molecular Imaging PicoPlus.

Supporting data

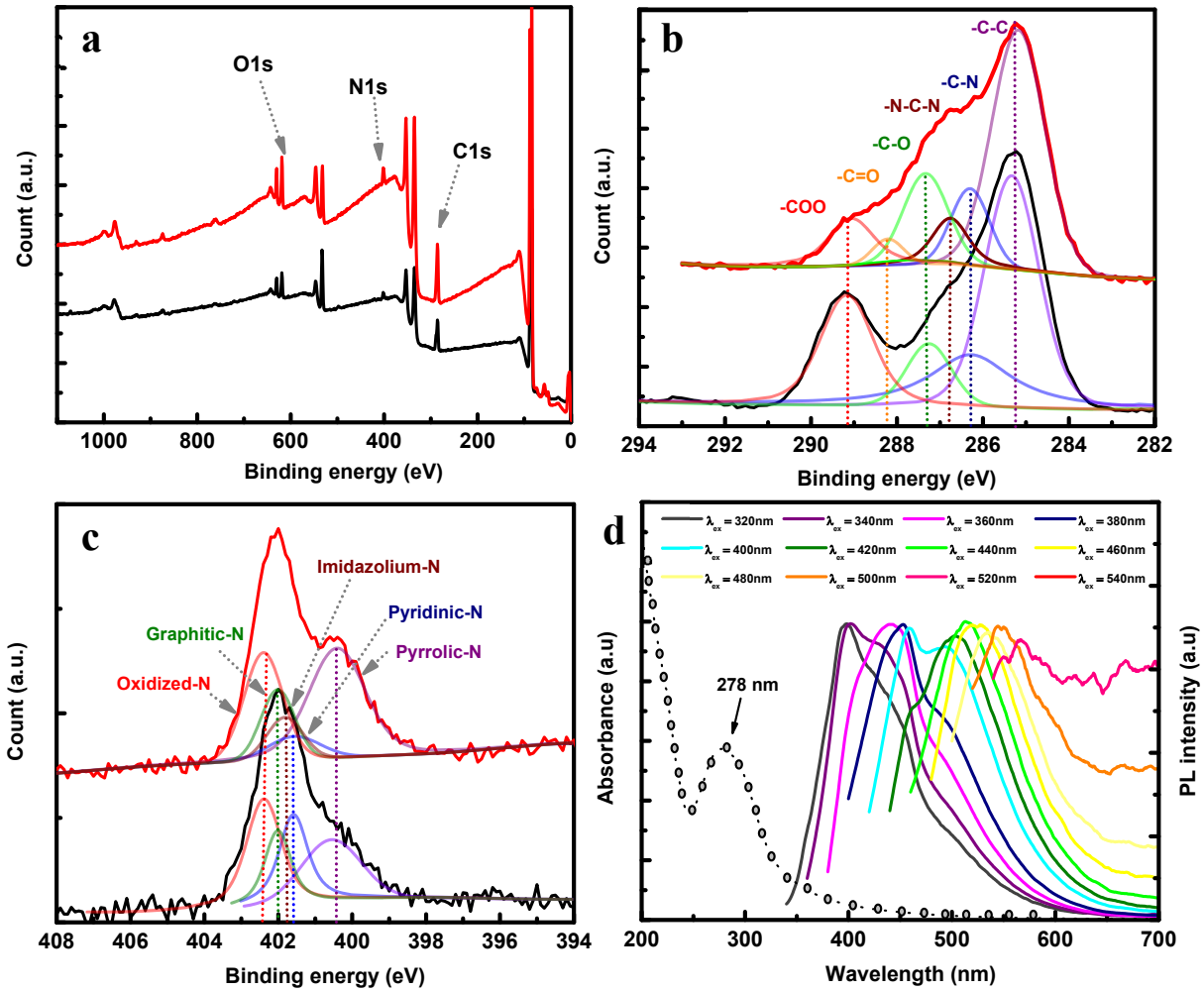

Figure 3.S1 XPS spectra of C-dots 3 (black curves) and Poly(VImM)/C-dots 3 (red curves): ***(a)*** Survey spectrum, ***(b)*** and ***(c)*** corresponding high resolution XPS spectra of C1s and N1s; ***(d)*** UV-Visible and Fluorescence spectra of C - dots -3

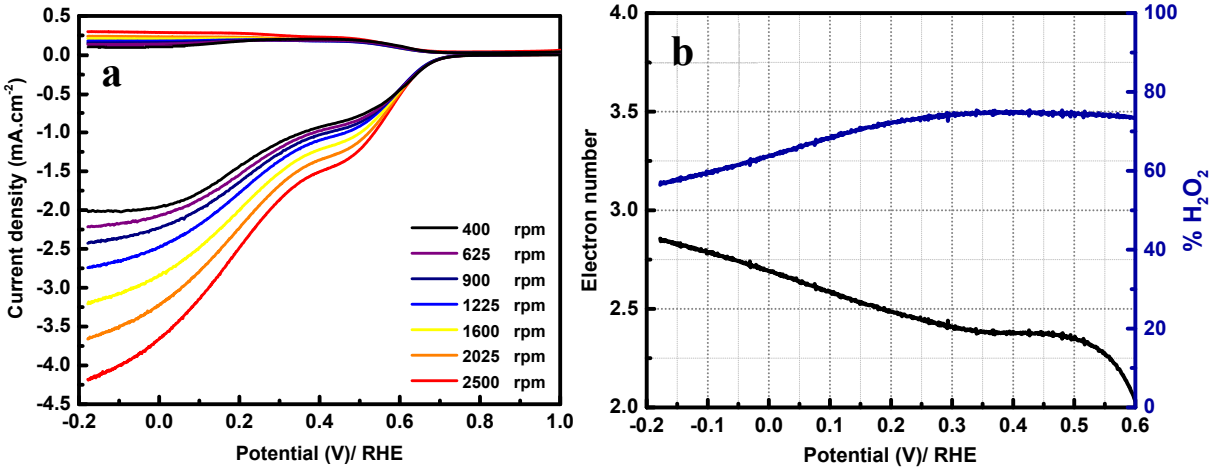

Figure 3.S2 (a) ORR polarization curves using RRDE at different rotations speeds for GC/C-dots 3 in O_2-saturated 0.1 M KOH solution ***(b)*** Evolution of the electron number and $\%H_2O_2$ as function of the potential of GC/C-dots -3 (dark curves)

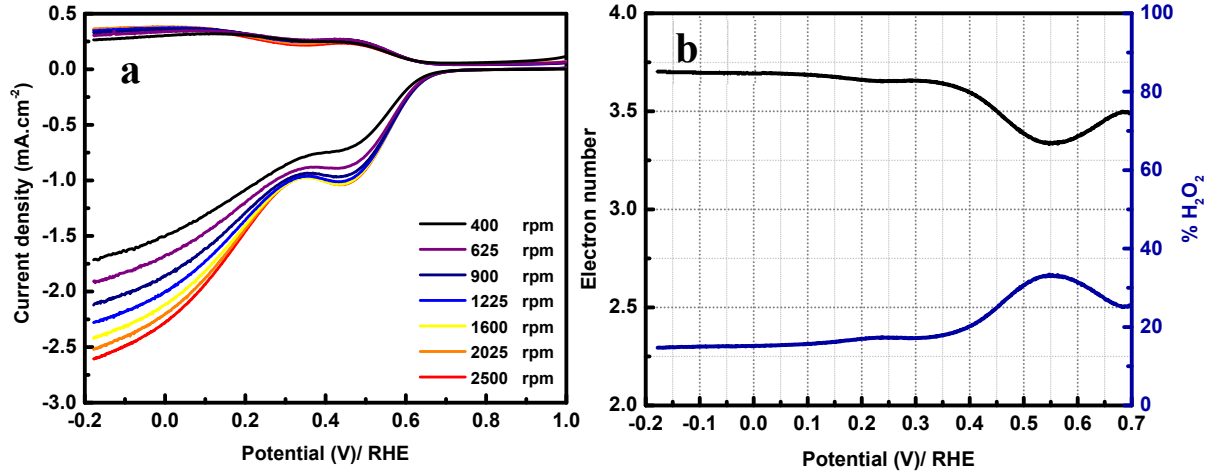

Figure 3.S3 (a) ORR polarization curves using RRDE at different rotations speeds for GC/Poly(VImM)/C - dots -2 in O_2-saturated 0.1 M KOH solution ***(b)*** Evolution of the electron number and $\%H_2O_2$ as function of the potential of (dark curves) GC/Poly(VImM)/C-dots -2

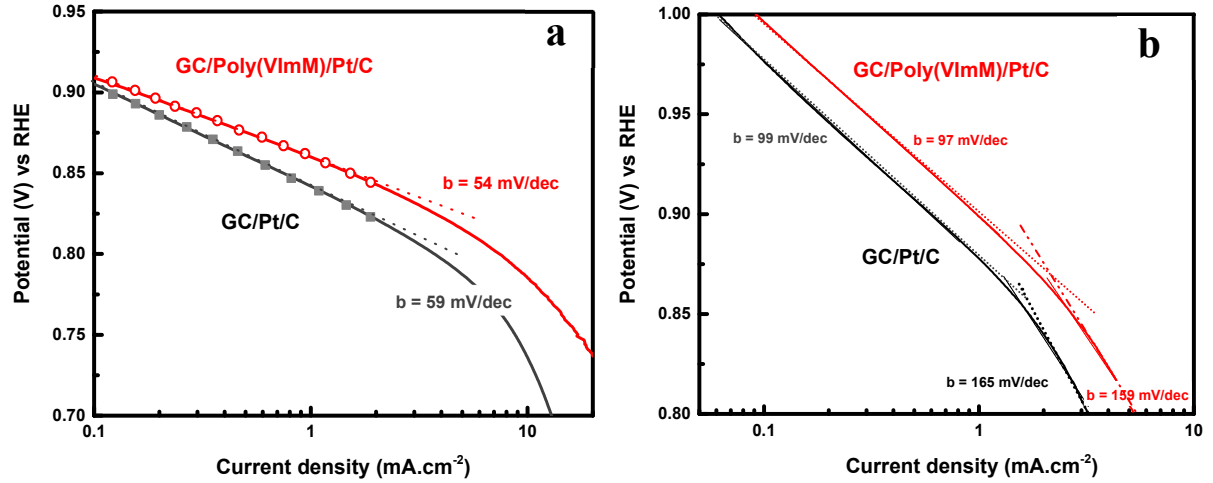

Figure 3.S4 Tafel plot of (red curves) GC/Poly(VImM)/Pt/C and (gray curves) GC/Pt/C in ***(a)*** alkaline conditions and ***(b)*** acidic conditions

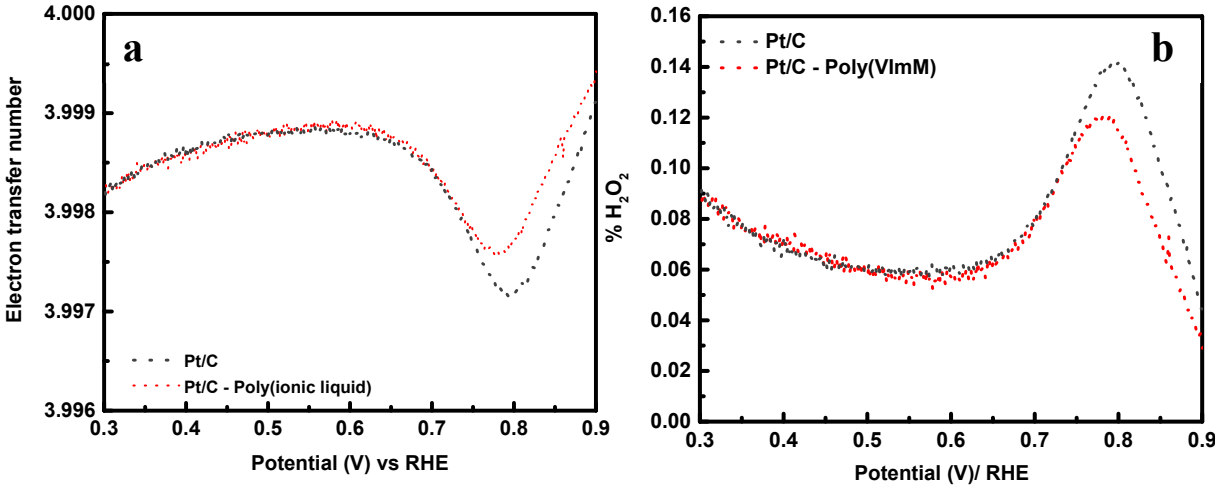

Figure 3.S5 ***(a)*** number of transferred electron and ***(b)*** quantity of hydrogen peroxide produced by (red curves) GC/Poly(VImM)/Pt/C and (gray curves) GC/Pt/C in 0.1 M O_2 – saturated $HClO_4$ solution

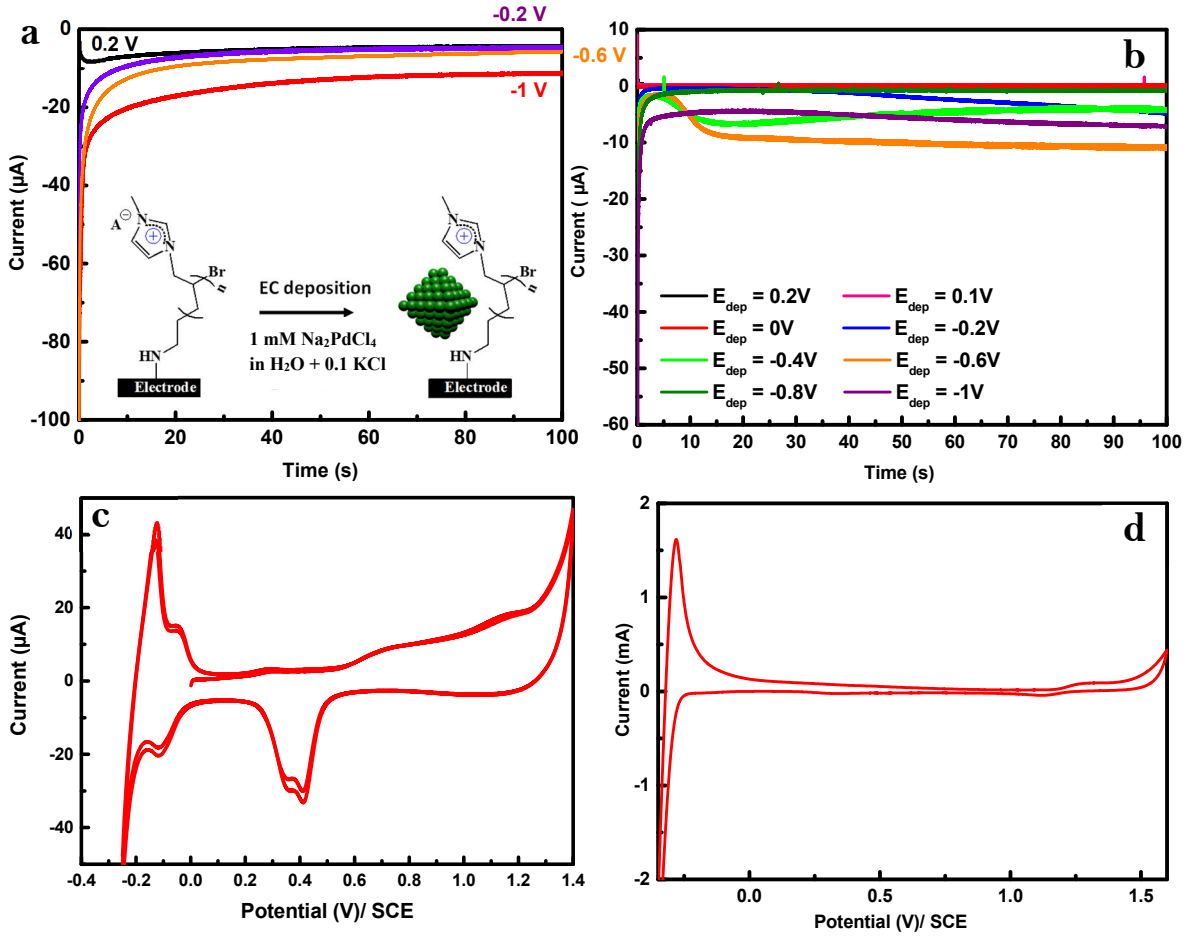

Figure 3.S6 Deposition curves obtained by chronoamperometry at different potentials in aqueous solution containing 0.1 M of KCl and 1 mM of ***(a)*** Na_2PdCl_4 and ***(b)*** K_2PtCl_4; electrochemical signal of ***(c)*** GC/PAMI/Pd NPs deposited at -0.2 V/ SCE and ***(d)*** GC/PAMI/Pt NPs deposited at -0.6 V/ SCE in aqueous solution containing 0.5 M of sulfuric acid.

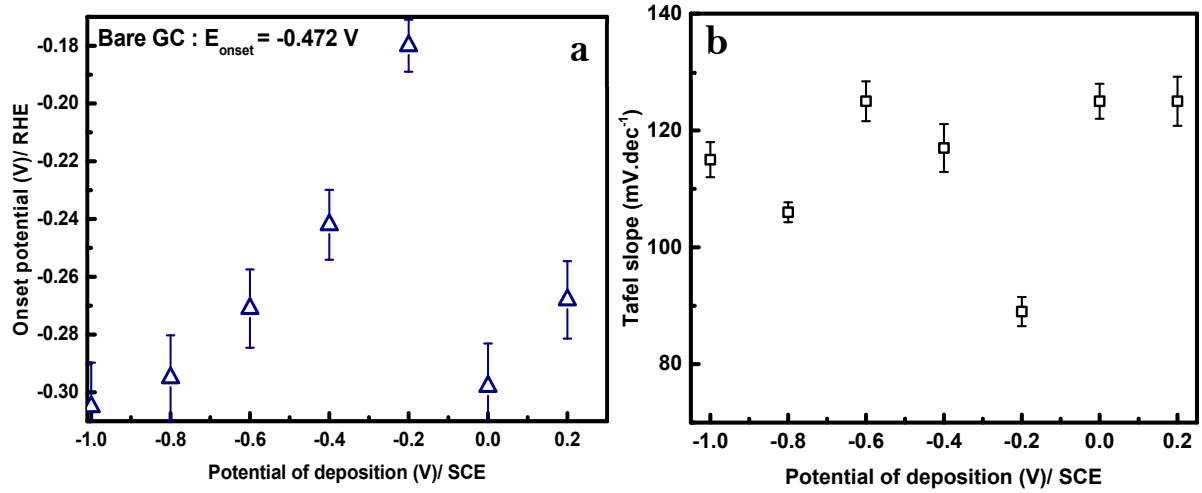

Figure 3.S7 Evolution of ***(a)*** Onset potential and ***(b)*** Tafel slope of GC/PAMI/Pd NPs as function of the deposition potentials.

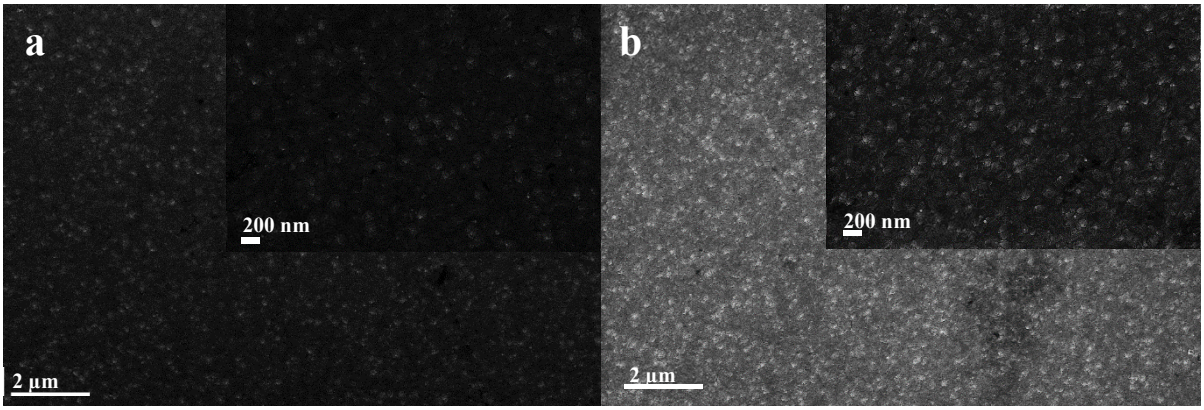

Figure 3.S8 SEM image of ***(a)*** ITO/PAMI/Pd^{exc} NPs deposited at -0.2 V/ SCE and ***(b)*** ITO/PAMI/Pt^{exc} NPs deposited at -0.6 V/ SCE

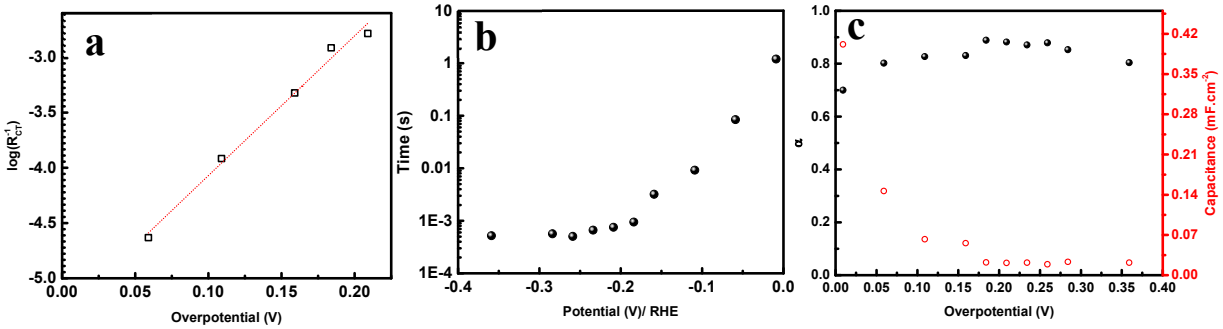

Figure 3.S9 (a) Variation of log(R_{CT}^{-1}) as function of overpotential, ***(b)*** Variation of time (s) in function of potential of the GC/PAMI/Pd^{exc} NPs electrode prepared at -0.2 V/ SCE and ***(c)*** Evolution of capacitance and exponent factor in function of the overpotential.

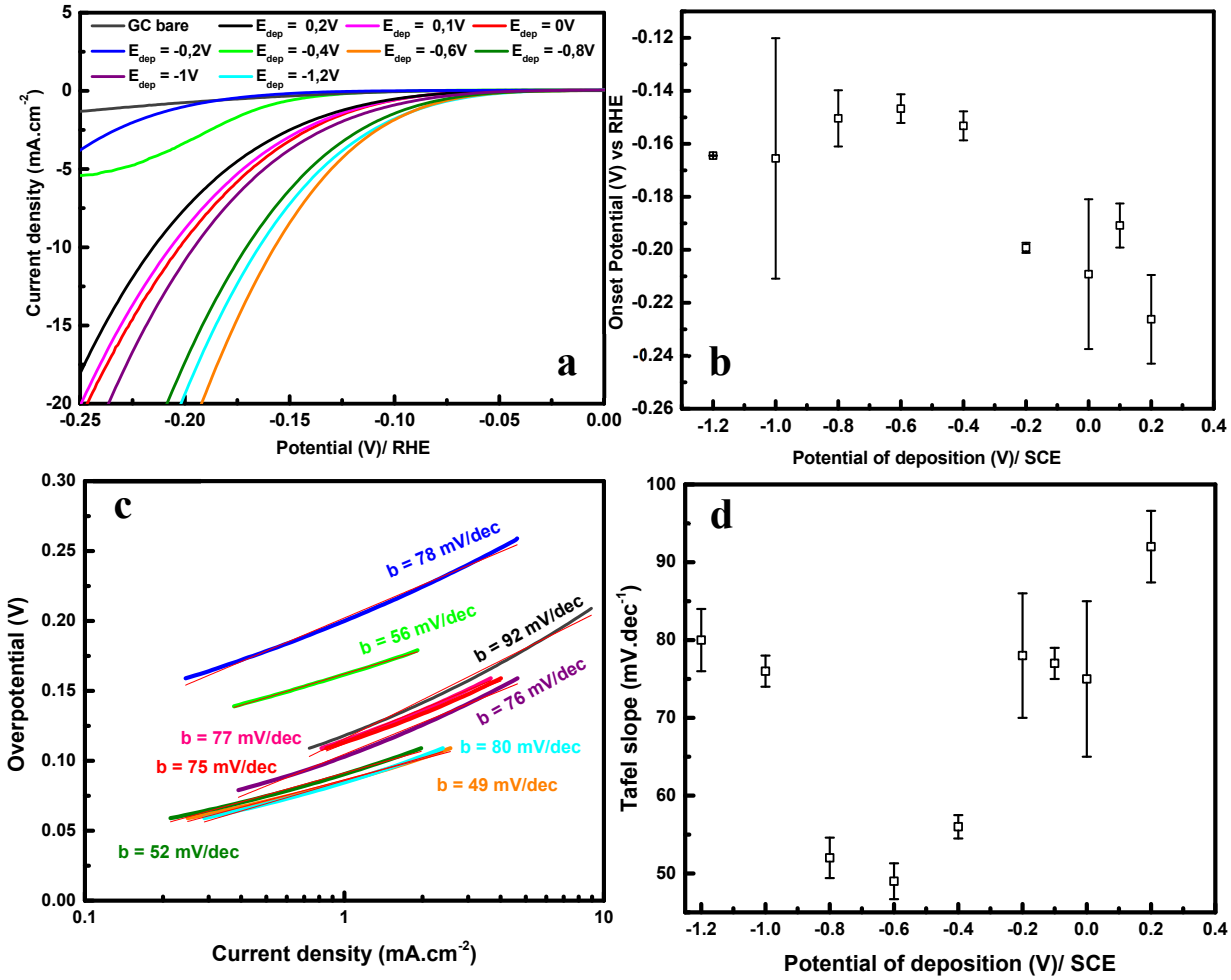

Figure 3.S10 (a) HER polarization curve (LSV) at 10 mV.s^{-1} in 0.5 M H_2SO_4 aqueous solution on GC/PAMI/Pt NPs deposited at different potentials; ***(b)*** Variation of onset potential as function of deposition potential and ***(c, d)*** Tafel slope as function of deposition potential.

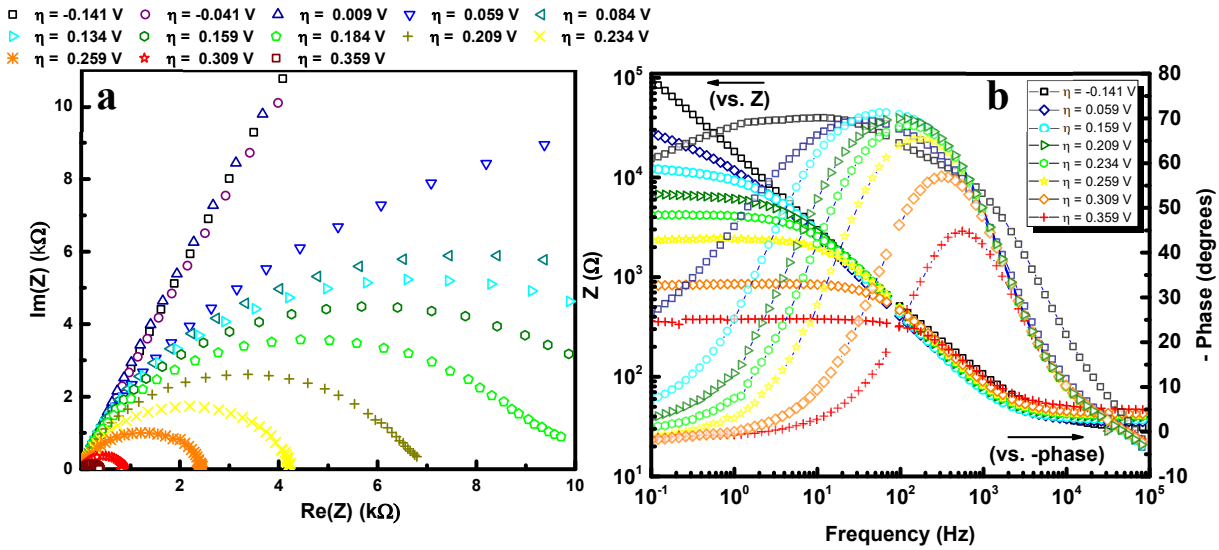

Figure 3.S11 (a) Nyquist plot and ***(b)*** Bode plot at different overpotential towards HER by using GC/PAMI/Pt NPs electrode

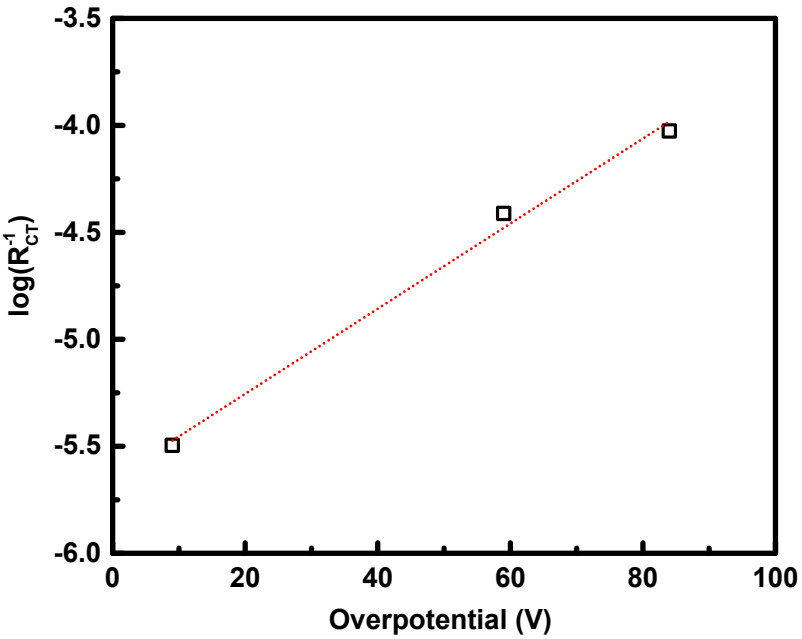

Figure 3.S12 Variation of log(R_{CT}^{-1}) as function of overpotential of the GC/PAMI/Pt^{exc} NPs electrode prepared at -0.6 V/ SCE

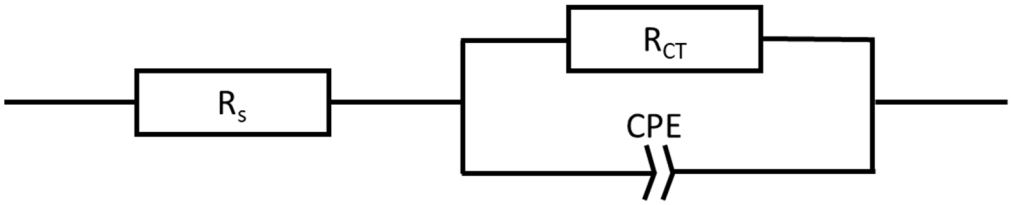

Figure 3.S13 Equivalent circuit using for EIS fitting

CHAPTER 4

SCANNING ELECTROCHEMICAL MICROSCOPY FOR LOCALIZED ELECTROCHEMISTRY: FROM CONVENTIONAL TO PROBE-LESS APPROACH

In this part, the scanning electrochemical microscopy (SECM) will be used to investigate the local electrochemical reactivity of different materials and the effect of surface functionalization. Thus, we purpose to probe the electron transfer properties of a single graphene layer (SGL) and modified SGL deposited onto flexible and insulating material. In addition, the SECM will be used to investigate surfaces bearing ionic liquid molecules including a thin layer and polymer ionic liquid.

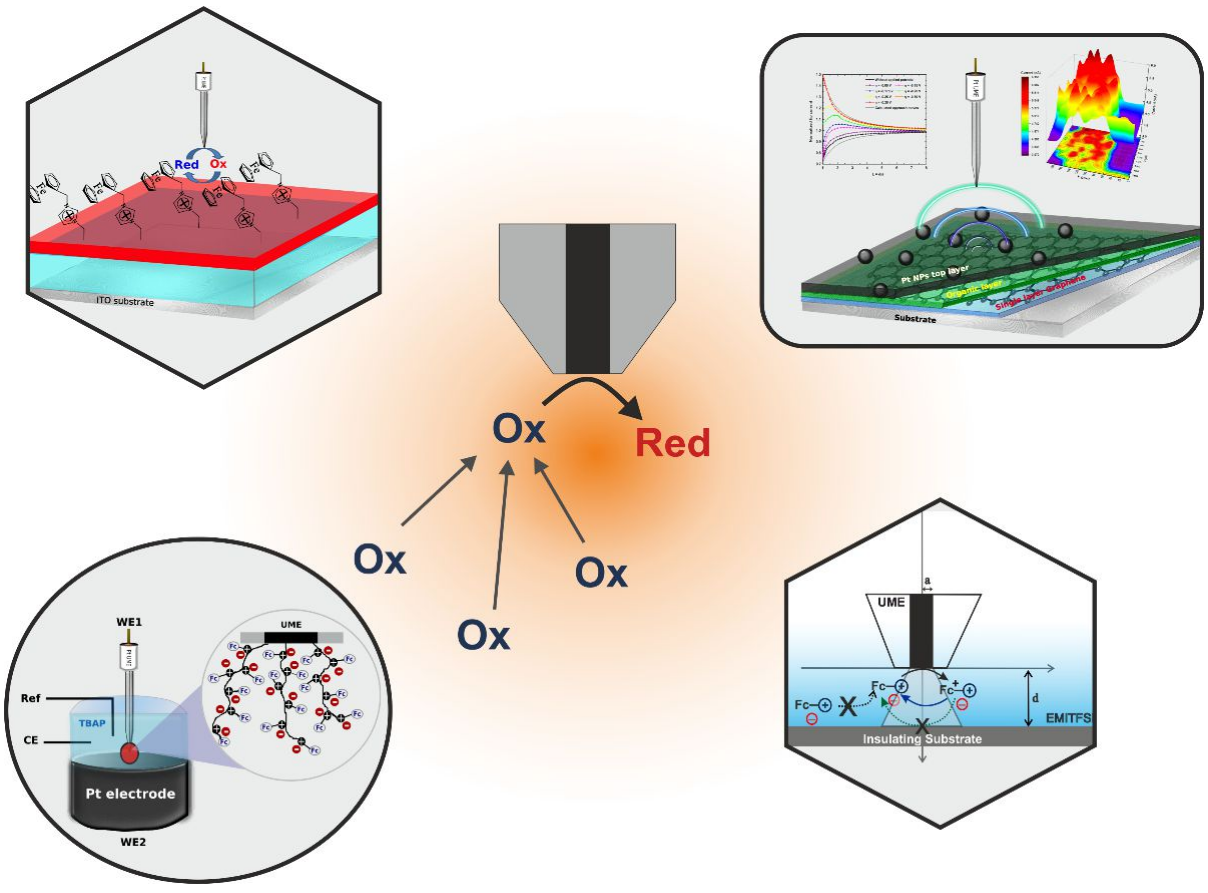

Keywords: scanning electrochemical microscopy (SECM), feedback, rate constant, charge transfer, localized electrochemistry, graphene, (polymer) ionic liquid, redox process, imaging mode.

OUTLINE

4.1 INTRODUCTION AND GENERAL PRINCIPLE OF SCANNING ELECTROCHEMICAL MICROSCOPY

Back to the history, in 1989, A.J. Bard and al[1,2] proposed a new electrochemical technique that provides the possibility to investigate the local electrochemical reactivity of a material (conductive or not) at micro/nanometer scale. This technique consists to measure the variation of the current recorded at an ultramicroelectrode tip, faradaic current, while approaching a surface of interest. The SECM require the use of reversible redox mediator that will ensure the feedback loop to probe the surface[3]. Since then, the SECM has been widely used for studying and resolving multiple problems at the local scale and become extremely powerful tool to study localized reactions in various electrochemical systems[4]. Among the large spectrum of applications, this technique has typically been utilized for investigating the electronic/electrochemical behaviors of diverse materials, for studying nanoparticle at individual level[5] or even for performing surface patterning with complex structures, etc[6].

4.1.1. Ultramicroelectrode

The notion of ultramicroelectrode is referred to electrodes that have a radius ranging from few nanometers to 25 µm. At such small scale, the edge effect is become comparable with the basal plan resulting to the change of the diffusion regime (Figure.4.1). Indeed, the mass transport, by means of diffusion, is high in the absence of convection. Typically, the mass transfer coefficient for a micro-disk electrode is:

$$m_O = \frac{4D}{\pi a} \qquad (4.1)$$

where D ($cm^2.s^{-1}$) is the diffusion coefficient of the O species and *a* is the radius of the electrode.

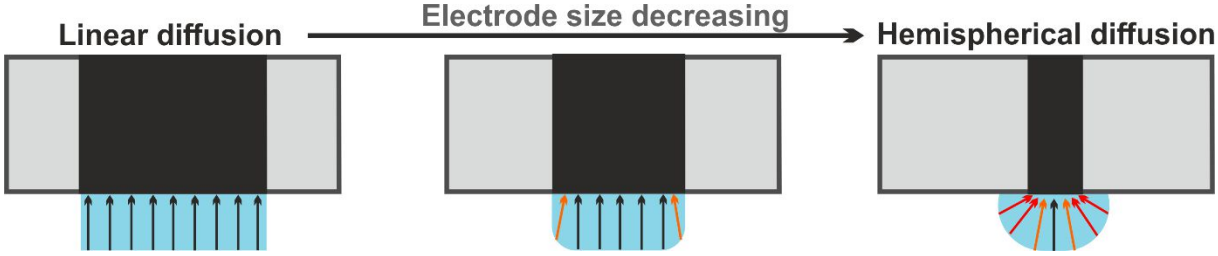

Figure 4.1 Variation of the diffusion regime in function of the electrode size

As a consequence, the current measured at the tip is referred to two-dimensional diffusion which make the system more complicated.

The diffusion is revealed by Fick's second law

$$\frac{i}{nFA} = \frac{\partial C_O(r,z,t)}{\partial t} = D\left(\frac{\partial^2 C_O(r,z,t)}{\partial^2 r} + \frac{1}{r}x\frac{\partial C_O(r,z,t)}{\partial r} + \frac{\partial^2 C_O(r,z,t)}{\partial z^2}\right) \qquad (4.2)$$

where r is referred to the radial displacement and z the linear one (perpendicular to the electrode)

5 boundary conditions are required to obtain solution from Eq.4.2

$$\text{At } t = 0, C_O(r,z,0) = C_{Obulk} \quad (4.3)$$

$$\text{At } x \to \infty, \lim_{x\to\infty} C_O(r,z,t) = C_{Obulk} \quad (4.4)$$

$$\text{At } z \to \infty, \lim_{z\to\infty} C_O(r,z,t) = C_{Obulk} \quad (4.5)$$

$$\text{At } r > a, \left.\frac{\partial C_O(r,z,t)}{\partial z}\right|_{z=0} = 0 \quad (4.6)$$

$$\text{At } r \le a, t > 0, C_O(r,z,t) = 0 \quad (4.7)$$

The solution of the equation (4.2) conducts to the current – time curve as followed:

$i = \frac{4nFAD_OC_{Obulk}}{\pi a} f(\tau) = 4nFD_OC_{Obulk}af(\tau)$ (4.8) with $A = \pi a^2$ for disk electrode and dimensionless term of time $\tau = 4D_Ot/a^2$.

At short time where $\tau < 1$, $\lim_{\tau\to 0} f(\tau) = \infty$, $\lim_{\tau\to 0} i = \infty$ (4.9)

At large time where $\tau > 1$, $\lim_{\tau\to 0} f(\tau) = 1$, $\lim_{\tau\to\infty} i = i_{SS} = 4nFD_OC_{Obulk}a$ (4.10)

From the Eq. 4.10, linear relationship can be obtained between the steady-state current and the diffusion coefficient of the redox species in solution which offer alternative way to Randle – Sevcik equation for measuring D_O value. Besides, by positioning the UME tip to a vertical axis piezo of a SECM setup, it is possible to obtain controllable displacement for investigating the local reactivity over a given substrate with and/or without applied biases. Among the different SECM approaches, two most relevant and popular mode are feedback mode and imaging mode.

4.1.2. Feedback mode

The following argumentation is based on the reduction of $Ox + 1e^- \leftrightarrows Red$. Accordingly, the backward reaction can also be explained in the same manner.

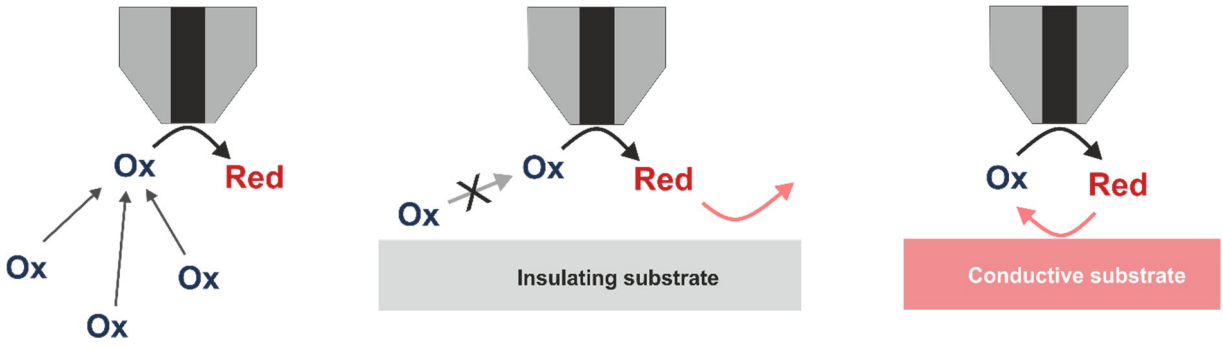

Figure 4.2 Working principle of SECM feedback mode; ***(a)*** semi-spherical diffusion far from the substrate, ***(b)*** blocking of diffusion provokes by insulating substrate and ***(c)*** Feedback loop at a conductive substrate.

The feedback mode consists to measure the current at the UME tip in function of the distance to the substrate to reveal the electronic/ electrochemical behaviors of the probed substrate. Indeed, far from the substrate (typically distance 4 times higher than the UME radius), the microelectrode is remained under steady-state conditions by semi-spherical diffusion resulting to a plateau (limiting current).

Close to the substrate, two possible extreme situations can occur. By approaching to an insulating substrate, the limiting current decreases exponentially with the distance, i.e. negative feedback, issue from the hindrance of the diffusion of the redox mediator from the bulk to the tip surface.

Theoretical evolution of the normalized tip current ($I_T(L) = i_T/i_{T,\infty}$) in function of the normalized distance L = d/a is

$$I_T(L) = \frac{i_{lim,L}}{i_{lim,L=\infty}} = \left[A + \frac{B}{L} + C.\exp\left(\frac{D}{L}\right) \right]^{-1} \quad (4.11); A - D = \text{Values depending on RG} = \frac{r_{electrode}}{a}$$

Contrarily, at a conductive surface, with or without applying potential, the vacancies localized at the surface of the substrate are involved in the oxidation process, i.e, the Red is oxidized into Ox which diffuses back to the UME resulting an electrochemical reaction loop. As a consequence, the UME current increases when the tip approaches the substrate producing a positive feedback (Figure 4.3).

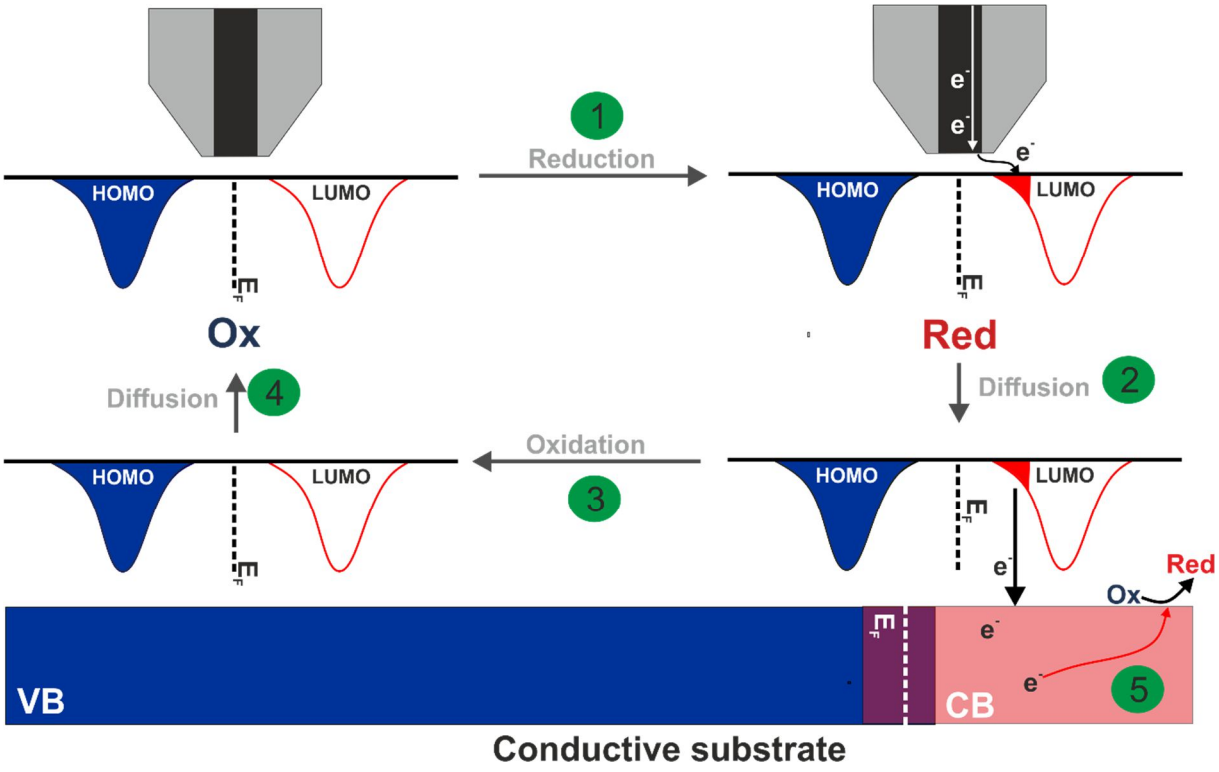

Figure 4.3 Working principle of SECM feedback mode on conductive substrate.

For Ox species used as mediator in solution, the positive feedback loop is ensured by the 5 following steps:

1st step: Generation of Red species by the UME tip;

2nd step: Diffusion of Red to the vicinity of the substrate;

3rd step: Electronic exchange with the substrate to generate Ox (illustrated in the Fig. 4.3);

4th step: Diffusion of Ox back to the tip;

5th step: Propagation of electron inside the substrate and backward reaction to ensure the electroneutrality.

Apparently, the diffusion of the redox molecules within the layer is strongly enhanced (Eq. 4.16).

$$i_{lim} = nFAm_O C_{Obulk} \tag{4.12}$$

$$m_O = \frac{i_{lim}}{nFAC_{Obulk}} \tag{4.13}$$

where

$$I_T(L) = \frac{i_{lim,L}}{i_{lim,L=\infty}} = k_1 + \frac{k_2}{L} + k_3.\exp(\frac{k_4}{L}); k_1 - k_4 = \text{Values depending on RG};\ k_4 < 0 \tag{4.14}$$

with L = d/a, which conducts to the distance – dependence relationship of mass transport coefficient

$$m_O = \frac{I_T(L)}{\pi a^2 nFC_{Obulk}} = \frac{4D_O}{\pi a}\left[k_1 + \frac{k_2}{L} + k_3.\exp(\frac{k_4}{L})\right] \tag{4.15}$$

$$\text{thus at } L \to 0, \lim_{L\to 0}\left[m_O(L)\right] = \infty \tag{4.16}$$

Consequently, the feedback mode allows probing the heterogeneous electron transfer kinetic at various substrate surfaces including conductors and semiconductors.

4.1.3. Imaging mode

In addition to the capability of probing the reactivity at one spot of the surface, the SECM allows to obtain an electrochemical reactivity map of the substrate. An SECM image can be obtained by scanning the UME tip in x – y plane and following the variation of the tip current as function of the tip location or following the variation of the z – values as function of tip location, so-called constant height and constant current mode, respectively[7]. Regardless to the selected mode, the recorded data reflect the heterogenous electron transfer rate occurred at the substrate. In this manner, a reactivity and/or conductivity map of the surface is constructed. As discussed in the previous part about the diffusion of the species from and to the tip, the resolution of the SECM technique is governed by the distance tip – substrate and the size of the microelectrode, which determined the diffusion layer. Theoretically, the resolution provides by a microelectrode is at least equal to its diameter.

4.2 SCANNING ELECTROCHEMICAL MICROSCOPY FOR FOLLOWING THE DOPING LEVEL OF GRAPHENE

Graphene supported flexible and transparent electrodes have been widely investigated using multidisciplinary approaches leading to their employment in optoelectronic devices as dye sensitized solar cell (DSSC)[8,9], electrochromic devices[10], organic light emitting diode (OLED)[11,12] and electrocatalysis[13]. However, the understanding of the local reactivity of single layer graphene (SLG) in solution is still restricted. Indeed, the control of the electrical double layer and the heterogeneous electron transfer processes at this interface are the key factor enabling further potential applications. The latter can be modulated by surface modification enabling the introduction of defects onto the graphene structure. It has been demonstrated, in the earlier reports, that the introduction of small concentrations of defects to the highly oriented pyrolytic graphite (HOPG) enhances the electron transfer kinetic up to 3 orders of magnitude[14]. As a consequence, among various surface functionalization approaches the electrochemical reduction of diazonium was widely studied for modifying carbon-based materials such as carbon nanotubes (CNTs)[15,16] and graphene[17]. This surface modification generates π-conjugated system breaking due to the formation of C sp^3 via C-C covalent bonds between the substrate and the organic layer. As an example, the introduction of nitrophenyl group to graphene/SiO_2 substrate, via spontaneous reduction, enhances the conductivity of the material when compared to pristine graphene[18].

Being known in the literature, SECM has been used for preparing well-defined patterns onto various substrates or studying the reactivity of a large number of materials, including carbon-based substrates[19]. The most relevant report investigating the role of the imperfections of chemical vapor deposition (CVD) graphene using scanning electrochemical microscopy (SECM) was performed by Abruna's group[20]. This work focused on the passivation of the defects by grafting a thin polymer layer. The authors have demonstrated that the defect density caused an increase of the electrochemical reactivity of the electrode material. Besides that, the SECM was used for the analysis and the patterning of graphene materials[21]. Even though recent advancements, the investigations of local electrochemical properties of single layer graphene deposited on insulating substrate are still scanty.

Single layer graphene (SLG) is an important 2D materials for both electron transport (high conductance) and electron transfer (heterogeneous catalysis), which make it qualified as an electrode material in both basic electrochemical investigations and applications including energy conversion and storage devices. Within this part, we report the electrochemical behaviors of single layer graphene/ethylene vinyl acetate/polyethylene terephthalate (SLG/PET) plastic film. Our approach consists to follow the local electrochemical reactivity of SLG/PET by using SECM configuration. Next, different surfaces functionalization scheme, from destructive approach by electrochemical reduction of the diazonium group to non-destructive approach via the drop casting of metal nanoparticles onto the SLG/PET substrate

were performed. The electron transfer properties of the SLG/PET as a function of the surface modification manners were investigated. This work was accomplished via a collaboration with the Prof. Z. Liu from Beijing Graphene Institute (BGI)[1] - Pekin University who provides the SLG/PET substrate.

4.2.1 Local reactivity of SLG/PET using SECM

Graphene/nanowire/plastic films were fabricated by a continuous large-scale roll-to-roll production of transparent conductive electrodes. The preparation procedure of SLG/NWs/EVA/PET (SLG/PET) and the characterizations of this material were reported in previous work[22]. Briefly, the continuous graphene film was grown on copper foil (5 cm x 5 m) using roll-to-roll (R2R) low-pressure chemical vapor deposition (CVD) method. In parallel, metal NWs (Ag or Cu) were coated onto EVA/PET (50 mm/75 mm) where EVA was treated by air plasma to increase the hydrophilicity of the film for having a good metal NWs dispersion. Then the graphene grown on Cu foil was hot laminated onto metal NWs mesh/EVA/PET forming unique laminated structure at 100 °C by using two rollers providing good adhesion and homogeneous film with minimum air traps. Finally, the graphene film was roll-to-roll delaminated from the copper foil by electrochemical bubbling delamination transfer method resulting to the formation of SLG/NWs/EVA/PET continuous film (5 cm x 5 m) with low defect density (I_D/I_G = 0.05 Fig 4.4c) and recycled copper foil (Scheme 4.1)[22].

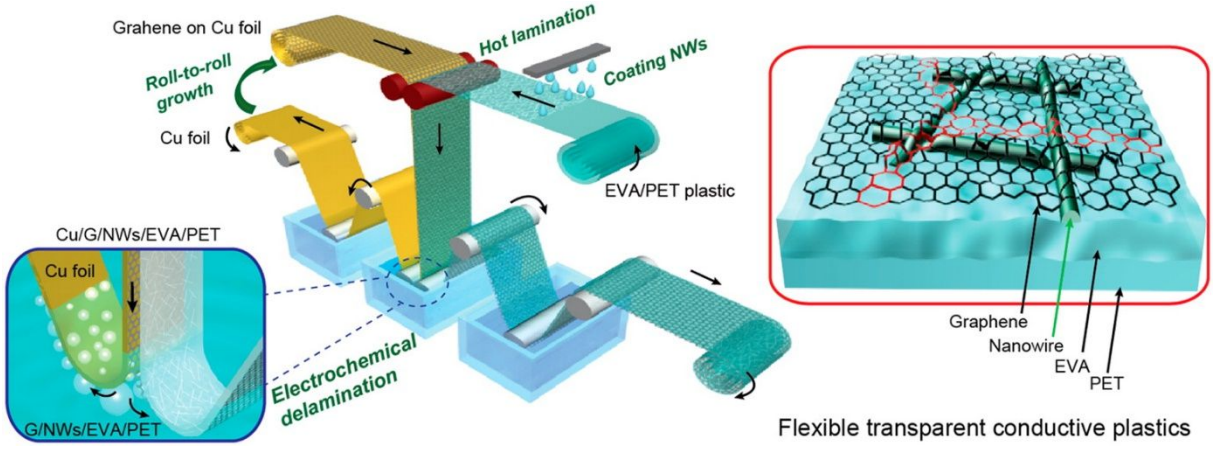

Scheme 4.1 Schematic and structure of graphene and metal nanowire hybrid films produced by a continuous roll-to-roll process.

The diameter of an individual Ag NWs is about 35 nm, and the graphene on PET sheet resistance was found to be ranged from 10 to 50 Ω/sq[22]. The generated SLG/PET was characterized using scanning electron microscopy (SEM) image, optical microscopy (OM) image and Raman spectroscopy as shown in Fig.4.4. All those characterizations clearly identify that the graphene is high-quality monolayer[22].

[1] http://bgi.tucoo.net/en/about-bgi-en/who-we-are/

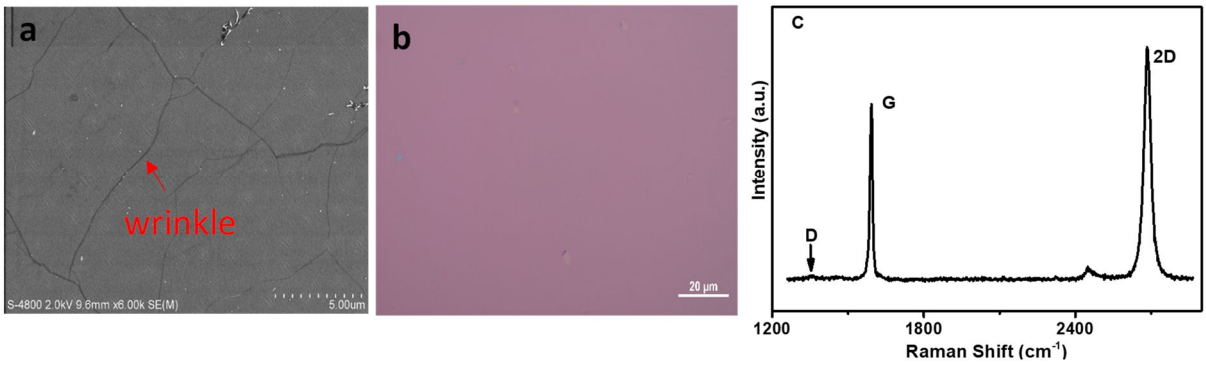

Figure 4.4 Characterization of graphene. ***(a)*** Scanning Electron Microscopy (SEM) image of SLG/PET; ***(b)*** Optical Microscopy (OM) image; ***(c)*** Raman spectrum. All those characterizations clearly identify that the graphene is high-quality monolayer[22].

As a starting point of this work, the pristine SLG/PET was electrochemically characterized by sweeping the potential in between 0.6 V and -1.5 V vs Fc^+/Fc in acetonitrile (MeCN) solution containing 1 mM of Fc and 0.1 M of $TBAPF_6$. As shown in Fig. 4.S1, only the reduction peak can be observed at -0.5 V corresponding to an extremely high ΔE (>1V) which is distorted from the conventional Nicholson and Shain theory[23]. From the cyclic voltammetry results, there is no doubt that SLG/PET presents a slow electron transfer process at a large electrode scale. For getting further information about the local heterogeneous electron transfer (HET) at the SLG/PET, SECM in feedback mode was performed in the presence of electron acceptor (TCNQ) or electron donor (Fc) redox couples.

Figure 4.5 shows a typical approach curves recorded onto unbiased SLG/PET using Fc as mediator. The curves show current decrease when the tip approaches the substrate suggesting either the absence of regeneration of the mediator or the presence of slow electron transfer rate at the SLG/PET surface.

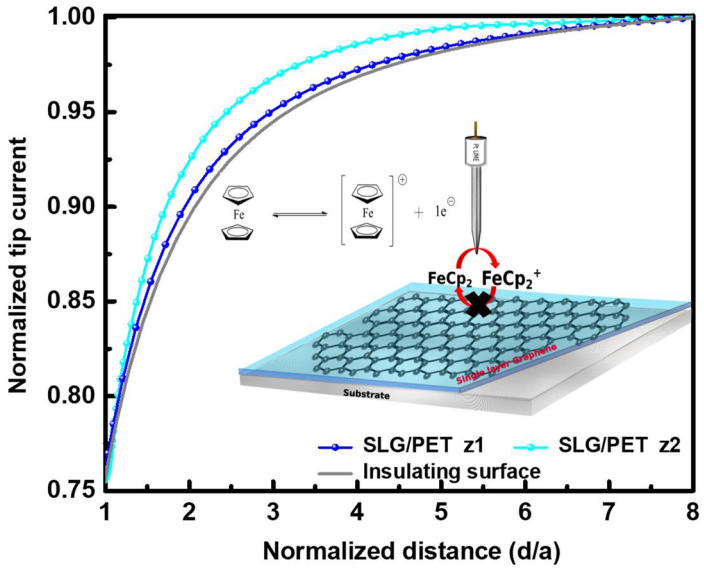

Figure 4.5 Approach curves onto SLG/PET using Fc as mediator (blue and cyan).

The SECM approach curves were recorded at different substrate locations and two behaviors were observed. The first one (blue curve) corresponds to a total negative feedback behavior suggesting the absence of the regeneration of the mediator and that the SLG/PET behave as an insulating surface toward the reduction of the ferrocenium to ferrocene. This curve matches perfectly with the theoretical approach curve expected for an insulating surface (solid line). The second behavior (cyan curve) displays a current decrease while the UME approaches the substrate but shows a deviation when compared to the expected negative feedback. This deviation highlights the existence of a slow regeneration of the ferrocene at the SLG/PET substrate and the curve fitting leads to extract the apparent electron transfer rate (k_{app}), which is found in the range of 10^{-4} cm.s^{-1} [24,25]. The SECM investigations using ferrocene as mediator lead to distinguish two areas with different local electrochemical reactivity. As known in the literature, the presence of metal on the under layer of graphene could provide an n-doped state of the graphene layer implying band-gap opening[26]. As a result, depending on the density of the metal NWs under the graphene sheet, the doping density differs between different graphene domains.

To get further insight, different biases were applied to the SLG/PET substrate with the aim to evaluate the impact of the driven force on the heterogeneous electron transfer (HET) at the surface (Fig.4.6). At overpotential η = applied potential – $E^0_{mediator}$ > -0.6 V, all the approach curves display a decrease of the measured current when the tip approach the substrate with an apparent electron transfer rate ranged between 10^{-4} and 10^{-3} cm.s^{-1}. The latter increases when the over potential become more negative, highlighting an accelerate electron transfer rate constant of the reaction ferrocenium to ferrocene at the SLG/PET surface. Further increase of the applied overpotential to the SLG/PET electrode induces a change of the shape of the approach curve and reaches a total positive feedback for an overpotential value around -1.4 V. This transition was observed at around η = -0.65 V. Two possibilities can explain this behavior either the electron donor properties of the electrode, upon applying negative potential, become dominant by enhancing the n-doping behavior of the graphene layer or the favorable evacuation of the generated hole at the interface. Both hypotheses conduce to an increase of the electron transfer (>10^{-2} cm.s^{-1} at -0.65 V) which is coherent with previous results[20]. Based on the Butler-Volmer model, the electron transfer rate reaction is linked to the overpotential via Eq.4.17:

$$k_f = k^0 . \exp\left(\frac{\alpha F}{RT} . \eta\right) \quad (4.17)$$

Inset in Fig. 4.6 shows a linear variation of ln(k) as a function of the overpotential. Thus, the intercept at η = 0 V gives the electron transfer rate at the standard potential of Fc which is found to be k^0 = 6. 10^{-4} cm.s^{-1} and the calculated charge transfer coefficient is α = 0.1. In general, the α value ranges from (0.3 – 0.7), however, a low value has already been reported

on modified electrode and was attributed to a pinhole in the self-assembled monolayer (SAM) and to the presence of defect and impurities within the graphene[27–30].

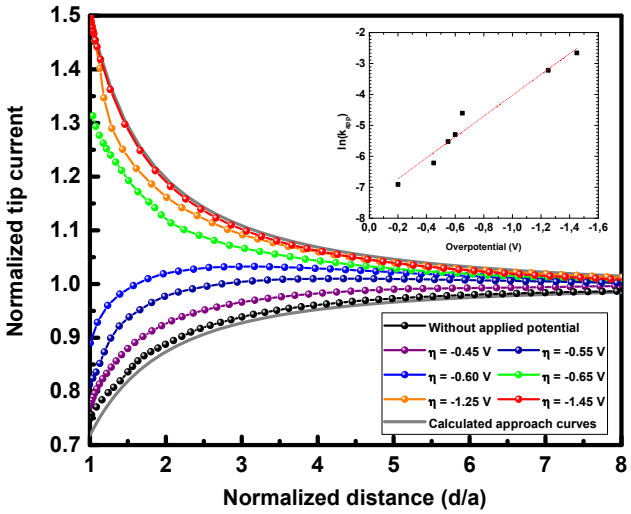

Figure 4.6 Approach curves onto biased graphene substrate: w/o bias (black), η = -0.45 V (purple), -0.55 V (dark blue), -0.60 V (blue), -0.65 V (green), -1.25 V (orange) and -1.45 V (red). (inset) Ln (k_{app}) in function of overpotential. Grey curves represent theoretical approach curves onto insulating and conducting substrates.

In order to get more information on the electronic properties of SLG/PET, the SECM response at the graphene substrate was investigated in the presence of reducing mediator, TCNQ (E^0 = - 0.5 V vs Fc^+/Fc). Similar to the case of ferrocene, the approach curves with the TCNQ on the SLG/PET were recorded on different substrate location and display two different shapes depending on the probed area. As illustrated in Fig. 4.7a, the screening of the SGL/PET surface shows either a total positive (red curve) or negative feedback (black curve).

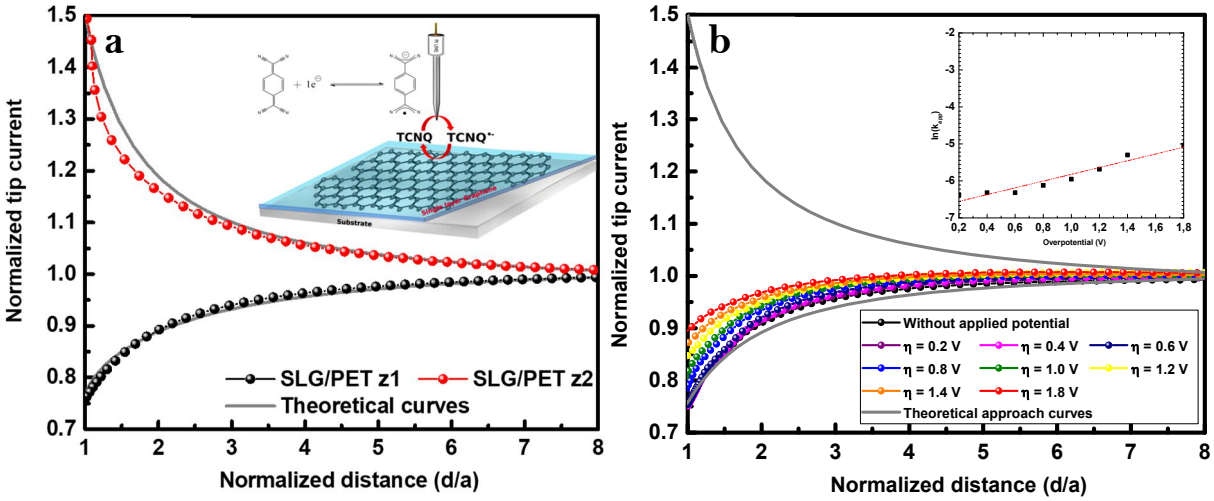

Figure 4.7 (a) Approach curves onto SLG/PET using TCNQ as mediator (black and red), ***(b)*** approach curves onto biased graphene substrate: w/o bias (black), η = 0.2 V (purple), 0.4 V (magenta), 0.6 V (dark blue), 0.8 V (blue), 1 V (green), 1.2 V (yellow), 1.4 V (orange) and 1.8 V (red). (inset) log (kapp) in function of overpotential. Grey curves represent theoretical approach curve onto insulating and conducting substrates.

In the zone z1, (black curve) the oxidation of $TCNQ^{\bullet-}$ at the substrate is not favored providing a total negative feedback. However, by changing to the area z2 (red curve) a positive feedback was observed with a k_{app} = 2. 10^{-2} $cm.s^{-1}$. The obtained results might be related to the variation of the n-doped density of the graphene layer which is linked to a non-homogeneous dispersion of the metal NWs mesh. In addition, the approach curves are performed in the same area using Fc followed by the TCNQ as redox probe. Interestingly, it was found that the positive feedback with the TCNQ correspond to the area where the Fc exhibits a total negative feedback, while the negative feedback obtained with the TCNQ correspond to the area where the Fc shows a slow electron transfer at the SGL/PET. All these results suggest the presence of correlation between the response of Fc and TCNQ on the probed area highlighting the presence of two doping level within the graphene layer.

Besides that, different biases (from 0.2 V to 1.8 V) were applied to the substrate and the corresponding approach curves at the location z1 (Fig. 4.7b) were recorded given intermediate feedback with a k^0 = 1.2. 10^{-3} $cm.s^{-1}$ and α = 0.024 (Fig. 4.7b Inset). The low charge transfer coefficient reflects is the presence of another factor that inhibits the electron transfer at the graphene surface, i.e. the structure of the interface graphene/electroactive species/solution.

Indeed, the TCNQ with aromatic ring has been reported to be able to generate π-π stacking interaction with the graphene producing a graphene/TCNQ complexes[31,32]. It was demonstrated that the adsorption of TCNQ induced by long-range Coulomb interactions results to close-packed island aggregations of this molecule at the graphene/insulator surface[33]. Therefore, the electron abundant of TCNQ and/or $TCNQ^{\bullet-}$ can be delocalized to the π – conjugated system of SLG generating an n-doped layer of TCNQ at the interface that acts as a barrier toward the electrochemical oxidation of $TCNQ^{\bullet-}$ generated at the tip. In the following, the impact of surface modification on the electron transfer properties at the local scale will be investigated.

4.2.2 Surface modification of SLG/PET and SECM investigations

The surface modification of graphene was performed by grafting an organic layer through the electrochemical reduction of p-nitrophenyl diazonium. By sweeping the potential between 0.3 V and -1.25 V vs Ag|AgCl in acetonitrile solution containing 1 mM of p-nitrophenyl diazonium and 0.1 M of $TBAPF_6$, a reduction peak is observed at -0.6 V corresponding to the reduction of diazonium group (Fig. 4.8a).

The current density decreases upon continuous cycling suggesting the formation of the organic layer at the surface and the blocking effect induced by the organic film (Fig. 4.8a)[34,35]. Next, the modified electrode was characterized by electrochemistry in acidified MeCN (0.1 M sulfuric acid). As shown in Fig. 4.8b, by sweeping the potential to -1.8 V vs Ag|AgCl in acidic media, the attached nitro groups ($R\text{-}NO_2$) were reduced to amine groups ($R\text{-}NH_2$) and substituted hydroxylamine groups (R-NHOH) via 6 and 4 (H^++4e^-) pathways, respectively[36].

For the anodic side, a redox signal was observed at E^0 = 0.35 V corresponding to the reversible electrochemical response of hydroxylamine/nitroso redox couple ($2e^- + 2H^+$)[37]. The electrochemical characterization confirms the occurrence of the grafting of nitro-phenyl layer onto SLG.

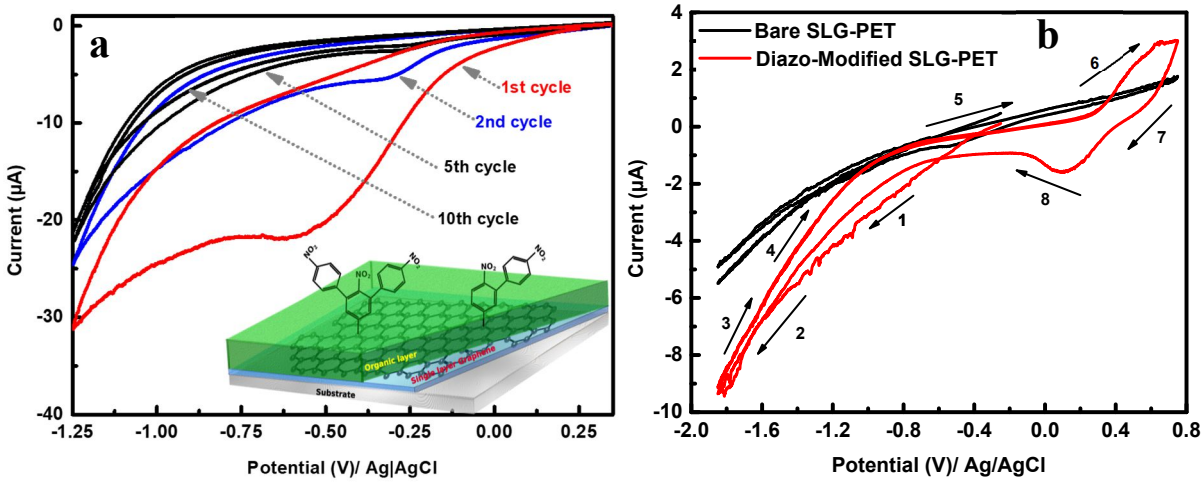

Figure 4.8 ***(a)*** Cyclic voltammograms for the reduction of 1 mM of p-nitrophenyl diazonium in MeCN solution with 0.1 M of $TBAPF_6$; ***(b)*** Cyclic voltammograms of immobilized p-nitrophenyl layer/SLG/PET in MeCN solution containing 0.1M of H_2SO_4 (red curve) and pristine SLG/PET (black curve).

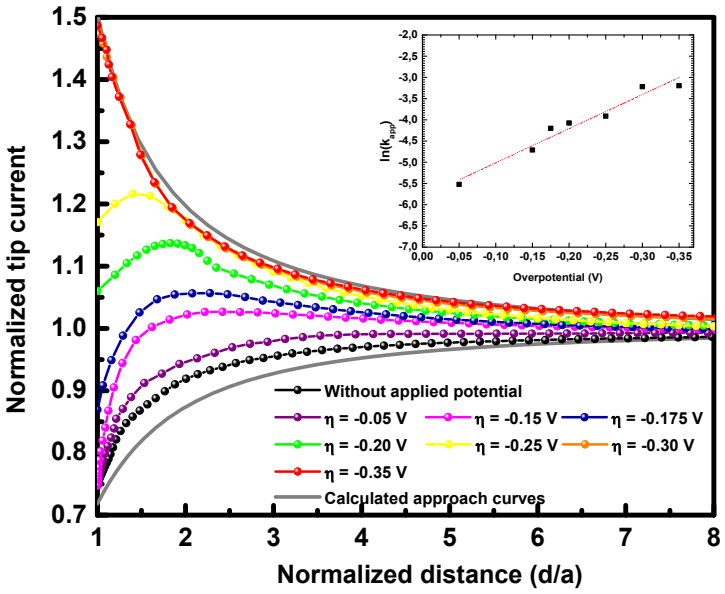

Figure 4.9 Approach curves onto biased diazo modified SLG/PET using Fc as mediator: w/o bias (black), η = -0.05 V (purple), -0.15 V (magenta), -0.175 V (blue), -0.2 V (green), -0.25 V (yellow), -0.3 V (orange) and -0.35 V (red). (inset) log (kapp) in function of overpotential. Grey curves represent theoretical approach curve onto insulating and conducting substrates.

To investigate the charge transfer at the modified interface NO_2-Phenyl/SLG/PET, approach curves using Fc as mediator were performed (Figure 4.9). For un-biased substrate (black curve in Figure 4.9) the approach curve shows the presence of Fc regeneration at the surface with a k_{app} = 3.3. 10^{-3} $cm.s^{-1}$. After the substrate polarization, the transition from current

decrease to a current increase occurred at lower overpotential (-0.2 V) when compared to the un-modified SLG/PET (-0.6 V) with a charge transfer coefficient $\alpha = 0.21$ and $k^0 = 3.03.\ 10^{-3}$ $cm.s^{-1}$.

From Figures 4.9 and 4.6, the variation of the current from the experimental approach curves as a function of the applied overpotential was plotted for SLG/PET and modified SLG/PET at normalized distance (L = d/a) value of 1.5 (Figure 4.10). The transition from slow to fast electron transfer was found to be 400 mV shifted for the modified graphene electrode suggesting an increase of the work function of SLG/PET by the introduction of nitrophenyl layer. Indeed, the surface functionalization generates defects on the single layer graphene produced by the covalent bonding between the aryl and the graphene layer. The presence of the organic layer creates not only $\pi - \pi$ conjugated system breaking, but also a chemical doping of the graphene. Thus, the presence of an electron withdrawing head group, $-NO_2$, decreases the electron density of the graphene layer generating a p-doped like behaviors of the graphene substrate. The electron accumulation at the interface organic layer/solution permits the acceleration of the electrochemical reduction process, i.e. the reduction of Fc^+ at the SLG substrate. It was also demonstrated that binding the single layer graphene with an aryl group increases the conductivity of the substrate[18], and as consequence enhances the electron transfer rate.

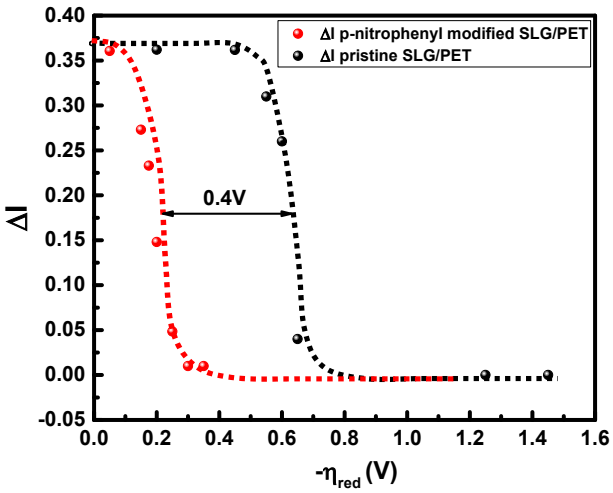

Figure 4.10 Variation of the normalized current with the overpotential for bare SLG (black) and modified SLG/PET (red).

Meantime, the chemical induced breakdown of the conjugated system of SLG/PET can also inhibit the formation of the TCNQ islands at the surface. It should be noted that due to the slow electrochemical response toward redox reaction, the electrochemical grafting of the p-nitrophenyl diazonium onto the graphene surface cannot generate a compact organic film leading to the pinhole effect in which the electroactive species can diffuse to the SLG. The combination of these factors results on the positive feedback observed with TCNQ on the modified SLG/PET (Fig. 4.11).

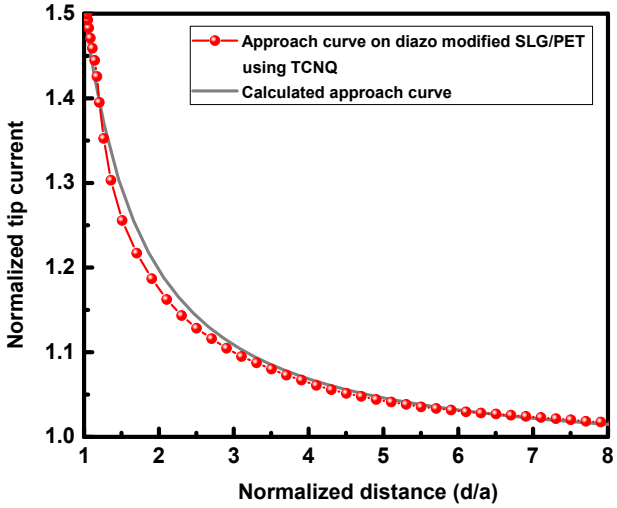

Figure 4.11 Approach curves onto diazo modified SLG/PET using TCNQ as mediator (red), theoretical approach curve for conducting substrate (grey).

One has to note that unlike SGL/PET substrate, all the recorded approach curves after surface functionalization exhibit similar shape whatever the probed area. This finding confirms that the surface grafting acquires to the graphene substrate homogeneous electronic properties and doping. The HET rate was found to be increased by 2 orders of magnitude (> 4. 10^{-2} cm.s^{-1}). Consequently, the formation of a p-n junction that involves the electron rich organic layer (accumulation of electron) and electron deficient graphene layer (accumulation of holes) has to be taken in consideration for explaining the enhancement of the charge transfer through the interface substrate/solution.

Besides changing the electronic properties of single layer graphene via a destructive approach, such as electrochemical grafting, non-destructive methods can also be used for modulating the electronic properties of the graphene-based materials. As mentioned above, the graphene single layer is supported by a metal NWs mesh on plastic film. The interaction between the metal and the graphene was revealed from the SLG side in the previous part. However, the electron transport in between the metal and the SLG cannot be exploited from the metal side which is taken, for the next step, in consideration by drop-casting Pt nanoparticles (NPs, 50 nm) onto the graphene layer. As the NPs were deposited by drop-casting, the interconnectivity between different particles is not ensured. Thus, the electron density of the nanoparticles is not sufficient for providing a fast electron transfer rate[38,39]. First, a series of approach curves using Fc and TCNQ as mediators were performed using Pt NPs deposited onto a glass slide as a substrate. In both cases negative feedback is observed (Figure 4.S2) indicating the absence of regeneration of the mediator at the Pt NPs/insulating interface. This result is expected because the size of the used UME (10 mm) is larger than the particle size around 50 nm or even an agglomerate particle unless their size exceeds the UME size which is not observed in our case (Figure 4.S3). However, by depositing the Pt NPs onto SLG/PET, positive feedback was recorded for both TCNQ and Fc with a high electron transfer rate k_{app} = 6. 10^{-2} cm.s^{-1} and 4. 10^{-2} cm.s^{-1}, respectively (Figure 4.12). As discussed before, the Pt NPs can also act as an

electron reservoir which can be transferred to the graphene substrate inducing electron deficient at the metal surface and electron rich density at the graphene layer. The electrons provided by the Pt NPs increase the electron density of the graphene and thus enhance the activity of the graphene layer toward the electrochemical reaction of both oxidized and reduced mediator at the Pt NPs/SLG/PET surface.

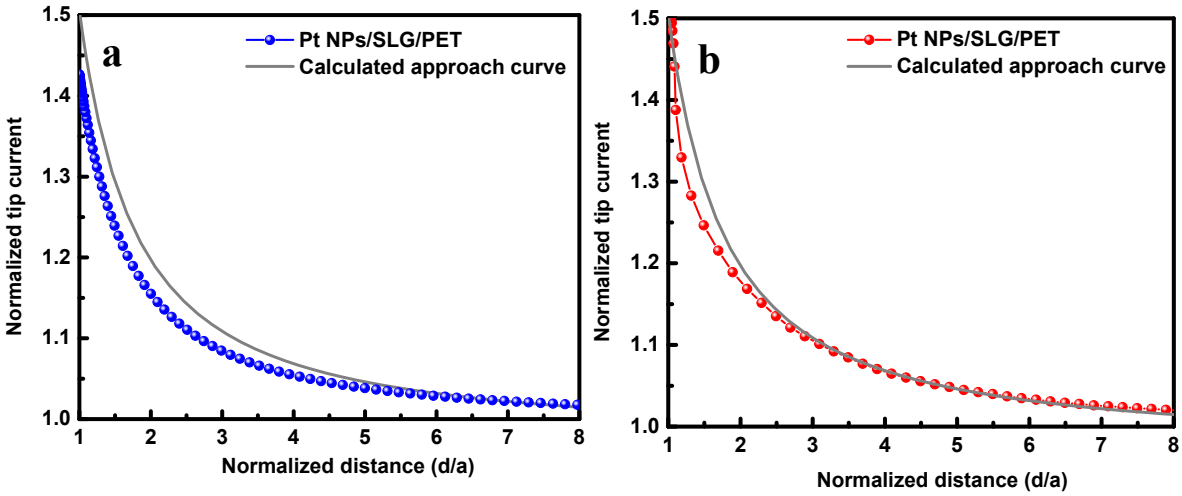

Figure 4.12 Approach curves onto Pt NPs/ SLG/PET using ***(a)*** Fc and ***(b)*** TCNQ as mediator, theoretical approach curve for conducting substrate (grey).

Next, a new interface was generated by depositing Pt NPs on pre-modified SLG/PET with p-nitrophenyl layer. The presence of the Pt NPs was verified using atomic force microscopy (AFM) (Figure 4.S4). Interestingly, the Fc approach curve displays a positive feedback with a HET rate around 6. 10^{-2} cm.s^{-1} (Figure 4.13a) while the electron transfer toward the oxidation of $TCNQ^{\bullet-}$ was dramatically decreased giving k_{app} ~10^{4} cm.s^{-1} (Figure 4.13b).

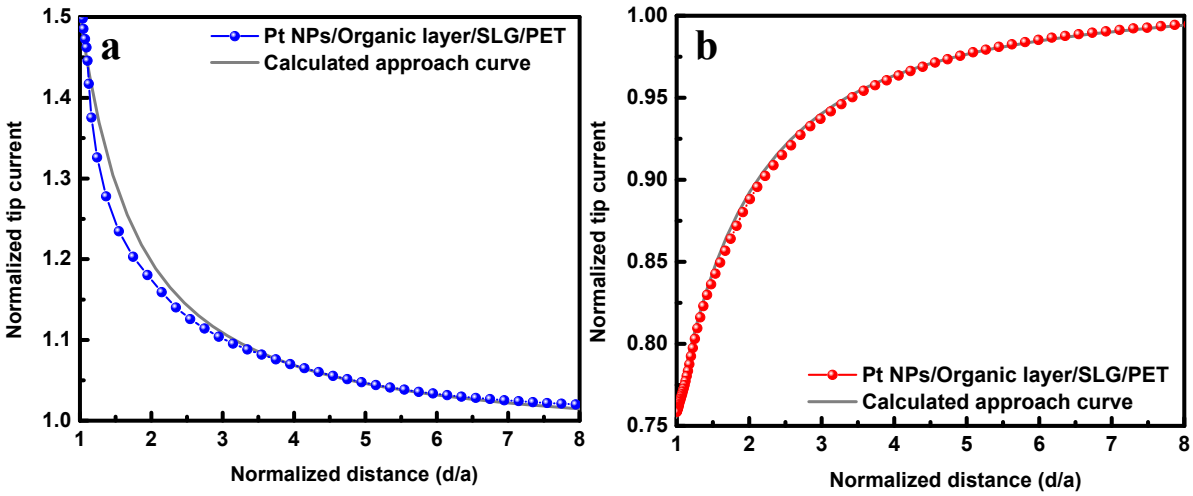

Figure 4.13 Approach curves onto Pt NPs/organic layer/SLG/PET using ***(a)*** Fc and ***(b)*** TCNQ as mediator, theoretical approach curve for conducting substrate (grey).

Thus, by introducing the organic layer in between the SLG surface and the Pt NPs film, the electronic properties of the substrate changes. As a consequence, the electrons accumulated at the organic layer are transferred to the Pt NPs which can act as an electron acceptor reservoir

and thus, enhances the electron density at the surface of Pt NPs and favors the reaction involving ferrocenium.

The mapping of the substrate was recorded using SECM imaging mode. Thus, by fixing a distance at 5 µm from the substrate, the tip current was recorded after displacement over 200 mm x 200 mm areas (Figure 4.14).

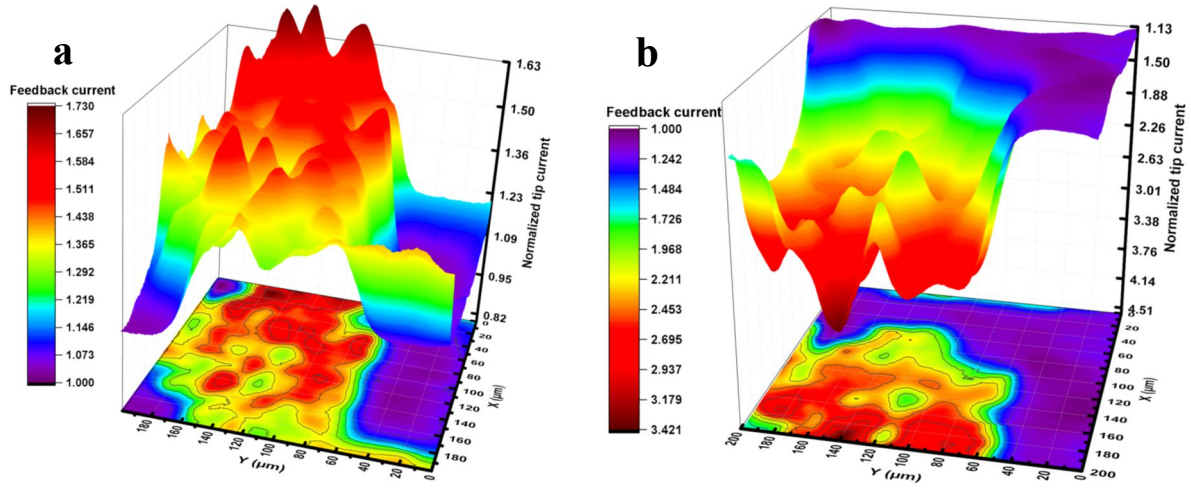

Figure 4.14 SECM image of 200 µm x 200 µm area onto Pt NPs/organic layer/SLG/PET using ***(a)*** Fc and ***(b)*** TCNQ as mediator.

The SECM images provide an overall view of the electrochemical reactivity of the surface. As shown in Figure 4.14a, the Pt NPs/modified SLG/PET displays increase of the feedback current in the case of ferrocene as a redox probe. In this region the Pt NPs were revealed strongly by Fc (red part). In the case of TCNQ as mediator, the conductive region observed with ferrocene behaves as an insulator-like film (Figure 4.14b). One has to note, that both SECM images were recorded in the same area. In addition, the comparison of the SECM images demonstrates that the area where the Fc probe gives negative feedback due to the absence of NPs on the organic layer, a positive feedback is recorded with TCNQ. These results match perfectly the results obtained from the feedback mode.

4.2.3 Influence of the supporting substrate to the electrochemical behaviors of SLG

In the previous part, the influence of the front side (graphene side) modification on the electronic properties of single layer graphene was evaluated. However, the influence of the supporting substrate of graphene has not been taken into consideration. In this study, the SLG supported on copper foil is then investigated. As displayed in the figure 4.15, the reactivity of the graphene layer differs by using two opposed substrates, PET/EVA and copper foil. Unlike reported behaviors of SLG/PET in the presence of ferrocene (negative feedback), the replacement from PET to copper foil as underlying substrate conducts to a change of both conductivity and reactivity at the graphene surface.

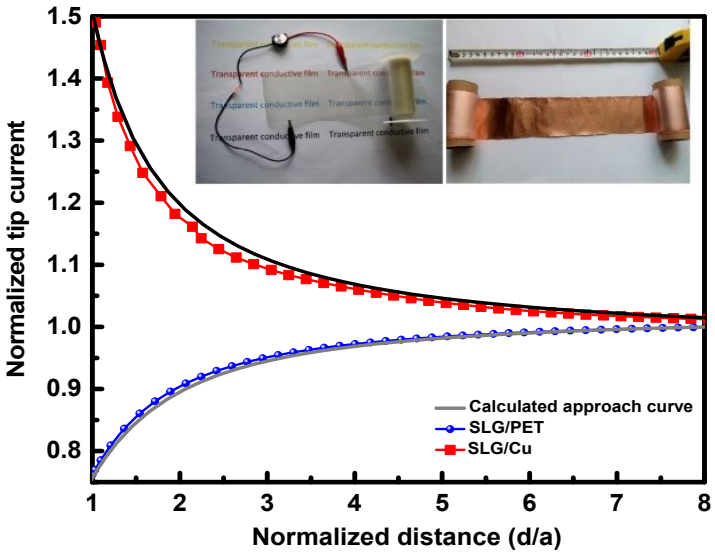

Figure 4.15 Approach curves using Fc onto (blue) SLG/PET and (red) SLG/Cu.

In the present case, a positive feedback was obtained indicating a reinforcement of n-doped character of the graphene layer. It has been demonstrated that the graphene has n-doped character when deposited onto metals as Al, Cu, Ag and p-doped behavior when deposited onto Au or Pt surfaces[40]. In the same study, Giovannetti et al.[40] have reported that the chemisorbed graphene onto copper foil possesses a calculated shift of fermi level around 0.5 eV (d_{M-G} = 0.3 nm) compared to pristine graphene. Consequently, from electrochemical point of view, the presence of copper foil induces a diminution of the overpotential for n-doping graphene layer by 0.5 V. Interestingly, when compare with the previous results on the evolution of the feedback curve as function of the overpotential of SLG/PET, similar overpotential value of 0.55 V (Figure 4.10, black dots) was found to be necessary to switch from p-doped to n-doped graphene. This value confirms the important role of the supporting layer to the electronic properties of the deposited graphene sheets.

In order to get more information about the influence of the supporting layer on the properties of graphene, an electrochemical treatment was performed to gradually oxidize copper layer to copper oxide, affording new interface of SLG/CuO_x/Cu. The generation of copper was performed in 1 M KOH solution by using chronoamperometry at different polarization time. The presence of the copper oxide was revealed by both XPS and SEM. The figure 4.16a displays the apparition of a strong Cu^{2+} satellite peaks at 943 eV and 962 eV confirming the formation of Cu_2O. In addition, the presence of a peak at around 934 eV corresponding to the broader shift confirms the presence of CuO. From SEM images, compared to the smooth surface of pristine G/Cu the presence of CuO_x needle-like structure is observed. Interestingly, the majority of the needles growth in the underneath of the graphene layer (Figure 4.16 d-e), suggesting the formation of new interface SLG/CuO_x/Cu.

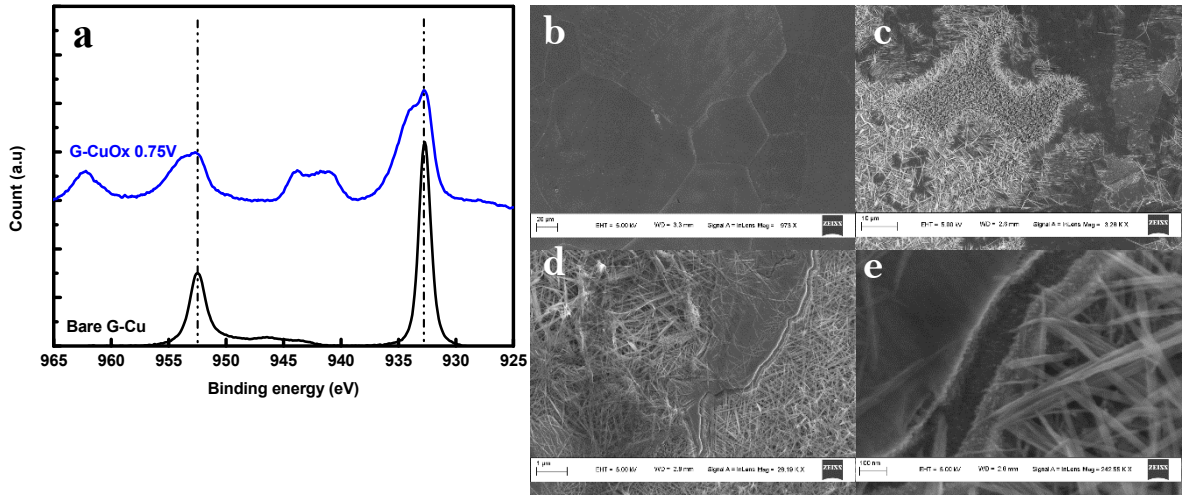

Figure 4.16 (a) XPS spectra of Cu(2p) from pristine SLG/Cu (black) and SLG/CuO_x/Cu (blue); SEM images of ***(b-e)*** pristine SLG/Cu and (c-e) SLG/CuO_x/Cu modified at 0.75 V for 60 min in 1 M KOH solution.

The local reactivity of the modified substrates was evaluated by using Fc^+/Fc redox couple in SECM configuration. The feedback curves displayed in the figure 4.17 shows a gradual decrease of the electron transfer rate by approaching to negative feedback as function of the oxidation time.

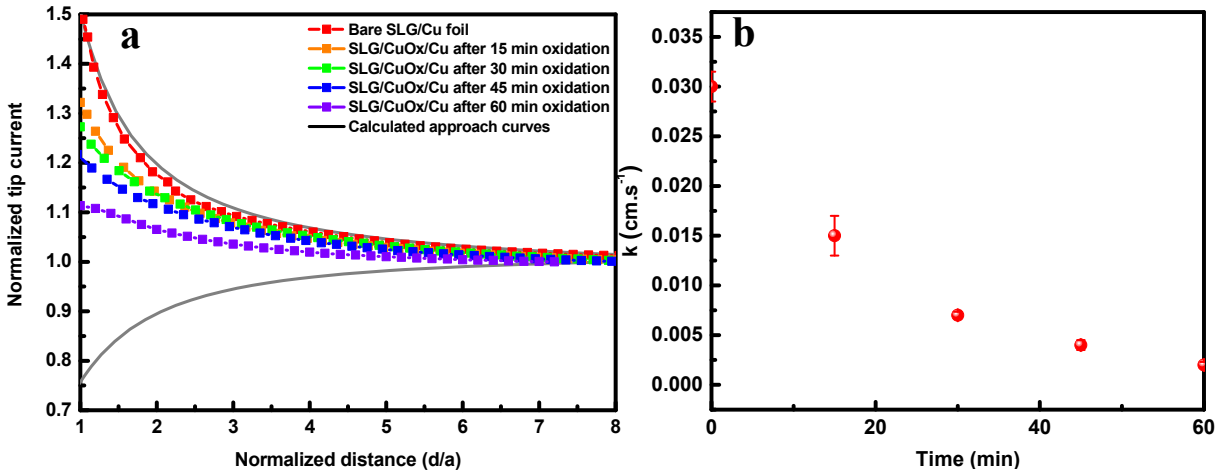

Figure 4.17 (a) Approach curves onto SLG/CuO_x/Cu using Fc as mediator. Theoretical approach curve for conducting and insulating substrates (grey); ***(b)*** Electron transfer rate as function of oxidation times.

The electron transfer rate was exponentially decreased in function of the oxidation time and reached 3.10^{-3} $cm.s^{-1}$ after 60 min treatment. By coupling the SEM images and the electrochemical behaviors of the modified layers, the decrease of HET rate can be attributed to the growth of the oxide layer which have semi-conductive behaviors[41]. Basing on the local reactivity of the SLG deposited onto different substrates (PET, Cu, CuO_x), it can be concluded that the electronic properties of the graphene layer is strongly depended on the electronic properties of the supporting layer.

In summary, the electronic properties of single layer graphene deposited onto flexible and transparent support were investigated by SECM. The variation of the feedback curves as a function of the nature of the mediator indicates the presence of different electronic interactions occurring between graphene single layer and the electroactive species. In addition, the functionalization of the graphene layer with the p-nitrophenyl layer through the electroreduction of diazonium group has also been examined. The observed increase of the electrochemical response can be explained by the formation of the p-n junction due to the withdrawing effect of the organic layers which provides double benefits. Firstly, the organic layer (n-doped layer) enhances the electron transfer from the substrate to the oxidized species in solution. Secondly, the chemical p-doped graphene provides accessible sites for the reduction process by preventing adsorption of aromatic compounds. With further modification of the substrate with platinum nanoparticles, the electrochemical responses toward the oxidizing and reducing mediators are inverted. Furthermore, the supporting layer provides a crucial role onto the electronic properties of the graphene sheets. Overall, the local electrochemical reactivity of the graphene monolayer can be tailored by modifying its structure via different approaches. Besides the fundamental knowledge of the surface modification of SLG/PET, we believe that the capacity to tune the electronic and electrochemical properties of the large scale SLG/PET could be used in a large spectrum of application such as touch screens, smart materials, molecular electronic, and for energy storage and conversion.

4.3 SECM IN IONIC LIQUID MEDIA AND OVER IONIC LIQUID LAYERS

4.3.1 SECM in ionic liquid media

The masse transport of redox species in ionic liquid solution differ from that measured in usual solvent. Different measurements were performed providing comparable results, typically $3.9.10^{-7}$ $cm^2.s^{-1}$ for ferrocene in imidazolium based ionic liquid $[EMI^+][TFSI^-]$[42]. This value is much lower than that found in acetonitrile solution ($D = 2.10^{-5}$ $cm^2.s^{-1}$) that cause non-negligible change in the electrochemical response of the redox species. In this context, the deep understanding of the electron transfer and the masse transport at the surface of a material provides a considerable role for improving the efficiency of different electrochemical processes in ionic liquid media. We report, in the present part, the use of the feedback mode via scanning electrochemical microscopy followed by cyclic voltammetry to investigate the heterogeneous electron transfer kinetic in IL media at very thin double junction within the gap UME/substrate, metal/IL/insulator (1) and metal/IL/metal (2).

An ultramicroelectrode (UME), attached to a vertical axis piezo of a SECM setup, was approached to the substrate through an ionic liquid solution ($[EMI^+][TFSI^-]$) containing 10 mM of 1-ferrocenylmethyl-3-methyl imidazolium TFSI as redox mediator. The electrochemical signals provided by the redox mediator were recorded at different distance between the tip and the conducting substrate (Figure 4.18b). Indeed, independent to the

distance L, the steady-state current is always satisfied. From the value of the limiting current in the bulk solution (black curve in Figure 4.18b), the diffusion coefficient of the [FcMIm$^+$M] [TFSI$^-$] can be calculated via the equation 4.10[1].

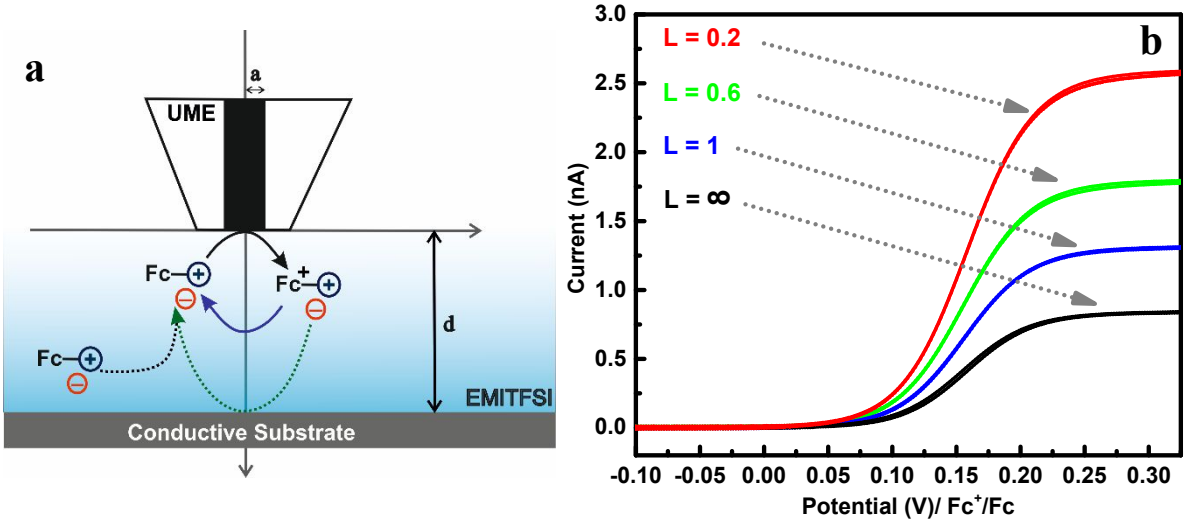

Figure 4.18 (a) Scheme of the investigation of the electrochemical behaviors of the 10 mM of FcIL in [EMIm$^+$][TFSI$^-$] solution on conductive substrate; ***(b)*** Cyclic voltammograms at different distance tip – substrate (L =d/a) : (black) L = ∞, (blue) L = 1, (green) L = 0.6, (red) L = 0.2.

As shown in the figure 4.18b, the CV at L = ∞ represents a well-defined diffusion-controlled system with a plateau current recorded at 50 mV.s^{-1} as a scan rate with a value of $D_{[FcMIm+M]}$ = 4.6.10^{-7} cm^2.s^{-1} observed in [EMI$^+$][TFSI$^-$] solution which is 2 orders of magnitude lower than the same molecule in acetonitrile solution. Nevertheless, the limiting current increases exponentially by approaching the UME to the substrate below L = 1. Despite the variation of the diffusion coefficient in ionic liquid the recorded SECM CV's at different distances over conducting substrate, behave similar to those obtained in classical solvent (acetonitrile).

However, by approaching the UME to an insulating substrate, a transition of diffusional regimes was observed under the same conditions. Unlike reported work on the electrochemical responses of the redox mediator by lowering the distance tip- insulating substrate where steady-state current decreases exponentially with the distance[43], peak-like shape cyclic voltammograms is observed. This behavior is mainly due to a considerable planar diffusion contribution (Figure 4.19b).

Far from the substrate, the plateau current was obtained as in the previous case where the mass transport is controlled by the radial diffusion. However, at L = 1, peak-like current was observed from the CV at 5 µm Pt UME corresponding to the early-stage formation of metal/thin liquid film/insulator double junctions. A well-defined reversible peak-shape CV was even emphasized by approaching the tip closer to the substrate (L = 0.2).

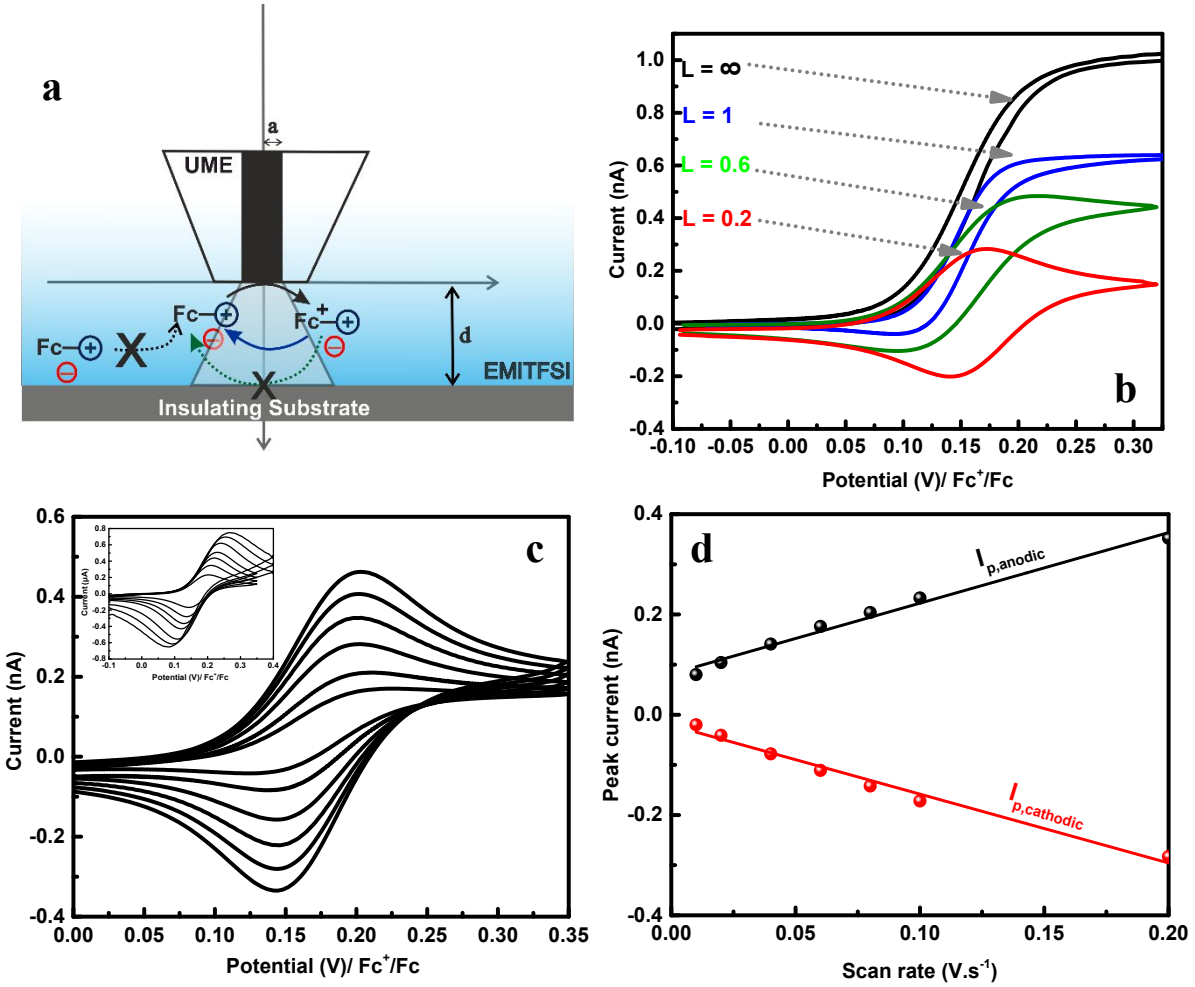

Figure 4.19 ***(a)*** Scheme of the investigation of the electrochemical behaviors of the FcIL in $[EMI^+][TFSI^-]$ solution on insulating substrate; ***(b)*** Cyclic voltammograms at different distance tip – substrate (L =d/a) : (black) L = ∞, (blue) L = 1, (green) L = 0.6, (red) L = 0.2; ***(c)*** CVs at different scan rate from 10 $mV.s^{-1}$ to 100 $mV.s^{-1}$, inset: CVs from 0.1 $V.s^{-1}$ to 2 $V.s^{-1}$ at L = 0.2; ***(d)*** Variation of the peak current in function of the scan rate.

At this position, the oxidation and the reduction peaks of FcIL are observed with a peak-to-peak separation less than 20 mV which is attributed to a thin film character. The phenomenon that can be occurred in this configuration is mainly due to the high viscosity of the ionic liquid, $[EMI^+][TFSI^-]$ (35.55 cP at 25°C[44]). The proposed behavior can induce important effects to the electrochemical response at the UME where the diffusion of the redox mediator from and to the electrode surface is inhibited by amplifying the physical obstruction due to the presence of the UME. Perhaps, a meta-state is generated in which all the FcIL molecules are captured inside the small volume defined by the UME and the substrate as presented in the Figure 4.19a. Besides, the low diffusion coefficient of FcIL induces extremely slow mass transport process (~ second scale, i.e negligible compared to the electron transfer rate) which is in the same potential sweeping scale. Therefore, at the reverse scan, the generated oxidized species are localized at the vicinity of the electrode and susceptible for reduction without any overpotential ($\Delta E < 20$ mV). In addition, a linear relationship between the anodic and

cathodic peak currents as function of the scan rate is obtained (Figure 4.19d) which can be referred, in this case, to a quasi-immobilized electroactive layer.

As demonstrated in the previous parts, in highly viscous solvents, case of ionic liquid, the diffusion is strongly affected. Indeed, to get insight on the mass transport in such solvent, approach curves were performed and recorded as shown in the figure 4.20. By using an approach rate about 2 $\mu m.s^{-1}$, the responses do not fit with the SECM steady-state theory. The feedback curve obtained by using insulating substrate shows unusual behavior where the current is less sensible with the variation of the distance and starts to decrease at $L < 1$. Nevertheless, the currents obtained by cyclic voltammetry at $L < 1$ show a net decrease of the oxidative current.

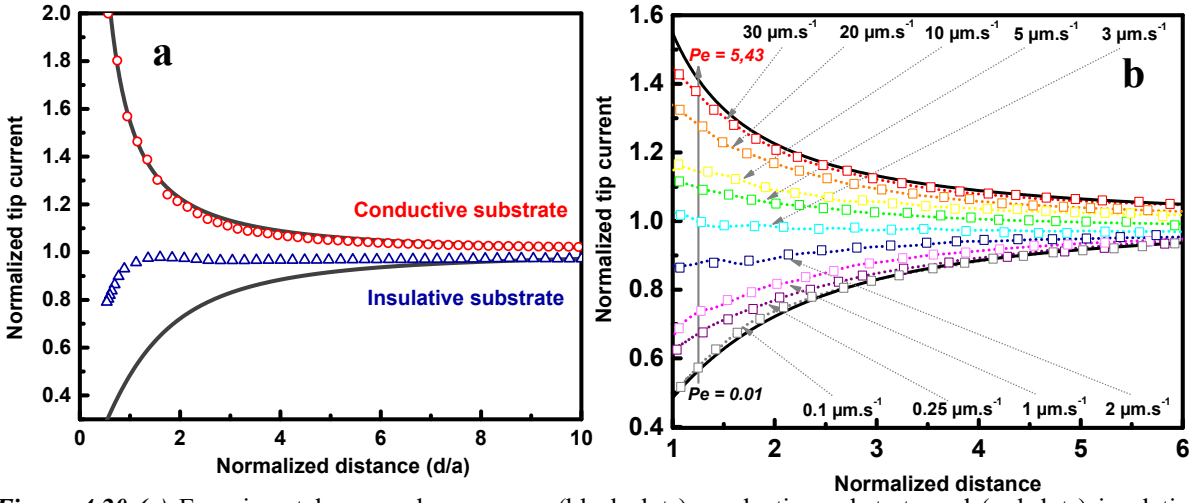

Figure 4.20 (a) Experimental approach curves on (black dots) conducting substrate and (red dots) insulating substrate. Solid lines correspond to the theoretical approach curves; ***(b)*** Evolution of the feedback curves in function of the approach rate ranging from 0.1 $\mu m.s^{-1}$ to 30 $\mu m.s^{-1}$ on insulating substrate.

Two contradictory observations can be correlated by adding the contribution of the convection into the mass transport[43]. Nkuku and LeSuer[45] proposed new SECM model in deep eutectic solvent via introduction of convection term on the total mass transport during the tip's approach. The combination of the diffusion and the convection is ensured by the Peclet number which is equal to υ_a/D where υ is the tip velocity. It has been demonstrated that at Pe values below 0.01, the convection is negligible compared to the mass transport. However, when the Pe value is beyond 1, the convection contributes significantly to the process. Typically, at an approach rate around 0.1 $\mu m.s^{-1}$ (Pe = 0.01), the feedback curve fits completely with the theoretical approach curve. By increasing the tip velocity from 0.1 $\mu m.s^{-1}$ to 30 $\mu m.s^{-1}$ (Pe = 0.01-5.43), the feedback curves onto insulating substrate switch from fully negative to positive (Figure 4.20b) where the contribution of the convection becomes dominated in the mass transport.

Independent to the approach rate, the cyclic voltammograms at different scan rate offer the real behaviors of the redox species at the vicinity of the microelectrode as mentioned in the

previous part. From that point of view, it is possible to reconstruct a more reliable approach curve by eliminating the contribution of the convection via the plateau current from the CVs recorded at different distance tip – substrate. Interestingly, from the steady state current values of different CVs, the variation of the i_z/i_∞ as function of the normalized distance tip – substrate is plotted as shown in the Figure 4.21. Importantly, even though the substrate is insulating or conductive, the evolution of the normalized current fits perfectly with the expected theoretical approach curves which are calculated under steady-state conditions. From the obtained results, the experimental feedback curves can not only be obtained by amperometric approach techniques with low tip velocity but also by means of cyclic voltammetry technique.

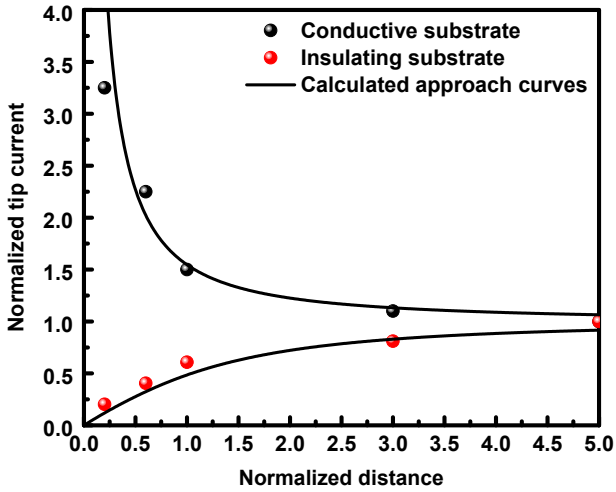

Figure 4.21 Reconstruction of the approach curve by means of the plateau currents collected from CVs at different distances (black dots) tip – conductive substrate and (red dots) tip – insulating substrate. Solid lines correspond to the theoretical approach curves.

In conclusion, the formation of the extremely thin layer of ferrocenated ionic liquid in EMITFSI solution reveals several effects to the charge transfer and the diffusion of the redox species at the vicinity of the electrode materials. This present work can open new understanding of the redox phenomena occurring at the interface between ionic liquid solution and the electrode surface and for further applications concerning the use of ionic liquid as both solvent and/or active materials.

4.3.2 SECM over thin layer of electroactive ionic liquid generated by click chemistry

As reported in the chapter 2, the surface modification of thin layer of ferrocenated ionic liquid onto electrode surface by click chemistry was performed. In this part, the investigation of the electroactive top layer was performed by employing the Scanning Electrochemical Microscopy (SECM). Via the feedback mode, the local reactivity of the substrate can be revealed at unbiased state. First, the feedback mode's responses on grafted azido-phenyl layer generated after 10 cycles were investigated by using two redox mediators: decamethylferrocene ($DmFc^+/DmFc$, E^0 = 0.1 V vs. SCE) and ferrocene (Fc^+/Fc, E^0 = 0.4 V

vs. SCE). For both redox couples, the normalized current at the microelectrode (UME) decreases as the Pt tip approaches the azido-phenyl modified ITO. This behavior, negative feedback, indicates the absence of regeneration of the mediator at the surface. Moreover, the experimental approach curves show a good agreement with the theoretical approach curve for an insulating substrate, demonstrating the insulating properties of the modified electrode and confirm the formation of dense layer free of pinholes (Fig.4.22b).

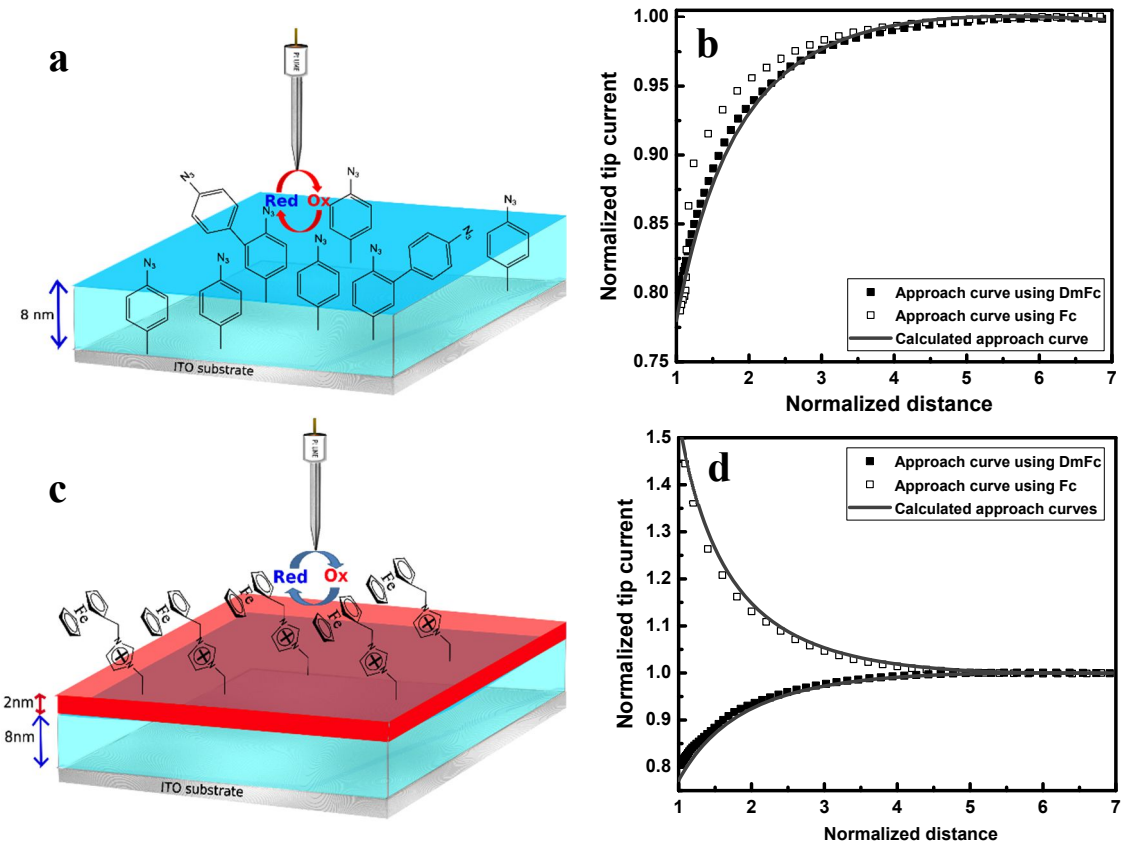

Figure 4.22 Scheme for investigating the electrochemical behaviors of ***(a)*** azido-phenyl modified electrode and ***(c)*** after immobilization of [FcPIm$^+$][Br$^-$] by click chemistry. Corresponding experimental approach curves using two redox mediators: DmFc$^+$/DmFc (■), Fc$^+$/Fc (□) and the theoretical approach curves (solid lines) for ***(b)*** azido-phenyl modified electrode and ***(d)*** after immobilization of [FcPIm$^+$][Br$^-$] by click chemistry.

However, after the grafting a top layer of ferrocenyl-imidazolium (Figure 4.22c), two different behaviors are observed, as illustrated in Fig. 4.22d. In the case of DmFc, negative feedback is obtained, and the experimental curve matches the theoretical approach curve for an insulating substrate. This result indicates the absence of interaction between the DmFc$^+$ generated at the UME and the attached Fc head group, and the absence of any interaction with the ITO electrode through pinholes and/or tunneling. By contrast, in the case of the Fc$^+$/Fc redox couple, the normalized current increases rapidly as the UME approaches the modified substrate. A positive feedback is observed, and the experimental approach curve matches the theoretical curve expected for a conducting substrate under diffusion control. The increase in the current during the approach curve is due to the oxidation of the grafted Fc head groups by

the Fc^+ generated at the UME. The fact that two similar redox mediators show opposite behaviors can be explained by the difference in the standard potential of the probes. For comparison, similar behavior was observed for Fc groups attached to the insulating n-Si surface[46]. Indeed, as the standard potential of the Fc mediator is close to that of the immobilized ferrocenyl-imidazolium, the facile and efficient oxidation of the attached Fc by oxidized Fc^+ diffusing from the tip becomes possible, inducing regeneration of the Fc mediator at the interface. Overall, the SECM investigations demonstrate that the electron transfer at the modified interface can be considered as an extremely fast and efficient process.

4.3.3 SECM over polymer layer of ionic liquid

Being described in the chapter 3, the presence of polymeric ionic liquid layer at the electrode surface does not block the diffusion of the active species from the bulk to the electrode surface and enhances the electron transfer towards inner sphere molecules. In order to confirm the results obtained from cyclic voltammetry and electrochemical impedance spectroscopy, scanning electrochemical microscopy, SECM, was employed to investigate the local electrochemical properties of the interface. For comparison, the SECM investigations were performed using two redox probes (inner and outer sphere) over GC modified with the initiator (Br terminated GC) and over the poly(IL)/GC after SI-ATRP polymerization.

In this case, the SECM configuration allows the investigation of the surfaces at their open circuit potential (unbiased substrate). Figure 4.23a depicts the approach curve in the presence of FcMeOH and shows an enhancement of the current when the UME approaches the surface for both investigated surfaces. The increase of the current is related to the regeneration of FcMeOH at the electrode surface which enhances the flux of the FcMeOH in the vicinity of the UME. This behavior indicates the presence of thin layer of Br terminated layer (lower than 5nm) and that the polymer brushes structure maintains the access of the redox probe to the GC surface.

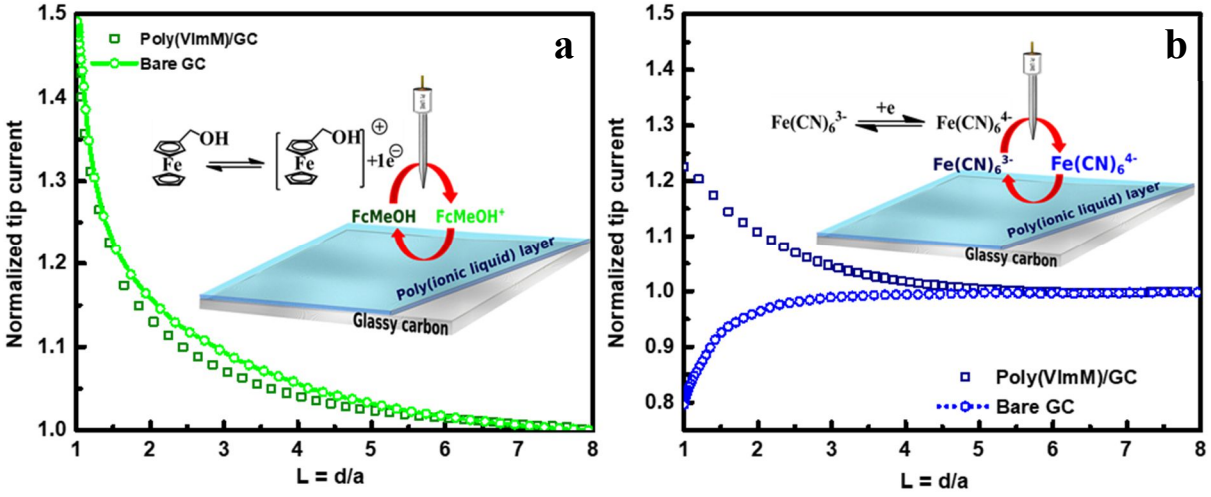

Figure 4.23 SECM approach curves at bare GC and poly(VImM) using ***(a)*** ferrocene methanol and ***(b)*** potassium ferricyanide at 1 mM in 0.1 M KOH aqueous solution

However, in the case of ferricyanide, two different opposite behaviors were observed (Figure 4.23b). On GC/Br initiator electrode, the current decreases while the UME approaches the surface indicating that the backward reaction ($Fe(CN)_6^{4-} \rightarrow Fe(CN)_6^{3-} + e^-$) at the substrate occurs with a low electron transfer. In the case of GC/poly(VImM) substrate, a positive feedback is observed confirming the occurrence of the backward reaction at the polymer interface. The observed positive feedback is related to the presence of ferricyanide moieties within the poly(VImM). These electrochemical investigations demonstrate that the poly(VImM) brush structure enhances the electrochemical response of an inner-sphere probe.

4.4 POLYMERIC FERROCENE BASED IONIC LIQUID FOR PROBE-LESS SECM

4.4.1 Electrochemical behaviors of poly(FcIL) film on ultramicroelectrode

In this part, we purpose to study the electrochemical behaviors of immobilized polymer redox ionic liquid, Poly(1-allyl-3-ferrocenylmethylimidazolium bromide) (Poly(FcIm), by using Surface-initiated Atom Transfer Radical Polymerization on Pt UME surface. SI-ATRP was chosen due to the robustness via covalent bond attachment and capacity to generate polymer brushes with controlled thickness. This method has already been reported to perform the polymerization of 2-hydroxyethyl methacrylate (PHEMA) on microelectrode arrays as platform for Hg^+ sensing[5]. However, there is no report on SI-ATRP polymerization onto single UME. The SI-ATRP procedure was kept similar as described in the previous part (chapter 2 and 3).

As the first report on immobilizing a redox-active polymer ionic liquid onto the ultramicroelectrode, the electrochemical response of the modified Pt UME in electrolytic solution was performed by cyclic voltammetry at different scan rate ranging from 0.01 to 20 $V.s^{-1}$ as shown in the figure 4.24a-b. The reversible redox system at 0.17 $V/E_{Fc+/Fc}$ corresponds to the typical electrochemical response of the Fc moieties within the polymeric ionic liquid. Unlike the response of the microelectrode in the presence of redox probe in solution with plateau current, the peak-like shape confirms the presence of immobilized ferrocene moieties at the UME.

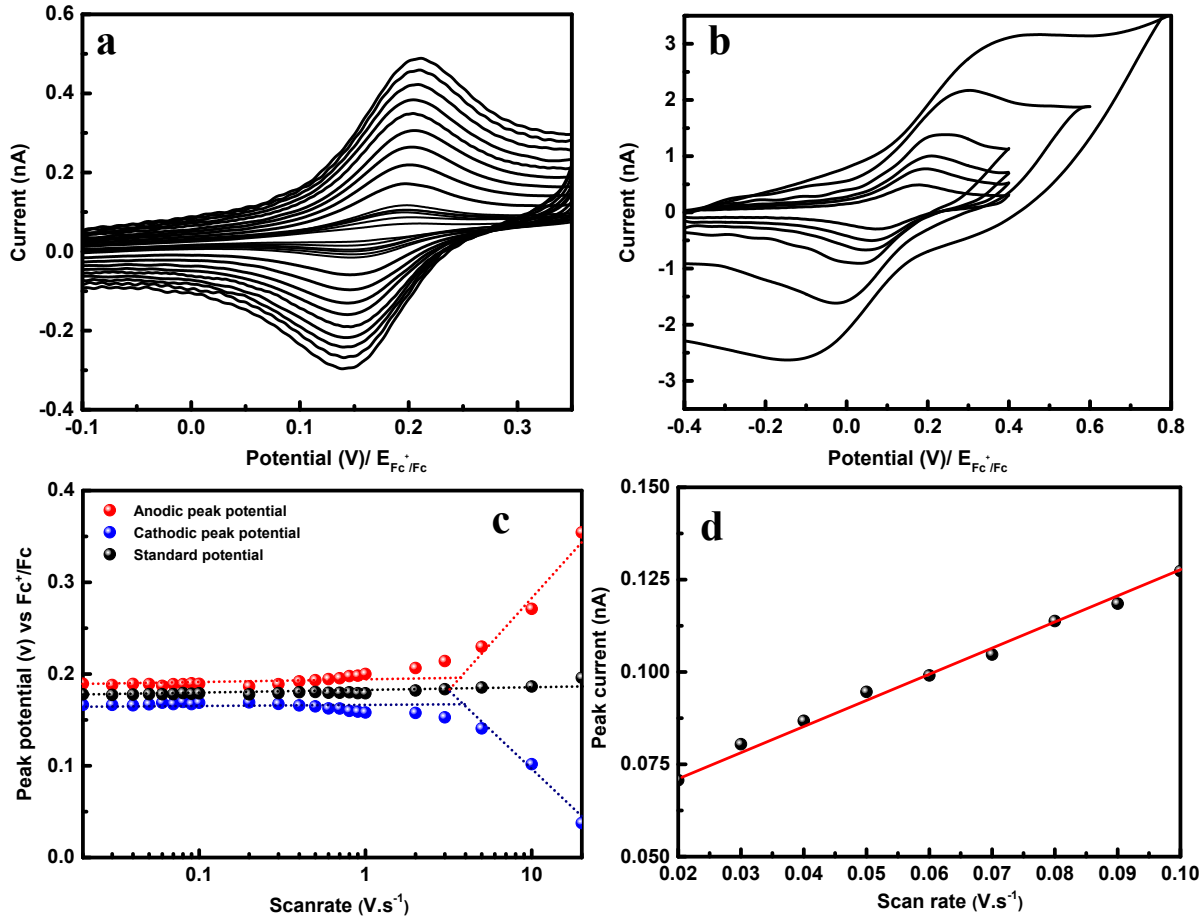

Figure 4.24 Cyclic voltammograms of the Pt UME/Poly(FcIL) electrode recorded at different scan rates : ***(a)*** from 20 mV.s^{-1} to 1 V.s^{-1} ; ***(b)*** from 1 V.s^{-1} to 20 V.s^{-1} ;***(c)*** Variation of the peak potentials in function of the scan rate; ***(d)*** Variation of the oxidation peak current in function of the scan rate.

The electron transfer kinetic was then investigated by plotting the variation of the peak potential as function of the logarithm of the scan rate. According to the Laviron's formalism, the calculated electron transfer rate constant is 253 s^{-1} which is similar to that reported on large electrode GC/Poly(FcIL)[47]. At low scan rate (below 0.1 V.s^{-1}), the current varies linearly with the scan rate highlighting the presence of a non-diffusive process. However, at high scan rate the current is proportional to the square root of the scan rate suggesting the limitation by the electron transfer and/or the apparent diffusion of the polymer chain thanks to the flexibility of the attached brushes polymer (Figure 4.24d). Such behavior has been already described in the literature[48].

4.4.2 *SECM study by using UME/ poly(FcIL) tip*

Later, the modified electrode was used to probe a conducting substrate in the presence of a redox mediator, decamethylferrocene, using the SECM approach curve. The choice of the mediator is due to its standard potential (E° = - 0.3 V/ $E_{Fc+/Fc}$) that is not interfered with the electrochemical active window of immobilized ferrocene moieties. As consequence, the difference of electron transfers kinetic, if it happens, is mainly due to the physical presence of the polymer layer by excluding the possible contribution from the attached redox moieties. As

shown in the figure 4.25, the recorded approach curve displayed no difference in term of feedback curve compared to bare Pt UME. This result appears coherent with the previous electrochemical response of the modified electrode using cyclic voltammetry.

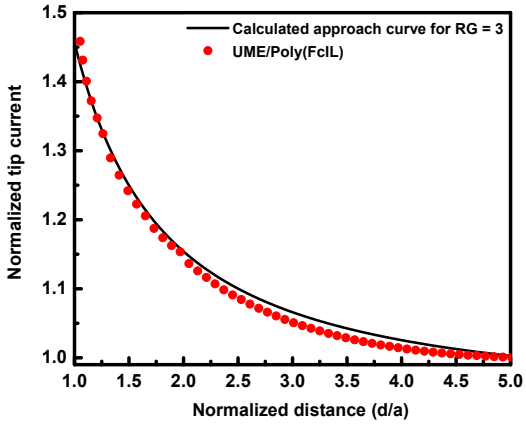

Figure 4.25 Approach curves onto Pt substrate by using Pt UME/Poly(FcIL) in a MeCN solution containing 0.05 mM of DmFc as mediator and 0.1 M of $TBAPF_6$.

After achieving the positive feedback curve, the modified electrode was kept close to the conducting substrate (L = 1). Next, a cyclic voltammogram was recorded by sweeping the potential from -0.6 V to 0.4 V/ $E_{Fc+/Fc}$. This experiment will lead to record the electrochemical signals of the redox molecules in solution (DmFc) and the immobilized ones (Fc). At a potential lower than 0 V/ $E_{Fc+/Fc}$, a well-defined plateau current was obtained resulting from the response of the $DmFc^+$/DmFc. Interestingly, by sweeping the potential from 0 to 0.4 V, a plateau current was observed which could be attributed to the electrochemical signal of the immobilized Fc moieties (Figure 4.26). For comparison, the CV recorded far from the substrate (L=10) displays a steady state shape for DmFc, while a peak shape is obtained for the immobilized Poly(FcIL). Thus, the increase of the current of DmFc, at lower UME/substrate distance, is consistent with the obtained positive feedback (Figure 4.25). However, for immobilized poly(FcIL) the electrochemical behavior is unexpected since it changes from immobilized (non-diffusive) to diffusional system.

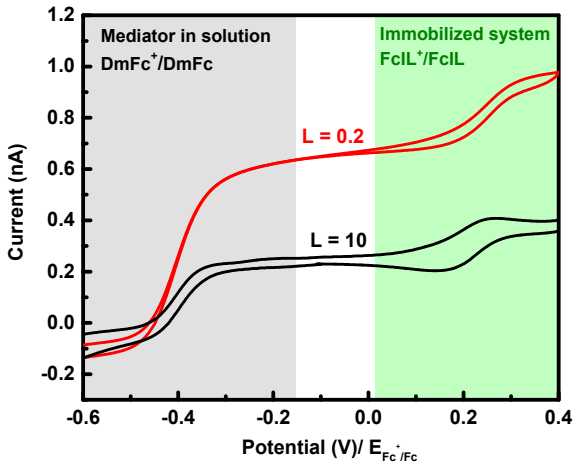

Figure 4.26 Cyclic voltammograms at different distance tip – substrate recorded at the Pt UME/Poly(FcIL) in a MeCN solution containing 0.05 mM of DmFc and 0.1 M of $TBAPF_6$.

These intriguing results conduct us to perform further investigations for understanding this behavior. Next, the DmFc solution was removed from the SECM electrochemical cell and was replaced by a MeCN solution containing only 0.1 M $TBAPF_6$ as supporting electrolyte. Different cyclic voltammograms were recorded by varying the tip – substrate distance as shown in the figure 3.27.

To follow the evolution of the electrochemical response, different CVs were recorded at different distance tip – substrate ranging from L = 0.2 to 3. The displacement of the tip is carried out by manual control considering the initial UME position located at 5 µm (L = 1) from the substrate determined during the approach curve in the presence of DmFc as a redox probe (Figure 4.25).

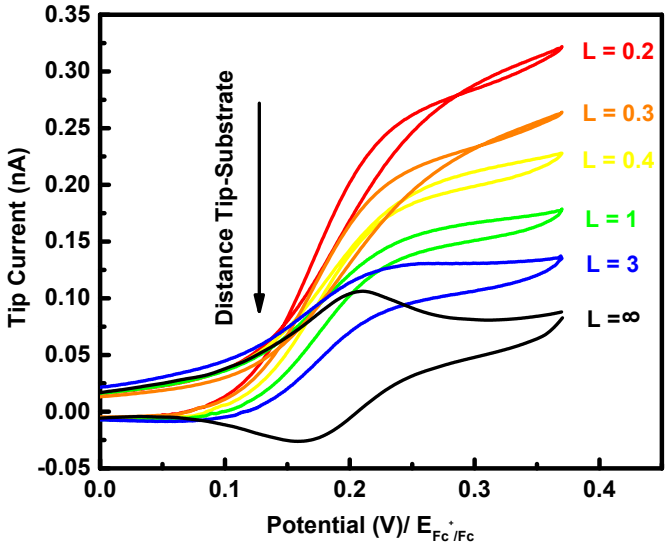

Figure 4.27 Cyclic voltammograms at different distance tip – substrate recorded at the Pt UME/Poly(FcIL) in a MeCN solution containing 0.1 M of $TBAPF_6$.

Far from the substrate L>3, the recorded CV at the modified UME displays a peak shape behavior confirming the presence of immobilized poly(FcIL) (black curve). For L=3 (blue curve) the shape of the CV changes from total peak shape to a mixed situation corresponding to a peak shape and steady state. Interestingly, at L = 1, instead of obtaining peak-like CV as previously presented, a plateau current was achieved. Further approach of the poly(FcIL)/UME to the substrate, displays a sigmoidal CV with an increase of the plateau current. In order to confirm this result, different CVs at L= 0.2 were recorded by varying the scan rate from 0.01 to 0.4 $V.s^{-1}$ as presented in the figure 4.7. The Figure 4.27 shows that the values of the steady state current remain unchanged while varying the scan rate. This result confirms the establishment of steady state regime of the attached poly(FcIL) in confined tip/substrate distance. In a typical SECM experiment, redox mediator in solution, the steady state current increases with decrease of the separate tip/substrate distance which is originated from the feedback loop due to the regeneration of the mediator at the conducting substrate. However, in our case the observed current increase could not be explained by the redox

feedback loop since the Fc species are attached onto the surface and the separate tip/substrate distance is in the μm range. The current enhancement could be due to the mechanical properties, for instance the flexibility, of the polymer brushes that induce a diffusion-like process in which the charge propagation results from an electron hopping between the Fc moieties within the film. The latter is expected to increase in confined media when the poly(FcIL)/UME is brought closer to the substrate. Overall, the performed SECM experiments are unprecedented and exhibit unusual electrochemical behavior presenting a change from peak-like to steady state CV of the immobilized poly(FcIL).

Even though the Fc moieties are immobilized onto the electrode surface, a diffusion process could occur, resulting from the flexibility of the polymer chain. Demaille et al[49,50] reported a diffusion coefficient of redox poly(ethylene glycol) immobilized onto Au tip by self-assembled monolayer (SAM). The methodology consists to compress the polymer modified Au tip onto a conductive substrate (few nanometer separate distance) and to follow the movement of the Fc heads. It was demonstrated that the mechanical force induces a diffusion loop of the Fc moieties in between the tip and the substrate with an apparent diffusion coefficient in the order of 10^{-9} – 10^{-8} $cm^2.s^{-1}$ via the following equation $i = \frac{2\pi FDR_{tip}\Gamma}{a}$ (4.18)

where a is the monomer statistical length, R_{tip} the radius of the UME, Γ the chain surface coverage. In our case, due to the high flexibility of the system via brush-like polymer chains, the diffusion of Fc moieties is probably occurring in confined medium (modified UME close to the substrate). By considering the difference of the geometry of the tip, the apparent diffusion coefficient of the immobilized Poly(FcIL) can be estimated using the formula $i = \frac{4FDR_{tip}\Gamma}{a}$ (4.19). For tip/substrate distance L=0.2 (red curve in Figure 4.27) the calculated apparent diffusion coefficient is around 0.8 10^{-9} $cm^2.s^{-1}$. Recently, the diffusion coefficient of immobilized flexible redox layer has been measured using Randles-Sevcik equation[48]. Indeed, during the electrochemical characterization of poly(FcIL)/UME in electrolytic solution, the current became linear with the square root of the scan rate at higher scan rate (Figure 4.24b). This linearity indicates an additional dependence of the electron transfer rate on the diffusion of the ferrocene head groups to and from the surface. In other words, the mass transport follows a semi-infinite diffusion process within this time scale. The diffusion constants of ferrocene could be determined from the anodic peak current using the Randles-Sevcik equation $i_p = 0.4463nFAC\left(\frac{nFvD}{RT}\right)^{1/2}$ (4.20) . In this equation, the concentration, C, can be replaced by Γ/e, with e being the layer thickness and Γ de surface concentration. A s result, the diffusion coefficient of Fc in poly(FcIL)/UME is estimated at 1.9 10^{-12} $cm^2.s^{-1}$. Simple comparison shows a difference of about 3 order of magnitude in the diffusion coefficient when comparing the poly(FcIL) far from the substrate (L>4) and close to

the substrate (L=0.2). The transition from peak shape behavior to steady state could be related to the variation of the diffusion coefficient in confined media (the tip is close to the substrate) and thus the flexibility of the poly(FcIL) increases with the decreases of the tip/substrate distance.

Unlike the diffusion mentioned by Demaille et al.[50] where the oxidized Fc heads generated from the tip diffuse to the substrate and come back to the tip, the present notion of diffusion includes several factors (translocation of ions, electrophoretic migration of ions, charge diffusion resulting from the change of the viscoelastic properties of the polymer in the presence/absence of electric field). The latter could induce a change in term of electron transfer rate and the electron transport through the film and the configuration of the polymer layer.

In addition, a series of experiment were performed by changing the chemical environment, scan rate, and distance. Two mixtures of an ionic liquid, EMITFSI, and MeCN with different proportion were used for this study. As expected, similar behavior was obtained, i.e. by approaching the modified tip to the substrate, a transition between the peak – like current to plateau current is observed. For the mixture 1 composed of EMITFSI:MeCN (70:30 v/v), the current intensity is lower than in the case of the mixture 2 (70 MeCN: 30 EMITFSI (v/v)), resulting from the different viscosity of the medium. In addition, the higher concentration of EMITFSI induces a delay for the switching between the two regimes (Figure 4.28 b and e). At an intermediate distance (L = 1), the current obtained in the solution 2 is less dependent on the scan rate than the values recorded in the solution 1. However, at a smaller distance L=0.2, plateau currents were obtained for both cases.

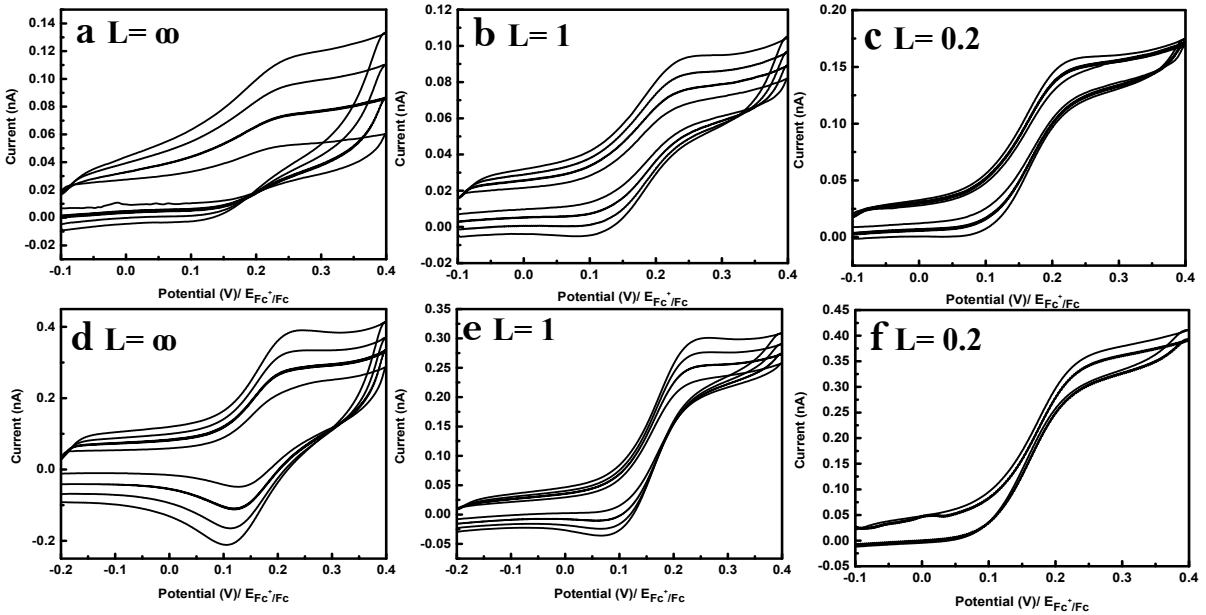

Figure 4.28 Cyclic voltammograms at different distance tip – substrate ***(a, d)*** L = ∞, ***(b, e)*** L = 1, ***(c, f)*** L = 0,2 and different scan rate (0,02 to 0,2 V.s^{-1}) recorded at the Pt UME/Poly(FcIL) in (a,b,c) EMITFSI/ACN 7:3 (v/v) and (d,e,f) EMITFSI/ACN 3:7 (v/v).

However, the proposed explanation is only a hypothesis and other phenomenon could explain this unexpected behavior. Thus, during the CV measurement, the formation of an electric field is expected. Owning a high concentration of cationic imidazolium species, the Poly(FcIL) is susceptible to the electric field and the cation is attracted to the negative side via the electric force $\vec{F} = q\vec{E}$, where E is the electric field and q is the net charge on the object. Furthermore, the anion from the bulk moves to the positive side (UME) with the opposite force. For non-uniform electric field, the electric flux is designed to be:

$$\phi = \int \vec{E} d\vec{S} = \frac{q}{2\varepsilon_0}\left(1 - \frac{d}{\sqrt{d^2 + R^2}}\right) \quad (4.21)$$ where d the distance between 2 electrodes, R the radius of the substrate. When d << R, the electric flux becomes: $$\phi = \frac{q}{2\varepsilon_0}\left(1 - \frac{d}{R}\right) \quad (4.22)$$

Therefore, by approaching the tip to the substrate, the electric flux passing the substrate increases.

As consequence, the imidazolium rings will move with a velocity controlled by the Coulombic forces and the viscosity drag forces. It is known that the electrophoretic mobility (μ) that relates the applied electric field to the velocity as: $$\mu = \frac{\varepsilon_m \xi}{\eta} \quad (4.23)$$ with ξ is the zeta potential, ε_m is the permittivity of the liquid and η is the viscosity of the liquid. Perhaps, by this way, the polymer chain is in an outstretched configuration (Scheme 4.2c). This hypothesis is consistent with the first proposed explanation based on the change of the flexibility and thus the diffusion coefficient.

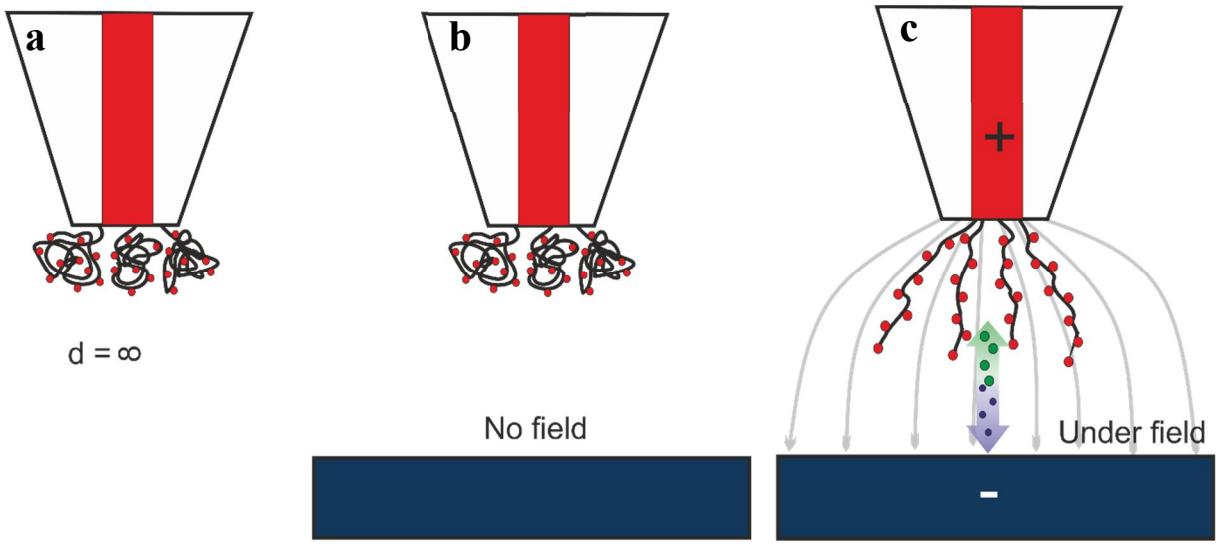

Scheme 4.2 Possible mechanism for the enhancement of the measured current: ***(a)*** configuration in absence of substrate, ***(b)*** configuration of Poly(FcIL)/UME in presence of insulating substrate and ***(c)*** configuration of the polymer chains in presence of conductive substrate

To confirm the crucial role of the imidazolium rings, the poly(vinylferrocene) modified UME was used to perform the same experiment. As presented in the figure 4.S8, there is no a clear increase of the faradic current when the tip approach the substrate. Moreover, at the explored UME/substrate distance (L between 3 and 0.2), the transition between peak –shape to steady state is not fully observed with the poly(vinylferrocene). This result, highlight the role of the ionic liquid within the polymer structure in the observed phenomena.

In addition, a well-defined structure of the polymer brushes enhanced the electron transport via hopping by independent channels with a decrease of the perturbation (Scheme 4.3). Considering a Fc^+ head at a layer n and a Fc head at a layer n+1, the electron hopping can be occurred as $Fc^+_{(n)} \rightleftarrows Fc^+_{(n+1)} + Fc_{(n)}$. The charge mobility is calculated as $\mu = \upsilon_d / E$ (4.24) with E is the electric field and ν_d is the charge drift velocity which can be considered as a ratio between the hopping distance (λ) and the hopping time (τ), i.e. $\upsilon_d = \lambda / \tau = \lambda k_{ex}$ (4.25) with k_{ex} is the hopping frequency or the rate constant for governing the hopping (s^{-1}). It has been demonstrated that the dependency of the mobility on the electric field is as followed[51]:

$\mu E = \lambda A' \exp(-\Delta G_0^{\neq} / RT) \exp(\alpha n F \lambda E) / RT$ (4.26), with $\lambda A' \exp(-\Delta G_0^{\neq} / RT)$ is the contribution of the diffusion and the remaining part represents the perturbation due to the presence of the electric field. By approaching the tip to the substrate, an increase of the electric field is expected which induces a strong enhancement of the charge mobility, i.e. the hopping rate.

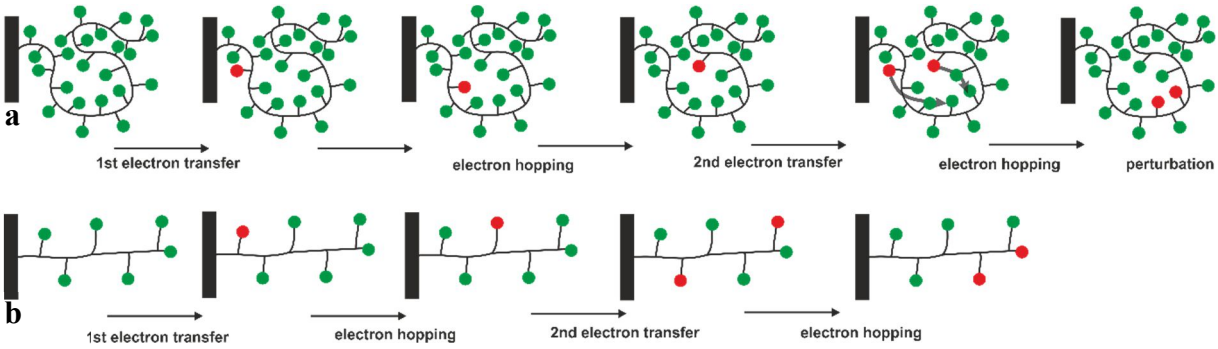

Scheme 4.3 Possible pathway of electron hopping in two configurations: ***(a)*** w/o electric field and ***(b)*** under electric field.

As a consequence, the measured diffusion coefficient can be expressed as $D_{exp} = D_0 + D_{ET}$ (4.27)[51] with D_0 is the diffusion coefficient in the absence of any self-exchange reactions and D_{ET} is the diffusion due to the self-exchange reactions, which is expressed as followed:

$D_{ET} = \frac{\pi k_{ex} \delta^2 c}{4}$ (4.28) where c the concentration of the co-reactant with which the diffusing molecules exchanges electrons and δ the distance between the centers of 2 species when the electron exchange occurs. In solution, the value of D_0 is typically much larger than the D_{ET}. However, in the situation where the electroactive species are immobilized onto the electrode

surface, smaller diffusion coefficient D_0 ($<10^{-8}$ $cm^2.s^{-1}$) is obtained, inducing a considerable contribution from the diffusion by self-exchange reactions.

In order to verify the hypothesis about the generation of electric field in the presence of a conductive substrate, the same experiment was performed by approaching the modified UME onto an insulating glass substrate as presented in the figure 4.29 and 4.S9. The peak-like behavior remains visible whatever the selected tip – substrate distance. Interestingly, by approaching the tip to the insulating substrate, a diminution of the current is obtained. In the absence of the formation of the electric field in between the UME and the substrate, the polymer brushes may be in a depleted configuration as presented in the scheme 4.2b.

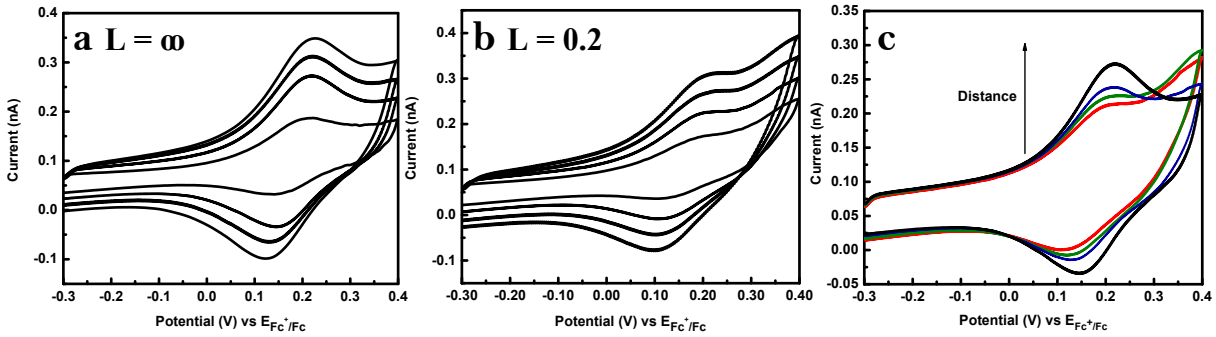

Figure 4.29 Cyclic voltammograms at different distance tip – substrate ***(a)*** L = ∞, ***(b)*** L = 0.2 and different scan rate (0.02 to 0,2 $V.s^{-1}$); ***(c)*** CVs recorded at various distance (v = 0.1 $V.s^{-1}$) recorded at the Pt UME/Poly(FcIL) in MeCN solution containing 0.1 M $TBAPF_6$

The change in the configuration of the polymer chains due to the concentration of electrolyte has been recently reported by Rodríguez-Lopez et al.[52] Briefly, different cyclic voltammograms were recorded in organic solvents containing millimolar concentration of redox-active polymer (VioRAP) and various concentration of supporting electrolyte. As a consequence, increasing the concentration of electrolyte induces a transition from peak-shape current to plateau current. The variation of the electrochemical response in function of the concentration of electrolyte is attributed to the dependence of the electrostatic interaction of permanent charged RAP on the ionic strength due to the supporting electrolyte in solution, resulting to a modulation of the hydrodynamic radius of the polymer chains. As conclusion, it has been claimed that the electrostatic interaction has strong impact on the electrochemical response of the redox-active polymer. As mentioned in the chapter 2, the ionic flux is described as $J_i = -D_i \nabla c_i - \frac{z_i F}{RT} D_i \nabla \phi + u c_i$ (2.9), which is depending on the velocity of the ion. In our study, as being supposed that the polymer layer is swelled by approaching the substrate, it is worth noting that the electrostatic interaction is facilitated by generating ion channels, resulting to higher ionic flux, i.e. a higher electron transfer/transport rate. By analogy with Rodríguez-Lopez et al work, approaching the modified UME to the conducting substrate the local concentration of the electrolyte could change which may explain the

variation of the CV behavior from peak-shape to steady state. In this case, the performed SECM experiments could be treated as a Scanning Ion Conductance Microscopy SICM.

In summary, the increase of the current by decreasing the distance tip – conductive substrate observed in the figure 4.27 and 4.28 could be attributed to: (i) Change of the dynamic of the polymer brushes in confined media inducing increase of the diffusion coefficient of the redox-active group (Fc). (ii) An increase of the hopping rate by increasing the electric field, (iii) An increase of the diffusion of the anion from the bulk to the polymer layer, (iv) A change of the configuration of the polymer (outstretched brushes) by displacement of the imidazolium centers in the presence of the field, (v) Finally, at a smaller distance, the establishment of feedback loop (regeneration of the attached mediator) is not fully excluded.

4.4.3 Probe-less SECM by using modified ultramicroelectrode

Even if the origin of the change from the peak shape to steady state still not clear, the experimental results demonstrate clearly the occurrence of this change. The interesting properties of the Poly(FcIL) when approaching conductive substrates, conduce us to further investigate the modified surface to probe the reactivity of the surface by using feedback mode. As displayed in the figure 4.30, the current intensity increases by approaching the tip to the substrate showing a positive feedback behavior. The interaction between the Poly(FcIL) and the substrate starts at a separate distance L bellow 1, while for a mediator in solution this interaction is observed at L bellow 4 (see Figure 4.25).The observed distance delay is comparable to the one observed when the approach curve is recorded in viscous media and could reflect a delay in the establishment of the feedback loop due to a lower diffusion coefficient[53]. Despite the origin of the feedback, this experiment demonstrates the possibility to use Poly(FcIL) modified UME for probing conducting substrate.

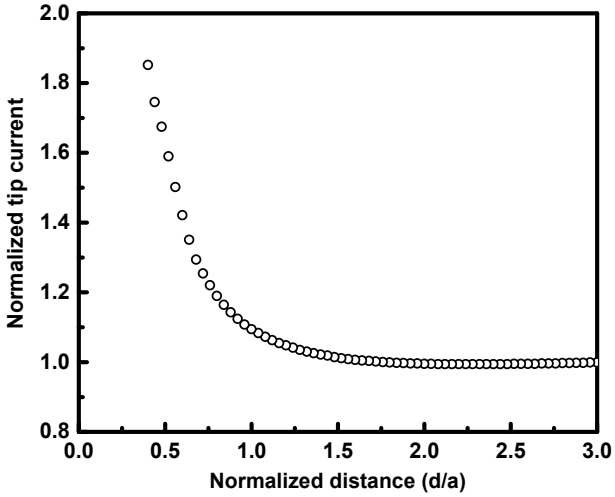

Figure 4.30 Approach curves onto Pt substrate by using Pt UME/Poly(FcIL) in a MeCN solution containing 0.1 M of $TBAPF_6$ by applying 0.35 V vs $E_{Fc+/Fc}$ to the tip w/o bias to the substrate.

As discussed in the previous part of this chapter, the cyclic voltammetry at different distance allows to reconstruct the approach curve with high accuracy. As illustrated in the figure 4.31,

the red dots represent the variation of the measured steady state current, $I_{normalized}$, at different L ranging from 3 to 0.2. Interestingly, these values match with the experimental approach curve recorded in the absence of the mediator in solution (grey curve).

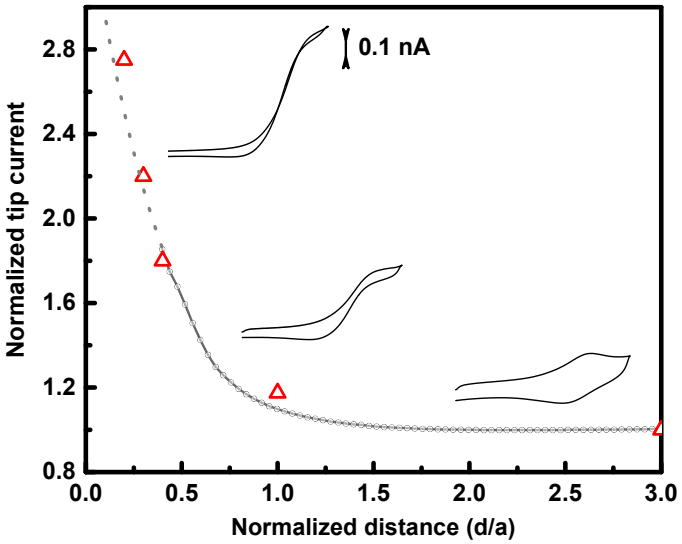

Figure 4.31 Approach curves reconstructed by cyclic voltammograms at different distances by using Pt UME/Poly(FcIL). (Solid curve) Experimental approach curve; (dot line) Extension of the experimental curve.

In summary, we have shown the possibility to immobilized task-specific ionic liquid on ultramicroelectrode by using SI-ATRP. The presence of poly(FcIm) was evidenced by following the redox signal of ferrocene group. As a result, the presence of imidazolium ring influences strongly the kinetic heterogeneous electron transfer and electron transport. In addition, the presence of a conductive substrate generates an electric field in between that influences strongly the viscoelastic properties of the polymer layer, resulting to a change of the flexibility of the chains and the accessibility of the anion from the bulk. In the other hand, a new kind of SECM setup can be developed with an electrolytic free solution to characterize the immobilized redox molecules. Besides, we believe that the large variety of task specific ionic liquid monomer described in the literature can be used for surface functionalization at micro/nano scale and open a new possibility for tuning of new properties of the surface at small scale. Particularly, we will develop this new approach for analyzing biological systems such as cells.

4.5 CONCLUSION

The local reactivity of nanomaterials is far different from the macroscopic behaviors where a collective response is observed. By using an ultramicroelectrode, the scanning electrochemical microscopy provides a powerful tool for investigating the local behaviors of a material with and/or without applied bias. This technique can cover a large range of application from fundamental studies to application in diverse fields, including energy storage and conversion systems. In this chapter, the SECM technique has been used for (1) studying the properties of graphene-based materials, (2) investigating the properties in solution of ionic liquid and over an ionic liquid layer, and (3) possible application in energy field by following the lithiation/delithiation process.

In the first part, it is known that graphene becomes nowadays emerging materials for multi-purposes. However, the electronic/electrochemical properties of the graphene – based materials are still opened for research. Within this context, we have followed the change in the electrochemical properties of graphene after several functionalization. The switching properties of the materials are attributed to a change of the Fermi level depending on the surface modification. By using electrochemical tools, the pristine SLG can be tuned into p-type or n-type graphene. Interestingly, the modulation of the doping type of graphene can be electrochemically followed by using SECM.

In the second part, the localized electrochemical properties of the (redox)-ionic liquids have been revealed. At a very close distance tip – insulating substrate in an ionic liquid solution containing a redox molecule, immobilized – like system is obtained instead of diffusion-controlled system as reported in literature. It is further demonstrated to be related to the high viscosity of the ionic liquid medium, resulting to a non-diffusive like system. In parallel, the electrochemical signature of the immobilized redox-ionic liquid has also been investigated, suggesting 2-D charge transport within a top compact single layer of ferrocenated ionic liquid. Furthermore, the polymeric ionic liquid is proven to be capable to accelerate the electron transfer with inner sphere probe (e.g. $K_3Fe(CN)_6$). Interestingly, by immobilizing the polymer FcIL onto an ultramicroelectrode surface was used as probe-less in SECM configuration. The results demonstrate the change of the electrochemical signal of the attached Fc moieties from peak shape to sigmoidal shape. In addition, the poly(FcIL)/UME could be used for recording approach curve in the absence of redox mediator in solution.

4.6 REFERENCES

(1) Kwak, J.; Bard, A. J. Scanning Electrochemical Microscopy. Theory of the Feedback Mode. *Anal. Chem.* **1989**, *61* (11), 1221–1227.

(2) Bard, A. J.; Fan, F.-R. F. R. F.; Kwak, J.; Lev, O. Scanning Electrochemical Microscopy. Introduction and Principles. *Anal. Chem.* **1989**, *61* (2), 132–138.

(3) Bard, A. J.; Faulkner, L. R. *Electrochemical methods: Fundamentals and Applications*, John Wiley & Sons, INC, 2nd edition; 2001.

(4) Polcari, D.; Dauphin-Ducharme, P.; Mauzeroll, J. Scanning Electrochemical Microscopy: A Comprehensive Review of Experimental Parameters from 1989 to 2015. *Chem. Rev.* **2016**, *116* (22), 13234–13278.

(5) Schuewer, N.; Tercier-Waeber, M.-L.; Danial, M.; Klok, H.-A. Voltammetric Detection of Hg2+ Using Peptide-Functionalized Polymer Brushes. *Aust. J. Chem.* **2012**, *65* (8), 1104–1109.

(6) Ku, S.-Y.; Wong, K.-T.; Bard, A. J. Surface Patterning with Fluorescent Molecules Using Click Chemistry Directed by Scanning Electrochemical Microscopy. *J. Am. Chem. Soc.* **2008**, *130* (8), 2392–2393.

(7) Bard, A. J.; Mirkin, M. V. *Scanning Electrochemical Microscopy*, 2nd edition; CRC Press, 2012.

(8) Bae, J.; Park, Y. J.; Lee, M.; Cha, S. N.; Choi, Y. J.; Lee, C. S.; Kim, J. M.; Wang, Z. L. Single-Fiber-Based Hybridization of Energy Converters and Storage Units Using Graphene as Electrodes. *Adv. Mater.* **2011**, *23* (30), 3446–3449.

(9) Punckt, C.; Roy-mayhew, J. D.; Bozym, D. J.; Punckt, C.; Aksay, I. A. Functionalized Graphene as a Catalytic Counter Electrode in Dye-Sensitized Solar Cells. *ACS Nano* **2010**, *4* (10), 6203–6211.

(10) Polat, E. O.; Balcı, O.; Kocabas, C. Graphene Based Flexible Electrochromic Devices. *Sci. Rep.* **2014**, *4*, 6484.

(11) Tae-Hee, H.; Youngbin, L.; Mi-Ri, C.; Seong-Hoon, W.; Sang-Hoon, B.; Byung Hee, H.; Jong-Hyun, A.; Tae-Woo, L. Extremely Efficient Flexible Organic Light-Emitting Diodes with Modified Graphene Anode. *Nat. Photonics* **2012**, *6* (2), 105–110.

(12) Li, N.; Oida, S.; Tulevski, G. S.; Han, S.-J.; Hannon, J. B.; Sadana, D. K.; Chen, T.-C. Efficient and Bright Organic Light-Emitting Diodes on Single-Layer Graphene Electrodes. *Nat. Commun.* **2013**, *4*, 2294.

(13) Qu, L.; Liu, Y.; Baek, J. B.; Dai, L. Nitrogen-Doped Graphene as Efficient Metal-Free Electrocatalyst for Oxygen Reduction in Fuel Cells. *ACS Nano* **2010**, *4* (3), 1321–1326.

(14) Robinson, R. S. Morphology and Electrochemical Effects of Defects on Highly Oriented Pyrolytic Graphite. *J. Electrochem. Soc.* **1991**, *138* (8), 2412.

(15) Bahr, J. L.; Tour, J. M. Highly Functionalized Carbon Nanotubes Using in Situ Generated Diazonium Compounds. *Chem. Mater.* **2001**, *13* (14), 3823–3824.

(16) Banerjee, S.; Hemraj-Benny, T.; Wong, S. S. Covalent Surface Chemistry of Single-Walled Carbon Nanotubes. *Adv. Mater.* **2005**, *17* (1), 17–29.

(17) Englert, J. M.; Dotzer, C.; Yang, G.; Schmid, M.; Papp, C.; Gottfried, J. M.; Steinrück, H.-P.; Spiecker, E.; Hauke, F.; Hirsch, A. Covalent Bulk Functionalization of Graphene. *Nat. Chem.* **2011**, *3* (4), 279–286.

(18) Huang, P.; Zhu, H.; Jing, L.; Zhao, Y.; Gao, X. Graphene Covalently Binding Aryl Groups: Conductivity Increases Rather than Decreases. *ACS Nano* **2011**, *5* (10), 7945–7949.

(19) Amemiya, S.; Chen, R.; Nioradze, N.; Kim, J. Scanning Electrochemical Microscopy of Carbon Nanomaterials and Graphite. *Acc. Chem. Res.* **2016**, *49* (9), 2007–2014.

(20) Tan, C.; Rodríguez-López, J.; Parks, J. J.; Ritzert, N. L.; Ralph, D. C.; Abruña, H. D.

Reactivity of Monolayer Chemical Vapor Deposited Graphene Imperfections Studied Using Scanning Electrochemical Microscopy. *ACS Nano* **2012**, *6* (4), 3070–3079.

(21) Hu, R.; Cola, B. A.; Haram, N.; Barisci, J. N.; Lee, S.; Stoughton, S.; Wallace, G.; Too, C.; Thomas, M.; Gestos, A.; Dela Cruz, M. E.; Ferraris, J. P.; Zakhidov, A. A.; Baughman, R. H. Harvesting Waste Thermal Energy Using a Carbon-Nanotube-Based Thermo-Electrochemical Cell. *Nano Lett.* **2010**, *10* (3), 838–846.

(22) Deng, B.; Hsu, P. C.; Chen, G.; Chandrashekar, B. N.; Liao, L.; Ayitimuda, Z.; Wu, J.; Guo, Y.; Lin, L.; Zhou, Y.; Aisijiang, M.; Xie, Q.; Cui, Y.; Liu, Z.; Peng, H. Roll-to-Roll Encapsulation of Metal Nanowires between Graphene and Plastic Substrate for High-Performance Flexible Transparent Electrodes. *Nano Lett.* **2015**, *15* (6), 4206–4213.

(23) Nicholson, R. S.; Shain, I. Theory of Stationary Electrode Polarography: Single Scan and Cyclic Methods Applied to Reversible, Irreversible, and Kinetic Systems. *Anal. Chem.* **1964**, *36* (4), 706–723.

(24) Lefrou, C.; Cornut, R. Analytical Expressions for Quantitative Scanning Electrochemical Microscopy (SECM). *ChemPhysChem* **2010**, *11* (3), 547–556.

(25) Zhong, J. H.; Zhang, J.; Jin, X.; Liu, J. Y.; Li, Q.; Li, M. H.; Cai, W.; Wu, D. Y.; Zhan, D.; Ren, B. Quantitative Correlation between Defect Density and Heterogeneous Electron Transfer Rate of Single Layer Graphene. *J. Am. Chem. Soc.* **2014**, *136* (47), 16609–16617.

(26) Vita, H.; Böttcher, S.; Horn, K.; Voloshina, E. N.; Ovcharenko, R. E.; Kampen, T.; Thissen, A.; Dedkov, Y. S. Understanding the Origin of Band Gap Formation in Graphene on Metals: Graphene on Cu/Ir(111). *Sci. Rep.* **2014**, *4* (111), 5704.

(27) Ritzert, N. L.; Rodríguez-López, J.; Tan, C.; Abruña, H. D. Kinetics of Interfacial Electron Transfer at Single-Layer Graphene Electrodes in Aqueous and Nonaqueous Solutions. *Langmuir* **2013**, *29* (5), 1683–1694.

(28) Kiani, A.; Alpuche-aviles, M. A.; Eggers, P. K.; Jones, M.; Gooding, J. J.; Paddon-row, M. N.; Bard, A. J. Scanning Electrochemical Microscopy . 59 . Effect of Defects and Structure on Electron Transfer through Self-Assembled Monolayers. *Langmuir* **2008**, No. 13, 2841–2849.

(29) Gu, A. G.; Ebejer, N.; Snowden, M. E.; Macpherson, J. V; Unwin, P. R. Structural Correlations in Heterogeneous Electron Transfer at Monolayer and Multilayer Graphene Electrodes. *J. Am. Chem. Soc* **2012**, *134* (134), 7258–7261.

(30) Finklea, H. O.; Avery, S.; Lynch, M. Blocking Oriented Monolayers of Alkyl Mercaptans on Gold Electrodes. *Langmuir* **1987**, *3* (8), 409–413.

(31) Hao, R.; Qian, W.; Zhang, L.; Hou, Y. Aqueous Dispersions of TCNQ-Anion-Stabilized Graphene Sheets. *Chem. Commun.* **2008**, No. 48, 6576–6578.

(32) Khanra, P.; Lee, C. N.; Kuila, T.; Kim, N. H.; Park, M. J.; Lee, J. H. 7,7,8,8-Tetracyanoquinodimethane-Assisted One-Step Electrochemical Exfoliation of Graphite and Its Performance as an Electrode Material. *Nanoscale* **2014**, *6* (9), 4864–4873.

(33) Tsai, H.-Z.; Omrani, A. A.; Coh, S.; Oh, H.; Wickenburg, S.; Son, Y.; Wong, D.; Riss, A.; Jung, H. S.; Nguyen, G. D.; Rodgers, G. F.; Aikawa, A. S.; Taniguchi, T.; Watanabe, K.; Zettl, A.; Louie, S. G.; Lu, J.; Cohen, M. L.; Crommie, M. F. Molecular Self-Assembly in a Poorly Screened Environment: F 4 TCNQ on Graphene/BN. *ACS Nano* **2015**, *9* (12), 12168–12173.

(34) Santos, L.; Ghilane, J.; Lacroix, J. C. Formation of Mixed Organic Layers by Stepwise Electrochemical Reduction of Diazonium Compounds. *J. Am. Chem. Soc.* **2012**, *134* (12), 5476–5479.

(35) Pinson, J.; Podvorica, F.; Pinson, J. Attachment of Organic Layers to Conductive or Semiconductive Surfaces by Reduction of Diazonium Salts. *Chem. Soc. Rev.* **2005**, *34*, 429–439.

(36) Fontaine, O.; Ghilane, J.; Martin, P.; Lacroix, J. C.; Randriamahazaka, H. Ionic Liquid Viscosity Effects on the Functionalization of Electrode Material through the Electroreduction

of Diazonium. *Langmuir* **2010**, *26* (23), 18542–18549.

(37) Delamar, M.; Désarmot, G.; Fagebaume, O.; Hitmi, R.; Pinsonc, J.; Savéant, J.-M. Modification of Carbon Fiber Surfaces by Electrochemical Reduction of Aryl Diazonium Salts: Application to Carbon Epoxy Composites. *Carbon N. Y.* **1997**, *35* (6), 801–807.

(38) Sun, T.; Yu, Y.; Zacher, B. J.; Mirkin, M. V. Scanning Electrochemical Microscopy of Individual Catalytic Nanoparticles. *Angew. Chemie - Int. Ed.* **2014**, *53* (51), 14120–14123.

(39) Quinn, B. M.; Prieto, I.; Haram, S. K.; Bard, A. J. Electrochemical Observation of a Metal/Insulator Transition by Scanning Electrochemical Microscopy. *J. Phys. Chem. B* **2001**, *105* (31), 7474–7476.

(40) Giovannetti, G.; Khomyakov, P. A.; Brocks, G.; Karpan, V. M.; Van Den Brink, J.; Kelly, P. J. Doping Graphene with Metal Contacts. *Phys. Rev. Lett.* **2008**, *101* (2), 4–7.

(41) Meyer, B. K.; Polity, A.; Reppin, D.; Becker, M.; Hering, P.; Klar, P. J.; Sander, T.; Reindl, C.; Benz, J.; Eickhoff, M.; Heiliger, C.; Heinemann, M.; Bläsing, J.; Krost, A.; Shokovets, S.; Müller, C.; Ronning, C. Binary Copper Oxide Semiconductors: From Materials towards Devices. *Phys. Status Solidi* **2012**, *249* (8), 1487–1509.

(42) Bentley, C. L.; Li, J.; Bond, A. M.; Zhang, J. Mass-Transport and Heterogeneous Electron-Transfer Kinetics Associated with the Ferrocene/Ferrocenium Process in Ionic Liquids. *J. Phys. Chem. C* **2016**, *120*, 16516–16525.

(43) Walsh, D. A.; Lovelock, K. R. J.; Licence, P.; Walsh, D. A. Ultramicroelectrode Voltammetry and Scanning Electrochemical Microscopy in Room-Temperature Ionic Liquid Electrolytes. *Chem Soc Rev* **2010**, *39*, 4185–4194.

(44) Barhdadi, R.; Laurent, M.; Troupel, M.; Marne, P. V. De. Determination of Viscosity , Ionic Conductivity , and Diffusion Coefficients in Some Binary Systems : Ionic Liquids + Molecular Solvents. *J. Chem. Eng. Data* **2006**, *51*, 680–685.

(45) Nkuku, C. A.; Lesuer, R. J. Electrochemistry in Deep Eutectic Solvents. *J. Phys. Chem. B* **2007**, *111*, 13271–13277.

(46) Hauquier, F.; Ghilane, J.; Fabre, B.; Hapiot, P. Conducting Ferrocene Monolayers on Nonconducting Surface. *J. Am. Chem. Soc.* **2008**, *130* (9), 2748–2749.

(47) Bui-Thi-Tuyet, V.; Trippe-Allard, G.; Ghilane, J.; Randriamahazaka, H. Surface and Electrochemical Properties of Polymer Brush-Based Redox Poly(Ionic Liquid). *ACS Appl. Mater. Interfaces* **2016**, *8* (42), 28316–28324.

(48) Steentjes, T.; Jonkheijm, P.; Huskens, J. Electron Transfer Processes in Ferrocene-Modified Poly(Ethylene Glycol) Monolayers on Electrodes. *Langmuir* **2017**, *33* (43), 11878–11883.

(49) Abbou, J.; Anne, A.; Demaille, C. Accessing the Dynamics of End-Grafted Flexible Polymer Chains by Atomic Force-Electrochemical Microscopy. Theoretical Modeling of the Approach Curves by the Elastic Bounded Diffusion Model and Monte Carlo Simulations. Evidence for Compression-Induced Late. *J. Phys. Chem. B* **2006**, *110* (45), 22664–22675.

(50) Anne, A.; Demaille, C.; Goyer, C. Electrochemical Atomic-Force Microscopy Using a Tip-Attached Redox Mediator. Proof-of-Concept and Perspectives for Functional Probing of Nanosystems. *ACS Nano* **2009**, *3* (4), 819–827.

(51) Buttry, D. A.; Anson, F. C. Electron Hopping vs. Molecular Diffusion as Charge Transfer Mechanisms in Redox Polymer Films. *J. Electroanal. Chem.* **1981**, *130* (C), 333–338.

(52) Burgess, M.; Hernández-Burgos, K.; Schuh, J. K.; Davila, J.; Montoto, E. C.; Ewoldt, R. H.; Rodríguez-López, J. Modulation of the Electrochemical Reactivity of Solubilized Redox Active Polymers via Polyelectrolyte Dynamics. *J. Am. Chem. Soc.* **2018**, *140* (6), 2093–2104.

(53) Ghilane, J.; Lagrost, C.; Hapiot, P. Scanning Electrochemical Microscopy in Nonusual Solvents: Inequality of Diffusion Coefficients Problem. *Anal. Chem.* **2007**, *79* (19), 7383–7391.

4.7 APPENDICES

For SECM measurements, a commercial four-electrode SECM cell was used. A silver wire and a platinum wire were used as a reference electrode (RE) and counter electrode (CE), respectively. An ultramicroelectrode with a diameter of 10 mm was used as working electrode. All the potentials were recalculated using the ferrocenium/ferrocene (Fc^+/Fc) redox couple as internal reference. Surface modification was carried out in a conventional electrochemical cell using silver/silver chloride (Ag|AgCl) as RE, stainless steel mesh as CE. The electrochemical and SECM measurements were performed using CHI920C bipotentiostat (CH Instruments, Austin, Texas).

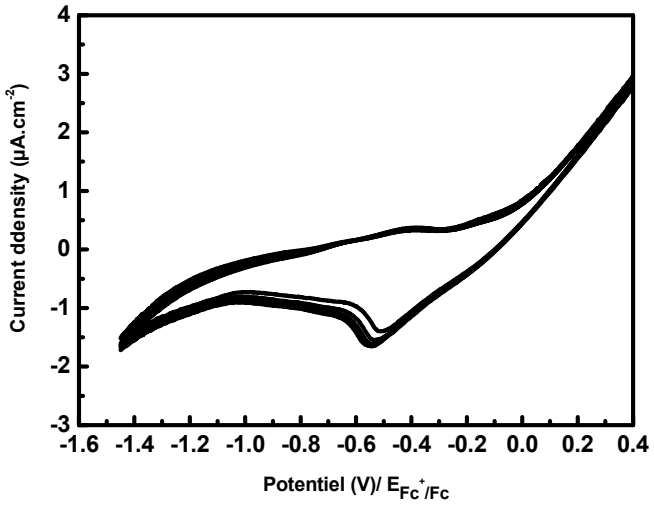

Figure 4.S1 Cyclic voltammograms of SLG/PET in MeCN solution containing 1 mM of ferrocene and 0.1 M of $TBAPF_6$

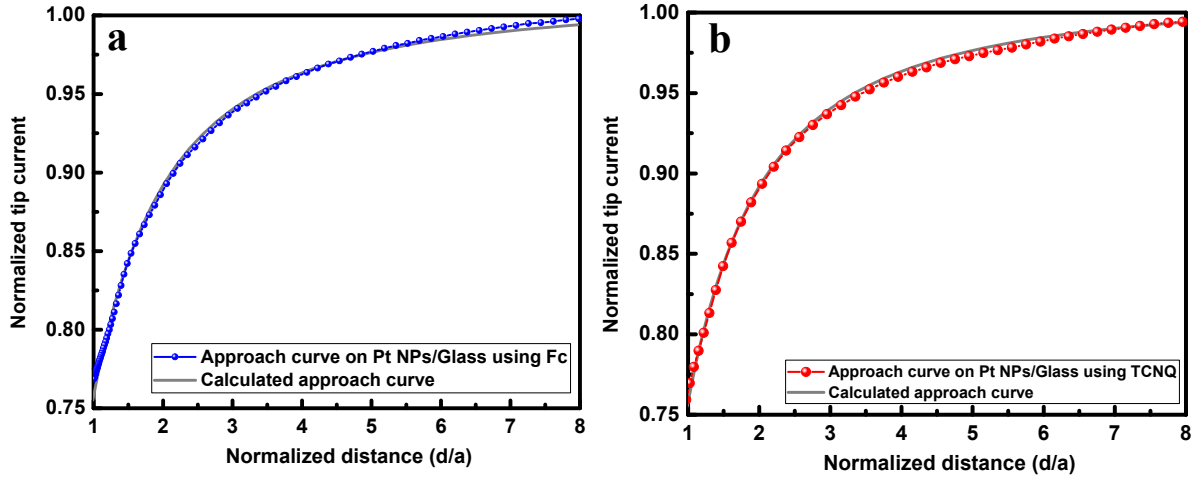

Figure 4.S2 (a) Approach curves onto Pt NPs/glass slide using Fc as mediator (blue curve), ***(b)*** Approach curves on Pt NPs/glass slide using TCNQ as mediator. Theoretical approach curves are in grey.

The Pt NPs were deposited onto the substrate as followed: 3 µl of a dispersed of 0.1 % wt. of Pt NPs (<50 nm) in water was drop-casted onto different substrates. The substrate was then dried in an oven at 50 °C for 5 hrs. before further uses. The electrochemical responses of Pt NPs deposited onto unmodified SLG/PET and onto glass slide were recorded by using

scanning electrochemical microscopy. As shown in the Figure 4.S2, the approach curves recorded with the Pt NPs deposited onto glass slide substrate gave negative feedbacks for both ferrocene and TCNQ. As a result, an insulating behavior was observed which is due not only to the leakage of charge density at the particle surfaces but also to the absence of charge propagation at the surface in order to ensure the electroneutrality of the system.

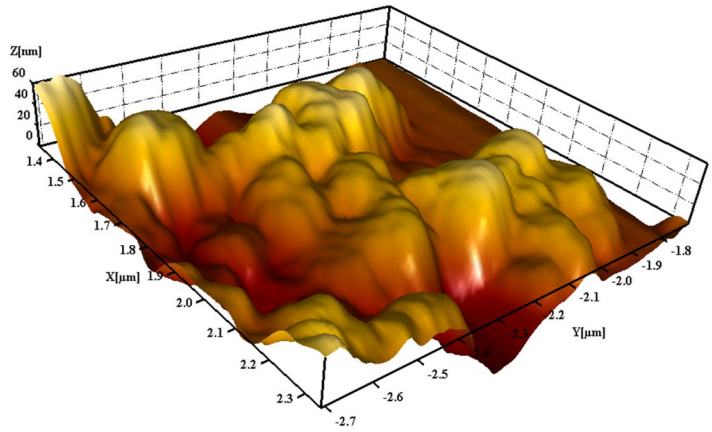

Figure 4.S3 3D-AFM image of Pt NPs onto glass substrate

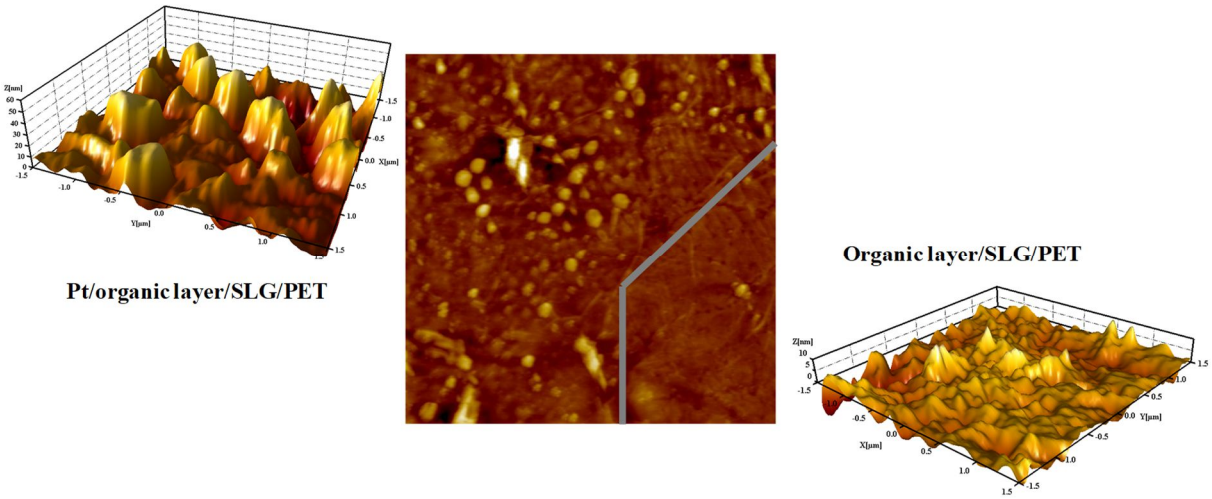

Figure 4.S4 2D and 3D-AFM images of Pt NPs/organic layer/SLG/PET

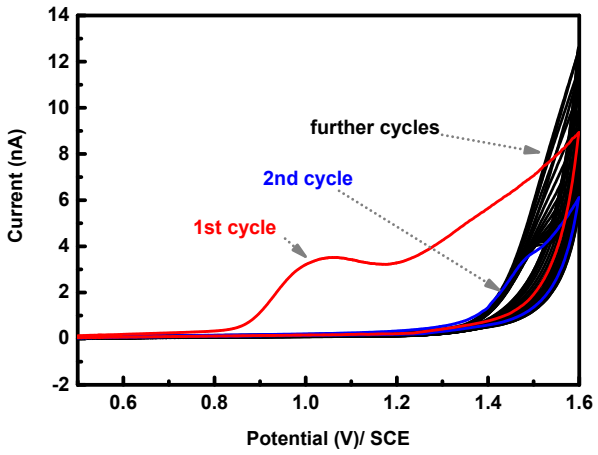

Figure 4.S5 Grafting of initiator layer via electrochemical oxidation in a aqueous solution of 3 mM of 2-bromoethylamine and 0.1 M of $LiClO_4$. 10 µm diameter Pt UME was used as working electrode

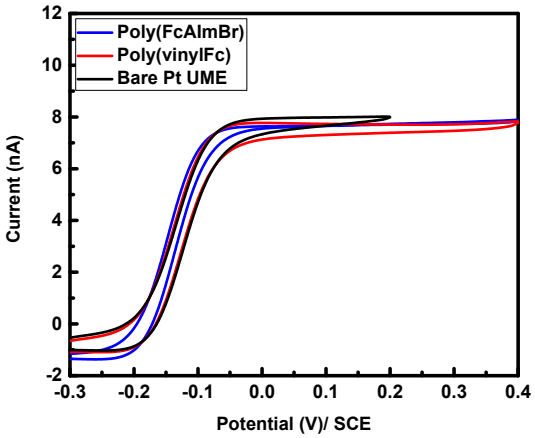

Figure 4.S6 CVs in electrolytic MeCN solution containing 2 mM of DmFc recorded with (black) Bare UME, (blue) Poly(FcIL) and (red) Poly(vinylFc)

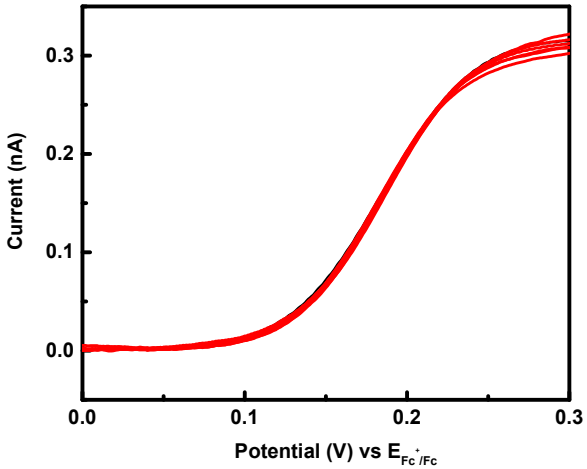

Figure 4.S7 CVs at different scan rate ranging from 10 $mV.s^{-1}$ to 0.4 $V.s^{-1}$ in electrolytic MeCN solution recorded with Poly(FcIL) modified UME at L = 0.2

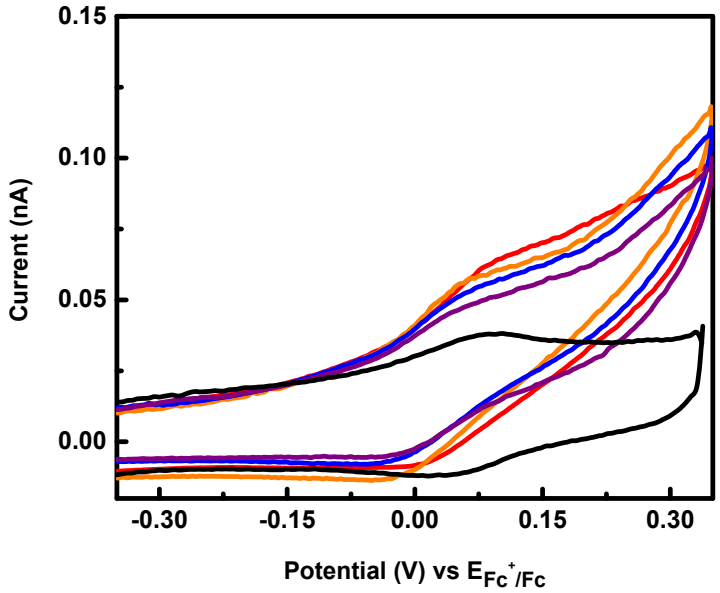

Figure 4.S8 Cyclic voltammograms at different distance tip – substrate recorded at the Pt UME/Poly(VFc) in a MeCN solution containing 0.1 M of $TBAPF_6$

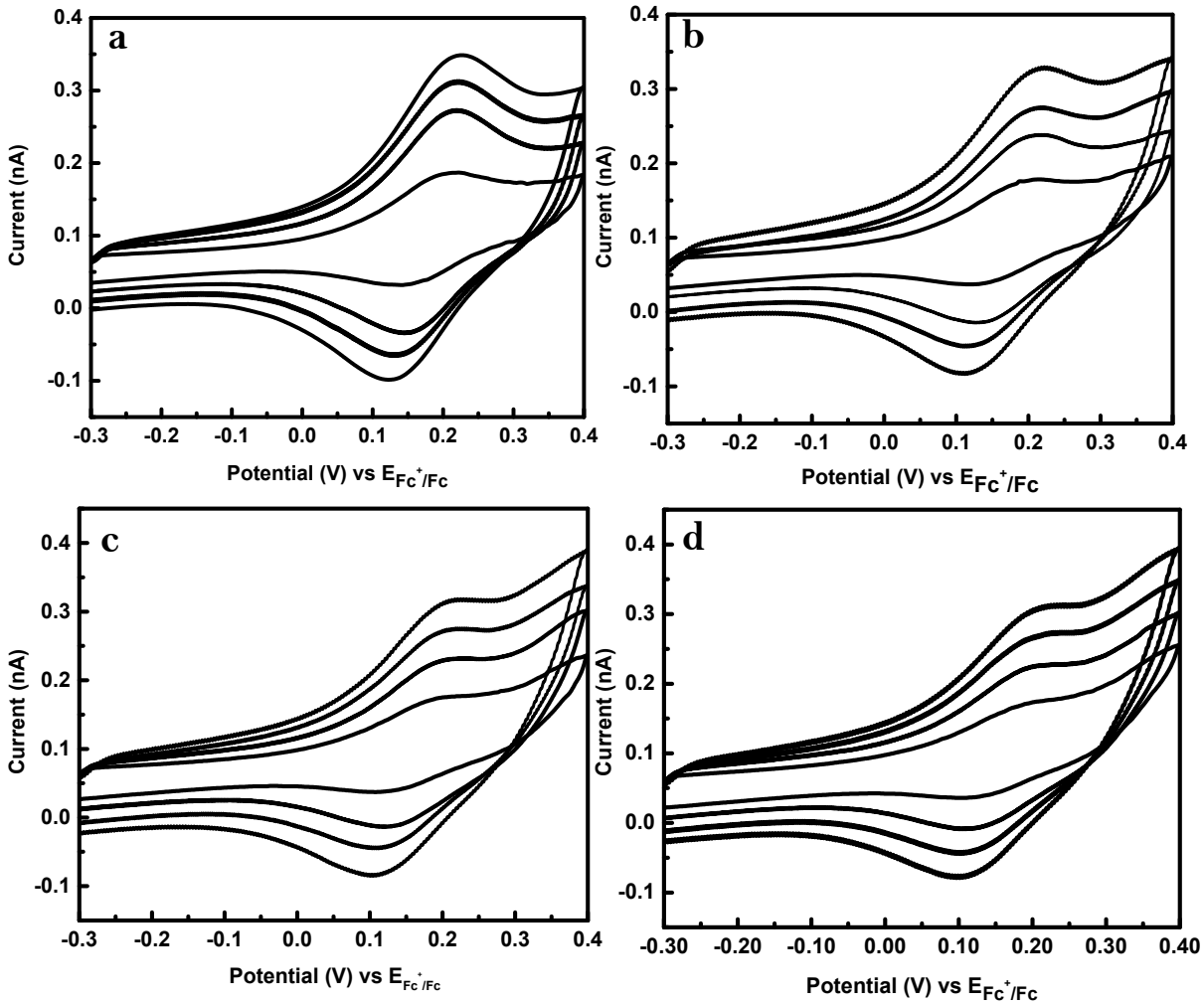

Figure 4.S9 Cyclic voltammograms at different distance tip – substrate ***(a)*** L = ∞; ***(b)*** L = 3; ***(c)*** L = 0.6 and ***(d)*** L = 0.2 and different scan rate (20 mV.s-1 to 0,2 V.s-1).

CHAPTER 5

MOLECULAR CONCEPT OF IONIC LIQUID FOR ENERGY STORAGE AND CONVERSION SYSTEMS: A PERSPECTIVE TOWARDS ARTIFICIAL SKIN

In this chapter, different possible applications in energy field by using (electroactive) ionic liquid-based materials will be reported. Moreover, the role of the surface modification to the energy conversion is investigated via studying the influence of the molecular structure to the triboelectrification effect.

Keywords: redox-flow lithium battery, supercapacitor – battery hybrid, (redox-active) (polymer) ionic liquids, surface modification, triboelectric effect, electrocatalysis.

OUTLINE

5.1 INTRODUCTION

In the era of 4.0 technology, i.e. current trend of automation and data exchange in manufacturing technologies, the development of extra-thin, light and flexible electronics devices open new horizon for different applications in smart interfaces, smart sensing, soft robotics, etc. Imagine a city which every surface can generate electricity from solar power or paper-thin television to electronic skin, etc. The surface functionalization offers advantageous properties to the surface by generating new interfaces. Indeed, the extreme layer of a material is always differed from the bulk atoms due to the leakage of coordination number which induces a change in term of surface energy, density of state and reactivity. As a consequence, the exposure of a material in air provokes problems by physio- and chemisorption of contaminations as corrosion, deactivation of the surface, etc. However, the obstacles can be turned over by introducing a protective layer, for example, an ultra-thin functional organic film which acts as a barrier to protect and/or to generate new interfaces with novel properties. Thus, the surface functionalization with an organic layer has widely investigated since the last century resulting from a large spectrum of approaches. The most relevant methods for making thin organic layer are named self-assembled monolayer (SAM) and electrochemical assisted approaches. In this context, highlighted examples and possible perspectives of potential utilization of Redox-IL and polymeric Redox-IL as (multi)functional materials in a large spectrum of application, such as energy storage and conversion, catalysis, stimulus surface, etc. are described.

5.2 CONCEPTS OF (REDOX)-IONIC LIQUID IN ENERGY STORAGE SYSTEMS

5.2.1 Redox Ionic liquids in redox – flow battery systems

This work is in collaboration with Prof. Qing Wang's group, Department of Materials Science & Engineering at National University of Singapore *(Nernstian-Potential-Driven Redox-Targeting Reactions of Battery Materials, Chem, 2017, 3, 1-14).*

Increasing demand of energy generates considerably pressure to various research fields for approaching to novel technologies towards efficient exploitation of renewable sources. Within this context, the energy conversion and storage have widely investigated involving photovoltaic, (photo) water splitting, batteries, etc. Very recently, new concept of energy storage using redox targeting redox-flow battery was introduced by Wang et al[1]. Unlike conventional RFB where the energy is stored in the liquid phase, in the redox-targeting RFB (RFLB), the energy is stored in 2 separate tanks composed by active solid phase (e.g. TiO_2 and $LiFePO_4$) (Figure 5.1a-b). In parallel, the power is generated in electrochemical cells similar to conventional flow batteries. There are considerable advantages of RFLB over other technologies in terms of energy density (10 times higher than the conventional redox flow systems)[1]. For charging and discharging the battery (Fig.5.1c-d), small electroactive molecules with suitable standard potential can be utilized as charge shuttles. A large variety of redox

molecules have already been tested in different battery materials. Whatever the RFB or RFLB, most of the redox mediators reported in the literature exhibit drawbacks resulting from low solubility. Therefore, the chemical structures influence significantly not only to the charge transfer in between the battery materials and the redox mediators in the mobile phase but also to the solubility in a solvent of interest.

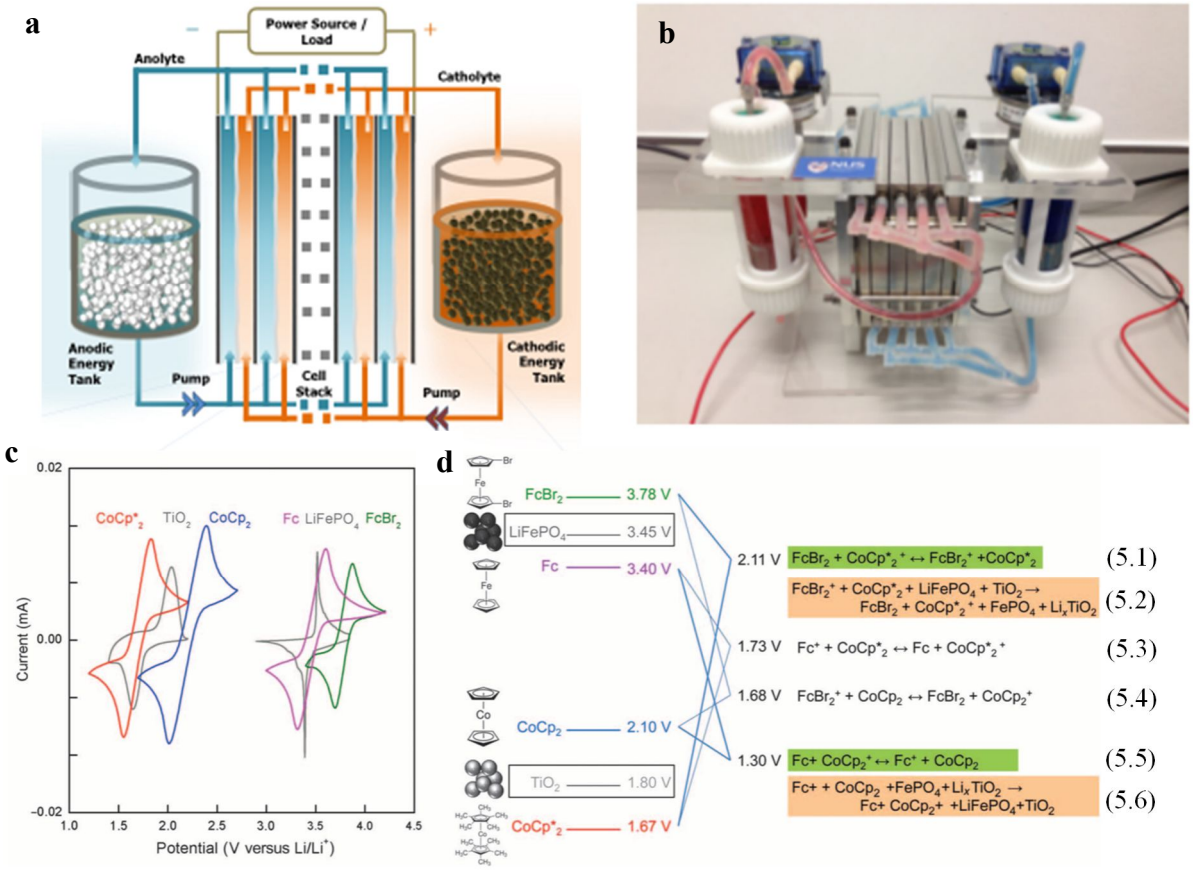

Figure 5.1 ***(a)*** Scheme for Redox flow lithium battery (RFLB), ***(b)*** stack cells, ***(c, d)*** Working principle of the redox targeting reactions in cathodic and anodic tanks. Adapted from Ref.1.

Considering the most developed vanadium based redox-flow battery (VBR), the cell voltage is around 1.2 V and the concentration of vanadium species is ranged from 1.6 M to 3 M, which limits its tanks energy density below 100 $Wh.L^{-1}$. As shown in the figure 5.2 (1 – 8), most of water-based systems provide an energy density lower than 100 $Wh.L^{-1}$.[2–7] Further developments have been demonstrated that non-aqueous systems combined with the utilization of organic and organometallic compounds offer higher energy density and cell voltage[8–16]. Except some compounds which have good solubility (> 2M) in aprotic solvents[17–21], most of redox molecules (e.g. Figure 5.2, 11-15) display lower solubility in these solvents[22–24]. For RFLB, in addition to the low solubility of the mediators, the voltage loss, which results from large potential difference between two molecules, is also major problem ($V^{loss}_{(FcBr2/Fc)}$ = 300 mV when paired with $LiFePO_4$[25], $V^{loss}_{(CoCp2*/CoCp)}$ = 540 mV for TiO_2[26]).

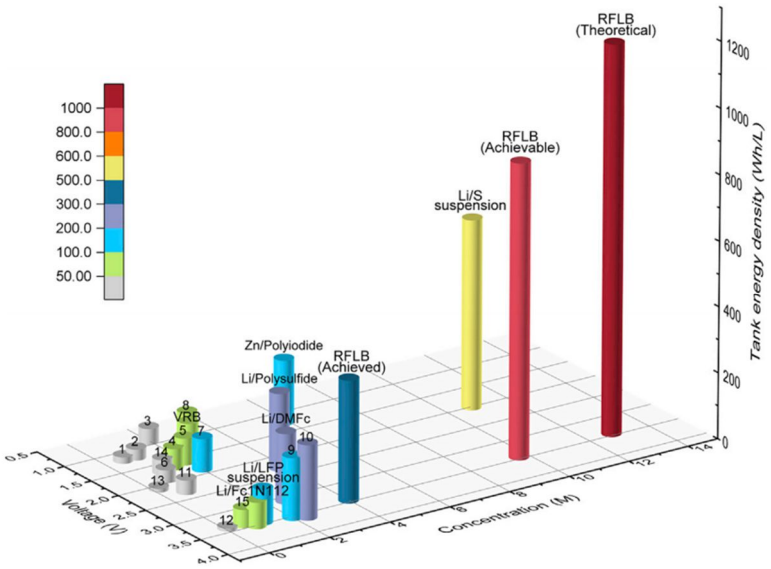

Figure 5.2 Energy density of some selected redox-flow systems. The theoretical energy density of a redox-targeting-based redox flow lithium battery (RFLB) is calculated on the basis of 50% porosity of LFP loaded with 1.4 M redox mediators. 1–8 represent water-based systems: 2,6-DHAQ/$K_4Fe(CN)_6$, Fe/Cr, AQDS/Br_2, polysulfide/Br_2, soluble Pb-Acid, BTMAP-Fc/BTMAP-Vi, and Zn/Br_2, FcNCl/MV. 9 and 10 represent non-aqueous systems: Li/TEMPO, Li/MTLT ionic liquid; 11–15 represent all-organic or organometallic systems: FL/DBMMB, all $Cr(acac)_3$, all $V(acac)_3$, $CoCp_2$/Fc, Li/Fc. The abbreviations are explained in Table 5.S1

In this context, tailoring the physical-chemical properties at the molecular scale becomes crucial not only for boosting the activities of the existed materials but also for creating new type of molecular entities for storing and releasing energy. The proposed strategy of using redox active ionic liquids is not only important for increasing the charge storage efficiency but also for the mechanistic investigation of the influence of charged molecules to the processes at the interface between electrodes and solution. In this collaborative work, we have introduced ferrocenated imidazolium ionic liquid as single – molecule redox – targeting (SMRT) for LFP – based RFLB.

The working principle of SMRT consists to use a suitable redox molecule that has identical standard potential to the LFP. As depicted in Figure 5.3a, the battery operation can be described with two associated events occurring in the cell and tank.

$$RM \rightleftharpoons RM^+ + e \qquad (5.7)$$

$$LiFePO_4 + RM^+ \rightleftharpoons FePO_4 + RM + Li^+ \qquad (5.8)$$

In the cell, a simple electrochemical reaction is necessary for generating oxidized species (RM^+) (Eq. 5.7) whereas in the storage tank, the oxidized molecules undergo reversible SMRT reaction to regenerate RM and delithiate LFP (Eq. 5.8).

The principle of the SMRT reaction is illustrated in Figure 5.3c. At the standard condition, Equation 2 stays at equilibrium because both the molecule and material share the same standard potential ($E°_{RM+/RM} = E°_{FePO4/LiFePO4}$). Upon charging or discharging, the equilibrium potential

of RM (E_{RM}) varies with the activities of the oxidized and reduced states, as governed by the Nernst equation:

$$E_{RM} = E^{0}_{RM^{+}/RM} + \frac{RT}{F}\ln\frac{a_{RM^{+}}}{a_{RM}} \quad (5.9)$$

However, the equilibrium potential of $LiFePO_4$ involve the presence of 2 phases, for which the activities of LFP and $FePO_4$ are equal to unity, inducing the Eq. 5.10

$$E_{LiFePO_4} = E^{0}_{FePO_4/LiFePO_4} + \frac{RT}{F}\ln(a_{Li^{+}}) \quad (5.10)$$

$$\Delta E = \frac{RT}{F}\ln\frac{a_{RM^{+}}}{a_{RM}} - \frac{RT}{F}\ln(a_{Li^{+}}) = \frac{RT}{F}\ln\frac{a_{RM^{+}}}{a_{Li^{+}}.a_{RM}}, \quad (5.11) \text{ where } E°_{RM^{+}/RM} = E°_{FePO_4/LiFePO_4}.$$

Then, the difference of potential between the molecule and the solid material, provides driving force for the reaction described in the Eq. 5.8. During the charging process, more RM^{+} is formed in the catholyte by RM oxidation on the electrode (Equation 5.7), and Li^{+} ions move away to the anodic compartment for charge balancing, which concertedly results in a positive ΔE. Hence, electrons are driven to transfer from the valence band of p-type $LiFePO_4$ to the lowest unoccupied molecular orbital of RM^{+}, accompanied by Li^{+} extraction to form $FePO_4$ (Figure 5.3c). Conversely, during the discharging process, more RM and Li^{+} ions are accumulated in the catholyte. ΔE then becomes negative, and consequently electrons are driven to transfer from the highest occupied molecular orbital of RM to the conduction band of n-type $FePO_4$, concomitantly with Li^{+} insertion into the material forming $LiFePO_4$

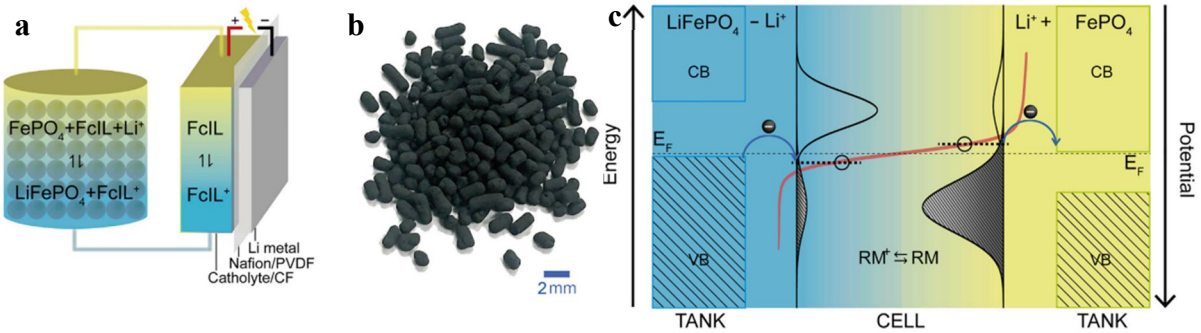

Figure 5.3 Working Principle of the Single-Molecule Redox-Targeting (SMRT) Reaction. ***(a)*** Schematic of an RFLB half-cell with $LiFePO_4$ granules filled in the energy storage tank. Lithium foil and carbon felt (CF) were used as the anode and cathode, respectively. The Nafion/polyvinylidene fluoride (PVDF) composite membrane was used as a separator in the RFLB to prevent crossover of FcIL; ***(b)*** The $LiFePO_4$ granules; ***(c)*** Energy diagram and charge transfer of the SMRT reactions of RM^{+} with $LiFePO_4$ upon charging and RM with $FePO_4$ upon discharging. The thick dashed line marks the formal potential of RM/RM^{+}, and the thin dashed line indicates the Fermi level of solid material.

To validate the SMRT reactions, the 1-Ferrocenylmethyl-3-methylimidazolium TFSI (Figure 5.4A), FcIL, was chosen as mediator. As presented in the figure 5.4B (orange curve), the cyclic voltammogram of this molecule (50 mM) in 1 M of LiTFSI/propylene carbonate (PC) electrolyte shows its half-wave potential around 3.43 V/$E_{Li^+/Li}$, which coincides with the potential obtained with the $LiFePO_4$. Moreover, the FcIL offers higher solubility, beyond 1.45 M in carbonated based electrolyte[27,28] than non-modified Fc (<0.2 M). For simulating the reaction in the tank, a specific experiment was constructed. The electrode was firstly modified with a dense layer of alumina followed by deposition of a top layer of $LiFePO_4/FePO_4$. The presence of alumina film prevents electrical contact between the electrode surface and the active material. The voltammogram was recorded in absence of the FcIL in electrolytic PC solution, affording obtention of non-faradic current (grey curve). In presence of the FcIL molecule (50 mM), not only an increase of the recorded current is observed but also the shape of the voltammogram changes (green curve). Under finite diffusion regime through the alumina layer, the Fc^+IL generated at the FTO surface is reduced to FcIL at the interface of $LiFePO_4$/solution (Eq. 5.8) and diffuses back to the electrode surface while the Li^+ diffuse to the Li – electrode, resulting to a diffusion-controlled system. For the backward reaction, similar argumentation can be applied. In summary, the FcIL molecule is validated as a bifunctional mediator for LFP-based RFLBs.

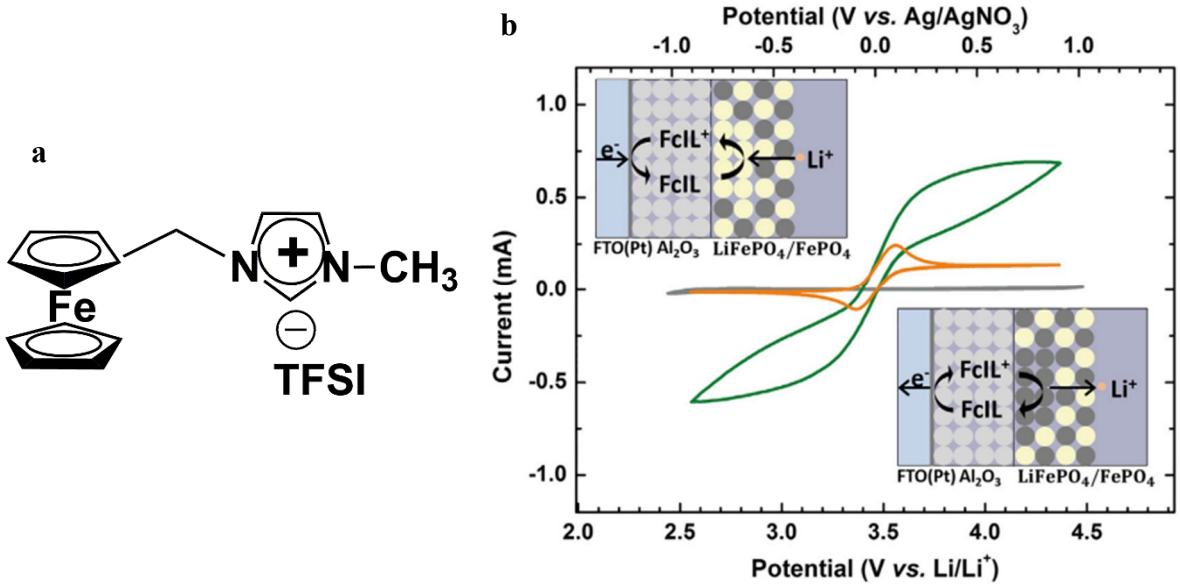

Figure 5.4 ***(a)*** molecular structure of FcIL; ***(b)*** cyclic voltammograms of 50 mM FcIL on a double-layer electrode in the absence (orange) and presence (green) of $FePO_4/LiFePO_4$ (1:1). For comparison, the gray curve shows the CV of a $FePO_4/LiFePO_4$-coated double-layer electrode in the absence of FcIL in the electrolyte. The electrolyte was 1 M LiTFSI/PC. The scan rate was 2 $mV.s^{-1}$. The insets illustrate the reaction of FcIL on the double layer electrode.

Both static and flow cells were used to examine the SMRT reactions for battery applications. As shown in Figures 5.5A–C, when 0.44 M equivalent $LiFePO_4$ powder was introduced into the cathodic compartment, the static cell revealed an extended voltage plateau beyond the

capacity of 0.50 M FcIL in the catholyte. This counts for more than 50% utilization of the material via the SMRT reactions, whereas the $LiFePO_4$ powder itself shows very little capacity in the absence of FcIL (Figure 5.S1). Distinct from the previously reported two-molecule redox systems[25,26] or single molecule with multiple redox potentials[29,30], the cell exhibits only one voltage plateau, which considerably eliminates the voltage loss and thus unprecedentedly improves the voltage efficiency to about 95%. The cell retains around 90% capacity after five cycles, revealing reasonably good stability of the system. Some electrolyte was found trapped at the gasket gap after the test, which could partly account for the capacity drop over the testing.

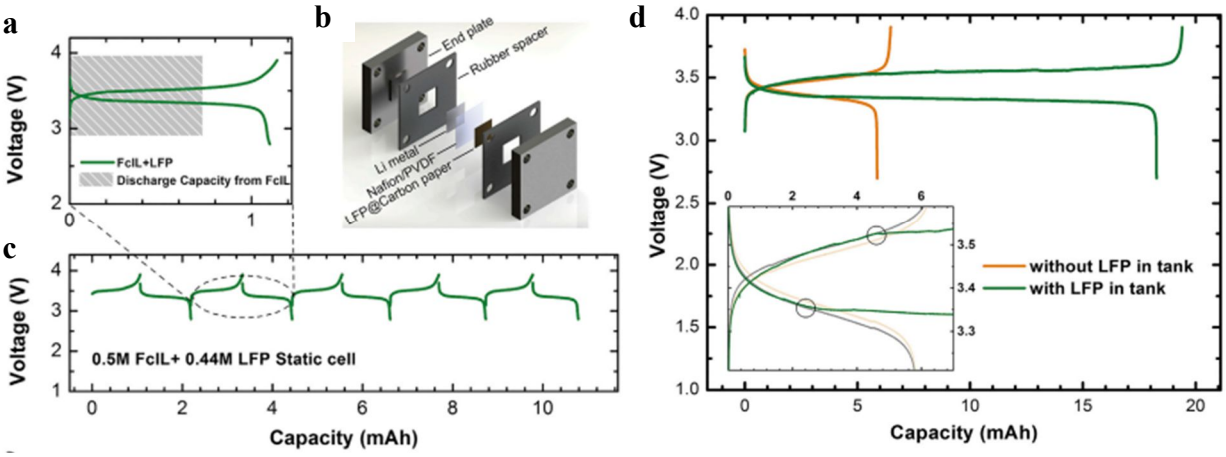

Figure 5.5 SMRT Reaction for Static and Flow Battery Applications. ***(a)*** A typical galvanostatic voltage profile of a static cell with 0.50 M FcIL in the catholyte and 0.44 M equivalent $LiFePO_4$ on the cathode. The shaded area indicates the capacity from FcIL. The electrolyte was 1 M LiTFSI/PC. The current density was 0.025 $mA.cm^{-2}$. ***(b)*** Exploded view of the static cell. ***(c)*** Voltage profiles of the static cell for five consecutive cycles. ***(d)*** Voltage profiles of flow cells with 0.20 M FcIL in the catholyte and 0.37 M equivalent $LiFePO_4$ granules in the tank. The inset is the enlarged voltage profiles of the flow cells after IR correction. The electrolyte was 1 M LiTFSI/PC. The current density was 0.025 $mA.cm^{-2}$.

To further demonstrate the feasibility of the SMRT reaction for RFLBs, a flow cell was tested. As seen in Figure 5.5d, after adding 0.37 M (13.1 mAh) equivalent $LiFePO_4$ granules to the tank, the voltage plateau of 0.20 M FcIL was greatly elongated, which exceeds the discharge capacity of the molecule by 2.1 times. In flow through mode, the reactions between the redox molecules and solid material are considerably improved owing to the forced mass transport, which results in enhanced utilization of $LiFePO_4$ up to 95% (the capacity extension is 12.4 mAh). Benefitting from the SMRT reaction, the flow cell exhibited a voltage efficiency over 94%, which is on a par with or even superior to other rival battery technologies. The Coulombic efficiency was around 90% for the flow cell, which is presumably due to the crossover of redox molecules upon prolonged test as a slight color change of the anolyte was observed after disassembling the cell. Because the FcIL stays in a reduced state in anolyte, it would remain intact upon cycling. To eliminate the adverse effect of crossover, the same electrolyte composition in both the anolyte and catholyte could be used to reduce the concentration gradient and thus crossover. With the same electrolyte, the cycling stability of the flow cell was tested

at controlled capacity, which shows Coulombic efficiency >97% and negligible degradation over 50 cycles, revealing the robustness of the SMRT system.

As a proof-of-concept study, the tank energy density of the flow cell achieved is around 330 $Wh.L^{-1}$ considering ~83% effective porosity of the solid material in the tank. To evaluate the reachable energy density, $LiFePO_4$ granules were loaded in a glass bottle for pore-volume measurement. typical packing of the $LiFePO_4$ granules in a short stick shape in a 12.5-mL glass vial. The mass loading of the material is 18.5 g, which has a packing density and porosity of 1.48 g/mL and 59%, respectively, equivalent to 9.35 M effective concentration of redox species and Li^+ ions. The volumetric energy density of the cathodic tank ($Wh.L^{-1}$) can be calculated in terms of the following equation:

$$W = (Q.d.p + c.F.\frac{1-p}{3600}).E$$

Here, Q is the specific capacity of $LiFePO_4$ (170 $mAh.g^{-1}$), d is the density of $LiFePO_4$ (3.60 $g.mL^{-1}$), c is the concentration of FcIL in the catholyte, p is the porosity of $LiFePO_4$ granules packed in the tank, and E is the cell voltage (3.45 V). So, W is determined to be 942 $Wh.L^{-1}$ provided that the concentration of FcIL is 1.40 M, which is nearly 20 times the tank energy density of VRBs. By modifying the shape and dimension of the granules, as well as the loading method, the porosity can be further reduced to accommodate more solid material and thus an even higher energy density is expected.

The inset of Figure 5.4D shows the magnified voltage profiles of the flow cells with and without the solid material loaded in the tank. It is observed that during the charging process, the FcIL cell initially shared similar voltage changes to the FcIL/$LiFePO_4$ cell before its voltage started to rise more steeply and diverge from the latter at ~70% state of charge (SOC). As the cell voltage (after IR correction) is indicative of the equilibrium potential of $FcIL/FcIL^+$ in the catholyte, the divergence point broadly shows the transition state from which ΔE (Equation 5.11) starts to drive the forward SMRT reaction (Equation 5.8), which regenerates FcIL, retarding the voltage rise of the FcIL/$LiFePO_4$ cell. In comparison, the discharge curves of the two cells diverged at ~40% state of discharge (SOD), indicating an opposite scenario at which ΔE (Equation 5.11) starts to drive the backward SMRT reaction (Equation 5.8), which regenerates $FcIL^+$, impeding the voltage drop of the FcIL/$LiFePO_4$ cell. The difference in the starting point of SMRT reactions between the charging and discharging process is partly in good accordance with the little potential disparity between FcIL (3.43 V versus Li/Li^+) and $LiFePO_4$ (3.45 V versus Li/Li^+), which inherently results in a slight asymmetry in the reaction kinetics, with a more facilitated backward SMRT reaction than the forward reaction.

In summary, the Nernstian-potential-driven SMRT reaction presents an elegant way to improve voltage efficiency without sacrificing the salient features of redox-targeting-based RFLBs and simplify the electrolyte composition of the cell. The small potential difference originated from

the activity changes of redox active species during charge-discharge cycles enables reversible delithiation and lithiation of $LiFePO_4$, for which near-unity utilization yield and 95% voltage efficiency were achieved with a, single molecule. This also leads to a considerable enhancement in volumetric tank energy density to 330 $Wh.L^{-1}$, which is potentially optimized up to 942 $Wh.L^{-1}$.

5.2.2 Ionic liquids for fabrication of supercapacitor – battery hybrid

In complement with the use of redox ionic liquid in solution, the electrochemical assisted polymerisation of redox-ionic liquid (referred to SI-ATRP, chapter 2) has also been demonstrated to be promising for fabracation of thin-film supercapacitor-battery hybrid system. It is noted that a supercapacitor provide an energy storage mode via movement of charges from/to the electrodes while a battery stores charges by electron transfer/transport.

Due to different processes at the interface of electrode, supercapactors provide a high power density, resulting from the rapid release of a large amounts of energy based on its volume while batteries offer a high energy density, resulting from a higher energy storage in a given size or mass. In addition, for a battery, the life cycle is shortened by charging/discharging with a large pulsed current (e.g. risk of explosion for Li-ion batteries). In this context, organic battery has been proposed not only to resolve the risks issue from the utilization of lithium by achieving comparable performance but also to lower the cost, consequently allow large-scale deployment[31]. In addition, the organic – based battery offers more designable structures (flexible or implantable) without caring about the mechanical issue from the inorganic ones. Following this trend, we have developed the concept of hybrid organic supercapacitor – battery, which provides several advantages compared to the current state-of-the-art, including a high power and energy density, possible for the development of flexible and cost effective devices. For the proof-of-concept, we have used an asymetric system in which the anode and cathode is functionalized with oxidizable and reducible species, Poly(FcIL) and Poly(AQIL), respectively. Having an ionic skeleton, the imidazolium rings within the polymer chains supply high charge density, which is suitable for utilization as electrical double layer capacitor (EDLC) while the redox-active groups (Fc and AQ) furnish the redox battery behavior via electron storage by the following equations (protic solution):

$$2Fc \rightleftharpoons 2Fc^{+} + 2e^{-} + 2A^{-} \qquad \text{(anode)}$$

$$AQ + 2H^{+} + 2e^{-} \rightleftharpoons AQH_2 \qquad \text{(cathode)}$$

The theoretical cell voltage is defined by the difference between the 2 (standard) potentials of the electrodes, according to: cell voltage = cathode potential – anode potential[31], i.e. 0.6 V. Due to the confidential terms (Patent application procedure), the results of charging/discharging are not described in this thesis. Nevertheless, the calculated Ragone plot (power density ($W.kg^{-1}$) vs energy density ($Wh.kg^{-1}$)) of our system is presented in the figure 5.6. It is worth noting that

our system is located in the frontier between the electrochemical capacitors and batteries, i.e. hybrid supercapacitor – battery region by providing a power density ranging from 10^3 to 10^4 $W.kg^{-1}$ and an energy density up to 7 $Wh.kg^{-1}$.

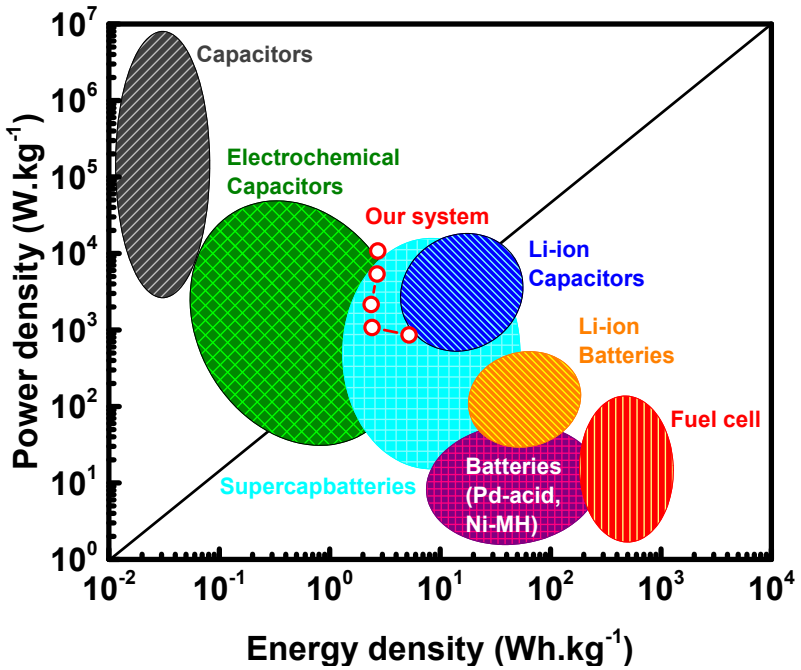

Figure 5.6 Ragone plot (P = f(E)) of the immobilized redox-active polymer ionic liquid at different C-rates.

5.3 ROLE OF SURFACE MODIFCATION IN ENERGY CONVERSION SYSTEMS

This work is in collaboration with Prof. Sang-Woo Kim's group, School of Advanced Materials Science and Engineering, Advanced Institute of Nanotechnology (SAINT), Sungkyunkwan University (SKKU), Suwon, Korea.

5.3.1 General principle of triboelectric nanogenerator (TENG)

In the daily life, numerous electronic devices are needed to ensure our best demands for healthcare, communication, transportation, etc. Typical examples that can be listed are laptops, GPS devices, glucose meter. However, each of these devices is produced for a specific purpose and sometimes needs to be connected to other devices. Furthermore, they are relatively cumbersome that reduce the mobility and the fashionable of the owner. Within this context, wearable technology has been nowadays becoming a hot trend in the field of electronic devices. Indeed, the devices can be directly printed onto the skin or to the clothes providing more immediate usage, better communication with the environment, more fashionable and more discreet. Consequently, the next few decades will be deserved for the development of smaller devices with a higher portability and more functionality. Such devices require a very low power that can be supplied by surrounding environmental energy, e.g. variation of the temperature, solar energy, wind power and friction, etc. Among these examples, the friction is the most popular form of energy. In daily life, friction is helpful for fabrication of cloth, for walking, prevents us from sliding, etc. Being known for thousand years, the most known case of

triboelectrification is lightning which is attributed to the friction of tiny water drops via convection in clouds. Starting from this concept, two distinct families of triboelectric generators has been developed, i.e. traditional triboelectric generators and triboelectric nanogenerator (TENG).

Wilhelm Holtz introduced the earliest machines in the 1860s. However, the latter are inefficient and present an unpredictable tendency for switching its polarity. These drawbacks are eliminated by the invention of James Wimshurst at the beginning of 1880s, so called Wimshurst machine which is based on the separation of electric charges through induction, in absence of any friction for its operation. Later, Robert J. Van de Graaff developed another electrostatic generator, which uses a rotating dielectric belts to accumulate charges on a hollow metal globe on the top, producing ultrahigh electric potential (up to megavolt scale). For discharging, visible sparks through large air barrier are even visible. Nevertheless, it is noted that these traditional generators are high voltage sources and there is no current flowing through unless there is a discharging.

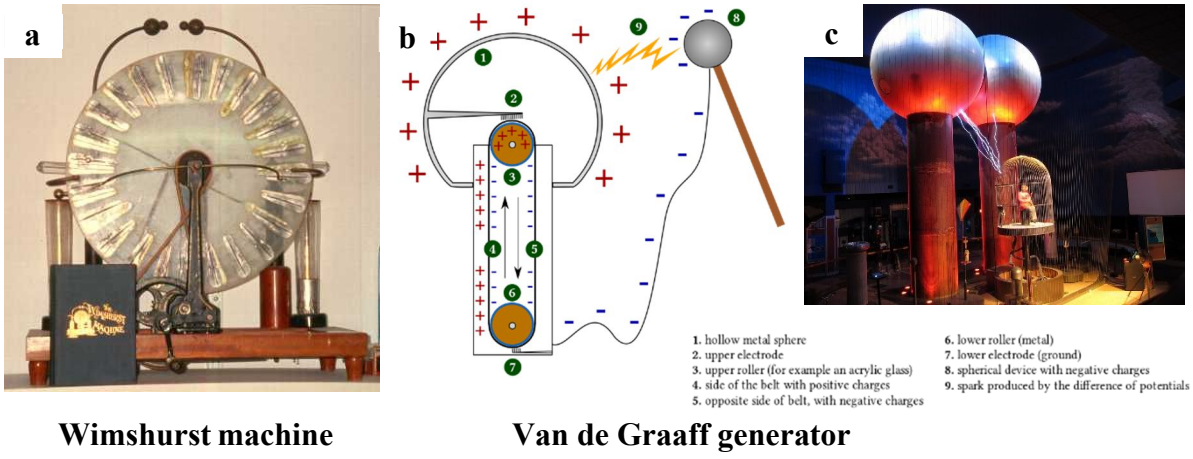

Figure 5.7 ***(a)*** Wimshurst machine (in the Jack Judson Collection at the Magic Lantern Collection in San Antonio, Texas.); ***(b)*** Schematic working principle of a Van de Graaff generator (Wikipedia) and ***(c)*** World's largest Van de Graaff generator at Boston Museum of Science)

In 2012, Wang and al[39] has proposed novel approach, triboelectric nanogenerator (TENG), by coupling the triboelectric effect and the electrostatic induction for fabricating flexible power sources towards flexible electronics. A typical power generator contains an inner circuit and an outer one. In the inner part, a potential is produced by triboelectric effect due to the charge transfer between a dielectric layer and another dielectric or inorganic film, resulting from the opposite polarity. In the outer circuit, a current is obtained by an electron flux between two backsides to balance the potential. Since then, the TENG has been widely investigated from the mechanistic studies to applications[40,41]. According to the literature, six different families of TENG have been reported[40], comprising vertical contact separation mode based TENG (dielectric to dielectric and metal to dielectric), lateral sliding mode based TENG (dielectric on

dielectric and metal on dielectric), rotation mode based TENG and single electrode mode based TENG (figure 5.8).

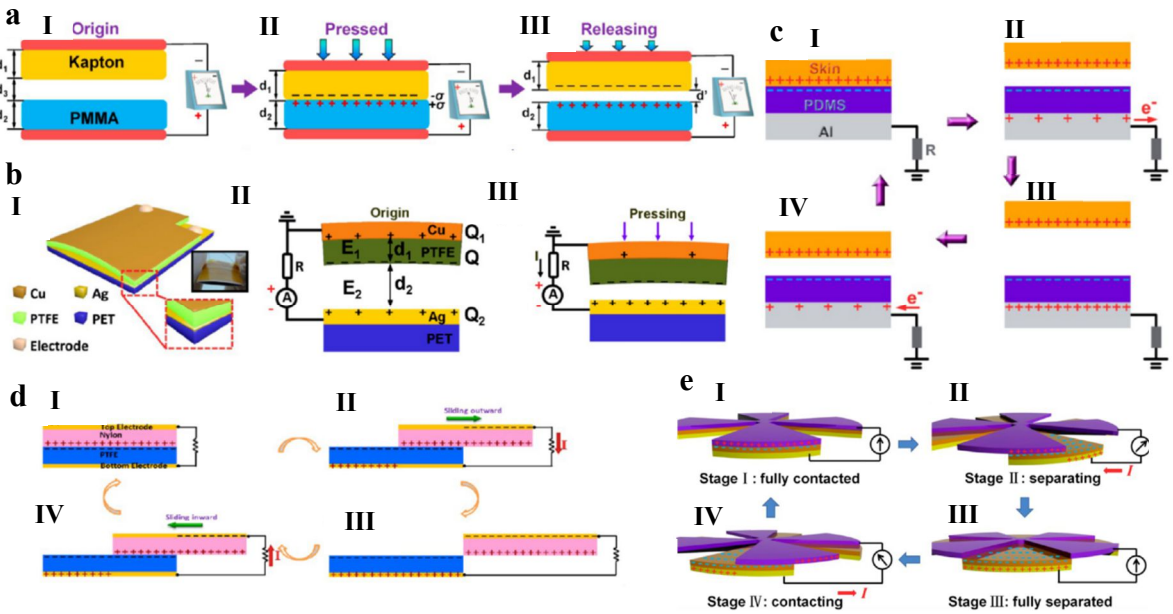

Figure 5.8 Working principle of different TENG modes: vertical contact separation (dielectric to dielectric ***(a)***[42] and metal to dielectric***(b)***)[43]; ***(c)*** single electrode mode[44]; ***(d)*** lateral sliding mode with dielectric on dielectric[45] and ***(e)*** rotation mode[46].

As mentioned above, the potential generated and the current collected in a nanogenerator depend strongly on the contact between the films in the inner circuit. Most of the materials exhibit the triboelectrification, e.g. polymer, silk, hair, etc. Consequently, the choices of the material for TENG are infinite. Nevertheless, the capability for a chosen material to gain/to lose electrons is determined by its polarity. In addition, the use of cumbersome materials conducts to a loss of volumetric generated power of TENG. In this context, molecular engineering provides excellent way to produce thinner devices with higher power density. Self-assembled monolayer, SAM, method for functionalizing the surface of Au electrode with different organic molecules has been reported. As results, an influence of the molecular structure onto the triboelectric effect is observed that could be attributed to the difference of polarity of various molecules[47]. It is known that the self-assembled monolayer is typically based on the adsorption of a thiol onto Au substrate that can provoke a low stability and durability to the TENG. This drawback can be resolved by the use of the electrochemical grafting, especially via diazonium reduction, affording covalent bonding between the electrode and the organic layer. In addition, the thickness of the organic layer could be modulated by changing the electrochemical deposition conditions. For this study, we attempt to investigate the influence of molecular structure on the triboelectric effect of the film. Consequently, various molecules have been chosen as shown in the figure 5.9.

5.3.2 Surface modification of flexible ITO by electrochemical reduction of diazonium derivatives and its characteristics

The electrochemical approaches generate radicals from oxidizable or reducible groups which can be attached onto a conductive/semiconductor substrates[48]. Among various available functional groups, the diazonium salts appear as one of the best candidate for generating thin, compact film which has been largely used in different applications as molecular electronic[49], sensors[50], smart surfaces[51], etc.

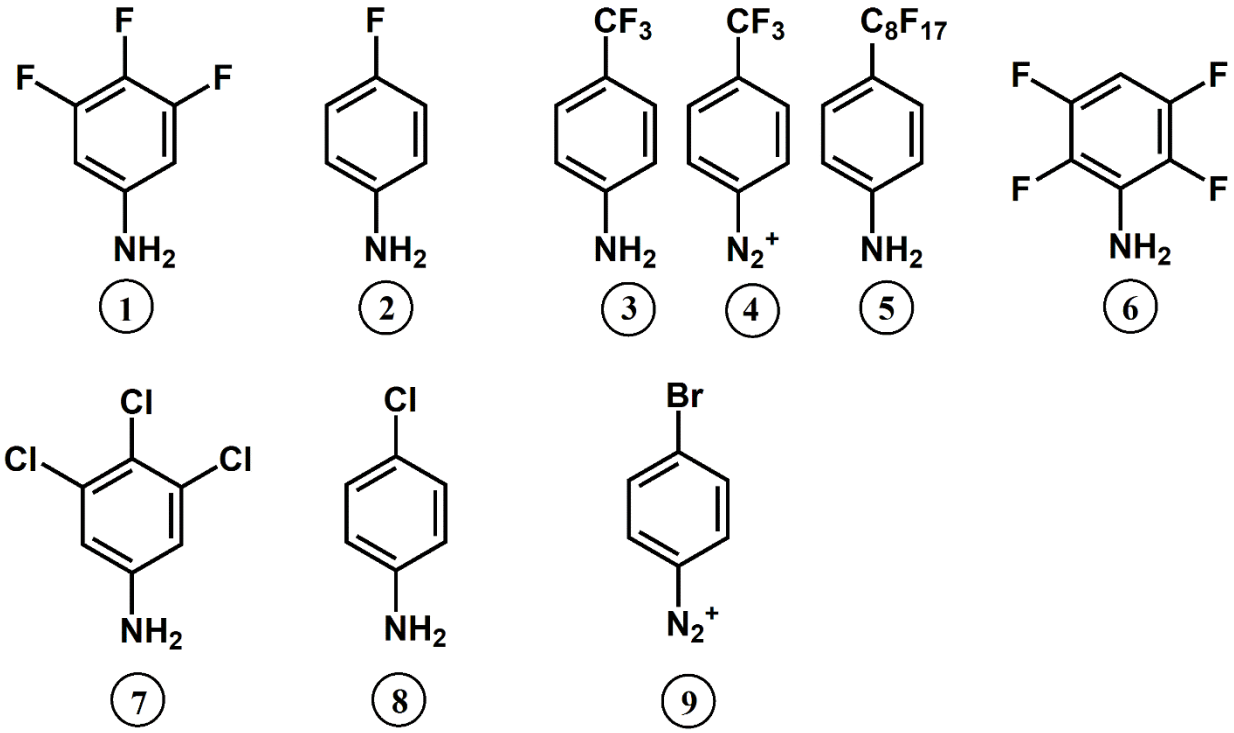

Figure 5.9 molecular structure of diazonium derivatives used for this study.

The electrochemical reduction of diazonium derivatives was performed in MeCN solution containing 1 mM of molecule of interest and 0.1 M of $TBAPF_6$. The aniline based molecule solutions are followed by addition of diazotization agent (3 equiv.), tert-butyl nitrite (t-BuNO), affording in-situ diazonium cation. Then, cyclic voltammetry was launched by sweeping the potential from 0.6 V to -0.8 V/SCE for 10 cycles. The used working electrode is a flexible ITO supported on PET (supplied from Aldrich). As an example, the cyclic voltammogram of electrografting using 3,4,5-trifluoroaniline is shown in the figure 5.10. For the first cycle, a net reduction peak is observed at around -0.2 V/SCE correspond to the formation of radicals at the vicinity of the electrode surface, which are rapidly attached to the surface, resulting to a dramatic decrease of the current since the second cycle. For the remaining molecules, similar CV shape was obtained with a variation of the reduction peak potential. Nevertheless, no clear faradic current is observed after ten reduction cycles.

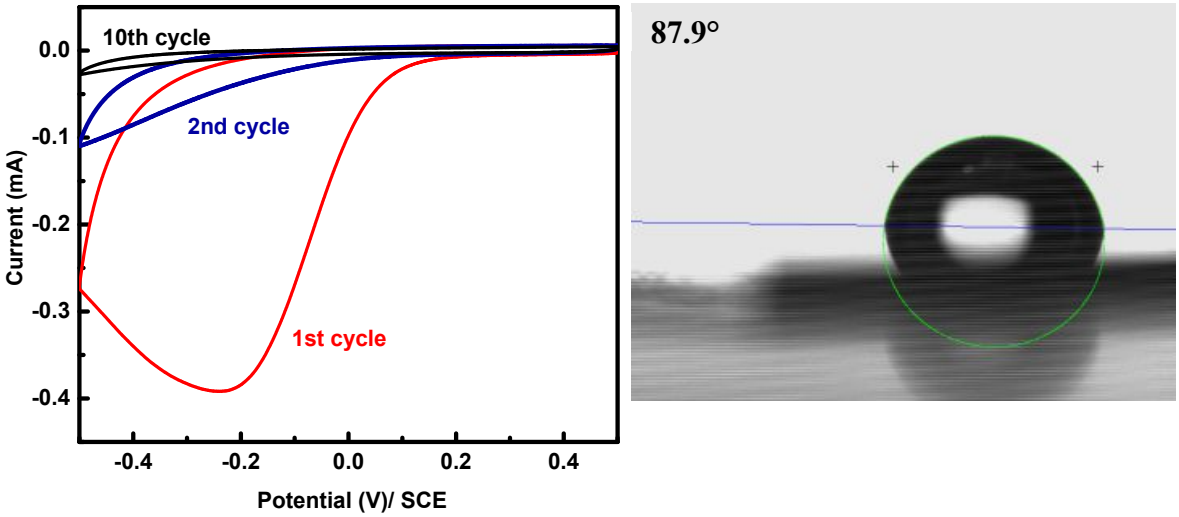

Figure 5.10 (a) Electrochemical grafting via reduction of 3,4,5-trifluoroaniline in a MeCN solution of 1 mM of 3,4,5-trifluoroaniline and 0.1 M of $TBAPF_6$. Scan rate = 100 $mV.s^{-1}$ and ***(b)*** CA measurement of the modified ITO/PET

The presence of the organic layer was firstly proven by a change of the contact angle. Thus, in presence of the 3,4,5-trifluorophenyl layer, an increase of the contact angle around 20° was observed compared to the bare ITO electrode (Figure 5.10b). In addition, the XPS measurements reveal the elemental composition at the surface of the surface of the electrode (Figure 5.11). The high-resolution spectrum of C(1s) displays 3 components located at 285 eV, 287 eV and 289 eV which are attributed to C – C, C – N and C – F bond, respectively. Moreover, the presence of F(1s) signal at 688 eV confirm the presence of the fluorinated layer at the ITO surface.

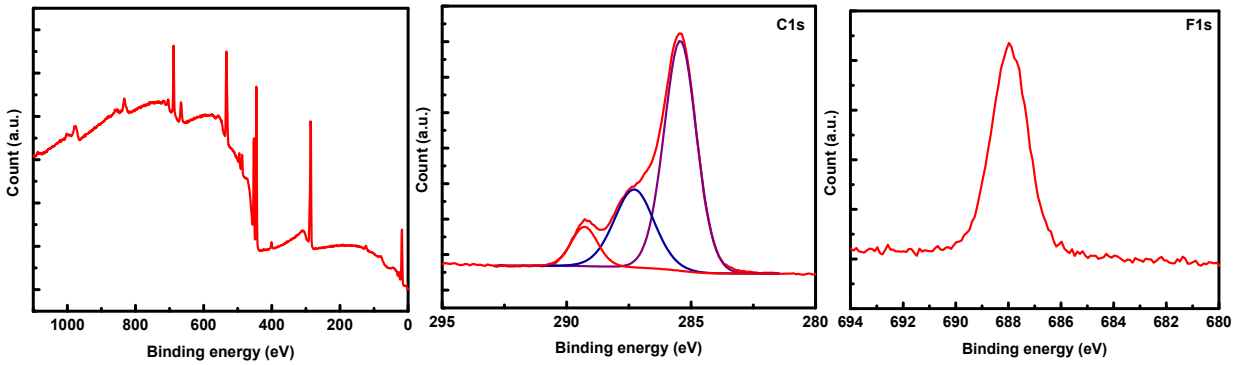

Figure 5.11 XPS spectra of 3,4,5-trifluorophenyl modified ITO/PET electrode. ***(a)*** Survey spectrum; ***(b, c)*** high resolution spectra of C1s and F(1s), respectively.

Also, the XPS has been recorded for the remaining molecules that evidenced the presence of the organic layer. For further studies, 3 fluorinated molecules will be used to investigate the influence of the molecular structure on the electronic properties of the final interface (Figure 5.12 a-c inset). Indeed, the Kelvin force microscopy has been used for investigating the morphology (KFM) and the surface potential of these surfaces (KPFM). The surface potential was investigated as followed. First, the surface potential of HOPG reference sample was

measured to set the surface potential of the reference. Then the surface potential of different samples was measured by KFM mode (non-contact mode). Finally, the surface potential of HOPG was measured again to confirm that there is no artefact due the degradation of the tip.

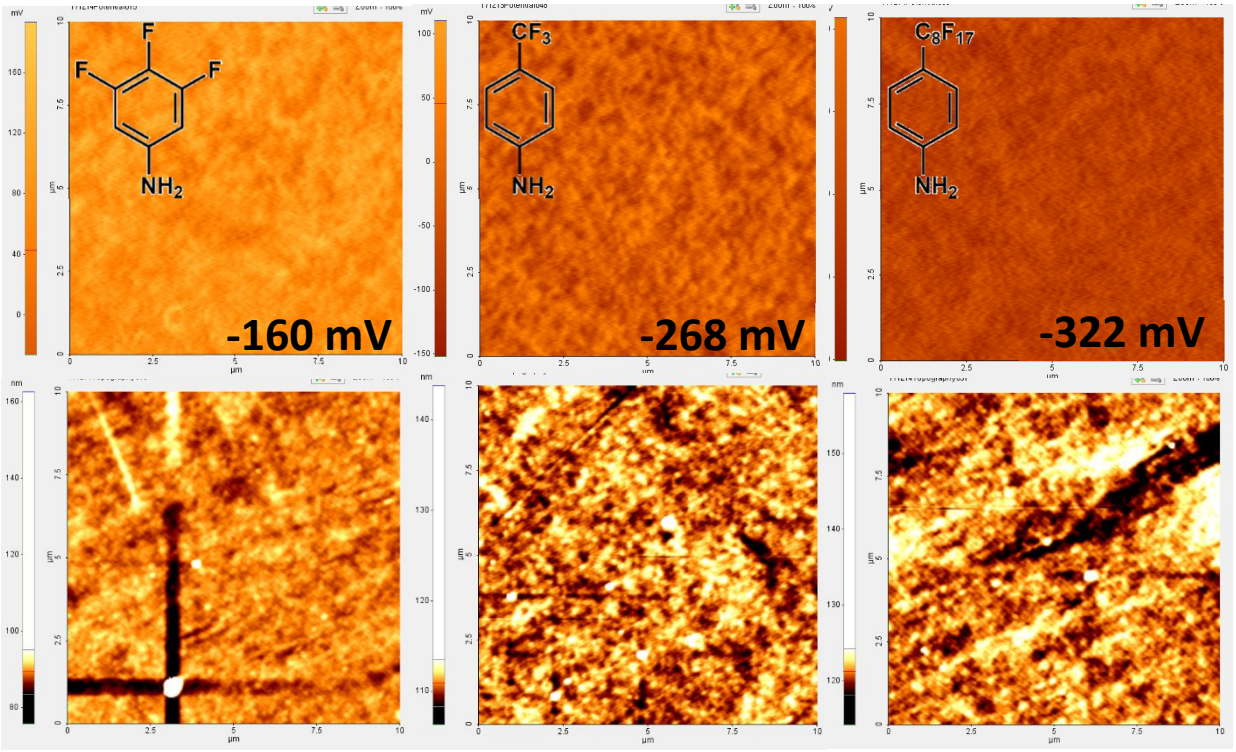

Figure 5.12 The surface potential and morphology were investigated by using KFM for ***(a, d)*** 3,4,5-trifluorophenyl, ***(b, e)*** 4-(trifluoromethyl)phenyl and ***(c, f)*** 4-(perfluoroctane)phenyl modified ITO.

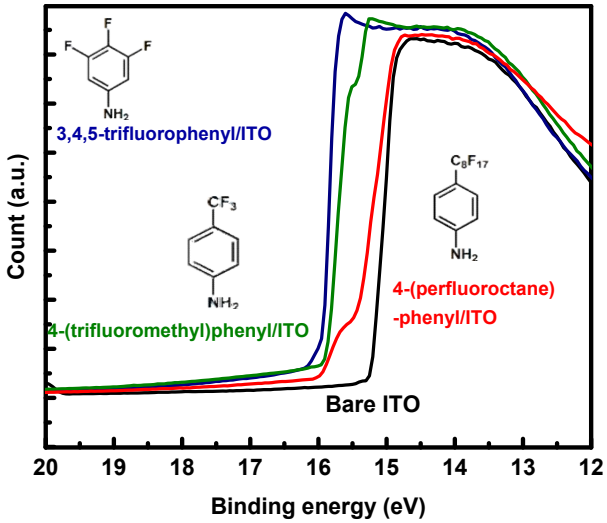

Figure 5.13 UPS spectra of (black) bare ITO/PET, (blue) 3,4,5-trifluorophenyl/ITO, (green) 4-(trifluoromethyl)phenyl/ITO and (red) 4-(perfluoroctane)phenyl/ITO

As presented in the figure 5.13 a-c, the surface potential of 3 substrates (3,4,5-trifluorophenyl, 4-(trifluoromethyl)phenyl and 4-(perfluoroctane)phenyl modified ITO) were recorded. By increasing the atomic percentage of the fluoride within the film, the surface potential is considerably increases from -160 mV (3,4,5-trifluorophenyl) to -322 mV (4-

(perfluoroctane)phenyl). This result suggests that the change of the quantity of F affect the characteristics of the surface, which is coherent with the work function measured with the ultraviolet photoelectron spectroscopy (UPS) (5.1 eV, 5.26 eV and 5.33 eV for 4-(perfluoroctane)phenyl, 4-(trifluoromethyl)phenyl and 3,4,5-trifluorophenyl/ITO, respectively) (Figure 5.13). The work function values were calculated by $\phi = h\nu - (\text{cutoff} - E_F)$.

5.3.3 Molecular influence to the triboelectric nanogenerators: mechanical – electrical converter

Then the modified electrodes were applied for TENG measurements by using vertical contact separation mode based TENG by using an Al-PTFE/Functionalized ITO system (dielectric-to-dielectric case) (Figure 5.8a). Three fluorinated layer modified ITO were used for the measurements and the open circuit voltage (V_{OC}) are reported in the figure 5.14a. At the initial state where no contact is established, there is no charge induced or generated, inducing to no difference of the electric potential. By applying external force, the 2 electrodes are kept in contact, resulting to a surface charge transfer due to the triboelectrification. As the TENG starts to be released, the top electrode, PTFE film reverts back to the initial position. Once the two electrodes are separated, a difference of electrical potential is established. By defining the electric potential of the ITO electrode is equal to zero, the electric potential at the PTFE electrode (top electrode) is calculated by[40]:

$U_{\text{top electrode}} = -\frac{\sigma d'}{\varepsilon_0}$ where σ us the triboelectric charge density, ε_0 is the vacuum permittivity and d' is the interlayer distance at a given state. As the V_{OC} is proportional to the distance between the electrodes, once the TENG is released, the voltage increases and reaches a maximal value where the top electrode is back to the initial state. Moreover, the voltage remains constant, indicating the input impedance of the electrometer is infinitively large. As displayed in the figure 5.14a, the recorded voltage for all the samples exhibits negative values, suggesting that the functionalized ITO substrates provide positive triboelectric effect compared to the PTFE (figure 5.14b). Then, the top electrode approaches to the bottom electrode, resulting to a drop of the V_{OC} to zero when the electrodes are in contact.

As presented in the figure 5.14a, the V_{OC} obtained for the 4-(perfluoroctane)phenyl/ITO is doubled compared to other substrates, suggesting a higher triboelectrification effect. John Carl Wilcke published *De electricitatibus contrariisa, 1757,* mentioning a series of triboelectric effect on static charges of different materials. Briefly, a material in the bottom range of the series, when touched to a material near the top, will acquire more negative charges. As a result, Teflon is one of the most negatively charged. As the work function of the 4-(perfluoroctane)phenyl/ITO is the lowest among 3 substrates, it is easier for exchanging the electron with the PTFE, conducting to accumulation of more positive charges at the interface.

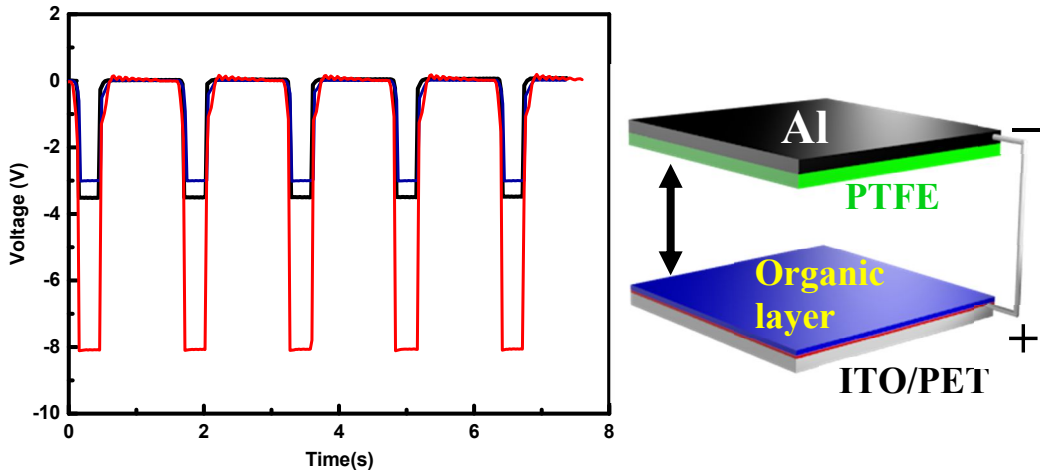

Figure 5.14 (a) Open circuit voltage of TENG with the functionalized ITO with (black) 3,4,5-trifluorophenyl/ITO, (blue) 4-(trifluoromethyl)phenyl/ITO and (red) 4-(perfluoroctane)phenyl/ITO; ***(b)*** configuration of TENG used for measurements.

The presented TENG must have two electrodes to form a closed circuit that complicates the engineering design of the cells, restricting their commercialization and large-scale deployment. To resolve this problem, single electrode cell, which is more practical, has been introduced. In our configuration, functionalized ITO substrates were used as bottom electrode and a piece of Nylon was used as a triboelectric generator. At the initial position, no change in the electrical potential is observed. When the Nylon is in contact with the functionalized ITO, the electrification occurs at the interface Nylon/Functionalized ITO. According to the triboelectric series, the Nylon is more triboelectric positive than the functionalized ITO, which induces negative charges at the surface of modified ITO, which is the contact electrification process. Once the separation of Nylon and ITO occurs, the charges located within the organic layer cannot be compensated, conducting to a charge separation at the interface ITO/organic film, i.e. positive charges in the ITO, resulting to a driven force for electron to flow from the ITO to the ground, conducting to the positive voltage. Then, when the Nylon substrate is put again in contact with the functionalized ITO, the negative charges at the surface of the substrate can be compensated by the opposite charges from the Nylon, resulting to an electron flow from the ground to the ITO, i.e. V_{OC} drops back to zero (Figure 5.15).

In this configuration, the 4-(perfluoroctane)phenyl/ITO exhibits higher V_{OC} (39.6 V) which can be attributed to the polarity of the molecule with a high density of fluoride that can be highly negative charged. As consequence, a lower V_{OC} of 37.9 V and 34.4 V can be explained for the 4-(trifluoromethyl)phenyl/ITO and 3,4,5-trifluorophenyl/ITO, respectively. When looking onto the molecular structure of the 3,4,5-trifluorophenyl/ITO, the position 3, 4 and 5 of the phenyl ring are blocked by the presence of fluoride, that inhibits the growth of further layer during the electrochemical grafting process. As consequence, the latter exhibits lowest quantity of fluoride which is responsible for the triboelectrification in this case of study.

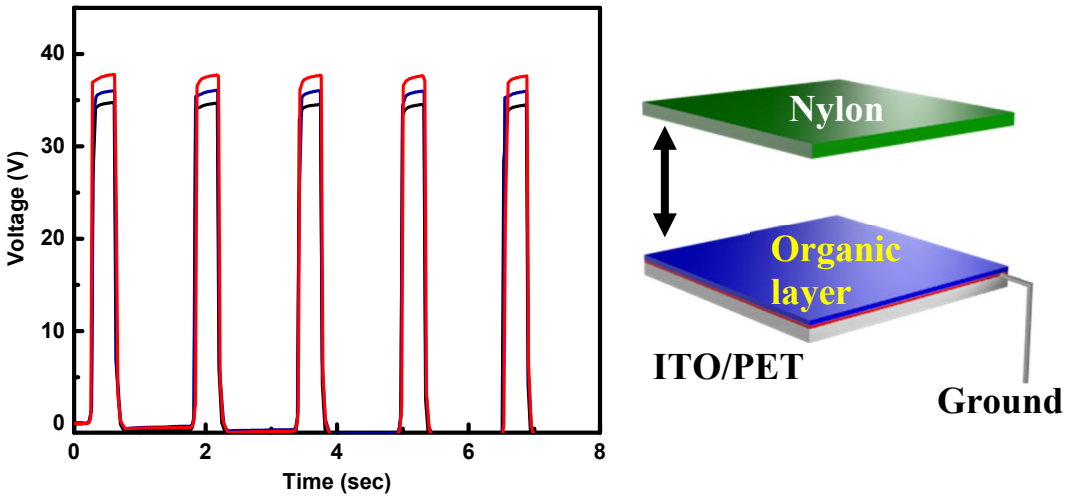

Figure 5.15 (a) Open circuit voltage of TENG with the functionalized ITO with (black) 3,4,5-trifluorophenyl/ITO, (blue) 4-(trifluoromethyl)phenyl/ITO and (red) 4-(perfluoroctane)phenyl/ITO; ***(b)*** configuration of TENG used for measurements.

In summary, the surface modification can be powerful tool for elaboration of triboelectric nanogenerators (TENG). As discussed in the present example, the molecular engineering plays a crucial role in the modulation of the performance of the TENG devices. Owing high density of charges within their structure, the ionic liquid-based materials can also be applied for the nanogenerator application, resulting to a modified flexible ITO electrode with polymeric ionic liquids. Combining with the results reported in the previous parts, is it possible to fabricate a multifunctional membrane which possesses an ability to either convert energy from mechanical form into electrical one which can be store by redox reaction.

5.4 CONCLUSION

This chapter provide an overview of the possible uses of the ionic liquids in energy applications, including energy storage and conversion systems. These results are seen as a promising way for fabricating electronic skin with multifunctional purposes, comprising the ability to convert environmental energy into electricity which can be stored via supercapacitor – battery hybrid system.

In the first part, the ferrocenated ionic liquid has been used as bi-functional mediator that ensure the charging and discharging in a redox-flow lithium battery via single molecule redox targeting model. The present system provides not only negligible voltage loss but also high energy density (up to 942 $Wh.L^{-1}$). In addition to the use of the FcIL in solution, the polymeric ferrocenated ionic liquid and Poly(AQIL) have been demonstrated as promising candidate for developing supercabattery system by increasing either the power density and the energy density (104 $W.kg^{-1}$ and 7 $Wh.kg^{-1}$).

In the second part, the preliminary results present an important role of the surface functionalization to the conversion of mechanical to electrical energy by means of the triboelectrification process. Having high density of ionic species within the structure, the ionic liquid modified substrate can be expected as further use towards efficient nanogenerator.

5.5 REFERENCES

(1) Jia, C.; Pan, F.; Zhu, Y. G.; Huang, Q.; Lu, L.; Wang, Q. High – Energy Density Nonaqueous All Redox Flow Lithium Battery Enabled with a Polymeric Membrane. *Sci. Adv.* **2015**, *1* (10), 1–7.

(2) Lin, K.; Chen, Q.; Gerhardt, M. R.; Tong, L.; Bok, S. Alkaline Quinone Flow Battery. *Science (80-.).* **2015**, *349* (6255), 1529–1532.

(3) Beh, E. S.; De Porcellinis, D.; Gracia, R. L.; Xia, K. T.; Gordon, R. G.; Aziz, M. J. A Neutral PH Aqueous Organic-Organometallic Redox Flow Battery with Extremely High Capacity Retention. *ACS Energy Lett.* **2017**, *2* (3), 639–644.

(4) Soloveichik, G. L. Flow Batteries: Current Status and Trends. *Chem. Rev.* **2015**, *115* (20), 11533–11558.

(5) Ding, Y.; Yu, G. The Promise of Environmentally Benign Redox Flow Batteries by Molecular Engineering. *Angew. Chemie - Int. Ed.* **2017**, *56* (30), 8614–8616.

(6) Hu, B.; DeBruler, C.; Rhodes, Z.; Liu, T. L. Long-Cycling Aqueous Organic Redox Flow Battery (AORFB) toward Sustainable and Safe Energy Storage. *J. Am. Chem. Soc.* **2017**, *139* (3), 1207–1214.

(7) Huskinson, B.; Marshak, M. P.; Suh, C.; Er, S.; Gerhardt, M. R.; Galvin, C. J.; Chen, X.; Aspuru-Guzik, A.; Gordon, R. G.; Aziz, M. J. A Metal-Free Organic-Inorganic Aqueous Flow Battery. *Nature* **2014**, *505* (7482), 195–198.

(8) Liu, Q.; Sleightholme, A. E. S.; Shinkle, A. A.; Li, Y.; Thompson, L. T. Non-Aqueous Vanadium Acetylacetonate Electrolyte for Redox Flow Batteries. *Electrochem. commun.* **2009**, *11* (12), 2312–2315.

(9) Liu, Q.; Shinkle, A. A.; Li, Y.; Monroe, C. W.; Thompson, L. T.; Sleightholme, A. E. S. Non-Aqueous Chromium Acetylacetonate Electrolyte for Redox Flow Batteries. *Electrochem. commun.* **2010**, *12* (11), 1634–1637.

(10) Ding, Y.; Zhao, Y.; Yu, G. A Membrane-Free Ferrocene-Based High-Rate Semiliquid Battery. *Nano Lett.* **2015**, *15* (6), 4108–4113.

(11) Ding, Y.; Zhao, Y.; Li, Y.; Goodenough, J. B.; Yu, G. A High-Performance All-Metallocene-Based, Non-Aqueous Redox Flow Battery. *Energy Environ. Sci.* **2017**, *10* (2), 491–497.

(12) Winsberg, J.; Hagemann, T.; Janoschka, T.; Hager, M. D.; Schubert, U. S. Redox-Flow Batteries: From Metals to Organic Redox-Active Materials. *Angew. Chemie - Int. Ed.* **2017**, *56* (3), 686–711.

(13) Ding, Y.; Li, Y.; Yu, G. Exploring Bio-Inspired Quinone-Based Organic Redox Flow Batteries: A Combined Experimental and Computational Study. *Chem* **2016**, *1* (5), 790–801.

(14) Wei, X.; Xu, W.; Huang, J.; Zhang, L.; Walter, E.; Lawrence, C.; Vijayakumar, M.; Henderson, W. A.; Liu, T.; Cosimbescu, L.; Li, B.; Sprenkle, V.; Wang, W. Radical Compatibility with Nonaqueous Electrolytes and Its Impact on an All-Organic Redox Flow Battery. *Angew. Chemie - Int. Ed.* **2015**, *54* (30), 8684–8687.

(15) Hwang, B.; Park, M. S.; Kim, K. Ferrocene and Cobaltocene Derivatives for Non-Aqueous Redox Flow Batteries. *ChemSusChem* **2015**, *8* (2), 310–314.

(16) Zhao, Y.; Ding, Y.; Song, J.; Li, G.; Dong, G.; Goodenough, J. B.; Yu, G. Sustainable Electrical Energy Storage through the Ferrocene/Ferrocenium Redox Reaction in

Aprotic Electrolyte. *Angew. Chemie - Int. Ed.* **2014**, *53* (41), 11036–11040.

(17) Wei, X.; Xu, W.; Vijayakumar, M.; Cosimbescu, L.; Liu, T.; Sprenkle, V.; Wang, W. TEMPO-Based Catholyte for High-Energy Density Nonaqueous Redox Flow Batteries. *Adv. Mater.* **2014**, *26* (45), 7649–7653.

(18) Li, B.; Nie, Z.; Vijayakumar, M.; Li, G.; Liu, J.; Sprenkle, V.; Wang, W. Ambipolar Zinc-Polyiodide Electrolyte for a High-Energy Density Aqueous Redox Flow Battery. *Nat. Commun.* **2015**, *6*, 1–8.

(19) Fan, F. Y.; Woodford, W. H.; Li, Z.; Baram, N.; Smith, K. C.; Helal, A.; McKinley, G. H.; Carter, W. C.; Chiang, Y. M. Polysulfide Flow Batteries Enabled by Percolating Nanoscale Conductor Networks. *Nano Lett.* **2014**, *14* (4), 2210–2218.

(20) Takechi, K.; Kato, Y.; Hase, Y. A Highly Concentrated Catholyte Based on a Solvate Ionic Liquid for Rechargeable Flow Batteries. *Adv. Mater.* **2015**, *27* (15), 2501–2506.

(21) Cong, G.; Zhou, Y.; Li, Z.; Lu, Y. C. A Highly Concentrated Catholyte Enabled by a Low-Melting-Point Ferrocene Derivative. *ACS Energy Lett.* **2017**, *2* (4), 869–875.

(22) Huang, Q.; Wang, Q. Next-Generation, High-Energy-Density Redox Flow Batteries. *Chempluschem* **2015**, *80* (2), 312–322.

(23) Wang, Y.; He, P.; Zhou, H. Li-Redox Flow Batteries Based on Hybrid Electrolytes: At the Cross Road between Li-Ion and Redox Flow Batteries. *Adv. Energy Mater.* **2012**, *2* (7), 770–779.

(24) Zhao, Y.; Ding, Y.; Li, Y.; Peng, L.; Byon, H. R.; Goodenough, J. B.; Yu, G. A Chemistry and Material Perspective on Lithium Redox Flow Batteries towards High-Density Electrical Energy Storage. *Chem. Soc. Rev.* **2015**, *44* (22), 7968–7996.

(25) Huang, Q.; Li, H.; Grätzel, M.; Wang, Q. Reversible Chemical Delithiation/Lithiation of LiFePO4: Towards a Redox Flow Lithium-Ion Battery. *Phys. Chem. Chem. Phys.* **2013**, *15* (6), 1793–1797.

(26) Pan, F.; Yang, J.; Huang, Q.; Wang, X.; Huang, H.; Wang, Q. Redox Targeting of Anatase TiO2 for Redox Flow Lithium-Ion Batteries. *Adv. Energy Mater.* **2014**, *4* (15), 1400567.

(27) Fontaine, O.; Lagrost, C.; Ghilane, J.; Martin, P.; Trippé, G.; Fave, C.; Lacroix, J. C.; Hapiot, P.; Randriamahazaka, H. N. Mass Transport and Heterogeneous Electron Transfer of a Ferrocene Derivative in a Room-Temperature Ionic Liquid. *J. Electroanal. Chem.* **2009**, *632* (1–2), 88–96.

(28) Forgie, J. C.; El Khakani, S.; MacNeil, D. D.; Rochefort, D. Electrochemical Characterisation of a Lithium-Ion Battery Electrolyte Based on Mixtures of Carbonates with a Ferrocene-Functionalised Imidazolium Electroactive Ionic Liquid. *Phys. Chem. Chem. Phys.* **2013**, *15* (20), 7713–7721.

(29) Zhu, Y. G.; Du, Y.; Jia, C.; Zhou, M.; Fan, L.; Wang, X.; Wang, Q. Unleashing the Power and Energy of LiFePO4-Based Redox Flow Lithium Battery with a Bifunctional Redox Mediator. *J. Am. Chem. Soc.* **2017**, *139* (18), 6286–6289.

(30) Huang, Q.; Yang, J.; Ng, C. B.; Jia, C.; Wang, Q. A Redox Flow Lithium Battery Based on the Redox Targeting Reactions between LiFePO $_4$ and Iodide. *Energy Environ. Sci.* **2016**, *9* (3), 917–921.

(31) Muench, S.; Wild, A.; Friebe, C.; Häupler, B.; Janoschka, T.; Schubert, U. S. Polymer-Based Organic Batteries. *Chem. Rev.* **2016**, *116* (16), 9438–9484.

(32) Kim, S.; Wee, J.; Peters, K.; Huang, H. Y. S. Multiphysics Coupling in Lithium-Ion Batteries with Reconstructed Porous Microstructures. *J. Phys. Chem. C* **2018**, *122* (10), 5280–5290.

(33) Tavassol, H.; Jones, E. M. C.; Sottos, N. R.; Gewirth, A. A. Electrochemical Stiffness in Lithium-Ion Batteries. *Nat. Mater.* **2016**, *15* (11), 1182–1188.

(34) Barker, J. In-Situ Measurement of the Thickness Changes Associated with Cycling of Prismatic Lithium Ion Batteries Based on LiMn2O4 and LiCoO2. *Electrochim. Acta* **1999**, *45* (1–2), 235–242.

(35) Lee, J. H.; Lee, H. M.; Ahn, S. Battery Dimensional Changes Occurring during Charge/Discharge Cycles - Thin Rectangular Lithium Ion and Polymer Cells. *J. Power Sources* **2003**, *119–121*, 833–837.

(36) Fu, R.; Xiao, M.; Choe, S. Y. Modeling, Validation and Analysis of Mechanical Stress Generation and Dimension Changes of a Pouch Type High Power Li-Ion Battery. *J. Power Sources* **2013**, *224*, 211–224.

(37) Nadimpalli, S. P. V.; Sethuraman, V. A.; Abraham, D. P.; Bower, A. F.; Guduru, P. R. Stress Evolution in Lithium-Ion Composite Electrodes during Electrochemical Cycling and Resulting Internal Pressures on the Cell Casing. *J. Electrochem. Soc.* **2015**, *162* (14), A2656–A2663.

(38) Bucci, G.; Swamy, T.; Bishop, S.; Sheldon, B. W.; Chiang, Y.-M.; Carter, W. C. The Effect of Stress on Battery-Electrode Capacity. *J. Electrochem. Soc.* **2017**, *164* (4), A645–A654.

(39) Fan, F. R.; Tian, Z. Q.; Lin Wang, Z. Flexible Triboelectric Generator. *Nano Energy* **2012**, *1* (2), 328–334.

(40) Wang, Z. L. Triboelectric Nanogenerators as New Energy Technology for Self-Powered Systems and as Active Mechanical and Chemical Sensors. *ACS Nano* **2013**, *7* (11), 9533–9557.

(41) Wang, Z. L. Triboelectric Nanogenerators as New Energy Technology and Self-Powered Sensors - Principles, Problems and Perspectives. *Faraday Discuss.* **2014**, *176*, 447–458.

(42) Zhu, G.; Pan, C.; Guo, W.; Chen, C. Y.; Zhou, Y.; Yu, R.; Wang, Z. L. Triboelectric-Generator-Driven Pulse Electrodeposition for Micropatterning. *Nano Lett.* **2012**, *12* (9), 4960–4965.

(43) Zhong, J.; Zhong, Q.; Fan, F.; Zhang, Y.; Wang, S.; Hu, B.; Wang, Z. L.; Zhou, J. Finger Typing Driven Triboelectric Nanogenerator and Its Use for Instantaneously Lighting up LEDs. *Nano Energy* **2013**, *2* (4), 491–497.

(44) Yang, Y.; Zhou, Y. S.; Zhang, H.; Liu, Y.; Lee, S.; Wang, Z. L. A Single-Electrode Based Triboelectric Nanogenerator as Self-Powered Tracking System. *Adv. Mater.* **2013**, *25* (45), 6594–6601.

(45) Wang, S.; Lin, L.; Xie, Y.; Jing, Q.; Niu, S.; Wang, Z. L. Sliding-Triboelectric Nanogenerators Based on in-Plane Charge-Separation Mechanism. *Nano Lett.* **2013**, *13* (5), 2226–2233.

(46) Lin, L.; Wang, S.; Xie, Y.; Jing, Q.; Niu, S.; Hu, Y.; Wang, Z. L. Segmentally Structured Disk Triboelectric Nanogenerator for Harvesting Rotational Mechanical Energy. *Nano Lett.* **2013**, *13* (6), 2916–2923.

(47) Wang, S.; Zi, Y.; Zhou, Y. S.; Li, S.; Fan, F.; Lin, L.; Wang, Z. L. Molecular Surface

Functionalization to Enhance the Power Output of Triboelectric Nanogenerators. *J. Mater. Chem. A* **2016**, *4* (10), 3728–3734.

(48) Bélanger, D.; Pinson, J. Electrografting: A Powerful Method for Surface Modification. *Chem. Soc. Rev.* **2011**, *40* (7), 3995–4048.

(49) Lao, C.; Li, Y.; Wong, C. P.; Wang, Z. L. Enhancing the Electrical and Optoelectronic Performance of Nanobelt Devices by Molecular Surface Functionalization. *Nano Lett.* **2007**, *7* (5), 1323–1328.

(50) Liu, G.; Böcking, T.; Gooding, J. J. Diazonium Salts: Stable Monolayers on Gold Electrodes for Sensing Applications. *J. Electroanal. Chem.* **2007**, *600* (2), 335–344.

(51) Kakade, B. a.; Pillai, V. K. Tuning the Wetting Properties of Multiwalled Carbon Nanotubes by Surface Functionalization. *J. Phys. Chem. C* **2008**, *112* (9), 3183–3186.

(52) Gattrell, M.; Gupta, N.; Co, A. A Review of the Aqueous Electrochemical Reduction of CO2to Hydrocarbons at Copper. *J. Electroanal. Chem.* **2006**, *594* (1), 1–19.

(53) Garza, A.; Bell, A. T.; Head-Gordon, M. On the Mechanism of CO2 Reduction at Copper Surfaces: Pathways to C2 Products. *ACS Catal.* **2018**, acscatal.7b03477.

(54) Li, C. W.; Kanan, M. W. CO 2 Reduction at Low Overpotential on Cu Electrodes Resulting from the Reduction of Thick Cu 2O Films. *J. Am. Chem. Soc.* **2012**, *134* (17), 7231–7234.

(55) Loiudice, A.; Lobaccaro, P.; Kamali, E. A.; Thao, T.; Huang, B. H.; Ager, J. W.; Buonsanti, R. Tailoring Copper Nanocrystals towards C2 Products in Electrochemical CO2 Reduction. *Angew. Chemie - Int. Ed.* **2016**, *55* (19), 5789–5792.

(56) Nie, X.; Esopi, M. R.; Janik, M. J.; Asthagiri, A. Selectivity of CO_2 Reduction on Copper Electrodes: The Role of the Kinetics of Elementary Steps. *Angew. Chemie* **2013**, *125* (9), 2519–2522.

(57) Kim, C.; Jeon, H. S.; Eom, T.; Jee, M. S.; Kim, H.; Friend, C. M.; Min, B. K.; Hwang, Y. J. Achieving Selective and Efficient Electrocatalytic Activity for CO_2 Reduction Using Immobilized Silver Nanoparticles. *J. Am. Chem. Soc.* **2015**, *137* (43), 13844–13850.

(58) Liu, S.; Tao, H.; Zeng, L.; Liu, Q.; Xu, Z.; Liu, Q.; Luo, J. L. Shape-Dependent Electrocatalytic Reduction of CO2to CO on Triangular Silver Nanoplates. *J. Am. Chem. Soc.* **2017**, *139* (6), 2160–2163.

(59) Rosen, B. A.; Salehi-khojin, A.; Thorson, M. R.; Zhu, W.; Whipple, D. T.; Kenis, P. J. A.; Masel, R. I. Ionic Liquid – Mediated Selective Conversion of CO2 to CO at Low Overpotentials. *Science (80-.).* **2011**, *334* (November), 643–644.

(60) Zheng, Y.; Jiao, Y.; Ge, L.; Jaroniec, M.; Qiao, S. Z. Two-Step Boron and Nitrogen Doping in Graphene for Enhanced Synergistic Catalysis. *Angew. Chemie - Int. Ed.* **2013**, *52* (11), 3110–3116.

(61) Shao, Y.; Zhang, S.; Engelhard, M. H.; Li, G.; Shao, G.; Wang, Y.; Liu, J.; Aksay, I. A.; Lin, Y. Nitrogen-Doped Graphene and Its Electrochemical Applications. *J. Mater. Chem.* **2010**, *20* (35), 7491–7496.

(62) Yang, S.; Zhi, L.; Tang, K.; Feng, X.; Maier, J.; M??llen, K. Efficient Synthesis of Heteroatom (N or S)-Doped Graphene Based on Ultrathin Graphene Oxide-Porous Silica Sheets for Oxygen Reduction Reactions. *Adv. Funct. Mater.* **2012**, *22* (17), 3634–3640.

(63) Sun, H.; Gao, N.; Dong, K.; Ren, J.; Qu, X. Graphene Quantum Dots-Band-Aids Used

for Wound Disinfection. *ACS Nano* **2014**, *8* (6), 6202–6210.

(64) Yang, J.; Zhang, X.; Ma, Y. H.; Gao, G.; Chen, X.; Jia, H. R.; Li, Y. H.; Chen, Z.; Wu, F. G. Carbon Dot-Based Platform for Simultaneous Bacterial Distinguishment and Antibacterial Applications. *ACS Appl. Mater. Interfaces* **2016**, *8* (47), 32170–32181.

(65) Singh, V. V.; Jurado-Sánchez, B.; Sattayasamitsathit, S.; Orozco, J.; Li, J.; Galarnyk, M.; Fedorak, Y.; Wang, J. Multifunctional Silver-Exchanged Zeolite Micromotors for Catalytic Detoxification of Chemical and Biological Threats. *Adv. Funct. Mater.* **2015**, *25* (14), 2147–2155.

5.6 APPENDICES

Table 5.S1 List of abbreviations of various flow batteries in Figure 5.2

Abbreviation	Full name
2,6-DHAQ/$K_4Fe(CN)_6$	2,6-dihydroxyanthraquinone/ferrocyanide
Fe/Cr	Iron/chromium
AQDS/Br_2	9,10-anthraquinone-2,7-disulfonic acid/bromine
Soluble lead-acid	Lead-acid flow battery based on soluble lead methanesulfonate
BTMAP-Fc/BTMAP-Vi	Bis((3-trimethylammonio)propyl)ferrocene dichloride/ bis(3-trimethylammonio)propylviologen tetrachloride
FcNCl/MV	(Ferrocenylmethyl)trimethylammonium chloride/ methyl viologen
Li/TEMPO	Li-metal/ 2,2,6,6-tetramethylpiperidine-1-oxyl
Li/MTLT ionic liquid	Li-metal/ 4-methoxy-2,2,6,6-tetramethylpiperidine 1-oxyl + lithium bis(trifluoromethanesulfonyl) imide
FL/DBMMB	9-fluorenone/2,5-di-tert-butyl-1-methoxy-4-[2'-Methoxyethoxy]benzene
all $Cr(acac)_3$	Chromium acetylacetonate
all $V(acac)_3$	Vanadium acetylacetonate
$CoCp_2$/Fc	Cobaltocene/ ferrocene
Li/Fc	Li-metal/ ferrocene
VRB	All-vanadium redox flow battery
Li/Fc1N112	Li-metal/ ferrocenylmethyl dimethyl ethyl ammonium
Li/DMFc	Li-metal/1,1-dimethylferrocene
RFLB	Redox targeting based redox flow lithium battery

CHAPTER 6

GENERAL CONCLUSIONS AND PERSPECTIVES

6.1 GENERAL CONCLUSIONS

Within this thesis, we propose a series of RIL by introducing oxidative and/or reducible groups (ferrocene, anthraquinone, viologen, etc.) to the imidazolium's and ammonium's structure. Besides, we have also prepared bi/multi-functional ionic liquids by combining redox-active groups and polymerizable unit (vinyl, methacrylate, etc.) within the cationic skeleton. The presence of such monomer units provides possibility to perform the polymerization affording polymeric redox-active ionic liquids. In the vicinity of positive charge induced from different cation centers (imidazolium, ammonium, etc.), the electrochemical response of the redox-active components is strongly affected. Unlike conventional redox-active molecules, (Redox)-ionic liquids provide multiple role in electrochemistry, i.e, simultaneously act as solvent, supporting electrolyte and electrochemical active materials.

In the chapter 2, different approaches have been proposed for immobilization of different ionic liquids onto electrode surfaces from thin layers to polymeric films. The thin layer of electroactive ionic liquid has been performed via electrochemical grafting of the linker, 4-azidoaniline, followed by click chemistry with 1-ferrocenylmethyl-3-propargylimidazolium. Interestingly, independent to the number of electrochemical grafting cycles, a single layer of ferrocenated ionic liquids is obtained at the top of the modified electrode. However, a different of the electron transfer rate constant is strongly depending on the thickness of the primary layer. Furthermore, the surface characterization techniques confirm the presence of the ionic liquid layer. In addition to the surface modification with thin layer of ionic liquid, a biredox ionic liquid molecule, FcAQIm, has been used for generating multi-redox state of the modified surface. The immobilization has been performed by stepwise process. Importantly, the bi-redox layer exhibits not only 3 redox states within a narrow potential window but also an enhancement of the capacitance (3 times compared to the bare GC). In parallel, the functionalization of the electrode with polymeric layers is also important approach for attaching more quantity of the ionic liquid molecules. We have demonstrated a possibility to polymerize the FcIL by electrodeposition under cathodic polarization. Apart from the detection of the immobilized ferrocene moieties at the surface, the modified electrodes have been used as stable quasi-reference electrode in non-aqueous and ionic liquid solution with negligible potential shift after numerous cycles (< 10 mV for 500 cycles). Besides, this reference electrode can be prepared and used in confined electrochemical cell, e.g. SECM. Later, another approach has been reported to polymerize the ionic liquid-based monomer via SI-ATRP process. Indeed, 3 monomers have been used, varying from monoredox to biredox molecules. As an interesting

result, all of the immobilized polymeric ionic liquids exhibit self-electrolytic behavior which is one of the particularity of the ionic liquid. Moreover, the biredox polymer, Poly(FcAQIm) presents a strong enhancement either the multiredox-state characteristic and the capacitance (30 times higher compared to the bare electrode).

In continuation of the previous works, in the chapter 3, the application of polymeric ionic liquid in the field of electrocatalysis has been reported. The immobilized polymeric ionic liquids (Poly(VImM) and PAMI) have been used as active catalysts towards oxygen reactions, including oxygen reduction and evolution reactions. It has been evidenced that the presence of the polymer layer enhances not only the adsorption of oxygen but also the ionic conduction. Moreover, the brush-structure coupled with high density of positive charges create water channels that favors the accessibility of the oxygen, resulting to higher oxygen concentration inside the film. More interestingly, we have experimental evidences that poly(ionic liquids) can provide host-guest platform for preparation of hybrid PIL/metal NPs with simple drop-casting procedure, resulting to a synergetic effect, i.e. enhancement of catalytic activity (a gain of 40 mV was obtained by using PIL/Pt NPs compared to only Pt NPs). This approach has been proven to provide a vast increase of the performance (n_e approaches to 4) to low efficient catalysts, e.g. Au NPs. In addition, profiting cationic behavior of the polymer, 2 electrochemical approaches have been developed in order to generate homogeneous film of polymeric ionic liquid decorated with metallic nanoparticles. As aforementioned, the self-electrocatalytic behavior of the PIL allows the electrochemical deposition of metallic nanoparticles in electrolytic-free medium. This approach provides thin and homogeneous layer which is compose of multiple nanoparticles embedded inside the polymeric layer. The hybrid layers provide high catalytic performance by using less quantity of material (2 orders of magnitude).

In parallel with the surface functionalization using (poly)-ionic liquids, the use of ionic liquid, EMIES, has been explored towards synthesis of carbon quantum dots with ten of nanometers in size. The EMIES has been evidenced to be either solvent and nitrogen source for doping the final particles, conducting to N,S-doped C-dots. Importantly, this family of material exhibits a strong affinity for electrochemical generation of hydrogen peroxide resulting from oxygen reduction reaction in alkaline solution (higher than 90 % over a broad potential ranging from 0.6 V to -0.2V/RHE. Consequently, this approach paves the way for replacing the anthraquinone process which is relatively expensive.

Appearing as novel materials, the electron transfer/transport through and within the layer is still matter for exploration. Within this context, the scanning electrochemical microscopy setup has been used for investigating the localized electrochemical behaviors in/over the ionic liquid layers. In presence of redox molecule in an ionic liquid medium, EMITFSI, a formation of immobilized-like layer of the Fc moieties inside the junction between the UME and an insulator has been observed. Inversely, close to a conductive substrate, an immobilized Poly(FcIL) on UME exhibits diffusion-controlled regime with appearance of plateau current. More

importantly, feedback curve has been recorded in absence of any redox mediator in solution, resulting probably from a scanning ionic conductance microscopy approach. Even though the explanation of these phenomena is still opened, they question about previous studies using approach curves in ionic liquid media, resulting to re-evaluation of the charge transfer kinetic in ionic liquid solutions and over ionic liquid layers.

Besides, the SECM setup has also been used to investigate the electronic/electrochemical properties of the graphene-based materials. Thus, by functionalizing the single layer graphene with different approaches, varying from destructive (electrografting of diazonium salts) to non-destructive one (drop-casting of Pt NPs), a modulation from p-type and n-type graphene is observed and followed by SECM. Consequently, this study proposes new routes for modulating the Fermi level of graphene-based materials, affording interesting interfaces in diverse applications.

In the last part, preliminary results by using ionic liquids for different applications in energy fields are reported. Thus, the ferrocenated ionic liquid has been interestingly proved to have a bifunctionality aspect for charging and discharging the RFLB. As a result, the use of the ionic liquid allows to avoid the voltage loss due to the use of 2 redox mediators in RFLB and increase the energy density (up to 942 $Wh.L^{-1}$). In addition to the use of FcIL in solution, the polymer ionic liquids have been demonstrated to provide suitable configuration for preparation of supercapacitor – battery hybrid, which give either higher power density (up to 10^4 $W.kg^{-1}$) and higher energy density (7 $Wh.kg^{-1}$). An exploratory study has been performed to evaluate the influence of the surface modification to the triboelectrification effect of the ITO substrates. As consequence, the triboelectrification effect change by changing the ratio the fluoride within the film, resulting from a crucial change of the work function of the material. As a result, the open circuit potential change in function of the molecular structure of the surface.

Altogether, the reported results pave the way for generating and utilization of novel family of materials based on ionic liquids for multifunctional purposes, especially in the energy field and fabrication of flexible electronic skin.

6.2 PERSPECTIVE

In this part, some perspectives will be proposed for preparation of highly efficient thin film catalysts for conversion of solar/electrical energy to chemical bonds via catalytic activation of small molecules. As long-term goals, we aim to develop electronic skin which has high energetical autonomous.

Flexible supercabattery coupled with electrochemical actuator

For energy storage, there are two typical systems which have been widely investigated and commercialized, i.e. electrochemical capacitor and battery. It is noted that electrochemical capacitor or supercapacitor stores energy in an electric field by the electrical double layer of the electrode materials (Figure 6.1a). As the operation of a supercapacitor is based on the adsorption of ions at the surface of the electrode, the system allows to store and deliver a large amount of power within short time (high power density). And battery systems are based on the exchange of electron between two chemical reactions, i.e. oxidation and reduction that occurs at the anode and the cathode, respectively (Figure 6.1b). As the energy is stored by electrochemical reaction that involves the electron transfer and ionic transport, high energy density can be obtained. By Having large amount of ionic species within the polymer layer, the redox polymeric ionic liquids could provide in parallel higher power density and higher energy density than other systems, resulting to a supercabattery system. This notion is attributed to an energy storage system that provide high ability to store either energy and power.

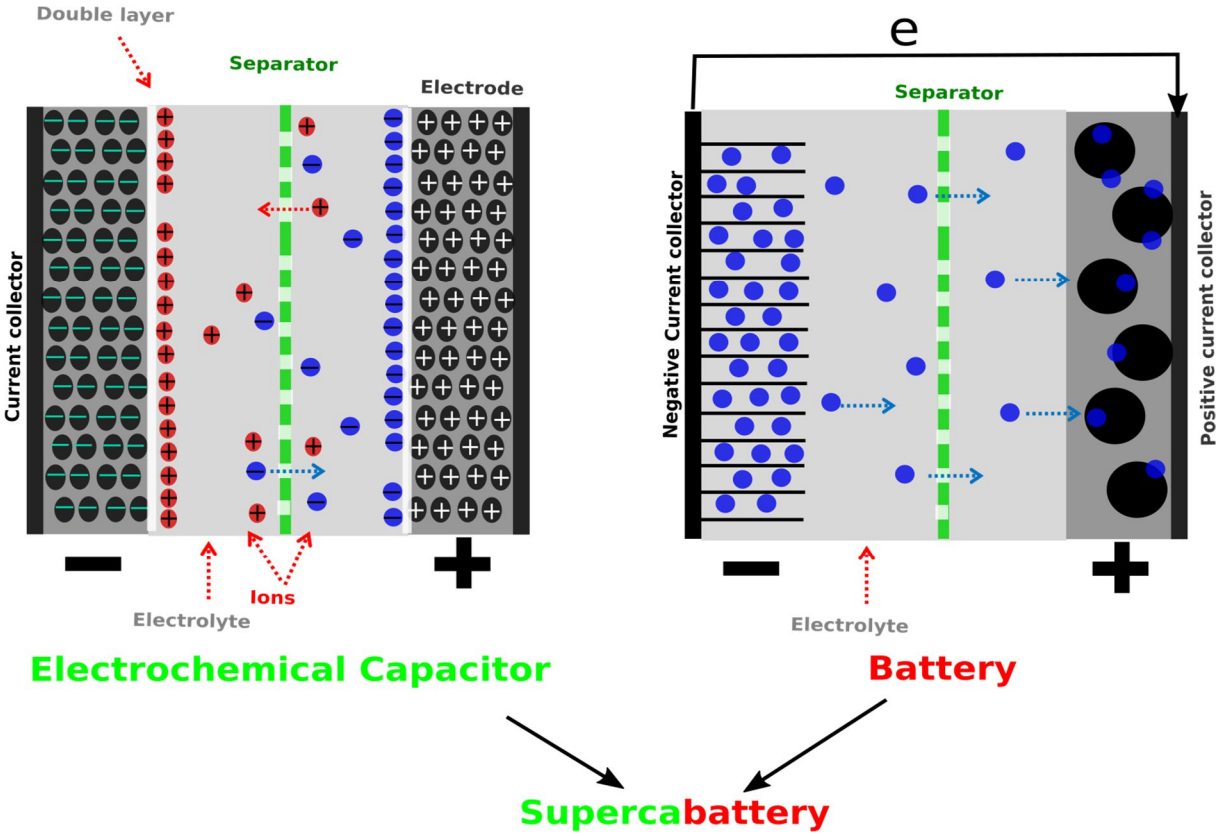

Figure 6.1 Working principle of ***(a)*** supercapacitor and ***(b)*** battery

For future development, instead of using asymmetric system in which the Poly(FcIL) is used as anode and the Poly(AQ) is used as cathode, a symmetric system is considered. This approach is composed of 2 working electrodes made through the same manner, i.e. modification by using Poly(FcAQIL) as shown in the chapter 2. As demonstrated in the chapter 2, the capacitance observed for the GC/Poly(FcAQIm) is 30 times higher than bare GC electrode, suggesting a higher capacitance compared to the one given by a simple Poly(FcIL) or Poly(AQIL).

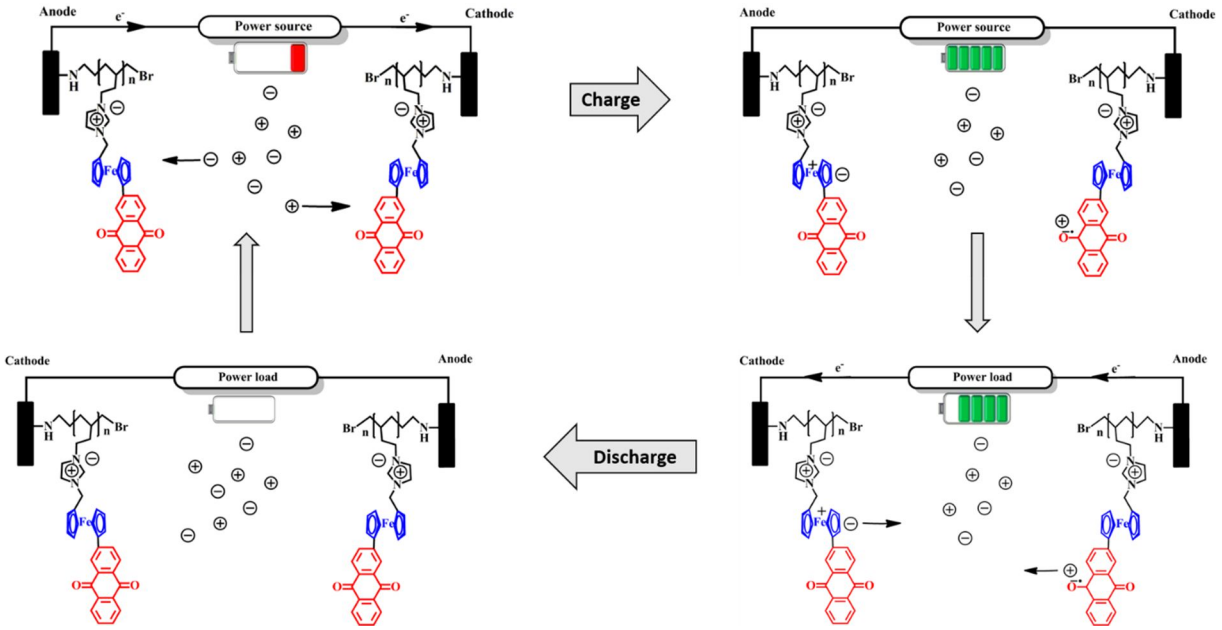

Figure 6.2 Schematic electrochemical processes during charging/discharging cycle.

As consequence, the use of the bi-redox system provides a higher power density. In principle, during the charging process in protic solution,

At the anode, $FcAQIm^+ A^- \longrightarrow Fc^+AQIm^+ A^- + 1e^- + 1A^-$ (6.1)

At the cathode, $FcAQIm^+ A^- + 2e^- + 2H^+ \longrightarrow FcAQH_2 Im^+ A^-$ (6.2)

and during the discharging process,

At the anode, $FcAQIm^+ A^- \longleftarrow Fc^+AQIm^+ A^- + 1e^- + 1A^-$ (6.3)

At the cathode, $FcAQIm^+ A^- + 2e^- + 2H^+ \longleftarrow FcAQH_2 Im^+ A^-$ (6.4)

In addition to the hybrid behaviors of the immobilized redox-active polymer ionic liquids, they provide a possibility towards the fabrication of organic systems. For SI-ATRP, the thickness of the polymer is estimated to be in the range of 30 nm for all the used monomers. Furthermore, it has been described in the chapter 2 the possibility to functionalize flexible substrates with these polymer ionic liquids, comprising flexible ITO/PET and 3D – Ni foam. Consequently, this approach put forward the fabrication of ultrathin/wearable organic supercabattery.

Besides, it is known that the intercalation of ions into a solid matrix cause mechanical stress inside the material during charging/discharging process[1,2]. This phenomenon is more severe in the case of Li-ion composite[3–5], inducing a power loss due to the contraction of the material to

the equilibrium state by means of delithiation[6,7]. Nevertheless, the flexibility of the polymer chains (cf. chapter 4) allows the insertion of anion into the polymer layer without any perturbation. In addition, the intercalation of the ions into the ionic liquid framework increase the electron transfer kinetic. Thus, we can imagine an energy storage system combined with an electrochemical actuator where the expansion is expected during the charging process.

Nanofilm catalyst towards activation of small molecules

In the previous part, the surface modification has been demonstrated to have an impact to the conversion of the mechanical energy to the electricity, which can be store either by battery systems or via chemical bonds. As presented in the chapter 3, the electrocatalytic performance of the poly(VImM) and the influence of the molecular structure on the catalytic activity have been evidenced. According to an estimation, there are around a million of possible ionic liquids which could have different physical-chemical properties. Consequently, the performance of the immobilized polymer ionic liquids can be improved by utilizing different molecular designs. Moreover, the immobilized ionic liquid can provide a host-guest platform for the generation of hybrid catalysts for catalytic activation of different reactions, comprising evolution oxygen and hydrogen evolution reactions, and oxygen reduction reaction. In this part, different routes are discussed for developing/boosting the performance of the system towards higher energy conversion efficiency.

For fabrication of ionic liquid – based film as catalysts towards electrical – chemical conversion, fundamental studies about the electrodeposition of different metal nanoparticles can be further investigated. Indeed, in presence of the polymeric ionic liquid, high density of cationic charges invokes the change of the size, the morphology, the exposed crystallographic facets of the deposited nanoparticles. Consequently, a theoretical coupled with experimental investigation allow to modulate the performance of the nanoparticles deposited in presence of polymer ionic liquid films. Exempt the utilization of Pd and Pt nanoclusters as decorators for boosting the performance of the final interface, other available metallic nanoparticles are possible, such as Cu, Ag, MoS_2, etc. The use of these metals paves the way for making efficient multifunctional catalysts, especially for carbon dioxide reduction with high selectivity. It is reported in the literature that copper – based catalysts offer a great selectivity towards production of hydrocarbon[8–12] while the Ag produce majorly carbon monoxide (CO)[13,14]. Interestingly, Rosen et al. have reported the used of ionic liquid, 1-ethyl-3-methylimidazolium tetrafluoroborate, as mediator for generation of CO at low overpotential by using a silver electrode[15].

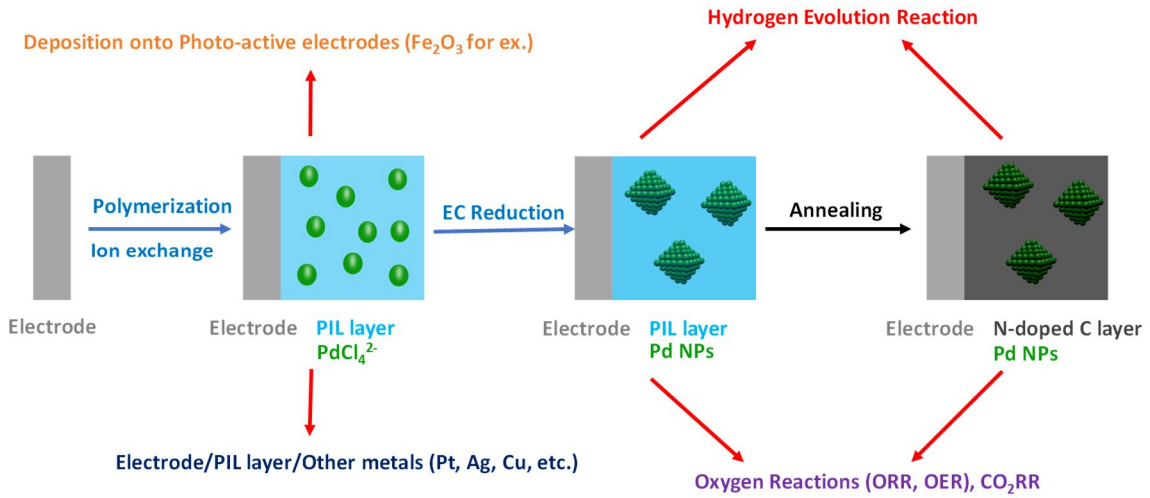

Figure 6.3 Different possibilities to develop more efficient catalysts towards activation of various reactions.

Up to now, all of the reported poly(ionic liquid) – based electrocatalysts have been utilized as prepared without further thermal treatments. However, it is worth noting that most of carbonaceous catalysts require high – temperature treatment for achieving their best performance[16–18]. Consequently, the immobilized ionic liquid layer could be further transformed into N-doped carbon layer decorated with nanoparticles via annealing. In addition, at high temperature, the metallic nanoparticles can be further crystallized, affording higher density of the active facets, suggesting an enhancement of the catalytic activity.

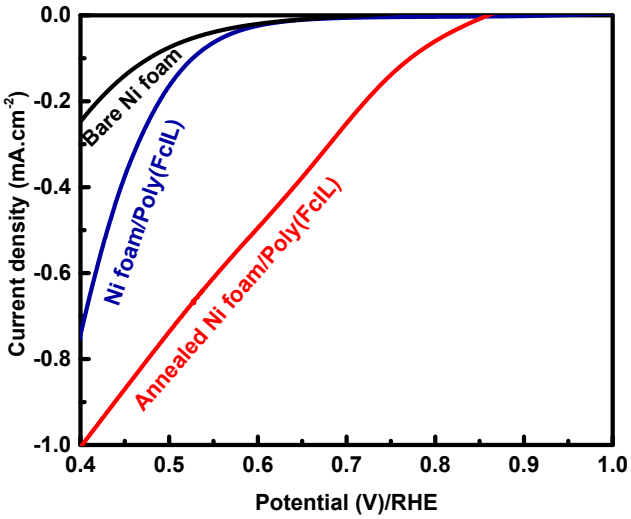

Figure 6.4 Polarization curves recorded with (black) bare Ni foam, (blue) Ni foam/Poly(FcIL) and (red) Ni foam/(Poly(FcIL) treated by annealing at 450° C for 2hrs, in O_2 – saturated KOH solution. Scan rate = 10 mV.s^{-1}

The figure 6.4 presents an example of the crucial role of the annealing for enhancing the performance of ionic liquid-based materials. For this preliminary study, a Ni foam was used as substrate for immobilization of Poly(FcIL) by using SI-ATRP procedure (cf. Chapter 2). Then, the modified substrate was investigated for oxygen reduction reaction in alkaline solution. As result, a net difference of catalytic activity towards oxygen reduction reaction can be easily observed before and after thermal treatment by using Ni foam/Poly(FcIL). After annealing at 450 °C for 2hrs for converting the polymer layer onto Fe,N – doped carbon film, the catalytic

performance of the annealed Ni/Poly(FcIL) electrode is strongly increased with a shift of onset potential about 250 mV compared to non-treated Ni/Poly(FcIL).

Thermoelectrochemical cell

Very recently, new concept of energy storage using thermocell has been developed at Prof. Wallace's group[19,20]. In conventional energy conversion, a fuel is needed to generate higher valued products; e.g. photo/electro water splitting is used to convert solar power into chemical bonding and combustion of fossil fuel is typical chemical energy/heat conversion, etc. However, these technologies suffer from numerous inconvenient from economic to ecologic point of view. Within this context, thermo-cells can provide some advantages, such as continuous transformation from heat to electricity via the dependency of electrochemical redox potential on the temperature, simple design, zero carbon emission, etc.

In the thermo-cells, small electroactive molecules with suitable standard potential can be utilized as charge shuttles for charging and discharging the cell by Seebeck effect. Besides, as the working principle of the cell engages a difference of temperature, the choice of solvent with high thermal resistance is crucial. A large variety of redox molecules have already been tested. Unfortunately, the most of the redox mediators reported in the literature exhibit drawbacks resulting from the limited concentration due to their low solubility in various solvents 0. As a consequence, the chemical structures influence significantly not only to the charge transfer in between the battery materials and the redox mediators in the mobile phase but also to the solubility in a solvent of interest, where introduction of redox active ionic liquids.

The following points are proposed and will be carried out for the next steps to study the influence of different redox active ionic liquids to the efficiency of the thermocell system:

(1) Charge transfer kinetic and mass transport by evaluating different redox active ionic liquid structures. These parameters can be obtained by *Electrochemical Impedance Spectroscopy (EIS)* from utilization of several ionic liquids. These molecules are liquid at room temperature with great solubility in a large spectrum of common organic solvents. Interestingly, due to the electron withdrawing effect caused by imidazolium or quaternary ammonium center, the standard potential of the ferrocenated ionic liquids can be modulated. However, there is no systematic study up-to-date on the influence of the nature and the quantity of charge hold by electroactive ionic liquids at the interface electrode/solution. The influence of the electrode materials (CNTs, Graphene, etc.) will also be investigated. This investigation will allow not only a better understanding on the charge transport profiles and the diffusion but also important step forward to optimize the system.

(2) Energy storage efficiency by thermo-cell system. By using various electrode materials different redox active ionic liquids will be tested via the following redox couple Eq. 6.5 and figure 6.5:

(3) $FcIL \rightleftharpoons Fc^{+}IL + e^{-}$ (6.5)

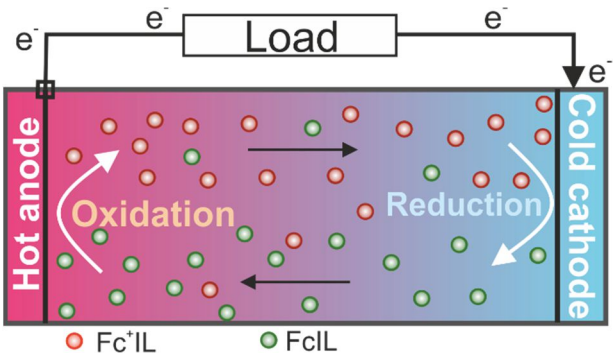

Figure 6.5 Working principle of a thermocell using FcIL mediator

Furthermore, the conventional ionic liquids have been demonstrated to have higher accessible thermal window than other organic solvent. Consequently, owing ionic properties, it is noted that the redox ionic liquids can be used as prepared, without diluting with other electrolytic solvent.

(4) Cell design and elaboration procedure for fabrication of the devices

Triboelectrochemical cell

As mentioned in the previous chapter, the triboelectric effect is induced by friction. It is noted that by definition, friction occurs whenever 2 bodies slides against each other (horizontal or vertical mode). By consequent, apart from the generated triboelectrification, the friction can also produce local heat at the contact interface. Assumed that all of the energy is dissipated as triboelectric effect and heat on the sliding contact surfaces, the energy transformation can be given by:

$E = F_{Friction}.d = E_{tribo} + Q$ where $F_{Friction}$ is the friction force, d is the distance of sliding, E is the energy transformed to the triboelectrification and Q is the heat generated at the interface.

Consequently, the heat generated at the contact surfaces is depending on the coefficient of friction, the contact pressure and the relative sliding velocity. By combining with the working principle of the thermocell, a new type of electrochemical system can be proposed. Accordingly, by sliding a plaque of dielectric on a metallic substrate, the frictional heating could induce a local difference of temperature, which can induce an oxidation/reduction of the mediator in solution. Typical working principle of the cell can be illustrated in the figure 6.6.

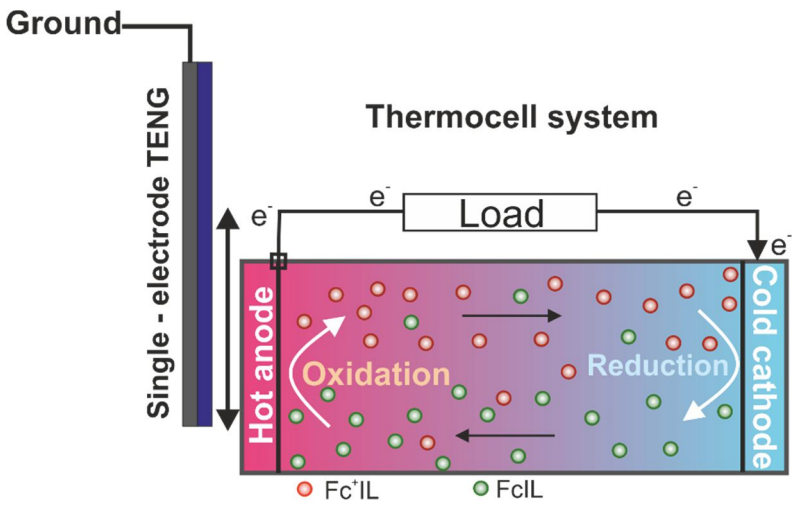

Figure 6.6 Working principle of a TENG coupled thermocell using FcIL mediator

6.3 REFERENCES

(1) Kim, S.; Wee, J.; Peters, K.; Huang, H. Y. S. Multiphysics Coupling in Lithium-Ion Batteries with Reconstructed Porous Microstructures. *J. Phys. Chem. C* **2018**, *122* (10), 5280–5290.

(2) Tavassol, H.; Jones, E. M. C.; Sottos, N. R.; Gewirth, A. A. Electrochemical Stiffness in Lithium-Ion Batteries. *Nat. Mater.* **2016**, *15* (11), 1182–1188.

(3) Barker, J. In-Situ Measurement of the Thickness Changes Associated with Cycling of Prismatic Lithium Ion Batteries Based on LiMn2O4 and LiCoO2. *Electrochim. Acta* **1999**, *45* (1–2), 235–242.

(4) Lee, J. H.; Lee, H. M.; Ahn, S. Battery Dimensional Changes Occurring during Charge/Discharge Cycles - Thin Rectangular Lithium Ion and Polymer Cells. *J. Power Sources* **2003**, *119–121*, 833–837.

(5) Fu, R.; Xiao, M.; Choe, S. Y. Modeling, Validation and Analysis of Mechanical Stress Generation and Dimension Changes of a Pouch Type High Power Li-Ion Battery. *J. Power Sources* **2013**, *224*, 211–224.

(6) Nadimpalli, S. P. V.; Sethuraman, V. A.; Abraham, D. P.; Bower, A. F.; Guduru, P. R. Stress Evolution in Lithium-Ion Composite Electrodes during Electrochemical Cycling and Resulting Internal Pressures on the Cell Casing. *J. Electrochem. Soc.* **2015**, *162* (14), A2656–A2663.

(7) Bucci, G.; Swamy, T.; Bishop, S.; Sheldon, B. W.; Chiang, Y.-M.; Carter, W. C. The Effect of Stress on Battery-Electrode Capacity. *J. Electrochem. Soc.* **2017**, *164* (4), A645–A654.

(8) Gattrell, M.; Gupta, N.; Co, A. A Review of the Aqueous Electrochemical Reduction of CO2to Hydrocarbons at Copper. *J. Electroanal. Chem.* **2006**, *594* (1), 1–19.

(9) Garza, A.; Bell, A. T.; Head-Gordon, M. On the Mechanism of CO2 Reduction at Copper Surfaces: Pathways to C2 Products. *ACS Catal.* **2018**, acscatal.7b03477.

(10) Li, C. W.; Kanan, M. W. CO 2 Reduction at Low Overpotential on Cu Electrodes Resulting from the Reduction of Thick Cu 2O Films. *J. Am. Chem. Soc.* **2012**, *134* (17), 7231–7234.

(11) Loiudice, A.; Lobaccaro, P.; Kamali, E. A.; Thao, T.; Huang, B. H.; Ager, J. W.; Buonsanti, R. Tailoring Copper Nanocrystals towards C2 Products in Electrochemical CO2 Reduction. *Angew. Chemie - Int. Ed.* **2016**, *55* (19), 5789–5792.

(12) Nie, X.; Esopi, M. R.; Janik, M. J.; Asthagiri, A. Selectivity of CO $_2$ Reduction on Copper Electrodes: The Role of the Kinetics of Elementary Steps. *Angew. Chemie* **2013**, *125* (9), 2519–2522.

(13) Kim, C.; Jeon, H. S.; Eom, T.; Jee, M. S.; Kim, H.; Friend, C. M.; Min, B. K.; Hwang, Y. J.

Achieving Selective and Efficient Electrocatalytic Activity for CO_2 Reduction Using Immobilized Silver Nanoparticles. *J. Am. Chem. Soc.* **2015**, *137* (43), 13844–13850.

(14) Liu, S.; Tao, H.; Zeng, L.; Liu, Q.; Xu, Z.; Liu, Q.; Luo, J. L. Shape-Dependent Electrocatalytic Reduction of CO2to CO on Triangular Silver Nanoplates. *J. Am. Chem. Soc.* **2017**, *139* (6), 2160–2163.

(15) Rosen, B. A.; Salehi-khojin, A.; Thorson, M. R.; Zhu, W.; Whipple, D. T.; Kenis, P. J. A.; Masel, R. I. Ionic Liquid – Mediated Selective Conversion of CO2 to CO at Low Overpotentials. *Science (80-.).* **2011**, *334* (November), 643–644.

(16) Zheng, Y.; Jiao, Y.; Ge, L.; Jaroniec, M.; Qiao, S. Z. Two-Step Boron and Nitrogen Doping in Graphene for Enhanced Synergistic Catalysis. *Angew. Chemie - Int. Ed.* **2013**, *52* (11), 3110–3116.

(17) Shao, Y.; Zhang, S.; Engelhard, M. H.; Li, G.; Shao, G.; Wang, Y.; Liu, J.; Aksay, I. A.; Lin, Y. Nitrogen-Doped Graphene and Its Electrochemical Applications. *J. Mater. Chem.* **2010**, *20* (35), 7491–7496.

(18) Yang, S.; Zhi, L.; Tang, K.; Feng, X.; Maier, J.; M??llen, K. Efficient Synthesis of Heteroatom (N or S)-Doped Graphene Based on Ultrathin Graphene Oxide-Porous Silica Sheets for Oxygen Reduction Reactions. *Adv. Funct. Mater.* **2012**, *22* (17), 3634–3640.

(19) Hu, R.; Cola, B. A.; Haram, N.; Barisci, J. N.; Lee, S.; Stoughton, S.; Wallace, G.; Too, C.; Thomas, M.; Gestos, A.; Dela Cruz, M. E.; Ferraris, J. P.; Zakhidov, A. A.; Baughman, R. H. Harvesting Waste Thermal Energy Using a Carbon-Nanotube-Based Thermo-Electrochemical Cell. *Nano Lett.* **2010**, *10* (3), 838–846.

(20) Zhang, L.; Kim, T.; Li, N.; Kang, T. J.; Chen, J.; Pringle, J. M.; Zhang, M.; Kazim, A. H.; Fang, S.; Haines, C.; Al-Masri, D.; Cola, B. A.; Razal, J. M.; Di, J.; Beirne, S.; MacFarlane, D. R.; Gonzalez-Martin, A.; Mathew, S.; Kim, Y. H.; Wallace, G.; Baughman, R. H. High Power Density Electrochemical Thermocells for Inexpensively Harvesting Low-Grade Thermal Energy. *Adv. Mater.* **2017**, *29* (12), 1–7.